EPIGENETIC REGULATION AND TUMOR IMMUNOTHERAPY

EDITED BY: Mingzhu Yin, Qin Yan, Jian Cao and Bihui Huang
PUBLISHED IN: Frontiers in Immunology and Frontiers in Oncology

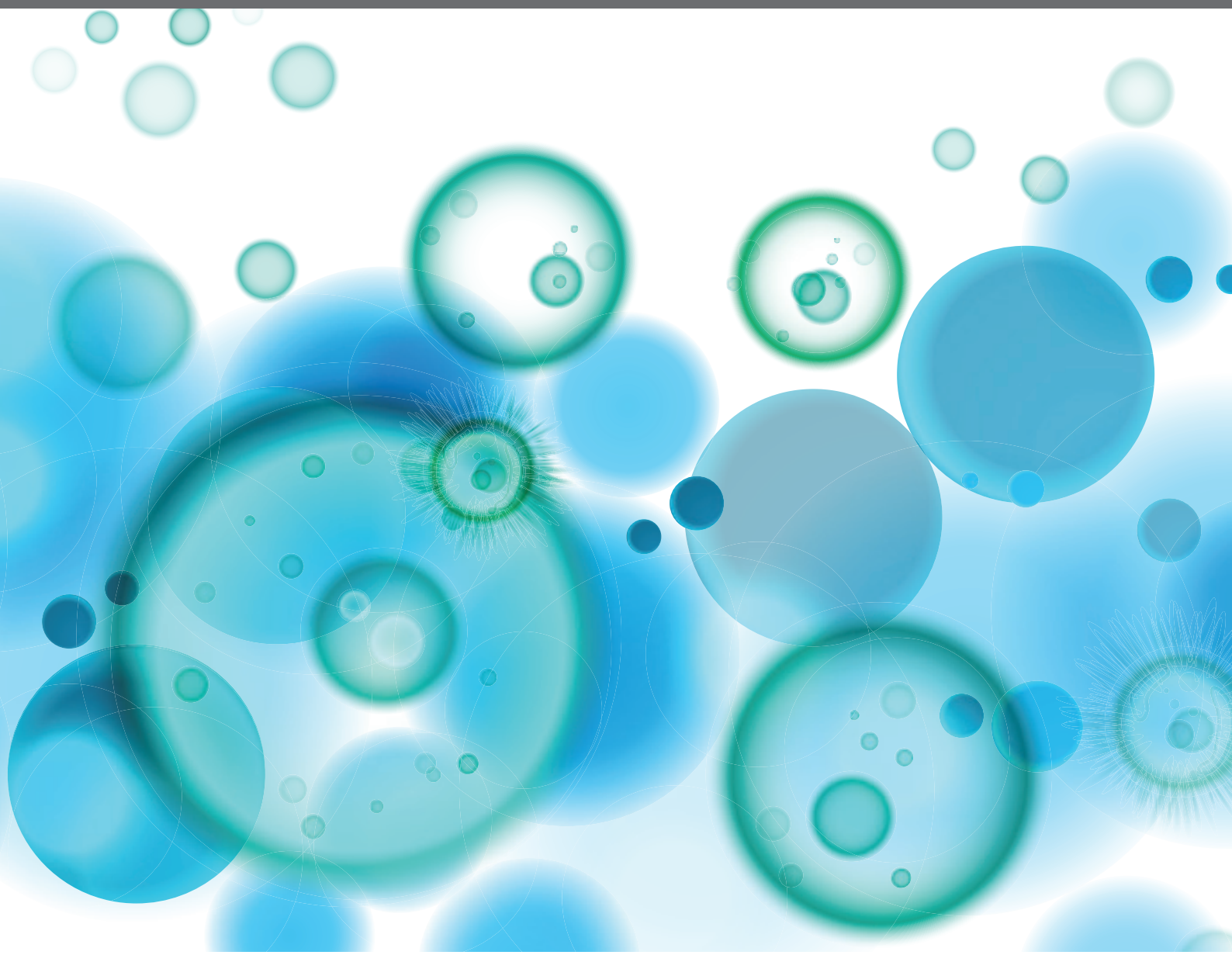

frontiers Research Topics

ISSN 1664-8714
ISBN 978-2-88976-246-0
DOI 10.3389/978-2-88976-246-0

About Frontiers

Frontiers is more than just an open-access publisher of scholarly articles: it is a pioneering approach to the world of academia, radically improving the way scholarly research is managed. The grand vision of Frontiers is a world where all people have an equal opportunity to seek, share and generate knowledge. Frontiers provides immediate and permanent online open access to all its publications, but this alone is not enough to realize our grand goals.

Frontiers Journal Series

The Frontiers Journal Series is a multi-tier and interdisciplinary set of open-access, online journals, promising a paradigm shift from the current review, selection and dissemination processes in academic publishing. All Frontiers journals are driven by researchers for researchers; therefore, they constitute a service to the scholarly community. At the same time, the Frontiers Journal Series operates on a revolutionary invention, the tiered publishing system, initially addressing specific communities of scholars, and gradually climbing up to broader public understanding, thus serving the interests of the lay society, too.

Dedication to Quality

Each Frontiers article is a landmark of the highest quality, thanks to genuinely collaborative interactions between authors and review editors, who include some of the world's best academicians. Research must be certified by peers before entering a stream of knowledge that may eventually reach the public - and shape society; therefore, Frontiers only applies the most rigorous and unbiased reviews.
Frontiers revolutionizes research publishing by freely delivering the most outstanding research, evaluated with no bias from both the academic and social point of view. By applying the most advanced information technologies, Frontiers is catapulting scholarly publishing into a new generation.

What are Frontiers Research Topics?

Frontiers Research Topics are very popular trademarks of the Frontiers Journals Series: they are collections of at least ten articles, all centered on a particular subject. With their unique mix of varied contributions from Original Research to Review Articles, Frontiers Research Topics unify the most influential researchers, the latest key findings and historical advances in a hot research area! Find out more on how to host your own Frontiers Research Topic or contribute to one as an author by contacting the Frontiers Editorial Office: frontiersin.org/about/contact

EPIGENETIC REGULATION AND TUMOR IMMUNOTHERAPY

Topic Editors:
Mingzhu Yin, Central South University, China
Qin Yan, Yale University, United States
Jian Cao, The State University of New Jersey, United States
Bihui Huang, Sun Yat-sen University, China

Citation: Yin, M., Yan, Q., Cao, J., Huang, B., eds. (2022). Epigenetic Regulation and Tumor Immunotherapy. Lausanne: Frontiers Media SA.
doi: 10.3389/978-2-88976-246-0

Table of Contents

frontiers | Frontiers in Oncology

EDITORIAL
published: 05 May 2022
doi: 10.3389/fonc.2022.893157

Editorial: Epigenetic Regulation and Tumor Immunotherapy

*Hongyin Sun[1], Bihui Huang[2], Jian Cao[3], Qin Yan[4] and Mingzhu Yin[1]**

[1] Department of Dermatology, Hunan Engineering Research Center of Skin Health and Disease, Hunan Key Laboratory of Skin Cancer and Psoriasis, Xiangya Hospital, Central South University, Changsha, China, [2] Scientific Research Center, The Seventh Affiliated Hospital, Sun Yat-sen University, Shenzhen, China, [3] Department of Medicine, Robert Wood Johnson Medical School, Cancer Institute of New Jersey Rutgers, the State University of New Jersey, New Brunswick, NJ, United States, [4] Department of Pathology, Yale School of Medicine, New Haven, CT, United States

Keywords: epigenetic regulation, tumor immunotherapy, tumor immune microenvironment, methlation, acetylation

Editorial on the Research Topic

Epigenetic Regulation and Tumor Immunotherapy

Epigenetics is the study of DNA sequence-independent heritable changes in phenotype and gene expression. Major epigenetic mechanisms include DNA methylation, histone modification, chromatin structure regulation, and non-coding RNA regulation. Emerging evidence suggests that epigenetic regulation plays central roles in tumor immunosurveillance, including tumor antigen production, the interaction between tumor cells and immune cells, and T cell development, priming, activation, and exhaustion. On the other hand, tumors commonly hijack various epigenetic mechanisms to escape immune restriction (1, 2). Therefore, modulating epigenetic regulators can normalize the impaired immunosurveillance and/or trigger antitumor immune responses. Numerous preclinical and clinical studies revealed that epigenetic agents, including DNMT inhibitors (3), HDAC inhibitors (4), EZH2 inhibitors (5), LSD1 inhibitors (6), KDM5 inhibitors (7), G9a inhibitors (8), and BET inhibitors (9–11), have the capacity to induce anti-tumor immune responses and modulate tumor immune microenvironment. Currently, hundreds of clinical trials that combine epigenetic agents and immune checkpoint inhibitors (ICI) are ongoing, aiming to achieve synergistic effects, reduce adverse effects, and overcome intrinsic and acquired resistance. Thus, combining epigenetic therapy with immunotherapy is a promising new strategy to improve clinical outcomes.

This Research Topic leads to a better understanding of epigenetics in tumor immunity and immunotherapy and highlights the clinical significance of epigenetic drugs. This Research Topic accepted a total of 18 articles from 123 authors, demonstrating great interest in this field. Our topic can be mainly divided into the following topics:

METHYLATION

Abnormal methylation patterns of tumor cells are mainly manifested in the overall hypomethylation of the genome and hypermethylation of CpG islands. The hypermethylation in the promoter regions of tumor suppressor genes and DNA repair leads to the extinction of these genes and the development of cancer. Nevertheless, the hypomethylation in the regulatory regions of oncogenes increases their expression and leads to tumorigenesis (12). In this Research Topic, Zheng et al. explored whether epigenetic regulation associated with DNA methylation could

OPEN ACCESS

Edited and reviewed by:
Katy Rezvani,
University of Texas MD Anderson Cancer Center, United States

****Correspondence:***
Mingzhu Yin
yinmingzhu@csu.edu.cn

Specialty section:
This article was submitted to Cancer Immunity and Immunotherapy, a section of the journal Frontiers in Oncology

Received: *10 March 2022*
Accepted: *28 March 2022*
Published: *05 May 2022*

Citation:
Sun H, Huang B, Cao J, Yan Q and Yin M (2022) Editorial: Epigenetic Regulation and Tumor Immunotherapy. Front. Oncol. 12:893157. doi: 10.3389/fonc.2022.893157

underlie increasing PD-L1 expression by disulfiram (DSF). They found that DSF inhibited DNMT1 expression and activity, thus leading to IRF7 hypomethylation and PD-L1 upregulation in Triple Negative Breast Cancer (TNBC) cell lines. They further observed that co-treatment of DSF and anti-PD-1 Ab increased CD8+ tumor-infiltrating lymphocytes (TIL) and enhanced the therapeutic effects of ICB *in vivo*, which provide a novel combination therapy strategy for TNBC. Based on patients' overall survival (OS), Yang et al. Established a prognostic risk score system using 18 immune-related methylation genes (IRMGs) of 1057 breast cancer patients from the TCGA cohort and GSE72308 cohort. Patients in the low-risk group had a higher immune score and stromal score compared with the high-risk group. The characteristics based on 18-IRMGs signature were related to the tumor immune microenvironment and affected the abundance of tumor-infiltrating immune cells. As the result, the proposed 18-IRMGs signature could be a potential marker for breast cancer prognostication. Enhancer of zeste homolog 2 (EZH2) is a negative regulator of early NK cell differentiation and function through trimethylation of histone H3 lysine 27 (H3K27me3). Yu et al. deleted *Ezh2* from immature NK cells and downstream progeny to explore its role in NK cell maturation by single-cell RNA sequencing. They indicated a novel role for the EZH2-AP-1-KLRG1 axis in altering the NK cell maturation trajectory and NK cell-mediated cytotoxicity, which suggested that EZH2 plays a critical role in NK development by activating AP-1 family gene expression independent of its methyltransferase activity.

Different from DNA methylation, RNA methylation modifications, including N6-methyladenosine (m6A), 5-methylcytosine (m5C), and N1-methyladenosine (m1A), mainly regulate genetic expression at the post-transcriptional level (13, 14). Liu et al. comprehensively assessed N1-methyladenosine (m1A) methylation modification patterns in 474 ovarian cancer (OC) patients and linked them to immune infiltration characteristics in the tumor microenvironment (TME). They demonstrated that individual tumor m1A modification patterns can predict patient survival, stage and grade. A high m1Ascore is usually accompanied by a better survival advantage and a lower mutational load. Patients with high m1Ascore showed marked therapeutic benefits and clinical outcomes in terms of chemotherapy and immunotherapy, which provide clinicians with new ideas for immuno-oncology and individualized immunotherapy in OC. Recently, m6A RNA methylation is an emerging epigenetic modification, which has been associated with the progression of several cancers (15, 16). ALKBH5 and YTHDF1 are regarded as the eraser and reader in N6-methyladenosine (m6A) modification, respectively. The former has been shown to regulate suppressive immune cell accumulation in melanoma (17, 18), and the latter can improve the efficiency of mRNA translation (19). Using consensus clustering based on the expression of ALKBH5 and YTHDF1, Yan et al. divided the patients with colon adenocarcinoma (COAD) into two clusters. Cluster 2 (high expression of ALKBH5 and lesser so of YTHDF1) had stronger immune infiltration, higher expression of targets of ICIs, more TMB, and a larger proportion of deficiency in mismatch repair-microsatellite instability-high (dMMR-MSI-H) status than Cluster 1 (high expression of YTHDF1 and lesser so of ALKBH5). ALKBH5 and YTHDF1 influence immune contexture and can potentially transform cold tumors into hot tumors in patients with COAD. In addition, m6A modification accelerates Snail1 expression in HeLa cells (20), indicating the indirect regulation of Snail1 by methylation. Snail1, a key inducer of epithelial-mesenchymal transition (EMT), plays a critical role in tumor metastasis. Tang et al. reviewed the pathways and molecules involved in the maintenance of Snail1 level and the significance of Snail1 in tumor immune evasion and demonstrated that Snail1 can function as a biomarker to predict tumor relapse and patient prognosis. Furthermore, Snail1 is implicated in chemotherapy and radiotherapy resistance, thereby the author proposes that chemotherapy or radiotherapy combined with Snail1 inhibitors may be a promising therapeutic approach to combat tumors.

ACETYLATION

Acetylation is the addition of acetyl groups to lysine residues in a protein that occurs in the presence of acetyltransferase, which is a dynamic and reversible process involving both histone acetyltransferases (HATs) and histone deacetylases (HDACs). HATs are figuratively called "writers", which are responsible for covalently attaching an acetyl group to the lysine residue of a protein, while HDACs are called "erasers" and mediate the removal of this acetyl group (21). Evidence has shown that acetylation is one of the most important modifications used to alter protein activity and precisely regulate and control cellular functions. In recent studies, many researchers have found that HDAC inhibitors also have significant effects on host immunosuppressive cells, and MDSCs are important immunosuppressive cells in the tumor microenvironment (22). Thereby some researchers regard MDSCs as targets of tumor therapy. Cui et al. summarized the effects and the underlying mechanisms of different HDAC inhibitors on the immunosuppressive function and expansion of MDSCs based on the findings of relevant studies, which may improve their therapeutic effects on tumors.

LONG NON-CODING RNA REGULATION

Long non-coding RNA (lncRNA) has been reported to play diverse roles in various biological processes (23), which can modulate transcriptional and post-transcriptional genes and regulate the expression of tumor suppressors or initiators, and thereby confers the occurrence and progression of cancer (24). In this topic, Xu et al. constructed a novel hypoxia-related long non-coding RNAs (HRL) signature that could distinguish lower-grade glioma (LGG) patients with similar expression levels of immune checkpoints and might predict the efficacy of immune checkpoint inhibitors. Additionally, hypoxia-related pathways and immune pathways were enriched in the high-risk group, and a high risk score indicated low tumor purity

and high immune infiltration. LINC00941 and BASP1-AS1 could significantly affect the proliferation of glioma cells. These results reveal that HRLs could be novel biomarkers to predict the prognosis of LGG patients and potential targets for LGG treatment. Simultaneously, Yu et al. built a prognostic model signature based on six key immune-related lncRNAs (irlncRNAs) (H19, ST3GAL6-AS1, AL162231.2, SOX21-AS1, AC006213.5, and AC002456.1) in glioblastoma multiforme (GBM) patients. PLAU was predicted as a target of lncRNA-H19 and mainly enriched in the malignant related pathways. Moreover, three hub genes KRT8, NGFR, and TCEA3 among GBM subtypes (GSs) were screened and validated to potentially play oncogenic roles in GBM. These results suggested that the irlncRNAs had promising potential for immunotherapy of GBM.

In addition to the above three topics, Ma et al. found that SAMD9 (Sterile Alpha Motif Domain-Containing Protein 9) was highly expressed in glioma and closely related to histological and genetic features in CGGA and TCGA databases. They present evidence to show that there was a positive association between SAMD9 and malignancy characters in LGG. Immune infiltration analysis demonstrated that high SAMD9 expression resulted in an accumulation of macrophages by CIBERSORT and TIMER databases, the same trends were also verified using clinical specimens with IHC staining. In addition, silencing of SAMD9 by shRNA in LN229 cells attenuated the infiltration abilities of M2 macrophage. Taken together, the authors revealed that SAMD9 may be a diagnostic or prognostic indicator for LGG and also a new potential therapeutic target for treating gliomas. Moreover, Xu et al. identified IFN-γ response clusters, which might be used to improve the prognostic accuracy of immune contexture in the clear cell renal cell carcinoma (ccRCC) microenvironment. Immune-cold RANBP2-type and C3HC4-type zinc finger containing 1 $(RBCK1)^{high}$ patients have pro-tumorigenic immune infiltration and significantly worse outcomes than $RBCK1^{low}$ patients based on results from multi-omics to real-world data, which highlights the association between tumor alterations and immune phenotype. Furthermore, Zhou and Jin presented the expression and biological function of B7 homolog 3 protein (B7-H3) in distinct cancer and normal cells, as well as B7-H3-mediated signal pathways in cancer cells and B7-H3-based tumor immunotherapy strategies, which provides a comprehensive overview that encompasses B7-H3's role in TME to its potential as a target in cancer immunotherapy.

CONCLUSION

In aggregate, this Research Topic summarized recent development on the central roles of epigenetic regulation in tumor immunosurveillance and the mechanisms of epigenetic regulation. This topic provides new prognostic biomarkers, as well as promising therapeutic approaches and novel combination therapy strategies for several tumors.

AUTHOR CONTRIBUTIONS

All authors listed have made a substantial, direct, and intellectual contribution to the work and approved it for publication.

REFERENCES

1. Topper MJ, Vaz M, Marrone KA, Brahmer JR, Baylin SB. The Emerging Role of Epigenetic Therapeutics in Immuno–Oncology. *Nat Rev Clin Oncol* (2020) 17(2):75–90. doi: 10.1038/s41571–019–0266–5
2. Chen X, Pan X, Zhang W, Guo H, Cheng S, He Q, et al. Epigenetic Strategies Synergize With PD–L1/PD–1 Targeted Cancer Immunotherapies to Enhance Antitumor Responses. *Acta Pharm Sin B* (2020) 10(5):723–33. doi: 10.1016/j.apsb.2019.09.006
3. Luo N, Nixon MJ, Gonzalez–Ericsson PI, Sanchez V, Opalenik SR, Li H, et al. DNA Methyltransferase Inhibition Upregulates MHC–I to Potentiate Cytotoxic T Lymphocyte Responses in Breast Cancer. *Nat Commun* (2018) 9(1):248. doi: 10.1038/s41467–017–02630–w
4. Woods DM, Sodré AL, Villagra A, Sarnaik A, Sotomayor EM, Weber J. HDAC Inhibition Upregulates PD–1 Ligands in Melanoma and Augments Immunotherapy With PD–1 Blockade. *Cancer Immunol Res* (2015) 3 (12):1375–85. doi: 10.1158/2326–6066.CIR–15–0077–T
5. Goswami S, Apostolou I, Zhang J, Skepner J, Anandhan S, Zhang X, et al. Modulation of EZH2 Expression in T Cells Improves Efficacy of Anti–CTLA–4 Therapy. *J Clin Invest* (2018) 128(9):3813–8. doi: 10.1172/JCI99760
6. Sheng W, LaFleur MW, Nguyen TH, Chen S, Chakravarthy A, Conway JR, et al. LSD1 Ablation Stimulates Anti–Tumor Immunity and Enables Checkpoint Blockade. *Cell* (2018) 174(3):549–63. doi: 10.1016/j.cell.2018.05.052
7. Wu L, Cao J, Cai WL, Lang SM, Horton JR, Jansen DJ, et al. KDM5 Histone Demethylases Repress Immune Response *via* Suppression of STING. *PloS Biol* (2018) 16(8):e2006134. doi: 10.1371/journal.pbio.2006134
8. Huang T, Zhang P, Li W, Zhao T, Zhang Z, Chen S, et al. G9A Promotes Tumor Cell Growth and Invasion by Silencing CASP1 in non–Smallcell Lung Cancer Cells. *Cell Death Dis* (2017) 8(4):e2726. doi: 10.1038/cddis.2017.65
9. Yin M, Guo Y, Hu R, Cai WL, Li Y, Pei S, et al. Potent BRD4 Inhibitor Suppresses Cancer Cell–Macrophage Interaction. *Nat Commun* (2020) 11 (1):1833. doi: 10.1038/s41467–020–15290–0
10. Deng G, Zeng F, Su J, Zhao S, Hu R, Zhu W, et al. BET Inhibitor Suppresses Melanoma Progression *via* the Noncanonical NF–κb/SPP1 Pathway. *Theranostics* (2020) 10(25):11428–43. doi: 10.7150/thno.47432
11. Deng G, Zeng F, He Y, Meng Y, Sun H, Su J, et al. Eef2k Silencing Inhibits Tumor Progression Through Repressing SPP1 and Synergizes With BET Inhibitors in Melanoma. *Clin Transl Med* (2022) 12(2):e722. doi: 10.1002/ctm2.722
12. Yoo CB, Jones PA. Epigenetic Therapy of Cancer: Past, Present and Future. *Nat Rev Drug Discovery* (2006) 5(1):37–50. doi: 10.1038/nrd1930
13. Zhao BS, Roundtree IA, He C. Post–Transcriptional Gene Regulation by mRNA Modifications. *Nat Rev Mol Cell Biol* (2017) 18(1):31–42. doi: 10.1038/nrm.2016.132
14. Boccaletto P, Machnicka MA, Purta E, Piatkowski P, Baginski B, Wirecki TK, et al. MODOMICS: A Database of RNA Modification Pathways. *Nucleic Acids Res* (2018) 46(D1):D303–7. doi: 10.1093/nar/gkx1030
15. Liu ZX, Li LM, Sun HL, Liu SM. Link Between M6a Modification and Cancers. *Front Bioeng Biotechnol* (2018) 6:89. doi: 10.3389/fbioe.2018.00089
16. Sun T, Wu R, Ming L. The Role of M6a RNA Methylation in Cancer. *BioMed Pharmacother* (2019) 112:108613. doi: 10.1016/j.biopha.2019.108613
17. Zheng G, Dahl JA, Niu Y, Fedorcsak P, Huang CM, Li CJ, et al. ALKBH5 is a Mammalian RNA Demethylase That Impacts RNA Metabolism and Mouse Fertility. *Mol Cell* (2013) 49(1):18–29. doi: 10.1016/j.molcel.2012.10.015
18. Li N, Kang Y, Wang L, Huff S, Tang R, Hui H, et al. ALKBH5 Regulates antiPD–1 Therapy Response by Modulating Lactate and Suppressive Immune Cell Accumulation in Tumor Microenvironment. *Proc Natl Acad Sci USA* (2020) 117(33):20159–70. doi: 10.1073/pnas.1918986117

19. Wang X, Lu Z, Gomez A, Hon GC, Yue Y, Han D, et al. N6–MethyladenosineDependent Regulation of Messenger RNA Stability. *Nature* (2014) 505(7481):117–20. doi: 10.1038/nature12730
20. Li J, Chen F, Peng Y, Lv Z, Lin X, Chen Z, et al. N6–Methyladenosine Regulates the Expression and Secretion of TGFbeta1 to Affect the EpithelialMesenchymal Transition of Cancer Cells. *Cells* (2020) 9(2):296. doi: 10.3390/cells9020296
21. Narita T, Weinert BT, Choudhary C. Functions and Mechanisms of Nonhistone Protein Acetylation. *Nat Rev Mol Cell Biol* (2019) 20(3):156–74. doi: 10.1038/s41580–018–0081–3
22. Li M, Zha X, Wang S. The Role of N6–Methyladenosine mRNA in the Tumor Microenvironment. *Biochim Biophys Acta Rev Cancer* (2021) 1875(2):188522. doi: 10.1016/j.bbcan.2021.188522
23. Peng WX, Koirala P, Mo YY. LncRNA–Mediated Regulation of Cell Signaling in Cancer. *Oncogene* (2017) 36(41):5661–7. doi: 10.1038/onc.2017.184
24. Yang G, Lu X, Yuan L. LncRNA: A Link Between RNA and Cancer. *Biochim Biophys Acta* (2014) 1839(11):1097–109. doi: 10.1016/j.bbagrm.2014.08.012

Conflict of Interest: The authors declare that the research was conducted in the absence of any commercial or financial relationships that could be construed as a potential conflict of interest.

Publisher's Note: All claims expressed in this article are solely those of the authors and do not necessarily represent those of their affiliated organizations, or those of the publisher, the editors and the reviewers. Any product that may be evaluated in this article, or claim that may be made by its manufacturer, is not guaranteed or endorsed by the publisher.

frontiers in Immunology

ORIGINAL RESEARCH
published: 16 April 2021
doi: 10.3389/fimmu.2021.659659

SAMD9 Is Relating With M2 Macrophage and Remarkable Malignancy Characters in Low-Grade Glioma

Wenping Ma[1,2,3,4,5], *Kenan Zhang*[1], *Zhaoshi Bao*[2,5]*, *Tao Jiang*[1,2,3,4,5]* and *Ying Zhang*[1,5]*

[1] Department of Molecular Neuropathology, Beijing Neurosurgical Institute, Capital Medical University, Beijing, China, [2] Department of Neurosurgery, Beijing Tiantan Hospital, Capital Medical University, Beijing, China, [3] Center of Brain Tumor, Beijing Institute for Brain Disorders, Beijing, China, [4] China National Clinical Research Center for Neurological Diseases, Beijing, China, [5] Chinese Glioma Genome Atlas Network (CGGA) and Asian Glioma Genome Atlas Network (AGGA), Beijing, China

OPEN ACCESS

Edited by:
Mingzhu Yin,
Central South University, China

Reviewed by:
Aleksandra Ellert-Miklaszewska,
Nencki Institute of Experimental Biology (PAS), Poland
Minghui Zhang,
Harbin Medical University Cancer Hospital, China

***Correspondence:**
Ying Zhang
zhangy_bni@163.com
Tao Jiang
taojiang1964@163.com
Zhaoshi Bao
baozhaoshi@bjtth.org

Specialty section:
This article was submitted to Cancer Immunity and Immunotherapy, a section of the journal Frontiers in Immunology

Received: 28 January 2021
Accepted: 19 March 2021
Published: 16 April 2021

Citation:
Ma W, Zhang K, Bao Z, Jiang T and Zhang Y (2021) SAMD9 Is Relating With M2 Macrophage and Remarkable Malignancy Characters in Low-Grade Glioma. Front. Immunol. 12:659659. doi: 10.3389/fimmu.2021.659659

Immunoreactions regulated by TAMs (Tumor-associated macrophages) play a pivotal role in tumorigenesis and metastasis. In recent decades, treatments based on immune regulation have achieved revolutionary breakthroughs in cancer targeted therapies. The phenotypes of TAMs in gliomas are more heterogeneous and inherently complex than can be simply defined by classification into the M1 and M2 polarized states. The detailed mechanisms surrounding infiltrating macrophage phenotype and glioma characteristics remain undefined. SAMD9 (Sterile Alpha Motif Domain-Containing Protein 9) was found to be highly expressed in glioma and closely related to histological and genetic features in CGGA and TCGA databases. Simultaneously, we present evidence to show that there was a positive association between SAMD9 and malignancy characters in LGG. Univariable and Multivariate proportional hazard Cox analysis showed that SAMD9 was an independent prognostic factor for LGG. Surprisingly, Gene Ontology (GO) analysis showed SAMD9 expression level was remarkably well correlated with immunological responses and the Kyoto Encyclopedia of Genes and Genomes (KEGG) analysis supported the connection with immune responses and tumorigenesis. Immune infiltration analysis demonstrated that high SAMD9 expression resulted in an accumulation of macrophages by CIBERSORT and TIMER databases, especially positively related to macrophage total marker gene AIF1 and Macrophage M2 marker gene CD163. IHC staining further indicated a high correlation of SAMD9 with those specific macrophage markers in the immune response. Human THP-1 cells were induced into M2 macrophages, which were then co-cultured with LN229 cells. Silencing of SAMD9 by shRNA in LN229 cells attenuated the infiltration abilities of M2 macrophage. SAMD9 explored immune response via relating of M2 macrophage *in vitro*. Our results revealed SAMD9 acted as the malignancy characters in LGG, enrichment with M2 macrophage.

Keywords: SAMD9, low grade glioma, immunity, macrophage, overall survival, tumor character

INTRODUCTION

Glioma is a kind of tumor originates from glial cells or precursor cells (1–3). It is the most common type of primary tumors in the central nervous system (4–6). Traditionally, the standard treatment for gliomas consisted of total tumor surgical resection, followed by radiotherapy and concurrent chemotherapy with TMZ (temozolomide) (7–9). However, using those comprehensive complex treatments, the overall survival achieved in glioma is not more than around 15 months, indicating the need for new innovative treatments which anchor the character and heterogeneity of glioma and expose the potential vital factors affecting tumorigenesis (6). Immunoreactions regulated by the TAM play a pivotal role throughout tumor angiogenesis and metastasis, also some immunotherapies have achieved revolutionary breakthroughs in cancer targeted therapies. Therapeutics targeting the programmed cell death (PD)-1 protein and its ligands, PD-L1, such as the FDA-approved Nivolumab, an anti-PD-1 monoclonal antibody for use in melanoma, Hodgkin's lymphoma and squamous cell lung cancer, have achieved great responses in clinical treatments (10–13). TAMs are abundant in many solid tumors characterized by diversity and plasticity, including classically M1 macrophage or M2 macrophage under different stimulation (14–16). M1 macrophages increase proinflammatory cytokine production along with the Th1 type immune response and regulate host-cell antigen presentation responses to high levels of pathogens (bacteria and viruses) and tumor cells. M2-type macrophages release anti-inflammatory factors that activate a Th2 type immune response and promote tumor growth by facilitating immune infiltration, tissue remodeling, and angiogenesis (17–20). The role of the immune response in central nervous tumors was once a controversial issue due to special structure blood-brain barrier, lacking typical lymphatic ducts and special macrophage cells (21). Although the use of immunotherapies has become a powerful strategy to effectively reduce tumor size and prolong survival in peripheral tumors (22, 23) immune response target drugs have had less dramatic benefit for glioma patients (24–28). Therefore, it was urgent and important to search for immune-related targets in gliomas.

Deleterious mutations of SAMD9 are key enabling factors for some autoimmune diseases and cancers, as well as the pathogenesis of myelodysplastic syndromes (MDS), esophageal and lung tumorigenesis (29). Our previous studies have shown that knocking down SAMD9 in glioma cells decreases glioblastoma progression (30). We reveal that elevated SAMD9 expression is closely correlated with increasing WHO grade. Furthermore, knockdown of SAMD9 attenuated the proliferation, migration and invasion of glioblastoma cells and reduced the activity of the PI3K/AKT signaling pathway (29). Till now, the detailed regulatory mechanism of SAMD9 and its impact on tumor immunity in gliomas has not been reported, whether SAMD9 could influence the immune response in gliomas is still unclear. In this paper we show that SAMD9 was elevated in low grade gliomasand acted as an indicator of poor prognosis with malignancy characteristics, IDH wild type, MGMT unmethylation and 1p/19q non-codeletion. Further analysis of glioma databases revealed that SAMD9 function was closely related to immune responses and SAMD9 enrichment was accompanied by a high M2 phenotype macrophage infiltration. The distinct correlation of SAMD9 expression levels and accumulation of macrophages implied a role for SAMD9 in governing the fate of infiltrating M2 macrophages in LGG. We verified the expression levels of SAMD9 and abundance of macrophages using clinical specimens and obtained the same trends as previously indicated by bioinformatics analysis. We further explored the molecular activity surrounding infiltrated macrophages and found SAMD9 could enhance the infiltration ability of M2 macrophage cells in vitro. In summary, our findings revealed that SAMD9 may serve as a key factor of gliomas immunity and act as an independent prognosis factor.

MATERIALS AND METHODS

Databases and Samples

The RNA-seq data, clinical and survival information were downloaded from CGGA database (http://www.cgga.org.cn). For the TCGA validation cohort (616 patients), the RNA-seq data and corresponding clinical information were obtained from TCGA database (http://cancergenome.nih.gov/). In total, 325 samples of RNA sequencing data from CGGA mRNA sequence database 1, 616 samples of TCGA mRNA sequence database (http://cancergenome.nih.gov/), and 693 samples of RNA sequencing data from CGGA database 2 (http://www.cgga.org) were collected in this study. We retrospectively analyzed the CGGA databases which mainly included the age, grade, IDH type, MGMT promoter methylation status, TCGA molecular subtypes (31), five molecular subtypes, radiotherapy and chemotherapy characters. Simultaneously, TCGA database was included for validation, which mostly contained the same clinical features described previously. Clinical specimens were collected from glioma patients admitted for operation in Beijing Tiantan Hospital.

Survival Prognostication

The beginning of OS was included from the initial diagnosis and the ending period was calculated to the last follow up or death. The survival data were downloaded for the CGGA and TCGA databases. All samples were divided into high and low expression groups according to the median value of SAMD9. The prognostic value of SAMD9 in these cohorts was evaluated by Kaplan-Meier with log-rank test.

The GO and KEGG Pathway Analysis

A gene annotation and analysis resource database that detailed integrated ontology sources, including GO analysis and KEGG Pathway was carried out to evaluate the SAMD9 associated biological processes and risk score in CGGA and TCGA databases.

Cibersort

CGGA and TCGA database were analyzed by the CIBERSORT software (https://cibersort.stanford.edu). Ten types of immune cells were evaluated in CIBERSORT to estimate the correlation of SAMD9 and infiltrating immune cells.

TIMER Module (Tumor IMmune Estimation Resource)

Immune infiltration associated with SAMD9 expression levels in LGG were selected and visualized by TIMER Module (https://cistrome.shinyapps.io/timer/) online system.

Cox Proportional Hazards Analysis

Univariate and multivariate Cox proportional hazards analysis were carried out to explore whether the risk score was an independent prognostic factor and screen out the most valuable independent prognostic factors.

Immune Functions Analysis

GSVA (Gene Set Enrichment Analysis) was performed with R software as previously (31). The relationship between SAMD9 expression and immune functions was evaluated by Pearson correlation analysis. Immune function scores were calculated by GSVA analysis and the immune function gene set was downloaded from AmiGO 2 (http://amigo.geneontology.org/amigo/landing). The classification of immune functions was according to the guidelines of AmiGO 2.

Nomogram Model Prediction

SAMD9, other partial factors such as pathological grade, age, 1p/19q status, radio status, and IDH were established using Cox regression in CGGA LGG and TCGA LGG database. Calibration curves were conducted at 1-, 3-, and 5-year time points. nomogram model was used to evaluate clinical risk score.

Cell Culture, Lentivirus Infection, and Macrophage Polarization

Human glioma LN229 and THP-1 cells were purchased from Chinese Academy of Sciences (China), LN229 cells were cultured in DMEM medium and THP-1 cells were cultured in RPMI 1640 medium with a humidified atmosphere of 5% CO_2 at 37°C, which containing 10% fetal bovine serum (FBS, Gibco), 100 IU/mL penicillin and 100 μg/mL streptomycin (Gibco, Thermo Scientific, NY, USA). Lentiviruses was constructed through short hairpin (sh)-RNA targeting human SAMD9 (Genepharma, Shanghai, China). LN229 cell (60%-70% density) were transfected with lentivirus vector at a multiplicity of infection of 10-15, LN229cells were infected by the viruses for 36-48 h, then they were cultured in medium containing puromycin for selecting stable SAMD9-knockdown cells. The knockdown efficiency was verified by Western blotting. the shRNA sequences were as follows (SAMD9-Homo-571, 5'-GGGTAAAGAGAACCCAGATAT-3'; SAMD9-Homo-1074, 5'-GCATTCGAGA GCCAAGATTTG-3'; non-targeting control, 5'-TTCTCCGAACG TGTCACGT-3'). To polarize M0 macrophages, THP-1 cells (2.5×10^5) were plated into 6-well plate and treated with 320 nM phorbol 12-myristate 13-acetate (PMA; Sigma, St. Louis, MO, USA) at 37°C for 6h. To polarize M2 macrophages, then added M2-polarizing reagents (20 ng/ml IL-4 plus 20 ng/ml IL-13), incubated at 37°C for 72 h (32–35).

M2 Macrophage Infiltration Assays

M2 macrophage infiltration assays were conducted by seeding 2.5×10^5 M2 macrophage cells (300μl) without serum for 12 h in the upper chamber of a Transwell plate (size 5μm, Corning, NY, USA). 2.5×10^5 LN229 glioma cells were cultured with10% FBS in bottom plate(700μl), each experiment. After incubation at 37°C for 24 h, the cells in the upper chamber were fixed in 4% formalin and stained with 0.1% crystal violet. The infiltrated M2 macrophage cells were counted in three randomly selected fields from each membrane and each experiment was performed three times (29, 36–38).

Semi-Quantitative Immunohistochemistry

Paraffin sections were made as previously described (39, 40). After deparaffinization, sections were immersed in 100% ethanol, 96% ethanol, and 75% ethanol, and subjected to heat-induced antigen retrieval at 120°C for 10 min, After cooling to room temperature, each slide was incubated with the primary antibody overnight at 4C, then incubated with the secondary antibody for 1 h. Color development was produced using DAB staining for 5 min and hematoxylin counterstained for 1 min. In our research, we stained the serial sections of the same glioma tissue and observed in the same visual field. Positive expression of SAMD9 was located in cytoplasm of tumor cells. SAMD9 and other protein expression levels were evaluated independently by two experienced pathologists using the following method. A: Cell staining intensity (at 10x20 magnification, 3 different fields of view were observed and the average counts of 3 fields taken), the count scoring was as follows: negative staining, 0 point; weakly positive staining, 1 point; positive staining but with light brown background, 2 points; positive staining without background, 3 points. B: Area staining intensity (at 10 x 4 magnification the total positive area was observed and evaluated): positive area = 0%, 0 point; positive area =1%-25%, 1 point; positive area = 26%-50%, 2 points; positive area = 51%-75%, 3 points; positive area>75%, 4 points. C: The degree of positive staining for each section was determined by multiplication of the values for A and B: 1-3 was classified as weakly positive (+); 4-6 as positive (++); and 7-12 as strongly positive (+++).

Other Analysis

Heatmap was plotted by R-CRAN-Package pheatmap through Raivo Kolde·GitHub (http://cran.r-project.org), Before data entry, the data of CGGA and TCGA was applied with log transformation by mean value of gene and normalized the rows of those data.

Statistical Analysis

Student's t-test or the chi-squared test were performed to clarify the differences in clinicopathological characteristics among these samples. $p < 0.05$ was considered statistically significant. correlation analysis of various factors and graphic work were

accomplished by R language (Version 4.0.2) and SPSS (SPSS Inc., Chicago, Ill., USA).

Ethics

We confirmed that the research involving experiments on human subjects met the ethical standards of the Helsinki Declaration in 1975. The research was approved by the ethics committee of Beijing Tiantan Hospital, Capital Medical University, and all patient and their relatives had provided written informed consent.

RESULTS

SAMD9 Expression is Significantly Correlated With Malignancy Degree and Subtype Feature in Lower Grade Gliomas

To further explore the role of SAMD9 in the malignant progression of glioma, we analyzed its expression levels in different grades in CGGA dataset 1, TCGA dataset, and CGGA dataset 2 of glioma. SAMD9 expression levels increased along with grade II to III progression very significantly in glioma (**Figure 1A**), it also showed an increasing grade III to IV tendency in the TCGA database (**Figure 1A**). We also detected the expression of SAMD9 in clinical glioma specimens and observed that SAMD9 was indeed increased with tumor grade and increased in high-grade gliomas (**Figure 1E**). IDH mutation is a principal driver gene in low grade gliomas, with an incidence of more than 70% (41). we therefore explored the relationship between SAMD9 expression and the status of *IDH*. In both the CGGA database 1 and TCGA database, patients with high SAMD9 expression were synchronized with wild type *IDH*, whereas most of those with low SAMD9 expression associated with the *IDH* mutation status (**Figure 1B**). The alkylating drug TMZ is routinely used for chemotherapy in glioma patients and *MGMT* promoter status was identified as a useful predictive biomarker for TMZ efficacy (42). We assessed the SAMD9 transcription level and the status of *MGMT* promoter methylation in both the CGGA sequence database 1 and TCGA sequence database. Patients with lower SAMD9 expression were found to have the *MGMT* promoter methylated, conversely, those with high SAMD9 expression associated with the unmethylated *MGMT* promoter (**Figure 1C**). The correlation between SAMD9 expression and glioma subtypes could also reflect SAMD9 function attributed to human glioma characteristics. We also systematically characterized the molecular features of classified lower grade gliomas through IDH and 1p/19q status. Patients with high expressions of SAMD9 were more concentrated in the astrocytoma than oligodendrocyte type. This information is highly consistent across the CGGA database 1 and TCGA databases (**Figure 1D**). These results indicated that lower expression of SAMD9 may be correlated with better prognosis of gliomas. we also achieved the same tendency characters of SAMD9 in CGGA database 2 (**Supplementary Figure 1**).

Landscape of the Correlations of SAMD9 Accompanied With Classical Genetic Alterations and Clinical Character of Glioma

Oncoprint plots were used to visualize the correlation between SAMD9 expression level and classical genetic alterations in CGGA and TCGA dataset by complex Heatmap package. In CGGA dataset 1, we noticed that with increasing expression of SAMD9, patients tended towards a higher grade, *IDH* wild type, intact 1p/19q, *PTEN* mutation, and *MGMT* promoter unmethylation. We obtained more reliable and robust results with the large sample TCGA database. Furthermore, *MGMT* promoter unmethylation and fewer *ATRX* mutations appeared frequently in SAMD9 high expressing patients. Even more remarkable was a gain of chromosome 7 and loss of chromosome 10 in those patients. The high expression of SAMD9 showed a consistent trend with the typical malignant genetic features disclosing malignancy characters in gliomas. The high expression of SAMD9 synchronized with malignancy characters indicate the oncogenic nature of SAMD9 which may play an important role in the biological process of tumorigenesis (**Figure 2** and **Tables 1**, **2**).

SAMD9 mRNA Expression Levels Predicted Overall Survival in All Grade Glioma and Especially in Lower Grade Glioma Patients

SAMD9 expression level was sufficient to predict OS (overall survival) of patients with glioma in three datasets. The patients of all glioma, LGG and glioblastoma (GBM) were divided into two groups on the basis of Grade type derived from CGGA database 1 (**Figures 3A–C**). Patients with higher SAMD9 expression exhibited shorter OS in Kaplan-Meier analyses in all glioma and LGG (**Figure 3A** $p < 0.0001$; **Figure 3B** $p < 0.0001$). To avoid the possible bias caused by a single database, we further expanded sample volumes in the TCGA database and confirmed the true character of SAMD9, we revealed the OS analyses with SAMD9 expression level derived from TCGA dataset (**Figures 3D–F**). The half of patients with higher SAMD9 expression exhibited shorter OS in either all grades (**Figure 3D** $p < 0.0001$) or LGG (**Figure 3E** $p = 0.0026$), but not in GBM (**Figure 3F** $p = 0.75$). We also got the same trend in CGGA mRNA sequence database 2 and the OS distinguishing effects of SAMD9 expression level were very significant in all glioma and LGG (**Supplementary Figure 2A** $p < 0.0001$; **Supplementary Figure 2B** $p = 0.0002$).

Univariate and Multivariate Analysis Showed SAMD9 Together With Other Related Clinicopathological Factors of Prognostic Significance

To further explore SAMD9 function in different grades and determine whether the risk score was an independent and

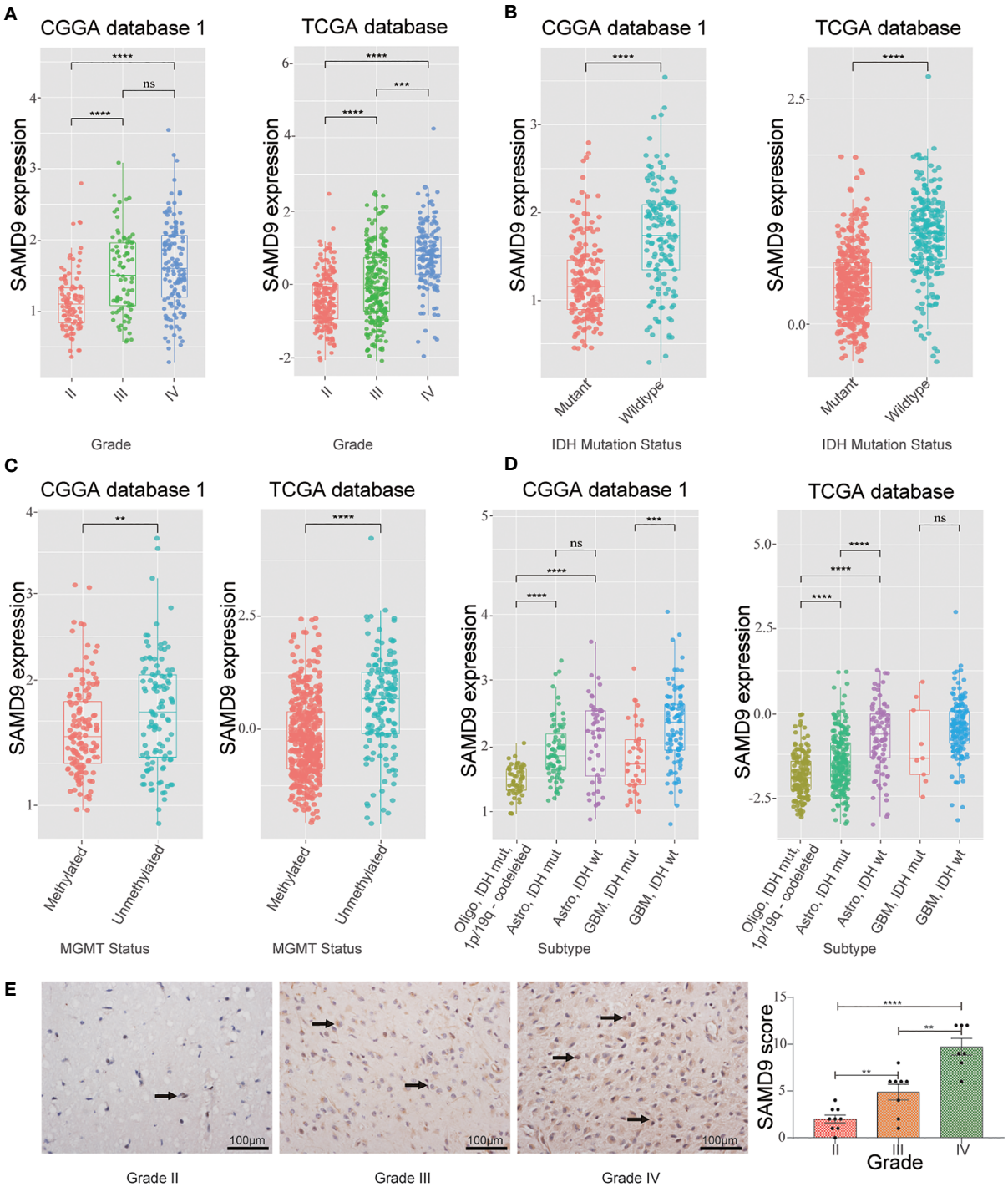

FIGURE 1 | WHO grade, IDH1 status, MGMT promoter methylation status and transcriptional characteristic subtype relative to SAMD9 expression. **(A)** The correlation of SAMD9 expression level with WHO grade. SAMD9 expression levels in glioma of WHO grade II-IV in CGGA database 1 and TCGA database, the difference between III & IV in TCGA database. **(B)** The relationship between *SAMD9* transcription level and *IDH1* mutation in CGGA and TCGA databases. **(C)** The correlation of *SAMD9* expression level and *MGMT* promoter methylation status, the difference in CGGA database 1 and in TCGA database. **(D)** The relationship between *SAMD9* transcription level and *IDH1* mutation in each transcriptional characteristic subtype in CGGA and TCGA databases. **(E)** SAMD9 expression in different grades of gliomas (Grade II, n=7; Grade III, n=8; Grade IV, n=9) detected by IHC analysis. Scale bar = 100 mm. **, ***, **** and ns indicate $p < 0.01$, $p < 0.001$, $p < 0.0001$ and no significance, respectively.

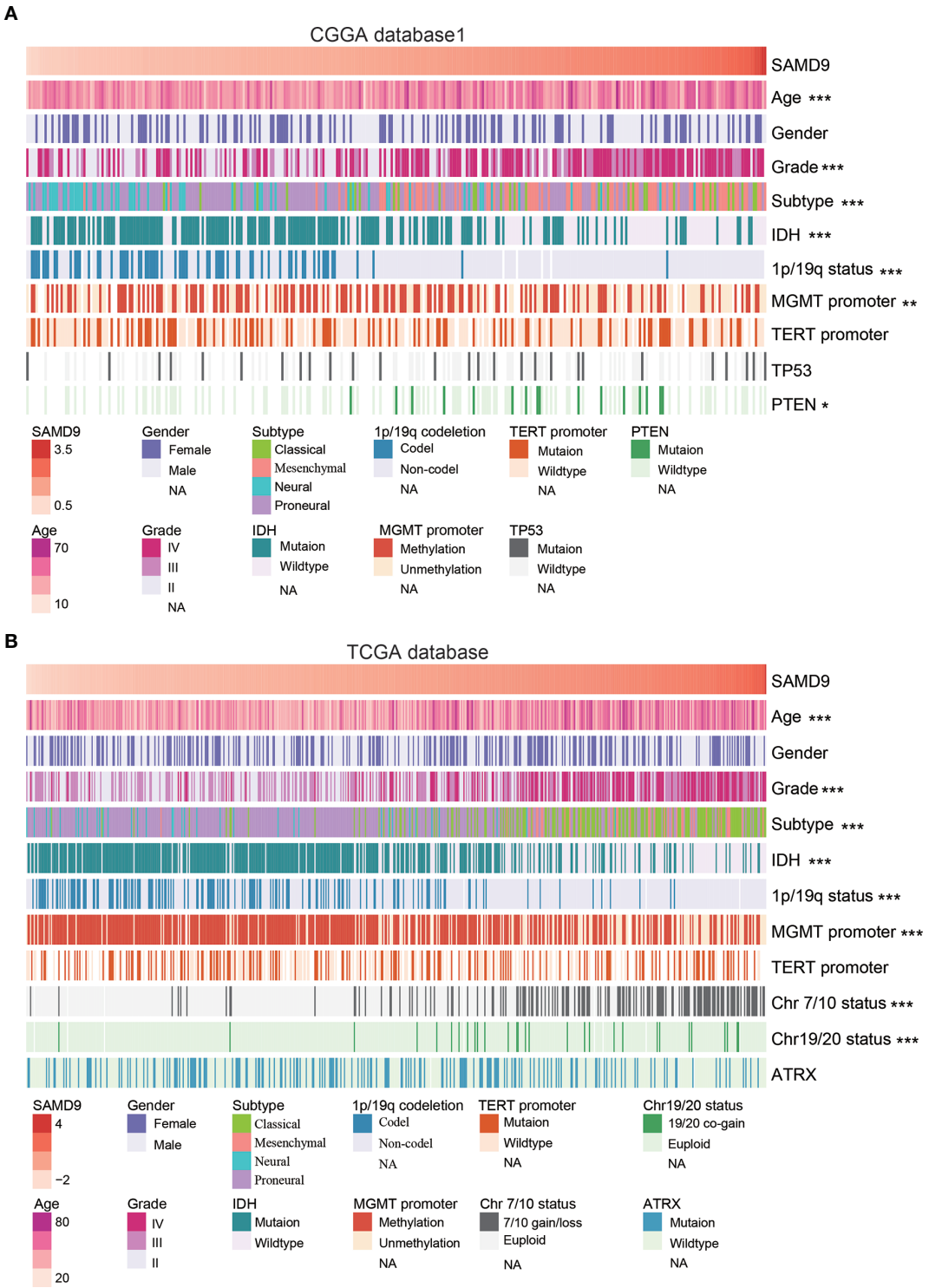

FIGURE 2 | SAMD9 transcription level accompanied with classical genetic alterations and clinical character of glioma. **(A)** With increasing expression of SAMD9 in CGGA database 1, patients characterized with age group, ***high grade, ***oligodendrocyte and GBM subtype, ****IDH* wild type, ***1p/19q intact, ***MGMT promoter unmethylation status, ***PTEN* mutation. **(B)** The correlation of *SAMD9* expression level in TCGA database with age group, ***high grade, ***oligodendrocyte and GBM subtype, ***IDH wild type, ***1p/19q intact ***MGMT promoter unmethylation status, ***Chromosome 7/10 Euploid, ***Chromosome 19/20 Euploid, *, **, and *** indicate $p < 0.05$, $p < 0.01$, $p < 0.001$, respectively.

TABLE 1 | Clinicopathological of SAMD9 expression in CGGA database 1.

Variable	Group	Total	SAMD9 Expression		*p*-value
		325	Low(-+)	High(++)	
			180	145	
Age					
	<=43	183	119	64	1.15E-04
	>43	142	61	81	
Gender					
	0	203	113	90	9.88E-01
	1	122	67	55	
Grade					
	II	103	86	17	6.25E-11
	III	79	37	42	
	IV	139	57	82	
Subtype					
	Classical	32	10	22	7.63E-15
	Mesenchymal	78	17	61	
	Neural	57	47	10	
	Proneural	158	106	52	
IDH1					
	0	149	48	101	3.42E-14
	1	175	131	44	
1p/19q status					
	0	250	112	138	6.15E-14
	1	67	65	2	
MGMT promoter					
	0	110	48	62	6.45E-03
	1	134	83	51	
TERT promoter					
	0	169	93	76	5.42E-01
	1	92	55	37	
TP53					
	0	89	40	49	9.42E-01
	1	27	13	14	
PTEN					
	0	100	52	48	2.76E-02
	1	16	3	13	

TABLE 2 | Clinicopathological of SAMD9 expression in TCGA database.

Variable	Group	Total	SAMD9 Expression		*p*-value
		601	Low(-+)	High(++)	
			317	284	
Age					
	<=43	266	185	81	3.59E-13
	>43	335	132	203	
Gender					
	0	351	193	158	2.22E-01
	1	250	124	126	
Grade					
	II	211	162	49	1.13E-28
	III	236	129	107	
	IV	154	26	128	
Subtype					
	Classical	149	20	129	3.23E-40
	Mesenchymal	35	1	34	
	Neural	36	31	5	
	Proneural	381	265	116	
IDH1					
	0	227	46	181	5.40E-35
	1	374	271	103	
1p/19q status					
	0	446	191	255	7.82E-18
	1	149	125	24	
MGMT promoter					
	0	147	45	102	3.88E-11
	1	420	263	157	
TERT promoter					
	0	162	96	66	4.26E-01
	1	155	84	71	
ATRX					
	0	422	215	207	1.37E-01
	1	174	101	73	
Chr19/20 status					
	0	564	311	253	6.10E-06
	1	29	3	26	
Chr7/10 status					
	0	448	294	154	4.61E-27
	1	145	20	125	

significant prognostic factor in glioma, we carried out univariate and multivariate Cox regression analyses in the above databases. In addition, univariate and multivariate Cox regression analyses showed SAMD9, together with classical malignancy features of glioma (gender, age, WHO grade, *IDH* status, 1p/19q status, *MGMT* promoter status, radiotherapy, and chemotherapy). The univariate and multivariate Cox regression analysis in CGGA database1 LGG identified SAMD9 expression (univariate hazard ratio (HR): 3.17, p = 8.71E-12; multivariate HR: 1.58, p = 3.61E-02), WHO grade (univariate HR: 3.75, p = 1.82E-09; multivariate HR: 3.29, p = 1.82E-09), 1p/19q codeletion (univariate HR: 0.15, p = 7.82E-09; multivariate HR: 0.22, p = 5.50E-05), radiotherapy (univariate HR: 0.54, p = 3.99E-02; multivariate HR: 0.44, p = 1.40E-02) (**Figure 4A**). We discovered SAMD9 together with WHO grade (red color) in LGG may serve as independent risk factors but irrelevant in GBM (**Figure 4B**), 1p/19q codeletion and radiotherapy were designated as protectable variances. We also analyzed *SAMD9* and the related clinical features in TCGA LGG database and got consistent trends. SAMD9 expression (univariate HR: 2.16, p = 1.42E-09; multivariate HR: 1.64, p=2.59E-04), WHO Grade (univariate HR: 3.32, p = 2.86E-06; multivariate HR: 1.94, p = 1.53E-02) and age (univariate HR: 1.07, p = 1.39E-12; multivariate HR:1.06, p = 1.15E-08), *IDH* mutation (univariate HR: 0.16, p = 1.22E-14; multivariate HR:0.29, p = 5.87E-04) (**Figure 4C**). We found *SAMD9* together with grade and age (red color) had clinical significance in LGG but evaluated no significance in GBM (**Figure 4D**), IDH mutation was a protective factor. Further similar trend results were obtained in CGGA database2 (**Supplementary Figures 3A, B**). In summary, SAMD9 may act as an independent prognostic factor in low-grade gliomas.

Nomogram Model Predicted the Overall Survival and Integrated Clinic Pathologic Risk Score

The clinical prognostic factors for overall survival were identified and incorporated to construct nomograms for 1-, 3- and 5-year overall survival, respectively (**Figures 5A, B**). These nomograms can easily be used by providers to estimate a

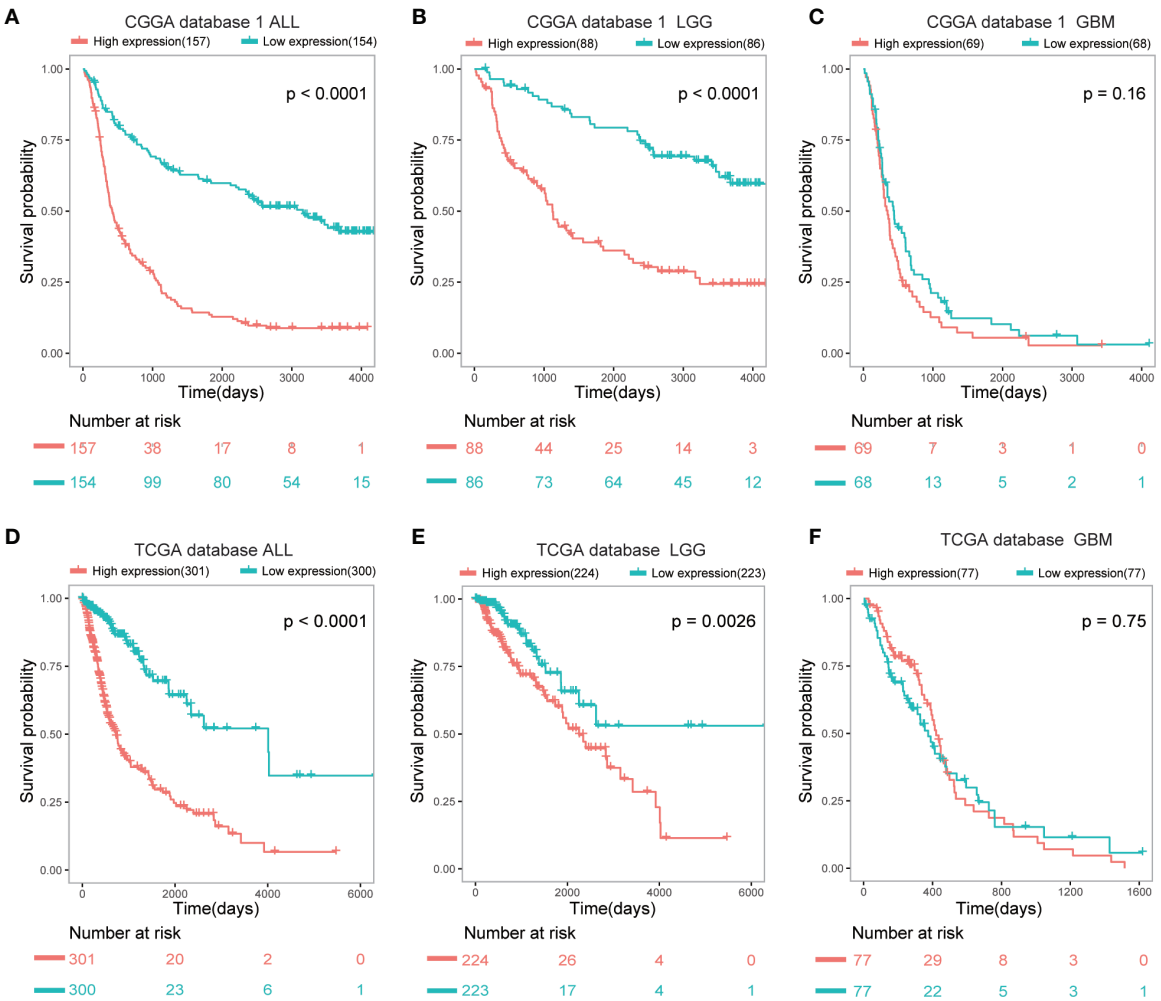

FIGURE 3 | Patients with higher SAMD9 level exhibit poorer OS. **(A)** Half of the patients with higher SAMD9 expression exhibited shorter OS in Kaplan-Meier analyses based on CGGA database 1 ALL, $p < 0.0001$. **(B)** The half of patients with higher SAMD9 expression exhibited shorter OS in Kaplan-Meier analyses based on CGGA database 1 LGG, $p < 0.0001$. **(C)** Half of patients with higher *SAMD9* expression exhibited shorter OS in Kaplan-Meier analyses based on CGGA database 1 GBM, $p = 0.16$. **(D)** Half of the patients with higher SAMD9 expression exhibited shorter OS in Kaplan-Meier analyses based on TCGA database ALL, $p < 0.0001$. **(E)** The half of patients with higher SAMD9 expression exhibited shorter OS in Kaplan-Meier analyses based on TCGA database LGG, $p = 0.0026$. **(F)** Half of patients with higher *SAMD9* expression exhibited shorter OS in Kaplan-Meier analyses based on TCGA database GBM, $p = 0.75$.

patient's prognosis; the only clinical details a provider needs to use these nomograms effectively are grade, 1p/19q codeletion status, radiotherapy status and SAMD9 expression levels. The calibration plot for the probability of survival at 1-, 3- and 5-years also showed optimal concordance with the prediction in the TCGA validation cohort. The C-indices respectively were 0.81 in CGGA database 1 LGG (**Figure 5A**) and 0.87 in TCGA database LGG (**Figure 5B**). We got an accurate and reliable 1-, 3- and 5-year predicting survival of glioma patients through these nomogram-based results. In addition, a calibration plot for probability of survival also showed satisfactory concordance with the prediction of 1-, 3-, and 5-year OS in CGGA database 2 (**Supplementary Figure 4**).

Functional Enrichment Analysis of Tightly Correlated Genes With SAMD9 in LGG

We analyzed related genes that tightly correlated with the SAMD9 expression levels of each sample in CGGA and TCGA databases ($R > 0.5$) by Pearson correlation analysis, then further explored the biological function of those related genes, and used the DAVID online system to annotate those significant enrichment functions. The enrichment results indicate different terms in the positive-expression. Comparisons of the TOP20 gene terms, mostly focused on the immune response and tumorigenesis in CGGA database1 LGG (twelve related functions) (**Figure 6A** and **Supplementary Table 1**) and were almost totally immune response related in the TCGA database

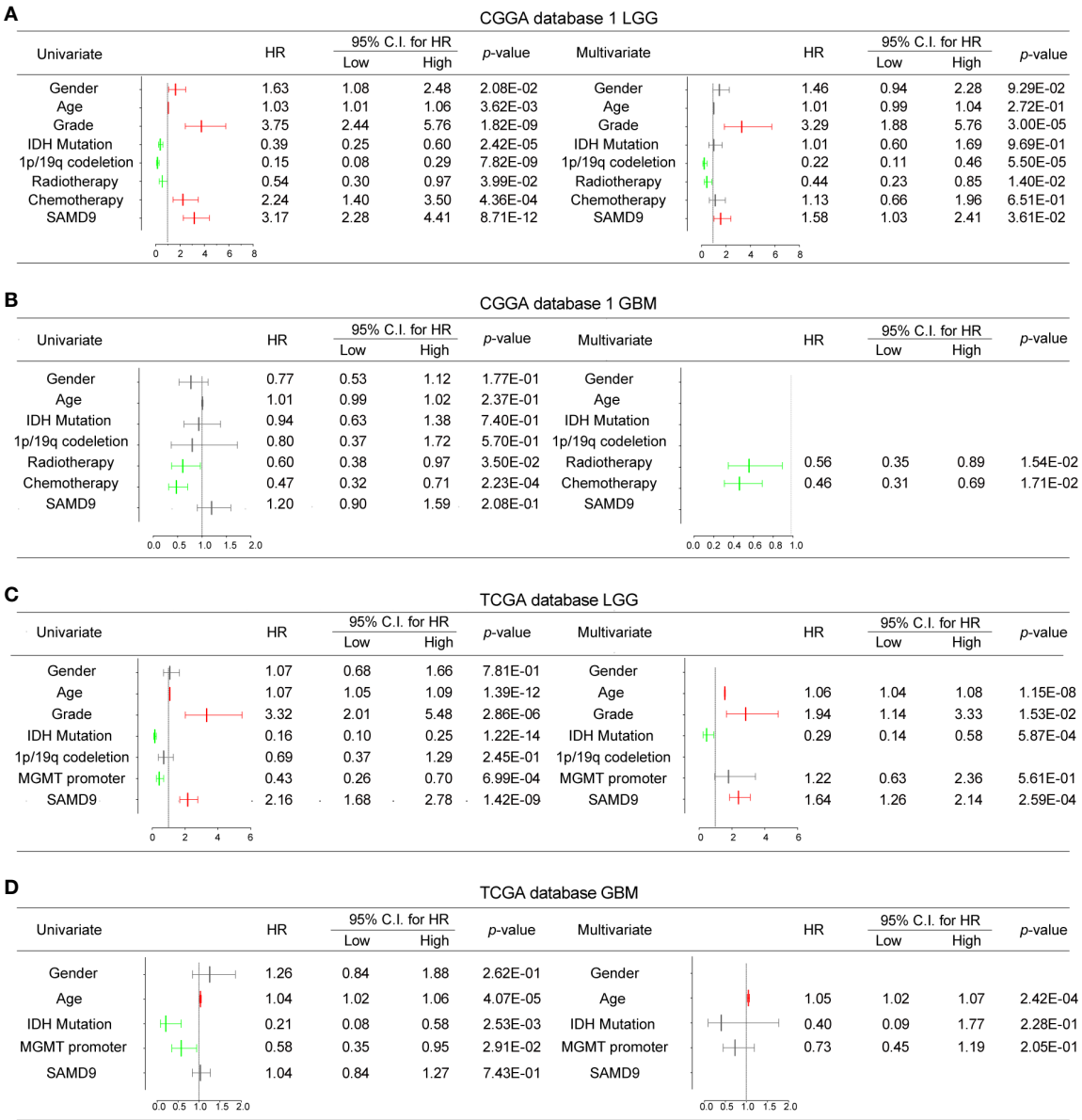

FIGURE 4 | Univariate and Multivariate Cox regression analyses and correlations with classic genetic alterations of SAMD9. **(A)** Univariate and Multivariate regression analyses of SAMD9 expression level and several related clinical variables in CGGA database 1 LGG, Red color indicates protective factor HR > 1, Green color indicates harmful factors HR < 1, Gray color represents HR crossing 1. HR of SAMD9 and Grade > 1, $p < 0.0001$. HR of 1p/19q codeletion < 1, $p < 0.0001$. HR of Radiotherapy < 1, $p < 0.0001$. **(B)** Univariate and Multivariate regression analyses of SAMD9 expression level and several related clinical variables in CGGA database 1 GBM, HR of Radiotherapy < 1, $p = 0.0154$. HR of 1p/19q codeletion < 1, $p = 0.0171$. **(C)** Univariate and Multivariate regression analyses of SAMD9 expression level and several related clinical variables in TCGA database LGG. HR of SAMD9 > 1, $p < 0.0001$. HR of Grade > 1, $p = 0.0153$. HR of Age > 1, $p < 0.0001$. **(D)** Univariate and Multivariate regression analyses of SAMD9 expression level and several related clinical variables in TCGA database GBM. HR of Age > 1, $p < 0.0001$.

LGG (fourteen functions) (**Figure 6B** and **Supplementary Table 2**). Through these GO and KEGG pathways validations, we strongly speculate that SAMD9 was directly correlated with immunological responses. Positive function analysis revealed activation of the immune response, myeloid leukocyte activation, regulation of cytokine production, lymphocyte activation, defense response to virus, cytokine-mediated signaling pathway, myeloid leukocyte activation, activation of immune response, T cell activation, Adaptive Immune System and regulation of type I interferon production. The top 5 molecular functions were located in immune response, cytokine production, defense response to virus. This founding illustrates that SAMD9 has a strong correlation with the immune system. To understand the role of SAMD9 in the immune

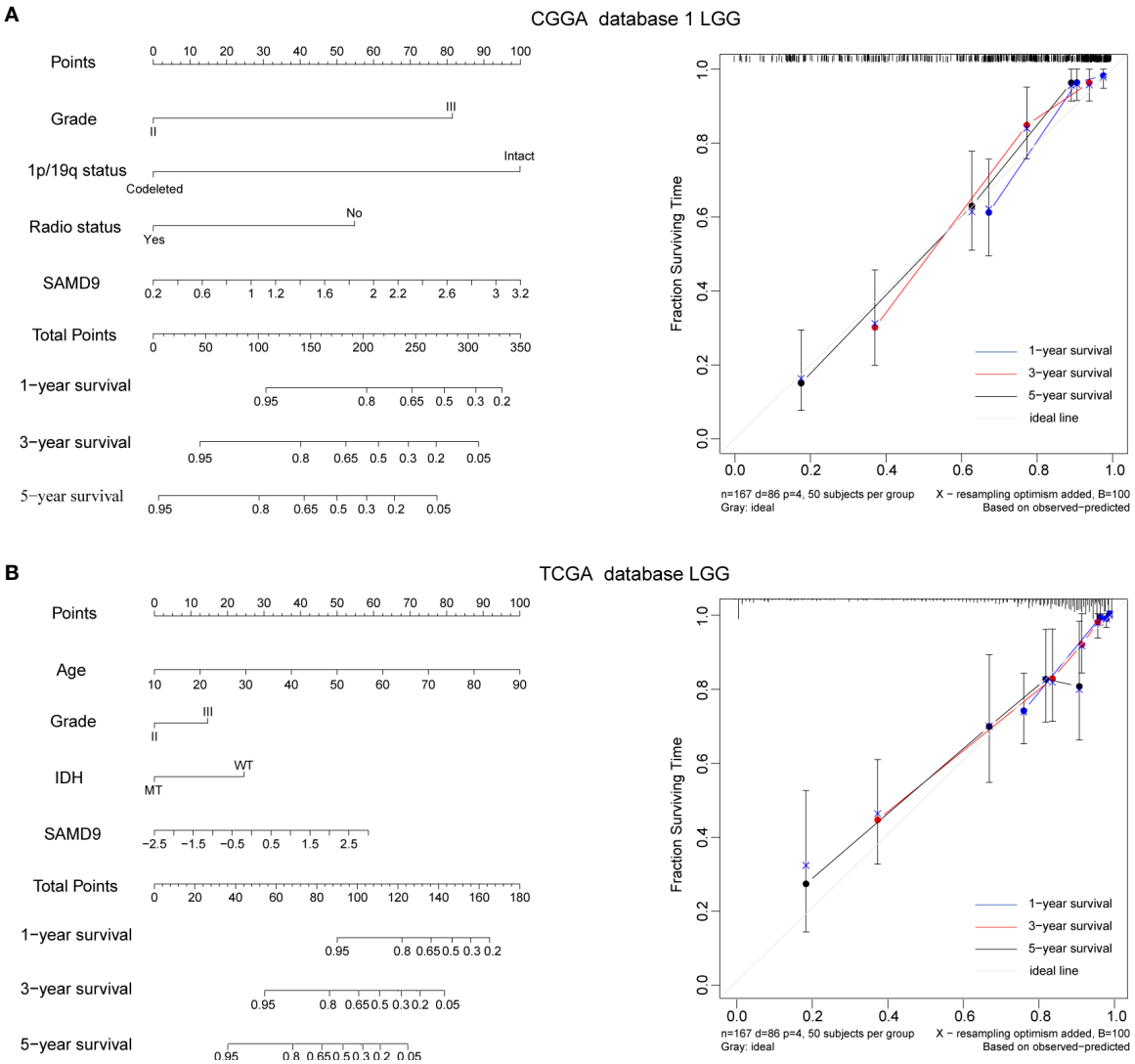

FIGURE 5 | Nomogram prediction model for overall survival (OS) and other integrated risk factors. **(A)** A nomogram was developed by integrating the SAMD9 expression with the clinicopathologic features, grade, 1p/19q codeletion status, radiotherapy status in the CGGA database 1 (left). Calibration plot of nomogram for predicting OS at 1- (blue line), 3- (red line) and 5- (black line) years, ideal line as control (white line) in the CGGA database 1 (right). **(B)** A nomogram was developed by integrating the SAMD9 expression with the clinicopathologic features, age, grade, IDH status (MT, mutant. WT, wild type.) in the TCGA database (left). Calibration plot of nomogram for predicting OS at 1- (blue line), 3- (red line) and 5- (black line) years, ideal line as control (white line) in the TCGA database LGG (right).

system, we performed a correlation coefficient analysis on data from the CGGA database1 LGG and the TCGA database LGG databases (**Figure 6C** and **Tables 3**, **4**). We observed that almost all of immune functions showed positive correlation with SAMD9; only the term of "T cell-mediated immune response" was found to be negatively correlated with SAMD9.To further explore the relationship between SAMD9 and immune responses, we detected nine immune-related checkpoints by Pearson correlation analysis and found that SAMD9 is positively associated with TIM3, CD276, and IDO1, these evaluations indicating SAMD9 maybe a potential antitumoral target by inhibiting these checkpoint proteins (**Figures 6D, E**). We also detected the SAMD9 and TIM3 protein levels in 20 LGG patients by IHC and found that SAMD9 expression positive correlated with TIM3 expression (**Figures 6F, G,** r = 0.59, p = 0.0019).

SAMD9 Relating M2 Macrophages in LGG and Enhances the Infiltration of M2 Macrophages *In Vitro*

All the above results confirmed that SAMD9 may serve as an independent influencing factor for malignancy of LGG, poor prognostic survival and enriched with immune related

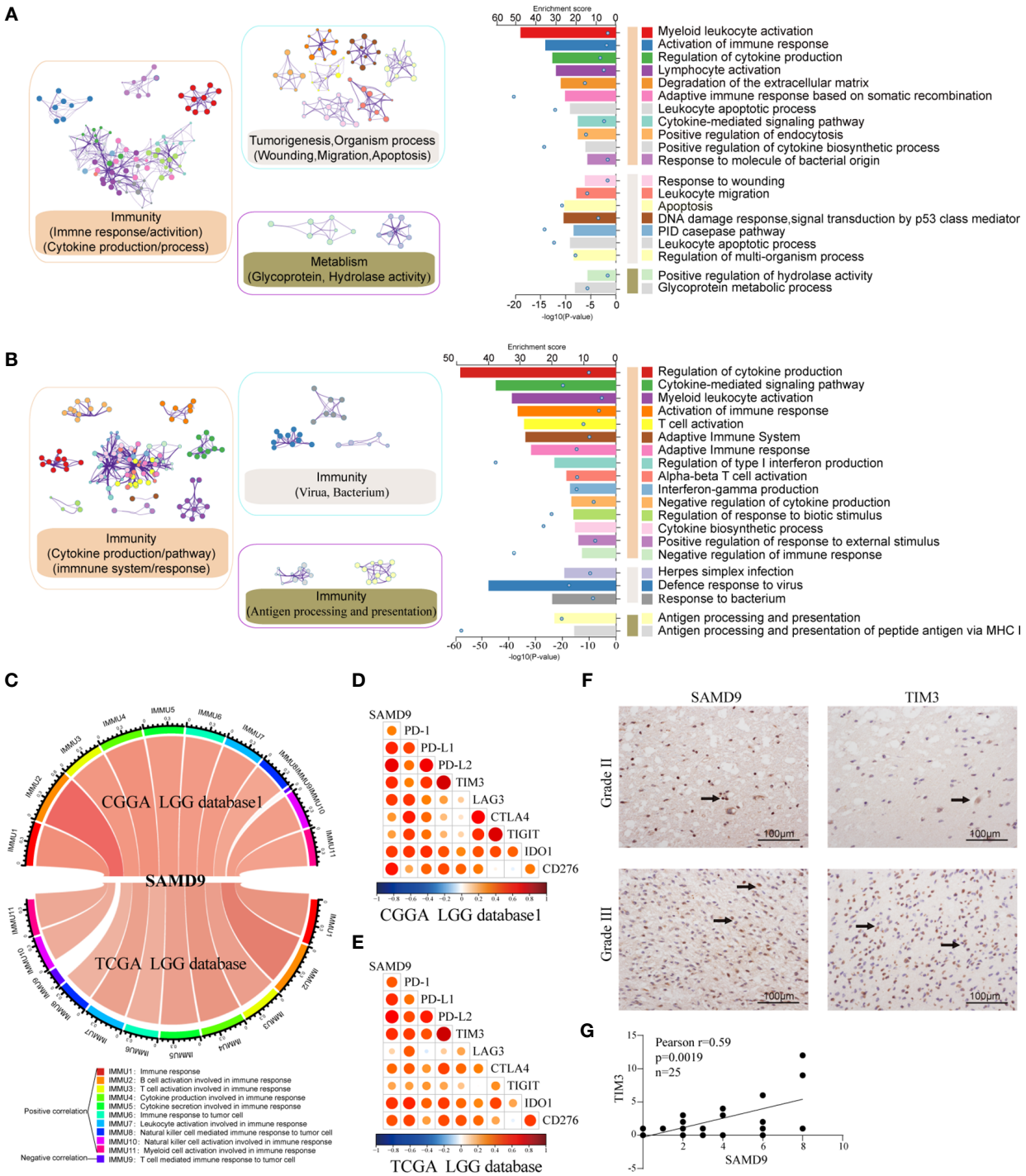

FIGURE 6 | Functional analysis of SAMD9 correlated genes relative to immune response. **(A, B)**. Functional enrichments of SAMD9 related genes (R > 0.5) in CGGA database 1and CGGA database, Cluster showed the possible functions of TOP 20 genes terms and description annotated the detailed pathways. Blue dots represent the enrichment scores of difference terms in the upper axis, the *P*-value of difference terms in the lower axis, all analysis was calculated by Metascape online. **(C)** The correlation coefficient between SAMD9 and different immune cells in CGGA and TCGA databases. IMMU9 represent a negative correlation and other IMMNUs represent a positive correlation. **(D, E)** Correlation Analysis of SAMD9 and nine immune-related checkpoints (PD-1, PD-L1, PD-L2, TIM3, LAG3, CTLA4, TIGIT, IDO1, CD276) in CGGA database 1 LGG and TCGA database LGG. Color depth and circle square represent the degrees of correlation. **(F)** SAMD9 and TIM3 expression levels in glioma specimens determined by IHC analysis in grade II and III. Scale bar = 100 μm. **(G)** Correlation analysis of SAMD9 and TIM3 immunohistochemical scores. X-axis, SAMD9 staining score; y-axis, TIM3 staining score; correlation coefficient r = 0.59; p = 0.0019.

TABLE 3 | SAMD9 and related immune scores in CGGA database 1 LGG.

SAMD9	IMMU1	IMMU2	IMMU3	IMMU4	IMMU5	IMMU6	IMMU7	IMMU8	IMMU9	IMMU10	IMMU11
r	0.553098	0.677422	0.514613	0.543303	0.50371	0.493287	0.497261	0.439126	0.036262	0.483541	0.46568

TABLE 4 | SAMD9 and related immune scores in TCGA database LGG.

SAMD9	IMMU1	IMMU2	IMMU3	IMMU4	IMMU5	IMMU6	IMMU7	IMMU8	IMMU9	IMMU10	IMMU11
r	0.507254	0.594908	0.456405	0.496002	0.446906	0.383906	0.444729	0.364097	-0.18261	0.385898	0.410394

biological progress (myeloid leukocyte activation, activation of immune response, regulation of cytokine production, defense response to virus, immune checkpoints) that regulate glioma character phenotype.To further explore the cells that have the remarkable significant impact on SAMD9, we evaluated the classical proportions of 10 types of infiltrating immune cells (B cells, plasma cells, T cells, NK cells, monocytes, macrophages, dendritic cells, mast cells, eosinophils, neutrophils) using the Cell-type Identification by Spearman's rank correlation test in both CGGA and TCGA datasets. Among these immune cells, we found that macrophages significantly infiltrated in LGG gliomas and were highly consistent with SAMD9 expression in both CGGA database 1 LGG and TCGA databases LGG. The abundance of macrophage was correlated with LGG glioma in those databases (**Figures 7A, B**) (R = 0.32, p = 9.6E-06; R = 0.34, p = 1.1E-13). The partial correlation between the SAMD9 expression level and the six immune cell types: B cell, CD4 T cell, CD8 T cell, neutrophils, macrophages and dendritic cells in the tumor microenvironment was systematically estimated based on the Tumor Immune Estimation Resource (TIMER) algorithm. there was a highly significant correlation between measurements of macrophage infiltration and SAMD9 expression in LGG (**Figure 7C**) (partial.cor = 0.551, p = 7.78E-39). Although five other immune cell types showed significantly in LGG, they did not match the data in CIBERSORT. In conclusion, samples with higher *SAMD9* expression exhibited apparent concordance with encirclement of macrophage cells. The classical phenotype markers of M (*AIF1*), M1 (*IL12A*, *TNF, NOS2, PTGS2*) and M2 (*IL10*, *CCL163*, *TGFB1, CSF1R)* were analyzed in CGGA and TCGA database and found *SAMD9* had stronger positive correlation with M (*AIF1*) and M2 (*IL10*, *CCL163*, *TGFB1, CSF1R)* markers, but inconsistent correlation with M1 (*IL12A*, *TNF, NOS2, PTGS2*) markers (**Figures 7D, E**). Furthermore, we examined the expression levels of related proteins in clinical samples using IHC staining and performed correlation analysis of SAMD9 and those markers. Detailed antibody information in **Table 5**. The results showed that there was higher staining intensity of macrophage total marker AIF1 and M2 marker CD163in WHO grade III than grade II and significantly correlated with SAMD9 (Total Macrophage and SAMD9 Pearson r = 0.47, p = 0.029. Macrophage M2 and SAMD9 Pearson r = 0.55, p = 0.0086). but M1 marker TNF expressed lower grade III than grade II and showed no significant correlation with SAMD9 (Total Macrophage & SAMD9 Pearson r = 0.06, p = 0.85) (**Figure 7F**). To explore the effects of SAMD9 -on M2 macrophage migrative activity, we stably knocked down SAMD9 expression level in LN229 gliomas cells (**Figure 7G**). THP-1 cells were differentiated into M2 macrophage according to classical inducing methods (32, 33). Stable silencing of SAMD9 in LN229 cells reduced the infiltration of M2 macrophage (NC group & shSAMD9 1, p <0.01; NC group & shSAMD9 2, p <0.001) (**Figure 7H**).

DISCUSSION

New strategies for immune targeted cancer therapy could be anchored in specifically interfering with the M2-like TAM signaling cascade pathway or switching polarization of tumor-promoting M2-like TAMs to a tumoricidal M1-like phenotype. The greater infiltration of TAMs is proportionally correlated with a long term of negative prognosis, as observed in experimental animals and clinical research (43–45). TAMs play major roles in tumor progression and it was widely recognized that the M2 phenotype provided an advantage to high grade gliomas (46, 47). There was a fierce dispute about the macrophage polarization state and the proportions of M1 versus M2 in LGG because of the prolonged dynamic stable state of low-grade gliomas (47–49).

SAMD9 expression levels maybe a robust index for the evaluation of the degree of the immune response, deleterious mutations of SAMD9 is the cause of some autoimmune diseases and cancers (50, 51). The IFN-γ binding element is located within the SAMD9 promoter in humans and IFN is the cytokine produced by gliomas, influencing the immune response through TAMs (52, 53). We have revealed that knocking down SAMD9 expression levels in glioma cells decreased the glioblastoma cell progression via the AKT/PI3K pathway, but the detailed mechanism of how SAMD9 affected the occurrence of gliomas and its impact on tumor immunity has not been reported in gliomas (29).

This is the first report to demonstrate that SAMD9 has a role not only as a significance marker related to malignancy characteristics in glioma, but also may as an independent prognostic indicator in lower grade glioma patients; further study found that SAMD9 influences the immune response by increasing the ability of M2 macrophage to infiltrate *in vitro*.

LGG is a transient dynamic quiescence state which almost always invariably develops into secondary glioblastoma (sGBM) (54, 55). Many tumor-related events occur prior to reaching this stage, which potentially provides an optimal intervention window for glioma. Therefore, an urgent strategy is now needed to exploit the novel factors involved in macrophage function in tumorigenesis and metastasis. Revealing the

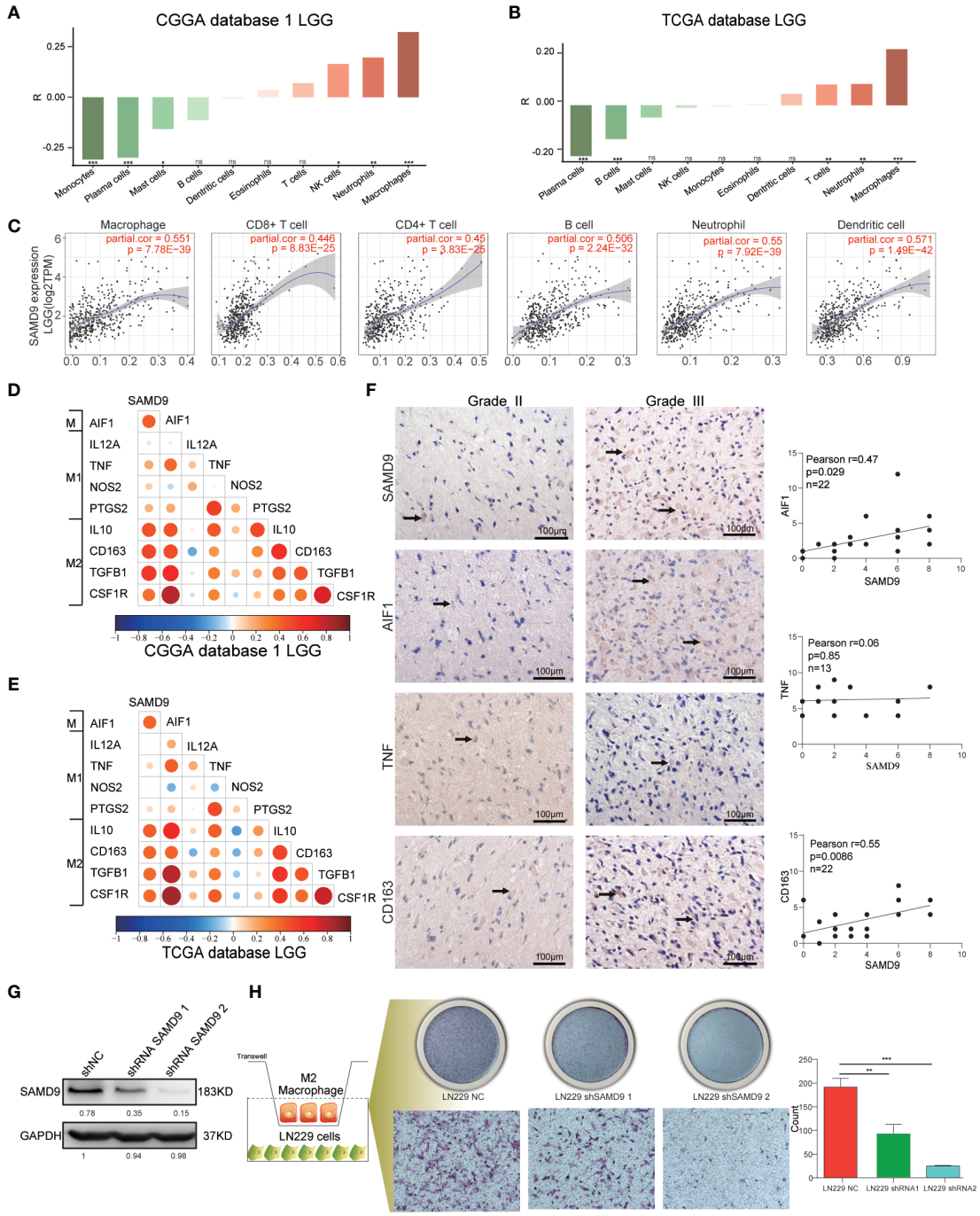

FIGURE 7 | SAMD9 enrichment with M2 macrophages in LGG. **(A, B)** The correlation between SAMD9 and ten types of infiltrating immune cells (B cells, plasma cells, T cells, NK cells, monocytes, macrophages, dendritic cells, mast cells, eosinophils, neutrophils) in CGGA database 1 LGG, Correlation between SAMD9 and macrophages in CGGA database 1 LGG (R = 0.32, p = 9.6E-06) and in TCGA database LGG (R = 0.34, p = 1.1E-13). **(C)** Correlation between SAMD9 and the six immune cell types (B cells, CD4 T cells, CD8 T cells, neutrophils, macrophages and dendritic cells) on TIMER algorithm, macrophages, partial.cor = 0.551, p = 7.78E-39. **(D, E)** Nine classical phenotype markers of M (*AIF1*), M1 (*IL12A*, *TNF, NOS2, PTGS2*) and M2 (*IL10*, *CCL163*, *TGFB1, CSF1R)* were analyzed in CGGA and TCGA database, Color depth and circle square represent the degrees of correlation. **(F)** SAMD9, AIF1, CD163 and TNF expression levels in glioma specimens determined by IHC analysis in grade II and III. Scale bar = 100 μm. Correlation analysis of SAMD9 and related proteins immunohistochemical scores. X-axis, SAMD9 staining score; y-axis, AIF1, CD163 and TNF staining score; Correlation coefficient between SAMD9 and AIF1, r = 0.47; p = 0.029. Correlation coefficient between SAMD9 and TNF, r = 0.06; p = 0.85. Correlation coefficient between SAMD9 and CD163, r = 0.55; p =0.0086. **(G)** Western blots of LN229 cells with stable expression of shSAMD9. **(H)** Infiltration of M2 macrophage in LN229 NC (left), LN229 shSAMD9 1 (middle), LN229 shSAMD9 2 (right). LN229 NC & LN229 shSAMD9 1, **. LN229 NC & LN229 shSAMD9 2, ***.*, **, ***, **** and ns indicate $p < 0.05$, $p < 0.01$, $p < 0.001$, $p < 0.0001$ and no significance, respectively.

TABLE 5 | Detailed antibody information.

Antibody	Number	Antibody dilution
Anti-SAMD9	(ab121664)	1:200
Anti-TNF	(ab270264)	1:150
Anti-TIM3	(ab241332)	1:200
Anti-CD163	(ab189915)	1:200
Anti-AIF1	(ab204493)	1:200

molecular function of SAMD9 will determine its clinical application. SAMD9 may be a diagnostic or prognostic indicator for low grade glioma and also a new potential therapeutic target for treating gliomas. A better understanding of the role of SAMD9 in LGG and its detailed mechanism could certainly open up a new avenue for anti-glioma therapy. Future research will focus on the exploration of SAMD9 specific inhibitors and evaluating their therapeutic effect in gliomas.

DATA AVAILABILITY STATEMENT

The datasets presented in this study can be found in online repositories. The names of the repository/repositories and accession number(s) can be found in the article/**Supplementary Material**.

ETHICS STATEMENT

The studies involving human participants were reviewed and approved by the ethics committee of Beijing Tiantan Hospital, Capital Medical University. The patients/participants provided their written informed consent to participate in this study.

AUTHOR CONTRIBUTIONS

WM: data analysis and editing the manuscript. ZB: data collection and organization of CGGA database. YZ: data collection and organization of TCGA database. KZ: draw the figures. TJ: conception, supervision, and design of the manuscript. All authors contributed to the article and approved the submitted version.

FUNDING

This study was supported by the National Natural Science Foundation of China (81761168038, 81972337); Nature Science Foundation of Beijing (JQ20030).

SUPPLEMENTARY MATERIAL

The Supplementary Material for this article can be found online at: https://www.frontiersin.org/articles/10.3389/fimmu.2021.659659/full#supplementary-material

Supplementary Figure 1 | WHO grade, IDH1 status, MGMT promoter methylation status and transcriptional characteristic subtype relative to *SAMD9* expression. **(A)** The correlation of SAMD9 expression level with WHO grade. SAMD9 expression levels in glioma of WHO grade II-IV in CGGA database 2, ****$p < 0.01$. the difference between III & IV, ****$p < 0.0001$. **(B)** The relationship between SAMD9 transcription level and *IDH1* mutation in CGGA database 2. ****$p < 0.0001$. **(C)** The correlation of SAMD9 expression level and MGMT promoter methylation status, the difference in CGGA database 2, ****$p < 0.0001$. **(D)** The relationship between SAMD9 transcription level and *IDH1* mutation in each transcriptional characteristic subtype in CGGA database 2.

Supplementary Figure 2 | Patients with higher *SAMD9* level exhibit poorer OS. **(A)** Half of the patients with higher SAMD9 expression exhibited shorter OS in Kaplan-Meier analyses based on CGGA database 2 ALL, $p < 0.0001$. **(B)** The half of patients with higher SAMD9 expression exhibited shorter OS in Kaplan-Meier analyses based on CGGA database 2 LGG, $p = 0.0002$. **(C)** Half of patients with higher SAMD9 expression exhibited shorter OS in Kaplan-Meier analyses based on CGGA database 2 GBM, $p = 0.058$.

Supplementary Figure 3 | Univariate and Multivariate Cox regression analyses and correlations with classic genetic alterations of SAMD9. **(A)** Univariate and Multivariate regression analyses of SAMD9 expression level and several related clinical variables in CGGA database 2 LGG, Red color indicates protective factor HR > 1, Green color indicates harmful factors HR < 1, Gray color represents HR crossing 1. HR of SAMD9 and Grade > 1, $p < 0.0001$. HR of *IDH* mutation < 1, $p < 0.01$. HR of 1p/19q codeletion < 1, $p < 0.001$. **(B)** Univariate and Multivariate regression analyses of SAMD9 expression level and several related clinical variables in GBM CGGA database 2, HR of *IDH* mutation < 1, $p < 0.05$.

Supplementary Figure 4 | Nomogram prediction model for OS and other integrated risk factors. A nomogram was developed by integrating the SAMD9 expression with the clinicopathologic features, grade, IDH status, 1p/19q codeletion status in the CGGA database 2 (left). Calibration plot of nomogram for predicting OS at 1- (blue line), 3- (red line) and 5- (black line) years, ideal line as control (white line) in the CGGA database 2 (right).

Supplementary Figure 5 | SAMD9 expression comparation between normal brain and difference grade gliomas. Total of 207 normal brain tissues, 518 low-grade gliomas, and 207 high-grade gliomas were included in the comparisons. $p < 0.05$ LGG & Normal, $p < 0.05$ GBM & Normal.

REFERENCES

1. Liu C, Sage JC, Miller MR, Verhaak RG, Hippenmeyer S, Vogel H, et al. Mosaic analysis with double markers reveals tumor cell of origin in glioma. *Cell* (2011) 146(2):209–21. doi: 10.1016/j.cell.2011.06.014
2. Venkatesh HS, Johung TB, Caretti V, Noll A, Tang Y, Nagaraja S, et al. Neuronal Activity Promotes Glioma Growth through Neuroligin-3 Secretion. *Cell* (2015) 161(4):803–16. doi: 10.1016/j.cell.2015.04.012
3. Waker CA, Lober RM. Brain Tumors of Glial Origin. *Adv Exp Med Biol* (2019) 1190:281–97. doi: 10.1007/978-981-32-9636-7_18
4. Chang Y, Li G, Zhai Y, Huang L, Feng Y, Wang D, et al. Redox Regulator GLRX Is Associated With Tumor Immunity in Glioma. *Front Immunol* (2020) 11:580934. doi: 10.3389/fimmu.2020.580934
5. Touat M, Li YY, Boynton AN, Spurr LF, Iorgulescu JB, Bohrson CL, et al. Mechanisms and therapeutic implications of hypermutation in gliomas. *Nature* (2020) 580(7804):517–23. doi: 10.1038/s41586-020-2209-9
6. Hu H, Mu Q, Bao Z, Chen Y, Liu Y, Chen J, et al. Mutational Landscape of Secondary Glioblastoma Guides MET-Targeted Trial in Brain Tumor. *Cell* (2018) 175(6):1665–1678 e1618. doi: 10.1016/j.cell.2018.09.038

7. Oldrini B, Vaquero-Siguero N, Mu Q, Kroon P, Zhang Y, Galan-Ganga M, et al. MGMT genomic rearrangements contribute to chemotherapy resistance in gliomas. *Nat Commun* (2020) 11(1):3883. doi: 10.1038/s41467-020-17717-0
8. Baumert BG, Hegi ME, van den Bent MJ, von Deimling A, Gorlia T, Hoang-Xuan K, et al. Temozolomide chemotherapy versus radiotherapy in high-risk low-grade glioma (EORTC 22033-26033): a randomised, open-label, phase 3 intergroup study. *Lancet Oncol* (2016) 17(11):1521–32. doi: 10.1016/S1470-2045(16)30313-8
9. Eyupoglu IY, Buchfelder M, Savaskan NE. Surgical resection of malignant gliomas-role in optimizing patient outcome. *Nat Rev Neurol* (2013) 9(3):141–51. doi: 10.1038/nrneurol.2012.279
10. Chapel DB, Stewart R, Furtado LV, Husain AN, Krausz T, Deftereos G. Tumor PD-L1 expression in malignant pleural and peritoneal mesothelioma by Dako PD-L1 22C3 pharmDx and Dako PD-L1 28-8 pharmDx assays. *Hum Pathol* (2019) 87:11–7. doi: 10.1016/j.humpath.2019.02.001
11. Mahoney KM, Freeman GJ, McDermott DF. The Next Immune-Checkpoint Inhibitors: PD-1/PD-L1 Blockade in Melanoma. *Clin Ther* (2015) 37(4):764–82. doi: 10.1016/j.clinthera.2015.02.018
12. Weber JS, D'Angelo SP, Minor D, Hodi FS, Gutzmer R, Neyns B, et al. Nivolumab versus chemotherapy in patients with advanced melanoma who progressed after anti-CTLA-4 treatment (CheckMate 037): a randomised, controlled, open-label, phase 3 trial. *Lancet Oncol* (2015) 16(4):375–84. doi: 10.1016/S1470-2045(15)70076-8
13. Motzer RJ, Rini BI, McDermott DF, Redman BG, Kuzel TM, Harrison MR, et al. Nivolumab for Metastatic Renal Cell Carcinoma: Results of a Randomized Phase II Trial. *J Clin Oncol* (2015) 33(13):1430–7. doi: 10.1200/JCO.2014.59.0703
14. Rodell CB, Arlauckas SP, Cuccarese MF, Garris CS, Li R, Ahmed MS, et al. TLR7/8-agonist-loaded nanoparticles promote the polarization of tumour-associated macrophages to enhance cancer immunotherapy. *Nat BioMed Eng* (2018) 2(8):578–88. doi: 10.1038/s41551-018-0236-8
15. Oya Y, Hayakawa Y, Koike K. Tumor microenvironment in gastric cancers. *Cancer Sci* (2020) 111(8):2696–707. doi: 10.1111/cas.14521
16. Genard G, Lucas S, Michiels C. Reprogramming of Tumor-Associated Macrophages with Anticancer Therapies: Radiotherapy versus Chemo- and Immunotherapies. *Front Immunol* (2017) 8:828. doi: 10.3389/fimmu.2017.00828
17. Tao W, Chu C, Zhou W, Huang Z, Zhai K, Fang X, et al. Dual Role of WISP1 in maintaining glioma stem cells and tumor-supportive macrophages in glioblastoma. *Nat Commun* (2020) 11(1):3015. doi: 10.1038/s41467-020-16827-z
18. Ye L, He S, Mao X, Zhang Y, Cai Y, Li S. Effect of Hepatic Macrophage Polarization and Apoptosis on Liver Ischemia and Reperfusion Injury During Liver Transplantation. *Front Immunol* (2020) 11:1193. doi: 10.3389/fimmu.2020.01193
19. Tariq M, Zhang J, Liang G, Ding L, He Q, Yang B. Macrophage Polarization: Anti-Cancer Strategies to Target Tumor-Associated Macrophage in Breast Cancer. *J Cell Biochem* (2017) 118(9):2484–501. doi: 10.1002/jcb.25895
20. Zhao J, Zhang Z, Xue Y, Wang G, Cheng Y, Pan Y, et al. Anti-tumor macrophages activated by ferumoxytol combined or surface-functionalized with the TLR3 agonist poly (I : C) promote melanoma regression. *Theranostics* (2018) 8(22):6307–21. doi: 10.7150/thno.29746
21. Brown NF, Carter TJ, Ottaviani D, Mulholland P. Harnessing the immune system in glioblastoma. *Br J Cancer* (2018) 119(10):1171–81. doi: 10.1038/s41416-018-0258-8
22. Goodwin TJ, Shen L, Hu M, Li J, Feng R, Dorosheva O, et al. Liver specific gene immunotherapies resolve immune suppressive ectopic lymphoid structures of liver metastases and prolong survival. *Biomaterials* (2017) 141:260–71. doi: 10.1016/j.biomaterials.2017.07.007
23. Liu Z, Wang Y, Huang Y, Kim BYS, Shan H, Wu D, et al. Tumor Vasculatures: A New Target for Cancer Immunotherapy. *Trends Pharmacol Sci* (2019) 40 (9):613–23. doi: 10.1016/j.tips.2019.07.001
24. Kumagi T, Akbar SM, Horiike N, Onji M. Increased survival and decreased tumor size due to intratumoral injection of ethanol followed by administration of immature dendritic cells. *Int J Oncol* (2003) 23(4):949–55. doi: 10.3892/ijo.23.4.949
25. De Carli E, Delion M, Rousseau A. [Immunotherapy in brain tumors]. *Ann Pathol* (2017) 37(1):117–26. doi: 10.1016/j.annpat.2016.12.001
26. Liu EK, Sulman EP, Wen PY, Kurz SC. Novel Therapies for Glioblastoma. *Curr Neurol Neurosci Rep* (2020) 20(7):19. doi: 10.1007/s11910-020-01042-6
27. Stepanenko AA, Chekhonin VP. Recent Advances in Oncolytic Virotherapy and Immunotherapy for Glioblastoma: A Glimmer of Hope in the Search for an Effective Therapy? *Cancers (Basel)* (2018) 10(12):1–24. doi: 10.3390/cancers10120492
28. McGranahan T, Therkelsen KE, Ahmad S, Nagpal S. Current State of Immunotherapy for Treatment of Glioblastoma. *Curr Treat Options Oncol* (2019) 20(3):24. doi: 10.1007/s11864-019-0619-4
29. Ma W, Jin H, Liu W, Li X, Zhou X, Guo X, et al. Homeobox B8 Targets Sterile Alpha Motif Domain-Containing Protein 9 and Drives Glioma Progression. *Neurosci Bull* (2020) 36(4):359–71. doi: 10.1007/s12264-019-00436-y
30. Nagamachi A, Matsui H, Asou H, Ozaki Y, Aki D, Kanai A, et al. Haploinsufficiency of SAMD9L, an endosome fusion facilitator, causes myeloid malignancies in mice mimicking human diseases with monosomy 7. *Cancer Cell* (2013) 24(3):305–17. doi: 10.1016/j.ccr.2013.08.011
31. Li GZ, Wang Z, Zhang CB, Liu X, Cai JQ, Wang ZL, et al. Molecular and clinical characterization of TIM-3 in glioma through 1,024 samples. *Oncoimmunology* (2017) 6(8):e1328339. doi: 10.1080/2162402X.2017.1328339
32. Genin M, Clement F, Fattaccioli A, Raes M, Michiels C. M1 and M2 macrophages derived from THP-1 cells differentially modulate the response of cancer cells to etoposide. *BMC Cancer* (2015) 15:577. doi: 10.1186/s12885-015-1546-9
33. Wang D, Yang L, Yue D, Cao L, Li L, Wang D, et al. Macrophage-derived CCL22 promotes an immunosuppressive tumor microenvironment via IL-8 in malignant pleural effusion. *Cancer Lett* (2019) 452:244–53. doi: 10.1016/j.canlet.2019.03.040
34. Yang M, Ma B, Shao H, Clark AM, Wells A. Macrophage phenotypic subtypes diametrically regulate epithelial-mesenchymal plasticity in breast cancer cells. *BMC Cancer* (2016) 16:419. doi: 10.1186/s12885-016-2411-1
35. Cassetta L, Fragkogianni S, Sims AH, Swierczak A, Forrester LM, Zhang H, et al. Human Tumor-Associated Macrophage and Monocyte Transcriptional Landscapes Reveal Cancer-Specific Reprogramming, Biomarkers, and Therapeutic Targets. *Cancer Cell* (2019) 35(4):588–602 e510. doi: 10.1016/j.ccell.2019.02.009
36. Wang Y, Lyu Z, Qin Y, Wang X, Sun L, Zhang Y, et al. FOXO1 promotes tumor progression by increased M2 macrophage infiltration in esophageal squamous cell carcinoma. *Theranostics* (2020) 10(25):11535–48. doi: 10.7150/thno.45261
37. Xu J, Yu Y, He X, Niu N, Li X, Zhang R, et al. Tumor-associated macrophages induce invasion and poor prognosis in human gastric cancer in a cyclooxygenase-2/MMP9-dependent manner. *Am J Transl Res* (2019) 11 (9):6040–54.
38. Lee SM, Kim NH, Lee S, Kim YN, Heo JD, Rho JR, et al. (10Z)-Debromohymenialdisine from Marine Sponge Stylissa sp. Regulates Intestinal Inflammatory Responses in Co-Culture Model of Epithelial Caco-2 Cells and THP-1 Macrophage Cells. *Molecules* (2019) 24(18):1–15. doi: 10.3390/molecules24183394
39. Kelppe J, Thoren H, Ristimaki A, Haglund C, Sorsa T, Hagstrom J. BRAF V600E expression in ameloblastomas-A 36-patient cohort from Helsinki University Hospital. *Oral Dis* (2019) 25(4):1169–74. doi: 10.1111/odi.13072
40. Sousa DA, Silva K, Cascon CM, Silva FBF, Mello MFV, Leite JDS, et al. Epidermal growth factor receptor 2 immunoexpression in gastric cells of domestic cats with H. heilmannii infection. *Acta Histochem* (2019) 121 (4):413–8. doi: 10.1016/j.acthis.2019.03.004
41. Qian Z, Li Y, Fan X, Zhang C, Wang Y, Jiang T, et al. Molecular and clinical characterization of IDH associated immune signature in lower-grade gliomas. *Oncoimmunology* (2018) 7(6):e1434466. doi: 10.1080/2162402X.2018.1434466
42. Chai RC, Zhang KN, Liu YQ, Wu F, Zhao Z, Wang KY, et al. Combinations of four or more CpGs methylation present equivalent predictive value for MGMT expression and temozolomide therapeutic prognosis in gliomas. *CNS Neurosci Ther* (2019) 25(3):314–22. doi: 10.1111/cns.13040
43. Patel SJ, Sanjana NE, Kishton RJ, Eidizadeh A, Vodnala SK, Cam M, et al. Identification of essential genes for cancer immunotherapy. *Nature* (2017) 548 (7669):537–42. doi: 10.1038/nature23477
44. Chen JJ, Lin YC, Yao PL, Yuan A, Chen HY, Shun CT, et al. Tumor-associated macrophages: the double-edged sword in cancer progression. *J Clin Oncol* (2005) 23(5):953–64. doi: 10.1200/JCO.2005.12.172
45. Brower V. Macrophages: cancer therapy's double-edged sword. *J Natl Cancer Inst* (2012) 104(9):649–52. doi: 10.1093/jnci/djs235

46. De I, Steffen MD, Clark PA, Patros CJ, Sokn E, Bishop SM, et al. CSF1 Overexpression Promotes High-Grade Glioma Formation without Impacting the Polarization Status of Glioma-Associated Microglia and Macrophages. *Cancer Res* (2016) 76(9):2552–60. doi: 10.1158/0008-5472.CAN-15-2386
47. Sorensen MD, Dahlrot RH, Boldt HB, Hansen S, Kristensen BW. Tumour-associated microglia/macrophages predict poor prognosis in high-grade gliomas and correlate with an aggressive tumour subtype. *Neuropathol Appl Neurobiol* (2018) 44(2):185–206. doi: 10.1111/nan.12428
48. Szulzewsky F, Pelz A, Feng X, Synowitz M, Markovic D, Langmann T, et al. Glioma-associated microglia/macrophages display an expression profile different from M1 and M2 polarization and highly express Gpnmb and Spp1. *PloS One* (2015) 10(2):e0116644. doi: 10.1371/journal.pone.0116644
49. Gjorgjevski M, Hannen R, Carl B, Li Y, Landmann E, Buchholz M, et al. Molecular profiling of the tumor microenvironment in glioblastoma patients: correlation of microglia/macrophage polarization state with metalloprotease expression profiles and survival. *Biosci Rep* (2019) 39(6):1–12. doi: 10.1042/BSR20182361
50. Chefetz I, Ben Amitai D, Browning S, Skorecki K, Adir N, Thomas MG, et al. Normophosphatemic familial tumoral calcinosis is caused by deleterious mutations in SAMD9, encoding a TNF-alpha responsive protein. *J Invest Dermatol* (2008) 128(6):1423–9. doi: 10.1038/sj.jid.5701203
51. Davidsson J, Puschmann A, Tedgard U, Bryder D, Nilsson L, Cammenga J. SAMD9 and SAMD9L in inherited predisposition to ataxia, pancytopenia, and myeloid malignancies. *Leukemia* (2018) 32(5):1106–15. doi: 10.1038/s41375-018-0074-4
52. Hershkovitz D, Gross Y, Nahum S, Yehezkel S, Sarig O, Uitto J, et al. Functional characterization of SAMD9, a protein deficient in normophosphatemic familial tumoral calcinosis. *J Invest Dermatol* (2011) 131(3):662–9. doi: 10.1038/jid.2010.387
53. Tanaka M, Shimbo T, Kikuchi Y, Matsuda M, Kaneda Y. Sterile alpha motif containing domain 9 is involved in death signaling of malignant glioma treated with inactivated Sendai virus particle (HVJ-E) or type I interferon. *Int J Cancer* (2010) 126(8):1982–91. doi: 10.1002/ijc.24965
54. Claus EB, Walsh KM, Wiencke JK, Molinaro AM, Wiemels JL, Schildkraut JM, et al. Survival and low-grade glioma: the emergence of genetic information. *Neurosurg Focus* (2015) 38(1):E6. doi: 10.3171/2014.10.FOCUS12367
55. Xu Y, Geng R, Yuan F, Sun Q, Liu B, Chen Q. Identification of differentially expressed key genes between glioblastoma and low-grade glioma by bioinformatics analysis. *PeerJ* (2019) 7:e6560. doi: 10.7717/peerj.6560

Conflict of Interest: The authors declare that the research was conducted in the absence of any commercial or financial relationships that could be construed as a potential conflict of interest.

frontiers in Oncology

ORIGINAL RESEARCH
published: 17 May 2021
doi: 10.3389/fonc.2021.670490

Potential Impact of ALKBH5 and YTHDF1 on Tumor Immunity in Colon Adenocarcinoma

Guanyu Yan, Yue An, Boyang Xu, Ningning Wang, Xuren Sun†* and *Mingjun Sun*†*

Department of Gastroenterology, The First Hospital of China Medical University, Shenyang, China

OPEN ACCESS

Edited by:
Jian Cao,
Rutgers Cancer Institute of New Jersey, United States

Reviewed by:
Steven F. Gameiro,
McMaster University, Canada
Weimin Zhang,
Beijing Cancer Hospital, China

***Correspondence:**
Mingjun Sun
sunmjmw@163.com
Xuren Sun
sxr679@126.com

†*These authors have contributed equally to this work and share last authorship*

Specialty section:
This article was submitted to Cancer Immunity and Immunotherapy, a section of the journal Frontiers in Oncology

Received: *21 February 2021*
Accepted: *26 April 2021*
Published: *17 May 2021*

Citation:
Yan G, An Y, Xu B, Wang N, Sun X and Sun M (2021) Potential Impact of ALKBH5 and YTHDF1 on Tumor Immunity in Colon Adenocarcinoma. Front. Oncol. 11:670490. doi: 10.3389/fonc.2021.670490

Background: ALKBH5 and YTHDF1 are regarded as the eraser and reader, respectively, in N6-methyladenosine (m6A) modification. Recently, immune contexture has been drawing increasing attention in terms of the progression and treatment of cancers. This study aimed to determine the relationship between ALKBH5/YTHDF1 and immunological characteristics of colon adenocarcinoma (COAD).

Methods: Expression of ALKBH5 and YTHDF1 was investigated across TCGA and GEO validated in our study. Patients with COAD were divided into two clusters using consensus clustering based on the expression of ALKBH5 and YTHDF1. We then compared their clinical characteristics and performed gene set enrichment analysis (GSEA) to identify the functional differences. Immune infiltration analyses were conducted using ESTIMATE, CIBERSORT, and ssGSEA. In addition, we evaluated the expression of the targets of immune checkpoint inhibitors (ICIs) and calculated the tumor mutation burden (TMB) of the tumor samples. Weighted gene co-expression network analysis (WGCNA) was used to identify the genes related to both ALKBH5/YTHDF1 expression and immunity. GSE39582 was utilized for external validation of immunological features between the two clusters.

Results: Cluster 2 had high expression of ALKBH5 and lesser so of YTHDF1, whereas Cluster 1 had just the reverse. Cluster 1 had a higher N stage and pathological stage than Cluster 2. The latter had stronger immune infiltration, higher expression of targets of ICIs, more TMB, and a larger proportion of deficiency in mismatch repair-microsatellite instability-high (dMMR-MSI-H) status than Cluster 1. Moreover, WGCNA revealed 14 genes, including PD1 and LAG3, related to both the expression of ALKBH5/YTHDF1 and immune scores.

Conclusions: ALKBH5 and YTHDF1 influence immune contexture and can potentially transform cold tumors into hot tumors in patients with COAD.

Keywords: colon adenocarcinoma, ALKBH5, YTHDF1, immune contexture, m6A modification

INTRODUCTION

Colorectal cancer (CRC) ranks third in incidence, and its mortality ranks second in both sexes worldwide (1). Approximately 70–80% of patients with early stage CRC are eligible for surgery, and the five-year survival rate of these patients is approximately 90%. However, the five-year survival rate of patients with distant CRC (stage IV) is as low as 10–15% (2, 3).

Colon adenocarcinoma (COAD) is the main type of CRC that originates from adenomatous lesions and evolves into cancer due to the accumulation of genetic mutations (4). Recently, a study has shown that mutations can generate new antigens, which can be recognized by the immune system (5). Moreover, immunotherapy has proven to be effective in treating advanced carcinomas (6). Nevertheless, immunotherapy has limitations in some patients with microsatellite instability (MSI) and most patients with microsatellite stability (MSS) (7). Therefore, identification of novel immunotherapy markers and uncovering the underlying mechanisms of immune checkpoints would be important.

N6-methyladenosine (m6A) is the most abundant RNA modification that occurs in both coding and non-coding RNAs, and is a crucial post-transcriptional regulator in various cancers (8–11). Proteins involved in m6A modification may be divided into three categories: writer (catalyzes the occurrence of m6A modification), eraser (catalyzes the removal of m6A modification), and reader (recognizes and binds m6A modification) (12). Although tumor-intrinsic carcinogenic processes are vital, the impact of m6A modification on tumor and immunity is also worth attention. In recent years, some studies have suggested that targeting of dysregulated m6A regulators with small molecule inhibitors has potential in treating cancer. Given the functional importance of m6A modification in various cancers, targeted treatment against m6A regulators may be applicable in the clinic, in combination with chemotherapy or immunotherapy, to improve cancer therapy (13).

ALKBH5 plays the role of eraser in m6A modification and has been proven to regulate suppressive immune cell accumulation in melanoma (14, 15). In pancreatic ductal adenocarcinoma, ALKBH5 inhibits tumorigenesis by decreasing m6A modification of WIF-1 RNA and mediating the Wnt signaling pathway (16). On the other hand, YTHDF1 is a reader in m6A modification that can improve the efficiency of mRNA translation (17). It regulates the expression of lysosomal proteases in an m6A-dependent manner to control anti-tumor immunity and improve the efficacy of immunotherapy. Deficiency of YTHDF1 can enhance the therapeutic effect of PD-L1 checkpoint blockade (18).

To comprehensively understand the role of ALKBH5 and YTHDF1 in tumor immunity, we analyzed the transcriptome profiling data of colon adenocarcinoma from The Cancer Genome Atlas (TCGA) and Gene Expression Omnibus (GEO). We divided patients into two clusters based on the expression of ALKBH5 and YTHDF1 and compared their differences in clinical characteristics, biological pathways, immune infiltration, immune checkpoint expressions, and mutational landscapes using bioinformatics methods. Our results indicated that Cluster 2, with high expression of ALKBH5 and low expression of YTHDF1, had more immune infiltration, immune checkpoint inhibitor expression, and tumor mutation burden than Cluster 1, hence suggesting that Cluster 2 might respond better to immunotherapy. ALKBH5 and YTHDF1 may remarkably influence the immune contexture of colon adenocarcinoma.

MATERIALS AND METHODS

Data Sources and Preprocessing

Transcriptome profiling data (HTSeq-Counts and HTSeq-FPKM) with clinical information were downloaded from TCGA-COAD project by R (version 4.0.2) with R package TCGAbiolinks (19). Cases that contained intact clinical information (age, sex, T stage, N stage, M stage, and prognostic information) were included. Level 3 HTSeq-FPKM of 435 primary solid tumor samples were treated by log2(FPKM+1) transformation for further analyses, and HTSeq-Counts were used for differential analysis.

Simple nucleotide variation data (MuTect2) of 376 patients with COAD were collected using R package maftools (20). Due to the lack of mutation information for some patients with COAD, we only included 376 patients in the analysis involving mutational landscape. Waterfall plots were used to show the genetic mutation of patients using the R package ComplexHeatmap (21). Tumor mutation burden (TMB) was calculated based on simple nucleotide variation, defined as the number of mutations per megabase.

Expression profiling by GSE39582 array was downloaded from the Gene Expression Omnibus (GEO) database (https://www.ncbi.nlm.nih.gov/gds/) (22). The dataset with 566 colon cancer tissues was used to verify the immune characteristics of patients with colon cancer.

Immune Infiltration Analysis

ESTIMATE is a method that determines the fractions of stromal and immune cells based on gene expression signatures in tumor samples. It was applied to evaluate the tumor microenvironment (TME) of each patient with COAD, along with stromal score (stromal content), immune score (extent of immune cell infiltration), ESTIMATE score (synthetic mark of stroma and immune), and tumor purity by R package estimate (23).

CIBERSORT is a means of computing cell composition based on the expression profiles. This deconvolution algorithm was used to calculate the proportion of 22 immune cells in each patient with COAD (24). The sum of 22 immune cell type fraction in each sample was 1.

By applying the single-sample gene set enrichment analysis (ssGSEA) method from R package GSVA (25), we calculated the extent of infiltration of 28 immune cell types according to the expression levels of genes in 28 published gene sets for immune cells (26).

Consensus Clustering Based on ALKBH5 and YTHDF1

Expression of ALKBH5 and YTHDF1 was extracted and clustered coherently using the R package ConsensusClusterPlus (27). The samples were divided into two clusters. We used the R package CMScaller to identify the consensus molecular subtypes (CMS) of each sample (28). CMS is a robust classification system for CRC. Every CMS has distinct features: CMS1 (immune), CMS2 (canonical), CMS3 (metabolic), and CMS4 (mesenchymal) (29). A Sankey diagram was used to indicate the relationship between the two clusters and CMS.

Gene Set Enrichment Analysis

GSEA was performed using the R package clusterProfiler to discover the significant functional difference between the two clusters (30). Significant pathway enrichment was identified by the normalized enrichment score (|NES| >1), P value <0.05, and FDR q value <0.05.

Differential Expressed Genes

Expression profiling data (HTSeq-Counts) were compared to identify the DEGs of two clusters using the R package DESeq2 (31). The threshold values were |log2FoldChange | >1 and adjusted P value <0.05.

Weighted Gene Co-Expression Network Analysis

We performed WGCNA on DEGs using the R package WGCNA (32). To ensure that the constructed co-expression network approached scale-free distribution, we chose 5 as the soft power. We obtained nine modules and calculated their correlation with cluster, stromal score, immune score, ESTIMATE score, and tumor purity. Subsequently, we acquired 14 genes according to the calculation of module membership (MM) and gene significance (GS).

Functional Enrichment Analysis

Gene Ontology (GO) analysis was applied to understand the functions of 14 selected DEGs using the R package clusterProfiler (30). We then constructed a protein–protein interaction (PPI) network using the STRING database (33). Next, we analyzed the Spearman's correlation of gene–gene, gene–ESTIMATE, and gene–ssGSEA using the R package corrplot.

Specimen Collection and Real-Time Quantitative PCR

Twelve pairs of CRC tissues and their adjacent tissues were collected from the First Hospital of China Medical University with informed consent and approval from the Institutional Ethics Board of the First Hospital of China Medical University.

Total RNA was extracted using TRIzol reagent (Invitrogen). cDNA was synthesized using the PrimeScript RT Reagent Kit (TaKaRa). The SYBR Prime Script RT-PCR kit (TaKaRa) was used to perform RT-qPCR according to the manufacturer's protocol.

The primer sequences were as follows: ALKBH5-F, 5′-CGGC GAAGGCTACACTTACG-3′; ALKLBH5-R, 5′-CCACCAGCTT TTGGATCACCA-3′; YTHDF1-F, 5′-ACCTGTCCAGCTAT TACCCG-3′; YTHDF1-R, 5′-TGGTGAGGTATGGAATCG GAG-3′; GAPDH-F, 5′-CGGATTTGGTCGTATTGGG-3′; GAPDH-R, 5′-CTGGAAGATGGTGATGGGATT-3′.

Statistical Analysis

All statistical analyses were conducted by R (4.0.2) and SPSS (25.0) software. Figure panels were pieced together by Adobe Illustrator (CC 2019). Box plot analyses were performed using the Wilcoxon rank-sum test. Correlation analysis was performed using the Spearman's coefficient. Chi-square test was used to compare the clinical characteristics between the two clusters (Fisher's exact test was used when required). Multivariate logistic regression analysis was used to evaluate the clinical characteristics affecting the clusters. Survival curves were constructed using the Kaplan–Meier method (log-rank test). All hypothetical tests were two-sided, and a P value <0.05 was considered significant.

RESULTS

Identification of Immune-Related m6A Regulators and Consensus Clustering of Patients

First, we calculated four indices of ESTIMATE in each sample to assess the fractions of stromal and immune cells. In order to explore the role of m6A modification in tumor immunity of patients with COAD, 21 m6A regulators were identified, and correlation between the expression of m6A regulators and results of ESTIMATE was evaluated (**Figure 1A**). Considering the highest absolute value of correlation with immune score, ALKBH5 and YTHDF1 were included in subsequent analyses. Next, Wilcoxon rank-sum test was conducted between tumor and normal tissues using RNA-seq data of TCGA-COAD; the tumor tissues were found to have lower ALKBH5 expression and higher YTHDF1 expression than normal tissues (**Figures 1B, C**). We thereafter performed a consensus clustering on 435 TCGA-COAD samples according to the expression matrix of ALKBH5 and YTHDF1, and divided the samples into two clusters (**Figure 1D** and **Supplementary Figure 1**). The heatmap shows Cluster 1 (n = 217) to have low expression of ALKBH5 and high expression of YTHDF1 while Cluster 2 (n = 218) had low expression of YTHDF1 and high expression of ALKBH5. Since the two genes showed opposite trends in the two clusters, Spearman's correlation between ALKBH5 and YTHDF1 was investigated, and a weak, negative correlation (R = −0.30, P = 1.34e-10) was found (**Figure 1E**). To understand the features of the two clusters better, we evaluated the CMS of each sample and drew a Sankey diagram to indicate their relationship (**Supplementary Figure 2**).

Evaluation of Clinical Characteristics

To identify the differences in clinical characteristics between the two clusters, we drew a survival curve first, and found no significant difference in prognosis between the two clusters

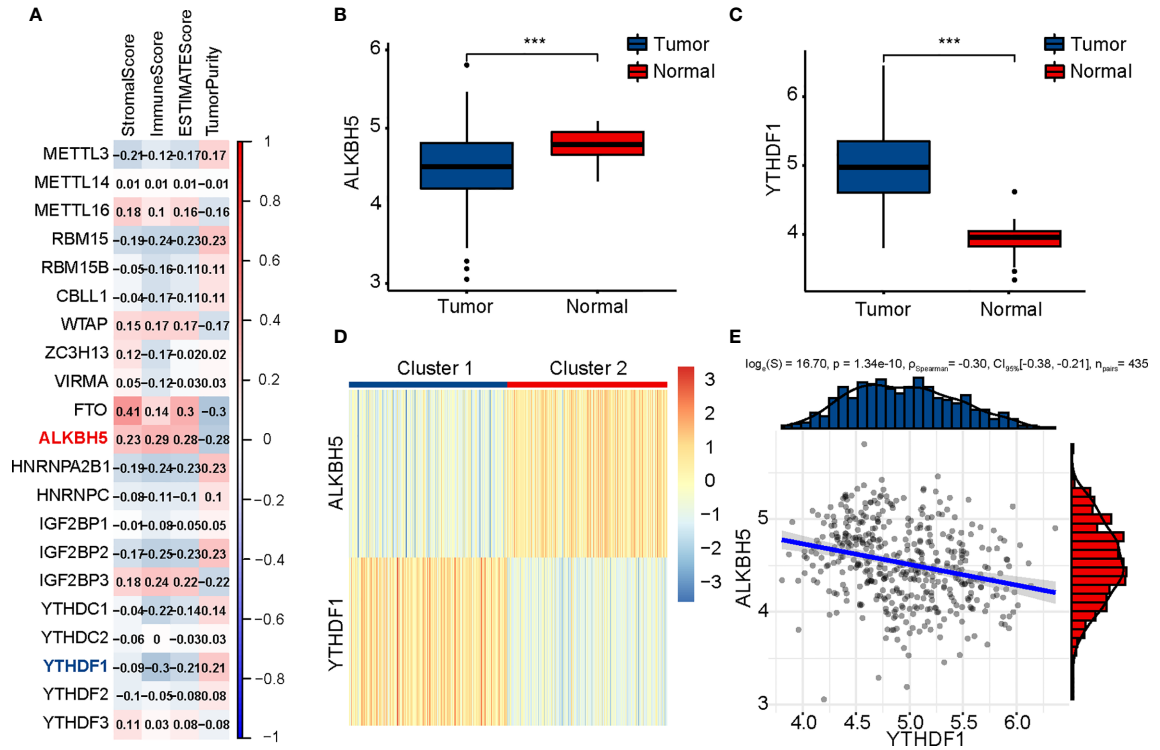

FIGURE 1 | Identification of m6A regulators related to immune score and clustering of TCGA-COAD patients based on ALKBH5 and YTHDF1. **(A)** Association between m6A regulators and results of ESTIMATE. **(B)** Comparison of ALKBH5 expression between tumor and normal tissues. **(C)** Comparison of YTHDF1 expression between tumor and normal tissues. **(D)** TCGA-COAD patients are divided into two clusters according to ALKBH5 and YTHDF1. **(E)** Association between ALKBH5 and YTHDF1 expression. The P values are labeled using asterisks (***P < 0.001).

(**Supplementary Figure 3**). Associated analysis showed Cluster 1 to have higher N stage, higher pathological stage, and lesser age than Cluster 2 (**Table 1**). Moreover, multivariate logistic regression analysis showed age, T stage, and N stage to be independent factors affecting clustering (**Table 2**).

Identification of Immune-Related Pathways by GSEA

GSEA was performed to understand the functional differences between the two clusters. All differentially expressed genes (Cluster 2 *vs.* Cluster 1) were included in the GSEA. We identified many significant pathways related to immunity in the enrichment of MSigDB Collection (c5.cp.v7.0.symbols.gmt), including adaptive immune response, cell killing, humoral immune response, positive regulation of cytokine production, T cell activation, and T cell proliferation (**Figure 2A**).

Comparison of Immune Infiltration

ESTIMATE, CIBERSORT, and ssGSEA were performed to understand the differences in immunological function better. Cluster 2 had higher stromal, immune, and ESTIMATE scores, and lower tumor purity than Cluster 1 in the ESTIMATE analysis (**Figures 2B–E**). Furthermore, CIBERSORT analysis demonstrated that Cluster 2 to have a higher proportion of CD8 T cells (**Figure 2F**). ssGSEA showed 25 immune cell subtypes (such as activated B cells, activated CD4 T cells, activated CD8 T cells, activated dendritic cells, natural killer

TABLE 1 | Clinical features of two clusters.

	Cluster 1	Cluster 2	P value
Number	217	218	
Age (median [IQR])	66.00 [56.00, 75.00]	71.00 [61.00, 80.00]	<0.001
Gender (%)			0.312
female	97 (44.7)	109 (50.0)	
male	120 (55.3)	109 (50.0)	
T stage (%)			0.42
T1	5 (2.3)	5 (2.3)	
T2	40 (18.4)	34 (15.6)	
T3	151 (69.6)	147 (67.4)	
T4	21 (9.7)	32 (14.7)	
N stage (%)			0.029
N0	114 (52.5)	141 (64.7)	
N1	60 (27.6)	41 (18.8)	
N2	43 (19.8)	36 (16.5)	
M stage (%)			0.098
M0	157 (80.5)	170 (87.2)	
M1	38 (19.5)	25 (12.8)	
Pathological stage (%)			0.033
Stage I	36 (16.6)	38 (17.4)	
Stage II	73 (33.6)	100 (45.9)	
Stage III	70 (32.3)	55 (25.2)	
Stage IV	38 (17.5)	25 (11.5)	

TABLE 2 | Multivariate Logistic Regression for clustering (Cluster 2 *vs*. Cluster 1).

Variables	Multivariate Logistic Regression	
	Odds Ratio (95% Confidence Interval)	P value
age	1.02 (1.01–1.04)	0.0032
T stage		0.0705
T2 *vs*. T1	0.46 (0.11–1.91)	0.2828
T3 *vs*. T1	0.35 (0.16–0.77)	0.0088
T4 *vs*. T1	0.50 (0.27–0.93)	0.028
N stage		0.0129
N1 *vs*. N0	1.72 (0.99–2.98)	0.0525
N2 *vs*. N0	0.86 (0.47–1.58)	0.6212

cells, and natural killer T cells) to be highly expressed in Cluster 2 (**Figure 2G**). A heatmap was prepared to show the overall conditions of the 28 immune cell subtypes in the two clusters (**Supplementary Figure 4**). Results indicated that Cluster 2 tended to have a stronger immune infiltration than Cluster 1, especially regarding CD8 T cells.

Evaluation of Sensitivity to Immunotherapy

To evaluate the sensitivity of patients with COAD to immunotherapy, we identified some targets of immunomodulatory drugs in clinical trials for metastatic colorectal cancer.

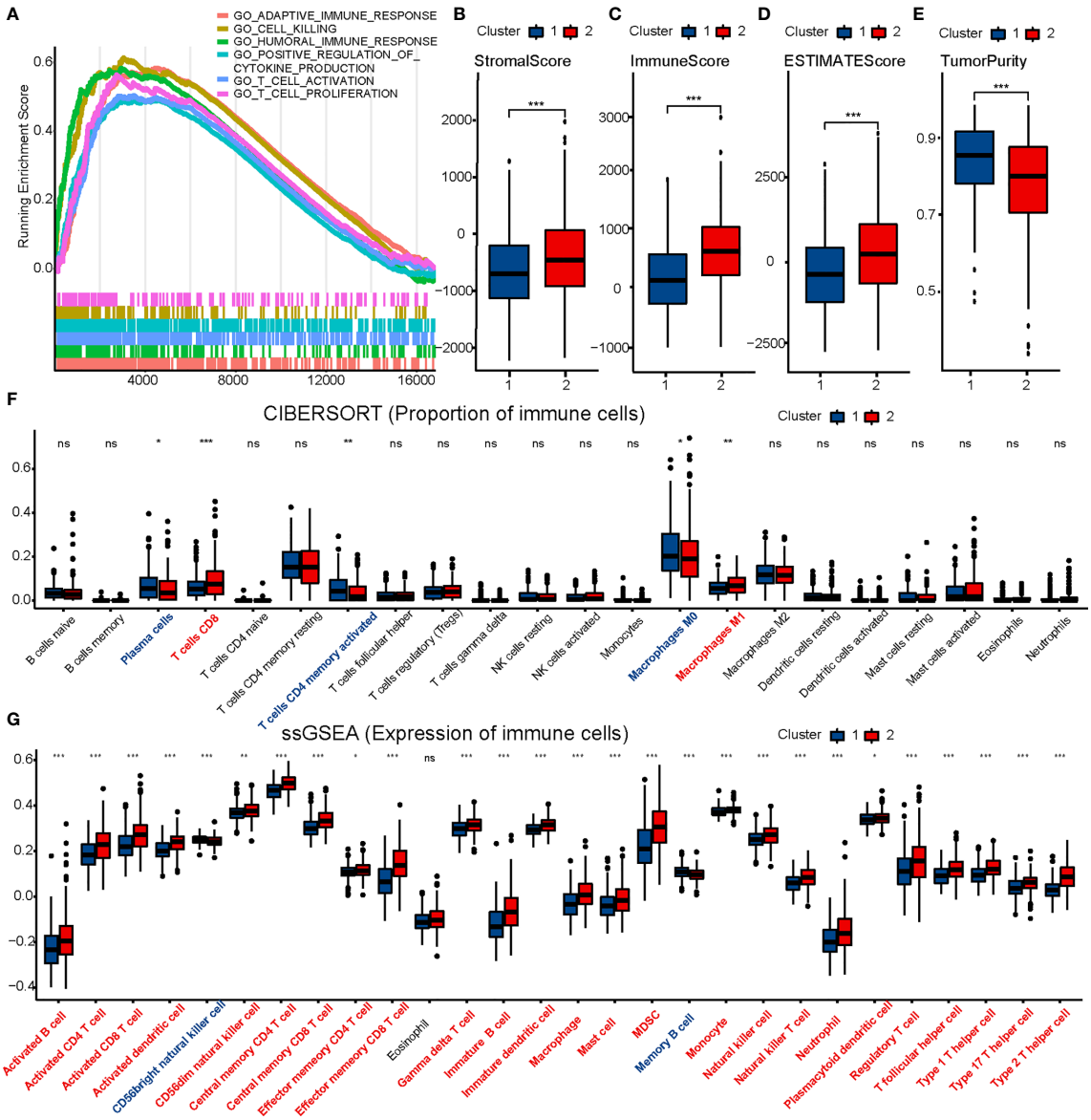

FIGURE 2 | Comparison of immune characteristics between two clusters. Comparison of functional enrichment **(A)**, stromal score **(B)**, immune score **(C)**, ESTIMATE score **(D)**, tumor purity **(E)**, proportion of immune cells **(F)** and expression of immune cells **(G)** between two clusters. The P values are labeled using asterisks (ns, no significance, *P < 0.05, **P < 0.01, ***P < 0.001).

We then compared the expression of these immunomodulatory targets between the two clusters and found most of the immunomodulatory targets (PD1, PDL1, PDL2, CTLA4, CD80, CD86, LAG3, TIM3, TIGHT, OX40, GITR, 4-1BB, ICOS, CD27, and CD70) to be expressed significantly higher in Cluster 2 (**Figures 3A–D**). The results suggested that Cluster 2 may show better response to immunotherapy than Cluster 1.

Comparison of Genetic Mutation

Different genetic mutations can influence the efficacy of immunotherapy differently; therefore, we evaluated the mutational conditions in COAD. Landscapes of mutation profiles between the two clusters are shown in **Figures 4A, B**. Cluster 2 had higher TMB and more numbers of MLH1, MSH2, MSH6, PMS2, POLE, and POLD1 mutations than Cluster 1 (**Figures 4C, D**), which once again indicated that the effect of immunotherapy may be better in Cluster 2.

WGCNA and Identification of Hub Genes Related With m6A and Immunity

We obtained 978 DEGs (721 upregulated and 257 downregulated) between the two clusters, and results were visualized using a volcano plot (**Figure 5A**). The genes were then considered for the WGCNA (**Figures 5B, C**). To identify a module related to both m6A and immunity, we performed a correlation between modules and traits (**Figure 5D**). The blue module was selected owing to its correlation with m6A (R = 0.32, P = 6e-12) and immunity (R = 0.85, P = 3e-124). Thereafter, we obtained 14 hub genes (WARS, SLC2A5, UBASH3B, NKG7, GNLY, GZMH, LAG3, GZMA, HAPLN3, CTSW, PDCD1, CCL4, RARRES3, and KIR2DL4) from the blue module based on MM >0.7 and GS >0.25 (**Figure 5E**).

Functional Enrichment of Hub Genes and Their Correlation With Immune Infiltration

To determine the biochemical functions of the 14 hub genes, we performed a GO enrichment analysis (**Figure 6A**). The most significant GO term was negative regulation of immune system. We also conducted PPI analysis and checked correlations across the genes (**Figures 6B, C**). Spearman's correlation analysis between genes and immune infiltration (ESTIMATE and ssGSEA) showed most of the genes to be significantly correlated with immunity (**Figures 6D, E**).

GEO Validation of Immune Characteristics Between Two Clusters

First, we divided 566 colon cancer samples from GSE39582 into two clusters in the same way as performed in TCGA (**Figure 7A**) and found the distribution of ALKBH5 and YTHDF1 expression in the two clusters to be quite similar to that in TCGA. We also calculated the Spearman's correlation coefficient for ALKBH5 and YTHDF1 (R = −0.36, P = 1.24e-18) (**Figure 7B**).

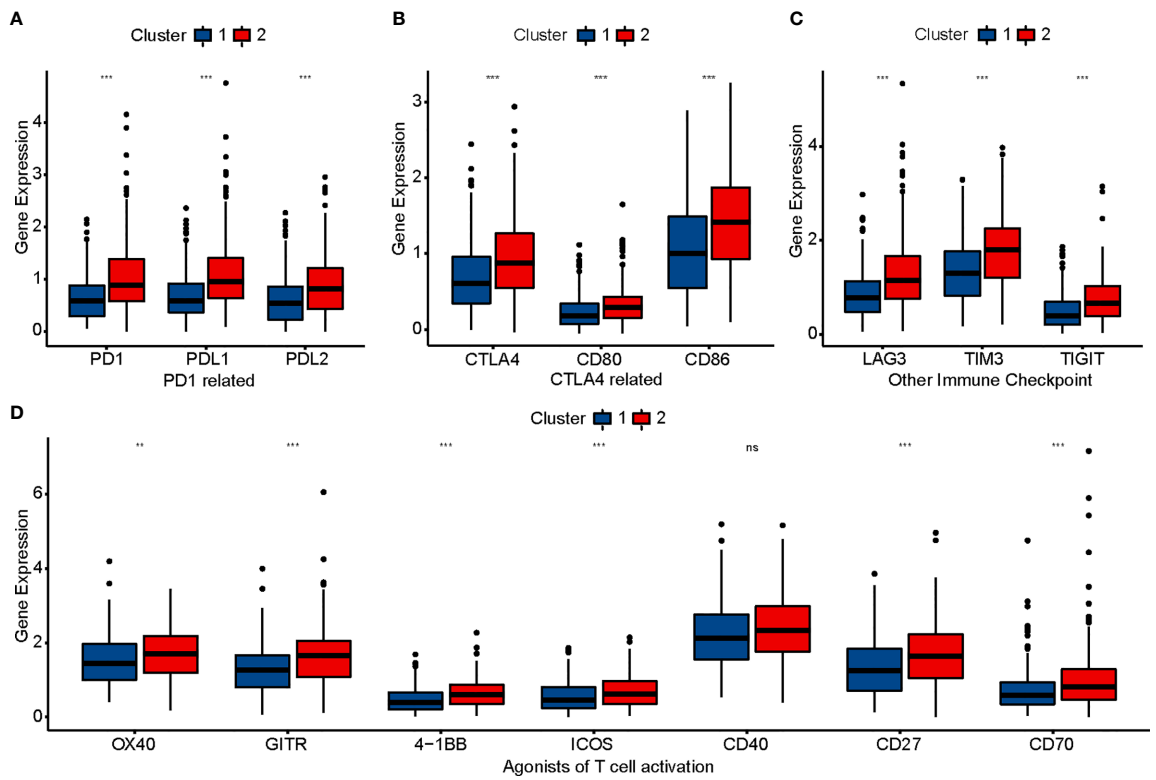

FIGURE 3 | Comparison of immunomodulatory drugs' targets in clinical trials for metastatic colorectal cancer between two clusters. The P values are labeled using asterisks (ns, no significance, **P < 0.01, ***P < 0.001).

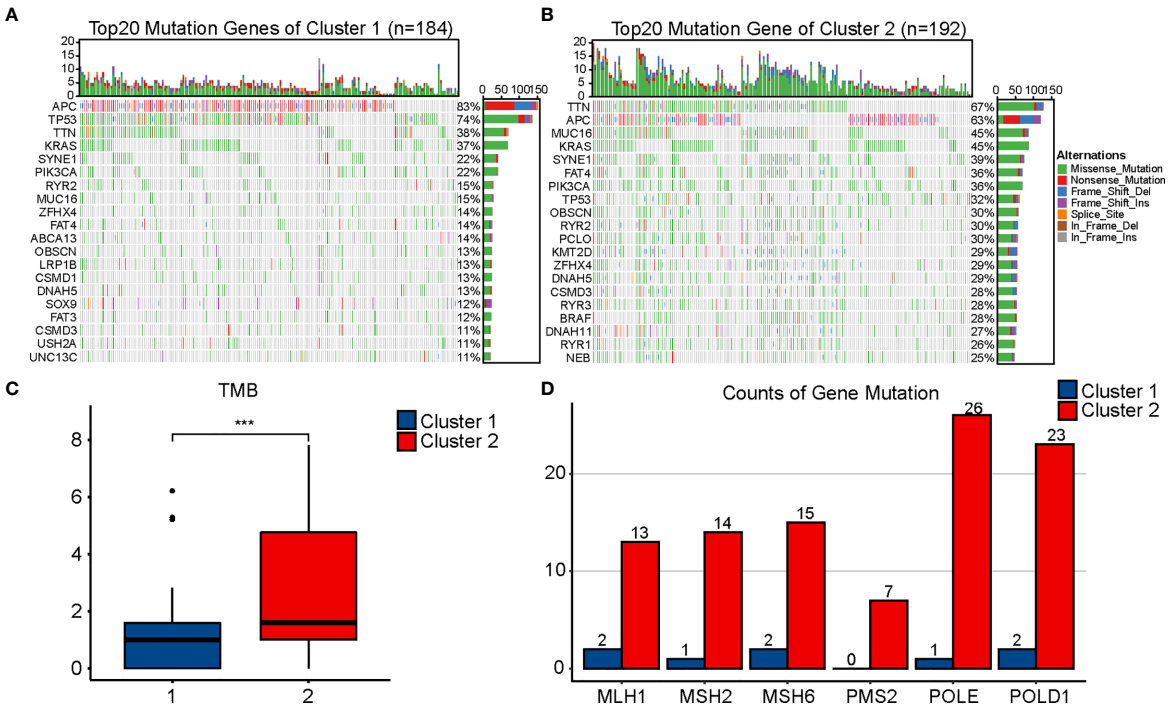

FIGURE 4 | Comparison of mutational landscapes between two clusters. Mutational landscape of Cluster 1 **(A)** and Cluster 2 **(B)**. **(C)** Comparison of tumor mutation burden (TMB) between two clusters. **(D)** Comparison of gene mutation related to mismatch repair and POLE proofreading domain between two clusters. The P values are labeled using asterisks (***P < 0.001).

The expression of immunomodulatory targets and extent of immune infiltration (ESTIMATE, CIBERSORT, and ssGSEA) were evaluated in the same manner (**Figures 7C–L**). Cluster 2 was clearly more active regarding the immune system than Cluster 1.

Verification of Expression Levels of ALKBH5 and YTHDF1 in CRC and Adjacent Tissues

We tested the expression levels of ALKBH5 and YTHDF1 in 12 CRC tissues and paired adjacent tissues using RT-qPCR. Results indicated CRC tissues to have lower expression of ALKBH5 and higher expression of YTHDF1 than the paired adjacent tissues (**Figure 8**).

DISCUSSION

ALKBH5 is expressed at low levels in colon cancer; its overexpression inhibits cell metastasis *in vivo* and cell invasion *in vitro*, thus suggesting it as a tumor suppressor (34). A recent study has reported that the expression and function of ALKBH5 in different types of cancer are variable (35). Although ALKBH5 has been proven to correlate with the response to anti-PD1 therapy in melanoma, the association between ALKBH5 expression and response to immunotherapy in patients with COAD still remains unclear (15). YTHDF1 is highly expressed and enhances stem cell-like activity in CRC (36). The high expression of YTHDF1 could lead to low immune cell abundance, since high stemness indices represent a low immune cell fraction and low PD-L1 expression (37). The expression of ALKBH5 and YTHDF1 in patients with COAD in our study was consistent with those in previous studies. In addition, we found a negative correlation between ALKBH5 and YTHDF1, suggesting that their functions may have a cross-talk or interaction upon m6A modification. A previous study had reported that ALKBH5 suppresses tumor progression in non-small cell lung cancer in a YTHDF1-dependent manner (38). Moreover, their relevance to the immune score in the ESTIMATE analysis was just the opposite. Therefore, both ALKBH5 and YTHDF1 may participate in the regulation of m6A modification, which can in turn influence immune infiltration and response to immunotherapy in patients with COAD.

We applied consensus clustering to divide patients with COAD from TCGA into two clusters: Cluster 1 (ALKBH5: low expression; YTHDF1: high expression) and Cluster 2 (ALKBH5: high expression; YTHDF1: low expression). Moreover, we investigated the relationship between the two clusters and the CMS. We found CMS2 to be mostly classified into Cluster 1, whereas CMS1 and CMS3 were mostly classified into Cluster 2. There was no difference in CMS4. CMS1 represented microsatellite instability immune type with hypermutation,

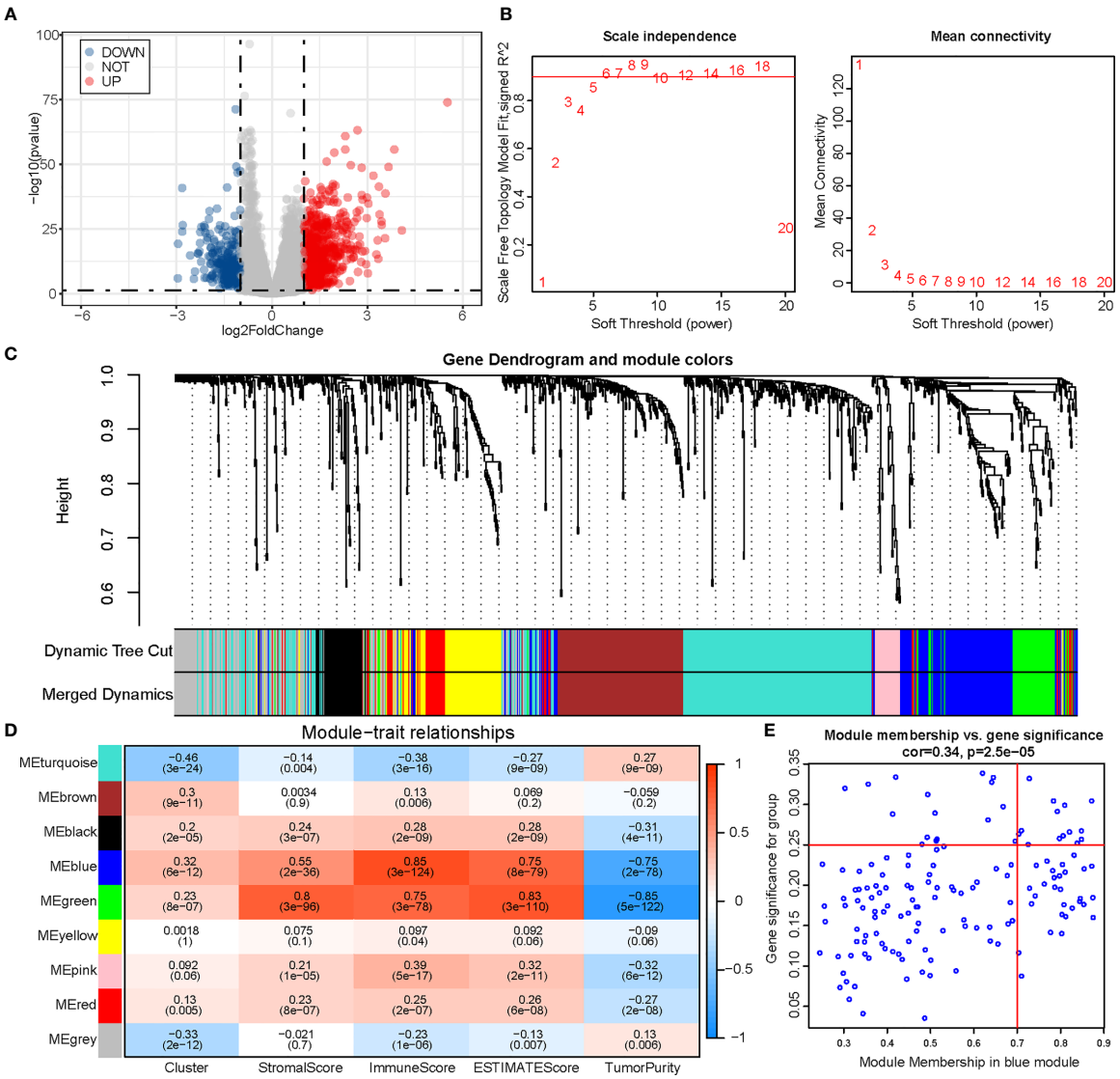

FIGURE 5 | Identification of module genes associated with both clustering and immunity in the WGCNA. **(A)** Volcano plot of differential analysis. **(B)** Analysis of network topology for soft powers. **(C)** Gene dendrogram and module colors. **(D)** Heatmap between module eigengenes and cluster, ESTIMATE results. **(E)** Scatter plot of module eigengenes in the blue module.

MSI, and strong immune activation; CMS2 represented canonical type with remarkable WNT and MYC activation; CMS3 represented metabolic type with epithelial and evident metabolic dysregulation (29). From the perspective of CMS, we inferred Cluster 2 to possibly possess more immune infiltration than Cluster 1. We then evaluated their clinical characteristics and discovered Cluster 1 to have a higher N stage than Cluster 2, which may have resulted from the inhibition of metastasis by ALKBH5.

To further investigate the functional differences between the two clusters, we used TCGA-COAD data for GSEA and found some immune-related pathways, such as adaptive immune response, cell killing, cytokine production, and T cell activation to be enriched in Cluster 2. This suggested that Cluster 2 may act more actively in immune response than Cluster 1.

Next, we compared the immune characteristics of the two clusters using the ESTIMATE, CIBERSORT, and ssGSEA methods. In the ESTIMATE analysis, Cluster 2 was proven to possess higher stromal, immune, and ESTIMATE scores than Cluster 1, thereby implying that Cluster 2 had a vibrant tumor immune microenvironment. In the CIBERSORT analysis, we found the proportion of CD8 T cells and M1 subtype macrophages to be significantly elevated in Cluster 2. Previous studies had demonstrated CD8 T cells to have the strongest effect on patient prognosis in most tumor-infiltrating immune cell subtypes (39). In the ssGSEA analysis, 25 immune cell subtypes showed significantly higher expression in Cluster 2, including

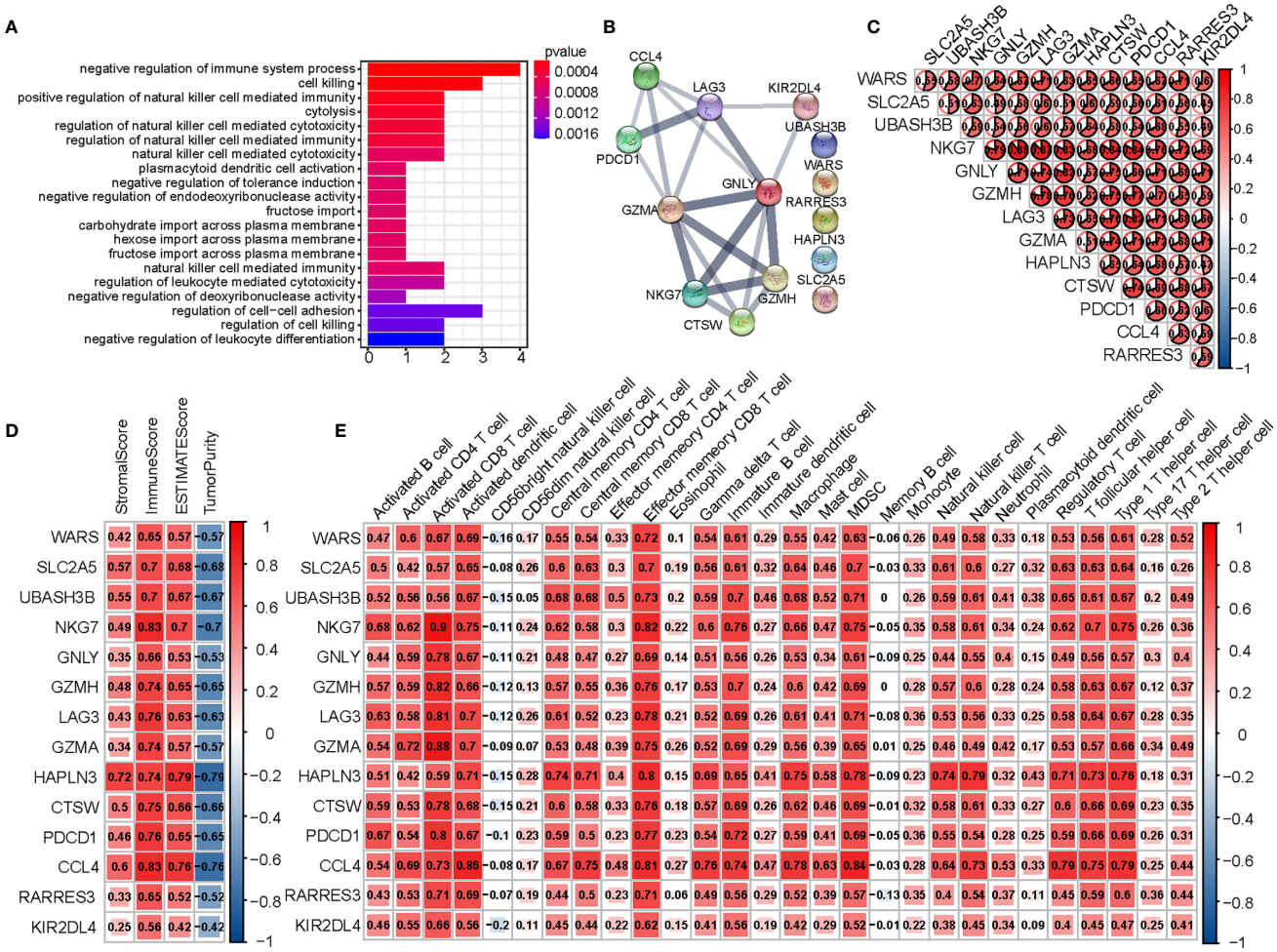

FIGURE 6 | Analysis of 14 hub genes. **(A)** The GO analysis of hub genes. **(B)** PPI network of hub genes. **(C)** Correlation between hub genes. **(D)** Correlation between hub genes and results of ESTIMATE. **(E)** Correlation between hub genes and expression of immune cells (ssGSEA).

CD8 T cells, T helper cells (CD4), dendritic cells (DCs), natural killer (NK) cells, natural killer T (NKT) cells, and macrophages. Tumor-infiltrating T cells have a major impact on the clinical attributes of CRC. High infiltration of CD8 T cells can predict the response to drugs and improve survival in patients with CRC and hepatic metastases (40). A previous study had illustrated that patients with high expression of Th1 have a prolonged prognosis, whereas those with high expression of Th17 have poor prognosis in CRC. In addition, the effect of Th1 seemed to surpass the effect of Th17 on survival (41). DCs have been reported as key antigen-presenting cells that promote anti-tumor immunity by activating T cells (42). Moreover, conventional type 1 dendritic cells are known to be recruited into the tumor microenvironment following stimulation by NK cells (43). The latter have cytotoxic capacity in anti-tumor immunity, and their extensive infiltration leads to a favorable outcome in CRC (44). NKT cells could reinvigorate the exhausted CD8 T cells in an anti-PD-1-resistant tumor model, hence playing a pivotal role in anti-tumor immunity (45). A previous study had shown that high NKT cell infiltration to be an independent favorable prognostic factor in CRC (46). Macrophages are conventionally divided into M1 (proinflammatory; anti-tumor) and M2 (anti-inflammatory; tumor-promoting) subtypes. According to the results of CIBERSORT analysis, Cluster 2 had a higher proportion of M1 subtype macrophages than Cluster 1, which suggested that Cluster 2 could easily achieve anti-tumor Th1-type responses while Cluster 1 tended to establish a tolerogenic microenvironment (47). Based on our study of immune contexture, Cluster 2 had more extensive immune cell infiltration than Cluster 1. Therefore, Cluster 2 may have more immunological competence and be more likely to benefit from immunotherapy.

Previous studies reported that programmed cell death 1 (PD1), programmed cell death 1 ligand 1 (PDL1), and cytotoxic T lymphocyte antigen 4 (CTLA4) are approved as targets of immune checkpoint inhibitors (ICIs) by the FDA (48). In addition, lymphocyte activation gene-3 (LAG3), T cell immunoglobulin-3 (TIM3), and T cell immunoglobulin and

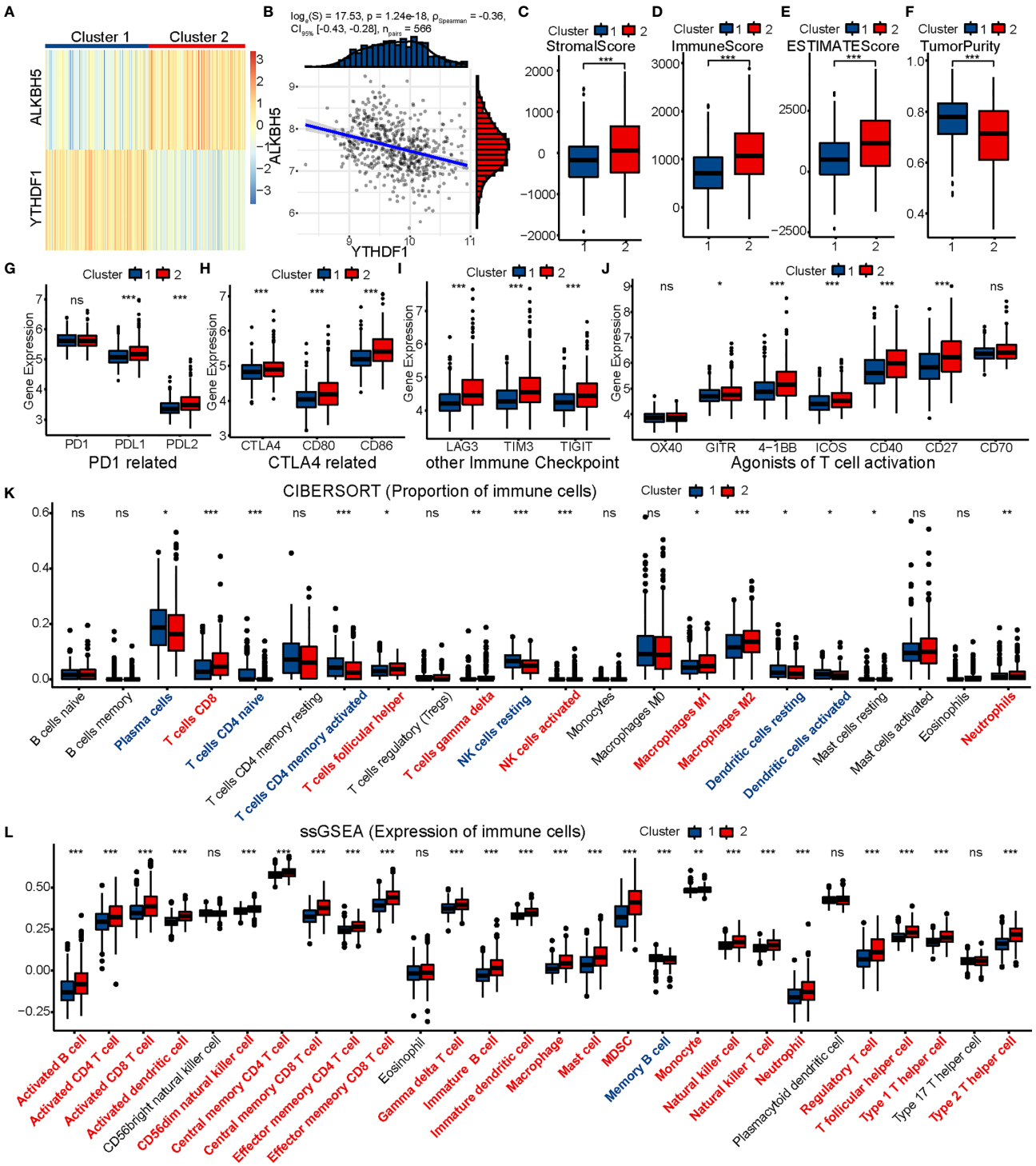

FIGURE 7 | GSE39582 validation of immune contexture between two clusters. **(A)** GSE39582 patients are divided into two clusters according to ALKBH5 and YTHDF1. **(B)** Association between ALKBH5 and YTHDF1 expression in GSE39582. **(C–K)** Comparison of stromal score **(C)**, immune score **(D)**, ESTIMATE score **(E)**, tumor purity **(F)**, targets of immunomodulatory drugs **(G–J)**, proportion of immune cells **(K)** and expression of immune cells **(L)** between two clusters. The P values are labeled using asterisks (ns, no significance, *P < 0.05, **P < 0.01, ***P < 0.001).

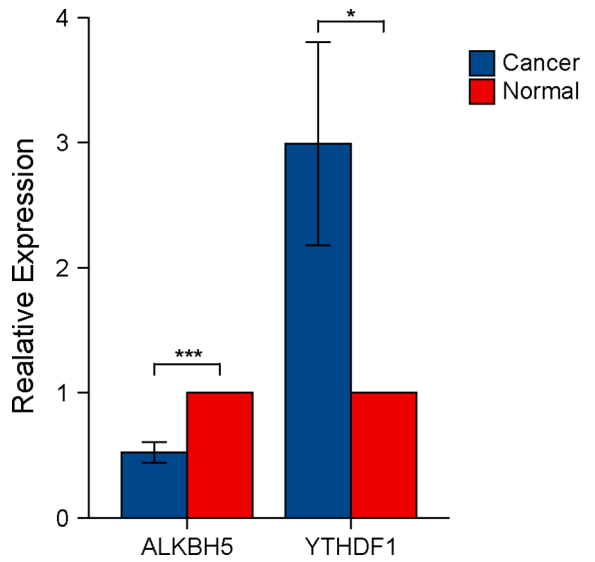

FIGURE 8 | Verification of ALKBH5 and YTHDF1 expression in CRC tissues using RT-qPCR. The P values are labeled using asterisks (ns, no significance, *P < 0.05, ***P < 0.001).

ITIM domain (TIGIT) are regarded as co-inhibitory receptor targets (49). In this study, we compared two clusters of immunomodulatory drugs, which have been included in clinical trials for metastatic CRC (48). Most of these targets were found to be significantly high in expression in Cluster 2.

Next, we analyzed the mutational landscapes of the two clusters, and found a remarkable difference between them. We found Cluster 2 to have more TMB than Cluster 1. TMB may affect the generation of immunogenic peptides and thereby influence the response to immunotherapy (50). Furthermore, CRC can be categorized into two groups based on microsatellite instability (MSI) and mismatch repair (MMR), namely dMMR-MSI-H and pMMR-MSI-L. The signature of dMMR-MSI-H in patients with CRC is a specific biomarker for evaluating the response to immunotherapy. In addition to the hypermutation caused by dMMR-MSI-H, POLE proofreading domain mutation also leads to a remarkable hypermutation, which may result in excellent prognosis (48). Our study suggested that Cluster 2 possesses a higher mutation rate of MMR-related genes (MLH1, MSH2, MSH6, and PMS2) and POLE/POLD1 than Cluster 1, hence implying that Cluster 2 would show better effect of immunotherapy.

We next performed WGCNA to identify the blue module that differed between the two clusters in relation to both ALKBH5/YTHDF1 and immune score. Based on MM and GS, we obtained 14 genes from this module, including PD1 (PDCD1) and LAG3. An explicit synergistic interaction between PD1 and LAG3 has already been reported, and they have been shown to mediate T cell exhaustion together (51); this probably occurs in Cluster 2. Therefore, we speculated that Cluster 2 could acquire a better response to immunotherapy than Cluster 1 by evaluating the extent of infiltration extent of immune cells, expression of ICIs, and mutational burden; this difference might result from m6A modification mediated by ALKBH5 and YTHDF1.

Based on the immunological features, Cluster 2 was considered to have a hot tumor, whereas Cluster 1 tended to be have a cold tumor (52). Since our RT-qPCR results verified the expression of ALKBH5 and YTHDF1 in 12 pairs of cancer and normal tissues, we inferred Cluster 1 to represent the overall immunological characteristics of COAD, thus showing poor immune response. ALKBH5 and YTHDF1 could possibly play a potential role in the transformation of cold to hot tumor in COAD.

Although the comprehensive analysis improved our understanding of the relationship between ALKBH5/YTHDF1 and immunity, and we used 566 patients with GSE39582 as the external validation set, there are still some limitations in the current study. First, it was a retrospective study. Therefore, a prospective study should be conducted in future in order to avoid analysis bias associated with retrospective studies. Moreover, the study was performed based on TCGA and GEO; we could not illustrate the expression of ALKBH5 and YTHDF1 from the protein level or demonstrate the direct mechanisms of ALKBH5/YTHDF1 in anti-tumor immunity. So further studies to unravel the direct mechanisms should be performed.

CONCLUSION

By clustering patients of TCGA-COAD and GSE39582 based on the expression of ALKBH5 and YTHDF1, we demonstrated Cluster 2 (ALKBH5: highly expressed; YTHDF1: lowly expressed) to have more infiltration of immune cells, expression of ICI targets, TMB, and proportion of dMMR-MSI-H than Cluster 1 (ALKBH5: lowly expressed; YTHDF1: highly expressed), thereby suggesting that Cluster 2 acquired better response to immunotherapy. Our findings illustrated that ALKBH5 and YTHDF1 have potential in tumor immunity and provided novel insights into the relationship between m6A modification and immunity.

DATA AVAILABILITY STATEMENT

The original contributions presented in the study are included in the article/**Supplementary Material**. Further inquiries can be directed to the corresponding authors.

ETHICS STATEMENT

The studies involving human participants were reviewed and approved by the institutional ethics board of the First Hospital of China Medical University. The patients/participants provided their written informed consent to participate in this study.

AUTHOR CONTRIBUTIONS

GY designed the study and wrote the manuscript. YA performed the literature search and collected data for the manuscript. BX analyzed the data. NW edited the figures and tables. MS and XS

revised the manuscript. All authors contributed to the article and approved the submitted version.

FUNDING

This work was supported by the National Natural Science Foundation of China (81670506).

ACKNOWLEDGMENTS

The authors thank the Department of Gastroenterology of First Hospital of China Medical University and the contributions from the TCGA and GEO network.

SUPPLEMENTARY MATERIAL

The Supplementary Material for this article can be found online at: https://www.frontiersin.org/articles/10.3389/fonc.2021.670490/full#supplementary-material

Supplementary Figure 1 | Heatmap corresponding to the consensus matrix for k = 2 using consensus clustering.

Supplementary Figure 2 | Relationship between the two clusters and the consensus molecular subtypes (CMS).

Supplementary Figure 3 | Survival analysis of 2 clusters.

Supplementary Figure 4 | Heatmap shows overall condition of 28 immune cells subtypes between 2 clusters.

REFERENCES

1. Sung H, Ferlay J, Siegel RL, Laversanne M, Soerjomataram I, Jemal A, et al. Global Cancer Statistics 2020: GLOBOCAN Estimates of Incidence and Mortality Worldwide for 36 Cancers in 185 Countries. *CA Cancer J Clin* (2021) 0:1–41. doi: 10.3322/caac.21660
2. Lombardi L, Morelli F, Cinieri S, Santini D, Silvestris N, Fazio N, et al. Adjuvant Colon Cancer Chemotherapy: Where We Are and Where We'll Go. *Cancer Treat Rev* (2010) 36 Suppl 3:S34–41. doi: 10.1016/S0305-7372(10)70018-9
3. Mattiuzzi C, Sanchis-Gomar F, Lippi G. Concise Update on Colorectal Cancer Epidemiology. *Ann Transl Med* (2019) 7(21):609. doi: 10.21037/atm.2019.07.91
4. Mutch MG. Molecular Profiling and Risk Stratification of Adenocarcinoma of the Colon. *J Surg Oncol* (2007) 96(8):693–703. doi: 10.1002/jso.20915
5. Riaz N, Morris L, Havel JJ, Makarov V, Desrichard A, Chan TA. The Role of Neoantigens in Response to Immune Checkpoint Blockade. *Int Immunol* (2016) 28(8):411–9. doi: 10.1093/intimm/dxw019
6. Chalabi M, Fanchi LF, Dijkstra KK, Van den Berg JG, Aalbers AG, Sikorska K, et al. Neoadjuvant Immunotherapy Leads to Pathological Responses in MMR-proficient and MMR-deficient Early-Stage Colon Cancers. *Nat Med* (2020) 26(4):566–76. doi: 10.1038/s41591-020-0805-8
7. Diaz LAJr, Le DT. PD-1 Blockade in Tumors With Mismatch-Repair Deficiency. *N Engl J Med* (2015) 373(20):1979. doi: 10.1056/NEJMc1510353
8. Yang D, Qiao J, Wang G, Lan Y, Li G, Guo X, et al. N6-Methyladenosine Modification of lincRNA 1281 is Critically Required for mESC Differentiation Potential. *Nucleic Acids Res* (2018) 46(8):3906–20. doi: 10.1093/nar/gky130
9. Zhou C, Molinie B, Daneshvar K, Pondick JV, Wang J, Van Wittenberghe N, et al. Genome-Wide Maps of m6A CircRNAs Identify Widespread and Cell-Type-Specific Methylation Patterns That Are Distinct From Mrnas. *Cell Rep* (2017) 20(9):2262–76. doi: 10.1016/j.celrep.2017.08.027
10. Alarcon CR, Lee H, Goodarzi H, Halberg N, Tavazoie SF. N6-Methyladenosine Marks Primary microRNAs for Processing. *Nature* (2015) 519(7544):482–5. doi: 10.1038/nature14281
11. Desrosiers R, Friderici K, Rottman F. Identification of Methylated Nucleosides in Messenger RNA From Novikoff Hepatoma Cells. *Proc Natl Acad Sci USA* (1974) 71(10):3971–5. doi: 10.1073/pnas.71.10.3971
12. Nombela P, Miguel-Lopez B, Blanco S. The Role of M(6)a, M(5)C and Psi RNA Modifications in Cancer: Novel Therapeutic Opportunities. *Mol Cancer* (2021) 20(1):18. doi: 10.1186/s12943-020-01263-w
13. Huang H, Weng H, Chen J. M(6)a Modification in Coding and Non-coding RNAs: Roles and Therapeutic Implications in Cancer. *Cancer Cell* (2020) 37(3):270–88. doi: 10.1016/j.ccell.2020.02.004
14. Zheng G, Dahl JA, Niu Y, Fedorcsak P, Huang CM, Li CJ, et al. ALKBH5 is a Mammalian RNA Demethylase That Impacts RNA Metabolism and Mouse Fertility. *Mol Cell* (2013) 49(1):18–29. doi: 10.1016/j.molcel.2012.10.015
15. Li N, Kang Y, Wang L, Huff S, Tang R, Hui H, et al. ALKBH5 Regulates anti-PD-1 Therapy Response by Modulating Lactate and Suppressive Immune Cell Accumulation in Tumor Microenvironment. *Proc Natl Acad Sci USA* (2020) 117(33):20159–70. doi: 10.1073/pnas.1918986117
16. Tang B, Yang Y, Kang M, Wang Y, Wang Y, Bi Y, et al. M(6)a Demethylase ALKBH5 Inhibits Pancreatic Cancer Tumorigenesis by Decreasing WIF-1 RNA Methylation and Mediating Wnt Signaling. *Mol Cancer* (2020) 19(1):3. doi: 10.1186/s12943-019-1128-6
17. Wang X, Lu Z, Gomez A, Hon GC, Yue Y, Han D, et al. N6-Methyladenosine-Dependent Regulation of Messenger RNA Stability. *Nature* (2014) 505(7481):117–20. doi: 10.1038/nature12730
18. Han D, Liu J, Chen C, Dong L, Liu Y, Chang R, et al. Anti-Tumour Immunity Controlled Through mRNA M(6)a Methylation and YTHDF1 in Dendritic Cells. *Nature* (2019) 566(7743):270–4. doi: 10.1038/s41586-019-0916-x
19. Colaprico A, Silva TC, Olsen C, Garofano L, Cava C, Garolini D, et al. TCGAbiolinks: An R/Bioconductor Package for Integrative Analysis of TCGA Data. *Nucleic Acids Res* (2016) 44(8):e71. doi: 10.1093/nar/gkv1507
20. Mayakonda A, Lin DC, Assenov Y, Plass C, Koeffler HP. Maftools: Efficient and Comprehensive Analysis of Somatic Variants in Cancer. *Genome Res* (2018) 28(11):1747–56. doi: 10.1101/gr.239244.118
21. Gu Z, Eils R, Schlesner M. Complex Heatmaps Reveal Patterns and Correlations in Multidimensional Genomic Data. *Bioinformatics* (2016) 32(18):2847–9. doi: 10.1093/bioinformatics/btw313
22. Marisa L, de Reynies A, Duval A, Selves J, Gaub MP, Vescovo L, et al. Gene Expression Classification of Colon Cancer Into Molecular Subtypes: Characterization, Validation, and Prognostic Value. *PLoS Med* (2013) 10(5):e1001453. doi: 10.1371/journal.pmed.1001453
23. Yoshihara K, Shahmoradgoli M, Martinez E, Vegesna R, Kim H, Torres-Garcia W, et al. Inferring Tumour Purity and Stromal and Immune Cell Admixture From Expression Data. *Nat Commun* (2013) 4:2612. doi: 10.1038/ncomms3612
24. Newman AM, Liu CL, Green MR, Gentles AJ, Feng W, Xu Y, et al. Robust Enumeration of Cell Subsets From Tissue Expression Profiles. *Nat Methods* (2015) 12(5):453–7. doi: 10.1038/nmeth.3337
25. Hanzelmann S, Castelo R, Guinney J. GSVA: Gene Set Variation Analysis for Microarray and RNA-seq Data. *BMC Bioinformatics* (2013) 14:7. doi: 10.1186/1471-2105-14-7
26. Bindea G, Mlecnik B, Tosolini M, Kirilovsky A, Waldner M, Obenauf AC, et al. Spatiotemporal Dynamics of Intratumoral Immune Cells Reveal the Immune Landscape in Human Cancer. *Immunity* (2013) 39(4):782–95. doi: 10.1016/j.immuni.2013.10.003
27. Wilkerson MD, Hayes DN. ConsensusClusterPlus: A Class Discovery Tool With Confidence Assessments and Item Tracking. *Bioinformatics* (2010) 26(12):1572–3. doi: 10.1093/bioinformatics/btq170
28. Eide PW, Bruun J, Lothe RA, Sveen A. CMScaller: An R Package for Consensus Molecular Subtyping of Colorectal Cancer Pre-Clinical Models. *Sci Rep* (2017) 7(1):16618. doi: 10.1038/s41598-017-16747-x
29. Guinney J, Dienstmann R, Wang X, de Reynies A, Schlicker A, Soneson C, et al. The Consensus Molecular Subtypes of Colorectal Cancer. *Nat Med* (2015) 21(11):1350–6. doi: 10.1038/nm.3967
30. Yu G, Wang LG, Han Y, He QY. clusterProfiler: An R Package for Comparing Biological Themes Among Gene Clusters. *OMICS* (2012) 16(5):284–7. doi: 10.1089/omi.2011.0118

31. Love MI, Huber W, Anders S. Moderated Estimation of Fold Change and Dispersion for RNA-seq Data With DESeq2. *Genome Biol* (2014) 15(12):550. doi: 10.1186/s13059-014-0550-8
32. Langfelder P, Horvath S. WGCNA: An R Package for Weighted Correlation Network Analysis. *BMC Bioinformatics* (2008) 9:559. doi: 10.1186/1471-2105-9-559
33. Szklarczyk D, Gable AL, Lyon D, Junge A, Wyder S, Huerta-Cepas J, et al. STRING v11: Protein-Protein Association Networks With Increased Coverage, Supporting Functional Discovery in Genome-Wide Experimental Datasets. *Nucleic Acids Res* (2019) 47(D1):D607–D13. doi: 10.1093/nar/gky1131
34. Yang P, Wang Q, Liu A, Zhu J, Feng J. ALKBH5 Holds Prognostic Values and Inhibits the Metastasis of Colon Cancer. *Pathol Oncol Res* (2020) 26(3):1615–23. doi: 10.1007/s12253-019-00737-7
35. Wang J, Wang J, Gu Q, Ma Y, Yang Y, Zhu J, et al. The Biological Function of m6A Demethylase ALKBH5 and its Role in Human Disease. *Cancer Cell Int* (2020) 20:347. doi: 10.1186/s12935-020-01450-1
36. Bai Y, Yang C, Wu R, Huang L, Song S, Li W, et al. YTHDF1 Regulates Tumorigenicity and Cancer Stem Cell-Like Activity in Human Colorectal Carcinoma. *Front Oncol* (2019) 9:332. doi: 10.3389/fonc.2019.00332
37. Malta TM, Sokolov A, Gentles AJ, Burzykowski T, Poisson L, Weinstein JN, et al. Machine Learning Identifies Stemness Features Associated With Oncogenic Dedifferentiation. *Cell* (2018) 173(2):338–54.e15. doi: 10.1016/j.cell.2018.03.034
38. Jin D, Guo J, Wu Y, Yang L, Wang X, Du J, et al. M(6)a Demethylase ALKBH5 Inhibits Tumor Growth and Metastasis by Reducing YTHDFs-mediated YAP Expression and Inhibiting Mir-107/LATS2-Mediated YAP Activity in NSCLC. *Mol Cancer* (2020) 19(1):40. doi: 10.1186/s12943-020-01161-1
39. Bruni D, Angell HK, Galon J. The Immune Contexture and Immunoscore in Cancer Prognosis and Therapeutic Efficacy. *Nat Rev Cancer* (2020) 20(11):662–80. doi: 10.1038/s41568-020-0285-7
40. Galon J, Costes A, Sanchez-Cabo F, Kirilovsky A, Mlecnik B, Lagorce-Pages C, et al. Type, Density, and Location of Immune Cells Within Human Colorectal Tumors Predict Clinical Outcome. *Science* (2006) 313(5795):1960–4. doi: 10.1126/science.1129139
41. Tosolini M, Kirilovsky A, Mlecnik B, Fredriksen T, Mauger S, Bindea G, et al. Clinical Impact of Different Classes of Infiltrating T Cytotoxic and Helper Cells (Th1, th2, Treg, th17) in Patients With Colorectal Cancer. *Cancer Res* (2011) 71(4):1263–71. doi: 10.1158/0008-5472.CAN-10-2907
42. Wculek SK, Cueto FJ, Mujal AM, Melero I, Krummel MF, Sancho D. Dendritic Cells in Cancer Immunology and Immunotherapy. *Nat Rev Immunol* (2020) 20(1):7–24. doi: 10.1038/s41577-019-0210-z
43. Bottcher JP, Bonavita E, Chakravarty P, Blees H, Cabeza-Cabrerizo M, Sammicheli S, et al. NK Cells Stimulate Recruitment of cDC1 Into the Tumor Microenvironment Promoting Cancer Immune Control. *Cell* (2018) 172(5):1022–37.e14. doi: 10.1016/j.cell.2018.01.004
44. Coca S, Perez-Piqueras J, Martinez D, Colmenarejo A, Saez MA, Vallejo C, et al. The Prognostic Significance of Intratumoral Natural Killer Cells in Patients With Colorectal Carcinoma. *Cancer* (1997) 79(12):2320–8. doi: 10.1002/(sici)1097-0142(19970615)79:12<2320::aid-cncr5>3.0.co;2-p
45. Bae EA, Seo H, Kim BS, Choi J, Jeon I, Shin KS, et al. Activation of NKT Cells in an Anti-PD-1-Resistant Tumor Model Enhances Antitumor Immunity by Reinvigorating Exhausted CD8 T Cells. *Cancer Res* (2018) 78(18):5315–26. doi: 10.1158/0008-5472.CAN-18-0734
46. Tachibana T, Onodera H, Tsuruyama T, Mori A, Nagayama S, Hiai H, et al. Increased Intratumor Valpha24-positive Natural Killer T Cells: A Prognostic Factor for Primary Colorectal Carcinomas. *Clin Cancer Res* (2005) 11(20):7322–7. doi: 10.1158/1078-0432.CCR-05-0877
47. Aras S, Zaidi MR. TAMeless Traitors: Macrophages in Cancer Progression and Metastasis. *Br J Cancer* (2017) 117(11):1583–91. doi: 10.1038/bjc.2017.356
48. Ganesh K, Stadler ZK, Cercek A, Mendelsohn RB, Shia J, Segal NH, et al. Immunotherapy in Colorectal Cancer: Rationale, Challenges and Potential. *Nat Rev Gastroenterol Hepatol* (2019) 16(6):361–75. doi: 10.1038/s41575-019-0126-x
49. Anderson AC, Joller N, Kuchroo VK. Lag-3, Tim-3, and TIGIT: Co-Inhibitory Receptors With Specialized Functions in Immune Regulation. *Immunity* (2016) 44(5):989–1004. doi: 10.1016/j.immuni.2016.05.001
50. Havel JJ, Chowell D, Chan TA. The Evolving Landscape of Biomarkers for Checkpoint Inhibitor Immunotherapy. *Nat Rev Cancer* (2019) 19(3):133–50. doi: 10.1038/s41568-019-0116-x
51. Andrews LP, Marciscano AE, Drake CG, Vignali DA. LAG3 (CD223) as a Cancer Immunotherapy Target. *Immunol Rev* (2017) 276(1):80–96. doi: 10.1111/imr.12519
52. Galon J, Bruni D. Approaches to Treat Immune Hot, Altered and Cold Tumours With Combination Immunotherapies. *Nat Rev Drug Discov* (2019) 18(3):197–218. doi: 10.1038/s41573-018-0007-y

Conflict of Interest: The authors declare that the research was conducted in the absence of any commercial or financial relationships that could be construed as a potential conflict of interest.

frontiers in Immunology

MINI REVIEW
published: 02 June 2021
doi: 10.3389/fimmu.2021.690207

Regulatory Effects of Histone Deacetylase Inhibitors on Myeloid-Derived Suppressor Cells

Yudan Cui[1,2], *Jingshan Cai*[1,2], *Wenxin Wang*[2] *and Shengjun Wang*[1,2*]

[1] Department of Laboratory Medicine, The Affiliated People's Hospital, Jiangsu University, Zhenjiang, China, [2] Department of Immunology, Jiangsu Key Laboratory of Laboratory Medicine, School of Medicine, Jiangsu University, Zhenjiang, China

Histone deacetylase inhibitors (HDACIs) are antitumor drugs that are being developed for use in clinical settings. HDACIs enhance histone or nonhistone acetylation and promote gene transcription *via* epigenetic regulation. Importantly, these drugs have cytotoxic or cytostatic properties and can directly inhibit tumor cells. However, how HDACIs regulate immunocytes in the tumor microenvironment, such as myeloid-derived suppressor cells (MDSCs), has yet to be elucidated. In this review, we summarize the effects of different HDACIs on the immunosuppressive function and expansion of MDSCs based on the findings of relevant studies.

Keywords: acetylation, histone deacetylases, inhibitors, myeloid-derived suppressor cells, immunosuppression

OPEN ACCESS

Edited by:
Mingzhu Yin,
Central South University, China

Reviewed by:
José Medina-Echeverz,
Bavarian Nordic, Germany
Ali Bettaieb,
Université de Sciences Lettres de Paris, France

***Correspondence:**
Shengjun Wang
sjwjs@ujs.edu.cn

Specialty section:
This article was submitted to Cancer Immunity and Immunotherapy, a section of the journal Frontiers in Immunology

Received: *02 April 2021*
Accepted: *17 May 2021*
Published: *02 June 2021*

Citation:
Cui Y, Cai J, Wang W and Wang S (2021) Regulatory Effects of Histone Deacetylase Inhibitors on Myeloid-Derived Suppressor Cells. Front. Immunol. 12:690207. doi: 10.3389/fimmu.2021.690207

INTRODUCTION

Myeloid-derived suppressor cells (MDSCs) are heterogeneous cells derived from bone marrow that can suppress the immune response (1, 2). MDSCs are produced in large quantities under pathological conditions, such as inflammation and cancer. The accumulation of MDSCs is a complex and gradual phenomenon that is regulated by many factors (3). MDSCs are composed of two major types of cells: the granulocytic or polymorphonuclear type (PMN-MDSCs), which are similar to neutrophils in phenotype and morphology, and the monocytic type (M-MDSCs), which are similar to monocytes in phenotype and morphology. In most types of cancer, PMN-MDSCs account for more than 80% of all MDSCs, while M-MDSCs are direct promoters of tumor metastasis (4). In mice, MDSCs are more common in tumors of the bone marrow, spleen, liver and other organs. PMN-MDSCs and M-MDSCs are defined as $CD11b^{+}Ly6G^{+}Ly6C^{lo}$ and $CD11b^{+}Ly6G^{-}Ly6C^{hi}$, respectively. In humans, MDSCs are most common in the blood and tumors of various organs. In peripheral blood mononuclear cells, PMN-MDSCs are defined as $CD11b^{+}CD14^{-}CD15^{+}$ or $CD11b^{+}CD14^{-}CD66b^{+}$, while M-MDSCs are defined as $CD11b^{+}CD14^{+}HLA\text{-}DR^{-/lo}CD15^{-}$. $Lin^{-}HLA\text{-}DR^{-}CD33^{+}$ cells are a group of mixed MDSCs containing more immature progenitor cells that have been proposed to be defined by 'early-stage MDSCs' (e-MDSCs). However, the same type of cells have yet to be identified in mice (5). The signals driving the development of MDSCs occur in two partially overlapping stages (6). In the first stage, the expansion and regulation of bone marrow cells occur in the bone marrow and spleen,

while the second stage is characterized by the transformation of neutrophils and monocytes into pathologically activated MDSCs, which primarily occurs in peripheral tissues (7). Several factors participate in MDSC-mediated immunosuppression, including arginase-1 (Arg-1), inducible nitric oxide synthase 2 (iNOS), transforming growth factor β (TGF-β), interleukin-10 (IL-10), cyclooxygenase 2 (COX2) and indoleamine 2,3-dioxygenase (IDO) (8, 9). Although MDSCs are involved in the suppression of different cells in the immune system, T cells are the primary targets of MDSCs. Both PMN-MDSCs and M-MDSCs can reduce the production of L-arginine through the expression of Arg-1 and iNOS, thereby inhibiting the function of T cells (10, 11). Furthermore, M-MDSCs and PMN-MDSCs also take advantage of different immunosuppressive mechanisms. M-MDSCs use NO and produce related cytokines to inhibit the ability of T cells to eliminate antigens (12), while PMN-MDSCs primarily inhibit the immune response in an antigen-specific manner. The induction of antigen-specific T cell tolerance is one of the primary characteristics of PMN-MDSCs (13, 14), and reactive oxygen species (ROS) production is crucial for this activity (8). In recent years, an understanding of the clinical importance of MDSCs has emerged. An initial study monitored MDSCs from cancer patients and analyzed the total MDSC population. The results showed that the number of peripheral blood MDSCs was positively correlated with the tumor stage and tumor burden of colorectal, breast, thyroid and nonsmall cell lung cancers (3, 15–21). In melanoma and hepatocellular carcinoma, both PMN-MDSCs and M-MDSCs were shown to be associated with a poorer prognosis (3, 22, 23). In nonsolid tumors, M-MDSC numbers were associated with reduced survival in multiple myeloma, Hodgkin's lymphoma, non-Hodgkin's lymphoma, and diffuse large B-cell lymphoma (24–26). Therefore, therapeutics targeting MDSCs have become an important means of tumor immunotherapy by inhibiting their differentiation, expansion and activity.

Immune checkpoint inhibitors, such as anti-PD-1 and anti-CTLA-4, have shown success in eradicating cancer by enhancing immune activation, but primary and secondary resistance are still problems (27). Epigenetic treatments for cancer include histone deacetylase inhibitors (HDACIs), DNA methyltransferase inhibitors (DNMTIs) and histone methyltransferase inhibitors (HMTIs), which can stimulate tumor cells and improve the antitumor response by host immune cells. Epigenetic treatments can improve the response of tumor patients to immune checkpoint blockade therapy (28). DNMTIs have been reported to be effective in the treatment of hematological malignancies in clinical studies (29), while HMTIs have been shown to play a role in the treatment of multiple myeloma (30). However, some DMNTIs and HMTIs have not shown clinical efficacy. HDACIs are a different class of small molecule drugs that can have a wide range of effects on tumor cells, including cell cycle arrest, apoptosis, cell differentiation, autophagy and antiangiogenesis (31). HDACIs can inhibit HDACs, and because these drugs have a more pronounced effect on the proliferation of malignant cells than nonmalignant cells, there is increasing interest in developing these drugs, especially as antitumor treatments. In recent studies, many researchers have found that HDACIs also have significant effects on host immunosuppressive cells. As MDSCs are important immunosuppressive cells in the tumor microenvironment (32), it is worth investigating the regulatory effects of HDACIs these cells.

ACETYLATION

Lysine acetylation is an evolutionarily conserved posttranslational modification that occurs in prokaryotes and eukaryotes. In general, two different types of protein acetylation occur in cells. In humans, 80-90% of proteins undergo cotranslational acetylation at the Nα end of the nascent polypeptide chain (43–45). The other common type of protein acetylation occurs at the ϵ-amino group of lysine. Acetylation was first discovered in histones (46). Subsequently, researchers observed acetylation modifications on nonhistones and identified histone acetyltransferases (HATs) and histone deacetylases (HDACs). In the past decade, advances in proteomics based on mass spectrometry have greatly expanded the classification of endogenous acetylated proteins, provided an objective perspective for the study of acetylation, and provided new insights into the scope and regulation of nonhistone acetylation. To reflect the degree of nonhistone acetylation, HATs and HDACs were renamed lysine acetyltransferases (KATs) and lysine deacetylases (KDACs), respectively (47) (ordinarily, the terms HATs and HDACs are used). Acetylation is a dynamic and reversible process involving both KATs and KDACs. KATs are responsible for covalently attaching an acetyl group to the lysine residue of a protein and are figuratively called "writers", while KDACs mediate the removal of this acetyl group and are called "erasers". Acetylation is the addition of acetyl groups to lysine residues in a protein that occurs in the presence of acetyl transferase. Acetylation is an important type of posttranslational modification for acetyl-CoA metabolism and cell signal transduction. In addition, acetylation is a widespread regulatory mechanism mediated by posttranslational modification in the subcellular organelles of the nucleus or cytoplasm and is involved in many processes, such as transcription, chemotaxis, metabolism, cell signal transduction, stress response, proteolysis, cell apoptosis, and neuron development (47). Evidence has shown that acetylation is one of the most important modifications used to alter protein activity and precisely regulate and control cellular functions.

HISTONE DEACETYLASES

HDACs can mediate the deacetylation of histones and nonhistone proteins and are a class of proteases that play important roles in chromosome structural modifications and gene expression regulation (48). Under normal conditions, the acetylation of histones is beneficial for the dissociation of DNA

and dense histone octamers, allowing the nucleosome structure to relax so that various transcription factors and cooperative transcription factors can bind to specific DNA binding sites and activate gene transcription. The deacetylation of histones has the opposite effect (49). In addition to regulating histone modification, HDACs also regulate the posttranslational acetylation of many nonhistones, including transcription factors, chaperones, and signaling molecules, leading to changes in protein stability, protein-protein interactions, and protein-DNA interactions (50). There are four classes of HDACs. Class I includes HDAC1, HDAC2, HDAC3 and HDAC8. Class II is further divided into IIa and IIb, with HDAC4, HDAC5, HDAC7 and HDAC9 belonging to class IIa, while class IIb includes HDAC6 and HDAC10. Class III is composed of sirtuin1-7, and class IV includes HDAC11 only. Classes I, II and IV enzymes are zinc ion dependent, while class III members are zinc ion independent (51). It is worth noting that nearly half of all deacetylases have weak or no deacetylase activity or target other types of acylation (47).

HISTONE DEACETYLASE INHIBITORS

HDACIs can inhibit the deacetylation of histones or nonhistone proteins and have direct inhibitory effects on tumor cells. Inhibiting HDACs can regulate the balance between proapoptotic and antiapoptotic proteins, leading to the death of tumor cells (52). While HDACIs have direct inhibitory effects on tumor cells, they can also regulate various components of the host immune system (53). Some researchers have found that the treatment of cancer patients with HDACIs can reduce the number of lymphocytes, indicating that HDACIs are immunocytotoxic (54, 55). On the other hand, some researchers have shown that HDACIs promote immune activity and can enhance cancer immunotherapy (56–58). Theoretically, targeted inhibition of HDACs is closely associated with adverse outcomes after trauma and can optimize treatment outcomes while reducing complications (59). Many isotype-specific HDACIs are now available and are undergoing clinical trials as antitumor agents (60). HDACIs can be structurally classified into at least four categories (hydrochlorates, cyclic peptides, fatty acids, and benzoamides) and can also be classified according to their HDAC specificity. Broad-spectrum HDACIs include panobinostat, belinostat, resminostat and trichostatin A. Butyrate and valproate inhibit class I and IIa HDACs. Romidepsin, entinostat (ENT) and mocetinostat are considered class I specific, and tubacin is HDAC6 specific (51). Due to the zinc ion-dependent nature of the domains of class I, II and IV HDACs, inhibitors occupying the zinc ion-binding site of the catalytic center will inhibit the activity of these enzymes. These HDACIs contain a pharmacophore, a cap structure, a linking unit and a zinc ion-binding group to chelate cations in the catalytic region of the target HDACs (27). Trichostatin A, vorinostat, belinostat, dacinostat, panobinostat and givinostat are HDACIs. Recent studies have shown that HDACIs also have crucial effects on host immunosuppressive cells, with MDSCs being important immunosuppressive cells in the tumor microenvironment (**Table 1**).

EFFECTS OF HDACIs ON MDSCs

Entinostat

ENT is a specific inhibitor of class I HDACs that targets immunosuppressive cells in the tumor microenvironment (61). ENT has been reported to have immunoregulatory activity (62) and has been used in the clinical treatment of breast and nonsmall cell lung cancers (63, 64). The clinical drug development of ENT focuses on the resistance mechanism of breast cancer to endocrine therapy and HER2-targeted drugs (63). Importantly, ENT can inhibit tumor cell proliferation, which can induce mitochondrial damage and lead to apoptosis. ENT increases the sensitivity of lung cancer cells to tumor necrosis factor-related apoptosis-inducing ligands and downregulates the expression of the antiapoptotic genes Bcl-2 and XIAP (64).

Using lung and renal cell carcinoma models, Orillion A and colleagues observed that the total number of MDSCs in tumors increased in the presence of ENT alone but only slightly increased after treatment with ENT combined with anti-PD-1. In addition, there was also a decline in immunosuppressive functions, showing that ENT can inhibit the levels of Arg-1, iNOS and COX2, thereby reducing the immunosuppressive

TABLE 1 | Effects of HDACIs on MDSCs.

HDACI	Classification	Effects on MDSCs	Ref
Entinostat	Class I	PMN-MDSC function inhibited	(33)
		M-MDSC migration inhibited	(34)
Valproic acid	Class I	PMN-MDSC function inhibited	(35)
		M-MDSC migration inhibited	(36)
Mocetinostat	Class I/IV	total number of MDSCs decreased	(37)
Vorinostat	Class I/II	MDSC apoptosis (at higher vorinostat concentrations)	(38)
		total number of MDSCs amplified (at lower vorinostat concentrations)	(39)
CG-745	Class I/IIb	total number of MDSCs decreased	(40)
ACY241	specific inhibitor of HDAC6	total number of MDSCs decreased	(41)
Trichostatin A	Broad spectrum (except HDAC8)	total number of MDSCs amplified (0.1-10 nM TSA)	(39)
		PMN-MDSC number decreased	(42)

effects of MDSCs (62). After treatment with ENT, the tumor-free survival of HER/neu transgenic breast cancer and Panco2 metastatic pancreatic cancer mouse models was significantly improved. ENT combined treatment with anti-PD-1 and anti-CTLA-4 was shown to inhibit the VEGF, ErbB and mTOR pathways in PMN-MDSCs as well as the activity of STAT3 and the activity of Arg-1 (33). Tomita et al. reported that the number of circulating PMN-MDSCs and M-MDSCs decreased in samples from breast cancer patients treated with ENT combined with an aromatase inhibitor (65). However, the immunosuppressive activity of PMN-MDSCs could specifically be reduced by ENT treatment, and there was no effect on M-MDSCs (66). The microenvironment before tumor metastasis has been shown to be established through the activities of M-MDSCs, suggesting that the number of M-MDSCs and niche-promoting molecules in the lung tissue before tumor metastasis can be reduced by low-dose 5-azacytidine (100 nM) and low-dose ENT (50 nM) treatment. Interestingly, the gene set related to the chemokine axis and immune cell migration was observed to be significantly altered by low-dose ENT treatment, and the expression of CCR2 in M-MDSCs in the bone marrow and lung was significantly downregulated after low-dose ENT treatment (34). CCR2 is a key regulator of the migration of M-MDSCs from the bone marrow to the tumor environment, suggesting that the transport of M-MDSCs to the premetastatic lung may be affected by low-dose ENT therapy at least partially through the downregulation of CCR2 (67, 68). In short, ENT can inhibit the function of PMN-MDSCs and the metastasis of M-MDSCs (**Figure 1**).

Valproic Acid

Valproic acid (VPA) is an anticonvulsant drug (69) and an HDACI (70, 71) that targets HDAC class I enzymes (HDAC1, 2 and 3). *In vitro* experiments by Xie Z et al. showed that VPA treatment can reduce the proportion of PMN-MDSCs, inhibit the immunosuppressive function of MDSCs in a dose-dependent manner and also reduce the level of Arg-1 by inhibiting IL-4Rα expression, thereby weakening the immunosuppressive function of MDSCs (35). In a recent study, VPA was shown to downregulate CCR2 expression in M-MDSCs, and the tumor invasion ability of these cells was also reduced (36). In addition, VPA was shown to decrease the immunosuppressive effects of MDSCs on $CD8^+$ T cells and NK cells, and the ability of these cells to kill tumors was also enhanced (36). Moreover, treatment with VPA combined with an anti-PD-L1 antibody blocked the immunosuppressive functions of MDSCs by activating IRF1/IRF8 (72).

Mocetinostat

Mocetinostat is a selective inhibitor of class I/IV HDAC, proteins involved in the epigenetic silencing of immunoregulatory genes in tumors and immune cells. The target gene promoters of mocetinostat are occupied by class I HDACs, and an increase in active histone markers is observed after mocetinostat treatment (37). Briere D and colleagues suggested that the number of MDSCs and Tregs could be reduced by mocetinostat treatment, with an increase in $CD8^+$ T cells observe in a tumor-bearing mouse model of colorectal cancer (37). However, the exact mechanism of action of mocetinostat remains unclear.

Vorinostat

Vorinostat (SAHA) is a nonspecific inhibitor of class I and class II HDACs and was the first HDACI drug approved by the Food And Drug Administration for clinical use in patients with cutaneous T cell lymphoma (73). Vorinostat can also reduce

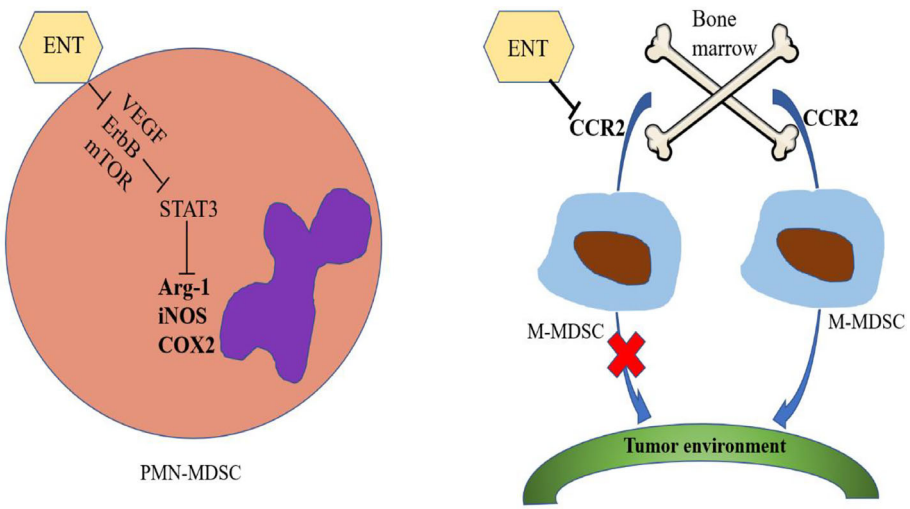

FIGURE 1 | Effects of entinostat on MDSCs. Entinostat inhibits the VEGF, ErbB and mTOR pathways in PMN-MDSCs, thereby inhibiting the activity of STAT3, which in turn reduces the activities of Arg-1, iNOS and COX2. Entinostat therapy inhibits the transport of M-MDSCs from bone marrow to the tumor environment by downregulating CCR2 expression.

acute graft-versus-host disease (GVHD) after allogeneic bone marrow transplantation by inhibiting the production of proinflammatory cytokines such as TNF-α, IL-1 and IFN-γ (73).

MDSCs were shown to be induced by both GM-CSF and vorinostat-induced tumor pressure *in vitro*, which can mediate MDSC apoptosis and contradicts the results of other researchers, possibly because different concentrations of vorinostat were used (38). In a spontaneous transgenic mouse melanoma model, treatment with vorinostat resulted in a significant delay in disease onset, downregulation of chemokine (c-c motif) ligand 2 (CCL2) and the recruitment of MDSCs (74). Kroesen M and colleagues showed that the number of M-MDSCs in the tumor microenvironment of 9464D tumor-bearing mice could be reduced by vorinostat treatment. Thus, vorinostat can create a permissible tumor microenvironment for tumor-directed mAb therapy by increasing the number of macrophage effector cells expressing high levels of Fc receptors (75).

CG-745

CG-745 is a specific inhibitor of class I and class IIb HDACs that exhibits anticancer effects on pancreatic, colorectal and nonsmall cell lung cancers (56). Kim YD and colleagues analyzed the distribution of immune cells in the tumor microenvironment and spleen and reported that CG-745 could inhibit M2 macrophage polarization and reduce the number of MDSCs (40). Therefore, the cytotoxicity of PBMCs and IFN-γ expression in Jurkat T cells could be increased by CG-745. H3 acetylation, which is an important factor during the differentiation of naïve $CD8^+$ T cells into memory T cells, was also induced (76).

ACY241

ACY241 is a specific inhibitor of HDAC6 that inhibits multiple myeloma when used in combination with immunoregulatory drugs and proteasome inhibitors (41). After treatment with ACY241, the number of MDSCs in patients with multiple myeloma was shown to significantly decrease. Bcl6 expression in $CD8^+$ T cells may be enhanced by ACY 241 through activation of the AKT/mTOR/NF-κB signaling pathway in $CD8^+$ T cells, thereby enhancing $CD8^+$ T cell activity (41).

Trichostatin A

Trichostatin A (TSA) is a natural antifungal metabolite produced by *Streptomyces* and is a broad-spectrum HDACI with no effect on HDAC8 (77). Rosboroug BR et al. observed that after GM-CSF-induced mouse bone marrow cells were treated with TSA (0.1-10 nM) and vorinostat (10-500 nM), CD11b+ GR1+ cells and MDSCs were strongly amplified (39). After TSA treatment of experimental autoimmune encephalomyelitis, PMN-MDSCs were present in reduced numbers in secondary lymphoid organs and migrated into the spinal cord without affecting monocytes, while the disease symptoms improved (42). Additionally, the numbers of Tregs and MDSCs were reduced in Her2/CT26 tumor-bearing mice treated with TSA (78).

CONCLUSION

In general, most HDACIs inhibit class I or class II HDACs. Among these molecules, the regulatory effects of entinostat on MDSCs have been reported the most often, probably because entinostat has been put into clinical use. In summary, entinostat inhibits the VEGF, ErbB and mTOR pathways in PMN-MDSCs, thereby inhibiting the activity of STAT3, which in turn reduces the activity of Arg-1, iNOS and COX2. Entinostat also inhibits the transport of M-MDSCs from bone marrow to the tumor environment by downregulating CCR2. Other HDACIs have antitumor effects by reducing the number of MDSCs, but the specific mechanism of action varies. Interestingly, increased concentrations of vorinostat can amplify the number of MDSCs. Why different concentrations of vorinostat lead to different results is worth further research. At the same time, these results suggest that different doses of HDACIs may have different effects, demonstrating that studies of HDACIs must involve strict control of the drug dose. HDACIs have been shown to be effective antitumor agents in clinical studies, but their success has been limited. In addition, these inhibitors can produce side effects, such as platelet reduction, nausea, vomiting, anorexia and fatigue.

In recent years, research on MDSCs has gradually increased, and some researchers regard MDSCs as targets of tumor therapy. Therefore, it is necessary to explore the regulatory effects of HDACIs on MDSCs, which may improve their therapeutic effects toward tumors.

AUTHOR CONTRIBUTIONS

YC drafted the manuscript. JC and WW discussed and revised the manuscript. SW designed the study and revised the manuscript. All authors contributed to the article and approved the submitted version.

FUNDING

This work was supported by the Research Project of the Jiangsu Commission of Health (grant No. K2019019) and the Jiangsu Province's Key Medical Talents Program (grant No. ZDRCB2016018).

REFERENCES

1. Liu G, Bi Y, Shen B, Yang H, Zhang Y, Wang X, et al. SIRT1 Limits the Function and Fate of Myeloid-Derived Suppressor Cells in Tumors by Orchestrating HIF-1alpha-dependent Glycolysis. *Cancer Res* (2014) 74 (3):727–37. doi: 10.1158/0008-5472.CAN-13-2584
2. Mantovani A. The Growing Diversity and Spectrum of Action of Myeloid-Derived Suppressor Cells. *Eur J Immunol* (2010) 40(12):3317–20. doi: 10.1002/eji.201041170
3. Veglia F, Perego M, Gabrilovich D. Myeloid-Derived Suppressor Cells Coming of Age. *Nat Immunol* (2018) 19(2):108–19. doi: 10.1038/s41590-017-0022-x

4. Mantovani A, Marchesi F, Malesci A, Laghi L, Allavena P. Tumour-Associated Macrophages as Treatment Targets in Oncology. *Nat Rev Clin Oncol* (2017) 14(7):399–416. doi: 10.1038/nrclinonc.2016.217
5. Bronte V, Brandau S, Chen S, Colombo M, Frey A, Greten T, et al. Recommendations for Myeloid-Derived Suppressor Cell Nomenclature and Characterization Standards. *Nat Commun* (2016) 7:12150. doi: 10.1038/ncomms12150
6. Condamine T, Mastio J, Gabrilovich DI. Transcriptional Regulation of Myeloid-Derived Suppressor Cells. *J Leukoc Biol* (2015) 98(6):913–22. doi: 10.1189/jlb.4RI0515-204R
7. Veglia F, Sanseviero E, Gabrilovich DI. Myeloid-Derived Suppressor Cells in the Era of Increasing Myeloid Cell Diversity. *Nat Rev Immunol* (2021) 1:1–14. doi: 10.1038/s41577-020-00490-y
8. Gabrilovich DI. Myeloid-Derived Suppressor Cells. *Cancer Immunol Res* (2017) 5(1):3–8. doi: 10.1158/2326-6066.CIR-16-0297
9. Feng S, Cheng X, Zhang L, Lu X, Chaudhary S, Teng R, et al. Myeloid-Derived Suppressor Cells Inhibit T Cell Activation Through Nitrating LCK in Mouse Cancers. *Proc Natl Acad Sci USA* (2018) 115(40):10094–9. doi: 10.1073/pnas.1800695115
10. Bronte V, Serafini P, Mazzoni A, Segal DM, Zanovello P. L-Arginine Metabolism in Myeloid Cells Controls T-Lymphocyte Functions. *Trends Immunol* (2003) 24(6):301–5. doi: 10.1016/s1471-4906(03)00132-7
11. Kamran N, Kadiyala P, Saxena M, Candolfi M, Li Y, Moreno-Ayala MA, et al. Immunosuppressive Myeloid Cells' Blockade in the Glioma Microenvironment Enhances the Efficacy of Immune-Stimulatory Gene Therapy. *Mol Ther* (2017) 25(1):232–48. doi: 10.1016/j.ymthe.2016.10.003
12. Gabrilovich DI, Ostrand-Rosenberg S, Bronte V. Coordinated Regulation of Myeloid Cells by Tumours. *Nat Rev Immunol* (2012) 12(4):253–68. doi: 10.1038/nri3175
13. Koehn B, Apostolova P, Haverkamp J, Miller J, McCullar V, Tolar J, et al. GVHD-Associated, Inflammasome-Mediated Loss of Function in Adoptively Transferred Myeloid-Derived Suppressor Cells. *Blood* (2015) 126(13):1621–8. doi: 10.1182/blood-2015-03-634691
14. Marigo I, Bosio E, Solito S, Mesa C, Fernandez A, Dolcetti L, et al. Tumor-Induced Tolerance and Immune Suppression Depend on the C/EBPbeta Transcription Factor. *Immunity* (2010) 32(6):790–802. doi: 10.1016/j.immuni.2010.05.010
15. Sun H, Zhou X, Xue Y, Wang K, Shen Y, Mao J, et al. Increased Frequency and Clinical Significance of Myeloid-Derived Suppressor Cells in Human Colorectal Carcinoma. *World J Gastroenterol* (2012) 18(25):3303–9. doi: 10.3748/wjg.v18.i25.3303
16. Zhang B, Wang Z, Wu L, Zhang M, Li W, Ding J, et al. Circulating and Tumor-Infiltrating Myeloid-Derived Suppressor Cells in Patients With Colorectal Carcinoma. *PloS One* (2013) 8(2):e57114. doi: 10.1371/journal.pone.0057114
17. Wang Y, Yin K, Tian J, Xia X, Ma J, Tang X, et al. Granulocytic Myeloid-Derived Suppressor Cells Promote the Stemness of Colorectal Cancer Cells Through Exosomal S100A9. *Adv Sci* (2019) 6(18):1901278. doi: 10.1002/advs.201901278
18. Diaz-Montero C, Salem M, Nishimura M, Garrett-Mayer E, Cole D, Montero AJ. Increased Circulating Myeloid-Derived Suppressor Cells Correlate With Clinical Cancer Stage, Metastatic Tumor Burden, and Doxorubicin-Cyclophosphamide Chemotherapy. *Cancer Immunol Immunother* (2009) 58 (1):49–59. doi: 10.1007/s00262-008-0523-4
19. Angell T, Lechner M, Smith A, Martin S, Groshen S, Maceri D, et al. Circulating Myeloid-Derived Suppressor Cells Predict Differentiated Thyroid Cancer Diagnosis and Extent. *Thyroid* (2016) 26(3):381–9. doi: 10.1089/thy.2015.0289
20. Tian X, Ma J, Wang T, Tian J, Zhang Y, Mao L, et al. Long Non-Coding RNA HOXA Transcript Antisense RNA Myeloid-Specific 1-HOXA1 Axis Downregulates the Immunosuppressive Activity of Myeloid-Derived Suppressor Cells in Lung Cancer. *Front Immunol* (2018) 9:473. doi: 10.3389/fimmu.2018.00473
21. Huang A, Zhang B, Wang B, Zhang F, Fan K, Guo Y. Increased CD14(+)HLA-DR (-/Low) Myeloid-Derived Suppressor Cells Correlate With Extrathoracic Metastasis and Poor Response to Chemotherapy in Non-Small Cell Lung Cancer Patients. *Cancer Immunol Immunother* (2013) 62(9):1439–51. doi: 10.1007/s00262-013-1450-6
22. Jordan K, Amaria R, Ramirez O, Callihan E, Gao D, Borakove M, et al. Myeloid-Derived Suppressor Cells are Associated With Disease Progression and Decreased Overall Survival in Advanced-Stage Melanoma Patients. *Cancer Immunol Immunother* (2013) 62(11):1711–22. doi: 10.1007/s00262-013-1475-x
23. Li X, Xing Y, Lei A, Xiao Q, Lin Z, Hong Y, et al. Neutrophil Count is Associated With Myeloid Derived Suppressor Cell Level and Presents Prognostic Value of for Hepatocellular Carcinoma Patients. *Oncotarget* (2017) 8(15):24380–8. doi: 10.18632/oncotarget.15456
24. Wang Z, Zhang L, Wang H, Xiong S, Li Y, Tao Q, et al. Tumor-Induced CD14+ HLA-DR (-/Low) Myeloid-Derived Suppressor Cells Correlate With Tumor Progression and Outcome of Therapy in Multiple Myeloma Patients. *Cancer Immunol Immunother* (2015) 64(3):389–99. doi: 10.1007/s00262-014-1646-4
25. Wu C, Wu X, Zhang X, Chai Y, Guo Q, Li L, et al. Prognostic Significance of Peripheral Monocytic Myeloid-Derived Suppressor Cells and Monocytes in Patients Newly Diagnosed With Diffuse Large B-Cell Lymphoma. *Int J Clin Exp Med* (2015) 8(9):15173–81.
26. Marini O, Spina C, Mimiola E, Cassaro A, Malerba G, Todeschini G, et al. Identification of Granulocytic Myeloid-Derived Suppressor Cells (G-MDSCs) in the Peripheral Blood of Hodgkin and Non-Hodgkin Lymphoma Patients. *Oncotarget* (2016) 7(19):27676–88. doi: 10.18632/oncotarget.8507
27. Gomez S, Tabernacki T, Kobyra J, Roberts P, Chiappinelli KB. Combining Epigenetic and Immune Therapy to Overcome Cancer Resistance. *Semin Cancer Biol* (2020) 65:99–113. doi: 10.1016/j.semcancer
28. Stone ML, Chiappinelli KB, Li H, Murphy LM, Travers ME, Topper MJ, et al. Epigenetic Therapy Activates Type I Interferon Signaling in Murine Ovarian Cancer to Reduce Immunosuppression and Tumor Burden. *Proc Natl Acad Sci* (2017) 114(51):E10981–E90. doi: 10.1073/pnas.1712514114
29. Mikkelsen S, Gillberg L, Lykkesfeldt J, Grønbæk K. The Role of Vitamin C in Epigenetic Cancer Therapy. *Free Radic Biol Med* (2021) S0891-5849 (21):00169–6. doi: 10.1016/j.freeradbiomed
30. Rabal O, San José-Enériz E, Agirre X, Sánchez-Arias J, de Miguel I, Ordoñez R, et al. *In Vivo* Design and Synthesis of Novel Epigenetic Inhibitors Targeting Histone Deacetylases, DNA Methyltransferase 1, and Lysine Methyltransferase G9a With Efficacy in Multiple Myeloma. *J Med Chem* (2021) 64(6):3392–426. doi: 10.1021/acs.jmedchem.0c02255
31. Khan O, La Thangue NB. HDAC Inhibitors in Cancer Biology: Emerging Mechanisms and Clinical Applications. *Immunol Cell Biol* (2012) 90(1):85–94. doi: 10.1038/icb.2011.100
32. Li M, Zha X, Wang S. The Role of N6-Methyladenosine mRNA in the Tumor Microenvironment. *Biochim Biophys Acta Rev Cancer* (2021) 1875(2):188522. doi: 10.1016/j.bbcan.2021.188522
33. Christmas BJ, Rafie CI, Hopkins AC, Scott BA, Ma HS, Cruz KA, et al. Entinostat Converts Immune-Resistant Breast and Pancreatic Cancers Into Checkpoint-Responsive Tumors by Reprogramming Tumor-Infiltrating Mdscs. *Cancer Immunol Res* (2018) 6(12):1561–77. doi: 10.1158/2326-6066.CIR-18-0070
34. Lu Z, Zou J, Li S, Topper MJ, Tao Y, Zhang H, et al. Epigenetic Therapy Inhibits Metastases by Disrupting Premetastatic Niches. *Nature* (2020) 579 (7798):284–90. doi: 10.1038/s41586-020-2054-x
35. Xie Z, Ago Y, Okada N, Tachibana M. Valproic Acid Attenuates Immunosuppressive Function of Myeloid-Derived Suppressor Cells. *J Pharmacol Sci* (2018) 137(4):359–65. doi: 10.1016/j.jphs.2018.06.014
36. Xie Z, Ikegami T, Ago Y, Okada N, Tachibana M. Valproic Acid Attenuates CCR2-Dependent Tumor Infiltration of Monocytic Myeloid-Derived Suppressor Cells, Limiting Tumor Progression. *Oncoimmunology* (2020) 9 (1):1734268. doi: 10.1080/2162402X.2020.1734268
37. Briere D, Sudhakar N, Woods DM, Hallin J, Engstrom LD, Aranda R, et al. The Class I/IV HDAC Inhibitor Mocetinostat Increases Tumor Antigen Presentation, Decreases Immune Suppressive Cell Types and Augments Checkpoint Inhibitor Therapy. *Cancer Immunol Immunotherapy* (2017) 67 (3):381–92. doi: 10.1007/s00262-017-2091-y
38. Wang HF, Ning F, Liu ZC, Wu L, Li ZQ, Qi YF, et al. Histone Deacetylase Inhibitors Deplete Myeloid-Derived Suppressor Cells Induced by 4T1 Mammary Tumors In Vivo and In Vitro. *Cancer Immunol Immunother* (2017) 66(3):355–66. doi: 10.1007/s00262-016-1935-1
39. Rosborough BR, Castellaneta A, Natarajan S, Thomson AW, Turnquist HR. Histone Deacetylase Inhibition Facilitates GM-CSF-Mediated Expansion of

Myeloid-Derived Suppressor Cells In Vitro and In Vivo. *J Leukoc Biol* (2012) 91(5):701–9. doi: 10.1189/jlb.0311119
40. Kim YD, Park SM, Ha HC, Lee AR, Won H, Cha H, et al. Hdac Inhibitor, Cg-745, Enhances the Anti-Cancer Effect of Anti-PD-1 Immune Checkpoint Inhibitor by Modulation of the Immune Microenvironment. *J Cancer* (2020) 11(14):4059–72. doi: 10.7150/jca.44622
41. Bae J, Hideshima T, Tai YT, Song Y, Richardson P, Raje N, et al. Histone Deacetylase (HDAC) Inhibitor ACY241 Enhances Anti-Tumor Activities of Antigen-Specific Central Memory Cytotoxic T Lymphocytes Against Multiple Myeloma and Solid Tumors. *Leukemia* (2018) 32(9):1932–47. doi: 10.1038/s41375-018-0062-8
42. Jayaraman A, Sharma M, Prabhakar B, Holterman M, Jayaraman S. Amelioration of Progressive Autoimmune Encephalomyelitis by Epigenetic Regulation Involves Selective Repression of Mature Neutrophils During the Preclinical Phase. *Exp Neurol* (2018) 304:14–20. doi: 10.1016/j.expneurol.2018.02.008
43. Brown J, Roberts W. Evidence That Approximately Eighty Per Cent of the Soluble Proteins From Ehrlich Ascites Cells Are Nalpha-Acetylated. *J Biol Chem* (1976) 251(4):1009–14.
44. Arnesen T, Van Damme P, Polevoda B, Helsens K, Evjenth R, Colaert N, et al. Proteomics Analyses Reveal the Evolutionary Conservation and Divergence of N-terminal Acetyltransferases From Yeast and Humans. *Proc Natl Acad Sci USA* (2009) 106(20):8157–62. doi: 10.1073/pnas.0901931106
45. Aksnes H, Van Damme P, Goris M, Starheim K, Marie M, Støve S, et al. An Organellar Nα-Acetyltransferase, naa60, Acetylates Cytosolic N Termini of Transmembrane Proteins and Maintains Golgi Integrity. *Cell Rep* (2015) 10(8):1362–74. doi: 10.1016/j.celrep.2015.01.053
46. Allfrey V, Faulkner R, Mirsky A. Acetylation and Methylation of Histones and Their Possible Role in the Regulation of RNA Synthesis. *Proc Natl Acad Sci USA* (1964) 51:786–94. doi: 10.1073/pnas.51.5.786
47. Narita T, Weinert BT, Choudhary C. Functions and Mechanisms of non-Histone Protein Acetylation. *Nat Rev Mol Cell Biol* (2019) 20(3):156–74. doi: 10.1038/s41580-018-0081-3
48. Bahl S, Seto E. Regulation of Histone Deacetylase Activities and Functions by Phosphorylation and Its Physiological Relevance. *Cell Mol Life Sci CMLS* (2020) 78(2):427–45. doi: 10.1007/s00018-020-03599-4
49. Zhao M, Tao Y, Peng G. The Role of Histone Acetyltransferases and Histone Deacetylases in Photoreceptor Differentiation and Degeneration. *Int J Med Sci* (2020) 17(10):1307–14. doi: 10.7150/ijms.43140
50. Glozak M, Sengupta N, Zhang X, Seto E. Acetylation and Deacetylation of Non-Histone Proteins. *Gene* (2005) 363:15–23. doi: 10.1016/j.gene.2005.09.010
51. Villagra A, Cheng F, Wang HW, Suarez I, Glozak M, Maurin M, et al. The Histone Deacetylase HDAC11 Regulates the Expression of Interleukin 10 and Immune Tolerance. *Nat Immunol* (2009) 10(1):92–100. doi: 10.1038/ni.1673
52. Minucci S, Pelicci P. Histone Deacetylase Inhibitors and the Promise of Epigenetic (and More) Treatments for Cancer. *Nat Rev Cancer* (2006) 6(1):38–51. doi: 10.1038/nrc1779
53. Shen L, Orillion A, Pili R. Histone Deacetylase Inhibitors as Immuno modulators in Cancer Therapeutics. *Epigenomics* (2016) 8(3):415–28. doi: 10.2217/epi.15.118
54. Wagner J, Hackanson B, Lübbert M, Jung M. Histone Deacetylase (HDAC) Inhibitors in Recent Clinical Trials for Cancer Therapy. *Clin Epigenet* (2010) 1:117–36. doi: 10.1007/s13148-010-0012-4
55. Subramanian S, Bates S, Wright J, Espinoza-Delgado I, Piekarz R. Clinical Toxicities of Histone Deacetylase Inhibitors. *Pharmaceuticals (Basel Switzerland)* (2010) 3(9):2751–67. doi: 10.3390/ph3092751
56. Kato Y, Yoshimura K, Shin T, Verheul H, Hammers H, Sanni T, et al. Synergistic *In Vivo* Antitumor Effect of the Histone Deacetylase Inhibitor MS-275 in Combination With Interleukin 2 in a Murine Model of Renal Cell Carcinoma. *Clin Cancer Res Off J Am Assoc Cancer Res* (2007) 13:4538–46. doi: 10.1158/1078-0432.Ccr-07-0014
57. Shen L, Ciesielski M, Ramakrishnan S, Miles KM, Ellis L, Sotomayor P, et al. Class I Histone Deacetylase Inhibitor Entinostat Suppresses Regulatory T Cells and Enhances Immunotherapies in Renal and Prostate Cancer Models. *PloS One* (2012) 7(1):e30815. doi: 10.1371/journal.pone.0030815
58. Christiansen A, West A, Banks K, Haynes N, Teng M, Smyth M, et al. Eradication of Solid Tumors Using Histone Deacetylase Inhibitors Combined With Immune-Stimulating Antibodies. *Proc Natl Acad Sci USA* (2011) 108(10):4141–6. doi: 10.1073/pnas.1011037108
59. Sillesen M, Bambakidis T, Dekker SE, Fabricius R, Svenningsen P, Bruhn PJ, et al. Histone Deactylase Gene Expression Profiles Are Associated With Outcomes in Blunt Trauma Patients. *J Trauma Acute Care Surg* (2016) 80(1):26–32. doi: 10.1097/TA.0000000000000896
60. Kim H, Bae S. Histone Deacetylase Inhibitors: Molecular Mechanisms of Action and Clinical Trials as Anti-Cancer Drugs. *Am J Trans Res* (2011) 3(2):166–79.
61. Freundt JK, Frommeyer G, Spieker T, Wotzel F, Grotthoff JS, Stypmann J, et al. Histone Deacetylase Inhibition by Entinostat for the Prevention of Electrical and Structural Remodeling in Heart Failure. *BMC Pharmacol Toxicol* (2019) 20(1):16. doi: 10.1186/s40360-019-0294-x
62. Orillion A, Hashimoto A, Damayanti N, Shen L, Adelaiye-Ogala R, Arisa S, et al. Entinostat Neutralizes Myeloid-Derived Suppressor Cells and Enhances the Antitumor Effect of PD-1 Inhibition in Murine Models of Lung and Renal Cell Carcinoma. *Clin Cancer Res* (2017) 23(17):5187–201. doi: 10.1158/1078-0432.CCR-17-0741
63. Trapani D, Esposito A, Criscitiello C, Mazzarella L, Locatelli M, Minchella I, et al. Entinostat for the Treatment of Breast Cancer. *Expert Opin Invest Drugs* (2017) 26(8):965–71. doi: 10.1080/13543784.2017.1353077
64. Ruiz R, Raez L, Rolfo C. Entinostat (SNDX-275) for the Treatment of non-Small Cell Lung Cancer. *Expert Opin Invest Drugs* (2015) 24(8):1101–9. doi: 10.1517/13543784.2015.1056779
65. Tomita Y, Lee M, Lee S, Tomita S, Chumsri S, Cruickshank S, et al. The Interplay of Epigenetic Therapy and Immunity in Locally Recurrent or Metastatic Estrogen Receptor-Positive Breast Cancer: Correlative Analysis of ENCORE 301, A Randomized, Placebo-Controlled Phase II Trial of Exemestane With or Without Entinostat. *Oncoimmunology* (2016) 5(11):e1219008. doi: 10.1080/2162402x.2016.1219008
66. Hashimoto A, Fukumoto T, Zhang R, Gabrilovich D. Selective Targeting of Different Populations of Myeloid-Derived Suppressor Cells by Histone Deacetylase Inhibitors. *Cancer Immunol Immunother* (2020) 69(9):1929–36. doi: 10.1007/s00262-020-02588-7
67. Qian BZ, Li J, Zhang H, Kitamura T, Zhang J, Campion LR, et al. CCL2 Recruits Inflammatory Monocytes to Facilitate Breast-Tumour Metastasis. *Nature* (2011) 475(7355):222–5. doi: 10.1038/nature10138
68. Bonapace L, Coissieux M, Wyckoff J, Mertz K, Varga Z, Junt T, et al. Cessation of CCL2 Inhibition Accelerates Breast Cancer Metastasis by Promoting Angiogenesis. *Nature* (2014) 515(7525):130–3. doi: 10.1038/nature13862
69. Duenas-Gonzalez A, Candelaria M, Perez-Plascencia C, Perez-Cardenas E, de la Cruz-Hernandez E, Herrera L. Valproic Acid as Epigenetic Cancer Drug: Preclinical, Clinical and Transcriptional Effects on Solid Tumors. *Cancer Treat Rev* (2008) 34(3):206–22. doi: 10.1016/j.ctrv.2007.11.003
70. Göttlicher M, Minucci S, Zhu P, Krämer O, Schimpf A, Giavara S, et al. Valproic Acid Defines a Novel Class of HDAC Inhibitors Inducing Differentiation of Transformed Cells. *EMBO J* (2001) 20(24):6969–78. doi: 10.1093/emboj/20.24.6969
71. Gurvich N, Tsygankova O, Meinkoth J, Klein P. Histone Deacetylase Is a Target of Valproic Acid-Mediated Cellular Differentiation. *Cancer Res* (2004) 64(3):1079–86. doi: 10.1158/0008-5472.can-03-0799
72. Adeshakin AO, Yan D, Zhang M, Wang L, Adeshakin FO, Liu W, et al. Blockade of Myeloid-Derived Suppressor Cell Function by Valproic Acid Enhanced anti-PD-L1 Tumor Immunotherapy. *Biochem Biophys Res Commun* (2020) 522(3):604–11. doi: 10.1016/j.bbrc.2019.11.155
73. Bolden J, Peart M, Johnstone R. Anticancer Activities of Histone Deacetylase Inhibitors. *Nat Rev Drug Discovery* (2006) 5(9):769–84. doi: 10.1038/nrd2133
74. Gatti L, Sevko A, De Cesare M, Arrighetti N, Manenti G, Ciusani E, et al. Histone Deacetylase Inhibitor-Temozolomide Co-Treatment Inhibits Melanoma Growth Through Suppression of Chemokine (C-C Motif) Ligand 2-Driven Signals. *Oncotarget* (2014) 5(12):4516–28. doi: 10.18632/oncotarget.2065
75. Kroesen M, Bull C, Gielen PR, Brok IC, Armandari I, Wassink M, et al. Anti-GD2 mAb and Vorinostat Synergize in the Treatment of Neuroblastoma. *Oncoimmunology* (2016) 5(6):e1164919. doi: 10.1080/2162402X.2016.1164919

76. Dispirito J, Shen H. Histone Acetylation At the Single-Cell Level: A Marker of Memory CD8+ T Cell Differentiation and Functionality. *J Immunol (Baltimore Md 1950)* (2010) 184(9):4631–6. doi: 10.4049/jimmunol.0903830
77. Tseng W, Tsai M, Chen N, Tarng D. Trichostatin A Alleviates Renal Interstitial Fibrosis Through Modulation of the M2 Macrophage Subpopulation. *Int J Mol Sci* (2020) 21(17):5966. doi: 10.3390/ijms21175966
78. Hong E, Heo E, Song J, Kwon B, Lee J, Park Y, et al. Trans-Scirpusin A Showed Antitumor Effects Via Autophagy Activation and Apoptosis Induction of Colorectal Cancer Cells. *Oncotarget* (2017) 8(25):41401–11. doi: 10.18632/oncotarget.17388

Conflict of Interest: The authors declare that the research was conducted in the absence of any commercial or financial relationships that could be construed as a potential conflict of interest.

frontiers in Immunology

ORIGINAL RESEARCH
published: 30 June 2021
doi: 10.3389/fimmu.2021.704557

Identification and Validation of Immune-Related Methylation Clusters for Predicting Immune Activity and Prognosis in Breast Cancer

Anli Yang[1†], Ying Zhou[2†], Yanan Kong[1†], Xiaoli Wei[3†], Feng Ye[1], Lijuan Zhang[1], Xian Zhong[4], Mingyue Li[5], Shilin Lu[6], Xin An[3] and Weikai Xiao[1,7*]*

[1] Department of Breast Oncology, State Key Laboratory of Oncology in South China, Collaborative Innovation Center for Cancer Medicine, Sun Yat-sen University Cancer Center, Guangzhou, China, [2] Department of Infectious Diseases and Endemic Disease Control, Haizhu District Center for Disease Control and Prevention, Guangzhou, China, [3] Department of Medical Oncology, State Key Laboratory of Oncology in South China, Collaborative Innovation Center for Cancer Medicine, Sun Yat-sen University Cancer Center, Guangzhou, China, [4] Department of Ultrasound, The First Affiliated Hospital of Sun Yat-sen University, Guangzhou, China, [5] Department of Pathology and Laboratory Medicine, Perelman School of Medicine, University of Pennsylvania, Philadelphia, PA, United States, [6] Zhongshan School of Medicine, Sun Yat-sen University, Guangzhou, China, [7] Department of Breast Cancer, Cancer Center, Guangdong Provincial People's Hospital, Guangdong Academy of Medical Sciences, Guangzhou, China

The role of DNA methylation of breast cancer-infiltrating immune cells has not been fully explored. We conducted a cohort-based retrospective study analyzing the genome-wide immune-related DNA methylation of 1057 breast cancer patients from the TCGA cohort and GSE72308 cohort. Based on patients' overall survival (OS), a prognostic risk score system using 18 immune-related methylation genes (IRMGs) was established and further validated in an independent cohort. Kaplan–Meier analysis showed a clear separation of OS between the low- and high-risk groups. Patients in the low-risk group had a higher immune score and stromal score compared with the high-risk group. Moreover, the characteristics based on 18-IRMGs signature were related to the tumor immune microenvironment and affected the abundance of tumor-infiltrating immune cells. Consistently, the 18-IRMGs signatures showed similar influences on immune modulation and survival in another external validation cohort (GSE72308). In conclusion, the proposed 18-IRMGs signature could be a potential marker for breast cancer prognostication.

Keywords: DNA methylation, IRMGs, immune infiltration, prognosis, breast cancer

OPEN ACCESS

Edited by:
Mingzhu Yin,
Central South University, China

Reviewed by:
Khaled Murshed,
Hamad Medical Corporation, Qatar
Lei Gu,
Max Planck Institute for Heart and Lung Research, Germany
Neeraj Kaushal,
St. John's University, United States

***Correspondence:**
Xin An
anxin@sysucc.org.cn
Weikai Xiao
xiaowk@sysucc.org.cn

[†]These authors have contributed equally to this work

Specialty section:
This article was submitted to Cancer Immunity and Immunotherapy, a section of the journal Frontiers in Immunology

Received: *03 May 2021*
Accepted: *16 June 2021*
Published: *30 June 2021*

Citation:
Yang A, Zhou Y, Kong Y, Wei X, Ye F, Zhang L, Zhong X, Li M, Lu S, An X and Xiao W (2021) Identification and Validation of Immune-Related Methylation Clusters for Predicting Immune Activity and Prognosis in Breast Cancer. Front. Immunol. 12:704557. doi: 10.3389/fimmu.2021.704557

Abbreviations: IRMGs, immune-related methylation genes; OS, overall survival; ROC, receiver operating characteristic; ICB, immune checkpoint blockade; CNS, central nervous system (CNS); TCGA, The Cancer Genome Atlas; GEO, Gene Expression Omnibus; IRGs, immune-related genes; LASSO, least absolute shrinkage and selection operator; CIBERSORT, Cell-type Identification By Estimating Relative Subsets Of RNA Transcripts; AUC, area under the curve; TIME, tumor immune microenvironment; GO, Geneontology; GSEA, Gene Set Enrichment Analysis; Her2, human epidermal growth factor receptor 2.

INTRODUCTION

The biological behavior and clinical outcome of breast cancer are highly heterogeneous (1, 2). The molecular properties of breast cancer cells have been extensively studied to identify subgroups of patients having different treatment responses and prognosis for targeted therapy based on biomarkers (3–5). However, the tumor microenvironment is a complex mixture of malignant and non-malignant cells including immune cells which can affect the behavior and clinical outcomes of breast cancer. Up to date, the classification of the tumor microenvironment and its impact on prognosis are still poorly understood.

Immune cells from the microenvironment of breast cancer play an important role in determining tumor progression. Single-cell RNA sequencing of breast cancer has confirmed that there is a complex mixture of immune T cell subtypes in tumors (6, 7). Besides, a large number of transcriptomics analyses have been used to explore the immune microenvironment of breast cancer, which indicated that patients with different expression of genes involving multiple immune cells had different survival rates (8–11). Most of the previous research methods to decipher the characteristics of tumor immune microenvironment infiltration were based on the transcriptome (8, 9). DNA methylation, RNA and protein levels can be used as prognostic markers (12). But these markers have their own advantages and disadvantages. For example, DNA methylation and RNA sequencing results can be obtained by high-throughput chip or sequencing (13), which is more efficient and economical. However, high-throughput protein detection is time-consuming and expensive, and has not been widely used. However, few studies have explored the impact of immune cell infiltration on cancer from the perspective of DNA methylation patterns.

DNA methylation has established its role as the main epigenetic driving force in cancer progression and development (14–19). However, its contribution to defining the characteristics of the tumor microenvironment is still poorly understood. It has recently been shown that DNA hypomethylation promotes immune escape in corresponding tumors (15, 20, 21). Furthermore, DNA methylation patterns that predict the response of non-small cell lung cancer to immune checkpoint blockade (ICB) treatment have been revealed (22). DNA methylation patterns are also closely related to cell lineage and high levels of DNA methylation are often detected in blood and skin lineage. Finally, DNA methylation is associated with cellular and cell-free DNA derived from peripheral blood cells (23–25), and has been introduced as a complementary method for classifying the central nervous system (CNS) tumors (26). However, DNA methylation has not been widely used to determine the immune environment that occurs in the microenvironment of breast cancer.

Here, we identified DNA methylation markers, establishing an 18 immune-related methylation genes (IRMGs) signature, which could reflect multiple tumor-related immune cell subpopulations and divided the tumors into two clusters with different clinical and molecular characteristics, which were then validated in an independent dataset. This proposed signature could effectively predict the immune activity of the breast cancer microenvironment and the clinical prognosis of the patients.

MATERIALS AND METHODS

Study Population

Breast cancer datasets from The Cancer Genome Atlas (TCGA) and Gene Expression Omnibus (GEO) were downloaded and the workflow is illustrated in **Figure 1**. GSE72308 contained a set of data obtained from methylation array analysis, which has been used to evaluate the characteristics of immune response based on DNA methylation in breast cancer and other cancers (27). Only patients who met the following criteria were selected: (1) confirmed pathological diagnosis of invasive breast cancer; (2) available DNA methylation and overall survival (OS) data. Patients without active follow-up and transcriptomic data in the TCGA were excluded. In this study, molecular subtypes classified based on immunohistochemical detection in TCGA and GSE72308 were used for analysis. The number of patients in different molecular subtypes in TCGA are: Basal (n=193), HER (n=282), LumA (n=581), LumB (n=219), Normal (n=143).The number of patients in different molecular subtypes in GSE72308 are: Basal (n=65), HER2 (n=56), LumA (n=52), LumB (n=63).This study was based on the analysis of the TCGA and GSE72308 cohort, and was therefore deemed exempt from institutional review board approval by The Sun Yat-sen University Cancer Center, and informed consent was waived. We conducted this study in accordance with the ethical standards of the World Medical Association Declaration of Helsinki.

Data Acquisition and Generation of Immune Methylation Profiles

First, we downloaded a list of immune-related genes (**Supplementary List 1**) from the Immunology Database and Analysis Portal (ImmPort, https://www.immport.org). A total of 1826 immune-related genes for subsequent analysis. Subsequently, we downloaded the methylation data of breast cancer patients from the TCGA and GSE72308 databases. The TCGA methylation profile was obtained from the Xena database (https://xenabrowser.net/). The GSE72308 methylation profile was obtained from the GEO database (https://www.ncbi.nlm.nih.gov/geo/). Finally, the DNA methylation sites of the aforementioned immune-related genes (1812 genes downloaded from ImmPort) were screened in the TCGA and GSE72308 methylation profile. The DNA methylation sites of these immune-related genes are defined as IRMGs.

Besides, the expression profiles of the TCGA cohort were downloaded from the TCGA data portal (https://portal.gdc.cancer.gov/repository). Then we extracted the DNA methylation quantitative index β values [βvalue=methylation signal/(methylation signal + non-methylation signal)]of these genes and the corresponding RNA expression profiles. Subsequently, the correlation between DNA methylation level and RNA expression level was analyzed one by one.

The ensemble IDs were mapped to gene symbols according to the annotation of Homo_sapiens.GRCh38.91.chr.gtf from the ENSEMBLE website. The "limma" package in R was used for gene expression normalization using the scale method (28). The average RNA expression was calculated for duplicates, and genes with low abundance were discarded.

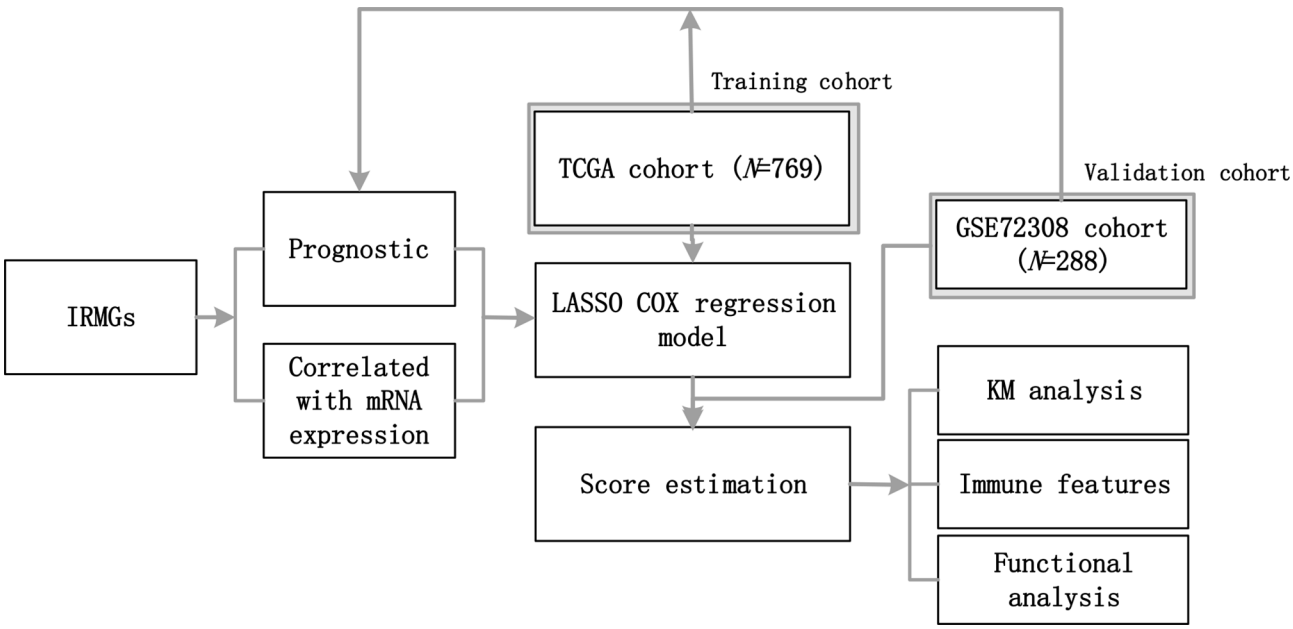

FIGURE 1 | The workflow of this study. A group of IRMGs related to the prognosis of breast cancer was identified in the TCGA and GSE72308 data cohort. Using the LASSO Cox regression model, a new immune methylation cluster was constructed in the TCGA cohort, and its key role in breast cancer immune status and the prognosis was validated in the GSE72308 cohort. IRMGs, immune-related methylation genes; TCGA, The Cancer Genome Atlas; GEO, Gene Expression Omnibus; LASSO, least absolute shrinkage and selection operator; KM, Kaplan-Meier.

Development of the DNA Methylation-Based Immune Profiling

The Univariate Cox regression was used to determine the immune-related methylation genes (IRMGs) associated with OS. The Least Absolute Shrinkage and Selection Operator (LASSO) Cox regression model was further applied to determine the key features and corresponding coefficients for the model construction (29). The LASSO Cox regression was performed using the "glmnet" package of the R software, and the ideal coefficient was estimated based on the partial likelihood deviation with ten-fold cross-validation (30). The optimal log λ was -4.37. To quantify the comprehensive impact of immune methylation status, a new score was calculated based on the features selected by the LASSO model.

First, we obtained IRMGs significantly related to the prognosis of TCGA and GSE72308 cohorts through the univariate cox regression analysis of IRMGs on overall survival. Then, IRMGs with a proper correlation between expression and DNA methylation level (r>0.2 and P<0.05) were selected and added to the LASSO cox regression model for modeling to calculate the score and standardization through the obtained coefficients using the following formula:

$$\mathrm{Sum} = \sum_{i=1}^{n}(\mathrm{IMRG} \times \mathrm{Coef}_i)\mathrm{Score} = (\mathrm{Sum} - \mathrm{Min})/\mathrm{Max}$$

Tumor Microenvironment and Function Analysis

The Cell-type Identification By Estimating Relative Subsets Of RNA Transcripts (CIBERSORT) analysis was used to identify immune cell types. The expression matrix was uploaded using the online analysis platform (https://cibersort.stanford.edu), and the proportion of infiltrating immune cells was estimated by the LM22 signature with 1000 permutations (31). Subsequently, the criterion of P<0.05 was used to select qualified samples. The xCell analysis was performed following its guidelines (https://xcell.ucsf.edu) (32). Immune and stromal scores were further estimated *via* the Estimation of Stromal and Immune cells in MAlignant Tumor tissues using Expression data (ESTIMATE) algorithm with the "estimate" package in R to quantify the immune and stromal components (33). The MCP-counter scores of immune-related active cells and fibroblasts were evaluated using the "MCPcounter" package in R (34). The cluster Profiler package of the R software was used for GO analysis (35). According to previous research, the "fGSEA" software package in R (version 4.0.1) was used to perform GSEA analysis to explore pathway enrichment between the low- and high-risk groups (36).

Statistical Analysis

The Univariate Cox regression was used to identify prognostically relevant IRMGs with a cutoff value of P<0.05. Crucial signatures involved in immune-related methylation clusters were identified using the LASSO Cox regression model. The optimal cut-off value for survival analysis was determined using the "survminer" package in R, and the OS of different subgroups were compared using the Kaplan-Meier method with the log-rank test. For the Kaplan-Meier analysis, the cut-off values for the score-high and score-low groups were based on the median score. The follow-up time was 6 years.

Time-dependent receiver operator characteristic (ROC) analyses were performed using the "timeROC" package in R (34). Spearman's correlation test was used for Score-related analysis. All statistical analyses were performed using the R software (Version 4.0.1). A *P* value of <0.05 was considered statistically significant, and all *P* values were two-tailed.

RESULTS

DNA Methylation-Based Immune Profiling of Breast Cancer

To explore the pattern of immune infiltration based on DNA methylation in breast cancer, we first compiled the TCGA methylation profile and GSE72308 methylation profile (**Figure 1**) to identify the corresponding IRMGs. A population of 769 and 288 patients from the TCGA and GSE72308 were included in this study. The IRMGs data from the TCGA and GSE72308 were subjected to univariate Cox proportional hazard regression analysis, of which a total of 226 IRMGs (**Supplementary List 2**) were found significantly related to the OS of breast cancer patients (P<0.05) in both cohorts and were identified as candidate markers (**Figures 2A–C**). Subsequently, 61 IRMGs (**Supplementary List 3**) were significantly correlated with corresponding mRNA expression (|r|>0.2, P<0.05) and were selected for the prognosis prediction model. Based on these, the LASSO Cox regression model was used to construct a prognostic model for the OS stratification of the patients from the TCGA data set (N=769). First, we determined the penalty value [log(lambda)=-4.37] according to the lowest point of the **Figure 2E** curve, and drew a vertical line at the position of log(Lambda)=-4.37 in **Figure 2D**. Each curve in **Figure 2D** represented a variable, and the curve that intersected with vertical line at the position of log(Lambda)=-4.37 was the final included in the model. The ordinate corresponding to the variable was the regression coefficient of the variable. In the regression equation, the regression coefficient represented the contribution of the variable.

18 IRMGs were selected according to the method of partial likelihood deviance, and the corresponding coefficients were generated with the best logλ of -4.37. **Supplementary List 4** shows the positions of these 18 IRMGs in the corresponding genes. The hazard ratio model consisting of 18 methylation sites (cg06735472, cg20862496, cg02172616, cg09108314, cg09369954, cg03779097, cg27460943, cg16633817, cg19901994, cg16265078, cg10942339, cg03240473, cg19266578, cg00668559, cg12697789, cg14993712, cg25562664, cg00743540) was selected as the best prognostic model for predicting OS (**Figures 2D, E**). The genes corresponding to these 18 methylation sites were SLURP1 (cg240862496), IL17RD(cg00743540), NFKBIE(cg00668559), OPRL1(cg19266578), NR3C2(cg27460943), ZC3HAV1L (cg14993712), EED(cg02172616), TXLNA(cg09369954), FGF2 (cg09108314), EED(cg16265078), TLR3(cg12697789), FAM3B (cg06735472), NR1I2(cg25562664), ROBO2(cg16633817),

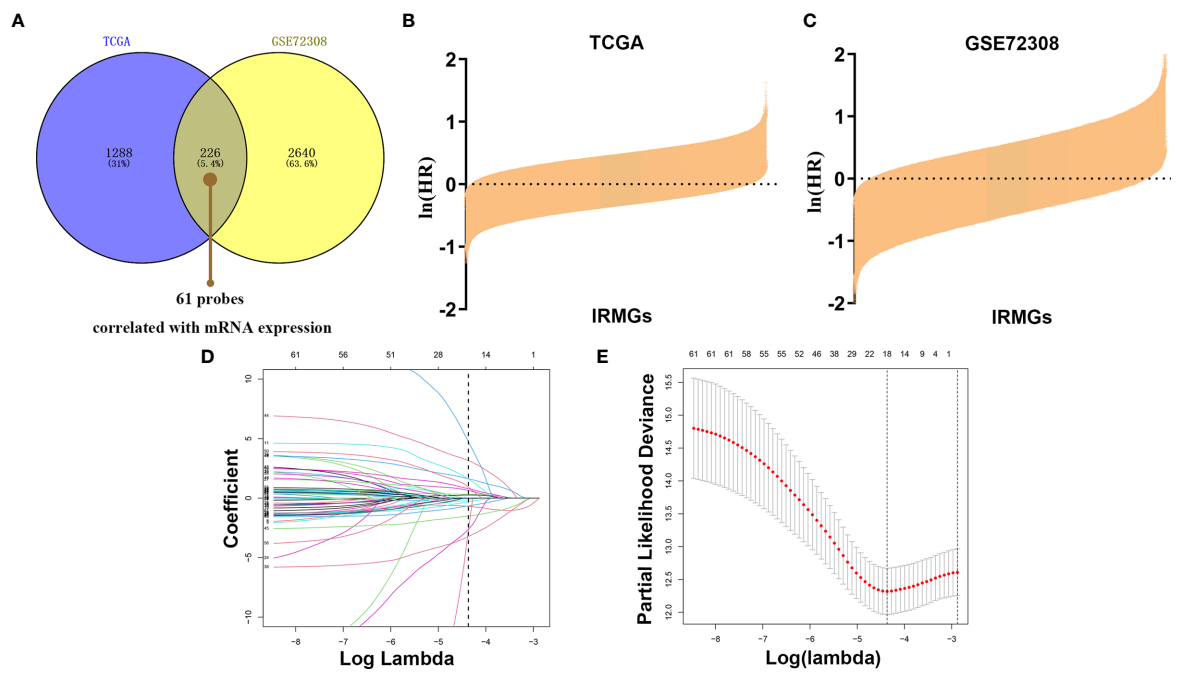

FIGURE 2 | Identification of prognostic IRMGs in breast cancer. **(A)** Venn plot shows that the 61 IRMGs identified in the two cohorts were associated with mRNA expression. **(B, C)** Bar graph showing the hazard ratio of IRMG in the TCGA cohort and GSE72308 cohort. The bars represent *95%CI*. The Univariate Cox regression was used for data analysis. **(D, E)** The LASSO Cox regression model was constructed from the 61 signature IRMGs, and the adjustment parameter (λ) was calculated based on the partial likelihood deviation with ten-fold cross-validation. The optimal log λ value is -4.37, as shown by the vertical black line in the curve. According to the best fit contour, an 18-IRMGs signature was determined. IRMGs, immune-related methylation genes; TCGA, The Cancer Genome Atlas; GEO, Gene Expression Omnibus; LASSO, least absolute shrinkage and selection operator.

PTK2B(cg19901994), OPRL1(cg03779097), MICB (cg10942339) and UMODL1(cg03240473). **Figure 3** shows the correlation coefficient and *P* value between the IRMGs selected by the LASSO model and their corresponding mRNA expression.

Kaplan-Meier analysis further confirmed the prognostic value of each of these 18 IRMGs (**Supplemental Figure 1**). Patients with higher methylation levels of cg03240473, cg19266578, cg00668559, cg12697789, cg14993712, cg25562664, and cg00743540 had poorer prognosis, while patients with higher methylation levels of cg06735472, cg20862496, cg02172616, cg09108314, cg09369954, cg03779097, cg27460943, cg16633817, cg19901994, cg16265078, cg10942339 had better prognosis; which was consistent with the results of the Lasso Cox regression analysis. The methylation values of the 18 IRMGs in TCGA and the corresponding *HR* and *95%CI* are shown in **Figures 4A, B**. Among the 18 IRMGs, 11 IRMGs was associated with improved prognosis while 7 with poor prognosis.

The risk score of the TCGA training cohort was calculated using the coefficients obtained by the above-mentioned LASSO algorithm. The risk score distribution of the 18 immune methylation markers in the TCGA training cohort is shown in **Figure 4C**. The risk scores of different molecular subtypes were significantly different, with HER2 positive scores being the highest, followed by the basal-like subtype and luminal B subtype. The risk score of these three subtypes was significantly higher than that of luminal A (**Figure 4D**). However, there was no significant correlation between the risk score and tumor size, lymph node metastasis, TNM stage, and age. The distribution of risk scores based on different survival time and survival status (alive or dead) is shown in **Figure 4E**. From this, we can observe that the patients who died (red dots) are more distributed in the high-risk group. Second, patients in the low-risk group had a longer survival time.

The 18-IRMGs Signature Was Significantly Associated With Molecular Characteristics and Immune Features

We first analyzed the enriched pathways of the 18-IRMGs signature through biological function enrichment analysis. The results showed that genes were significantly enriched in immune-related pathways of GO categories (**Figure 5A**), including humoral immune response, immunoglobulin production, T cell receptor complex, and immunoglobulin complex. Furthermore, Gene Set Enrichment Analysis (GSEA) analysis revealed 12 important pathways related to the 18-IRMGs signature, including adaptive immune response, T cell receptor complex, immunoglobulin complex, antigen binding, B cell receptor signaling pathway, lymphocyte-mediated immunity, neutrophil-mediated immunity, and more (**Figure 5B**). To study the effect of the 18-IRMGs signature on the immune microenvironment of breast cancer, we evaluated the immune score and stromal score between the high- and low-risk groups. The results showed a significant difference in immune score and stromal score between the high-risk and low-risk groups (**Figures 5C, D**). The immune score and stromal score of the low-risk group were significantly higher than that of the high-risk group ($P<0.05$).

Further, the ratio of 22 immune cell types between the two subgroups was analyzed. We first used the CIBERSORT algorithm to estimate the proportion of immune cells in the TCGA cohort (**Figure 5E**), and found that the low-risk group had a higher percentage of anti-tumor immune cells, including gamma delta (γδ) T cells ($P<0.05$), CD4+ memory T cells ($P<0.01$), mast cells ($P<0.01$), and resting dendritic cells ($P<0.01$). In addition, patients in the high-risk group showed a higher proportion of immunosuppressive cells, such as M0 macrophages. Although we

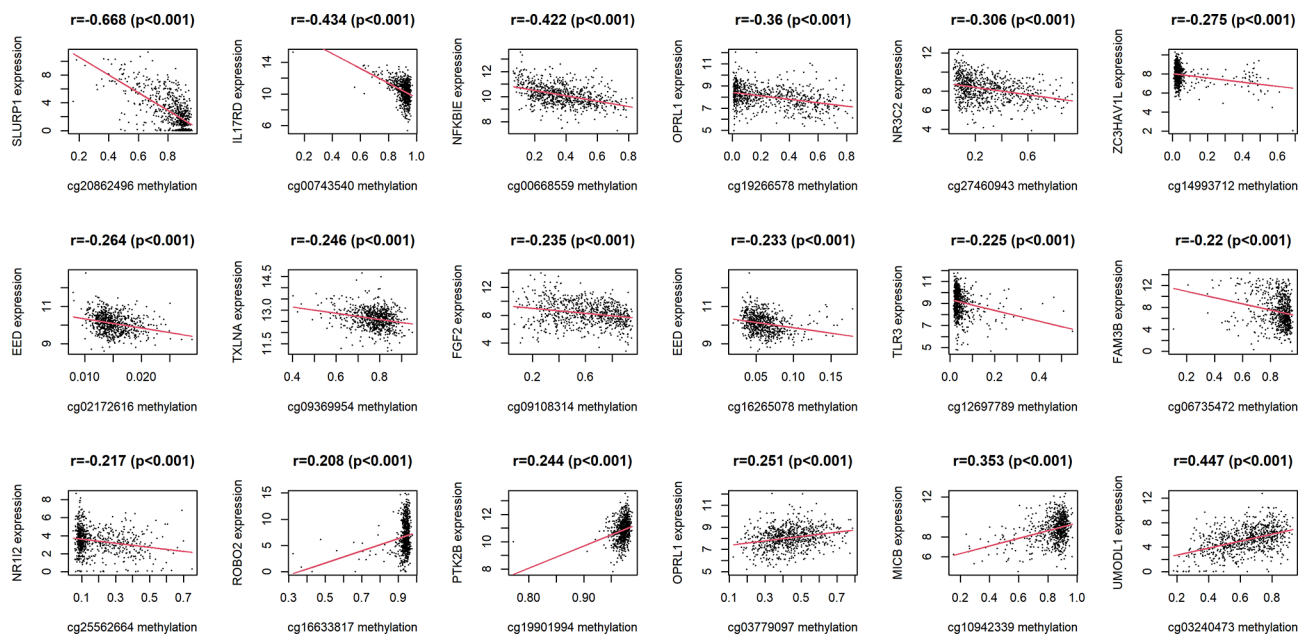

FIGURE 3 | The correlation between IRMGs identified in the LASSO model using the TCGA cohort and their corresponding mRNA expression levels.

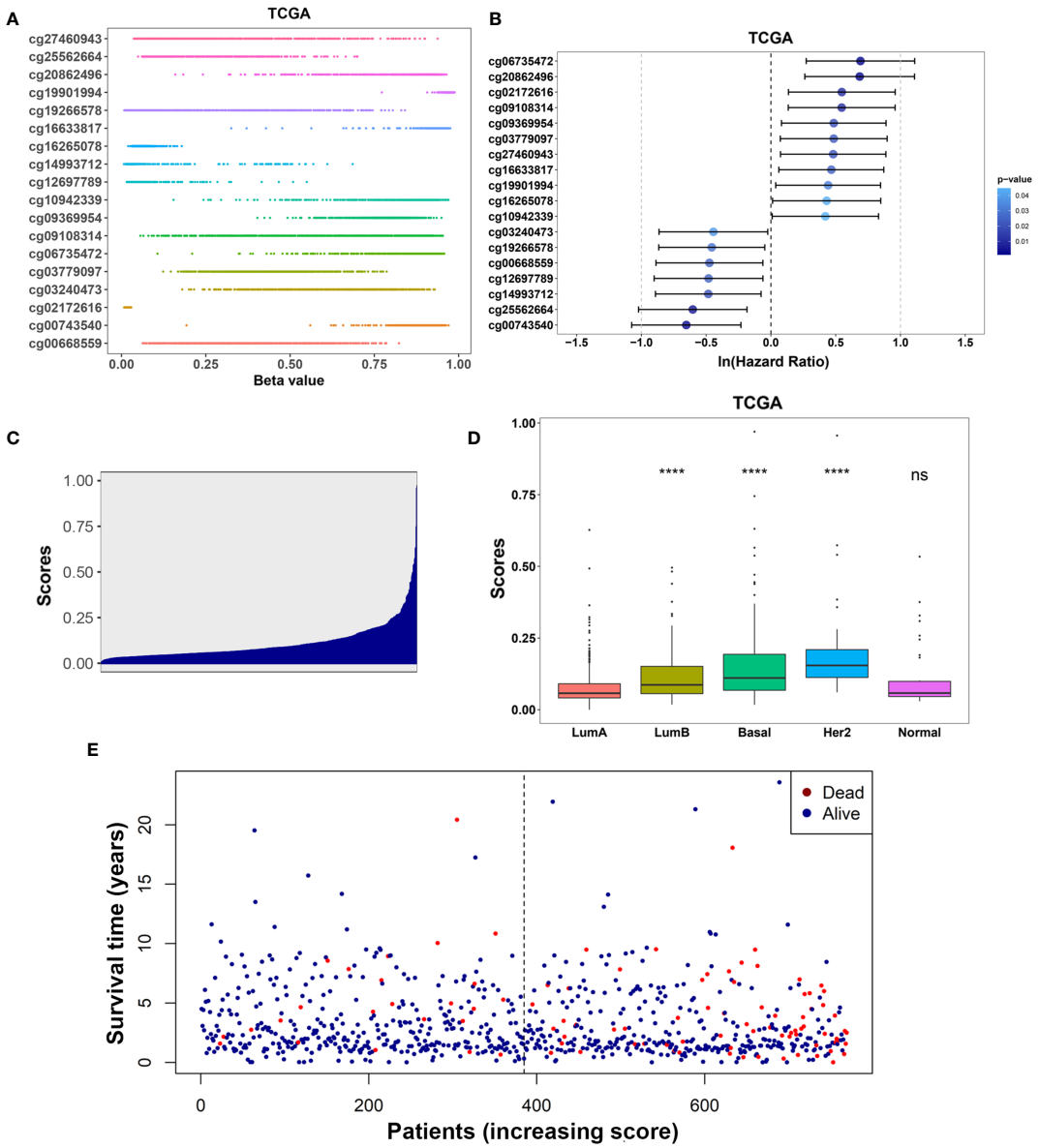

FIGURE 4 | **(A)** Distribution of methylation levels of the 18-IRMGs signature in the TCGA cohort; **(B)** Multivariate Cox regression analysis results of the 18-IRMGs signature corresponding to OS in the TCGA cohort. **(C)** Distribution of risk scores in the TCGA cohort; **(D)** Comparison of risk scores of different molecular subtypes in the TCGA cohort (****: p<=0.0001, ns: p>0.05); **(E)** The distribution of patients in different risk scores according to survival status and survival time. IRMGs, immune-related methylation genes; OS, overall survival; TCGA, The Cancer Genome Atlas; Her2, human epidermal growth factor receptor 2.

observed that the level of activated dendritic cells in the high-risk group was higher than that in the low-risk group, the absolute level in both groups was very low, even far lower than other types of immune cells. The effect of such a low level of activated dendritic cells may be almost negligible. Then, the MCP-counter algorithm was used to estimate the proportion of immune cells in the TCGA cohort (**Figure 5F**). Consistent with the above results, patients in the low-risk group also demonstrated a higher percentage of anti-tumor immune cells, including T cells, CD8+ T cells, cytotoxic T cells, B lineage, myeloid dendritic cells, and neutrophils. In addition, the risk score was negatively correlated with the mRNA expression of immune checkpoints CD27, CD40, ENTPD1, PDCD1, CD274, HAVCR2, CD33, CD4, TBX21, CD8B, and PRF1, but positively correlated with the expression of NOS2 (**Figure 5G**). We also observed that the risk score was mainly negatively correlated with the expression of immune checkpoints related to T cells.

Prognostic Value of the 18-IRMGs Signature

The development of convenient tools for early diagnosis and treatment guidance of diseases remains a critical clinical issue.

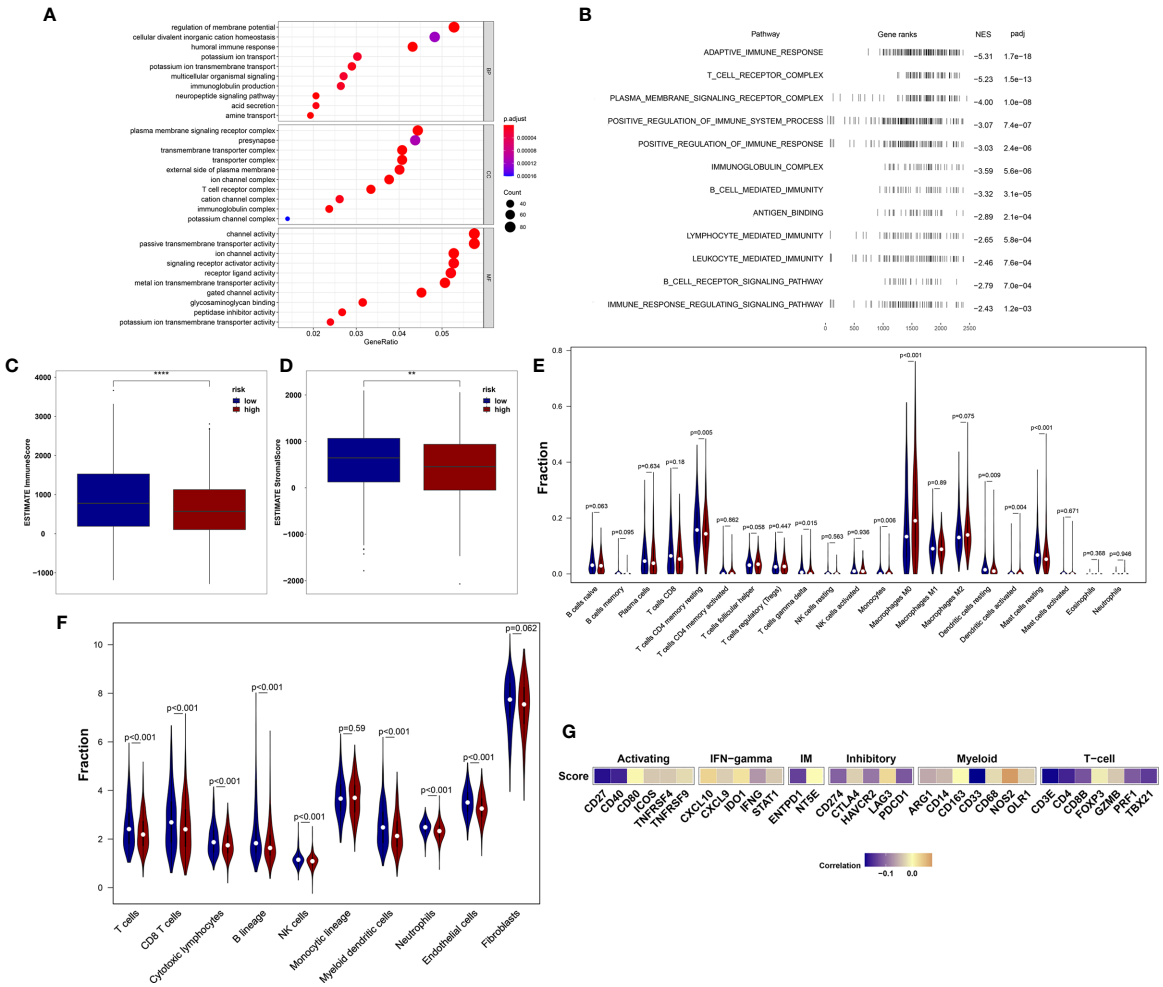

FIGURE 5 | 18-IRMGs signature related immune characteristics and immune cells. **(A)** GO analysis of the group based on18-IRMGs signature. **(B)** GSEA is related to immune-related signals based on the 18-IRMGs signature. **(C, D)** ESTIMATE immune score and stromal score between groups based on IMI (**: p<=0.01, ****: p<=0.0001). **(E)** Comparison of infiltrating immune cells (CIBERSORT) between the two risk groups. **(F)** Comparison of infiltrating immune cells (MCP counter) between the two risk groups. **(G)** Correlation between risk scores and immune-related genes in the TCGA cohort. IRMGs, immune-related methylation genes; GO, Geneontology; GSEA, Gene Set Enrichment Analysis; ESTIMATE, Estimation of Stromal and Immune cells in MAlignant Tumor tissues using Expression data; CIBERSORT, Cell-type Identification By Estimating Relative Subsets Of RNA Transcripts.

To further clarify the prognostic and prognostic value of the 18-IRMGs signature in breast cancer, ROC analysis, and the Kaplan-Meier method were used to assess the prognosis in the TCGA cohort.

First, the overall survival of patients with different risk scores was compared. In the TCGA cohort, patients in the low-risk group had a better OS than those in the high-risk group (**Figure 6A**). A time-related ROC analysis was performed and the area under the curve (AUC) was calculated at different time points based on the availability of data (**Figures 6B–D**). The results suggested that the corresponding AUCs of the ROC analysis for 1-, 3-, and 5-year follow-up in the TCGA cohort were 0.788, 0.771, and 0.721, respectively (**Figures 6B–D**). This indicated that the 18-IRMGs signature had good prognostic value in both short-term and long-term follow-up.

Validation of the 18-IRMGs Signature for Breast Cancer Survival Prediction in an Independent Cohort

The GSE72308 was used as the independent external validation cohort (*N*=288). First, the methylation values of the 18 IRMGs and risk score distribution of all the patients in the GSE72308 cohort are shown in **Figures 7A, B**. Consistent with the TCGA cohort, in the GSE72308 cohort, it was also observed that the HER2 positive subtype had the highest risk score, followed by basal-like subtypes and luminal B subtypes. The risk scores of these three subtypes were significantly higher than the luminal A subtype (**Figure 7C**). Similarly, high- or low-risk patients were grouped according to the median risk score. The results showed that the 18-IRMGs signature performed well, and compared with the high-risk group, the OS of patients in the low-risk group was

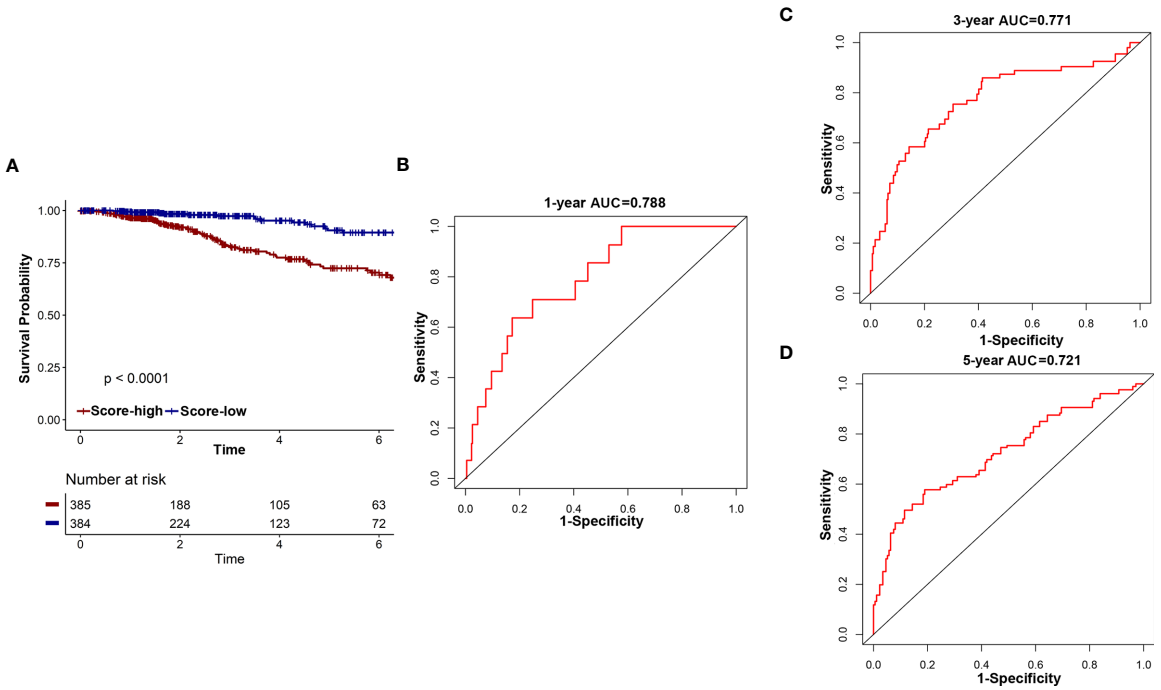

FIGURE 6 | The potential indicator value of 18-IRMGs signature in the prognosis of TCGA breast cancer. **(A)** Kaplan-Meier plot of OS between the two risk groups in the TCGA cohort. The log-rank test was used for data analysis. **(B–D)** Time-dependent ROC analysis (1, 3, and 5 years) based on 18-IRMGs signature in breast cancer patients in the TCGA cohort. IRMGs, immune-related methylation genes; OS, overall survival; ROC, receiver operating characteristic; TCGA, The Cancer Genome Atlas; AUC, area under the curve.

significantly longer ($P<0.05$) (**Figure 7H**). The ROC curve over time shows that the 18-IRMGs signature had good accuracy, with 0.839 for 1 year-AUC, 0.712 for 3 years-AUC, and 0.723 for 5 years-AUC (**Figures 7D–F**). The distribution of risk scores of breast cancer patients from the GSE72308 cohort based on different survival time and survival status (alive or dead) was also shown in **Figure 7G**.

DISCUSSION

In this study, we provided new insights into the heterogeneity of the tumor immune microenvironment of breast cancer and confirmed that the specific characteristics of immune methylation have an important prognostic value. We analyzed the relationship between DNA methylation and tumor immunity of breast cancer through the IRGMs set, and identified two immune methylation clusters significantly related to patient survival, which was then validated in an independent cohort. These demonstrated the relationship between immune methylation characteristics and corresponding immune cell infiltration in the tumor microenvironment and patient prognosis.

Some recent studies have suggested that there are abnormal methylation events in breast tumors, and specific DNA methylation patterns may be closely related to breast cancer immune microenvironment, molecular subtypes, and recurrence. Dedeurwaerder et al. (37) conducted DNA methylation analysis on 248 breast tissues and found that DNA methylation analysis can reflect the cell type composition of the tumor microenvironment, especially the T lymphocyte infiltration of the tumor. What they found also strongly proved that DNA methylation can indeed help better understand the complex relationship between tumor cells and the immune microenvironment. Holm et al. (38) used an array-based methylation assay to analyze the methylation status of 807 cancer-related genes in 189 fresh frozen primary breast tumors and 4 normal breast tissue samples. They found that basal-like, luminal A and luminal B subtypes of breast cancer have specific methylation characteristics, suggesting that methylation may play an important role in the development of breast cancer. Kamalakaran et al. (39) found that the DNA methylation pattern in luminal breast cancer is different from non-luminal subtypes, and the DNA methylation pattern can be independent of other clinical variables to identify the risk of recurrence.

Based on the TCGA data set of 769 breast cancer samples that met the inclusion criteria, the current study has identified prognostic immune methylation features with potential clinical applicability. The risk score obtained from the 18-IRMGs signature effectively divided breast cancer patients into high-risk and low-risk groups. In the TCGA cohort, the OS of the high-risk group was shorter than that of the low-risk group ($p<0.001$) and also demonstrated good prognostic performance (AUC of 1, 3, and 5 years are 0.788, 0.771, and 0.721, respectively). Besides, the results of the univariate Cox regression (**Figure 4B**) and Kaplan-Meier (**Supplementary Figure 1**) for 18 individual immune

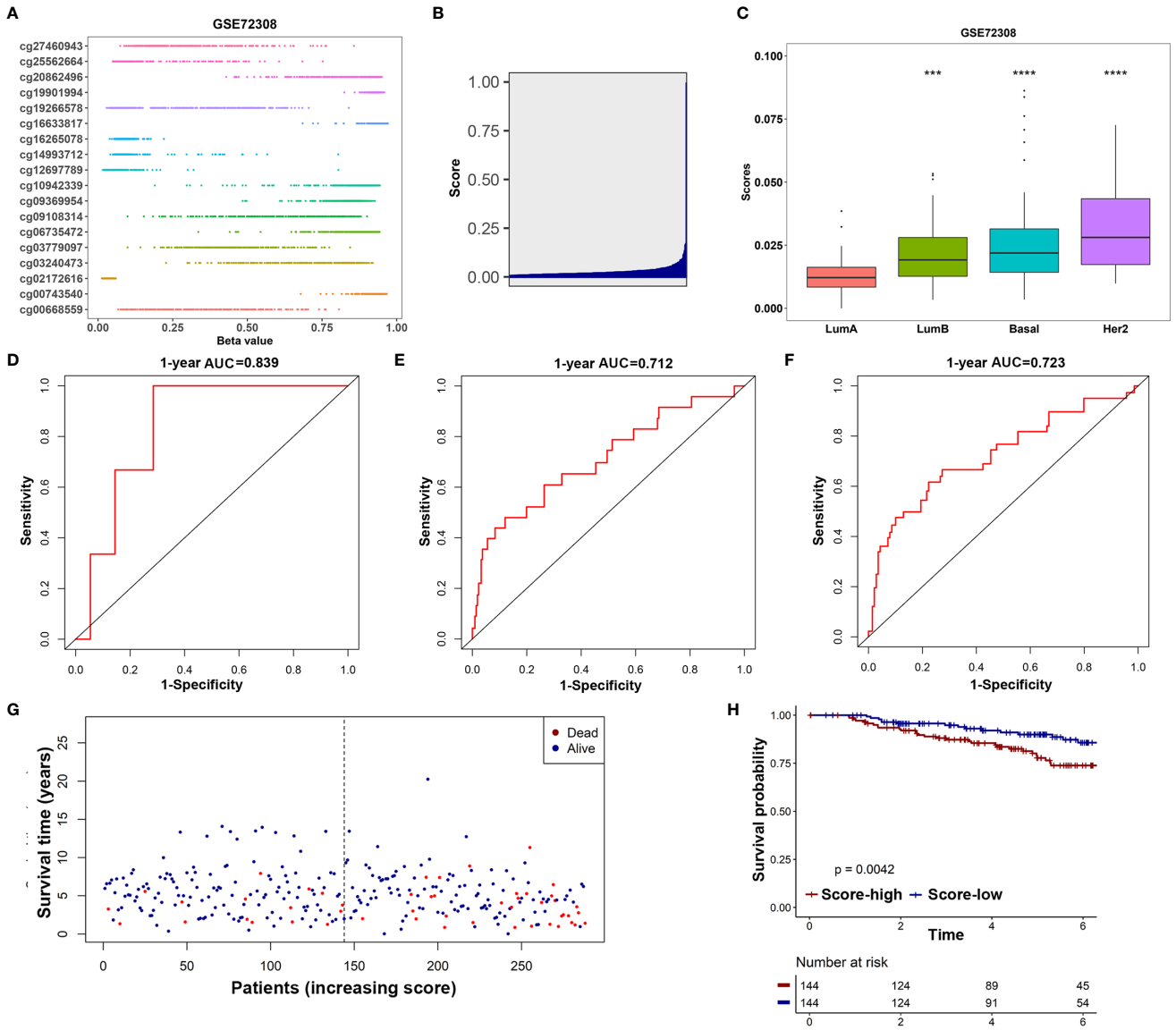

FIGURE 7 | Validation of the prognostic value of 18-IRMGs signature for OS in the GSE72308 cohort. **(A)** Distribution of methylation levels of 18 IRMGs in the GSE72308 cohort; **(B)** Distribution of risk scores in the GSE72308 cohort; **(C)** Comparison of risk scores of different molecular subtypes in the GSE72308 cohort (***: p<=0.001, ****: p<=0.0001); **(D–F)** Time-dependent ROC analysis (1, 3, and 5 years) based on 18-IRMGs signature in breast cancer patients in the GSE72308 cohort; **(G)** The distribution of patients of different risk scores according to survival status and survival time; **(H)** Kaplan-Meier plot of OS between the two risk groups in the GSE72308 cohort. The log-rank test was used for data analysis. IRMGs, immune-related methylation genes; OS, overall survival; ROC, receiver operating characteristic; AUC, area under the curve; Her2, human epidermal growth factor receptor 2.

methylation sites showed that each immune methylation site could also distinguish high-risk and low-risk patients. This indicated that a single immune methylation site may play a role in prognostic prediction, and the combination of 18 methylation sites provided better prognostication ability. Based on our existing knowledge, the prognostic value of related multiple immune methylation signatures in breast cancer has not been reported. Therefore, this study provides new insights on the combination of epigenetic biomarkers helping to improve the risk stratification and survival prediction of breast cancer patients.

Considering that ideal prognostic markers can also effectively stratify risk in other independent cohorts, we used the GSE72308 cohort to further evaluate the practicality of the 18-IRMGs signature. It performed well in distinguishing the low-risk and high-risk groups of the GEO cohort, and the prediction accuracy of the GSE72308 cohort was consistent with the TCGA cohort (1-year-AUC=0.839, 3-years-AUC =0.712, and 5-years-AUC=0.723).

The blockade of immune checkpoints such as PD-1, PD-L1, and CTLA-4 has shown impressive results in a series of solid

cancers (especially melanoma and non-small cell lung cancer). Currently, there are many ongoing and planned trials of these drugs in breast cancer. However, only a small percentage of breast cancer patients respond to immune checkpoint blockade (ICB) treatment, and the identification of ICB response biomarkers and drug resistance modifiers is a key challenge. DNA methylation plays a vital role in cell lineage regulation and can be used as a specific molecular marker for immune response measurement. The role of DNA methylation in the immune response to cancer is becoming increasingly important and it is currently considered to be closely related to the efficacy of immunotherapy for melanoma and other tumors. Recently, Duruisseaux M et al. (22) found that a microarray DNA methylation signature could predict the efficacy of anti-PD-1 therapy in stage IV NSCLC patients. Similarly, Kim et al. also found that methylation patterns could predict the clinical benefit of immunotherapy in lung cancer (40). In the present study, our proposed 18-IRMGs signature was found to be significantly related to the prognosis of breast cancer patients.

Further analyses showed that the characteristics based on 18-IRMGs signature were related to the tumor immune microenvironment and affected the abundance of tumor-infiltrating immune cells. The stromal cell score and the immune score of the high-risk group were significantly lower than the low-risk group. Further analysis showed that in the low-risk group, the infiltration level of quiescent mast cells, CD4 memory T cells, mast cells, gamma delta T cells and resting dendritic cells was higher than the high-risk group. In contrast, the infiltration level of macrophages M0 cells in the high-risk group were higher than those in the low-risk group. Although we observed that the activated dendritic cells in the high-risk group was higher than that in the low-risk group, the absolute level in both groups was very low, even far lower than other types of immune cells. The effect of such a low level of activated dendritic cells may be almost negligible. In general, the significant difference in survival rate between the two groups may be related to the difference in the immune microenvironment of the two groups. This finding is consistent with the results of previous studies, which showed that patients with low immune scores had a worse survival than patients with high immune scores.

Undeniably, our research had several limitations. First, despite the identification and validation of the 18-IRMGs signature, additional prospective external verification is required in a multicenter cohort to confirm the study findings. Second, it is necessary to further study the regulatory mechanism of DNA methylation in tumor immune microenvironment(TIME) to reshape TIME and improve precision immunotherapy for breast cancer. Third, there is no data on DNA methylation in breast cancer patients receiving immunotherapy, so it is unclear whether they could also be used as a marker for predicting ICB efficacy. Fourth, this study mainly used two independent databases (GSE72308 and TCGA data sets) to analyze the relationship between IRMG and immune activity. The results of this study have not been verified by extensive *in vitro* experiments. Fifth, we did not find any significant correlation between TNM staging and the 18-IRMGs signature, suggesting that the two are independent of each other in judging prognosis.

CONCLUSION

In summary, we identified and validated an 18-IRMGs signature that was significantly associated with OS in independent cohorts. The proposed 18-IRMGs signature demonstrated promising accuracy in stratifying breast cancer patients based on their survival differences and could be used as a guide to assess the need for adjuvant therapy. In addition, the 18-IRMGs signature was closely related to the tumor immune microenvironment and may be used to select patients who respond to immunotherapy.

DATA AVAILABILITY STATEMENT

The data used and analyzed during the current study areavailable from the corresponding author on reasonable request.

AUTHOR CONTRIBUTIONS

AY, YZ,YK, and XW conceived and designed the experiments. AY, YZ,YK, XW, FY, LZ, XZ, ML, SL, XA, and WX performed the experiments and analyzed the data. XA and WX wrote the paper. All authors contributed to the article and approved the submitted version.

FUNDING

This research is funded by the National Natural Science Foundation of China (approval No.: 8203066), Guangzhou basic and applied basic research project (approved in 2021), and special science and Technology Fund (Doctoral entrepreneurship project) of Guangdong People's Hospital and Guangdong Provincial Medical Research Fund (a2021080).

SUPPLEMENTARY MATERIAL

The Supplementary Material for this article can be found online at: https://www.frontiersin.org/articles/10.3389/fimmu.2021.704557/full#supplementary-material

Supplementary Figure 1 | Kaplan-Meier plot of overall survival for 18 individual immune methylation sites showed that each immune methylation site could distinguish high-risk and low-risk patients in the TCGA cohort. The log-rank test was used for data analysis.

Supplementary List 1 | List of 1812 immune-related genes from ImmPort.

Supplementary List 2 | A total of 226 IRMGs were found significantly related to the OS of breast cancer patients.

Supplementary List 3 | The 61 IRMGs were used in prognostic prediction models.

Supplementary List 4 | The positions of the 18 IRMGs in the corresponding genes.

REFERENCES

1. Srivastava S, Koay EJ, Borowsky AD, De Marzo AM, Ghosh S, Wagner PD, et al. Cancer Overdiagnosis: A Biological Challenge and Clinical Dilemma. *Nat Rev Cancer* (2019) 19(6):349–58. doi: 10.1038/s41568-019-0142-8
2. Ding S, Chen X, Shen K. Single-Cell RNA Sequencing in Breast Cancer: Understanding Tumor Heterogeneity and Paving Roads to Individualized Therapy. *Cancer Commun (Lond)* (2020) 40(8):329–44. doi: 10.1002/cac2.12078
3. Harbeck N, Gnant M. Breast Cancer. *Lancet* (2017) 389(10074):1134–50. doi: 10.1016/S0140-6736(16)31891-8
4. Guan X, Ma F, Li C, Wu S, Hu S, Huang J, et al. The Prognostic and Therapeutic Implications of Circulating Tumor Cell Phenotype Detection Based on Epithelial-Mesenchymal Transition Markers in the First-Line Chemotherapy of HER2-Negative Metastatic Breast Cancer. *Cancer Commun (Lond)* (2019) 39(1):1. doi: 10.1186/s40880-018-0346-4
5. Waks AG, Winer EP. Breast Cancer Treatment: A Review. *JAMA* (2019) 321 (3):288–300. doi: 10.1001/jama.2018.19323
6. Wagner J, Rapsomaniki MA, Chevrier S, Anzeneder T, Langwieder C, Dykgers A, et al. A Single-Cell Atlas of the Tumor and Immune Ecosystem of Human Breast Cancer. *Cell* (2019) 177(5):1330–45.e18. doi: 10.1016/j.cell.2019.03.005
7. Jackson HW, Fischer JR, Zanotelli V, Ali HR, Mechera R, Soysal SD, et al. The Single-Cell Pathology Landscape of Breast Cancer. *Nature* (2020) 578 (7796):615–20. doi: 10.1038/s41586-019-1876-x
8. Zheng S, Zou Y, Liang JY, Xiao W, Yang A, Meng T, et al. Identification and Validation of a Combined Hypoxia and Immune Index for Triple-Negative Breast Cancer. *Mol Oncol* (2020) 14(11):2814–33. doi: 10.1002/1878-0261.12747
9. Zheng S, Zou Y, Xie X, Liang JY, Yang A, Yu K, et al. Development and Validation of a Stromal Immune Phenotype Classifier for Predicting Immune Activity and Prognosis in Triple-Negative Breast Cancer. *Int J Cancer* (2020) 147(2):542–53. doi: 10.1002/ijc.33009
10. Ali HR, Chlon L, Pharoah PD, Markowetz F, Caldas C. Patterns of Immune Infiltration in Breast Cancer and Their Clinical Implications: A Gene-Expression-Based Retrospective Study. *PloS Med* (2016) 13(12):e1002194. doi: 10.1371/journal.pmed.1002194
11. Yi L, Wu G, Guo L, Zou X, Huang P. Comprehensive Analysis of the PD-L1 and Immune Infiltrates of M(6)A RNA Methylation Regulators in Head and Neck Squamous Cell Carcinoma. *Mol Ther Nucleic Acids* (2020) 21:299–314. doi: 10.1016/j.omtn.2020.06.001
12. Gu L, Frommel SC, Oakes CC, Simon R, Grupp K, Gerig CY, et al. BAZ2A (TIP5) Is Involved in Epigenetic Alterations in Prostate Cancer and its Overexpression Predicts Disease Recurrence. *Nat Genet* (2015) 47(1):22–30. doi: 10.1038/ng.3165
13. Wang Q, Gu L, Adey A, Radlwimmer B, Wang W, Hovestadt V, et al. Tagmentation-Based Whole-Genome Bisulfite Sequencing. *Nat Protoc* (2013) 8(10):2022–32. doi: 10.1038/nprot.2013.118
14. Gu L, Wang L, Chen H, Hong J, Shen Z, Dhall A, et al. CG14906 (Mettl4) Mediates M(6)A Methylation of U2 snRNA in Drosophila. *Cell Discovery* (2020) 6:44. doi: 10.1038/s41421-020-0178-7
15. Fleischer T, Tekpli X, Mathelier A, Wang S, Nebdal D, Dhakal HP, et al. DNA Methylation at Enhancers Identifies Distinct Breast Cancer Lineages. *Nat Commun* (2017) 8(1):1379. doi: 10.1038/s41467-017-00510-x
16. Feinberg AP, Koldobskiy MA, Göndör A. Epigenetic Modulators, Modifiers and Mediators in Cancer Aetiology and Progression. *Nat Rev Genet* (2016) 17 (5):284–99. doi: 10.1038/nrg.2016.13
17. Fleischer T, Frigessi A, Johnson KC, Edvardsen H, Touleimat N, Klajic J, et al. Genome-Wide DNA Methylation Profiles in Progression to *in Situ* and Invasive Carcinoma of the Breast With Impact on Gene Transcription and Prognosis. *Genome Biol* (2014) 15(8):435. doi: 10.1186/s13059-014-0435-x
18. Klughammer J, Kiesel B, Roetzer T, Fortelny N, Nemc A, Nenning KH, et al. The DNA Methylation Landscape of Glioblastoma Disease Progression Shows Extensive Heterogeneity in Time and Space. *Nat Med* (2018) 24(10):1611–24. doi: 10.1038/s41591-018-0156-x
19. Sina AA, Carrascosa LG, Trau M. DNA Methylation-Based Point-Of-Care Cancer Detection: Challenges and Possibilities. *Trends Mol Med* (2019) 25 (11):955–66. doi: 10.1016/j.molmed.2019.05.014
20. Briand J, Nadaradjane A, Bougras-Cartron G, Olivier C, Vallette FM, Cartron PF. Diuron Exposure and Akt Overexpression Promote Glioma Formation Through DNA Hypomethylation. *Clin Epigenet* (2019) 11(1):159. doi: 10.1186/s13148-019-0759-1
21. Das D, Ghosh S, Maitra A, Biswas NK, Panda CK, Roy B, et al. Epigenomic Dysregulation-Mediated Alterations of Key Biological Pathways and Tumor Immune Evasion are Hallmarks of Gingivo-Buccal Oral Cancer. *Clin Epigenet* (2019) 11(1):178. doi: 10.1186/s13148-019-0782-2
22. Duruisseaux M, Martínez-Cardús A, Calleja-Cervantes ME, Moran S, Castro de Moura M, Davalos V, et al. Epigenetic Prediction of Response to Anti-PD-1 Treatment in Non-Small-Cell Lung Cancer: A Multicentre, Retrospective Analysis. *Lancet Respir Med* (2018) 6(10):771–81. doi: 10.1016/S2213-2600(18)30284-4
23. Houseman EA, Accomando WP, Koestler DC, Christensen BC, Marsit CJ, Nelson HH, et al. DNA Methylation Arrays as Surrogate Measures of Cell Mixture Distribution. *BMC Bioinf* (2012) 13:86. doi: 10.1186/1471-2105-13-86
24. Moss J, Magenheim J, Neiman D, Zemmour H, Loyfer N, Korach A, et al. Comprehensive Human Cell-Type Methylation Atlas Reveals Origins of Circulating Cell-Free DNA in Health and Disease. *Nat Commun* (2018) 9 (1):5068. doi: 10.1038/s41467-018-07466-6
25. Shao F, Yang X, Wang W, Wang J, Guo W, Feng X, et al. Associations of PGK1 Promoter Hypomethylation and PGK1-Mediated PDHK1 Phosphorylation With Cancer Stage and Prognosis: A TCGA Pan-Cancer Analysis. *Cancer Commun (Lond)* (2019) 39(1):54. doi: 10.1186/s40880-019-0401-9
26. Capper D, Jones D, Sill M, Hovestadt V, Schrimpf D, Sturm D, et al. DNA Methylation-Based Classification of Central Nervous System Tumours. *Nature* (2018) 555(7697):469–74. doi: 10.1038/nature26000
27. Jeschke J, Bizet M, Desmedt C, Calonne E, Dedeurwaerder S, Garaud S, et al. DNA Methylation-Based Immune Response Signature Improves Patient Diagnosis in Multiple Cancers. *J Clin Invest* (2017) 127(8):3090–102. doi: 10.1172/JCI91095
28. Ritchie ME, Phipson B, Wu D, Hu Y, Law CW, Shi W, et al. Limma Powers Differential Expression Analyses for RNA-Sequencing and Microarray Studies. *Nucleic Acids Res* (2015) 43(7):e47. doi: 10.1093/nar/gkv007
29. Tibshirani R. The Lasso Method for Variable Selection in the Cox Model. *Stat Med* (1997) 16(4):385–95. doi: 10.1002/(SICI)1097-0258(19970228)16:4<385::AID-SIM380>3.0.CO;2-3
30. Friedman J, Hastie T, Tibshirani R. Regularization Paths for Generalized Linear Models *via* Coordinate Descent. *J Stat Softw* (2010) 33(1):1–22. doi: 10.18637/jss.v033.i01
31. Newman AM, Liu CL, Green MR, Gentles AJ, Feng W, Xu Y, et al. Robust Enumeration of Cell Subsets From Tissue Expression Profiles. *Nat Methods* (2015) 12(5):453–7. doi: 10.1038/nmeth.3337
32. Aran D, Hu Z, Butte AJ. xCell: Digitally Portraying the Tissue Cellular Heterogeneity Landscape. *Genome Biol* (2017) 18(1):220. doi: 10.1186/s13059-017-1349-1
33. Yoshihara K, Shahmoradgoli M, Martínez E, Vegesna R, Kim H, Torres-Garcia W, et al. Inferring Tumour Purity and Stromal and Immune Cell Admixture From Expression Data. *Nat Commun* (2013) 4:2612. doi: 10.1038/ncomms3612
34. Blanche P, Dartigues JF, Jacqmin-Gadda H. Estimating and Comparing Time-Dependent Areas Under Receiver Operating Characteristic Curves for Censored Event Times With Competing Risks. *Stat Med* (2013) 32(30): 5381–97. doi: 10.1002/sim.5958
35. Yu G, Wang LG, Han Y, He QY. Clusterprofiler: An R Package for Comparing Biological Themes Among Gene Clusters. *OMICS* (2012) 16 (5):284–7. doi: 10.1089/omi.2011.0118
36. Hänzelmann S, Castelo R, Guinney J. GSVA: Gene Set Variation Analysis for Microarray and RNA-Seq Data. *BMC Bioinf* (2013) 14:7. doi: 10.1186/1471-2105-14-7
37. Dedeurwaerder S, Desmedt C, Calonne E, Singhal SK, Haibe-Kains B, Defrance M, et al. DNA Methylation Profiling Reveals a Predominant Immune Component in Breast Cancers. *EMBO Mol Med* (2011) 3(12):726–41. doi: 10.1002/emmm.201100801
38. Holm K, Hegardt C, Staaf J, Vallon-Christersson J, Jönsson G, Olsson H, et al. Molecular Subtypes of Breast Cancer Are Associated With Characteristic DNA Methylation Patterns. *Breast Cancer Res* (2010) 12(3):R36. doi: 10.1186/bcr2590
39. Kamalakaran S, Varadan V, Giercksky Russnes HE, Levy D, Kendall J, Janevski A, et al. DNA Methylation Patterns in Luminal Breast Cancers Differ From Non-Luminal Subtypes and Can Identify Relapse Risk Independent of Other Clinical Variables. *Mol Oncol* (2011) 5(1):77–92. doi: 10.1016/j.molonc.2010.11.002

40. Kim JY, Choi JK, Jung H. Genome-Wide Methylation Patterns Predict Clinical Benefit of Immunotherapy in Lung Cancer. *Clin Epigenet* (2020) 12 (1):119. doi: 10.1186/s13148-020-00907-4

Conflict of Interest: The authors declare that the research was conducted in the absence of any commercial or financial relationships that could be construed as a potential conflict of interest.

frontiers in Immunology

REVIEW
published: 19 July 2021
doi: 10.3389/fimmu.2021.701006

B7-H3/CD276: An Emerging Cancer Immunotherapy

Wu-Tong Zhou[1] *and Wei-Lin Jin*[1,2*]

[1] *Institute of Nano Biomedicine and Engineering, Shanghai Engineering Center for Intelligent Diagnosis and Treatment Instrument, Department of Instrument Science and Engineering, Key Laboratory for Thin Film and Microfabrication Technology of Ministry of Education, School of Electronic Information and Electronic Engineering, Shanghai Jiao Tong University, Shanghai, China,* [2] *Institute of Cancer Neuroscience, Medical Frontier Innovation Research Center, The First Hospital of Lanzhou University, The First Clinical Medical College of Lanzhou University, Lanzhou, China*

Immunotherapy aiming at suppressing tumor development by relying on modifying or strengthening the immune system prevails among cancer treatments and points out a new direction for cancer therapy. B7 homolog 3 protein (B7-H3, also known as CD276), a newly identified immunoregulatory protein member of the B7 family, is an attractive and promising target for cancer immunotherapy because it is overexpressed in tumor tissues while showing limited expression in normal tissues and participating in tumor microenvironment (TME) shaping and development. Thus far, numerous B7-H3-based immunotherapy strategies have demonstrated potent antitumor activity and acceptable safety profiles in preclinical models. Herein, we present the expression and biological function of B7-H3 in distinct cancer and normal cells, as well as B7-H3-mediated signal pathways in cancer cells and B7-H3-based tumor immunotherapy strategies. This review provides a comprehensive overview that encompasses B7-H3's role in TME to its potential as a target in cancer immunotherapy.

Keywords: B7-H3/CD276, immune checkpoint, tumor microenvironment, tumor immunology, cancer immunotherapy

OPEN ACCESS

Edited by:
Mingzhu Yin,
Central South University, China

Reviewed by:
Wenping Ma,
Capital Medical University, China
Lisa Sevenich,
Georg Speyer Haus, Germany

****Correspondence:***
Wei-Lin Jin
ldyy_jinwl@lzu.edu.cn;
weilinjin@yahoo.com

Specialty section:
This article was submitted to Cancer Immunity and Immunotherapy, a section of the journal Frontiers in Immunology

Received: *27 April 2021*
Accepted: *05 July 2021*
Published: *19 July 2021*

Citation:
Zhou W-T and Jin W-L (2021) B7-H3/CD276: An Emerging Cancer Immunotherapy. Front. Immunol. 12:701006. doi: 10.3389/fimmu.2021.701006

INTRODUCTION

Immunotherapy that results in remarkable and durable responses across many different tumor types in patients by promoting antitumor immune responses has revolutionized the treatment of cancer over the past decade (1). Cancer immunotherapies based on immune evasion mechanisms, which are represented by B7-H1/PD-1 pathway targeting (anti-PD therapy), have achieved higher objective response rates in patients with considerably fewer immune-related adverse events than immune enhancement, indicating that normalization cancer immunotherapy has come of age with

Abbreviations: PD-1, Programmed cell death protein 1; TME, Tumor microenvironment; B7-H3, B7 homolog 3 protein; DCs, Dendritic cells; MMP, Matrix metallopeptidase; TLT-2, TREM-like transcript 2; CRC, Colorectal cancer; IHC, Immunohistochemistry; NSCLC, Non-small cell lung cancer; MCC, Merkel cell carcinoma; GM-CSF, Granulocyte–macrophage colony stimulating Factor; CSC, Cancer stem cells; EMT, Endothelial-to-mesenchymal; MKP, MAP kinase phosphatase; Cyt.c, Cytochrome c; NF-κB, Nuclear factor kappa B; CICs, Cancer initiating cells; JK , Janus kinase; STAT, Signal transducer and activator of transcription; NK, Natural killer cells; ADCC, Antibody-dependent cell-mediated cytotoxicity, ADCs, Antibody–drug conjugates; DCs, Dendritic cells; BsAbs, Bispecific antibodies; TriKEs, Trispecific Killer Engagers, CAR, Chimeric antigen receptor; CNS, Central nervous system.

the strenuous efforts expended to enhance clinical efficacy. The concept of immune normalization emphasizes the importance of specifically correcting immune deficiencies to restore natural antitumor immune capacity (2). The B7 superfamily provides the second signal of the T-cell activation process, which is necessary to ensure an appropriate immune response; several members of the B7 superfamily, which is represented by B7-H1/PD-1, have been implicated in immune deficiency in the tumor microenvironment (TME) (3–5). The B7 superfamily can be divided into three groups in accordance with the signals that they transduct during T-cell activation: I) costimulatory, II) coinhibitory, and III) costimulatory/inhibitory (6).

B7 homolog 3 protein (B7-H3), also known as CD276, is an immune checkpoint molecule and a costimulatory/coinhibitory immunoregulatory protein that plays a dual role in the immune system (7). It was first cloned in 2001 from a cDNA library that was derived from human dendritic cells (DCs) (8). The human B7-H3 gene is located on chromosome 15, and the murine B7-H3 gene has been mapped to chromosome 9 (3). The human B7-H3 protein exists either as a transmembrane or soluble isoform. Transmembrane B7-H3 is a type I transmembrane protein that contains 316 amino acids and has a molecular weight of ~45–66 kDa (8, 9). It is composed of an extracellular domain, a transmembrane domain, and a short intracellular domain. The extracellular domain in murine B7-H3 (2IgB7-H3, B7-H3 VC) is composed of a single pair of immunoglobulin variable domain and constant domain and human B7-H3 (4IgB7-H3, B7-H3 VCVC) is composed of two pairs due to exon duplication (10, 11). Soluble B7-H3 (sB7-H3), which is cleaved from the surface by a matrix metallopeptidase (MMP) or produced through the alternative splicing of the intron, has also been detected in human sera (12, 13). The B7-H3 protein has also been found in the secretome, including exosomes and other extracellular vesicles (14). Asuthkar et al. found that B7-H3 induces greater exosome secretion and stimulates increased exosome size in D283 medulloblastoma cells (15).

TREM-like transcript 2 (TLT-2) has been identified as a potential receptor of B7-H3 (16). However, TLT-2 may not be the only receptor of B7-H3 considering that B7-H3 has many contradictory roles. In contrast to other immune checkpoints, B7-H3 not only influences innate and adaptive immunity but also regulates the aggressiveness of cancer cells through various nonimmunological pathways (17). Various anti-B7-H3 approaches have been studied in preclinical and clinical trials and have demonstrated their feasibility for clinical application (18).

B7-H3 IS HIGHLY EXPRESSED IN DIFFERENT TYPES OF HUMAN CANCERS

In most normal human tissues, B7-H3 mRNA is expressed widely, whereas the B7-H3 protein is relatively rarely present; the difference between the mRNA and protein expression patterns of B7-H3 suggests that B7-H3 has a tight post-transcriptional regulation mechanism (19). Evidence suggests that miR-124 may cause translational repression by playing a tumor suppressor role and targeting the 3′-UTR of B7-H3 (20). Furthermore, miR-29 overexpression can inhibit B7-H3 expression levels, which play a crucial role in promoting medulloblastoma angiogenesis (21). Besides, B7-H3 expression is negatively regulated by miR-128 in colorectal cancer (CRC) (22).

We obtained datasets on the differential expression of B7-H3 in distinct cancers from the Oncomine online database (**Figure 1**) and B7-H3 transcripts across all tumor samples and paired normal tissues from the Gene Expression Profiling Interactive Analysis (GEPIA) online database (**Figure 2**). We could find that CD 276 is highly expressed in both mRNA and protein level in tumor cells.

B7-H3 has been extensively studied in various cancers, including but not limited to breast cancer, lung cancer, ovarian cancer, brain tumor, gastric cancer, and squamous cell carcinoma (**Table 1**). Its presence has been correlated with worsened prognosis, poor survival, and recurrence rate. B7-H3's capability to confer enhanced invasive and migratory properties has been further studied by using *in vitro* cancer models and is highlighted below.

B7-H3 in Breast Cancers

Breast cancer is the most frequently diagnosed cancer in women worldwide and the second leading cause of cancer deaths among women (31, 32). A study on American Joint Committee on Cancer stages I to III primary breast cancers and normal breast specimens found that B7-H3 was expressed in 32 out of 82 primary breast tumors and compared with normal breast tissue, B7-H3 expression in primary tumors had a significant correlation with increased tumor size and lymph vascular invasion (33). By utilizing immunohistochemistry (IHC), Yu et al. discovered that the positive rate of B7-H3 was 56.8% (42/74) in 74 specimens of breast cancer tissues and was higher than 43.2% (32/74) in 74 specimens of adjacent tissues (23).

B7-H3 in Lung Cancers

B7-H3 has been studied in non-small cell lung cancer (NSCLC). NSCLC is one of the cancers with the highest morbidity and mortality worldwide (34). Studies have shown that B7-H3 molecules are closely related to the invasion, metastasis, proliferation, and prognosis of NSCLC tumors (35). Yonesaka et al. evaluated B7-H3 expression levels in NSCLC tumors by using IHC and found that 74% of the tumor samples expressed B7-H3 with a staining pattern of 1+, 2+, or 3+ (24). Moreover, Wang et al. found that CD276 silencing inhibited cell invasion and migration by reducing integrin-associated protein expression (35). These studies indicated that in NSCLC, the presence of B7-H3 contributes to the capability of malignant neoplasms to progress and metastasize.

B7-H3 in Ovarian Cancers

B7-H3 has also attracted interest in the field of ovarian cancer research. By applying IHC, Zang et al. found that B7-H3 expression was present in 96 out of 103 (93%) ovarian tumors (25). Notably, in the ovarian TME, stromal cells express B7-H3 at higher levels than tumor cells (36). Cai et al. assessed the expression of B7 checkpoint molecules in OvCa and found that

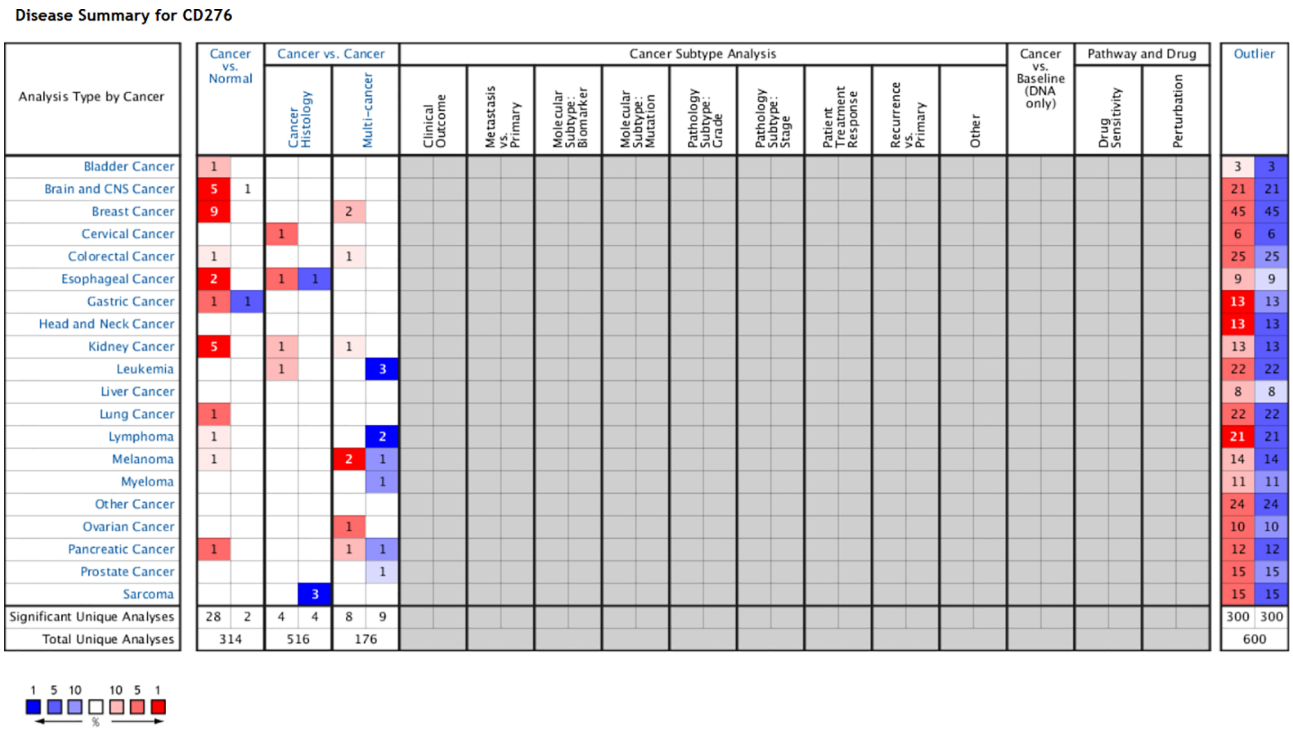

FIGURE 1 | B7-H3 differential expression datasets in distinct cancers. P-value equals 0.05, fold change equals 2, red indicates high expression, and the darker the color, the higher the expression, blue indicates vice versa (only comparisons within the same row). Gray and blank means no data. Cell color is determined by the best gene rank percentile for the analyses within the cell (Note: an analysis may be counted in more than one cancer type). www.oncomine.org.

B7-H3, but not PD-L1, was highly expressed and that the high expression of B7-H3 was associated with dysfunction in tumor-infiltrating T cells (37).

B7-H3 in Brain Cancers

Multiple studies have shown that B7-H3 is present in a range of brain cancers. Different types of gliomas have different B7-H3 expression levels. Weak B7-H3 expression was found in oligodendroglioma and choroid plexus papilloma specimens. B7-H3 was expressed at moderate-to-high levels in medulloblastoma, ependymocytoma, glioblastoma, anaplastic astrocytoma, glioblastoma multiforme, and diffuse intrinsic pontine glioma (3, 38). The differential expression of B7-H3 in different types of gliomas requires further study. A previous study showed that all 16/21 meningioma specimens presented high B7-H3 expression with strong membrane staining in almost 100% of tumor cells and that B7-H3 expression in the five remaining meningioma tissues was moderate to high (26). B7-H3 expression was detected in 75%–90% of the tumor tissues in six out of eight cases, and extremely low levels of B7-H3 were detected in normal brain tissues (27). Wang et al. revealed that 2IgB7-H3, but not 4IgB7-H3, was specifically expressed in gliomas; they also demonstrated for the first time that 2IgB7-H3 was a valuable biomarker for the diagnosis of glioma (39). Proctor et al. found that B7-H3 was the most prevalent and abundant inhibitory immune checkpoint protein quantified in meningioma (26).

B7-H3 in Other Cancers

Li et al. demonstrated that B7-H3 promoted gastric cancer cell migration and invasion and that its upregulation enhanced tumor infiltration depth (28). Wang et al. found that B7-H3 was involved in the progression of esophageal squamous cell carcinoma and the tumor escape of immunosurveillance (29). Varki et al. discovered that in patients who were positive for HIV and had cutaneous squamous cell carcinoma, the significantly higher B7-H3 expression levels of tumor cells in immunocompetent patients than in immunosuppressed individuals was largely driven by reduced B7-H3 expression (30). Besides, Tetzlaff et al. found that B7-H3 expression in Merkel cell carcinoma (MCC)-associated endothelial cells correlates with locally aggressive primary tumor features and increased vascular density (40).

B7-H3 in Normal Cells

Human B7-H3 protein is not expressed constitutively on monocytes, B, T, or NK cells but can be induced on these cell types (8, 11). Phorbol myristate acetate plus ionomycin can induce the surface expression of B7-H3 on T, B, and NK cells (11). Anti-IgM also promotes B7-H3 expression on murine B cells. Anti-CD40 can induce B7-H3 expression on murine macrophages and B cells. LPS stimulates B7-H3 protein expression on murine DC and macrophages. In murine DCs, B7-H3 mRNA expression is stimulated by IFN-γ but is suppressed by IL-4 (41). B7-H3 expression can be induced by

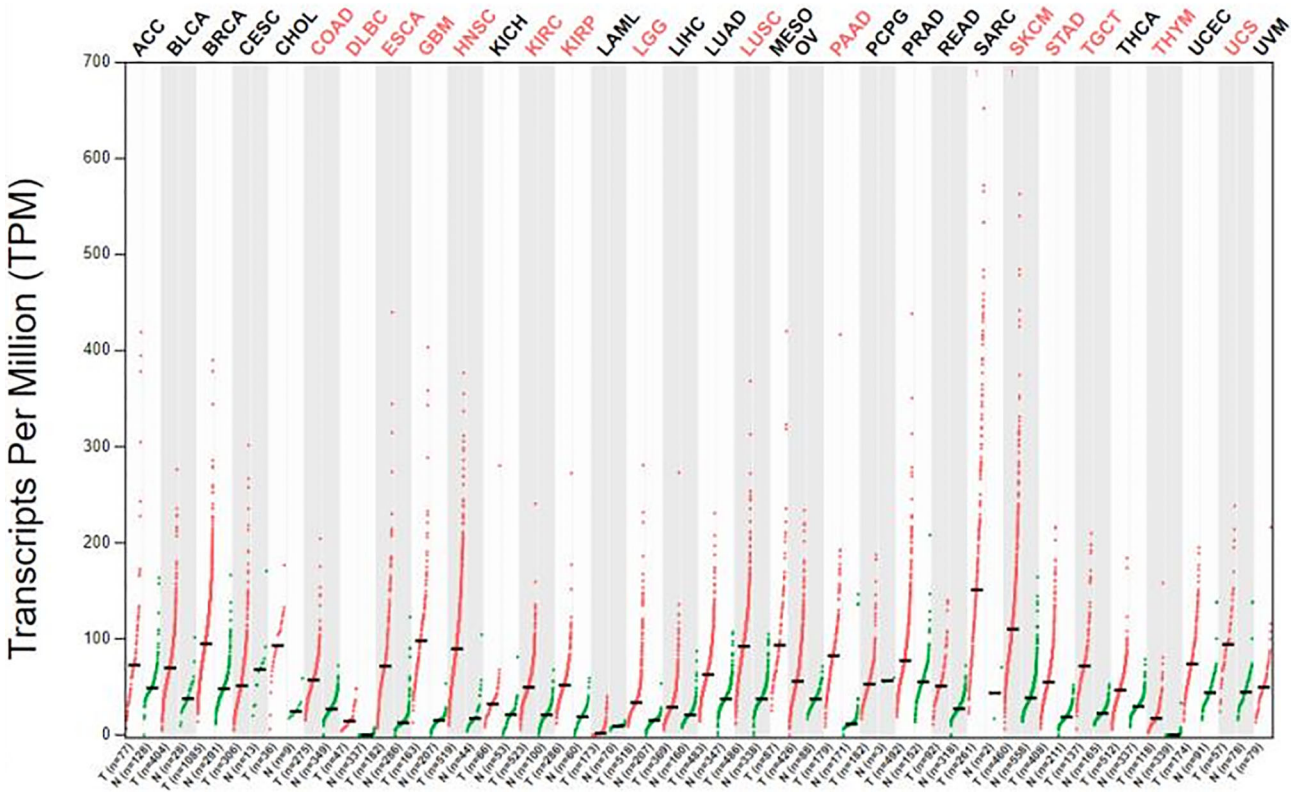

FIGURE 2 | The gene expression profile across all tumor samples and paired normal tissue (dot plot). Labels upward the figure show different types of tumor marked different color, red show statistic data have significant difference, black show statistic data have no significant difference; The X axis is the number of tumor samples (T) in red and normal samples (N) in green for each tumor. The Y axis is transcripts per million (TPM). gepia.cancer-pku.cn

TABLE 1 | Expression and diverse roles of B7-H3 in multiple types of human cancers.

Cancer type	Case number	Positive rate (%)	Cell category	Function	Reference
Breast cancer	74	56.8 (42/74)	Cancer tissue	B7-H3 participated in the occurrence and metastasis of breast cancer	(23)
	74	43.2 (32/74)	Adjacent tissue		
Non-small cell lung cancer	82	74	Tumor samples	B7-H3 impaired anti-PD-1 therapy in NSCLC	(24)
Ovarian cancer	103	93	Tumor samples	B7-H3 downregulated T cell mediated antitumor immunity	(25)
Meningioma	21	76.2	Tumor cells	B7-H3 expression was elevated in patients with gene mutations related to the PI3K/AKT/mTOR pathway	(26)
	8	75	Tumor tissues	B7-H3 protein might play important roles in meningioma immune responses	(27)
Gastric cancer	120	69.2	Cancer tissues	B7-H3 silencing downregulates CXCR4	(28)
Esophageal squamous cell carcinoma	66	69.7	Cancer tissues	Knockdown of B7-H3 on tumor cells suppressed ESCC cell migration and invasion	(29)
Cutaneous squamous cell carcinoma	66	85	Tumor tissues	B7-H3 expression was the only parameter in immunocompetent individuals that was significantly different from that in immunosuppressed patients	(30)

Not all clinical studies were included in this table due to the space limitation.

the granulocyte–macrophage-colony-stimulating factor LPS on monocytes and by IFN-γ on DCs (8, 11). B7-H3 also has functions in somatic cells. B7-H3 is highly expressed on osteoblasts during embryogenesis and is crucial for osteoblastic differentiation and bone mineralization (42).

B7-H3 is overexpressed in numerous tumor types. It is not expressed or expressed at low levels in either lymphoid cells or lymphocytes but exhibits increased expression when induced. These expression patterns imply that B7-H3 may play an important role in tumor development and cancer immunity.

THE SIGNALING PATHWAYS MEDIATED BY B7-H3 IN A DISTINCT MANNER

The high expression of B7-H3 in tumor tissues has aroused researchers' interest in the role of B7-H3 in the TME. A large body of experimental evidence indicates that B7-H3 can affect the progression of tumors through immune-dependent and nonimmune pathways.

Immune-Dependent Direction

Co-Stimulatory Role

B7-H3 has been suggested to play conflicting molecular roles in the immune system. B7-H3 was originally identified as a co-stimulatory molecule. In the presence of the anti-CD3 antibody, human B7-H3 protein increases the proliferation of CD4+ and CD8+ T-cells and enhances cytotoxic T-cell activity (8). CRC-bearing mouse models treated with adenoviral B7-H3 showed suppressed tumor growth and reduced secondary metastasis occurrence with significantly higher frequencies of IFN-γ-producing CD8+ T cells and higher IL-12 levels than the control group mice (43, 44).

Co-Inhibitory Role

In addition to its co-stimulatory role, B7-H3 plays a co-inhibitory role in antitumor immunity. Several current studies have shown that B7-H3 inhibits the proliferation of CD4+ and CD8+ T-cells and reduces the production of IL-2 and IFN-γ possibly through the suppression of NF-κB, the nuclear factor of activated T-cells, and activator protein-1-mediated signaling pathways (41, 45) (**Figure 3**). During T-cell activation, B7-H3 potently and consistently inhibits of T-cell proliferation and IFN-γ, IL-13, IL-10, and IL-2 production (**Figure 3**). In addition to its inhibitory effect on T-cells, B7-H3 inhibits NK cell activity. 4Ig-B7-H3-transfected CHO-K cells avoided NK-cell-mediated cytotoxicity with an unclear receptor (11, 46). Recently, Wang et al. found that cancer stem cells (CSCs) utilize B7-H3 to evade immune surveillance during head and neck squamous cell carcinoma initiation, development, and metastasis (47). The suppressive immune microenvironment shaped by B7-H3 helps cancer avoid immune destruction (48).

Non-Immune Direction

In addition to its role in immunological pathways, B7-H3 has nonimmunological protumorigenic functions, such as the

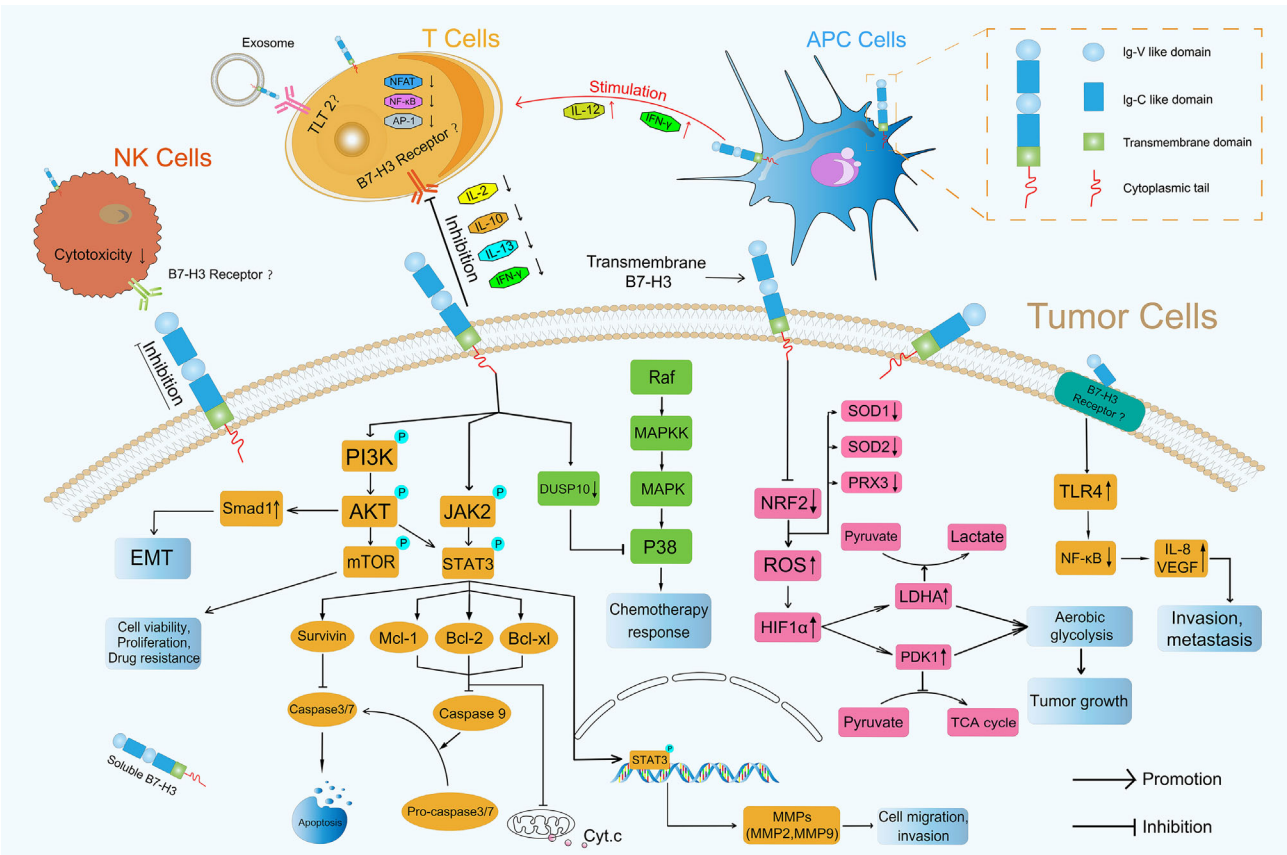

FIGURE 3 | Roles of B7-H3 in TME. B7-H3 can affect the progression of tumors through immune-dependent and nonimmune pathways.

promotion of migration and invasion, antiapoptosis, cell viability, chemoresistance, and endothelial-to-mesenchymal (EMT) transition. In tumor cells, it also participates in reprogramming metabolism through vital intracellular signal transduction pathways.

PI3K/AKT

Many articles have reported that the PI3K/AKT signaling pathway which is activated by phosphorylation is involved in the invasion of cancer cells (49–51) and participates directing immune cell differentiation and function (52). Li et al. found that B7-H3 overexpression promoted the migration and invasion of human bladder cancer cells and that B7-H3 knockdown suppressed the expression of MMP2 and MMP9 *via* the PI3K/AKT/STAT3 signaling pathway (53) (**Figure 3**). Nunes-Xavier et al. used API-2 (triciribidine, an AKT inhibitor) and RAD-001 (everolimus, a mTOR inhibitor) to target the PI3K/AKT/mTOR pathway and discovered that the inhibition of cell viability and proliferation in B7-H3 knockdown tumor cells was enhanced relative to that in their counterparts (54) (**Figure 3**). Jiang et al. found that B7-H3 upregulated Smad1 expression *via* the PI3K/AKT pathway, downregulated β-catenin and E-cadherin expression, and increased vimentin and N-cadherin expression, indicating that B7-H3 promoted EMT in colorectal cancer (55) (**Figure 3**). The expression of MMP2, MMP9 and EMT formation can contribute to mechanical microenvironment shaping in TME (48).

NF-κB

NF-κB transcription factors are activated as a response to a variety of signals (56). Wang et al. revealed that B7-H3 knockdown obviously reduced the phosphorylation levels of AKT, NF-κB, and STAT3 in HCT116 and RKO cells and that the NF-κB pathway had a major effect on B7-H3-induced VEGFA expression in CRC cells (57). Xie et al. proved that sB7-H3 first upregulated TLR4 expression, then activated NF-κB signaling, and finally promoted IL-8 and VEGF expression and demonstrated for the first time that sB7-H3 promoted the invasion and metastasis of pancreatic carcinoma cells through the TLR4/NF-κB pathway (58) (**Figure 3**).

Ras/Raf/MEK/MAPK

MAPK pathways regulate various cellular processes through four major pathways as defined by their MAPK effector: ERK1/2, ERK5, JNKs, and p38 MAPK (59). Flem-Karlsen et al. found that the knockdown of B7-H3 increased the *in vitro* and vivo sensitivity of melanoma cells to the chemotherapeutic agents dacarbazine and cisplatin in parallel with a reduction in p38 MAPK phosphorylation; they also observed the increased expression of dual-specific MAP kinase phosphatase (MKP) DUSP10 (a MKP known to dephosphorylate and inactivate p38 MAPK) in B7-H3 knockdown cells, indicating that B7-H3-mediated chemoresistance in melanoma cells is driven through a mechanism involving the DUSP10-mediated inactivation of p38 MAPK (60) (**Figure 3**).

JAK2/STAT3

The JAK/STAT signaling pathway is a critical controller of cellular survival and proliferation and is involved in cell antiapoptosis (61). The JAK2/STAT3 pathway activates some apoptosis suppressors, including survivin, Mcl-1, Bcl-xL, and Bcl-2, that block caspase cascades and apoptosis initiation in tumor cells (62). The direct inhibition of effector caspases 3 and 7 by survivin results in the suppression of apoptosis (63). Mcl-1, Bcl-2, and Bcl-xL inhibit the release of Cytochrome c (Cyt.c), thus preventing Cyt.c from reaching the threshold necessary for caspase cascades (64) (**Figure 3**). Several studies have demonstrated that B7-H3 performs an antiapoptotic role in tumorigenesis *via* the JAK2/STAT3 pathway. Liu et al. discovered that the knockdown of B7-H3 abrogated the phosphorylation of STAT3 through the inactivation of JAK2 and led to the downregulation of the direct target genes of STAT3 and to the reduction in survivin. By contrast, the overexpression of B7-H3 increased the phosphorylation of JAK2 and STAT3, indicating that the JAK2/STAT3 pathway contributes to B7-H3-mediated drug resistance (65) (**Figure 3**). Li et al. found that shRNA-mediated B7-H3 silencing inhibited AKT, ERK, and JAK2/STAT3 phosphorylation in the N87 gastric cancer cell line (28). Zhang et al. demonstrated that the overexpression of B7-H3 induced resistance to apoptosis in colorectal cancer cell lines by upregulating the JAK2-STAT3 signaling pathway; this effect thus potentially provides new approaches to the treatment of colorectal cancer (66). Recently, Lu et al. showed that B7-H3-mediated colon cancer cell resistance to the cytotoxicity of Vδ2 T cells involved a molecular pathway comprising STAT3 activation and decreased ULBP2 expression (67). However, how B7-H3 activates the downstream JAK2/STAT3 pathway remains unknown, and its underlying mechanism remains a point of conjecture (68). Other novel mechanisms that remain undiscovered must be explored in future investigations.

Glucose Metabolic Signaling Pathway

B7-H3 also plays a crucial role in glucose metabolic reprogramming. Cancer cell metabolism is characterized by an increase in glycolysis and lactate production even in the presence of abundant oxygen; this phenomenon is known as the Warburg effect or aerobic glycolysis (69). Aerobic glycolysis confers a growth advantage to cancer cells by providing energy and biosynthetic building blocks (70). Lim et al. demonstrated that B7-H3 regulated glucose metabolism through ROS-mediated HIF1a stabilization, which contributed to B7-H3-enhanced tumor growth; B7-H3 suppresses NRF2 transcriptional activity, which in turn reduces transcription of the antioxidant enzymes SOD1, SOD2, and PRX3; B7-H3-induced ROS then stabilized HIF1α, thus increasing the expression of the glycolytic enzymes LDHA and PDK1, an effect that promoted pyruvate conversion into lactate while inhibiting pyruvate flux through the TCA cycle (71) (**Figure 3**), contributing to tumor metabolism microenvironment shaping (48). Moreover, in CRC cells, B7-H3 mediated the activation of STAT3 and the subsequent expression of HK2 to promote glycolysis (72).

B7-H3-BASED TUMOR IMMUNOTHERAPY STRATEGIES

Immunotherapy is a novel individualized treatment strategy wherein the immune system is activated or suppressed to amplify or diminish an immune response. It has been developed rapidly for the treatment of various forms of cancer in recent years. Immune-based therapies are gaining attention due to improvements in their clinical outcomes. The abnormal expression of B7-H3 is a possible biomarker and a promising immune checkpoint target for multiple cancer immunotherapy approaches, especially its expression on cancer initiating cells (CICs), since their eradication is a requirement for an anti-tumor therapy to be effective (73). Recent advances in molecular biology and antibody engineering have enabled targeting B7-H3 on the basis of multiple mechanisms. Information about clinical trials can be seen in **Table 2**.

Targeting B7-H3 With Blocking mAbs

Blocking mAbs can partially or completely neutralize inhibitory ligand-to-receptor interactions, thus allowing effector functions (18). The use of blocking mAbs against the immune checkpoints CTLA-4, programmed cell death protein 1 (PD-1), and PD-1 ligand 1 (PD-L1) has demonstrated significant clinical success in patients with a variety of cancers (74–76). This successful experience can be applied to B7-H3 as well. B7-H3 blocking with mAbs has been shown to increase CD8+ T-cell and NK-cell tumor infiltration, reduce tumor growth, and prolong survival in mouse models of hematopoietic cancers, ovarian cancer (37), melanoma (77) and CRC (78). However, the translation of this

TABLE 2 | Summary of the clinical trials on anti B7-H3 antibodies for hematologic and solid tumor malignancies.

Trial number	Description	Drug	Trial stage	Start date	Completion date	Status
Targeting B7-H3 through ADCC						
NCT01391143	Refractory cancer, melanoma, prostate, solid tumors	Enoblituzumab (MGA271)	Phase I	July, 2011	April 18, 2019	Completed
NCT02982941	Pediatric patients with relapsed or refractory solid tumors	MGA271	Phase I	December, 2016	May 22, 2019	Completed
NCT02923180	Localized intermediate- and high-risk prostate cancer	MGA271	Phase II	October, 2016	October, 2021	Active but not recruiting
Targeting B7-H3 through ADC therapies						
NCT03729596	Advanced solid tumors	MGC018 with or without MGA012	Phase I/II	November 21, 2018	May, 2025	Recruiting
NCT02475213	Patients with melanoma, squamous cell cancer of the head and neck, NSCLC, and other cancers	MGA271 with pembrolizumab	Phase I	July, 2015	October, 2022	Recruiting
Targeting B7-H3 with bispecific antibodies						
NCT02628535	Patients with unresectable or metastatic neoplasms	Orlotamab (MGD009)	Phase I	September, 2015	November 25, 2019	Terminated
Targeting B7-H3 with CAR T cells						
NCT04185038	Diffuse Intrinsic Pontine Glioma/Diffuse Midline Glioma and Recurrent or Refractory Pediatric Central Nervous System Tumors	–	Phase I	December, 2019	May, 2041	Recruiting
NCT04077866	Patients with Recurrent or Refractory Glioblastoma	–	Phase I/ Phase II	May 1, 2022	July 1, 2024	Recruiting
NCT04385173	Patients with Recurrent and Refractory Glioblastoma	–	Phase I	June 1, 2020	July 1, 2022	Recruiting
NCT04483778	Recurrent/Refractory Solid Tumors in Children and Young Adults	–	Phase I	July 13, 2020	December, 2040	Recruiting
Synergistic options with anti–B7-H3 therapies						
NCT02381314	Patients with melanoma, NSCLC, and other cancers	MGA271, ipilimumab	Phase I	March 26, 2015	September 26, 2018	Completed
NCT04129320	Squamous Cell Carcinoma of the Head and Neck	MGA271, MGA012	Phase II/ III	October, 2019	October, 2025	Not yet recruiting
NCT02475213	Safety Study in Refractory Cancer	MGA271, pembrolizumab or MGA012	Phase I	July, 2015	October, 2022	Active but not recruiting
NCT03406949	Relapsed/Refractory Cancer	MGD009/MGA012	Phase I	February 27, 2018	December, 2022	Active but not recruiting
NCT01099644	Patients with Desmoplastic Small Round Cell Tumors and Other Solid Tumors	^{131}I-8H9	Phase I	April, 2010	September, 2020	Active but not recruiting
NCT04022213	Patients with Desmoplastic Small Round Cell Tumors and Other Solid Tumors	^{131}I-8H9	Phase II	July 15, 2019	July 2024	Recruiting
NCT04167618	Recurrent or Refractory Medulloblastoma	^{177}Lu-DTPA-8H9	Phase 1/ Phase 2	January 15, 2021	December 15, 2024	Not yet recruiting
NCT04315246	Leptomeningeal Metastasis from Solid Tumors	^{177}Lu-DTPA-8H9	Phase 1/ Phase 2	December 31, 2020	December 31, 2024	Not yet recruiting

Not all clinical studies were included in this table due to the space limitation.

strategy into the clinical setting has been hampered by the lack of human B7-H3-specific blocking mAbs.

Targeting B7-H3 Through ADCC

Antibody-dependent cell-mediated cytotoxicity (ADCC) refers to the binding of the antibody Fab to malignant cells. Moreover, Fc can bind to FcR on the surfaces of killer cells to mediate the direct killing of target cells. Loo et al. developed MGA271, a B7-H3-reactive, Fc-engineered mAb that mediates potent antitumor activity *in vitro* and in tumor xenografts; this characteristic, together with the favorable safety profile of MGA271 in cynomolgus monkey toxicology studies, supports its exploration in the treatment of B7-H3-positive cancers (79) (**Figure 4**).

Targeting B7-H3 Through Antibody–Drug Conjugates Therapies

Antibody–drug conjugates (ADCs) combine the target specificity of a mAb with cytotoxic agents to deliver the cytotoxic agents to a tumor and improve therapeutic indexes. Scribner et al. developed MGC018, an anti-B7-H3 ADC that incorporated an aduocarmycin-based DNA alkylating payload *via* a cleavable valine–citrulline linker. MGC018 exhibited potent antitumor activity in a range of human tumor xenografts, mediated bystander killing, and showed a favorable safety profile in cynomolgus monkeys (80).

Targeting B7-H3 With CD3-Engaging Bispecific Antibodies

Bispecific antibodies (BsAbs) are another option that is beginning to pick up steam in the area of tumor immunotherapy. BsAbs are artificially generated antibodies that are composed of the fragments of two distinct Abs and combining two specificities. One arm can bind to the CD3 component of the TCR complex on T cells, whereas the other arm recognizes a tumor-specific antigen, such as B7-H3. In this way, T cells are recruited to the tumor site and activated to kill cancer cells (81). The anti-CD3 antibody that is chemically conjugated with the anti-B7-H3 mAb antibody has been clinically approved (82). The anti-CD3 × anti-B7-H3 bispecific antibody (B7-H3 Bi-Ab) was then used to direct activated T cells

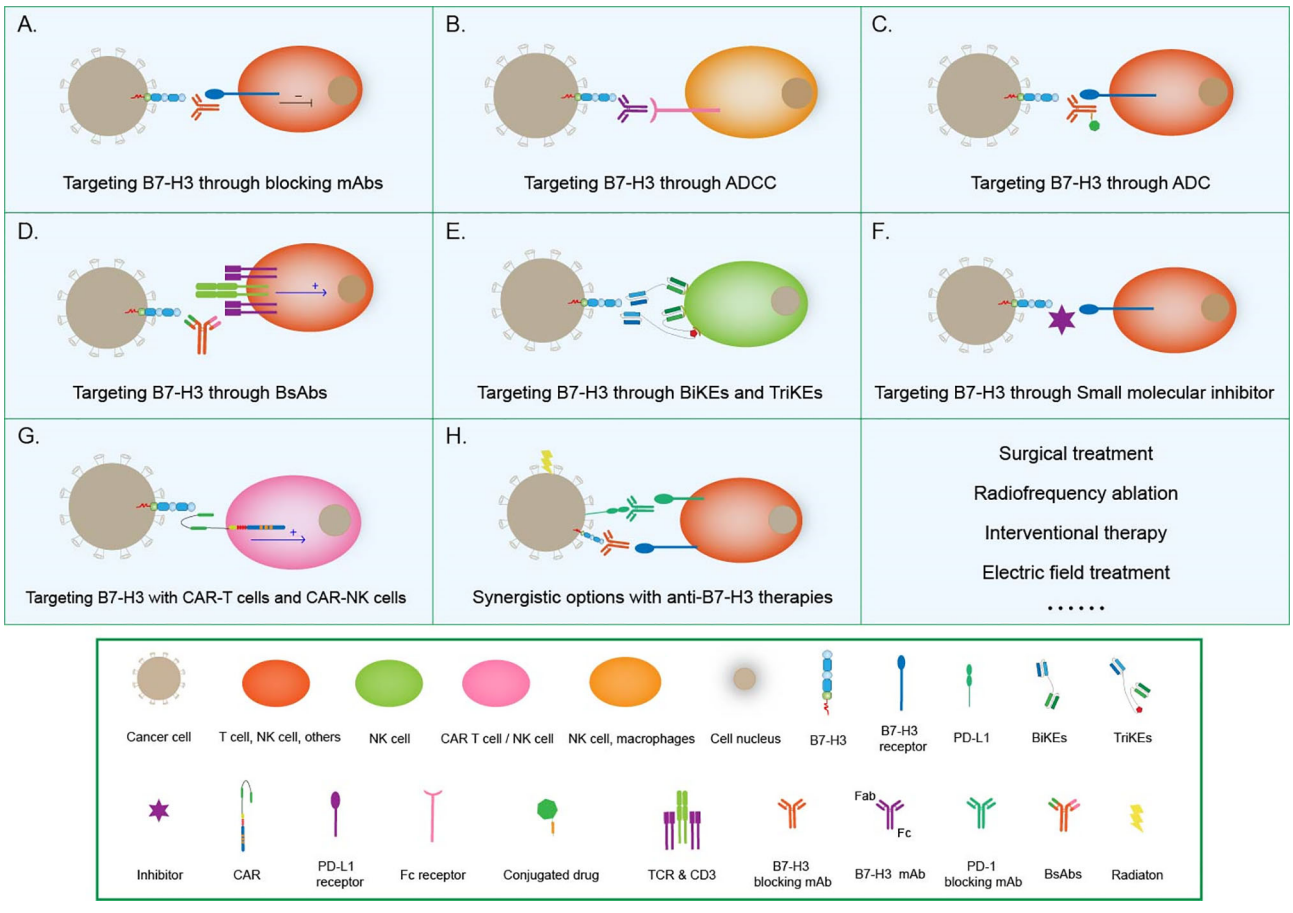

FIGURE 4 | Tumor immunotherapy strategies based on B7-H3. **(A)** Targeting B7-H3 with blocking mAbs; **(B)** Targeting B7-H3 through ADCC; **(C)** Targeting B7-H3 through ADC therapies; **(D)** Targeting B7-H3 with CD3-engaging BsAbs; **(E)** BiKEs and TriKEs; **(F)** Targeting B7-H3 with small-molecule inhibitors; **(G)** Targeting B7-H3 with CAR T cells and CAR-NK cells; **(H)** Synergistic options with anti B7-H3 therapies.

to kill tumor targets (83). The activated T cell armed with B7-H3 Bi-Ab exhibited increased specific cytotoxicity and cytokine production and suppressed B7-H3-positive cancer growth in the SCID–Beige murine model.

Bi and Tri-Specific Killer Engagers

Bispecific killer engagers (BiKEs) or trispecific killer engagers (TriKEs) form an antigen-specific immunological synapse between NK and tumor cells, thereby triggering NK-cell-mediated tumor cell lysis. BiKEs consist of an anti-CD16 scFv linked to an scFv that is specific for a tumor-expressed antigen, and TriKEs comprise the two scFvs mentioned above and a cytokine, most frequently IL-15 (84). Vallera et al. generated a B7-H3/IL-15 TriKE that used the scFv of the B7-H3-specific mAb 376.96; when deployed against PDAC, this TriKE resulted in a significant reduction in tumor load *in vitro* and in murine models (85). The same group had bioengineered a second-generation TriKE with human IL-15 as a modified crosslinker between an anti-B7-H3 scFv and a humanized camelid anti-CD16 single domain antibody. The latter allowed the improved function of IL15, thus enhancing the activation and proliferation of NK cells and the killing of ovarian cancer cells *in vitro* and in murine models (86).

Targeting B7-H3 With Small-Molecule Inhibitors

In addition to conventional therapeutic mAbs, small-molecule inhibitors have also begun to capture interest in the immune-oncology field (87). Small-molecule inhibitors are low-molecular-weight organic compounds (dinucleotides and peptides) that bind to specific biological targets, blocking specific antigen-antibody binding. They are readily used because of their advantages, including cheap manufacturing costs, ease of delivery due to their oral administration route, excellent tissue distribution due to their size, and short half-lives, over antibodies. A small-molecule inhibitor can be designed on the basis of the FG loop of the IgV domain of B7-H3 that is involved in T-cell activation to target this specific ligation area (88). Small molecule immunotherapy can provide an alternative treatment modality either alone or complementary to or synergistic with extracellular checkpoint mAbs to address low clinical response and drug resistance. The future research should continue to focus on discovery of novel small molecules with distinct chemo-types and higher potency (89).

Targeting B7-H3 With Chimeric Antigen Receptor T Cells and Chimeric Antigen Receptor NK Cells

Chimeric antigen receptor (CAR) T-cell technology is another effective way to target B7-H3 for immunotherapy. Autologous T cells or NK cells are engineered with a CAR that targets a tumor antigen and adoptively transferred to patients to kill cancer cells. Thus far, this technology has been successfully applied only in hematologic cancers. Although this area of research is challenging, efforts are being made to translate CAR-T cell therapy into the treatment of solid tumors (18). B7-H3-redirected CAR-T cells can effectively control GBM growth (90, 91) and are highly active against atypical teratoma-like rhabdomyoma *in vitro* and in xenograft murine models (92). Majzner et al. reported a CAR-T cell system directed at B7-H3 with strong activity against a wide array of xenograft pediatric cancer models, including liquid, solid, and central nervous system (CNS) tumors; they also demonstrated that, as has emerged for many CAR therapeutics, CAR T cell activity is dependent on antigen density (38). Furthermore, Yang et al. developed a tandem CAR T cell system that exhibited enhanced antitumor activity and tumor control in several preclinical models (93). Tang et al. presented the results of the first-in-human clinical study on B7-H3-targeted CAR T cells for the treatment of recurrent anaplastic meningioma and provided evidence that the local delivery of B7-H3-targeted CAR T cells could suppress tumor progression without off-tumor toxicity or serious side effects, thus indicating the tolerability, safety, and potential efficacy of this therapy (94). Recently, NK-cells have been used to generate CAR-NK cells, which controlled the growth of human NSCLC cells grafted in murine models and prolonged survival (95). Lei et al. reported that a pan-histone deacetylase inhibitor can enhance the antitumor activity of B7-H3-specific CAR T cells in solid tumors (96).

Synergistic Options With Anti–B7-H3 Therapies

With the successful experience of traditional immunotherapy, Combination therapy for improving the effect of immunotherapy and the survival rate of patients through combination of different immunotherapies has attracted increasing attention. Recent studies have shown that the combination of a variety of chemotherapeutics with checkpoint inhibitors exerts great synergistic effects that enhance the prospects of their full utilization in standard clinical practice.

Combination therapy involving multiple immune checkpoint inhibitors is emerging rapidly as a means for cancer treatment. Larkin et al. found that in patients with PD-L1-negative tumors, the combination of Nivolumab (PD-1 blockade) and ipilimumab (CTLA-4 blockade) was more effective than either agent alone (97). Xu et al. developed anti-B7-H3/PD-1 bispecific fusion proteins that simultaneously engaged the tumor-associated marker B7-H3 and the immune-suppressing ligand PD-L1 and enhanced ADCC to promote potent and highly selective tumor killing (98). Yonesaka et al. discovered that anti-B7-H3 immunotherapy combined with anti-PD-1/PD-L1 antibody therapy is a promising approach for the treatment of B7-H3-expressing NSCLCs (24).

B7-H3 gene silencing and combination drug therapy can also improve the rate of tumor elimination. Zhang et al. demonstrated that in U937 cells, B7-H3-targeting shRNA significantly enhanced sensitivity to chemotherapeutic drugs (99). Liu et al. examined the role of B7-H3 in paclitaxel resistance in several metastatic breast cancer cell lines; their results indicated that the B7-H3-shRNA-induced knockdown of the B7-H3 protein in these cells resulted in increased sensitivity to paclitaxel (65). Both studies showed that silencing B7-H3 significantly enhanced tumor cell chemosensitivity

and drug-induced apoptosis, thus providing a rationale for the potential synergistic effects between the B7-H3 blockade and chemotherapy or targeted therapy for patients with a variety of cancers.

Radiation is an additional avenue that can be considered for application in a future clinical setting in combination with B7-H3 targeting. Twyman-Saint Victor et al. demonstrated that PD-L1 on melanoma cells allowed tumors to escape anti-CTLA4-based therapy, and the combination of radiation, anti-CTLA4, and anti-PD-L1 promoted response and immunity through distinct mechanisms (100). 8H9 is distinct from other B7-H3–specific antibodies in that it binds to the FG loop of B7-H3, a region that is critical to its immunologic function (101).

Given the multiple steps involved in anticancer immunity, the potential to enhance cancer immunotherapy *via* rational combinations by modulating different biological steps in immunity simultaneously or in rapid sequence is quite broad (102). Besides immunotherapies, some non-immunotherapies such as surgical treatment (103), radiofrequency ablation (104), interventional therapy (105), electric field treatment (106) should been also taken into consideration.

CONCLUSIONS AND OUTLOOK

B7-H3 is a novel immune checkpoint from the B7 family. In this review, we analyzed the transcription and expression levels of B7-H3 in different tumors by utilizing bioinformatics tools, provided a comprehensive view of B7-H3's role in the TME, and summarized different B7-H3-based cancer immunotherapy strategies along with their corresponding clinical trials. The prospect of B7-H3 as a target for cancer immunotherapy which stems from its special expression patterns on tumor cells and the safety profile has stimulated the progress of B7-H3-targeting therapeutic strategies. The success of immunotherapies such as targeting PD-1 and CTLA4, also provide researchers' example and direction to develop new immunotherapy that target B7-H3. However, the unknown identity of the B7-H3 receptor greatly hinders the development of B7-H3 antagonists. Improving the understanding of B7-H3-mediated molecular processes for the regulation of tumorigenesis will open new avenues for developing novel therapeutic strategies for human cancers. Notably, organoids have attracted increasing attention in tumor research in recent years given their advantageous capability to reproduce tissue structure and organ function. The future trend of tumor immunotherapy involves studying cell therapy in different organoids on the basis of the new immune checkpoint B7-H3. To develop the diagnostic and therapeutic potential of B7-H3 completely, its expression in serum, pre-malignant lesions, tumor-associated vasculature, CSC, CIC, metastases and recurrence requires further investigation. Future studies aiming to delineate the precise cellular and molecular mechanisms based on B7-H3-mediated tumor promotion will provide further insights into the cell biology of tumor development and cancer immunotherapy.

AUTHOR CONTRIBUTIONS

The corresponding author W-LJ instructed the manuscript completion. The first author W-TZ contributed to manuscript writing and revising. All authors contributed to the article and approved the submitted version.

FUNDING

This study was supported by grants from the National Key Research and Development Program of China (no. 2017FYA0205302) to W-LJ.

REFERENCES

1. Egen JG, Ouyang W, Wu LC. Human Anti-Tumor Immunity: Insights From Immunotherapy Clinical Trials. *Immunity* (2020) 52:36–54. doi: 10.1016/j.immuni.2019.12.010
2. Sanmamed MF, Chen L. A Paradigm Shift in Cancer Immunotherapy: From Enhancement to Normalization. *Cell* (2018) 175:313–26. doi: 10.1016/j.cell.2018.09.035
3. Li G, Quan Y, Che F, Wang L. B7-H3 in Tumors: Friend or Foe for Tumor Immunity? *Cancer Chemother Pharmacol* (2018) 81:245–53. doi: 10.1007/s00280-017-3508-1
4. Loos M, Hedderich DM, Friess H, Kleeff J. B7-H3 and Its Role in Antitumor Immunity. *Clin Dev Immunol* (2010) 2010:683875. doi: 10.1155/2010/683875
5. Pollizzi KN, Powell JD. Integrating Canonical and Metabolic Signalling Programmes in the Regulation of T Cell Responses. *Nat Rev Immunol* (2014) 14:435–46. doi: 10.1038/nri3701
6. Zang X, Allison JP. The B7 Family and Cancer Therapy: Costimulation and Coinhibition. *Clin Cancer Res* (2007) 13:5271–9. doi: 10.1158/1078-0432.CCR-07-1030
7. Hofmeyer KA, Ray A, Zang X. The Contrasting Role of B7-H3. *Proc Natl Acad Sci USA* (2008) 105:10277–8. doi: 10.1073/pnas.0805458105
8. Chapoval AI, Ni J, Lau JS, Wilcox RA, Flies DB, Liu D, et al. B7-H3: A Costimulatory Molecule for T Cell Activation and IFN-Gamma Production. *Nat Immunol* (2001) 2:269–74. doi: 10.1038/85339
9. Zou W, Chen L. Inhibitory B7-Family Molecules in the Tumour Microenvironment. *Nat Rev Immunol* (2008) 8:467–77. doi: 10.1038/nri2326
10. Sun M, Richards S, Prasad DV, Mai XM, Rudensky A, Dong C. Characterization of Mouse and Human B7-H3 Genes. *J Immunol* (2002) 168:6294–7. doi: 10.4049/jimmunol.168.12.6294
11. Steinberger P, Majdic O, Derdak SV, Pfistershammer K, Kirchberger S, Klauser C, et al. Molecular Characterization of Human 4Ig-B7-H3, a Member of the B7 Family With Four Ig-like Domains. *J Immunol* (2004) 172:2352–9. doi: 10.4049/jimmunol.172.4.2352
12. Chen W, Liu P, Wang Y, Nie W, Li Z, Xu W, et al. Characterization of a Soluble B7-H3 (sB7-H3) Spliced From the Intron and Analysis of sB7-H3 in the Sera of Patients With Hepatocellular Carcinoma. *PloS One* (2013) 8:e76965. doi: 10.1371/journal.pone.0076965
13. Zhang G, Hou J, Shi J, Yu G, Lu B, Zhang X. Soluble CD276 (B7-H3) is Released From Monocytes, Dendritic Cells and Activated T Cells and is Detectable in Normal Human Serum. *Immunology* (2008) 123:538–46. doi: 10.1111/j.1365-2567.2007.02723.x
14. Flem-Karlsen K, Tekle C, Andersson Y, Flatmark K, Fodstad O, Nunes-Xavier CE. Immunoregulatory Protein B7-H3 Promotes Growth and

Decreases Sensitivity to Therapy in Metastatic Melanoma Cells. *Pigm Cell Melanoma R* (2017) 30:467–76. doi: 10.1111/pcmr.12599
15. Purvis IJ, Velpula KK, Guda MR, Nguyen D, Tsung AJ, Asuthkar S. B7-H3 in Medulloblastoma-Derived Exosomes; A Novel Tumorigenic Role. *Int J Mol Sci* (2020) 21:7050. doi: 10.3390/ijms21197050
16. Hashiguchi M, Kobori H, Ritprajak P, Kamimura Y, Kozono H, Azuma M. Triggering Receptor Expressed on Myeloid Cell-Like Transcript 2 (TLT-2) is a Counter-Receptor for B7-H3 and Enhances T Cell Responses. *P Natl Acad Sci USA* (2008) 105:14744–4. doi: 10.1073/pnas.0807700105. (vol 105, pg 10495, 2008).
17. Yang S, Wei W, Zhao Q. B7-H3, a Checkpoint Molecule, as a Target for Cancer Immunotherapy. *Int J Biol Sci* (2020) 16:1767–73. doi: 10.7150/ijbs.41105
18. Picarda E, Ohaegbulam KC, Zang X. Molecular Pathways: Targeting B7-H3 (CD276) for Human Cancer Immunotherapy. *Clin Cancer Res* (2016) 22:3425–31. doi: 10.1158/1078-0432.CCR-15-2428
19. Flem-Karlsen K, Fodstad O, Tan M, Nunes-Xavier CE. B7-H3 in Cancer - Beyond Immune Regulation. *Trends Cancer* (2018) 4:401–4. doi: 10.1016/j.trecan.2018.03.010
20. Wang L, Kang FB, Sun N, Wang J, Chen W, Li D, et al. The Tumor Suppressor miR-124 Inhibits Cell Proliferation and Invasion by Targeting B7-H3 in Osteosarcoma. *Tumour Biol* (2016) 37:14939–47. doi: 10.1007/s13277-016-5386-2
21. Purvis IJ, Avilala J, Guda MR, Venkataraman S, Vibhakar R, Tsung AJ, et al. Role of MYC-miR-29-B7-H3 in Medulloblastoma Growth and Angiogenesis. *J Clin Med* (2019) 8:1158. doi: 10.3390/jcm8081158
22. Hu X, Xu M, Hu Y, Li N, Zhou L. B7-H3, Negatively Regulated by Mir-128, Promotes Colorectal Cancer Cell Proliferation and Migration. *Cell Biochem Biophys* (2021) 79:397–405. doi: 10.1007/s12013-021-00975-0
23. Cong F, Yu H, Gao X. Expression of CD24 and B7-H3 in Breast Cancer and the Clinical Significance. *Oncol Lett* (2017) 14:7185–90. doi: 10.3892/ol.2017.7142
24. Yonesaka K, Haratani K, Takamura S, Sakai H, Kato R, Takegawa N, et al. B7-H3 Negatively Modulates CTL-Mediated Cancer Immunity. *Clin Cancer Res* (2018) 24:2653–64. doi: 10.1158/1078-0432.CCR-17-2852
25. Zang X, Sullivan PS, Soslow RA, Waitz R, Reuter VE, Wilton A, et al. Tumor Associated Endothelial Expression of B7-H3 Predicts Survival in Ovarian Carcinomas. *Mod Pathol* (2010) 23:1104–12. doi: 10.1038/modpathol.2010.95
26. Proctor DT, Patel Z, Lama S, Resch L, van Marle G, Sutherland GR. Identification of PD-L2, B7-H3 and CTLA-4 Immune Checkpoint Proteins in Genetic Subtypes of Meningioma. *Oncoimmunology* (2019) 8:e1512943. doi: 10.1080/2162402X.2018.1512943
27. Deng J, Ma M, Wang D, Zhu H, Hua L, Sun S, et al. Expression and Clinical Significance of Immune Checkpoint Regulator B7-H3 (CD276) in Human Meningioma. *World Neurosurg* (2020) 135:e12–8. doi: 10.1016/j.wneu.2019.10.044
28. Li Y, Yang X, Wu Y, Zhao K, Ye Z, Zhu J, et al. B7-H3 Promotes Gastric Cancer Cell Migration and Invasion. *Oncotarget* (2017) 8:71725–35. doi: 10.18632/oncotarget.17847
29. Wang L, Cao NN, Wang S, Man HW, Li PF, Shan BE. Roles of Coinhibitory Molecules B7-H3 and B7-H4 in Esophageal Squamous Cell Carcinoma. *Tumour Biol* (2016) 37:2961–71. doi: 10.1007/s13277-015-4132-5
30. Varki V, Ioffe OB, Bentzen SM, Heath J, Cellini A, Feliciano J, et al. Pd-L1, B7-H3, and PD-1 Expression in Immunocompetent vs. Immunosuppressed Patients With Cutaneous Squamous Cell Carcinoma. *Cancer Immunol Immunother* (2018) 67:805–14. doi: 10.1007/s00262-018-2138-8
31. Ferlay J, Soerjomataram I, Dikshit R, Eser S, Mathers C, Rebelo M, et al. Cancer Incidence and Mortality Worldwide: Sources, Methods and Major Patterns in GLOBOCAN 2012. *Int J Cancer* (2015) 136:E359–386. doi: 10.1002/ijc.29210
32. Wilson KE, Bachawal SV, Abou-Elkacem L, Jensen K, Machtaler S, Tian L, et al. Spectroscopic Photoacoustic Molecular Imaging of Breast Cancer Using a B7-H3-targeted Icg Contrast Agent. *Theranostics* (2017) 7:1463–76. doi: 10.7150/thno.18217
33. Arigami T, Narita N, Mizuno R, Nguyen L, Ye X, Chung A, et al. B7-H3 Ligand Expression by Primary Breast Cancer and Associated With Regional Nodal Metastasis. *Ann Surg* (2010) 252:1044–51. doi: 10.1097/SLA.0b013e3181f1939d
34. Castellanos JR, Purvis IJ, Labak CM, Guda MR, Tsung AJ, Velpula KK, et al. B7-H3 Role in the Immune Landscape of Cancer. *Am J Clin Exp Immunol* (2017) 6:66–75.
35. Li F, Chen H, Wang D. Silencing of CD276 Suppresses Lung Cancer Progression by Regulating Integrin Signaling. *J Thorac Dis* (2020) 12:2137–45. doi: 10.21037/jtd.2020.04.41
36. MacGregor HL, Sayad A, Elia A, Wang BX, Katz SR, Shaw PA, et al. High Expression of B7-H3 on Stromal Cells Defines Tumor and Stromal Compartments in Epithelial Ovarian Cancer and Is Associated With Limited Immune Activation. *J Immunother Cancer* (2019) 7:357. doi: 10.1186/s40425-019-0816-5
37. Cai DL, Li JM, Liu DF, Hong SJ, Qiao Q, Sun QL, et al. Tumor-Expressed B7-H3 Mediates the Inhibition of Antitumor T-Cell Functions in Ovarian Cancer Insensitive to PD-1 Blockade Therapy. *Cell Mol Immunol* (2020) 17:227–36. doi: 10.1038/s41423-019-0305-2
38. Majzner RG, Theruvath JL, Nellan A, Heitzeneder S, Cui Y, Mount CW, et al. Car T Cells Targeting B7-H3, a Pan-Cancer Antigen, Demonstrate Potent Preclinical Activity Against Pediatric Solid Tumors and Brain Tumors. *Clin Cancer Res* (2019) 25:2560–74. doi: 10.1158/1078-0432.CCR-18-0432
39. Wang ZX, Yang JF, Zhu YB, Zhu Y, Zhang B, Zhou YH. Differential Expression of 2igB7-H3 and 4igB7-H3 in Cancer Cell Lines and Glioma Tissues. *Oncol Lett* (2015) 10:2204–8. doi: 10.3892/ol.2015.3611
40. Aung PP, Parra ER, Barua S, Sui D, Ning J, Mino B, et al. B7-H3 Expression in Merkel Cell Carcinoma-Associated Endothelial Cells Correlates With Locally Aggressive Primary Tumor Features and Increased Vascular Density. *Clin Cancer Res* (2019) 25:3455–67. doi: 10.1158/1078-0432.CCR-18-2355
41. Suh WK, Gajewska BU, Okada H, Gronski MA, Bertram EM, Dawicki W, et al. The B7 Family Member B7-H3 Preferentially Down-Regulates T Helper Type 1-Mediated Immune Responses. *Nat Immunol* (2003) 4:899–906. doi: 10.1038/ni967
42. Suh WK, Wang SX, Jheon AH, Moreno L, Yoshinaga SK, Ganss B, et al. The Immune Regulatory Protein B7-H3 Promotes Osteoblast Differentiation and Bone Mineralization. *Proc Natl Acad Sci USA* (2004) 101:12969–73. doi: 10.1073/pnas.0405259101
43. Lupu CM, Eisenbach C, Kuefner MA, Schmidt J, Lupu AD, Stremmel W, et al. An Orthotopic Colon Cancer Model for Studying the B7-H3 Antitumor Effect In Vivo. *J Gastrointest Surg* (2006) 10:635–45. doi: 10.1007/BF03239969
44. Lupu CM, Eisenbach C, Lupu AD, Kuefner MA, Hoyler B, Stremmel W, et al. Adenoviral B7-H3 Therapy Induces Tumor Specific Immune Responses and Reduces Secondary Metastasis in a Murine Model of Colon Cancer. *Oncol Rep* (2007) 18:745–8. doi: 10.3892/or.18.3.745
45. Prasad DVR, Nguyen T, Li ZX, Yang Y, Duong J, Wang Y, et al. Murine B7-H3 is a Negative Regulator of T Cells. *J Immunol* (2004) 173:2500–6. doi: 10.4049/jimmunol.173.4.2500
46. Castriconi R, Dondero A, Augugliaro R, Cantoni C, Carnemolla B, Sementa AR, et al. Identification of 4Ig-B7-H3 as a Neuroblastoma-Associated Molecule That Exerts a Protective Role From an NK Cell-Mediated Lysis. *Proc Natl Acad Sci USA* (2004) 101:12640–5. doi: 10.1073/pnas.0405025101
47. Wang C, Li Y, Jia L, Kim JK, Li J, Deng P, et al. CD276 Expression Enables Squamous Cell Carcinoma Stem Cells to Evade Immune Surveillance. *Cell Stem Cell* (2021) 28:1–17. doi: 10.1016/j.stem.2021.04.011
48. Jin MZ, Jin WL. The Updated Landscape of Tumor Microenvironment and Drug Repurposing. *Signal Transduct Target Ther* (2020) 5:166. doi: 10.1038/s41392-020-00280-x
49. Li H, Zhang B, Liu Y, Yin C. EBP50 Inhibits the Migration and Invasion of Human Breast Cancer Cells Via LIMK/Cofilin and the PI3K/Akt/mTOR/MMP Signaling Pathway. *Med Oncol* (2014) 31:162. doi: 10.1007/s12032-014-0162-x
50. Niu H, Wu B, Peng Y, Jiang H, Zhang Y, Wang J, et al. RNA Interference-Mediated Knockdown of RhoGDI2 Induces the Migration and Invasion of Human Lung Cancer A549 Cells Via Activating the PI3K/Akt Pathway. *Tumour Biol* (2015) 36:409–19. doi: 10.1007/s13277-014-2671-9
51. Wu XY, Chen Y, Li G, Xia L, Gu RM, Wen X, et al. Her3 is Associated With Poor Survival of Gastric Adenocarcinoma: Her3 Promotes Proliferation, Survival and Migration of Human Gastric Cancer Mediated by PI3K/AKT

Signaling Pathway. *Med Oncol* (2014) 31:1–11. doi: 10.1007/s12032-014-0903-x
52. El Hage A, Dormond O. Combining Mtor Inhibitors and T Cell-Based Immunotherapies in Cancer Treatment. *Cancers (Basel)* (2021) 13:1359. doi: 10.3390/cancers13061359
53. Li YC, Guo GN, Song J, Cai ZP, Yang J, Chen ZW, et al. B7-H3 Promotes the Migration and Invasion of Human Bladder Cancer Cells Via the PI3K/Akt/STAT3 Signaling Pathway. *J Cancer* (2017) 8:816–24. doi: 10.7150/jca.17759
54. Nunes-Xavier CE, Karlsen KF, Tekle C, Pedersen C, Oyjord T, Hongisto V, et al. Decreased Expression of B7-H3 Reduces the Glycolytic Capacity and Sensitizes Breast Cancer Cells to AKT/mTOR Inhibitors. *Oncotarget* (2016) 7:6891–901. doi: 10.18632/oncotarget.6902
55. Jiang B, Zhang T, Liu F, Sun ZZ, Shi HP, Hua D, et al. The Co-Stimulatory Molecule B7-H3 Promotes the Epithelial-Mesenchymal Transition in Colorectal Cancer. *Oncotarget* (2016) 7:31755–71. doi: 10.18632/oncotarget.9035
56. Napetschnig J, Wu H. Molecular Basis of NF-kappaB Signaling. *Annu Rev Biophys* (2013) 42:443–68. doi: 10.1146/annurev-biophys-083012-130338
57. Wang RQ, Ma YC, Zhan SH, Zhang GB, Cao L, Zhang XG, et al. B7-H3 Promotes Colorectal Cancer Angiogenesis Through Activating the NF-Kappa B Pathway to Induce VEGFA Expression. *Cell Death Dis* (2020) 11:55. doi: 10.1038/s41419-020-2252-3
58. Xie C, Liu DQ, Chen QJ, Yang C, Wang B, Wu HS. Soluble B7-H3 Promotes the Invasion and Metastasis of Pancreatic Carcinoma Cells Through the TLR4/NF-Kappa B Pathway. *Sci Rep* (2016) 6:27528. doi: 10.1038/srep27528
59. Qi MS, Elion EA. MAP Kinase Pathways. *J Cell Sci* (2005) 118:3569–72. doi: 10.1242/jcs.02470
60. Flem-Karlsen K, Tekle C, Oyjord T, Florenes VA, Maelandsmo GM, Fodstad O, et al. P38 MAPK Activation Through B7-H3-Mediated DUSP10 Repression Promotes Chemoresistance. *Sci Rep-Uk* (2019) 9:5839. doi: 10.1038/s41598-019-42303-w
61. Girardi T, Sulima SO, Vereecke S, Khan Y, Fancello L, Flickinger Z, et al. The T-Cell Leukemia Associated Ribosomal Rpl10 R98s Mutation Enhances Jak-Stat Signaling. *Haematologica* (2017) 102:159–9. doi: 10.1038/leu.2017.225
62. Raible DJ, Frey LC, Brooks-Kayal AR. Effects of JAK2-STAT3 Signaling After Cerebral Insults. *JAKSTAT* (2014) 3:e29510. doi: 10.4161/jkst.29510
63. Capalbo G, Dittmann K, Hausmann E, Weiss C, Rodel C, Rodel F. Survivin As A Novel Target Protein for Reducing the Proliferation of Cancer Cells. *Strahlenther Onkol* (2009) 185:157–7. doi: 10.3892/br.2018.1077
64. Buki A, Okonkwo DO, Wang KKW, Povlishock JT. Cytochrome C Release and Caspase Activation in Traumatic Axonal Injury. *J Neurosci* (2000) 20:2825–34. doi: 10.1523/JNEUROSCI.20-08-02825.2000
65. Liu H, Tekle C, Chen YW, Kristian A, Zhao YH, Zhou M, et al. B7-H3 Silencing Increases Paclitaxel Sensitivity by Abrogating Jak2/Stat3 Phosphorylation. *Mol Cancer Ther* (2011) 10:960–71. doi: 10.1158/1535-7163.Mct-11-0072
66. Zhang T, Jiang B, Zou ST, Liu F, Hua D. Overexpression of B7-H3 Augments Anti-Apoptosis of Colorectal Cancer Cells by Jak2-STAT3. *World J Gastroenterol* (2015) 21:1804–13. doi: 10.3748/wjg.v21.i6.1804
67. Lu H, Ma Y, Wang M, Shen J, Wu H, Li J, et al. B7-H3 Confers Resistance to Vgamma9Vdelta2 T Cell-Mediated Cytotoxicity in Human Colon Cancer Cells Via the STAT3/ULBP2 Axis. *Cancer Immunol Immunother* (2021) 70:1213–26. doi: 10.1007/s00262-020-02771-w
68. Yang SY, Sales KM, Fuller B, Seifalian AM, Winslet MC. Apoptosis and Colorectal Cancer: Implications for Therapy. *Trends Mol Med* (2009) 15:225–33. doi: 10.1016/j.molmed.2009.03.003
69. Hanahan D, Weinberg RA. Hallmarks of Cancer: The Next Generation. *Cell* (2011) 144:646–74. doi: 10.1016/j.cell.2011.02.013
70. Heiden MGV, Cantley LC, Thompson CB. Understanding the Warburg Effect: The Metabolic Requirements of Cell Proliferation. *Science* (2009) 324:1029–33. doi: 10.1126/science.1160809
71. Lim S, Liu H, da Silva LM, Arora R, Liu ZX, Phillips JB, et al. Immunoregulatory Protein B7-H3 Reprograms Glucose Metabolism in Cancer Cells by ROS-Mediated Stabilization of HIF1 Alpha. *Cancer Res* (2016) 76:2231–42. doi: 10.1158/0008-5472.Can-15-1538
72. Shi T, Ma Y, Cao L, Chen W, Zhang X. B7-H3 Promotes Aerobic Glycolysis and Chemoresistance in Colorectal Cancer Cells by Regulating HK2. *Eur J Immunol* (2019) 49:95–5. doi: 10.1038/s41419-019-1549-6
73. Michelakos T, Kontos F, Barakat O, Maggs L, Schwab JH, Ferrone CR, et al. B7-H3 Targeted Antibody-Based Immunotherapy of Malignant Diseases. *Expert Opin Biol Ther* (2021) 21:587–602. doi: 10.1080/14712598.2021.1862791
74. Brahmer JR, Tykodi SS, Chow LQM, Hwu WJ, Topalian SL, Hwu P, et al. Safety and Activity of Anti-PD-L1 Antibody in Patients With Advanced Cancer. *New Engl J Med* (2012) 366:2455–65. doi: 10.1056/NEJMoa1200694
75. Hodi FS, O'Day SJ, McDermott DF, Weber RW, Sosman JA, Haanen JB, et al. Improved Survival With Ipilimumab in Patients With Metastatic Melanoma. *N Engl J Med* (2010) 363:711–23. doi: 10.1056/NEJMoa1003466
76. Topalian SL, Hodi FS, Brahmer JR, Gettinger SN, Smith DC, McDermott DF, et al. Safety, Activity, and Immune Correlates of Anti-PD-1 Antibody in Cancer. *New Engl J Med* (2012) 366:2443–54. doi: 10.1056/NEJMoa1200690
77. Lee YH, Martin-Orozco N, Zheng PL, Li J, Zhang P, Tan HD, et al. Inhibition of the B7-H3 Immune Checkpoint Limits Tumor Growth by Enhancing Cytotoxic Lymphocyte Function. *Cell Res* (2017) 27:1034–45. doi: 10.1038/cr.2017.90
78. Lu H, Shi T, Wang M, Li X, Gu Y, Zhang X, et al. B7-H3 Inhibits the IFN-gamma-dependent Cytotoxicity of Vgamma9Vdelta2 T Cells Against Colon Cancer Cells. *Oncoimmunology* (2020) 9:1748991. doi: 10.1080/2162402X.2020.1748991
79. Loo D, Alderson RF, Chen FZ, Huang L, Zhang WJ, Gorlatov S, et al. Development of an Fc-Enhanced Anti-B7-H3 Monoclonal Antibody With Potent Antitumor Activity. *Clin Cancer Res* (2012) 18:3834–45. doi: 10.1158/1078-0432.Ccr-12-0715
80. Scribner JA, Brown JG, Sharma S, Li H, Chiechi M, Li P, et al. Preclinical Development of MGC018, a Duocarmycin-Based Antibody-Drug Conjugate Targeting B7-H3 for Solid Cancer. *Cancer Res* (2018) 78:820. doi: 10.1158/1538-7445.AM2018-820
81. Weidle UH, Kontermann RE, Brinkmann U. Tumor-Antigen-Binding Bispecific Antibodies for Cancer Treatment. *Semin Oncol* (2014) 41:653–60. doi: 10.1053/j.seminoncol.2014.08.004
82. Ma J, Ma P, Zhao CH, Xue X, Han HM, Liu CZ, et al. B7-H3 as a Promising Target for Cytotoxicity T Cell in Human Cancer Therapy. *Oncotarget* (2016) 7:29480–91. doi: 10.18632/oncotarget.8784
83. Watchorn E. Irradiated Ergosterol and Calcium-Free Diet: Effect on Calcium and Phosphorus Metabolism. *Biochem J* (1930) 24:1560–3. doi: 10.1042/bj0241560
84. Davis ZB, Vallera DA, Miller JS, Felices M. Natural Killer Cells Unleashed: Checkpoint Receptor Blockade and BiKE/TriKE Utilization in NK-mediated Anti-Tumor Immunotherapy. *Semin Immunol* (2017) 31:64–75. doi: 10.1016/j.smim.2017.07.011
85. Kontos F, Kurokawa T, Vallera DA, Ferrone S, Ferrone CR. Il-15/B7-H3 TriKEs-Based Immunotherapy for Pancreatic Ductal Adenocarcinoma. *J Am Coll Surgeons* (2019) 229:S176–6. doi: 10.1016/j.jamcollsurg.2019.08.388
86. Vallera DA, Ferrone S, Kodal B, Hinderlie P, Bendzick L, Ettestad B, et al. Nk-Cell-Mediated Targeting of Various Solid Tumors Using a B7-H3 Tri-Specific Killer Engager In Vitro and In Vivo. *Cancers* (2020) 12:2659. doi: 10.3390/cancers12092659
87. Adams JL, Smothers J, Srinivasan R, Hoos A. Big Opportunities for Small Molecules in Immuno-Oncology. *Nat Rev Drug Discovery* (2015) 14:603–22. doi: 10.1038/nrd4596
88. Vigdorovich V, Ramagopal UA, Lazar-Molnar E, Sylvestre E, Lee JS, Hofmeyer KA, et al. Structure and T Cell Inhibition Properties of B7 Family Member. *B7-H3 Struct* (2013) 21:707–17. doi: 10.1016/j.str.2013.03.003
89. Chen S, Song Z, Zhang A. Small-Molecule Immuno-Oncology Therapy: Advances, Challenges and New Directions. *Curr Top Med Chem* (2019) 19:180–5. doi: 10.2174/1568026619666190308131805
90. Tang X, Wang YL, Huang JH, Zhang ZL, Liu FJ, Xu JG, et al. Administration of B7-H3 Targeted Chimeric Antigen Receptor-T Cells Induce Regression of Glioblastoma. *Signal Transduction Targeted Ther* (2021) 6:125. doi: 10.1038/s41392-021-00505-7
91. Nehama D, Di Ianni N, Musio S, Du HW, Patane M, Polloc B, et al. B7-H3-redirected Chimeric Antigen Receptor T Cells Target Glioblastoma and Neurospheres. *Ebiomedicine* (2019) 47:33–43. doi: 10.1016/j.ebiom.2019.08.030
92. Theruvath J, Sotillo E, Mount CW, Graef CM, Delaidelli A, Heitzeneder S, et al. Locoregionally Administered B7-H3-Targeted Car T Cells for

Treatment of Atypical Teratoid/Rhabdoid Tumors. *Nat Med* (2020) 26:712–+. doi: 10.1038/s41591-020-0821-8
93. Yang MJ, Tang X, Zhang ZL, Gu L, Wei H, Zhao SS, et al. Tandem CAR-T Cells Targeting CD70 and B7-H3 Exhibit Potent Preclinical Activity Against Multiple Solid Tumors. *Theranostics* (2020) 10:7622–34. doi: 10.7150/thno.43991
94. Tang X, Liu FJ, Liu ZY, Cao Y, Zhang ZL, Wang YL, et al. Bioactivity and Safety of B7-H3-targeted Chimeric Antigen Receptor T Cells Against Anaplastic Meningioma. *Clin Trans Immunol* (2020) 9:e1137. doi: 10.1002/cti2.1137
95. Yang S, Cao BH, Zhou GY, Zhu LP, Wang L, Zhang L, et al. Targeting B7-H3 Immune Checkpoint With Chimeric Antigen Receptor-Engineered Natural Killer Cells Exhibits Potent Cytotoxicity Against Non-Small Cell Lung Cancer. *Front Pharmacol* (2020) 11:1089. doi: 10.3389/fphar.2020.01089
96. Lei X, Ou Z, Yang Z, Zhong J, Zhu Y, Tian J, et al. A Pan-Histone Deacetylase Inhibitor Enhances the Antitumor Activity of B7-H3-Specific Car-T Cells in Solid Tumors. *Clin Cancer Res* (2021) 27:3757–71. doi: 10.1158/1078-0432.CCR-20-2487
97. Larkin J, Chiarion-Sileni V, Gonzalez R, Grob JJ, Cowey CL, Lao CD, et al. Combined Nivolumab and Ipilimumab or Monotherapy in Untreated Melanoma. *New Engl J Med* (2015) 373:23–34. doi: 10.1056/NEJMoa1504030
98. Xu Y, Xiao Y, Luo C, Liu QX, Wei AQ, Yang Y, et al. Blocking PD-1/PD-L1 by an ADCC Enhanced anti-B7-H3/PD-1 Fusion Protein Engages Immune Activation and Cytotoxicity. *Int Immunopharmacol* (2020) 84. doi: 10.1016/j.intimp.2020.106584
99. Zhang W, Wang J, Wang YF, Dong F, Zhu MX, Wan WL, et al. B7-H3 Silencing by RNAi Inhibits Tumor Progression and Enhances Chemosensitivity in U937 Cells. *Oncotargets Ther* (2015) 8:1721–33. doi: 10.2147/OTT.S85272
100. Twyman-Saint Victor C, Rech AJ, Maity A, Rengan R, Pauken KE, Stelekati E, et al. Radiation and Dual Checkpoint Blockade Activate Non-Redundant Immune Mechanisms in Cancer. *Nature* (2015) 520:373–7. doi: 10.1038/nature14292
101. Ahmed M, Cheng M, Zhao Q, Goldgur Y, Cheal SM, Guo HF, et al. Humanized Affinity-Matured Monoclonal Antibody 8h9 Has Potent Antitumor Activity and Binds to FG Loop of Tumor Antigen B7-H3. *J Biol Chem* (2015) 290:30018–29. doi: 10.1074/jbc.M115.679852
102. Hegde PS, Chen DS. Top 10 Challenges in Cancer Immunotherapy. *Immunity* (2020) 52:17–35. doi: 10.1016/j.immuni.2019.12.011
103. White AA, Lee DN, Mazzola E, Kucukak S, Polhemus E, Jaklitsch MT, et al. Adjuvant Therapy Following Induction Therapy and Surgery Improves Survival in N2-Positive Non-Small Cell Lung Cancer. *J Surg Oncol* (2021) 123:579–86. doi: 10.1002/jso.26305
104. Minami Y, Nishida N, Kudo M. Radiofrequency Ablation of Liver Metastasis: Potential Impact on Immune Checkpoint Inhibitor Therapy. *Eur Radiol* (2019) 29:5045–51. doi: 10.1007/s00330-019-06189-6
105. Bialosky JE, Beneciuk JM, Bishop MD, Coronado RA, Penza CW, Simon CB, et al. Unraveling the Mechanisms of Manual Therapy: Modeling an Approach. *J Orthop Sports Phys Ther* (2018) 48:8–18. doi: 10.2519/jospt.2018.7476
106. Lei KF, Ji WW, Goh A, Huang CH, Lee MY. Investigation of Uniform Sized Multicellular Spheroids Raised by Microwell Arrays After the Combined Treatment of Electric Field and Anti-Cancer Drug. *BioMed Microdevices* (2019) 21:94. doi: 10.1007/s10544-019-0442-5

Conflict of Interest: The authors declare that the research was conducted in the absence of any commercial or financial relationships that could be construed as a potential conflict of interest.

frontiers in Immunology

ORIGINAL RESEARCH
published: 03 August 2021
doi: 10.3389/fimmu.2021.719628

Comprehensive Characterization of RNA Processing Factors in Gastric Cancer Identifies a Prognostic Signature for Predicting Clinical Outcomes and Therapeutic Responses

Shenghan Lou[1†], Fanzheng Meng[2†], Xin Yin[1], Yao Zhang[1], Bangling Han[1] and Yingwei Xue[1]*

[1] Department of Gastroenterological Surgery, Harbin Medical University Cancer Hospital, Harbin, China, [2] Department of General Surgery, The First Affiliated Hospital of University of Science and Technology of China, Hefei, China

OPEN ACCESS

Edited by:
Mingzhu Yin,
Central South University, China

Reviewed by:
Fangrong Yan,
China Pharmaceutical University, China
Qing Zhang,
Shandong University, China
Yan Hou,
Peking University, China

***Correspondence:**
Yingwei Xue
xueyingwei@hrbmu.edu.cn

[†]These authors have contributed equally to this work

Specialty section:
This article was submitted to Cancer Immunity and Immunotherapy, a section of the journal Frontiers in Immunology

Received: *02 June 2021*
Accepted: *20 July 2021*
Published: *03 August 2021*

Citation:
Lou S, Meng F, Yin X, Zhang Y, Han B and Xue Y (2021) Comprehensive Characterization of RNA Processing Factors in Gastric Cancer Identifies a Prognostic Signature for Predicting Clinical Outcomes and Therapeutic Responses. Front. Immunol. 12:719628. doi: 10.3389/fimmu.2021.719628

RNA processing converts primary transcript RNA into mature RNA. Altered RNA processing drives tumor initiation and maintenance, and may generate novel therapeutic opportunities. However, the role of RNA processing factors in gastric cancer (GC) has not been clearly elucidated. This study presents a comprehensive analysis exploring the clinical, molecular, immune, and drug response features underlying the RNA processing factors in GC. This study included 1079 GC cases from The Cancer Genome Atlas (TCGA, training set), our hospital cohort, and two other external validation sets (GSE15459, GSE62254). We developed an RNA processing-related prognostic signature using Cox regression with the least absolute shrinkage and selection operator (LASSO) penalty. The prognostic value of the signature was evaluated using a multiple-method approach. The genetic variants, pathway activation, immune heterogeneity, drug response, and splicing features associated with the risk signature were explored using bioinformatics methods. Among the tested 819 RNA processing genes, we identified five distinct RNA processing patterns with specific clinical outcomes and biological features. A 10-gene RNA processing-related prognostic signature, involving *ZBTB7A*, *METTL2B*, *CACTIN*, *TRUB2*, *POLDIP3*, *TSEN54*, *SUGP1*, *RBMS1*, *TGFB1*, and *PWP2*, was further identified. The signature was a powerful and robust prognosis factor in both the training and validation datasets. Notably, it could stratify the survival of patients with GC in specific tumor-node-metastasis (TNM) classification subgroups. We constructed a composite prognostic nomogram to facilitate clinical practice by integrating this signature with other clinical variables (TNM stage, age). Patients with low-risk scores were characterized with good clinical outcomes, proliferation, and metabolism hallmarks. Conversely, poor clinical outcome, invasion, and metastasis hallmarks were enriched in the high-risk group. The RNA processing

signature was also involved in tumor microenvironment reprogramming and regulating alternative splicing, causing different drug response features between the two risk groups. The low-risk subgroup was characterized by high genomic instability, high alternative splicing and might benefit from the immunotherapy. Our findings highlight the prognostic value of RNA processing factors for patients with GC and provide insights into the specific clinical and molecular features underlying the RNA processing-related signature, which may be important for patient management and targeting treatment.

Keywords: RNA processing factors, alternative splicing event, drug response, prognostic model, immune heterogeneity, gastric cancer

INTRODUCTION

Gastric cancer (GC) is the third leading cause of cancer-related mortality and the fifth most frequently diagnosed malignancy worldwide (1), with almost 1,000,000 estimated new cases and 800,000 deaths each year (1, 2). Due to the lack of early symptoms, most patients with GC are usually diagnosed at an advanced stage (3). Despite effective treatment, relapse and metastasis are common in advanced GC, causing a fairly low 5-year survival rate (<20%) (4). To date, the tumor-node-metastasis (TNM) staging system remains the gold standard for predicting prognosis and guiding GC treatment decisions (5). However, the high heterogeneity leads to different outcomes among patients with the same TNM stage and treatments (6). Therefore, it is imperative to investigate the in-depth molecular mechanisms involved in GC occurrence and development to identify novel prognostic biomarkers and potential therapeutic targets.

RNA processing, connecting genotype to phenotype, is a process that converts the primary transcript RNA into mature RNA (7). RNA processing regulates activities as diverse as tissue-specific gene expression, apoptosis, and maturation of the immune response, among many others (8). Altered RNA processing functionally drives tumor initiation and maintenance, and may generate novel therapeutic opportunities (9). Given that dysregulated expression of RNA processing factors can contribute to abnormalities in a series of RNA processing phases, such as mRNA transport, editing, and decay (9), systematic examination of the role of RNA processing factors in GC is necessary.

RNA processing factors also function in intron removal and regulate alternative splicing events (ASEs) of individual genes (10). Aberrant selective RNA processing, especially alternative splicing, could cause a series of consequences, from changing the stability to adding or deleting structural domains and modifying the interactive relationship between proteins (11). Recently, we demonstrated that aberrant ASEs play an essential role in GC occurrence and development (12, 13). However, to date, the relationship between the dysregulated RNA processing factors and the aberrant ASEs has not been clearly elucidated.

In the present study, we systematically explored the expression profile of RNA processing factors and their prognostic values in 1079 patients with GC. We used three different GC cohorts, including RNA sequencing (RNA-seq) data and microarray data, to construct and validate the RNA processing-related prognostic signature. We constructed a composite prognostic nomogram to facilitate clinical practice by integrating this RNA processing-related signature with age and tumor stage. Then, we analyzed the association between the signature and clinical outcomes, genetic variants, pathway activation, immune heterogeneity, and drug response features. Besides, we profiled the ASEs underlying GC stratified by this risk signature and identified the corresponding functions.

MATERIALS AND METHODS

Gastric Cancer Dataset Source

We obtained 214 fresh frozen tumor specimens and clinical data from patients with GC who underwent gastrectomy as primary treatment at the Harbin Medical University (HMU) Cancer Hospital to construct the HMU-GC cohort. All samples were collected after written informed consent had been obtained from the patients. The study was approved by the HMU Cancer Hospital Institutional Review Board. RNA isolation, library construction, and mRNA sequencing were performed by Novogene (Beijing, China). The data were deposited in the Gene Expression Omnibus (GEO) repository (PRJNA718168).

We also systematically searched public gene expression data and complete clinical annotation in GEO and The Cancer Genome Atlas (TCGA) database. GC cohorts that: 1) had <150 patients; 2) lacked raw CEL files; 3) lacked basic clinical information (sex, age, TNM stage); or 4) lacked survival information were removed from further evaluation. Finally, four eligible GC cohorts, our HMU-GC cohort and three public datasets (GSE15459, GSE62254, TCGA-STAD), were included in the study for further analysis.

Data Preprocessing

For microarray data from the GEO database, the raw CEL files were downloaded. To calculate absolute mRNA expression levels, we used the RMA (Robust Multi-array Average) method provided through the affy package to obtain background-adjusted, quantile-normalized, and probe-level data-summarized values for all probe sets (14, 15). For high-throughput sequencing data from the HMU-GC and TCGA-

STAD datasets, raw read count values were transformed into transcripts per kilobase million (TPM) values, which are more similar to those generated from microarrays and are more comparable between samples (16). Batch effects from non-biological technical biases were corrected using the ComBat algorithm in the sva package (17).

The Affymetrix probe ID from the microarray data was annotated to gene symbols according to the GPL570 platform. For multiple probes that mapped to one gene, the mean expression value was considered. The Ensembl ID for mRNAs from high-throughput sequencing data was transformed to gene symbols *via* the biomaRt package (18). The mRNAs with TPM values of <1 in over 90% of samples were considered transcriptional noise and filtered out.

Collection of RNA Processing Factors

RNA processing factors, defined as genes that participate in any process involved in the conversion of ≥1 primary RNA transcripts into ≥1 mature RNA molecules, were first collected from the gene ontology (GO) term (GO:0006396) in the AmiGO database (19). RNA processing factors with sufficiently reliable expression, shared among the eligible GC cohorts, were retained for further analyses.

Unsupervised Clustering for RNA Processing Factors

Unsupervised clustering analysis was performed *via* hierarchical consensus clustering to identify the distinct RNA processing patterns based on the expression of RNA processing factors to classify patients for further analysis. The optimal number of clusters and their stability were determined by the consensus clustering algorithm. The above steps were performed using the ConsensusClusterPlus package, and 1000 repetitions were conducted to guarantee the stability of classification (20).

Gene set variation analysis (GSVA) was performed with the GSVA package (21), using the hallmark gene sets downloaded from MSigDB (22) to generate enrichment scores for each pathway per sample. Subsequently, we compared the GSVA enrichment score to explore the differences in biological functions and pathways among the distinct clusters. The overall survival (OS) of patients in the different RNA processing clusters was compared with Kaplan-Meier survival analysis with log-rank testing.

Identification of the RNA Processing-Related Prognostic Signature

Univariate Cox proportional hazards regression analysis was first performed on the expression matrix of RNA processing factors to estimate the relationship between RNA processing factors and prognosis (OS) in the TCGA-STAD cohort. RNA processing factors with p-value < 0.1 were selected as the potential prognosis-related RNA processing factors.

As the discovery cohort, the TCGA-STAD cohort was randomized into two subsets based on 5-fold sampling to enhance the robustness of this prognostic signature. The training set included 4-fold GC samples, and the internal testing set included the remaining 1-fold GC samples. The least absolute shrinkage and selection operator (LASSO) penalty was performed in the discovery cohort to build an optimal prognostic signature with the minimum number of RNA processing factors. Ten-fold cross-validation was conducted to tune the optimal value of the penalty parameter λ, which yields the minimum partial likelihood deviance. Finally, a set of RNA processing factors, the RNA processing-related prognostic signature, and their non-zero coefficients were identified.

The risk score for the signature was calculated for each sample based on the following formula:

$$\text{Risk Score} = \sum_{i=1}^{n} Coef_i \times E_i .,$$

where $Coef_i$ is the coefficient and E_i is the normalized expression value of each selected gene by log2 and z-score transformations. Patients were dichotomized into high-risk and low-risk groups using the cohort-specific median risk score as the cut-off. The performance of risk groups determined by the risk score was assessed based on the restricted mean survival (RMS) time difference between the high-risk and low-risk groups (23). Kaplan-Meier curves were generated for survival rates, with difference detection based on log-rank testing.

Development and Verification of a Composite RNA Processing–Clinical Prognostic Nomogram

Based on the multivariate analyses results, we integrated age, TNM stage, and the RNA processing-related prognostic signature to generate a composite prognostic model by applying a Cox proportional hazard regression in the TCGA-STAD cohort. The corresponding coefficients derived from the TCGA-STAD cohort were then used in the other two validation sets (HMU and GEO) for further validation. The prognostic value of the composite prognostic model was compared with the TNM staging system in terms of the concordance index (C-index), revealed by the RMS curve (24). The RMS represents the life expectancy at 60 months for patients with different risk scores. Finally, a nomogram was generated for model visualization and clinical application. The performance of the nomogram was evaluated by time-dependent receiver operator characteristic (ROC) analysis, calibration curve, and decision curve analysis (DCA) (25).

Construction of Regulatory Network Between RNA Processing Factors and ASEs

The corresponding alternative RNA splicing data of the TCGA-STAD cohort were downloaded from the TCGA SpliceSeq database (26). Splicing events in the dataset were divided into seven categories: exon skip (ES), retained intron (RI), alternate promoter (AP), alternate terminator (AT), alternate donor site (AD), alternate acceptor site (AA), and mutually exclusive exons (ME). To generate a reliable set of ASEs, we implemented a series of stringent filters, which included "percentage of samples with PSI value ≥ 75%" and "average PSI value ≥ 0.05". Only ASEs

meeting the above criteria were included for further analysis. Each splicing event was quantified by the percent spliced in (PSI) value (27), representing the ratio of included transcript reads in the total transcript reads.

To investigate the potential functions of RNA splicing, we performed enrichment analysis for all differential spliced genes in GC samples with lower risk (first quartile) and higher risk (fourth quartile) scores. These differential spliced genes were mapped to the Search Tool for the Retrieval of Interacting Genes/Proteins (STRING) database to observe the protein–protein interaction relationship (28). The protein interaction network was constructed to explore the potential impact of RNA splicing on protein-protein interactions in GC.

The potential association of the differential PSI values of ASEs between GC samples with lower and higher risk scores were predicted using RNA processing factors with significant expression levels. We calculated the Pearson's correlation for each RNA processing factor-ASE pair. The RNA processing factor-ASE pair with absolute correlation coefficients > 0.5 and Benjamini-Hochberg adjusted p-value < 0.05 were considered significant. The potential regulatory network was visualized with Cytoscape (29).

Immunohistochemical Analysis

Protein expression data were obtained from the Human Protein Atlas (HPA) database, the largest and most comprehensive database for evaluating protein distribution in human tissues (30). The protein expression of the selected RNA processing factors in normal and GC tissues was determined using the immunohistochemical staining images.

Bioinformatics Analyses

GO and Kyoto Encyclopedia of Genes and Genomes (KEGG) pathway enrichment analyses were utilized for gene set functional annotation. The functional enrichment of risk score-associated genes was investigated in gene set enrichment analysis (GSEA) using the clusterProfiler package (31, 32). We also performed GSVA to determine the functional differences between the risk groups. The mutation landscape was created with the maftools package with the initial removal of 100 FLAGS (frequently mutated genes) (33, 34). The presence of infiltrating stromal and immune cells in tumors was estimated with the estimate package (35). The population abundance of tissue-infiltrating immune and stromal cell populations was assessed with the MCPcounter package (36).

The gene module associated with the RNA processing-related prognostic signature was identified using weighted correlation network analysis (WGCNA) according to the protocol and recommendations of the WGCNA package (37). A scale-free topology fitting index (R^2) > 0.85 was set as the threshold to construct the weighted gene co-expression network. A minimum cluster size of 30 and a merge threshold function of 0.25 were chosen as the thresholds for identifying co-expressed gene modules. A biweight midcorrelation coefficient (r) ≥ 0.3 and p-value < 0.05 were set as the thresholds for determining gene modules associated with the prognostic signature.

Based on three public drug sensitivity databases, GDSC (Genomics of Drug Sensitivity in Cancer) (38), CTRP (Cancer Therapeutics Response Portal) (39), and PRISM (40), the pRRophetic package was applied for predicting chemotherapeutic response by using ridge regression to estimate the area under the dose–response curve (AUC) value for each sample (41, 42). The prediction accuracy was evaluated by 10-fold cross-validation based on each training set. Lower AUC values indicated increased sensitivity to treatment. Seven common chemotherapeutic agents (5-fluorouracil, cisplatin, oxaliplatin, capecitabine, paclitaxel, docetaxel, irinotecan) were selected for predicting the chemotherapeutic response (43). Furthermore, we predicted the relationship between the RNA processing-related prognostic signature and immunotherapy response using the Tumor Immune Dysfunction and Exclusion (TIDE) web tool (http://tide.dfci.harvard.edu/) (44). Patients with higher TIDE scores have a higher chance of antitumor immune escape, thereby exhibiting a lower immunotherapy response rate.

Statistical Analyses

All statistical tests were performed with R statistical software (v4.0.2) using Mann-Whitney testing for continuous data and Fisher's exact testing for categorical data. Correlation between two continuous variables was measured by Pearson's correlation coefficient. The hazard ratio (HR) and 95% confidence intervals (CI) were estimated by a Cox regression model using the survival package. Survival analysis was carried out using Kaplan–Meier methods. The statistical significance of differences was determined using log-rank testing. The RMS curve and RMS time difference were estimated with the survRM2 package. The time-dependent AUC was computed using the timeROC package. The C-index was compared with the compareC packages. For all statistical analyses, a two-tailed p-value < 0.05 was considered significant.

RESULTS

Overview of RNA Processing Factors in GC

A total of 1079 patients diagnosed with GC from four independent datasets (GSE15459, GSE62254, HMU-GC, TCGA-STAD) were ultimately included in this study. First, 929 genes, annotated as RNA processing factors in the GO term (GO:0006396), were acquired from the AmiGO database (**Supplementary Table 1**). After low-expression genes had been filtered out, 819 genes were present in all datasets (**Supplementary Table 2**). The entire workflow of this study, including the filtration of RNA processing factors, development and validation of a prognostic signature, the construction of a composite processing-clinical prognostic nomogram and, the analyses of signature-associated alteration of the ASEs and RNA expression profiles, are delineated in **Supplementary Figure 1**.

Identification of the Five Distinct RNA Processing Patterns

Patients with qualitatively different RNA processing patterns were classified using a meta-cohort (GSE15459, GSE62254,

HMU-STAD, TCGA-STAD). Five distinct patterns were eventually identified using unsupervised hierarchical clustering (**Figures 1A, B**): 385 cases in cluster 1, 171 cases in cluster 2, 206 cases in cluster 3, 174 cases in cluster 4, and 143 cases in cluster 5. Prognostic analysis of the five main RNA processing subtypes showed significant survival differences (log-rank test, $p < 0.01$; **Figure 1C**). Patients in clusters 2 and 3 had better prognosis than those in clusters 1 and 5 (**Figure 1C**).

We performed GSVA to explore the biological processes among these distinct RNA processing patterns. These five RNA processing subtypes showed significant enrichment of specific biological processes (**Figure 1D**). Clusters 2 and 3, correlated with good prognosis, were markedly enriched in the proliferation-specific pathways, such as the activation of the G2M checkpoint, E2F targets, and MYC targets pathway. Cluster 4, characterized by moderate prognosis, represented enriched pathways associated with metabolism activation, including the xenobiotic metabolism, bile acid metabolism, and estrogen response pathways. Clusters 1 and 5, associated with poor prognosis, were prominently related to stromal activation

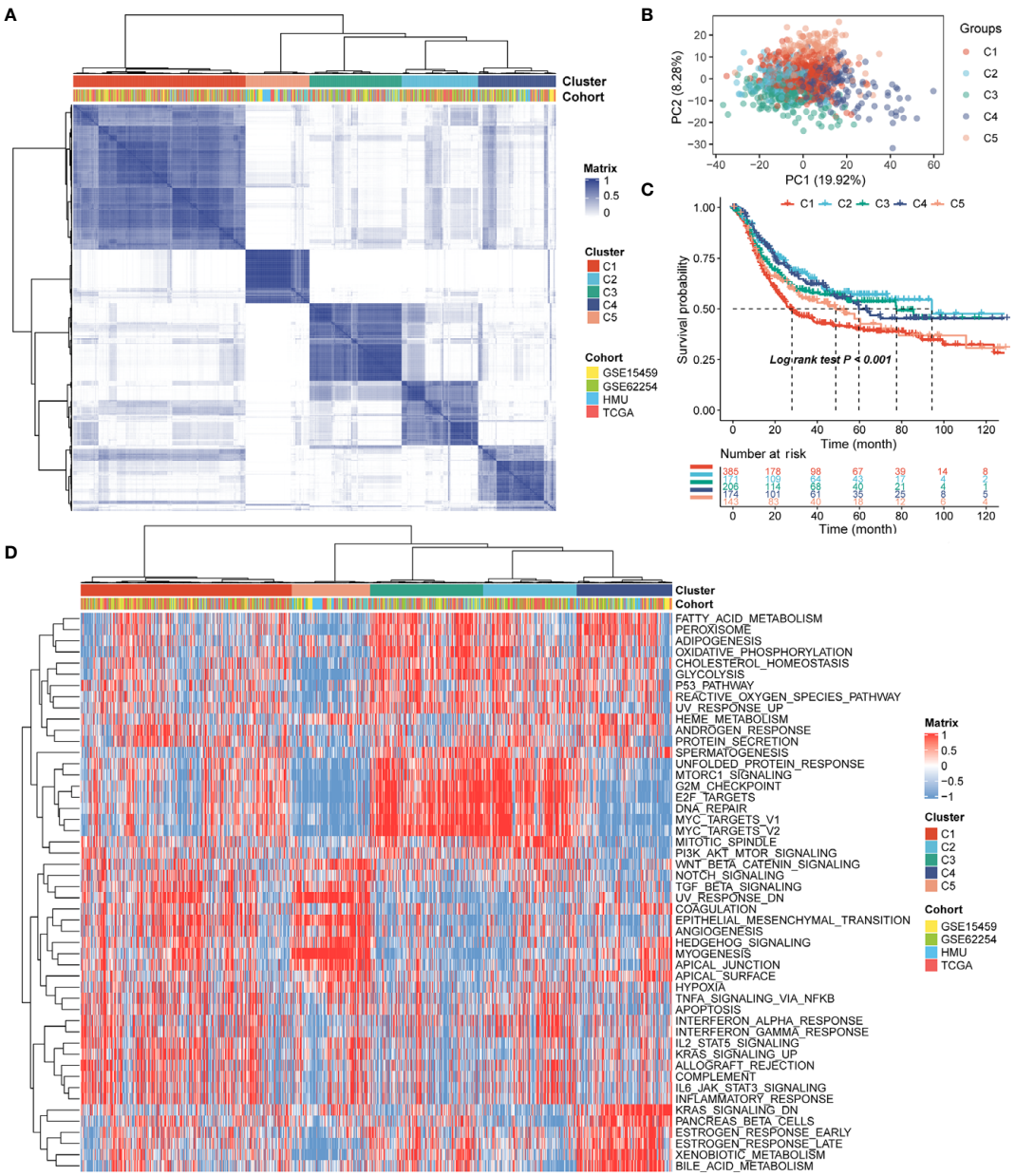

FIGURE 1 | Identification of the five distinct RNA processing patterns. **(A)** Heatmap showing consensus clustering analysis for the five defined RNA processing patterns. **(B)** Scatter plots showing principal component analysis (PCA) of the five distinct RNA processing patterns. **(C)** Kaplan–Meier survival analysis of OS for patients with the five distinct RNA processing patterns. **(D)** Heatmap showing GSVA scores of the hallmark gene sets for the five defined RNA processing patterns.

pathways, involving the epithelial–mesenchymal transition (EMT), transforming growth factor (TGF)-beta, and angiogenesis pathways. All these analyses suggest that RNA processing factors play an important role in GC occurrence and progression.

Identification of the RNA Processing-Related Prognostic Signature

Of the 819 RNA processing factors, 105 were associated with OS (**Supplementary Table 3**). Among these 105 factors, 51 factors (HR >1) were considered risk-associated, while the remaining 54 factors (HR <1) were considered protection-associated. We performed KEGG and GO functional enrichment analyses to study the more specific biological functions of these prognosis-related RNA processing factors. The results indicated that these factors were correlated with such key biological functions as RNA modification, regulation of RNA splicing, RNA transport, and spliceosome (**Figure 2A**).

To stratify the clinical outcomes of patients with the RNA processing factors readily and efficiently, we applied the LASSO Cox regression algorithm to the 105 factors in the TCGA training set. A total of 10 factors with non-zero coefficients were identified

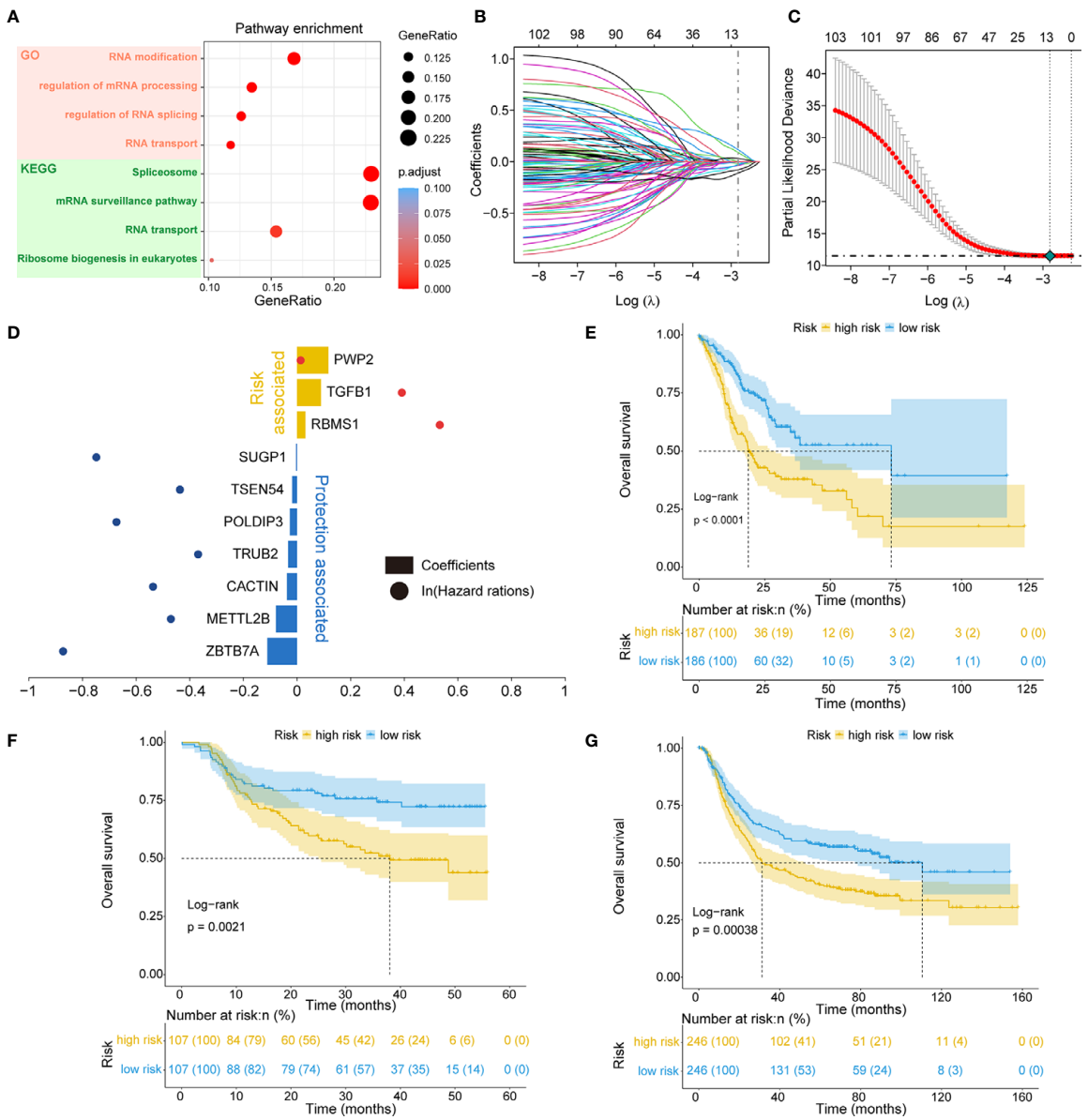

FIGURE 2 | Identification of the RNA processing-related prognostic signature. **(A)** Scatter plots showing functional enrichment analyses for the 105 OS-related RNA processing factors. **(B, C)** LASSO regression analysis of the 105 OS-related RNA processing factors. **(D)** The 10 genes included in the signature. Corresponding coefficients and HRs are depicted by horizontal bars and dots, respectively. **(E–G)** Kaplan–Meier OS curves with difference detection by log-rank test for patients from the training and validation datasets.

(**Figures 2B, C**). These LASSO-selected features were used to build the RNA processing-related signature (**Figure 2D**). The corresponding risk scores were computed for both the training and the validation datasets, according to the following formula:

$$\begin{aligned}\text{Risk Score} = & -0.111 \times ZBTB7A - 0.078 \times METTL2B - 0.037 \\ & \times CACTIN - 0.033 \times TRUB2 - 0.027 \\ & \times POLDIP3 - 0.018 \times TSEN54 - 0.003 \times SUGP1 \\ & + 0.031 \times RBMS1 + 0.089 \times TGFB1 + 0.116 \\ & \times PWP2\end{aligned}$$

We divided patients in all three datasets into high-risk and low-risk groups using their respective median risk score as the cutoff. Kaplan-Meier survival analysis determined that patients with low-risk scores had significantly longer OS than those with high-risk scores (TCGA training set: $p < 0.001$, HR = 0.455, 95% CI: 0.324-0.638; HMU validation set: $p = 0.002$, HR = 0.487, 95% CI: 0.304-0.778; GEO validation set: $p < 0.001$, HR = 0.633, 95% CI: 0.491-0.817; **Figures 2E–G**). Significant RMS time differences were also observed between the low-risk and high-risk groups at different time points; the RMS time differences increased as the follow-up duration was extended (**Table 1**). For example, the RMST differences between the two groups were 1 (TCGA), 4 (HMU), and 0 (GEO) months for OS at the first year of follow-up, which reached 11 (TCGA), 9 (HMU), and 7 (GEO) months at the fifth year.

We performed univariate and multivariate Cox regression analyses in the training and validation datasets to investigate the prognostic value of the RNA processing-related signature. The signature was the only prognostic factor in all three datasets (univariate cox analysis: $p < 0.05$; **Table 2**). After adjusting for other prognostic factors (age and TNM stage), the signature remained a significant independent prognostic factor in the HMU and TCGA cohorts (**Table 2**). Furthermore, we performed subgroup analyses according to age, sex, and TNM stage to explore the interaction effect between the signature and clinical characteristics. Subgroup analyses showed no statistically significant tests of interaction (**Table 3**), suggesting the robustness of this signature for different clinical features.

Identification of the Composite Prognostic Nomogram

In addition to the RNA processing-related signature, clinical characteristics, including age and TNM stage, might also be independent prognostic factors, suggesting their complementary value (**Table 2**). We integrated the signature with these significant clinical variables to further improve the prognostic accuracy, using the coefficients generated from the multivariate Cox regression model in the discovery cohort (TCGA cohort) and derived a composite prognostic model. A nomogram was then established for model visualization and clinical application (**Figure 3A**). The composite nomogram achieved significant improvement for assessing survival relative to the clinical model involving age and TNM stage (**Figure 3B**). The composite nomogram also performed better than the RNA processing-related signature and the clinical model for predicting GC prognosis (**Figure 3C**). The calibration curve detected an optimal prediction between the nomogram prediction and actual observations (**Figure 3D**).

Finally, we compared the clinical net benefit of the composite nomogram with that of the other two models through DCA curves. The composite nomogram demonstrated a larger net benefit than the RNA processing-related signature and basic clinical model within most of the above threshold probabilities (**Figure 3E**), indicating that the nomogram had the best clinical utility for predicting prognosis in patients with GC. All these findings were verified in the HMU (**Figures 3F–I**) and GEO validation datasets (**Figures 3J–M**), suggesting the reliability and stability of our composite nomogram.

Function Analysis of Genes Correlated With the RNA Processing-Related Prognostic Signature

Given that RNA processing factors are the main factors controlling the life cycle of RNAs in eukaryotes, we subsequently evaluated the RNA expression profile influenced by the RNA processing-related prognostic signature. In this case, we correlated the signature risk score with all robustly expressed mRNAs, generating a pre-ranked list sorted by the Pearson correlation coefficient, and further performed GSEA. The results indicated that invasion, metastasis, and immune hallmarks, such as EMT, myogenesis, angiogenesis,

TABLE 1 | RMS time (RMST) between the two risk groups at different time points.

Dataset	Time point	RMST[a]		RMST difference[b]	p-value
		Low risk (95% CI)	High risk (95% CI)		
TCGA cohort (n = 373)	**12 months**	11.236 (10.881, 11.590)	10.206 (9.722, 10.69)	1.030 (0.430, 1.629)	**<0.001**
	36 months	28.138 (26.304, 29.972)	21.273 (19.167, 23.378)	6.865 (4.073, 9.658)	**<0.001**
	60 months	40.810 (36.656, 44.964)	29.399 (25.410, 33.387)	11.411 (5.652, 17.170)	**<0.001**
HMU cohort (n = 214)	**12 months**	11.046 (10.594, 11.498)	11.072 (10.700, 11.444)	-0.026 (-0.612, 0.559)	0.93
	36 months	29.787 (27.582, 31.992)	25.915 (23.592, 28.237)	3.872 (0.670, 7.075)	**0.018**
	60 months	43.591 (39.832, 47.350)	34.980 (30.935, 39.025)	8.611 (3.089, 14.133)	**0.002**
GEO cohort (n = 492)	**12 months**	11.242 (10.965, 11.519)	11.115 (10.852, 11.377)	0.127 (-0.255, 0.509)	0.514
	36 months	28.479 (27.011, 29.948)	25.578 (24.070, 27.085)	2.901 (0.797, 5.006)	**0.007**
	60 months	42.934 (40.076, 45.792)	36.224 (33.359, 39.089)	6.710 (2.663, 10.757)	**0.001**

[a]*RMST, months.*

[b]*RMST difference = $RMST_{low\ risk} - RMST_{high\ risk}$.*

The bold value means the outcome is statistically significant.

TABLE 2 | Univariate and multivariate Cox analyses of the RNA processing-related signature.

Dataset	Factor	Univariate		Multivariate	
		HR (95% CI)	p-value	HR (95% CI)	p-value
TCGA cohort (n = 373)	**Risk score (increasing values)**	9.280 (4.746, 18.148)	**<0.001**	9.918 (4.926, 19.968)	**<0.001**
	Age (increasing years)	1.021 (1.005, 1.037)	**0.012**	1.027 (1.010, 1.045)	**0.002**
	Sex (male vs. female)	1.333 (0.936, 1.899)	0.112		
	TNM stage (III + IV vs. I + II)	1.891 (1.325, 2.698)	**<0.001**	2.101 (1.464, 3.015)	**<0.001**
HMU cohort (n = 214)	**Risk score (increasing values)**	2.819 (1.041, 7.637)	**0.041**	2.819 (1.041, 7.637)	**0.041**
	Age (increasing years)	1.009 (0.992, 1.027)	0.284		
	Sex (male vs. female)	0.984 (0.615, 1.574)	0.947		
	TNM stage (III + IV vs. I + II)	1.165 (0.710, 1.911)	0.545		
GEO cohort (n = 492)	**Risk score (increasing values)**	3.601 (2.002, 6.474)	**<0.001**	1.632 (0.879, 3.029)	0.121
	Age (increasing years)	1.006 (0.995, 1.018)	0.254		
	Sex (male vs. female)	1.056 (0.810, 1.377)	0.686		
	TNM stage (III + IV vs. I + II)	4.245 (3.097, 5.817)	**<0.001**	3.983 (2.878, 5.511)	**<0.001**

The bold value means the outcome is statistically significant.

hypoxia, inflammatory response, interferon-gamma response, and complement, were significantly enriched in GC samples with higher risk scores. In contrast, proliferation and metabolism hallmarks, such as G2M checkpoint, MYC targets, oxidative phosphorylation, fatty acid metabolism, and glycolysis, were significantly enriched in GC samples with lower risk scores (**Figure 4A**).

Furthermore, we used WGCNA to obtain the signature-related modules according to the approximate scale-free features. The top

TABLE 3 | Subgroup analysis of the RNA processing-related signature.

Data set	Factor	Subgroup analysis			p-value for interaction
		Samples	HR (95% CI)	p-value	
TCGA cohort (n = 373)	**Sex**				
	Female	133.000	12.071 (3.737, 38.996)	**<0.001**	0.651
	Male	240.000	8.271 (3.611, 18.945)	**<0.001**	
	Age				
	≤60	120.000	18.021 (4.949, 65.616)	**<0.001**	0.268
	> 60	249.000	7.543 (3.498, 16.267)	**<0.001**	
	Stage				
	Early (I and II)	164.000	7.482 (2.349, 23.831)	**0.001**	0.660
	Advanced (III and IV)	186.000	11.097 (4.527, 27.202)	**<0.001**	
HMU cohort (n = 214)	**Sex**				
	Female	77.000	2.162 (0.315, 14.849)	0.433	0.666
	Male	136.000	3.372 (1.037, 10.971)	**0.043**	
	Age				
	≤60	118.000	2.369 (0.563, 9.977)	0.240	0.691
	> 60	96.000	3.509 (0.883, 13.943)	0.075	
	Stage				
	Early (I and II)	67.000	1.243 (0.213, 7.264)	0.809	0.260
	Advanced (III and IV)	147.000	4.149 (1.234, 13.947)	**0.021**	
GEO cohort (n = 492)	**Sex**				
	Female	168.000	6.633 (2.354, 18.691)	**<0.001**	0.113
	Male	324.000	2.651 (1.290, 5.447)	**0.008**	
	Age				
	≤60	178.000	8.792 (3.039, 25.438)	**<0.001**	0.065
	> 60	314.000	2.583 (1.260, 5.291)	**0.010**	
	Stage				
	Early (I and II)	187.000	2.796 (0.784, 9.976)	0.113	0.312
	Advanced (III and IV)	305.000	1.331 (0.654, 2.708)	0.431	

The bold value means the outcome is statistically significant.

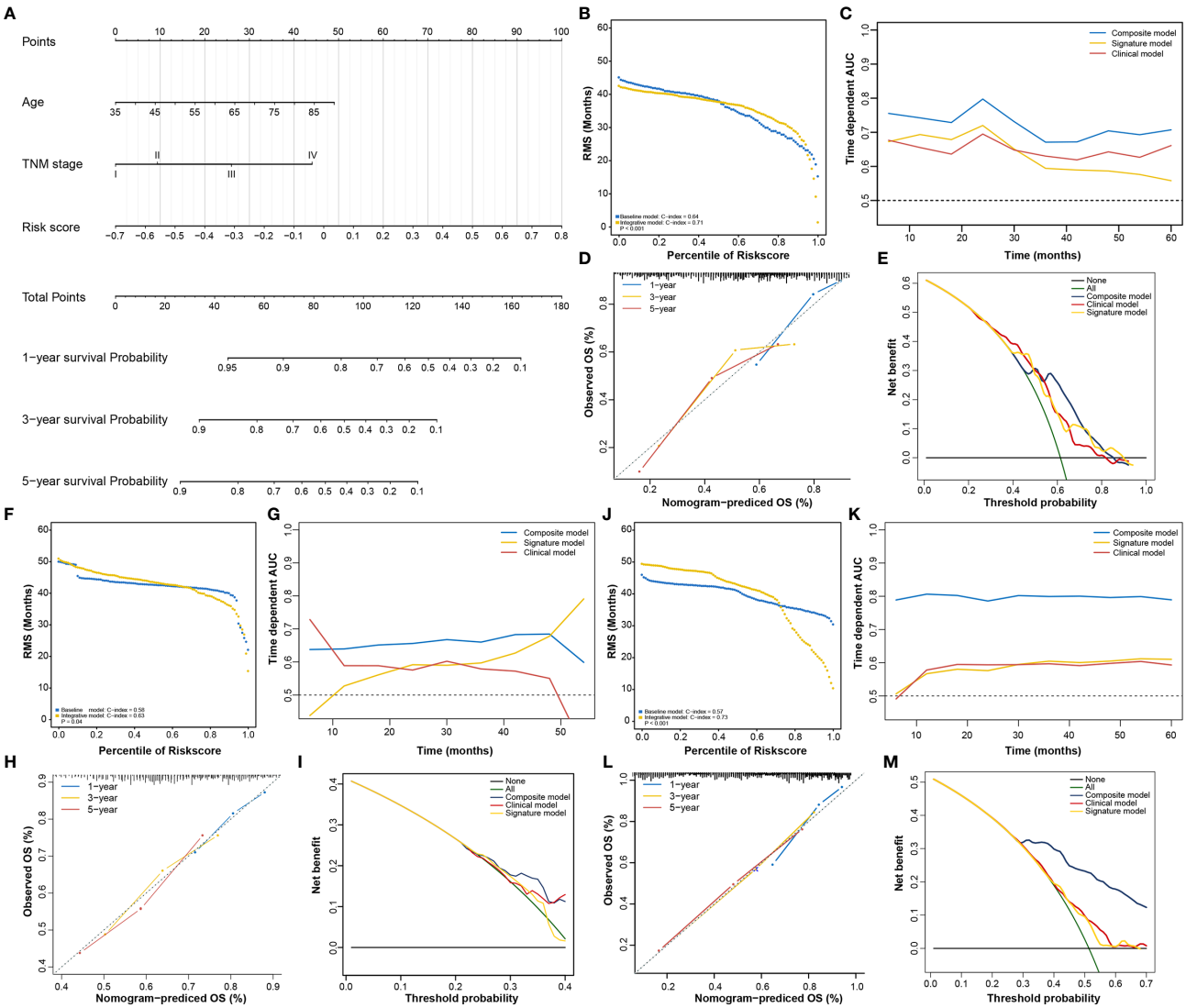

FIGURE 3 | Identification of the composite prognostic nomogram. **(A)** Composite nomogram prediction of 1-year, 3-year, and 5-year OS. **(B, F, J)** RMS curves for the composite prognostic nomogram and clinical model in the training and validation datasets. **(C, G, K)** Time-dependent ROC curves for the nomogram, signature model, and clinical model at different time points in the training and validation datasets. **(D, H, L)** Calibration curves of observed and predicted probabilities for the nomogram in the training and validation datasets. **(E, I, M)** DCA curves for the nomogram in the training and validation datasets.

5000 most variant genes, measured by the median absolute deviation (MAD), were selected for the WGCNA. We chose nine as the optimal soft threshold power to calculate the adjacency matrix, which was the lowest threshold to enable the scale-free R^2 to reach 0.85 (**Supplementary Figure 2**). We constructed a cluster dendrogram with the adjacency matrix; five color modules (blue, brown, turquoise, yellow, grey) were identified (**Figure 4B**). Genes that could not be included in any module were placed in the grey module and removed for the downstream analysis.

Next, we correlated the eigengene of the selected traits and modules to evaluate the module–trait relationships. Three modules (brown, turquoise, yellow) were highly significantly associated with the signature risk score ($|R| > 0.3$). The yellow and turquoise modules were positively correlated with the signature risk score. The brown module was negatively correlated with the signature risk score (**Figure 4C**). All modules also showed significant correlations between gene significance and module membership (**Supplementary Figure 3**), implying that the genes in these modules might play an essential biological role associated with the RNA processing-related prognostic signature.

We then performed functional enrichment analysis of the genes in each module to explore the biological functions of the signature-related modules. Consistent with the GSEA results, genes in the brown module were significantly enriched in the proliferation- and metabolism-related pathways (**Figure 4D**). For yellow module genes, the top enriched terms were allograft rejection, interferon-

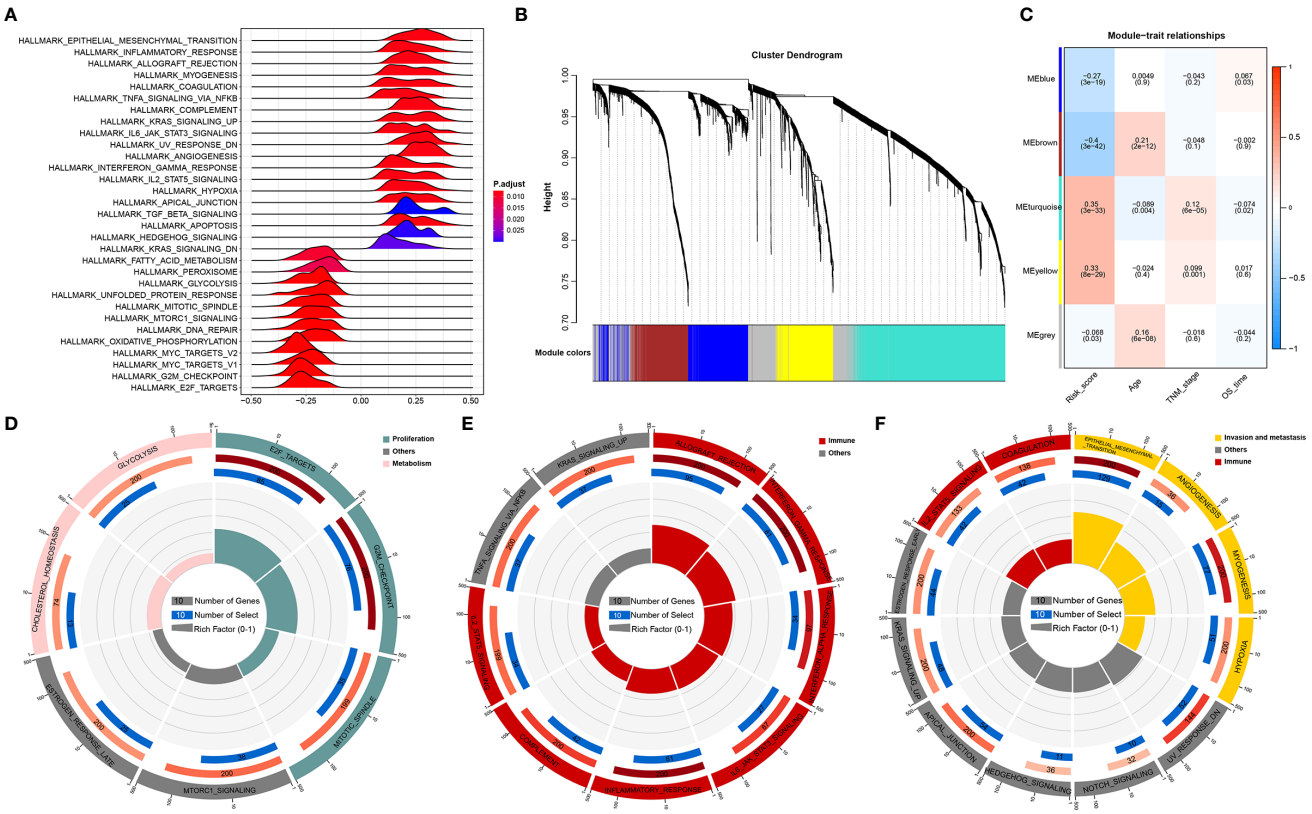

FIGURE 4 | Function analysis of genes correlated with the RNA processing-related prognostic signature. **(A)** GSEA of the hallmark gene sets for risk scores based on pre-ranked Pearson's correlation coefficients of risk score-associated mRNAs. **(B)** Clustering dendrogram of the top 5000 mRNAs with dissimilarity based on the topological overlap together with assigned module colors. **(C)** Module–trait relationships. Each row shows a module eigengene; each column corresponds to a clinical trait. Each cell contains the corresponding correlation (upper number) and p-value (lower number). **(D–F)** Functional enrichment analysis of the hallmark gene sets for the brown **(D)**, yellow **(E)**, and turquoise **(F)** modules.

gamma response, and inflammatory response, suggesting that the yellow module is involved in the immune response (**Figure 4E**). Genes in the turquoise module were associated with the development of malignant phenotypes, focusing on invasion and metastasis processes (**Figure 4F**). These findings imply that the RNA processing-related prognostic signature reflects the expression alterations of genes involved in multiple vital hallmarks (invasion, metastasis, proliferation, metabolism, immune response) in GC.

Expression and Clinical Features Underlying the RNA Processing-Related Prognostic Signature

All 1079 GC samples were pooled to explore the expression and clinical features of the RNA processing-related prognostic signature. All 10 LASSO-selected factors were significantly differentially expressed between the two risk groups (**Figures 5A, B**). Risk-associated genes showed higher expression levels in patients with high risk scores. In comparison, protection-associated genes showed higher expression levels in those with low risk scores (**Figures 5A, B**). Moreover, the immunohistochemical analysis *via* the HPA determined that most protection-associated genes showed lower protein expression levels in GC samples than in adjacent normal tissues; the protein products of the risk-associated genes showed an opposite trend (**Figure 5C**).

Moreover, we found that advanced tumor stage (stage III and IV) was significantly enriched in the high-risk group ($p < 0.001$; **Figures 5A, D**). A higher percentage of clusters 1 and 5, featuring poor prognosis and stromal activation, was enriched in the high-risk group ($p < 0.001$; **Figures 5A, E**). These results suggest that the identified RNA processing factors might be involved in GC occurrence and development and could serve as potential therapeutic targets.

Genetic Variants, Pathway Activation, and Immune Heterogeneity Underlying the RNA Processing-Related Prognostic Signature

Genomic data, including mutation profile and somatic copy number alteration (SCNA) data from the TCGA-STAD dataset, were first analyzed to explore the possible mechanisms underlying the RNA processing-related prognostic signature. A significantly higher tumor mutation burden (TMB) was

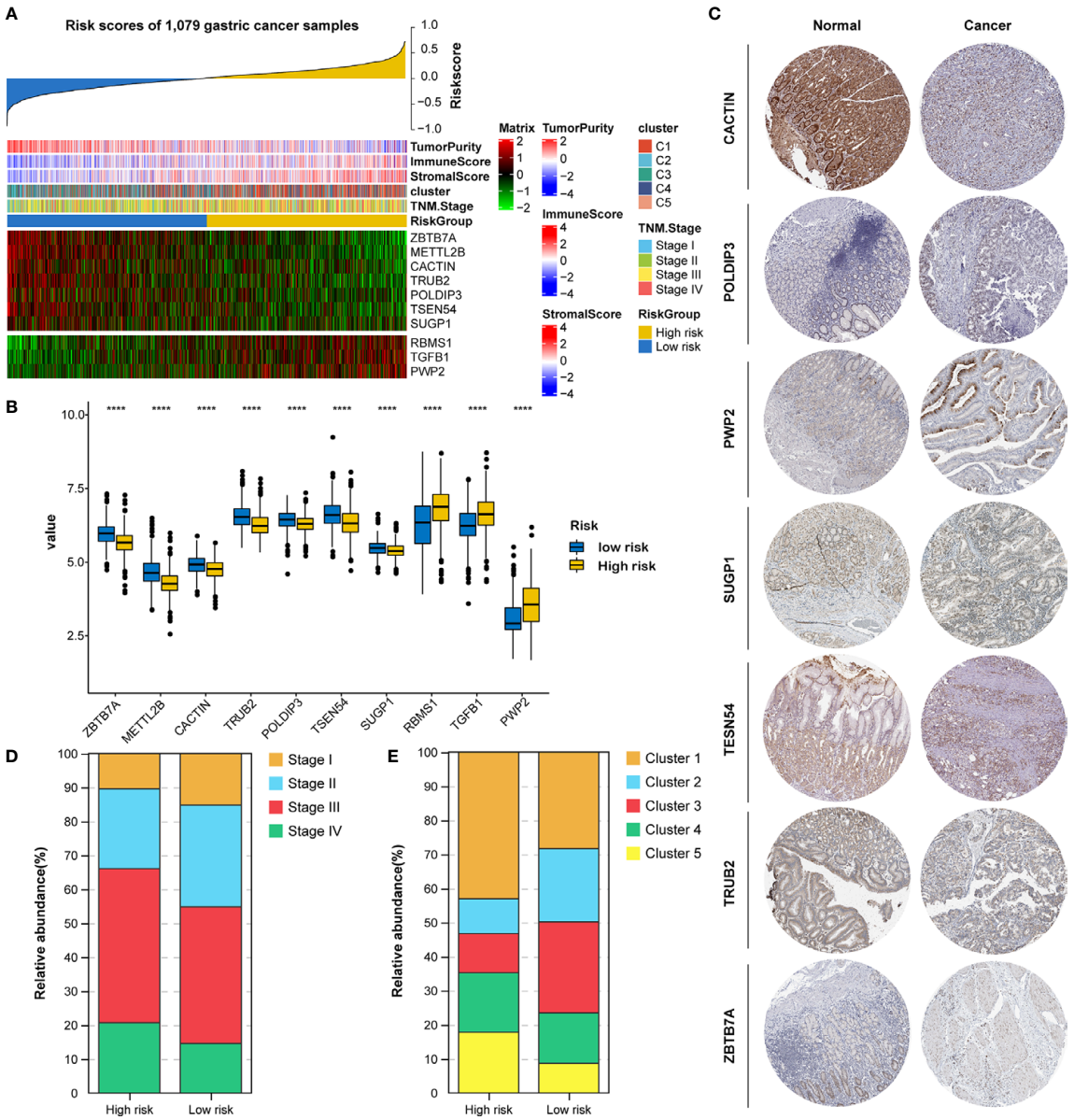

FIGURE 5 | Identification of expression and clinical features underlying the RNA processing-related prognostic signature. **(A)** Heatmap showing the expression patterns of 10 prognosis-associated RNA processing factors for the entire 1079-sample GC set sorted by the signature risk score in ascending order. **(B)** Differential expression of the 10 prognosis-associated RNA processing factors between the low-risk and high-risk groups. P values were obtained by the Mann-Whitney test. The asterisks represented the statistical P-value (****P < 0.0001). **(C)** Histogram showing the distribution of TNM stage between the low-risk and high-risk groups. **(D)** Histogram showing the distribution of the five distinct RNA processing patterns between the low-risk and high-risk groups. **(E)** Immunohistochemical analysis of the protein expression of the 7 prognosis-associated RNA processing factors in the HPA database.

detected in the low-risk group than in the high-risk group (**Figure 6A**). More mutations caused more neoantigens in cases with lower risk scores (first vs. fourth quartile; **Figure 6B**) (45). After filtering out genes with low-frequency mutations (5% of GC samples), we found 25 significantly mutated genes between the two groups (**Figure 6C**). All these significantly mutated genes were enriched in the low-risk group, and were involved in the UV response down pathway (adjusted p = 0.014). Subsequently, investigation of the data related to SCNA events revealed distinct chromosomal alteration patterns between the low-risk and high-risk groups (**Figure 6D**). A significantly greater fraction of genome gained was detected in the low-risk group (**Figure 6E**).

GSVA confirmed significant differences in biological functions between the high-risk and low-risk groups (**Figure 7A**). Consistent with the above results, stromal

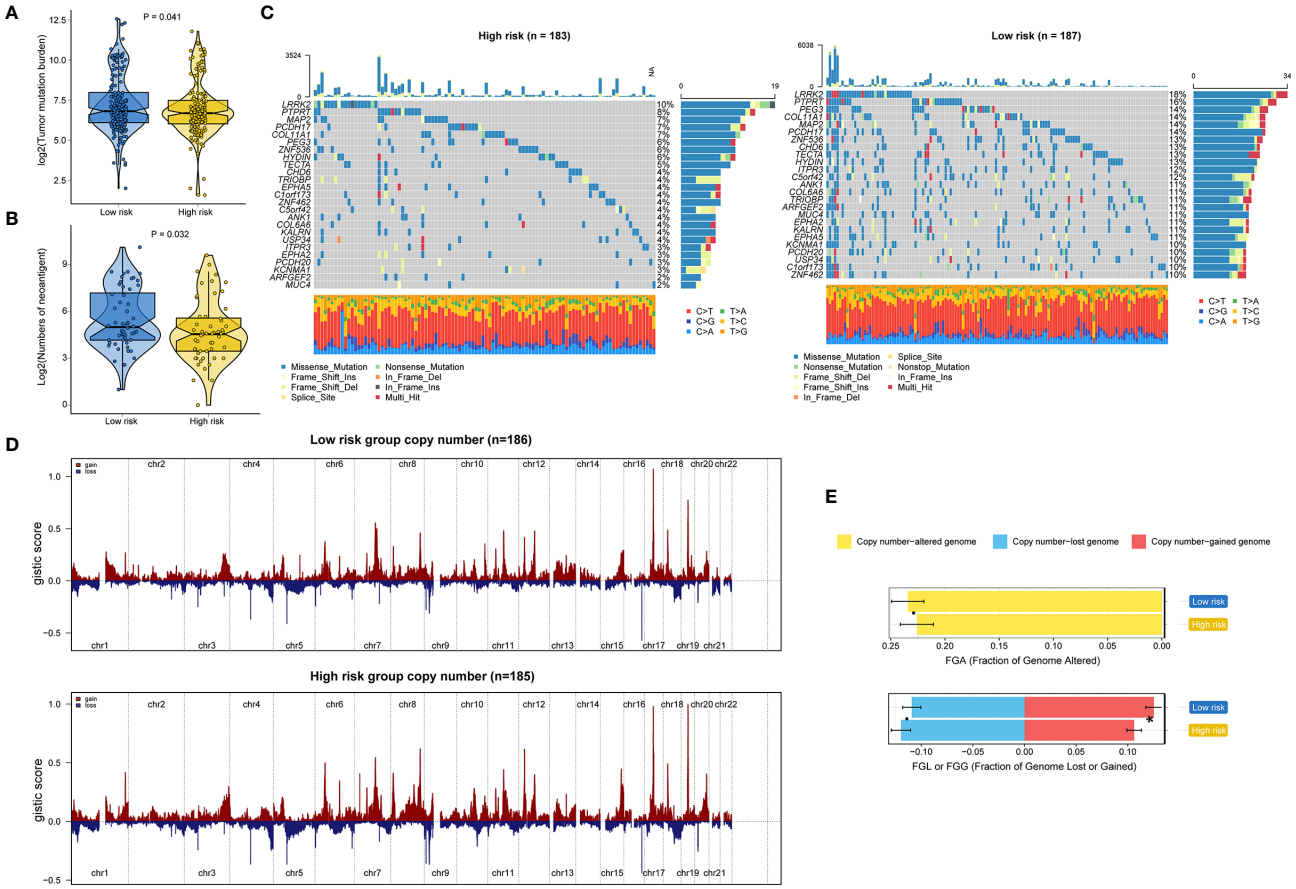

FIGURE 6 | Identification of genetic variants underlying the RNA processing-related prognostic signature. **(A)** Violin plot for the TMB between the low-risk and high-risk groups. **(B)** Violin plot for the number of neoantigens between the lower-risk and higher-risk groups. **(C)** Waterfall plot of the top 25 mutant genes in the low-risk and high-risk groups. **(D)** SCNA profiles with gains (red) and losses (blue) between the lower-risk and higher-risk groups. **(E)** Differential analysis of the fraction (%) of the genome altered, lost, and gained between the lower-risk and higher-risk groups. P values were obtained by the Mann-Whitney test. The asterisks represented the statistical P-value (*P < 0.05).

activation pathways, such as the EMT, TGF-beta, and angiogenesis pathways, were significantly enriched in the high-risk group (**Supplementary Table 4**). The immune-related pathways, such as the complement, interferon-alpha response, and interferon-gamma response pathways, were also significantly enriched in the high-risk group (**Figure 7A** and **Supplementary Table 4**).

As the high-risk group had marked enrichment of the stromal and immune activation pathways, we explored the relationship between the tumor microenvironment status and the RNA processing-related signature to characterize their immune heterogeneity. We found that both the stromal and immune scores, representing stromal and immune cell infiltration in tumor tissue, respectively, were significantly higher in the high-risk group (**Figures 7B, C**). The MCP-counter algorithm also determined a higher proportion of immune and stromal cells in the high-risk group (**Figures 7B, D**). Further, based on the pathology whole-slide images, samples with high risk scores had a higher percentage of tumor-infiltrating lymphocytes (including T cells, B cells, and natural killer cells) than those with low risk scores (**Figure 7E**) (46). These results indicate that the activation of stromal and immune components in the tumor microenvironment and the activated oncogenic pathways based on the proposed signature likely contribute to the worse prognosis in high-risk patients.

RNA Splicing Events Underlying the RNA Processing-Related Prognostic Signature

RNA processing factors dominate RNA splicing activities. Our outcomes showed that prognosis-associated RNA processing genes are closely correlated with RNA splicing-related activities (**Figure 8A**). Accordingly, we also comprehensively characterized ASEs in GC samples with different risk scores. Tens of thousands of seven ASE types were detected in each GC sample (**Figure 8A**). The proportion of these ASE types in the GC samples varied widely, from 0.5% to approximately 43% (**Figure 8A**). Although all GC samples shared similar ASE type patterns, the total number of detected ASEs gradually decreased along with the increasing risk

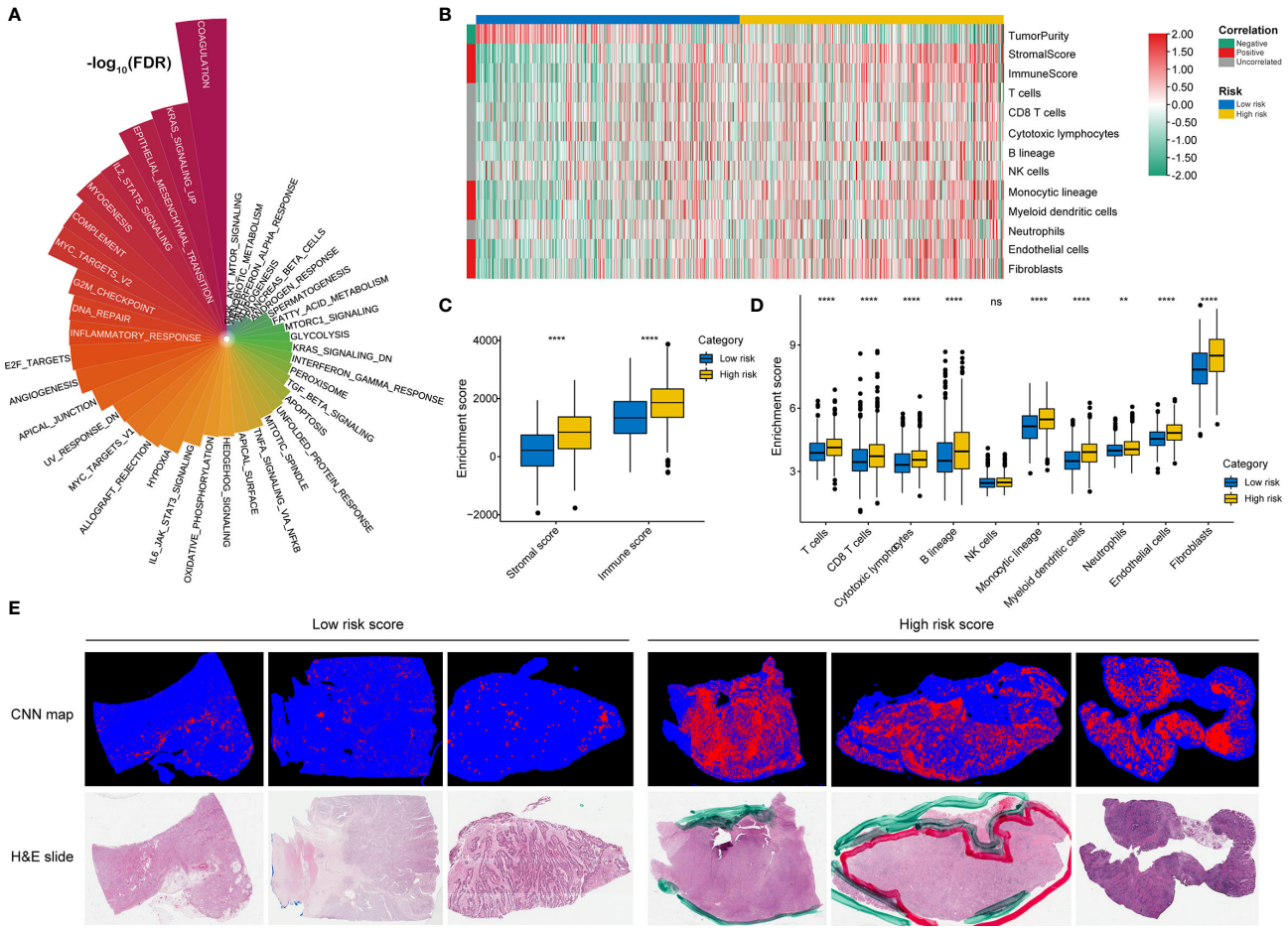

FIGURE 7 | Identification of immune heterogeneity underlying the RNA processing-related prognostic signature. **(A)** The differential analysis of GSVA scores between the low-risk and high-risk groups. The height and color represent the -log10(FDR). **(B)** Heatmap showing the immune cell infiltration between the high-risk and low-risk groups. **(C)** Differential expression of immune scores and stromal scores between the low-risk and high-risk groups. P values were obtained by the Mann-Whitney test. The asterisks represented the statistical P-value (ns, not statistical; **P < 0.01; ****P < 0.001). **(D)** Differential expression of immune and stromal cells between the low-risk and high-risk groups. P values were obtained by the Mann-Whitney test. The asterisks represented the statistical P-value (ns, not statistical; **P < 0.01; ****P < 0.001). **(E)** Tumor-infiltrating lymphocyte infiltration between the low-risk and high-risk groups determined by hematoxylin–eosin (H&E) whole-slide images. Red represents a positive TIL patch; blue represents a tissue region with no TIL patch, while black represents no tissue.

score ($p < 0.001$, R = -0.18). Moreover, ASEs were significantly higher in GC samples with lower risk scores (first quartile, n = 94) compared to those with higher risk scores (fourth quartile, n = 94) (**Supplementary Figure 4**).

We further identified differentially expressed RNA processing genes (absolute fold change > 1.2, false discovery rate [FDR] < 0.05) and ASEs with significantly different PSI values (absolute fold change > 1.5, FDR < 0.05) in GC samples with lower risk (first quartile, n = 94) and higher risk (fourth quartile, n = 94) scores (**Figure 8B**). We identified 358 ASEs from 327 genes, including 240 upregulated ASEs from 217 genes and 118 downregulated ASEs from 118 genes (**Supplementary Table 5**). For these ASEs with markedly different PSI values, we found that the frequency of all ASE types was significantly altered compared to the background ASEs (**Supplementary Figure 5**), suggesting that the presence of altered ASEs might be associated with GC prognosis.

We found that genes involved in the aberrant RNA splicing in GC (*CD44*), the RAS oncogene family (*RAB5C*, *RANN*), the TNF-α/NF-κB signaling pathway (e.g., *NR4A2*, *TANK*, *PFKFB3*), and the zinc finger protein family (e.g., *ZNF74*, *ZNF671*, *ZNF106*) were differentially spliced among GC samples with lower and higher risk scores (**Figure 8C**). We performed GO analysis of all differentially spliced genes to explore the role of alternative splicing underlying the RNA processing-related signature. These spliced genes were mainly related to cell–matrix adhesion and mesenchymal cell differentiation for biological process; cell projection membrane and cell–substrate junction for cellular component; and cadherin binding and guanyl nucleotide exchange factor activity for molecular function (**Table S6**). Our analysis indicates that differential ASEs participate in many cancer-related pathways, suggesting that ASEs are a critical mechanism underlying the prognostic value of RNA processing factors in GC.

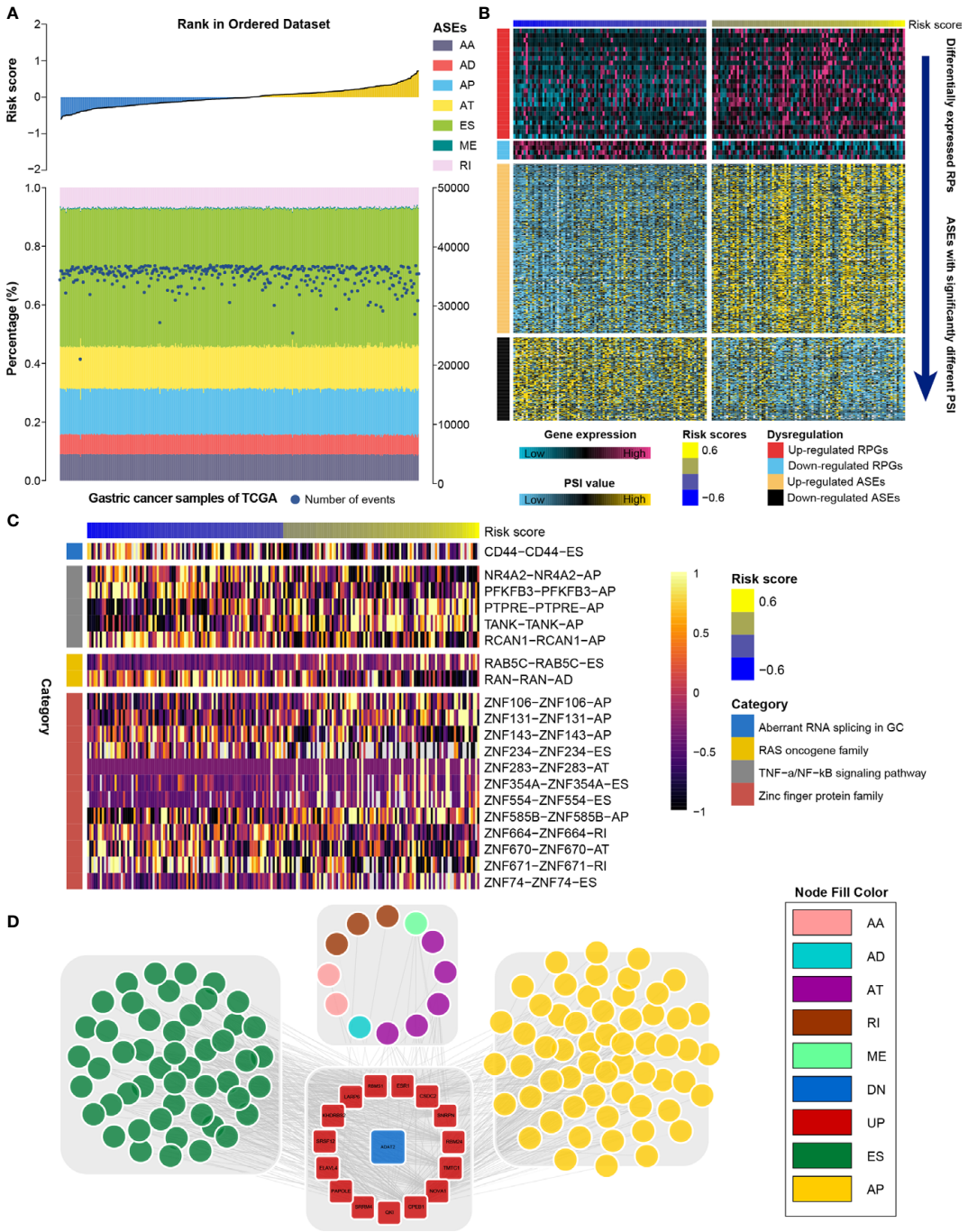

FIGURE 8 | Identification of the RNA splicing landscape underlying the RNA processing-related prognostic signature. **(A)** Proportions of ASEs in 375 TCGA samples sorted by increased risk score. Bars indicate the proportion of each ASE type. Dark blue dots indicate the number of ASEs in each sample. The risk scores in ascending order are shown in the top panel. **(B)** Heatmaps showing the expression levels of RNA processing factors (top panel) and PSI value of ASEs with significant differences between lower-risk and higher-risk groups (bottom panel). **(C)** Representative ASEs with differential PSI values between lower-risk and higher-risk groups. **(D)** Network plot showing the correlation between RNA processing factors and ASEs with significant differences between lower-risk and higher-risk groups.

RNA splicing might inevitably affect their protein characteristics. Therefore, we constructed a protein interaction network based on the spliced genes, presenting the interactive relationship in normal conditions and uncovering the potential influence of ASEs at protein level. After removing the isolated nodes, 228 genes were mapped in the protein interaction network. These spliced genes were closely linked to each other (**Supplementary Figure 6**). From the whole protein interaction

network, we identified six individual modules using the MCODE algorithm (47) (**Supplementary Figure 7**). Module enrichment analysis showed that most modules had biological functions with module specificity (**Supplementary Table 7**).

We explored the potential regulatory network among the significantly altered RNA processing genes and ASEs. A network with 549 pairwise correlations that ultimately involved 16 RNA processing genes and 119 ASEs was constructed (**Figure 8D**). Almost all ASEs followed the same expression trend as the RNA processing genes (**Supplementary Figure 8**). Most RNA processing genes were correlated with more than one ASE, and some played opposite roles in regulating different ASEs (**Figure 8D**). Besides, we found that different RNA processing genes competed for the same ASEs, partly explaining the diversity of splice isoforms created by only a few RNA processing factors.

Drug Response Features Underlying the RNA Processing-Related Signature

Given that genetic variants, pathway activation, immune heterogeneity, and splicing features were significantly different according to the RNA processing-related signature, we investigated the relationship between the prognostic signature and drug response to encourage personalized treatment decisions. As described earlier, the low-risk group presented a significantly higher TMB and neoantigens count than the high-risk group (**Figures 6A, B**), suggesting that the patients with low risk scores might benefit from immune checkpoint inhibitor treatment. Consistent with the idea, the TIDE algorithm determined that patients with low risk scores (45.56%, 246/540) might be more likely to respond to immunotherapy than those with high risk scores (33.58%, 181/539) ($p < 0.001$, odds ratio [OR] = 1.654, 95% CI: 1.284–2.134) (**Figures 9A, C** and **Supplementary Figure 9**).

We used two approaches to identify the drug response relationship between the selected chemotherapeutic agents and the identified signature. The analyses were performed using GDSC, CTRP, and PRISM-derived drug response data. First, differential drug response analysis between the higher-risk (first quartile) and lower-risk (fourth quartile) groups was conducted to identify chemotherapeutic agents with significantly different AUC values ($|\text{mean difference}| > 0.01$, $p < 0.05$). Next, Pearson correlation analysis between the AUC value and the risk score was performed to select agents with a significant correlation coefficient ($|R| > 0.1$, $p < 0.05$). Finally, we determined that patients with low-risk scores were more sensitive to two CTRP-derived compounds (5-fluorouracil and paclitaxel), and patients with high-risk scores were more sensitive to two GDSC-derived compounds (irinotecan and cisplatin) (**Figures 9A, B, D**).

DISCUSSION

In this study, we found that the general expression pattern of RNA processing factors correlates with specific clinical outcomes and hallmark features of GC. RNA processing factors that were significantly associated with the prognosis of patients with GC were also identified. We then constructed a 10-gene RNA processing-related prognostic signature to predict the prognosis of stratified patients with GC. The identified signature was integrated with clinical features to establish the composite prognostic nomogram, which reliably demonstrated accurate prognostic predictions for the patients. Finally, we identified the clinical outcomes, genetic variants, pathway activation, immune heterogeneity, alternative splicing landscape, and drug response features associated with the prognostic signature.

GC is a highly heterogeneous malignant tumor. Some patients with GC within the same TNM stage have differing responses to treatment and prognosis (6). Therefore, further stratification of patients with GC with definite TNM subgroups is urgently needed. RNA plays a crucial role in cell biological functions by passing genetic information from DNA to protein and regulating various biological processes (48). Dysregulation of RNA profiles is closely related to the malignant progression and prognosis of GC. The RNA expression profile and RNA fate are highly dependent on the RNA processing factors responsible for precise temporal and spatial coordinating gene expression (49). Here, we highlight the stratification ability of RNA processing factors in GC.

In the present study, we identified five distinct RNA processing patterns, characterized by different biological behaviors and prognoses (**Figure 1**). We confirmed the prognostic value of a signature built with 10 RNA processing genes in each cohort (**Figure 2** and **Table 1**). The risk score of the RNA processing-related signature was a stable, independent prognosis factor in both the training and validation datasets (**Tables 2**, **3**). Moreover, we established a composite nomogram by integrating the RNA processing-related signature with traditional stratifying factors (age and TNM stage). The composite nomogram showed improved prognostic accuracy, better predictive efficiency, and larger net benefits than the signature alone and the prognostic model of the traditional stratifying factors in each cohort (**Figure 3**). These results indicate that the signature is a powerful tool for predicting the prognosis of patients with GC stratified by TNM classification.

The RNA processing-related signature reflects the expression alterations of genes involved in multiple vital hallmarks in GC. We found that genes that correlated negatively with the signature were significantly enriched in the pathways associated with proliferation and metabolism. In contrast, genes with expression that related positively to the signature's risk score were significantly enriched in the invasion, metastasis, and immune biological processes (**Figure 4**). Among the 10 survival-related genes included in the signature, the risk-associated genes *PWP2* and *TGFB1* have been suggested to be associated with GC invasion and metastasis (50, 51), and *ZBTB7A*, a protection-associated gene, plays a tumor-suppressive role in GC cells (52). *METTL2B* was found to be RNA methyltransferases and play important roles in tumorigenesis (53). *CACTIN* involved in the regulation of innate immune response (54), contributing to the regulation of transcriptional activation of NF-kappa-B target genes in response to endogenous proinflammatory stimuli (55). *TRUB2*

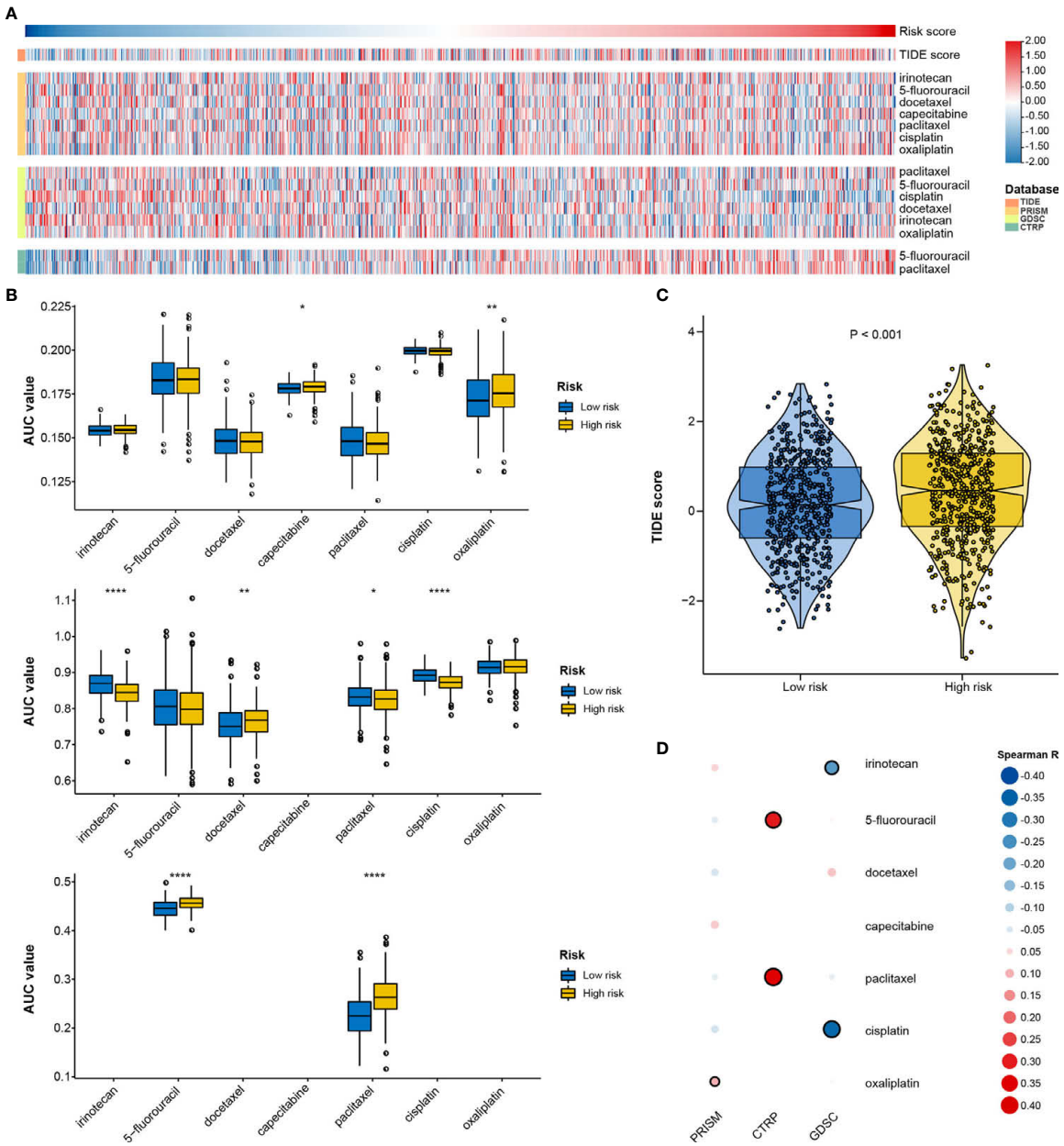

FIGURE 9 | Identification of drug response features underlying the RNA processing-related signature. **(A)** Heatmap showing the TIDE scores and AUC values for patients with GC with different risk scores. **(B)** Differential analysis of the selected chemotherapeutic agents for patients with GC with higher and lower risk scores in the PRISM, CTRP, and GDSC databases. P values were obtained by the Mann-Whitney test. The asterisks represented the statistical P-value (*P < 0.05; **P < 0.01; ****P < 0.001). **(C)** Violin plots of TIDE scores for patients with GC in the high-risk and low-risk groups. **(D)** Heatmap showing the Spearman correlation coefficient between the AUC values and the risk scores for the selected chemotherapeutic agents.

was a component of a functional protein-RNA module, which was required for intra-mitochondrial translation (56). *POLDIP3* was involved in regulation of translation, enhancing translational efficiency of spliced over non-spliced mRNAs (57). *TSEN54* participated the complex process for identification and cleavage of the splice sites in pre-tRNA. *SUGP1* and *RBMS1* were involved in RNA binding, playing a role in pre-mRNA splicing. These outcomes indicate that our study protocol can identify novel carcinogenesis-associated RNA processing genes that might serve as potential therapeutic targets. Future studies of these prognostic factors could identify novel mechanisms underlying RNA processing in GC.

We also determined that genetic variants, immune heterogeneity, and the alternative splicing landscape were also

significantly different between the high-risk and low-risk groups. The low-risk group had significantly higher TMB, more neoantigens, and greater fraction of genome gained than the high-risk group (**Figure 6**). Consistent with the GSEA result, the stromal and immune activation pathways were markedly enriched with increased risk scores (**Figure 4**). The ESTIMATE and MCP-counter algorithms and the pathology whole-slide images also suggested a higher proportion of immune and stromal cells in the high-risk group (**Figure 7**).

Currently, genome-wide analyses have begun to reveal the roles of ASEs correlated with GC progression and prognosis (12, 13). Abnormal ASEs of individual genes participate in several tumorigenic processes, such as proliferation, apoptosis, hypoxia, angiogenesis, immune escape, and metastasis (58, 59). For example, *CD44* splice variants participate in GC carcinogenesis, progression, and metastasis (60, 61). By revealing the ASE landscape in GC, we identified 358 ASEs correlated with GC prognosis. We also observed that *CD44* was differentially spliced in the lower-risk and higher-risk groups (**Figure 8**). Moreover, we identified the potential regulatory network between the altered RNA processing genes and the differential ASEs.

Further, we investigated the relationship between the signature and drug response to promote personalized treatment decisions. To date, immune checkpoint inhibitors have been approved for GC treatment. However, the response rate is relatively low (10–26%) (62–64). Therefore, it is critical to find new biomarkers for appropriate patient selection for immunotherapy. We determined that patients with low risk scores might benefit from immune checkpoint inhibitor treatment (**Figure 9**), suggesting that this RNA processing-related signature could be a predictive biomarker for immunotherapy in GC.

Chemotherapy remains the mainstay in GC treatment (43). We found that patients with low-risk scores might be more sensitive to 5-fluorouracil and paclitaxel, both cell cycle-nonspecific drugs. 5-Fluorouracil is an anti-cancer antimetabolite that inhibits tumor cell proliferation *via* DNA damage. Paclitaxel stabilizes microtubules and interferes with mitotic spindle formation, which leads to the inhibition of cancer cell proliferation. As mentioned above, the proliferation- and metabolism-related pathways were markedly enriched with decreased risk scores. The activation of these pathways, such as G2M checkpoint, DNA repair, and mitotic spindle, might be responsible for the higher sensitivity to 5-fluorouracil and paclitaxel.

On the other hand, patients with high-risk scores might be more sensitive to irinotecan and cisplatin, cell cycle-nonspecific anti-cancer drugs. Such drugs are not affected by the cell cycle phase and act upon rapidly dividing cancer cells for destruction. Therefore, GC characterized with a mesenchymal phenotype might be more sensitive to irinotecan and cisplatin. Whether a genetic variant, pathway activation, immune heterogeneity, splicing features, or chemotherapy and immunochemotherapy response feature, all the results aid understanding of the roles of RNA processing in GC. Our signature may further aid the design of a more reasonable and effective treatment regimen, contributing to precision therapy for individual patients with different risk levels.

This study has several strengths. First, we analyzed a large sample of 1079 patients with GC using either RNA-seq or microarray data, suggesting that our outcomes are likely highly reliable, robust, and independent of specific expression quantitative platforms. Second, the present study includes both our own RNA-seq dataset and public datasets, indicating the possibility of future verification of our risk signature in additional cohorts. Third, we used RMS time to demonstrate the clinical utility of the RNA processing-related signature. It is equivalent to the area under the Kaplan-Meier curve from the beginning of the study through that time point. The RMST difference means gain or loss in the event-free survival time between the groups during this period. As such, using the average survival time can be more easily understood by clinical communities. Meanwhile, RMST difference is valid and interpretable whether or not the proportional hazards assumption is violated (65). Despite these strengths, our study has its limitations as well. First, we used only two clinical characteristics (age and TNM stage) to construct the composite nomogram; additional clinical factors, such as Lauren subtype, microsatellite instability status, chemotherapy, surgery, and radiotherapy information, are warranted to refine the model. Second, further *ex vivo*, *in vitro*, and *in vivo* experiments regarding these prognosis-related RNA processing factors are required to validate our *in silico* results. Finally, the response of immunotherapy and chemotherapy should be further verified by clinical data in other cohorts.

In summary, our study highlights the prognostic value of RNA processing genes in GC and reveal an RNA processing-related prognostic signature for further improving the prognosis prediction of patients with GC with definite TNM subgroups. The clinical outcomes, genetic variants, pathway activation, immune heterogeneity, splicing features, and drug response features underlying the signature were also identified. Our findings provide a basis for understanding the roles of RNA processing and indicate the potential clinical implications of RNA processing factors in GC.

DATA AVAILABILITY STATEMENT

The datasets presented in this study can be found in online repositories. The names of the repository/repositories and accession number(s) can be found in the article/**Supplementary Material**.

ETHICS STATEMENT

The studies involving human participants were reviewed and approved by Institutional Review Board of the Harbin Medical University Cancer Hospital. The patients/participants provided their written informed consent to participate in this study.

AUTHOR CONTRIBUTIONS

SL, FM, and YX contributed to conception and design of the study. SL and FM organized the database. SL performed the statistical

analysis. SL wrote the first draft of the manuscript. SL, FM, XY, YZ and BH wrote sections of the manuscript. All authors contributed to the article and approved the submitted version.

FUNDING

This work was supported by funding from the Project Nn10 of Harbin Medical University Cancer Hospital (Grant Number Nn102017–03).

SUPPLEMENTARY MATERIAL

The Supplementary Material for this article can be found online at: https://www.frontiersin.org/articles/10.3389/fimmu.2021.719628/full#supplementary-material

Supplementary Figure 1 | The workflow of this study.

Supplementary Figure 2 | Identification of the soft threshold according to the standard of the scale-free network. The red line represents the threshold line of 0.85.

Supplementary Figure 3 | Intra-modular analysis for the signature-related modules. The scatterplot showing gene significance vs. module membership in the turquoise **(A)**, yellow **(B)**, and brown **(C)** modules.

Supplementary Figure 4 | The absolute numbers of all ASEs were compared in GC patients with higher-risk (first quartile) and lower-risk (fourth quartile) scores.

Supplementary Figure 5 | The distribution of splicing types for the differential and background ASEs. **(A)** The histogram showing ASE types' frequency for the differential and background ASEs. **(B)** The pie graph showing ASE types' frequency for the differential ASEs. **(C)** The pie graph showing ASE types' frequency for the background ASEs.

Supplementary Figure 6 | The protein interaction network for the spliced genes with significantly different PSI values.

Supplementary Figure 7 | The six individual modules from the protein interaction network determined by the "MCODE" algorithm.

Supplementary Figure 8 | The number of ASEs regulated by the 16 RNA processing factors.

Supplementary Figure 9 | Response rates of immunotherapy between two risk groups determined by the "TIDE" algorithm.

Supplementary Table 1 | 929 genes, annotated as RNA processing factors, acquired in the AmiGO database.

Supplementary Table 2 | 819 RNA processing factors involved in all data sets.

Supplementary Table 3 | 105 OS associated RNA processing factors.

Supplementary Table 4 | Difference of GSVA scores between the high-risk and low-risk groups.

Supplementary Table 5 | 358 differentially expressed ASEs and 28 differentially expressed RNA processing genes.

Supplementary Table 6 | GO analysis was performed for all differentially spliced genes.

Supplementary Table 7 | Module enrichment analysis for the six individual modules.

REFERENCES

1. Bray F, Ferlay J, Soerjomataram I, Siegel RL, Torre LA, Jemal A. Global Cancer Statistics 2018: GLOBOCAN Estimates of Incidence and Mortality Worldwide for 36 Cancers in 185 Countries. *CA Cancer J Clin* (2018) 68 (6):394–424. doi: 10.3322/caac.21492
2. Torre LA, Bray F, Siegel RL, Ferlay J, Lortet-Tieulent J, Jemal A. Global Cancer Statistics, 2012. *CA Cancer J Clin* (2015) 65(2):87–108. doi: 10.3322/caac.21262
3. Dai H, Chen H, Xu J, Zhou J, Shan Z, Yang H, et al. The Ubiquitin Ligase CHIP Modulates Cellular Behaviors of Gastric Cancer Cells by Regulating TRAF2. *Cancer Cell Int* (2019) 19:132. doi: 10.1186/s12935-019-0832-z
4. Katai H, Ishikawa T, Akazawa K, Isobe Y, Miyashiro I, Oda I, et al. Five-Year Survival Analysis of Surgically Resected Gastric Cancer Cases in Japan: A Retrospective Analysis of More Than 100,000 Patients From the Nationwide Registry of the Japanese Gastric Cancer Association (2001-2007). *Gastric Cancer* (2018) 21(1):144–54. doi: 10.1007/s10120-017-0716-7
5. Sasako M, Inoue M, Lin JT, Khor C, Yang HK, Ohtsu A. Gastric Cancer Working Group Report. *Jpn J Clin Oncol* (2010) 40 Suppl 1:i28–37. doi: 10.1093/jjco/hyq124
6. Tang S, Lin L, Cheng J, Zhao J, Xuan Q, Shao J, et al. The Prognostic Value of Preoperative Fibrinogen-to-Prealbumin Ratio and a Novel FFC Score in Patients With Resectable Gastric Cancer. *BMC Cancer* (2020) 20(1):382. doi: 10.1186/s12885-020-06866-6
7. Manning KS, Cooper TA. The Roles of RNA Processing in Translating Genotype to Phenotype. *Nat Rev Mol Cell Biol* (2017) 18(2):102–14. doi: 10.1038/nrm.2016.139
8. Tollervey D, Caceres JF. RNA Processing Marches on. *Cell* (2000) 103(5):703–9. doi: 10.1016/s0092-8674(00)00174-4
9. Obeng EA, Stewart C, Abdel-Wahab O. Altered RNA Processing in Cancer Pathogenesis and Therapy. *Cancer Discov* (2019) 9(11):1493–510. doi: 10.1158/2159-8290.CD-19-0399
10. Lu X, Zhou Y, Meng J, Jiang L, Gao J, Cheng Y, et al. RNA Processing Genes Characterize RNA Splicing and Further Stratify Colorectal Cancer. *Cell Prolif* (2020) 53(3):e12861. doi: 10.1111/cpr.12861
11. Matera AG, Wang Z. A Day in the Life of the Spliceosome. *Nat Rev Mol Cell Biol* (2014) 15(2):108–21. doi: 10.1038/nrm3742
12. Lou S, Zhang J, Zhai Z, Yin X, Wang Y, Fang T, et al. The Landscape of Alternative Splicing Reveals Novel Events Associated With Tumorigenesis and the Immune Microenvironment in Gastric Cancer. *Aging (Albany NY)* (2021) 12(3):4317–34. doi: 10.18632/aging.202393
13. Lou S, Zhang J, Zhai Z, Yin X, Wang Y, Fang T, et al. Development and Validation of an Individual Alternative Splicing Prognostic Signature in Gastric Cancer. *Aging (Albany NY)* (2021) 13(4):5824–44. doi: 10.18632/aging.202507
14. Irizarry RA, Bolstad BM, Collin F, Cope LM, Hobbs B, Speed TP. Summaries of Affymetrix GeneChip Probe Level Data. *Nucleic Acids Res* (2003) 31(4):e15. doi: 10.1093/nar/gng015
15. Gautier L, Cope L, Bolstad BM, Irizarry RA. Affy–Analysis of Affymetrix GeneChip Data at the Probe Level. *Bioinformatics* (2004) 20(3):307–15. doi: 10.1093/bioinformatics/btg405
16. Wagner GP, Kin K, Lynch VJ. Measurement of mRNA Abundance Using RNA-Seq Data: RPKM Measure Is Inconsistent Among Samples. *Theory Biosci* (2012) 131(4):281–5. doi: 10.1007/s12064-012-0162-3
17. Leek JT, Johnson WE, Parker HS, Jaffe AE, Storey JD. The Sva Package for Removing Batch Effects and Other Unwanted Variation in High-Throughput Experiments. *Bioinformatics* (2012) 28(6):882–3. doi: 10.1093/bioinformatics/bts034
18. Durinck S, Moreau Y, Kasprzyk A, Davis S, De Moor B, Brazma A, et al. BioMart and Bioconductor: A Powerful Link Between Biological Databases and Microarray Data Analysis. *Bioinformatics* (2005) 21(16):3439–40. doi: 10.1093/bioinformatics/bti525
19. Carbon S, Ireland A, Mungall CJ, Shu S, Marshall B, Lewis S. AmiGO: Online Access to Ontology and Annotation Data. *Bioinformatics* (2009) 25(2):288–9. doi: 10.1093/bioinformatics/btn615

20. Wilkerson MD, Hayes DN. ConsensusClusterPlus: A Class Discovery Tool With Confidence Assessments and Item Tracking. *Bioinformatics* (2010) 26 (12):1572–3. doi: 10.1093/bioinformatics/btq170
21. Hänzelmann S, Castelo R, Guinney J. GSVA: Gene Set Variation Analysis for Microarray and RNA-Seq Data. *BMC Bioinformatics* (2013) 14:7. doi: 10.1186/1471-2105-14-7
22. Liberzon A, Birger C, Thorvaldsdóttir H, Ghandi M, Mesirov JP, Tamayo P. The Molecular Signatures Database (MSigDB) Hallmark Gene Set Collection. *Cell Syst* (2015) 1(6):417–25. doi: 10.1016/j.cels.2015.12.004
23. Uno H, Claggett B, Tian L, Inoue E, Gallo P, Miyata T, et al. Moving Beyond the Hazard Ratio in Quantifying the Between-Group Difference in Survival Analysis. *J Clin Oncol* (2014) 32(22):2380–5. doi: 10.1200/JCO.2014.55.2208
24. Eng KH, Schiller E, Morrell K. On Representing the Prognostic Value of Continuous Gene Expression Biomarkers With the Restricted Mean Survival Curve. *Oncotarget* (2015) 6(34):36308–18. doi: 10.18632/oncotarget.6121
25. Vickers AJ, Elkin EB. Decision Curve Analysis: A Novel Method for Evaluating Prediction Models. *Med Decis Making* (2006) 26(6):565–74. doi: 10.1177/0272989X06295361
26. Ryan M, Wong WC, Brown R, Akbani R, Su X, Broom B, et al. TCGASpliceSeq a Compendium of Alternative mRNA Splicing in Cancer. *Nucleic Acids Res* (2016) 44(D1):D1018–22. doi: 10.1093/nar/gkv1288
27. Wang ET, Sandberg R, Luo S, Khrebtukova I, Zhang L, Mayr C, et al. Alternative Isoform Regulation in Human Tissue Transcriptomes. *Nature* (2008) 456(7221):470–6. doi: 10.1038/nature07509
28. Szklarczyk D, Gable AL, Lyon D, Junge A, Wyder S, Huerta-Cepas J, et al. STRING V11: Protein-Protein Association Networks With Increased Coverage, Supporting Functional Discovery in Genome-Wide Experimental Datasets. *Nucleic Acids Res* (2019) 47(D1):D607–607D613. doi: 10.1093/nar/gky1131
29. Shannon P, Markiel A, Ozier O, Baliga NS, Wang JT, Ramage D, et al. Cytoscape: A Software Environment for Integrated Models of Biomolecular Interaction Networks. *Genome Res* (2003) 13(11):2498–504. doi: 10.1101/gr.1239303
30. Thul PJ, Lindskog C. The Human Protein Atlas: A Spatial Map of the Human Proteome. *Protein Sci* (2018) 27(1):233–44. doi: 10.1002/pro.3307
31. Subramanian A, Tamayo P, Mootha VK, Mukherjee S, Ebert BL, Gillette MA, et al. Gene Set Enrichment Analysis: A Knowledge-Based Approach for Interpreting Genome-Wide Expression Profiles. *Proc Natl Acad Sci U S A* (2005) 102(43):15545–50. doi: 10.1073/pnas.0506580102
32. Yu G, Wang LG, Han Y, He QY. clusterProfiler: An R Package for Comparing Biological Themes Among Gene Clusters. *OMICS* (2012) 16(5):284–7. doi: 10.1089/omi.2011.0118
33. Shyr C, Tarailo-Graovac M, Gottlieb M, Lee JJ, van Karnebeek C, Wasserman WW. FLAGS, Frequently Mutated Genes in Public Exomes. *BMC Med Genomics* (2014) 7:64. doi: 10.1186/s12920-014-0064-y
34. Mayakonda A, Lin DC, Assenov Y, Plass C, Koeffler HP. Maftools: Efficient and Comprehensive Analysis of Somatic Variants in Cancer. *Genome Res* (2018) 28(11):1747–56. doi: 10.1101/gr.239244.118
35. Yoshihara K, Shahmoradgoli M, Martínez E, Vegesna R, Kim H, Torres-Garcia W, et al. Inferring Tumour Purity and Stromal and Immune Cell Admixture From Expression Data. *Nat Commun* (2013) 4:2612. doi: 10.1038/ncomms3612
36. Becht E, Giraldo NA, Lacroix L, Buttard B, Elarouci N, Petitprez F, et al. Estimating the Population Abundance of Tissue-Infiltrating Immune and Stromal Cell Populations Using Gene Expression. *Genome Biol* (2016) 17 (1):218. doi: 10.1186/s13059-016-1070-5
37. Langfelder P, Horvath S. WGCNA: An R Package for Weighted Correlation Network Analysis. *BMC Bioinformatics* (2008) 9:559. doi: 10.1186/1471-2105-9-559
38. Yang W, Soares J, Greninger P, Edelman EJ, Lightfoot H, Forbes S, et al. Genomics of Drug Sensitivity in Cancer (GDSC): A Resource for Therapeutic Biomarker Discovery in Cancer Cells. *Nucleic Acids Res* (2013) 41(Database issue):D955–61. doi: 10.1093/nar/gks1111
39. Basu A, Bodycombe NE, Cheah JH, Price EV, Liu K, Schaefer GI, et al. An Interactive Resource to Identify Cancer Genetic and Lineage Dependencies Targeted by Small Molecules. *Cell* (2013) 154(5):1151–61. doi: 10.1016/j.cell.2013.08.003
40. Corsello SM, Nagari RT, Spangler RD, Rossen J, Kocak M, Bryan JG, et al. Discovering the Anti-Cancer Potential of Non-Oncology Drugs by Systematic Viability Profiling. *Nat Cancer* (2020) 1(2):235–48. doi: 10.1038/s43018-019-0018-6
41. Geeleher P, Cox N, Huang RS. pRRophetic: An R Package for Prediction of Clinical Chemotherapeutic Response From Tumor Gene Expression Levels. *PloS One* (2014) 9(9):e107468. doi: 10.1371/journal.pone.0107468
42. Geeleher P, Cox NJ, Huang RS. Clinical Drug Response can be Predicted Using Baseline Gene Expression Levels and *In Vitro* Drug Sensitivity in Cell Lines. *Genome Biol* (2014) 15(3):R47. doi: 10.1186/gb-2014-15-3-r47
43. Arai H, Nakajima TE. Recent Developments of Systemic Chemotherapy for Gastric Cancer. *Cancers (Basel)* (2020) 12(5):1100. doi: 10.3390/cancers12051100
44. Jiang P, Gu S, Pan D, Fu J, Sahu A, Hu X, et al. Signatures of T Cell Dysfunction and Exclusion Predict Cancer Immunotherapy Response. *Nat Med* (2018) 24(10):1550–8. doi: 10.1038/s41591-018-0136-1
45. Rooney MS, Shukla SA, Wu CJ, Getz G, Hacohen N. Molecular and Genetic Properties of Tumors Associated With Local Immune Cytolytic Activity. *Cell* (2015) 160(1-2):48–61. doi: 10.1016/j.cell.2014.12.033
46. Saltz J, Gupta R, Hou L, Kurc T, Singh P, Nguyen V, et al. Spatial Organization and Molecular Correlation of Tumor-Infiltrating Lymphocytes Using Deep Learning on Pathology Images. *Cell Rep* (2018) 23(1):181–93.e7. doi: 10.1016/j.celrep.2018.03.086
47. Bader GD, Hogue CW. An Automated Method for Finding Molecular Complexes in Large Protein Interaction Networks. *BMC Bioinformatics* (2003) 4:2. doi: 10.1186/1471-2105-4-2
48. Fu Y, Dominissini D, Rechavi G, He C. Gene Expression Regulation Mediated Through Reversible M^6A RNA Methylation. *Nat Rev Genet* (2014) 15(5):293–306. doi: 10.1038/nrg3724
49. Coppin L, Leclerc J, Vincent A, Porchet N, Pigny P. Messenger RNA Life-Cycle in Cancer Cells: Emerging Role of Conventional and Non-Conventional RNA-Binding Proteins. *Int J Mol Sci* (2018) 19(3):650. doi: 10.3390/ijms19030650
50. Maehara Y, Kakeji Y, Kabashima A, Emi Y, Watanabe A, Akazawa K, et al. Role of Transforming Growth Factor-Beta 1 in Invasion and Metastasis in Gastric Carcinoma. *J Clin Oncol* (1999) 17(2):607–14. doi: 10.1200/JCO.1999.17.2.607
51. Zhou W, Li J, Lu X, Liu F, An T, Xiao X, et al. Derivation and Validation of A Prognostic Model for Cancer Dependency Genes Based on CRISPR-Cas9 in Gastric Adenocarcinoma. *Front Oncol* (2021) 11:617289. doi: 10.3389/fonc.2021.617289
52. Sun G, Peng B, Xie Q, Ruan J, Liang X. Upregulation of ZBTB7A Exhibits a Tumor Suppressive Role in Gastric Cancer Cells. *Mol Med Rep* (2018) 17 (2):2635–41. doi: 10.3892/mmr.2017.8104
53. Liu D, Li W, Zhong F, Yin J, Zhou W, Li S, et al. METTL7B Is Required for Cancer Cell Proliferation and Tumorigenesis in Non-Small Cell Lung Cancer. *Front Pharmacol* (2020) 11:178. doi: 10.3389/fphar.2020.00178
54. Atzei P, Gargan S, Curran N, Moynagh PN. Cactin Targets the MHC Class III Protein IkappaB-Like (IkappaBL) and Inhibits NF-kappaB and Interferon-Regulatory Factor Signaling Pathways. *J Biol Chem* (2010) 285(47):36804–17. doi: 10.1074/jbc.M110.139113
55. Suzuki M, Watanabe M, Nakamaru Y, Takagi D, Takahashi H, Fukuda S, et al. TRIM39 Negatively Regulates the NFκB-Mediated Signaling Pathway Through Stabilization of Cactin. *Cell Mol Life Sci* (2016) 73(5):1085–101. doi: 10.1007/s00018-015-2040-x
56. Arroyo JD, Jourdain AA, Calvo SE, Ballarano CA, Doench JG, Root DE, et al. A Genome-Wide CRISPR Death Screen Identifies Genes Essential for Oxidative Phosphorylation. *Cell Metab* (2016) 24(6):875–85. doi: 10.1016/j.cmet.2016.08.017
57. Liu L, Rodriguez-Belmonte EM, Mazloum N, Xie B, Lee MY. Identification of a Novel Protein, PDIP38, That Interacts With the P50 Subunit of DNA Polymerase Delta and Proliferating Cell Nuclear Antigen. *J Biol Chem* (2003) 278(12):10041–7. doi: 10.1074/jbc.M208694200
58. Oltean S, Bates DO. Hallmarks of Alternative Splicing in Cancer. *Oncogene* (2014) 33(46):5311–8. doi: 10.1038/onc.2013.533
59. Climente-González H, Porta-Pardo E, Godzik A, Eyras E. The Functional Impact of Alternative Splicing in Cancer. *Cell Rep* (2017) 20(9):2215–26. doi: 10.1016/j.celrep.2017.08.012
60. Chen XY, Wang ZC, Li H, Cheng XX, Sun Y, Wang XW, et al. Nuclear Translocations of Beta-Catenin and TCF4 in Gastric Cancers Correlate With

Lymph Node Metastasis But Probably Not With CD44 Expression. *Hum Pathol* (2005) 36(12):1294–301. doi: 10.1016/j.humpath.2005.09.003
61. Peng WZ, Liu JX, Li CF, Ma R, Jie JZ. hnRNPK Promotes Gastric Tumorigenesis Through Regulating CD44E Alternative Splicing. *Cancer Cell Int* (2019) 19:335. doi: 10.1186/s12935-019-1020-x
62. Muro K, Chung HC, Shankaran V, Geva R, Catenacci D, Gupta S, et al. Pembrolizumab for Patients With PD-L1-Positive Advanced Gastric Cancer (KEYNOTE-012): A Multicentre, Open-Label, Phase 1b Trial. *Lancet Oncol* (2016) 17(6):717–26. doi: 10.1016/S1470-2045(16)00175-3
63. Kang YK, Boku N, Satoh T, Ryu MH, Chao Y, Kato K, et al. Nivolumab in Patients With Advanced Gastric or Gastro-Oesophageal Junction Cancer Refractory to, or Intolerant of, at Least Two Previous Chemotherapy Regimens (ONO-4538-12, ATTRACTION-2): A Randomised, Double-Blind, Placebo-Controlled, Phase 3 Trial. *Lancet* (2017) 390(10111):2461–71. doi: 10.1016/S0140-6736(17)31827-5
64. Fuchs CS, Doi T, Jang RW, Muro K, Satoh T, Machado M, et al. Safety and Efficacy of Pembrolizumab Monotherapy in Patients With Previously Treated Advanced Gastric and Gastroesophageal Junction Cancer: Phase 2 Clinical KEYNOTE-059 Trial. *JAMA Oncol* (2018) 4(5):e180013. doi: 10.1001/jamaoncol.2018.0013
65. Royston P, Parmar MK. Restricted Mean Survival Time: An Alternative to the Hazard Ratio for the Design and Analysis of Randomized Trials With a Time-to-Event Outcome. *BMC Med Res Methodol* (2013) 13:152. doi: 10.1186/1471-2288-13-152

Conflict of Interest: The authors declare that the research was conducted in the absence of any commercial or financial relationships that could be construed as a potential conflict of interest.

Publisher's Note: All claims expressed in this article are solely those of the authors and do not necessarily represent those of their affiliated organizations, or those of the publisher, the editors and the reviewers. Any product that may be evaluated in this article, or claim that may be made by its manufacturer, is not guaranteed or endorsed by the publisher.

frontiers in Immunology

ORIGINAL RESEARCH
published: 13 August 2021
doi: 10.3389/fimmu.2021.739605

Prednisone Reprograms the Transcriptional Immune Cell Landscape in CNS Autoimmune Disease

He Li[1†], Yuehan Gao[1†], Lihui Xie[1†], Rong Wang[1†], Runping Duan[1†], Zhaohuai Li[1†], Binyao Chen[1], Lei Zhu[1], Xianggui Wang[2,3] and Wenru Su[1*]*

[1] State Key Laboratory of Ophthalmology, Zhongshan Ophthalmic Center, Sun Yat-sen University, Guangzhou, China, [2] Eye Center of Xiangya Hospital, Central South University, Changsha, China, [3] Hunan Key Laboratory of Ophthalmology, Xiangya Hospital, Central South University, Changsha, China

OPEN ACCESS

Edited by:
Mingzhu Yin,
Central South University, China

Reviewed by:
Hai-Feng Pan,
Anhui Medical University, China
Liwei Lu,
The University of Hong Kong, Hong Kong, SAR China

***Correspondence:**
Wenru Su
suwr3@mail.sysu.edu.cn
Xianggui Wang
wangxg@csu.edu.cn

[†]These authors have contributed equally to this work

Specialty section:
This article was submitted to Cancer Immunity and Immunotherapy, a section of the journal Frontiers in Immunology

Received: *11 July 2021*
Accepted: *29 July 2021*
Published: *13 August 2021*

Citation:
Li H, Gao Y, Xie L, Wang R, Duan R, Li Z, Chen B, Zhu L, Wang X and Su W (2021) Prednisone Reprograms the Transcriptional Immune Cell Landscape in CNS Autoimmune Disease. Front. Immunol. 12:739605. doi: 10.3389/fimmu.2021.739605

Glucocorticoids (GCs) are widely used immunosuppressive drugs for autoimmune diseases, although considerable gaps exist between current knowledge of the mechanisms of GCs and their conclusive immune-regulatory effects. Here we generated a single-cell transcriptional immune cell atlas based on prednisone-treated or untreated experimental autoimmune uveitis (EAU) mice. Immune cells were globally activated in EAU, and prednisone partially reversed this effect in terms of cell composition, gene expression, transcription factor regulation, and cell-cell communication. Prednisone exerted considerable rescue effects on T and B cells and increased the proportion of neutrophils. Besides commonly regulated transcriptional factors (Fosb, Jun, Jund), several genes were only regulated in certain cell types (e.g. Cxcr4 and Bhlhe40 in T cells), suggesting cell-type-dependent immunosuppressive properties of GC. These findings provide new insights into the mechanisms behind the properties and cell-specific effects of GCs and can potentially benefit immunoregulatory therapy development.

Keywords: prednisone, glucocorticoids, autoimmune uveitis, single-cell RNA sequencing, CNS autoimmune diseases

INTRODUCTION

Despite the expansion of novel immunosuppressants in the recent decades, glucocorticoids (GCs) remain the most widely used anti-inflammatory and immunosuppressive agents in clinical medicine. They are indispensable for achieving rapid disease control, especially of severe autoimmune diseases (1–4). However, the use of GCs is mostly based on historical experiences and knowledge from case series. For decades, the clinical application of GCs has exceeded our current knowledge of their immunosuppressive effects. Thus, there is an urgent need for research on the regulatory properties of GCs and their effects on the immune system.

Cytosolic GC receptors serve as the main mediators of the immunosuppressive and anti-inflammatory effects of GCs (5). Upon GC binding, they translocate into the nucleus, activate the

expression of anti-inflammatory proteins, and inhibit the production of pro-inflammatory proteins (2). Recent studies have also indicated other potential pathways associated with GCs, such as the regulatory properties of GC receptors without GC binding and even the receptor-independent effects of GCs (2, 6). Moreover, growing evidence suggests that the underlying mechanisms of GCs are cell type-dependent (7, 8). Due to this complexity, it is necessary to comprehensively depict the effects of GCs on the immune system from multiple perspectives and characterize the transcriptional modifications across different immune cell subpopulations.

Autoimmune diseases mainly affecting the central nervous system (CNS) include multiple types of diseases and affect millions of people (9). These diseases usually involve responses to self-antigen exposure and aberrant activation of the immune system. They are also chronic, painful, debilitating, and potentially life-threatening, thereby significantly affecting the quality of life. Among them, autoimmune uveitis, which mainly affects the vascular organs of the eye (iris, ciliary body, and choroid), is considered one of the principal causes of preventable blindness worldwide (10). It not only presents as an isolated entity or a part of a systemic autoimmune disease affecting CNS, but also allows direct observation of the inflammatory condition of the central nervous system, serving as a satisfactory model for CNS autoimmune disease studies. Moreover, GCs serve as the first-line systemic treatment for patients with sight-threatening uveitis, despite the lack of a comprehensive and in-depth understanding of their immunosuppressive properties (4, 10, 11).

To explore the effect of GCs on the immune system in the context of CNS autoimmune states, we developed experimental autoimmune uveitis (EAU) mouse models and performed single-cell profiling of the lymph node transcriptome (12, 13). We analyzed approximately 35,000 single cells of lymph nodes sampled from normal and EAU mice without additional treatment or prednisone. We investigated the effects of EAU and prednisone on the mouse immune system in the context of cell type composition, cell type-specific gene expression, transcription factor (TF) regulation, and intercellular communication. These showed widespread alterations in EAU, most strongly affecting CD4+ T cells. Interestingly, prednisone partly countered such alterations. Our results not only support the well-established participation of T cells and monocytes/macrophages in the onset of uveitis and effects of prednisone, but also comprehensively reveal the transcriptional modifications of the immune cell subsets at the single-cell level.

MATERIALS AND METHODS

EAU Model Induction and EAU Clinical Score

To induce EAU, the mice were injected subcutaneously with an emulsion, consisting of 2 mg/mL of human IRBP1-20 (GPTHLFQPSLVLDMAKVLLD, GiL Biochem, Shanghai, China) and complete Freund's adjuvant (BD Difco, San Jose, CA, USA) containing 2.5 mg of Mycobacterium tuberculosis strain H37Ra (BD Difco, San Jose, CA, USA) in a 1:1 volume ratio, were injected to mice (13). Additionally, 0.25 μg pertussis toxin (List Biological Laboratories, Campbell, California, USA) was dissolved in PBS, and injected on the same day and 2 days after immunization.

Funduscopic examination of EAU progress with the Micron IV fundus camera (Phoenix Co., Campbell, CA, USA) was performed, and the clinical findings were graded from 0 to 4 scoring based on observable infiltration and vasculitis in the retina (14). The clinical score was assessed in a blinded manner as followed: 0: Normal retina; 0.5/trace: minimal vasculitis; 1: Mild vasculitis; multiple, peripheral, and focal lesions; 2: Severe vasculitis (large size, thick wall, infiltrations); diffuse chorioretinal lesions and/or infiltrations; linear lesions; 3: Pattern of linear lesions; large confluent chorioretinal lesions; subretinal hemorrhages; 4: Large retinal detachment.

Treatment of Mice

Prednisone (Selleck Chemicals, Houston, TX, USA) was dissolved in DMSO (0.1%, Sigma). Mice with EAU induction were orally administered with prednisone (10 mg/kg/day) or vehicle control (0.1% DMSO) for 2 weeks after immunization (15). Each groups included six mice.

Lymph Node Collection and Single-Cell Suspension Preparation

Cervical dLNs isolated from the neck of mice were isolated into single cells by filtration through a with 20-μm strainer (352235, Falcon). After washing twice with PBS, the cells viability analyzed by Trypan blue in each sample exceeded 85%.

Flow Cytometric Analysis

After staining with live/dead dye (Thermo Fisher Scientific, Waltham, MA, USA), the cells were stained with surface markers: anti-mouse CD4 (GK1.5, catalog 100434, BioLegend), anti-mouse CD138 (Syndecan-1) (clone 281-2), anti-mouse CXCR5 (clone L138D7), anti-mouse PD-1 (clone 29F.1A12), anti-mouse CD90.2 (Thy-1.2) (clone 53-2.1), anti-human/mouse CD45R (B220) (clone RA3-6B2), anti-mouse F4/80 (clone BM8), anti-mouse CD11c (clone HL3) and analyzed *via* flow cytometry (BD LSRFortessa). After stimulation of 5 ng/ml phorbol myristate acetate (Sigma), 1 μg/ml brefeldin A (Sigma), and 0.5 mg/ml ionomycin (Sigma) at 37°C for 4 hours, and then fixation for 30 minutes and permeabilization for 1 hour at room temperature, the cells were stained with intracellular antibodies for 4°C overnight: anti-mouse IL-17A (TC11-18H10.1, catalog 506930, BioLegend), anti-mouse IFN-γ (XMG1.2, catalog 505808, BioLegend). The results were evaluated with FlowJo software (version 10.0.7, Tree Star, Ashland, OR, USA).

Single-Cell RNA Sequencing

We mix cells from cervical lymph nodes which from three group (normal, EAU treated with vehicle and EAU treated with prednisone) and each group includes three mice. After that,

three mix samples respectively from three groups are used to be sequenced. Before sequencing, we did not select immune cells *via* flow cytometry.

scRNA-Seq Data Processing

We used the Chromium Single Cell 5′ Library (10× Genomics chromium platform; Illumina NovaSeq 6000), Gel Bead and Multiplex Kit, and Chip Kit to acquire barcoded scRNA-seq libraries. Preparation of single-cell RNA libraries were performed with the Chromium Single Cell 5′ v2 Reagent (10× Genomics, 120237) kit. The quality of the libraries was tested with FastQC software. Demultiplexing and barcoding of the sequences from the 10× Genomics scRNA-seq platform alignment to the mm10 reference and quantification of sequencing reads for each sample were performed using CellRanger (Version 4.0.2, 10× Genomics) with default parameters.

scRNA-Seq Quality Control

For quality control, the Seurat package (version 3.1, https://github.com/satijalab/seurat) was used. Cells were filtered out if they showed greater than 15% of mitochondrial genes and fewer than 300 or greater than 10,000 detected genes. Genes not detected is also not include in analysis.

scRNA-Seq Analysis

For the scRNA-seq data analysis, we used Seurat package for normalization, dimensionality reduction, clustering as well as DEG analysis. We log-normalized the data with the 'NormalizeData()' before clustering and reduction and scaled the data with the top 2000 most variable genes by using the 'FindVariableFeatures()' script. The clustering and dimensionality method were used with the 'FindClusters()' at an appropriate resolution to identify significant clusters, which uses a shared nearest neighbor parameter optimized for each combined dataset modularity optimization-based clustering algorithm. 2-t-SNE clustering was performed using the 'RunTSNE()' function. DEGs were determined using the 'FindAllMarkers()' function. A disease-related DEG dataset was established (p value < 0.05, |Log2 fold-change| > 0.25).

GO Analysis

All GO enrichment analysis was performed using Metascape (www.metascape.org) (78) to visualize functional patterns in the gene clusters. Statistical analysis was used for GO and pathway enrichment analyses of the DEGs.

Transcription Factor-Target Gene Network Analysis

Based on the gene regulation identified in our scRNA-seq data, we utilized the GENIC3 R packages (version 1.6.0) (16), as well as the RcisTarget database (version 1.4.0) (17) of the SCENIC (version 1.1.2.2) (18) workflow to predict the transcription factor and their downstream genes. We used GENIE3 to computerize the genetic regulatory networks from our expression data, including EAU DEGs, prednisone DEGs or rescue DEGs, for each cell type. We further used RcisTarget databases to recognize the enriched transcription factor-binding motifs and those potential downstream genes (regulons). Figures showed the transcription factor targets with high-confidence annotation, with the Cytoscape software (version 3.7.1) (19).

Cell-Cell Communication Analysis

The intercellular communication was predicted with CellPhoneDB software (version 1.1.0) (www.cellphonedb.org) (20). We selected and analyzed the ligand-receptor pairs expressed in at least 10% of cells of a given type. The interaction was considered nonexistent if either the ligand or the receptor was undetectable. We compared the average expression of ligand-receptor pairs in different cell types, and selected pairs with $p < 0.05$ for further computerization of intercellular communication.

Statistical Analysis

GraphPad Prism Software was used to data analysis. The values are represented as the mean ± SD. Statistical analysis was performed using an unpaired, two-tailed Student's t-test or one-way ANOVA. p values above 0.05 were considered as not significant, NS; *, $p < 0.05$; **, $p < 0.01$; ***, $p < 0.001$; and ****, $p < 0.0001$.

RESULTS

Construction of Lymph Node Single-Cell Atlases of Normal and EAU mice

We first developed EAU mouse models by immunizing mice with the retinal protein interphotoreceptor retinoid-binding protein, and prepared non-treated mice as normal controls (see *Methods*). The EAU mice were evenly matched and randomized into two groups: (1) EAU group with no additional treatment and (2) prednisone group treated with prednisone (**Figure 1A**). After 14 days, the clinical scores of EAU mice were significantly increased compared to those of normal controls, indicating the onset of autoimmune uveitis in the mouse models (**Figure 1B**). In contrast, prednisone significantly reduced the inflammatory symptoms of EAU, as revealed by fundus photography and the clinical scores (**Figure 1B**).

To explore the underlying mechanisms of action of prednisone and the transcriptomes of lymph nodes of EAU mice, we generated single-cell RNA transcriptional profiles of immune cells from normal, EAU, and prednisone-treated EAU mice by isolating the lymph nodes of these mice and performing single-cell RNA sequencing. After the quality control process, we acquired 35000 high-quality immune cells for further analysis (see *Methods*) (**Figure 1C**). Then, we processed the sequencing data through integration, normalization, and clustering. We first identified six major cell types: (1) T cells, (2) B cells, (3) monocytes and conventional dendritic cells (cDCs), (4) macrophages, (5) neutrophils, and (6) plasmacytoid dendritic cells (pDCs), based on their corresponding marker genes (**Figures 1D, E** and **Supplementary Figure 1A**). We further differentiated cDCs and monocytes based on the expressions of *Ly6c2*, *Ccr2*, *Ccl22*, and *Fscn1* (**Supplementary Figures 1B, C**).

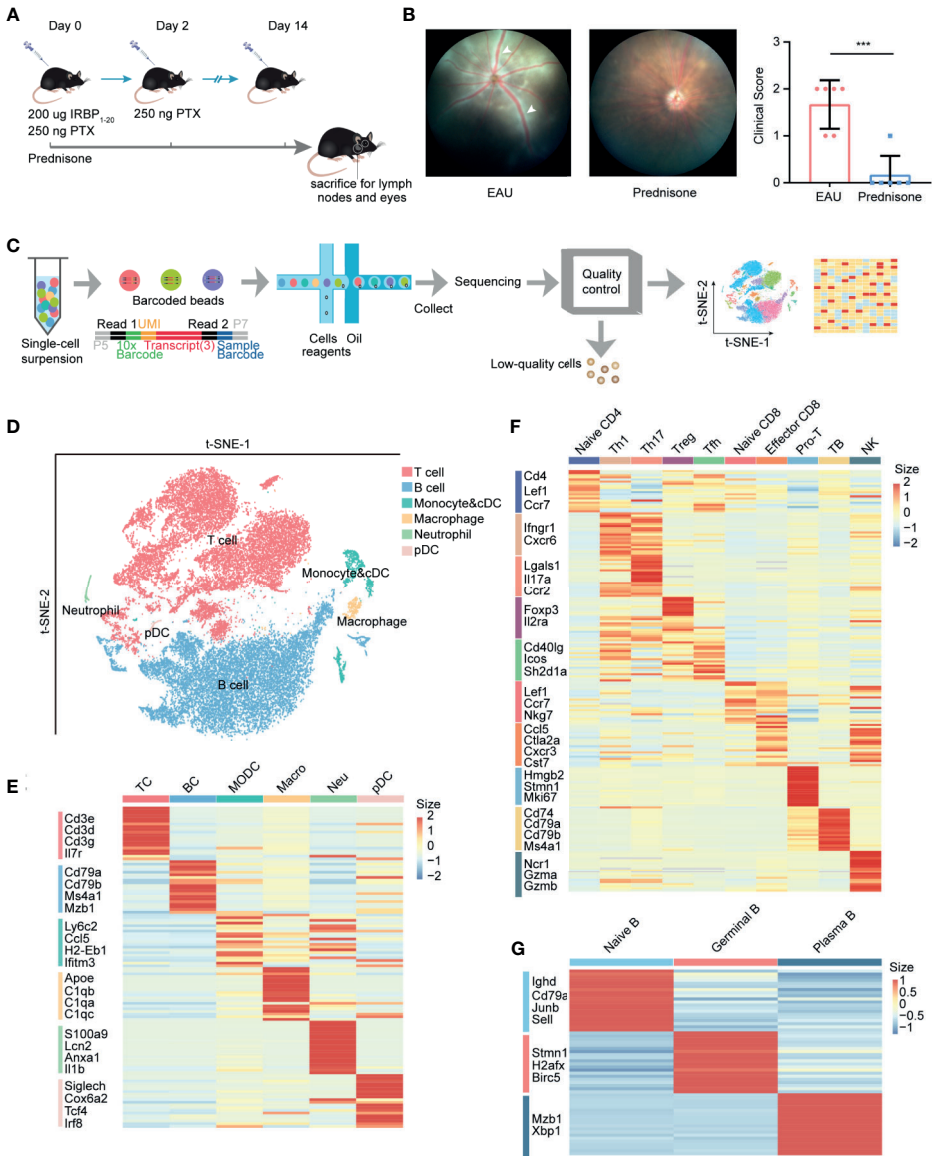

FIGURE 1 | study design and unbiased classification of immune cells by scRNA-seq. **(A)** research design. Cervical lymph nodes of EAU mice, prednisone-treated EAU mice, and normal subjects were studied. Cervical lymph nodes cells which from three group (normal, EAU treated with vehicle and EAU treated with prednisone) and each group includes three mice, were mixed. Three mix samples respectively from three groups are used to be sequenced without selection of immune cells *via* flow cytometry. IRBP, interphotoreceptor retinoid-binding protein. PTX, pertussis toxin. **(B)** Left: fundus photography of EAU and prednisone-treated EAU mice. Right: the clinical scores of EAU or prednisone-treated mice. Each group contains six mice. White Arrows indicate inflammatory exudation and vascular deformation. The P-values are exact two-sided generated by students' t test. ***$p < 0.001$. **(C)** Flowchart of the scRNA-seq process. **(D)** t-SNE embedding shows different cell types in lymph nodes. **(E)** Heatmap of marker genes for each type of cells. **(F)** Heatmap of marker genes for subtypes of T cells. **(G)** Heatmap of marker genes for subtypes of B cells.

To analyze T cell subsets in detail, T cells were subdivided into nine subsets with distinct properties (**Figure 1F** and **Supplementary Figures 2A, B**). The Th1 and Tfh clusters were further re-clustered based on the expressions of *Cxcr6* and *Tcf7* (**Supplementary Figures 2C–E**). Additionally, B cells were subdivided into three subpopulations: (1) naïve B cells, (2) germinal B cells, and (3) plasma B cells (**Figure 1G** and **Supplementary Figures 1D, E**).

Taken together, we constructed an integrative transcriptional atlas containing multiple immune cell subpopulations and established a cellular profile to further understand the effects of EAU and prednisone on the immune system.

Prednisone Affects Cell Type Composition

To depict the alterations in cell type composition in EAU and due to prednisone treatment, we investigated the changes in cell

type proportions in healthy, EAU, and prednisone-treated EAU mice (**Figure 2A**). In EAU mice, the proportions of Th1, Th17, Tfh, and proliferating T cells were increased, while the proportions of Treg cells and two CD8+T cell subsets were reduced (**Figure 2A**). B cell subsets were assumed to participate in disease progression, since the proportions of germinal and plasma B cells were also increased in EAU mice (**Figure 2A**). The proportions of myeloid leukocytes, including monocytes, pDCs, macrophages, and neutrophils, were also higher in EAU mice than in normal controls.

In the prednisone group, we observed widespread rescue effects of prednisone on nearly all immune cell types, especially

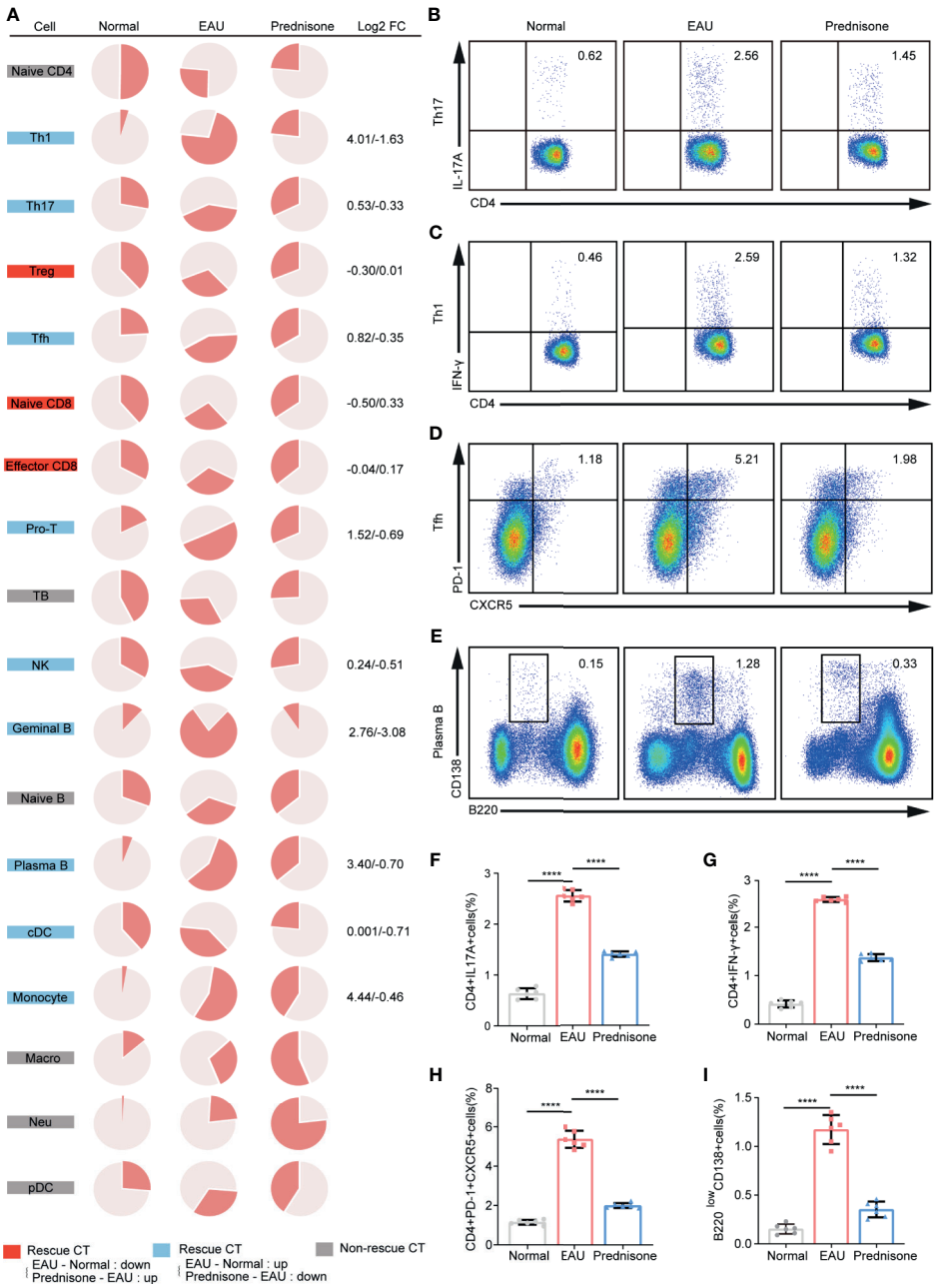

FIGURE 2 | The proportions of immune cells of EAU and prednisone-treated mice. **(A)** Pie charts of proportions of each type of cells in three group. The Log2FC values of the proportion were shown on the right. Normal, normal subject; EAU, experimental autoimmune uveitis mouse group; Prednisone, prednisone-treated mouse group. **(B–E)** Flow cytometry indicates the proportion of Th17 **(B)**, Th1 **(C)**, Tfh **(D)** and plasma B cells **(E)**, which was performed once with a cohort of 6 mice. **(F–I)** Bar plots show the proportions of Th17 **(F)**, Th1 **(G)**, Tfh **(H)** and plasma B cells **(I)** in normal controls, EAU mice treated with vehicle, and prednisone-treated EAU mice. Each group contains six mice. The P-values are exact two-sided generated by students' t test. ****$p < 0.0001$.

the lymphocyte subpopulations (**Figure 2A**). These rescue effects were highly evident among CD4+T cells, particularly Th1, Th17, and Tfh cells, indicating that prednisone may inhibit the differentiation of Th1, Th17, and Tfh cells (**Figure 2A**). Furthermore, we validated the changes in the proportions of these three cell types using flow cytometry (**Figures 2B–D**). We observed profound rescue effects of prednisone on Th1, Th17, and Tfh cells, consistent with the previous findings (**Figures 2F–H**). The alterations in the proportions of germinal and plasma B cells were reversed using prednisone treatment, suggesting that prednisone influences both humoral and cellular immunity to achieve its clinical benefit (**Figure 2A**). The proportion of plasma B cells was further validated using flow cytometry (**Figures 2E, I**).

Prednisone Reverses EAU-Associated Gene Expression Alteration in Lymph Nodes

To delineate the transcriptional changes caused by EAU and prednisone, we identified differentially expressed genes (DEGs) between normal and EAU mice (EAU DEGs) and between EAU and prednisone-treated EAU mice (prednisone DEGs) (**Figure 3A**). Based on these genes, we further distinguished "rescue DEGs", which refer to EAU DEGs that exhibited opposite regulatory tendencies after prednisone treatment (**Figure 3A**). We found that prednisone exerted considerable influence on the immune system of EAU mice, with 46 out of 139 upregulated EAU DEGs and 7 out of 62 downregulated EAU DEGs rescued by prednisone (**Figure 3A**).

To characterize the cell type-specific gene regulation profiles, we attributed EAU and rescue DEGs to eight major cell types: (1) T cells, (2) B cells, (3) natural killer (NK) cells, (4) monocytes, (5) cDCs, (6) pDCs, (7) macrophages, and (8) neutrophils (**Figure 3B**). T and B cells were the most strongly affected subsets based on their high rescue DEGs-to-EAU DEGs ratios (**Figure 3B**). Macrophages, pDCs, and NK cells, which may also serve as targets of prednisone, exhibited slightly smaller rescue DEGs-to-EAU DEGs ratios compared to those of T and B cells (**Figure 3B**).

To further explore the possible mechanisms of the immunosuppressive properties of prednisone, we analyzed the commonly and specifically rescued genes in the eight cell types, as shown in the Venn diagram (**Figure 3C**). The most commonly rescued genes were those that encode activator protein 1 (AP-1) transcription factor components, including *Fosb* (freq = 5), *Fos* (freq = 2), *Jun* (freq = 4), and *Jund* (freq = 4), and heat shock protein components, particularly *Hsp90aa1* (freq = 4) (**Figure 3C** and **Supplementary Figure 4A**). Glucocorticoids have been reported to downregulate the expression of several AP-1 components and reduce the DNA-binding ability of the AP-1 components to their cognate DNA motifs (1). Overall, these factors may play central roles in the immunosuppressive properties of prednisone to inhibit highly pro-inflammatory transcriptional signatures across different immune cell subsets in EAU.

In addition to widely regulated genes, we identified genes that were specifically rescued in different cell subsets. We found that *Cxcr4*, which plays a central role in cell homing and retention, was rescued in both T and B cells (21, 22). *Hif1a* was specifically rescued in T cells, while several *Ighg* family members were rescued in B cells. As for the genes in the non-lymphoid cells, both *Cxcl2* (rescued in monocytes and neutrophils) and *Cxcl10* (rescued only in monocytes) possibly contributed to the progression of uveitis by recruiting T cells and DCs (**Figure 3C**). Interestingly, in macrophages, we identified a specifically rescued gene, *Irgm1*, which is an important molecular regulator that promotes the disruption of the blood-brain barrier to initiate inflammation (23) (**Figure 3C**).

To better understand the effects of EAU and prednisone in the context of potential cellular functions, we performed Gene Ontology (GO) analysis on EAU, prednisone, and rescue DEGs in different cell subsets (**Figures 3D–F** and **Supplementary Figures 3A–D**). In EAU, T cells and monocytes exhibited significant alterations towards the "activation" side (**Supplementary Figure 3A**). Moreover, cDCs and B cells may participate in several immune processes in EAU, as they showed upregulated expressions of genes involved in inflammation, cytokine production, antigen presentation, and cell proliferation (**Supplementary Figure 3A**). Upon prednisone treatment, the activation of T cells and monocytes was robustly suppressed, with enrichment in "regulation of cytokine production" and "lymphocyte activation" (in T cells), as well as "myeloid leukocyte migration", "leukocyte chemotaxis" and "inflammatory response" (in monocytes) (**Supplementary Figure 3B**).

Regarding the rescue effect of prednisone on T cells, we identified categories closely associated with Th17, including "IL-17 signaling pathway", "Th17 cell differentiation", "proinflammatory lymphocyte activation", and "inflammatory response" (**Figure 3D**). We not only identified these categories, which were globally rescued in CD4+ and CD8+ T cells, but also found specifically rescued categories in CD4+ T cells, including "apoptotic signaling pathway" and "HSP90 chaperone cycle for steroid hormone receptors" (**Supplementary Figure 3C**). More specifically, the category "IL-17 signaling pathway" was rescued in Th17 cells, while "MAPK signaling pathway" and "inflammatory response" were rescued in Tfh cells (**Supplementary Figure 3D**). The rescued effect of prednisone on B cells was associated with "humoral immune response", "B cell-mediated immunity" and "regulation of B cell activation" (**Figure 3E**). In addition, the rescued DEG of myeloid leukocytes showed functional enrichment of "inflammatory response" (monocytes), "regulation of cell activation" (macrophages), "antigen processing and presentation" (pDC), and "cell killing" (NK cells) (**Figure 3F**).

EAU and Prednisone Affect Cell Type-Specific Gene Expression

To accurately explore the cell type-specific EAU, prednisone, and rescue DEGs, we further classified the DEGs into subpopulations defined in each cell type, generating gene regulatory networks across 18 types of immune cells. In **Figure 4A**, the sizes of the subpopulation circles suggest that both EAU and prednisone exhibit cell type-specific gene regulation effects.

In EAU, gene expression in plasma B cells was most strongly affected, suggesting the spontaneous production of

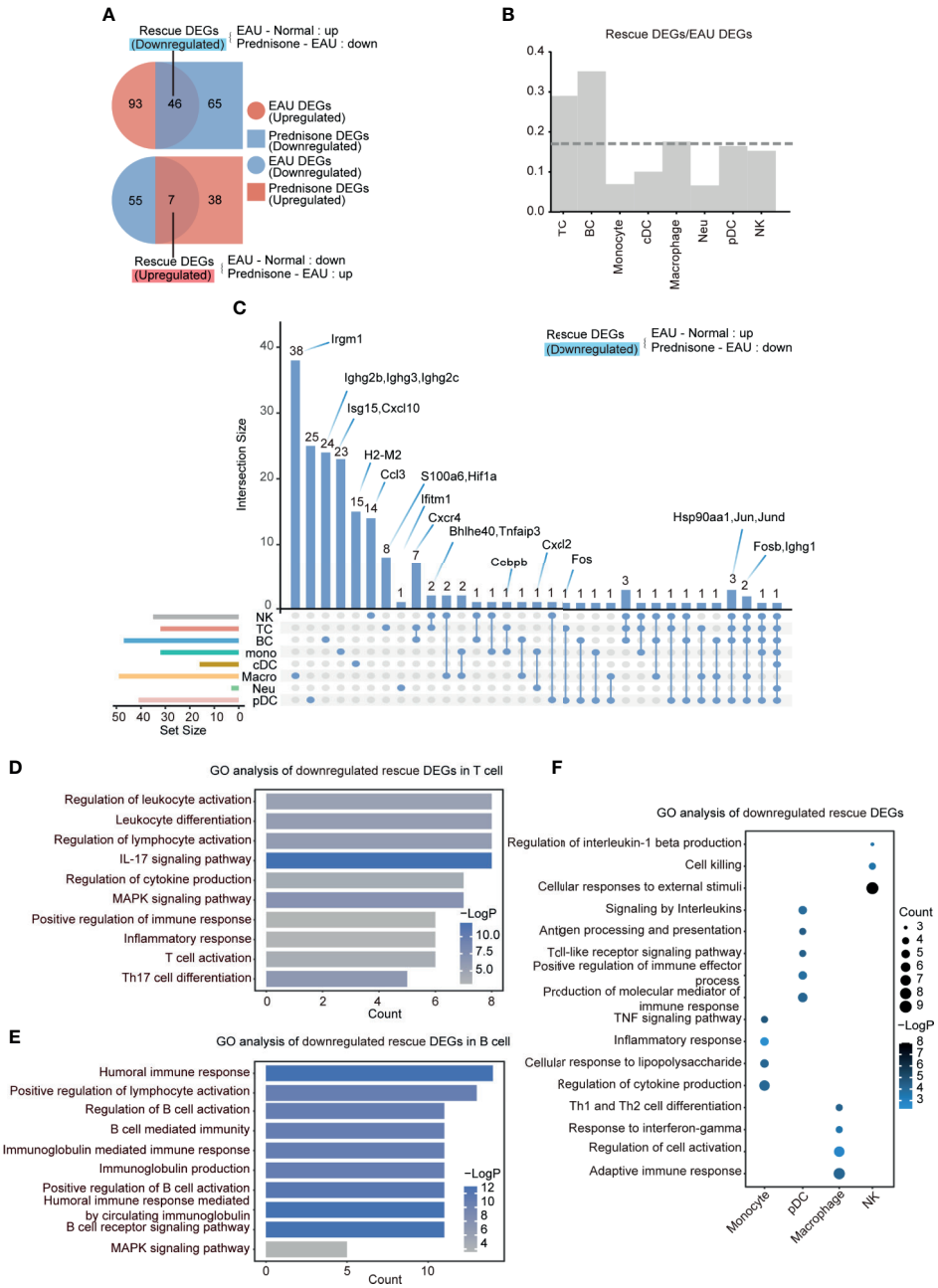

FIGURE 3 | Prednisone partly reversed the EAU-associated gene expression. **(A)** Venn diagrams of the numbers of EAU, prednisone and rescue DEGs. The overlapping parts indicate the numbers of downregulated rescue DEGs (top) and upregulated rescue DEGs (bottom). **(B)** Bar plots of the proportion of rescue DEGs compared to EAU DEGs. The dotted line indicates average proportion of rescue DEGs/EAU DEGs. **(C)** Venn diagram shows the downregulated DEGs in each cell types. Key genes were labeled on the top. **(D–F)** GO analysis of downregulated rescue DEGs in T cells **(D)**, B cells **(E)**, monocytes, pDCs, macrophages and NK cells **(F)**.

autoantibodies. As expected, Th1 and Th17 cells were the top two T cell subsets influenced by EAU, indicating the central role of activated CD4+T cells in EAU (**Figures 4A, B**) (24). Autoimmunity also had a considerable effect on myeloid leukocytes, including monocytes, macrophages, neutrophils, and DCs (**Figure 4A**). Moreover, prednisone alone significantly affected myeloid cells (monocytes, macrophages, neutrophils, and pDCs) and T cells. Not surprisingly, Th1, Th17, and Treg cells were the top three affected T cell subsets based on their large DEG numbers.

Strikingly, we identified the largest number of DEGs in the Treg subpopulation, although the numbers of EAU DEGs and

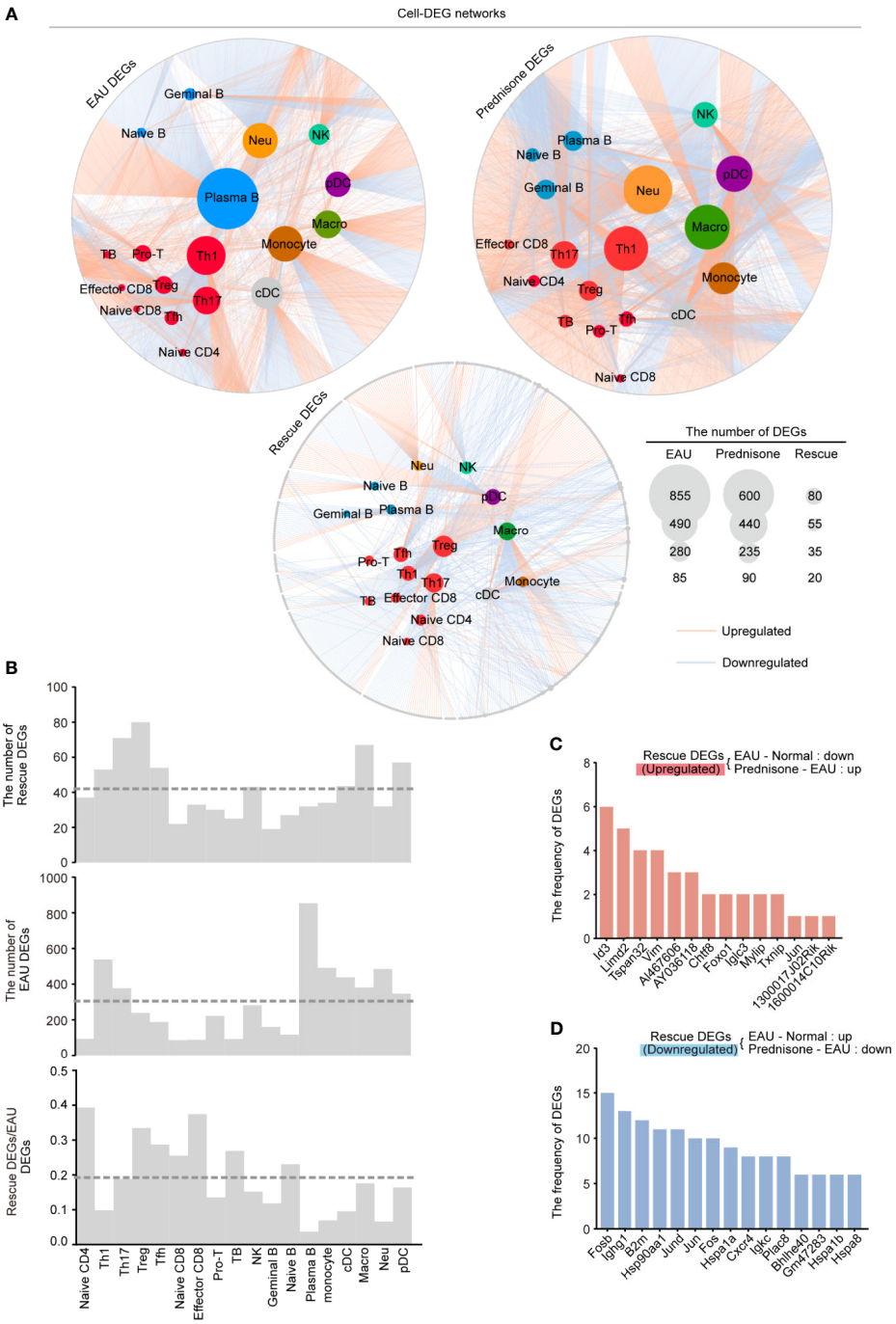

FIGURE 4 | Gene expression networks show cell-type-specific regulation among different cell types. **(A)** Network plots show the EAU, prednisone and rescue DEGs in each types of cells. The color of the internal nodes indicates cell types, and the gray edge represents DEGs. The lines between them attribute the DEGs to each cell types. **(B)** Bar plots show the number of rescue DEGs and EAU DEGs, and the rescue/EAU DEGs in each subtypes. The dotted line indicates average proportion of rescue DEGs/EAU DEGs. **(C, D)** Bar plots indicate the frequency of upregulated **(C)** and downregulated **(D)** rescue DEGs.

prednisone DEGs of Treg cells were relatively small compared to those of other cell subsets (**Figure 4A**). The rescue DEGs-to-EAU DEGs ratio further supported this observation, indicating an unexpected rescue effect of prednisone on Treg cells (**Figure 4B**). We also observed a considerable rescue effect on Th17 and Tfh cells and an unexpectedly strong rescue effect in naïve CD4+ T cells, naïve CD8+ T cells, and effector CD8+ T cells (**Figure 4B**). In contrast, given the relatively large numbers

of EAU and prednisone DEGs in B cells and myeloid cell subsets, the rescue effect seemed weak in these cell subsets, suggesting that the underlying mechanisms of action of prednisone may not involve directly countering the effects of EAU, but distinctly regulating these types of cells (**Figure 4B**).

Notably, *Id3*, *Limd2*, Tspan32, and *Vim* were downregulated in EAU and upregulated by prednisone in more than four cell types (**Figure 4C**). The rescued genes that were upregulated in EAU and downregulated by prednisone included genes encoding AP-1 components (*Fosb*, *Jund*, *Jun*, and Fos), immunoglobulins (*Ighg1* and *Igkc*), heat shock proteins (*Hsp9011a*, *Hspa1a*, *Hspa1b*, and *Hspa8*), and chemokine receptors (*Cxcr4*) (**Figure 4D**). Overall, these results provide a global assessment of the effects of EAU and prednisone on the immune system of mice at the single-cell level.

EAU and Prednisone Reprogram Transcriptional Regulatory Networks

Given the strong effect of EAU and prednisone on TFs as previously shown, we applied SCENIC to the transcriptional atlases and determined the critical TFs regulating EAU and prednisone DEGs in different cells types. Similarly, we defined "rescue TFs" as the TFs that were dysregulated in EAU and rescued by prednisone (**Figure 5A**). Interestingly, autoimmunity had a significant impact on mainly monocytes and cDCs, while prednisone alone had a widespread effect on nearly all cell types (**Figure 5B**). Although both the numbers of EAU and prednisone TFs were relatively small in T and B cells, both cell types were significantly influenced by rescue effects, which were likely due to the anti-inflammatory effects of prednisone on transcriptional regulatory networks (**Figure 5B**).

Furthermore, TFs regulated by EAU and prednisone were attributed to different types of immune cells, along with their theoretical downstream DEGs (**Figures 5C, D**). Our results showed that rescued TFs included AP-1 components (*Jund, Jun, Junb*, and *Fos*), leucine zipper (*Cebpb* and *Cebpd*), interferon regulatory factors (*Irf1, Irf5*, and *Irf8*), and amphoterin elements (*Hmgb1* and *Hmgb2*) (**Figures 5C, D**). The central roles of the AP-1 family are further indicated in **Figures 5E, F**, where two AP-1 components (*Jund* and *Jun*) not only appeared most frequently in the rescue list, but were also rescued in T cells, B cells, and DCs, which are essential in the pathogenesis of uveitis. In addition, the TFs *Hmgb2*, *Bhlhe40*, and *Cebpb* rescued in T and B cells may also play important roles in prednisone treatment. Focusing on the central CD4+ T cell subsets (Tfh, Th17, and Treg cells), we further identified TFs that may play key roles in both the effects of EAU and prednisone. In addition to AP-1 members, *Cebpb* and *Hif1a* were rescued in all three subsets. These findings provide evidence for the mechanisms of EAU pathogenesis and prednisone treatment (**Supplementary Figure B**).

Taken together, these data reveal that EAU-associated TF regulatory networks were strongly affected by prednisone and that AP-1 components were the TFs most frequently affected by EAU and prednisone.

Prednisone Alleviates Aberrant Intercellular Communication in EAU

The close communication between different types of immune cells forms the basis for effective immune responses, making it necessary to explore the intercellular interactions between immune cells. Thus, we explored the intercellular communication in EAU and upon prednisone treatment by determining the number of ligand-receptor pairs between different immune cell types and within the same cell type, indicating autocrine signaling (**Figure 6** and **Supplementary Figures 4C–E**).

We observed globally enhanced cell-cell communication in EAU mainly among myeloid cells, but not among T cells, probably because of the complex or even reversed transcriptional alterations in different T cell subsets (**Figure 6A**). Prednisone enhanced NK cell-associated communication and inhibited monocyte-associated communication (**Figure 6A**). The rescue effect, based on computational cell-cell communication, was primarily observed in macrophages, monocytes, and neutrophils (**Figure 6B**). We observed a strong impact of EAU and prednisone and a rescue effect on monocytes, macrophages, and neutrophils, indicating that these cells were highly sensitive to the changes in the immune system and presence of prednisone.

Then, we performed functional and pathway enrichment analyses on the rescued pairs to further examine the effects of prednisone. The erased pairs referred to the ligand-receptor pairs appear only in the EAU mice, not in the normal controls or prednisone-treated EAU mice (**Figure 6C**). Functionally, the eliminated interaction pairs were mostly associated with cell-cell adhesion and migration, inflammatory response, T cell activation and proliferation, and humoral immune response (**Figure 6C**). The most frequently rescued interaction pairs included the pro-inflammatory pair TNF-TNFRSF1A and B cell stimulatory pairs CD28-CD86 and CCL4-CCR5, which regulate immune cell migration (**Figure 6D**) (25, 26).

Furthermore, to better explore the changes in lymphocyte subsets, we reconstructed the cell-cell communication networks (**Figure 6E**). In EAU, the communication status of monocytes, macrophages, neutrophils, and T cells (Treg, Th17, and Mki67+ proliferating T cells) were significantly changed (**Figure 6E**). Prednisone seemed to have a complex influence on the communication networks, exhibiting both enhancing and inhibitory effects on all subsets (**Figure 6E**). As for the eliminated pairs, we observed widespread rescue effects on several CD4+ T cell subsets, including Treg, Th17, Tfh, Th1, and Mki67+ proliferating T cells (**Figure 6F**). The rescue effect on monocytes was also considerable, suggesting that monocytes may also play an important role in both the pathogenesis of uveitis and treatment with prednisone. In detail, eliminated interaction pairs that appeared frequently included CCL4-CCR5, CTLA4-CD86, CXCL10-CXCR3, and TNF-TNFRSF1 (**Figure 6G**), implying that prednisone may inhibit immune cell adhesion/migration, suppress inflammation, and control aberrant immune cell inactivation (25). Overall, abnormal intercellular communication patterns in EAU, especially those

FIGURE 5 | Changes of the transcription factors of EAU and prednisone-treated EAU mice. **(A)** Venn diagrams show the numbers of EAU, prednisone and rescue TFs. The overlapping parts indicate the numbers of upregulated or downregulated TFs. **(B)** Rose diagrams show the numbers of EAU, prednisone and rescue DEGs in each cell types. **(C, D)** Networks show the downregulated **(C)** and upregulated **(D)** EAU or prednisone TFs in each cell types. The circles indicate TFs. The gray edge indicates the downstream DEGs. The line between them indicates rescue TFs. **(E)** The upregulated rescue TFs in each cell types. **(F)** Bar plots indicate the frequency of downregulated rescue TFs.

that mediate migration and inflammation, were shown to be alleviated by prednisone.

DISCUSSION

Here, we presented an integrative and comprehensive immune cell atlas of EAU and prednisone-treated EAU mice at the single-cell level. We studied the transcriptional changes in EAU in terms of cell type composition, gene regulation, transcriptional regulation, and intercellular communication, providing clues about the processes involved in EAU. Comparative analysis of the transcriptional features in EAU and prednisone-treated EAU mice revealed the underlying mechanisms by which prednisone achieves rapid autoimmune disease control. Our results depict the immune cell atlases in EAU and upon prednisone treatment and provide resources for further research.

In EAU, a classical model of autoimmune diseases within CNS, retinal autoantigens drive the development of retinal inflammation, which involves nearly all types of immune cells

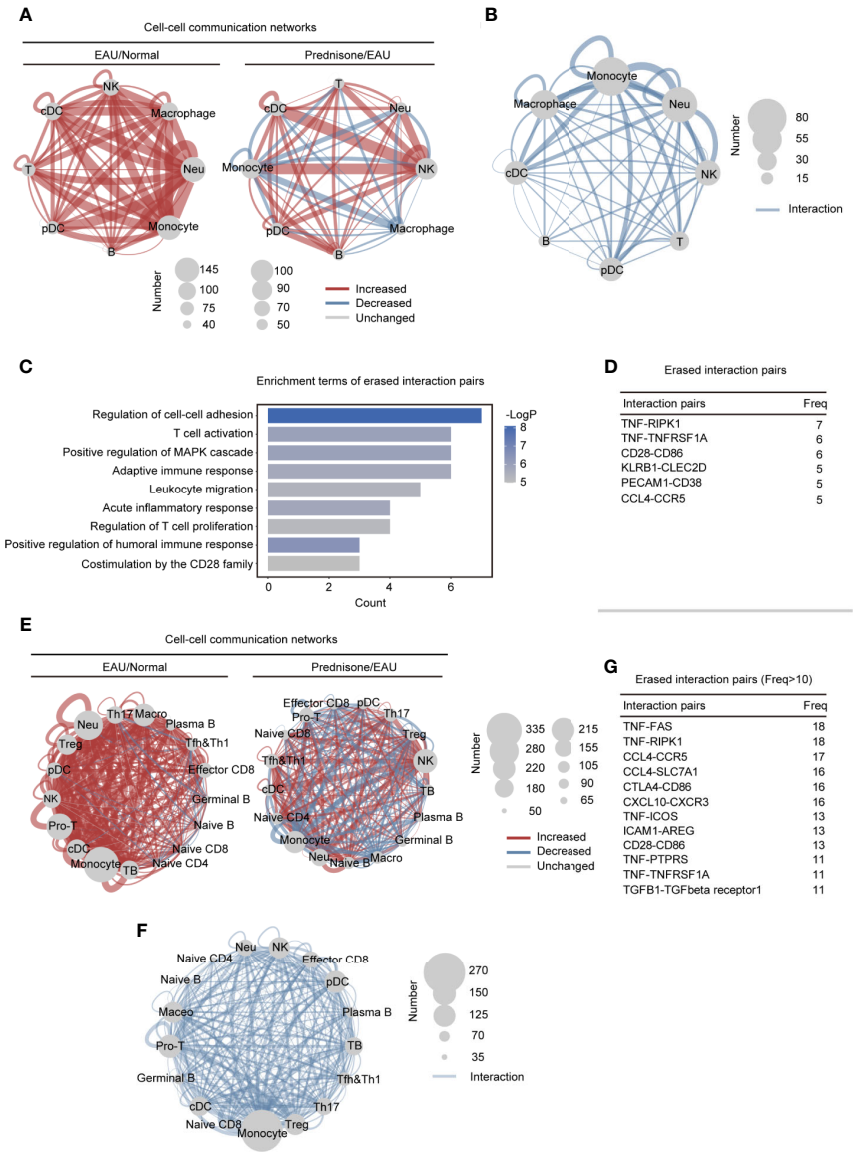

FIGURE 6 | Alteration of the intercellular interactions between different cell types in EAU and prednisone-treated EAU mice. **(A)** Networks of the alteration of the intercellular interactions between eight different types of cells in the EAU mice/normal controls (EAU/normal) and prednisone-treated EAU mice/EAU mice (prednisone/EAU) comparison. The lines indicate intercellular communication, the thickness of which corresponded to the number of intercellular ligand-receptor pairs. Abbreviations for each type of cells are the same as that in **Figure 5**. **(B)** Network plots show the rescue effect of prednisone in terms of cell-cell communication, similar to **(A)**. Ligand-receptor pairs are rescued when they appear only in the EAU mice, not in the normal controls or prednisone-treated EAU mice. **(C)** Functional enrichment analysis of the rescued pairs. **(D)** The frequency (Freq) of rescued intercellular interaction pairs in eight types of cells. **(E)** Same as **(A)**, network plots indicate intercellular interaction alteration in 17 types of cells in EAU/normal or prednisone/EAU comparison. **(F)** Same as **(B)**, network plots show the rescue effect of prednisone in terms of cell-cell communication. **(G)** The frequency (Freq) of rescued intercellular interaction pairs in 17 types of cells.

and multiple organs beyond the eye (12, 13, 24). High-dimensional assays and computational tools have allowed large-scale and comprehensive research on CNS autoimmune disease processes. Despite extensive investigation on CNS inflammatory diseases, including rheumatoid arthritis, multiple sclerosis, and experimental autoimmune encephalomyelitis, using bioinformatic methods, the transcriptional features of autoimmune uveitis have not been explored *via* high-throughput approaches (27). Moreover, a limited number of high-dimensional studies have focused on the EAU mouse model, which is the most important model for investigating the pathogenesis of uveitis and its associated therapies (13). Recently, several studies have revealed the transcriptional modifications in retinal endothelial cells and emphasized their potential roles in disease onset (28). However, most of these studies were based on bulk RNA sequencing and depicted only

the average transcriptional changes in autoimmune states (24, 28–30). In the current study, we depicted lymph node immune modifications in EAU from multiple aspects. Consistent with the current understanding and clinical features of EAU, we found an increase in the proportions of Th1 and Th17 cell and a decrease in the proportion of Treg cells (31). Specifically, our results, which showed that Th1, Th17, and Treg cells were the top three most significantly modified T cells in EAU, were consistent with those of previous studies (24). Previous studies have indicated that monocytes/macrophages cause pathogenic consequences, while dendritic cells manage antigen presentation in autoimmune states (31–33). Similarly, our results showed that myeloid clusters, including monocytes, macrophages, and cDCs, were strongly affected in EAU and that cell-cell communication was globally enhanced, as the hypersensitive immune system was activated by autoantigens.

GCs are currently the most widely used immunosuppressive agents for the control of severe autoimmune diseases and are the first-line systemic treatment for patients with sight-threatening uveitis (10). Despite their extensive clinical application in autoimmune uveitis, the underlying mechanisms by which GCs repress inflammatory gene expression remain poorly understood.

Thus, we conducted a comparative analysis of the transcriptomes of EAU mice and prednisone-treated EAU mice (12, 13). In our data, we showed that prednisone may induce anti-inflammatory effects by regulating immune cell composition, particularly of Th1, Tfh, Th17, and Mki67+ proliferating T cells. Among all immune cell subpopulations distinguished in the lymph nodes, CD4+ T cell subsets (Th1, Treg, Tfh, and Th17 cells) and myeloid cells were most strongly subjected to the rescue effects or prednisone, suggesting that these cells were the main responders to prednisone treatment (34). GCs have been reported to downregulate the constituent transcription factor AP-1 components Jun and Fos and reduce the DNA-binding ability of the AP-1 components to their cognate DNA motifs (2). Hsp90, an important GC receptor chaperone protein, is thought to be the key regulator of GC effects (35). Consistently, we found commonly rescued AP-1 components and *Hsp90aa1* in more than four types of immune cells. Analysis of the transcriptional regulatory networks further supported these findings. In addition, we also found the rescued genes *Id3*, *Tspan32*, and *Vim* in more than four types of cells, extending the transcriptional effects of prednisone and EAU. These three genes have been reported to be involved in lymphocyte development, Th cell immune response regulation, and lymphocyte/neutrophil apoptosis, respectively (36–39). Based on computational transcriptional regulatory networks, the TFs Cebpb and Bhlhe40, which were rescued in two types of cells, may also play a central role in the rescue effects of GCs.

Interestingly, we also identified cell type-specific rescued genes, indicating the complex modifications to immune cell transcriptomes due to prednisone. Chemokine genes, including *Cxcl2* (neutrophils and monocytes), *Ccl3* (NK cells), and *Cxcl10* (monocytes), and chemokine receptors, particularly *Cxcr4* (T and B cells), were found to correlate with the role of prednisone in regulating immune cell migration (25). Additionally, *Hif1a*, which is linked to the induction of Foxp3 and promotion of Treg differentiation, was specifically rescued in T cells (40). In macrophages, *Irgm1*, which is related to the disruption of the blood-brain barrier in the initiation of inflammation, was specifically rescued (23). The rescue effects of prednisone were further depicted from the perspective of cell-cell communication, highlighting the important migration-managing roles of myeloid cell subsets (34, 41, 42). Our findings corresponded to those of previous studies, which demonstrated monocyte/macrophages as the main effector cells in cell mediator release and inflammatory infiltration.

Taken together, our results provide single-cell expression landmarks that aid in systematically annotating immune cell types, identifying sets of genes and key TFs that are differentially regulated in EAU and by prednisone, and constructing cell-cell communication networks modulated in EAU and by prednisone. Our data help elucidate the complex processes involved in EAU and the mechanisms of action of GCs.

DATA AVAILABILITY STATEMENT

The single-cell sequencing data have been deposited at GSA with the project number PRJCA005205 and GSA accession number HRA000850.

ETHICS STATEMENT

The animal study was reviewed and approved by Ethics Committee of Zhongshan Ophthalmic Center, Sun Yat-Sen University.

AUTHOR CONTRIBUTIONS

WS designed the study. XW and HL conducted the experiment and acquired the data. RW analyzed the data and prepared the figures. YG, RD, and ZL wrote the manuscript. LX and LZ assisted the experiments. BC performed the statistical analyses. The manuscript was reviewed by all authors. Order of co-first author is based on the length of time spent on the project. All authors contributed to the article and approved the submitted version.

FUNDING

This work was supported by the National Key Research and Development Program of China (2017YFA0105804).

SUPPLEMENTARY MATERIAL

The Supplementary Material for this article can be found online at: https://www.frontiersin.org/articles/10.3389/fimmu.2021.739605/full#supplementary-material

REFERENCES

1. Cain DW, Cidlowski JA. Immune Regulation by Glucocorticoids. *Nat Rev Immunol* (2017) 17(4):233–47. doi: 10.1038/nri.2017.1
2. Quatrini L, Ugolini S. New Insights Into the Cell- and Tissue-Specificity of Glucocorticoid Actions. *Cell Mol Immunol* (2021) 18(2):269–78. doi: 10.1038/s41423-020-00526-2
3. Ronchetti S, Migliorati G, Bruscoli S, Riccardi C. Defining the Role of Glucocorticoids in Inflammation. *Clin Sci* (2018) 132(14):1529–43. doi: 10.1042/cs20171505
4. Chakraborty S, Pramanik J, Mahata B. Revisiting Steroidogenesis and its Role in Immune Regulation With the Advanced Tools and Technologies. *Genes Immun* (2021) 22(3):125–40. doi: 10.1038/s41435-021-00139-3
5. Simon C, Biddie S, John PJ, Sabo RE, Thurman TA, Johnson RL, et al. Stamatoyannopoulos and Gordon L. Hager: Transcription Factor AP1 Potentiates Chromatin Accessibility and Glucocorticoid Receptor Binding. *Mol Cell* (2011) 43(1):145–55. doi: 10.1016/j.molcel.2011.06.016
6. Boldizsar F, Talaber G, Szabo M, Bartis D, Palinkas L, Nemeth P, et al. Emerging Pathways of Non-Genomic Glucocorticoid (GC) Signalling in T Cells. *Immunobiology* (2010) 215(7):521–6. doi: 10.1016/j.imbio.2009.10.003
7. Love MI, Huska MR, Jurk M, Schöpflin R, Starick SR, Schwahn K, et al. Role of the Chromatin Landscape and Sequence in Determining Cell Type-Specific Genomic Glucocorticoid Receptor Binding and Gene Regulation. *Nucleic Acids Res* (2017) 45(4):1805–19. doi: 10.1093/nar/gkw1163
8. Hoffman JA, Papas BN, Trotter KW, Archer TK. Single-Cell RNA Sequencing Reveals a Heterogeneous Response to Glucocorticoids in Breast Cancer Cells. *Commun Biol* (2020) 3(1):126. doi: 10.1038/s42003-020-0837-0
9. Cooper GS, Bynum ML, Somers EC. Recent Insights in the Epidemiology of Autoimmune Diseases: Improved Prevalence Estimates and Understanding of Clustering of Diseases. *J Autoimmun* (2009) 33(3-4):197–207. doi: 10.1016/j.jaut.2009.09.008
10. Guly CM, Forrester JV. Investigation and Management of Uveitis. *BMJ* (2010) 341:c4976. doi: 10.1136/bmj.c4976
11. Franco LM, Gadkari M, Howe KN, Sun J, Kardava L, Kumar P, et al. Immune Regulation by Glucocorticoids Can Be Linked to Cell Type-Dependent Transcriptional Responses. *J Exp Med* (2019) 216(2):384–406. doi: 10.1084/jem.20180595
12. Bansal S, Barathi VA, Iwata D, Agrawal R. Experimental Autoimmune Uveitis and Other Animal Models of Uveitis: An Update. *Indian J Ophthalmol* (2015) 63(3):211–8. doi: 10.4103/0301-4738.156914
13. Caspi RR, Silver PB, Luger D, Tang J, Cortes LM, Pennesi G, et al. Mouse Models of Experimental Autoimmune Uveitis. *Ophthalmic Res* (2008) 40(3-4):169–74. doi: 10.1159/000119871
14. Chen J, Caspi RR. Clinical and Functional Evaluation of Ocular Inflammatory Disease Using the Model of Experimental Autoimmune Uveitis. *Methods Mol Biol* (2019) 1899:211–27. doi: 10.1007/978-1-4939-8938-6_15
15. Chen X, Hu X, Zou Y, Pi R, Liu M, Wang T, et al. Combined Treatment With Minocycline and Prednisone Attenuates Experimental Autoimmune Encephalomyelitis in C57 BL/6 Mice. *J Neuroimmunol* (2009) 210(1):22–9. doi: 10.1016/j.jneuroim.2009.02.016
16. Huynh-Thu VA, Irrthum A, Wehenkel L, Geurts P. Inferring Regulatory Networks from Expression Data Using Tree-Based Methods. *PLOS ONE* (2010) 5(9):e12776. doi: 10.1371/journal.pone.0012776
17. Verfaillie A, Imrichova H, Atak ZK, Dewaele M, Rambow F, Hulselmans G, et al. Marine and S. Aerts: Decoding the Regulatory Landscape of Melanoma Reveals TEADS as Regulators of the Invasive Cell State. *Nat Commun* (2015) 6 (1):6683. doi: 10.1038/ncomms7683
18. Aibar S, González-Blas CB, Moerman T, Huynh-Thu VA, Imrichova F, Hulselmans H, et al. Aerts: SCENIC: Single-Cell Regulatory Network Inference and Clustering. *Nat Methods* (2015) 14(11):1083–1086. doi: 10.1038/nmeth.4463
19. Shannon P, Markiel A, Ozier O, Baliga NS, Wang JT, Ramage D, et al. Cytoscape: A Software Environment for Integrated Models of Biomolecular Interaction Networks. *Genome Res* (2003) 13(11):2498–504. doi: 10.1101/gr.1239303
20. Vento-Tormo R, Efremova M, Botting RA, Turco MY, Vento-Tormo M, Meyer KB, et al. Single-Cell Reconstruction of the Early Maternal-Fetal Interface in Humans. *Nature* (2018) 563(7731):347–53. doi: 10.1038/s41586-018-0698-6
21. Nagafuchi Y, Shoda H, Sumitomo S, Nakachi S, Kato R, Tsuchida Y, et al. Immunophenotyping of Rheumatoid Arthritis Reveals a Linkage Between HLA-DRB1 Genotype, CXCR4 Expression on Memory CD4(+) T Cells, and Disease Activity. *Sci Rep* (2016) 6:29338. doi: 10.1038/srep29338
22. Schmidt TH, Bannard O, Gray EE, Cyster JG. CXCR4 Promotes B Cell Egress From Peyer's Patches. *J Exp Med* (2013) 210(6):1099–107. doi: 10.1084/jem.20122574
23. Wang C, Wang C, Dong H, Wu X-M, Wang C, Xia F, et al. Immune-Related GTPase Irgm1 Exacerbates Experimental Auto-Immune Encephalomyelitis by Promoting the Disruption of Blood–Brain Barrier and Blood–Cerebrospinal Fluid Barrier. *Mol Immunol* (2013) 53(1):43–51. doi: 10.1016/j.molimm.2012.06.009
24. Caspi RR. A Look at Autoimmunity and Inflammation in the Eye. *J Clin Invest* (2010) 120(9):3073–83. doi: 10.1172/JCI42440
25. Horai R, Caspi RR. Cytokines in Autoimmune Uveitis. *J Interferon Cytokine Res* (2011) 31(10):733–44. doi: 10.1089/jir.2011.0042
26. Dick AD, Forrester JV, Liversidge J, Cope AP. The Role of Tumour Necrosis Factor (TNF-Alpha) in Experimental Autoimmune Uveoretinitis (EAU). *Prog Retin Eye Res* (2004) 23(6):617–37. doi: 10.1016/j.preteyeres.2004.06.005
27. Meyer zu Hörste G, Gross CC, Klotz L, Schwab N, Wiendl H. Next-Generation Neuroimmunology: New Technologies to Understand Central Nervous System Autoimmunity. *Trends Immunol* (2020) 41(4):341–54. doi: 10.1016/j.it.2020.02.005
28. Lipski DA, Foucart V, Dewispelaere R, Caspers LE, Defrance M, Bruyns C, et al. Retinal Endothelial Cell Phenotypic Modifications During Experimental Autoimmune Uveitis: A Transcriptomic Approach. *BMC Ophthalmol* (2020) 20(1):106. doi: 10.1186/s12886-020-1333-5
29. Du Z, Wang Q, Huang X, Yi S, Mei S, Yuan G, et al. Effect of Berberine on Spleen Transcriptome and Gut Microbiota Composition in Experimental Autoimmune Uveitis. *Int Immunopharmacol* (2020) 81:106270. doi: 10.1016/j.intimp.2020.106270
30. Gonzales JA, Takhar JS, Joye A, Acharya NR, Chen C, Hinterwirth A, et al. Peripheral Blood Transcriptome in Patients With Sarcoidosis-Associated Uveitis. *Ocul Immunol Inflamm* (2021), 1–4. doi: 10.1080/09273948.2020.1861306
31. Diedrichs-Möhring M, Kaufmann U, Wildner G. The Immunopathogenesis of Chronic and Relapsing Autoimmune Uveitis - Lessons From Experimental Rat Models. *Prog Retin Eye Res* (2018) 65:107–26. doi: 10.1016/j.preteyeres.2018.02.003
32. Mochizuki M, Sugita S, Kamoi K. Immunological Homeostasis of the Eye. *Prog Retin Eye Res* (2013) 33:10–27. doi: 10.1016/j.preteyeres.2012.10.002
33. Forrester JV, Xu H, Kuffová L, Dick AD, McMenamin PG. Dendritic Cell Physiology and Function in the Eye. *Immunol Rev* (2010) 234(1):282–304. doi: 10.1111/j.0105-2896.2009.00873.x
34. Ehrchen JM, Roth J, Barczyk-Kahlert K. More Than Suppression: Glucocorticoid Action on Monocytes and Macrophages. *Front Immunol* (2019) 10:2028. doi: 10.3389/fimmu.2019.02028
35. Ouyang J, Chen P, Jiang T, Chen Y, Li J. Nuclear HSP90 Regulates the Glucocorticoid Responsiveness of PBMCs in Patients With Idiopathic Nephrotic Syndrome. *Int Immunopharmacol* (2012) 14(3):334–40. doi: 10.1016/j.intimp.2012.08.012
36. Yang CY, Best JA, Knell J, Yang E, Sheridan AD, Jesionek AK, et al. The Transcriptional Regulators Id2 and Id3 Control the Formation of Distinct Memory CD8+ T Cell Subsets. *Nat Immunol* (2011) 12(12):1221–9. doi: 10.1038/ni.2158
37. Kee BL, Rivera RR, Murre C. Id3 Inhibits B Lymphocyte Progenitor Growth and Survival in Response to TGF-β. *Nat Immunol* (2001) 2(3):242–7. doi: 10.1038/85303
38. Lombardo SD, Mazzon E, Basile MS, Campo G, Corsico F, Presti M, et al. Modulation of Tetraspanin 32 (TSPAN32) Expression in T Cell-Mediated Immune Responses and in Multiple Sclerosis. *Int J Mol Sci* (2019) 20(18):4323. doi: 10.3390/ijms20184323
39. Su L, Pan P, Yan P, Long Y, Zhou X, Wang X, et al. Role of Vimentin in Modulating Immune Cell Apoptosis and Inflammatory Responses in Sepsis. *Sci Rep* (2019) 9(1):5747. doi: 10.1038/s41598-019-42287-7
40. Clambey ET, McNamee EN, Westrich JA, Glover LE, Campbell EL, Jedlicka P, et al. Hypoxia-Inducible Factor-1 Alpha-Dependent Induction of FoxP3 Drives Regulatory T-Cell Abundance and Function During Inflammatory Hypoxia of the Mucosa. *Proc Natl Acad Sci USA* (2012) 109(41):E2784–93. doi: 10.1073/pnas.1202366109

41. Ronchetti S, Ricci E, Migliorati G, Gentili M, Riccardi C. How Glucocorticoids Affect the Neutrophil Life. *Int J Mol Sci* (2018) 19(12):4090. doi: 10.3390/ijms19124090
42. Vetillard M, Schlecht-Louf G. Glucocorticoid-Induced Leucine Zipper: Fine-Tuning of Dendritic Cells Function. *Front Immunol* (2018) 9:1232. doi: 10.3389/fimmu.2018.01232

Conflict of Interest: The authors declare that the research was conducted in the absence of any commercial or financial relationships that could be construed as a potential conflict of interest.

The handling editor declared a shared affiliation with one of the authors (XW) at time of review.

Publisher's Note: All claims expressed in this article are solely those of the authors and do not necessarily represent those of their affiliated organizations, or those of the publisher, the editors and the reviewers. Any product that may be evaluated in this article, or claim that may be made by its manufacturer, is not guaranteed or endorsed by the publisher.

frontiers in Immunology

ORIGINAL RESEARCH
published: 13 August 2021
doi: 10.3389/fimmu.2021.702244

Genome-Wide DNA Methylation Pattern in Whole Blood Associated With Primary Intracerebral Hemorrhage

Yupeng Zhang[1†], Hongyu Long[1†], Sai Wang[1], Wenbiao Xiao[1], Meishan Xiong[1], Jianyi Liu[1], Lei Chen[1], Ruijuan Chen[2], Xueli Wei[2], Yi Shu[3], Yi Zeng[2] and Le Zhang[1]*

[1] Department of Neurology, Xiangya Hospital, Central South University, Changsha, China, [2] Department of Geriatrics, Second Xiangya Hospital, Central South University, Changsha, China, [3] Department of Neurology, Second Xiangya Hospital, Central South University, Changsha, China

OPEN ACCESS

Edited by:
Mingzhu Yin,
Central South University, China

Reviewed by:
Wen Jiang,
Fourth Military Medical University, China
Suyue Pan,
Southern Medical University, China

***Correspondence:**
Le Zhang
zlzdzlzd@csu.edu.cn

[†]These authors have contributed equally to this work

Specialty section:
This article was submitted to Cancer Immunity and Immunotherapy, a section of the journal Frontiers in Immunology

Received: 29 April 2021
Accepted: 28 July 2021
Published: 13 August 2021

Citation:
Zhang Y, Long H, Wang S, Xiao W, Xiong M, Liu J, Chen L, Chen R, Wei X, Shu Y, Zeng Y and Zhang L (2021) Genome-Wide DNA Methylation Pattern in Whole Blood Associated With Primary Intracerebral Hemorrhage. Front. Immunol. 12:702244. doi: 10.3389/fimmu.2021.702244

Primary intracerebral hemorrhage (ICH) is a significant cause of morbidity and mortality throughout the world. ICH is a multifactorial disease that emerges from interactions among multiple genetic and environmental factors. DNA methylation plays an important role in the etiology of complex traits and diseases. We used the Illumina Infinium Human Methylation 850k BeadChip to detect changes in DNA methylation in peripheral blood samples from patients with ICH and healthy controls to explore DNA methylation patterns in ICH. Here, we compared genomic DNA methylation patterns in whole blood from ICH patients (n = 30) and controls (n = 34). The ICH and control groups showed significantly different DNA methylation patterns at 1530 sites (p-value < 5.92E-08), with 1377 hypermethylated sites and 153 hypomethylated sites in ICH patients compared to the methylation status in healthy controls. A total of 371 hypermethylated sites and 35 hypomethylated sites were in promoters, while 738 hypermethylated sites and 67 hypomethylated sites were in coding regions. Furthermore, the differentially methylated genes between ICH patients and controls were largely related to inflammatory pathways. Abnormalities in the DNA methylation pattern identified in the peripheral blood of ICH patients may play an important role in the development of ICH and warranted further investigation.

Keywords: intracerebral hemorrhage, epigenome-wide association study, epigenetics, DNA methylation, stroke

INTRODUCTION

ICH is a significant healthcare and financial burden on society and the families of patients. In Western populations, approximately 10% of all strokes are due to ICH (1), whereas 18.8%-55.4% of all strokes are due to ICH in China (2). ICH is a complex disease caused by environmental and genetic factors (3). Several studies have shown changes in gene expression in the brain following ICH (4, 5). However, the mechanism by which ICH causes these changes remains unknown. There has been recent increasing interest in the roles of epigenetic mechanisms and the interaction between the genome and environment in human diseases (6). Studies have confirmed that epigenetic modifications affect the regulation of gene expression and development, and

epigenetics is predicted to be an important part of future genetic studies of ICH (7). However, there are few reports on epigenetic mechanisms in ICH.

DNA methylation refers to the formation of a covalent bond between the 5' carbon atom of the cytosine of a DNA CpG (5'-cytosine guanine-3') dinucleotide and a methyl group by DNA methyltransferase, forming 5-methylcytosine (8). DNA hypermethylation can directly inhibit transcription or indirectly inhibit gene expression through transcriptional silencing (9). Methylated DNA in the human genome is an epigenetic marker of paramount importance for normal development. Changes in DNA methylation are associated with cardiovascular and cerebrovascular diseases, such as coronary heart disease, atherosclerosis, and cerebral infarction (10–12). Hypertension is the most important risk factor for ICH (13). Recent studies have found that the overall DNA methylation level of the peripheral blood of patients with essential hypertension was lower than that of the peripheral blood of healthy people (14). Furthermore, an epigenetic study showed that the level of global DNA hydroxymethylation in mouse brains was decreased after ICH (15). While DNA methylation has been linked to gene silencing, DNA hydroxymethylation is associated with actively transcribed genes (16). Therefore, we hypothesized that changes in DNA methylation play an important role in the development of ICH. DNA methylation exhibits strong tissue specificity, and studies of methylation patterns in peripheral blood samples from patients with many neurological diseases, such as Down Syndrome (17) and Parkinson's disease (18), have indicated that peripheral blood biomarkers are easily used in clinical practice. However, whether DNA methylation is changed in ICH injury remains unknown. In this study, we identified altered genome-wide DNA methylation patterns in whole blood from patients with ICH for the first time.

MATERIALS AND METHODS

Subjects

This case-control study recruited consecutive Han Chinese patients with acute ICH diagnosed at the Department of Neurology in Xiangya Hospital in Changsha, between August 2016 and October 2017. The inclusion criteria were as follows: diagnosis of ICH confirmed by computed tomography (CT) and/or magnetic resonance imaging (MRI); typical areas exhibiting ICH, especially hematoma in the basal ganglia; a clear history of hypertension; 18 years of age or older; and signed informed consent. Cases of mixed cerebrovascular disease (postinfarct hemorrhage or infarct after hemorrhage); ICH caused by arteritis, trauma, drug, tumor, cerebrovascular malformation, cerebral amyloid angiopathy, sinus thrombosis or aneurysm; and patients more than 2 weeks after the onset of ICH were excluded (19, 20). Age- and sex-matched healthy control subjects who had a routine physical check-up for the purpose of health maintenance at Xiangya Hospital were enrolled in the study. The control subjects had no symptoms or history of stroke, autoimmune disease, peripheral atherosclerotic disease, coronary artery disease or hematological disease. Finally, 30 patients and 34 controls were enrolled in the study following the procurement of written informed consent from all subjects. All research protocols were approved by the Ethics Committee of Central South University (No.201503225).

Information related to gender, age, body mass index (BMI), systolic blood pressure (SBP), diastolic blood pressure (DBP), fasting blood glucose (FBG), total cholesterol, triglyceride characteristics, high-density lipoprotein cholesterol, low-density lipoprotein cholesterol was recorded on admission. The hematoma volumes on admission to hospital were determined from base-line computed tomography scans (SOMATOM® Definition Flash; Siemens Healthcare, Erlangen, Germany) by the ABC/2 method for all patients. ICH patients and/or their caregivers were contacted and interviewed at 6 months after index ICH by telephone. We defined favorable outcome as achieving and retaining during entire follow-up an mRS ≤ 3.

Whole Blood DNA Extraction

Whole blood DNA was extracted from the blood samples of patients and control subjects using a commercial kit (Beijing Adly Biological Company, Beijing, China) according to the manufacturer's instructions. One microliter of DNA was diluted 10 times with distilled water and shaken evenly, and the DNA concentration (μg/μl) was measured using a NanoDrop spectrophotometer; DNA samples with an OD260/280 ratio from 1.7 to 2.0 were used for further experimentations. The integrity of all DNA samples was assessed by agarose gel electrophoresis and ethidium bromide staining. The main band of the sample electrophoresis is clear, not less than 10kb, no obvious degradation.

BeadChip DNA Methylation Assay

An Illumina Human Methylation 850k BeadChip Kit was used to determine the pattern and extent of DNA methylation in the samples. DNA samples were processed by a series of steps according to the manufacturer's protocols: DNA denaturation, whole genome amplification, fragmentation, precipitation, resuspension and hybridization. Signals (grayscale) from the final hybridization products were captured with the iScan system (Illumina, Inc.). The extent of methylation was determined by the β value, which was calculated as β= max (signal B, 0)/[max(signal A, 0)+ max (signal B, 0)+ 100]. The β values range from 0–1, indicating completely unmethylated to totally methylated DNA (21).

Validation of Methylation by Pyrosequencing

After analysis by Methylation 850k BeadChip, 6 CpG loci methylated to different extents (cg08909806, cg26620021, cg20460771, cg24507266, cg05799811, cg26934362) were selected. Then, we selected blood samples from 15 ICH cases and 15 sex- and age-matched control cases for bisulfite conversion of the target region using a PyroMark PCR kit (Qiagen, 59104). Pyrosequencing was performed using primers designed by PyroMark Assay Design 2.0 software (Qiagen, CA, USA). Pyrosequencing was performed using PyroMark Q96/48 ID (Qiagen, CA, USA).

Data and Bioinformatics Analyses

BeadStudio Methylation Module v3.2 software (Illumina, Inc.) (http://www.illumina.com) was used to analyze differential DNA methylation sites. Differential methylation sites with p-value<5.92 E-08 according to the Bonferroni correction method were screened to reduce the occurrence of class II statistical errors and ensure the accuracy of the research results. The R (https://www.r-project.org/, version 4.1.0) was used to perform all data analysis. Methylation of gene promoters was defined as methylation in the TSS1500 (upstream), TSS200 (upstream), 5' UTR and first exon regions. Methylation involving CpG island structures was defined as methylation of a CpG island or the N-shore, S-shore, N-shelf and S-shelf regions, with shores occurring 0–2 kb from a CpG island and shelves occurring 2–4 kb from a CpG island. Differentially methylated genes were selected using the DAVID bioinformatics database (http://david.abcc.ncifcrf.gov/home.jsp/). Pathways enriched in differentially methylated genes were determined using the Gene Ontology (GO) (http://geneontology.org/) and KEGG (http://www.genome.jp/kegg/) databases, and GO terms and KEGG pathways with a Bonferroni corrected p-value of less than 0.05 were reported. Used Pearson's chi-squared test to compare the distribution of hypomethylation and hypermethylation sites with all probes. The relationship between DNA methylation and clinical outcomes/hematoma volumes was analyzed by Pearson correlation analysis. Measured data are expressed as the mean ± SD. Differences in counted data were statistically analyzed with the chi-square test, and differences in measured data were analyzed by Student's t-test. p-value < 0.05 indicated statistical significance.

RESULTS

Characteristics of Cases and Controls

The total sample population of 64 individuals comprised 30 (aged 41–75 years, the mean age is 54.7) unrelated patients diagnosed with ICH and 34 (aged 33–74 years, the mean age is 54.9) age- and sex-matched unrelated controls (**Table 1**).

TABLE 1 | Demographic and clinical characteristics of ICH and control group.

	Patients n=30	Controls n=34	*p*
Age	54.90 ± 7.91	54.71 ± 9.65	0.931
Sex (M/F)	19/11	23/11	0.717
SBP/mmHg	159.7 ± 23.82	138.53 ± 23.59	0.000*
DBP/mmHg	93.7 ± 11.98	86.97 ± 12.76	0.036*
hypertension	30/30	16/34	0.000*
Diabetes	1/30	0/34	0.283
Smoking	11/30	10/34	0.537
Drinking	9/30	9/34	0.754
TC/(mmol/L)	4.97 ± 1.16	4.72 ± 0.81	0.396
TG/(mmol/L)	1.96 ± 0.60	2.07 ± 1.31	0.665
LDL-C/(mmo l/L)	3.20 ± 0.90	2.65 ± 0.73	0.021
HDL-C/(mmol/L)	1.11 ± 0.30	1.19 ± 0.26	0.245
Hematoma volumes/ml	16.95 ± 11.88	/	

Data presented as mean± SD or n (%).
SBP, systolic blood pressure; DBP, diastolic blood pressure; TC, total cholesterol; TG, triglycerides; HDL-C, high-density lipoprotein cholesterol; LDL-C, low-density lipoprotein cholesterol.
**P<0.05.*

Overall Changes in Blood Genomic DNA Methylation in Patients With ICH

To assess differences in methylation between the ICH cases and the control group, we conducted genome-wide analysis of DNA methylation in samples from these groups using the Illumina Infinium Human Methylation 850k BeadChip, which allows methylation-specific hybridization to an array of 844668 DNA methylation sites spanning the entire human genome. β-values for sites exhibiting differential DNA methylation between controls (n = 34) and patients with ICH (n= 30) are reported. Statistical analysis showed a total of 1530 loci showing differential DNA methylation between the two groups (defined using cutoff *p*-values < 5.92 E-08) (**Figure 1**). These substantially methylated sites appear to be randomly distributed on 22 chromosomes (**Figure 2**). Of these differential methylation sites, 1377 sites were hypermethylated, and 153 sites were hypomethylated (yielding a ratio of 9) compared to the methylation status of those sites in the control samples (**Figure 3**). The 10 methylation sites with the most significant differences in methylation level are listed in **Table 2**.

Biological information was available for 1157 sites of the 1530 positive sites, and there were 5 sites that overlap with genetic variant regions (22). Further analysis of DNA functional domains among the hypermethylated sites revealed 414 sites located in noncoding regions (27%), 738 sites in coding regions (47%), 377 sites in promoters (24%) and 34 in the termini of 3' untranslated regions (UTRs) (2%). Among the hypomethylated sites, 45 sites were in noncoding intergenic regions (28%), 76 sites were in coding regions (46%), 36 sites were in promoters

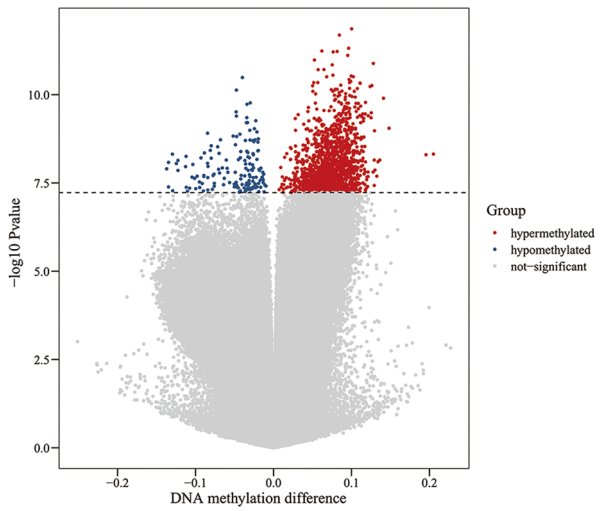

FIGURE 1 | Volcano plot for differential DNA methylation analysis of ICH group and control group. The x-axis shows the DNA methylation difference (delta β), the y-axis shows the – log10 p-value of each CpG site. The dashed line indicates statistically significant (P <5.92 E-08). Red represents hypermethylation sites, blue represents hypomethylation sites, and gray represents no significant.

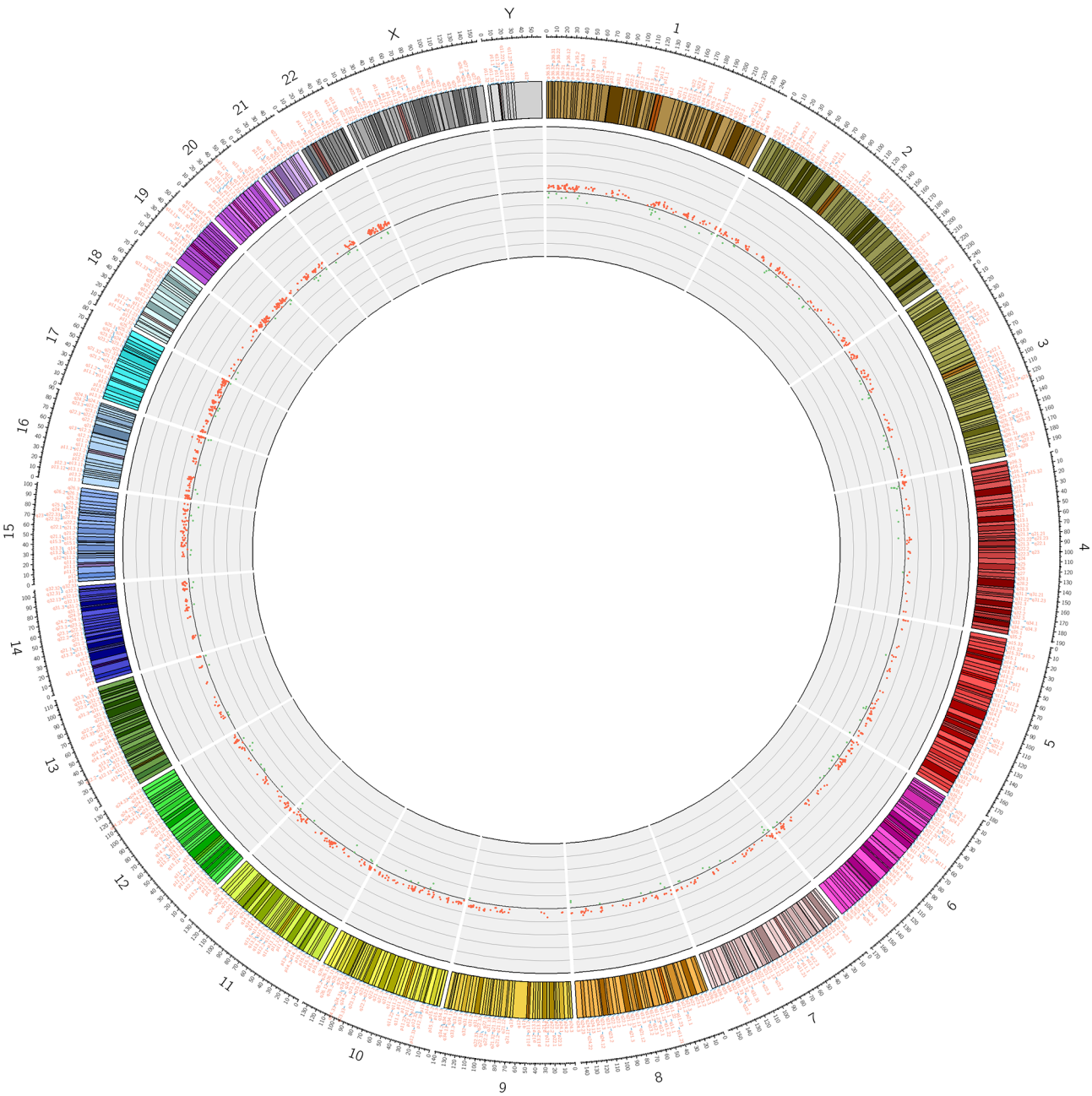

FIGURE 2 | Differential methylation site (P <5.92 E-08) circos diagram. The distribution of 1530 differential DNA methylation sites on 22 chromosomes, the outer layer is the physical location of the chromosome; the middle layer is the chromosome segment; the inner layer is the methylation of the site, red indicates hypermethylation, and green indicates hypomethylation.

(22%), and 7 (4%) were in the end of a 3' UTR. There was no significant difference in the distribution of hypomethylation and hypermethylation sites compared with all probes on the 850k Illumina array (**Figure 4**).

Among the 1530 positive sites, 406 were in promoter regions (**Figure 5**), and among these sites, 371, accounting for 91.38% of the total, were hypermethylated, and 35, accounting for 8.62% of the total, were hypomethylated. Among the 406 methylation sites in promoter regions, 42 were located in a CpG island, 46 were in a north (N)-shore, 59 were in a south (S)-shore, 227 were in an open area, 14 were in a north (N)-shelf, and 18 were in a south (S)-shelf.

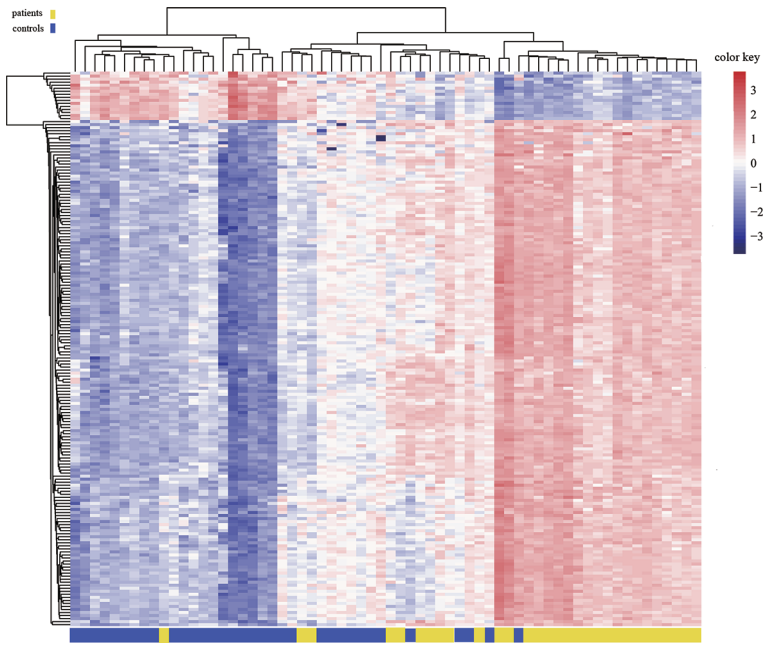

FIGURE 3 | Heat map generated from clustering-analysis of microarray data illustrating differentially methylated DNA sites in blood whole genome in the ICH patient group (n = 30) relative to the control group (n = 34). Blue and red represent levels of hypomethylation and hypermethylation, respectively, whereas white indicates no change in methylation, relative to control.

TABLE 2 | Top ten hyper- and hypo- methylated sites in whole blood genome in ICH.

	TargetID	delta β	*P* value	CHR	GROUP	GENE_NAME
Top ten hypermethylated sites	cg02902412	0.195492157	5.03851E-09	18	Body	*ATP9B*
	cg26934362	0.148252941	8.89275E-10	5	Body	*LPCAT1*
	cg14407179	0.141003922	1.26452E-10	7	Body	*ADAP1*
	cg05799811	0.136335294	7.13005E-09	1	Body	*CD247*
	cg15693299	0.134005882	7.95408E-09	12	TSS1500	*LOC360030*
	cg27642002	0.132466667	2.04617E-08	11	Body	*CLMP*
	cg17972213	0.130166667	1.36499E-08	1	Body	*S1PR1*
	cg13528873	0.129541176	1.0542E-09	6	Body	*GMDS*
	cg20673867	0.129247059	7.13057E-09	9	Body	*MOB3B*
	cg23474890	0.129145098	3.7247E-08	12	Body	*BCL7A*
Top ten hypomethylated sites	cg23351010	-0.1346	4.09969E-08	3	TSS1500;Body	*FLJ10213;PPP4R2*
	cg03330490	-0.13452549	8.20857E-09	10	Body	*HHEX*
	cg08301869	-0.129437255	5.27767E-08	4	Body	*TBC1D14*
	cg11546475	-0.124476471	8.93678E-09	11	Body	*CAT*
	cg07801620	-0.122456863	7.25833E-09	8	1stExon;Body;5'UTR	*PLEC1*
	cg23749353	-0.112090196	5.59553E-09	12	Body	*CORO1C*
	cg05756780	-0.111927451	4.17303E-08	1	Body	*IL6R*
	cg09447621	-0.110345098	5.38782E-08	11	Body	*B3GAT1*
	cg16284789	-0.107533333	4.42562E-08	1	Body	*IL10*
	cg26246740	-0.1034	9.43931E-09	10	TSS1500	*WDFY4*

Validation of Methylation by Pyrosequencing

Because previous studies found a good correlation between percent methylation determined by Illumina array and pyrosequencing (23), we randomly selected 6 differential DNA methylation sites for cross-validation with pyrosequencing. Data on both the differential DNA methylation sites and the mean signals for these sites collected by Illumina Infinium Human Methylation 850k BeadChip and pyrosequencing were analyzed. Data on individual sites from Illumina 850k BeadChip array and pyrosequencing were highly correlated, and the means of the differential DNA methylation sites ranged from 0.899 to 0.971 (p-value<0.001) (**Figures 6A–F**).

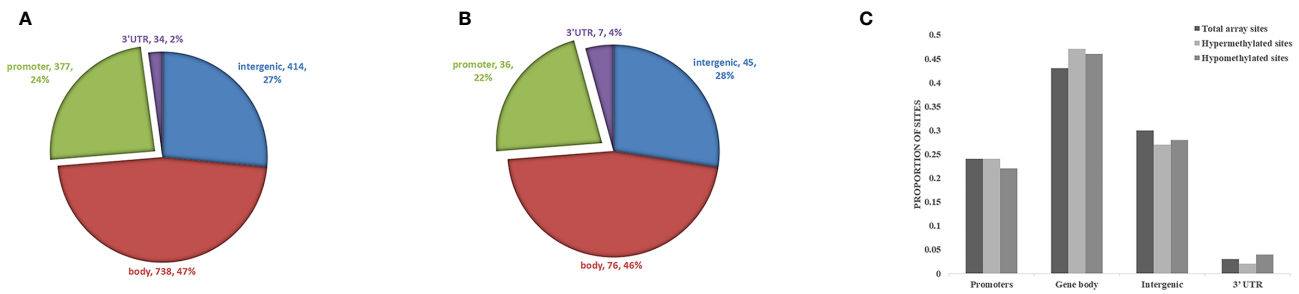

FIGURE 4 | Analysis of differentially methylated DNA sites in reference to genomic structure domains in ICH. **(A)** The distribution of hypermethylation sites, **(B)** the distribution of hypomethylation sites. **(C)** Compared the distribution of hypomethylation and hypermethylation sites with all probes on the Illumina array.

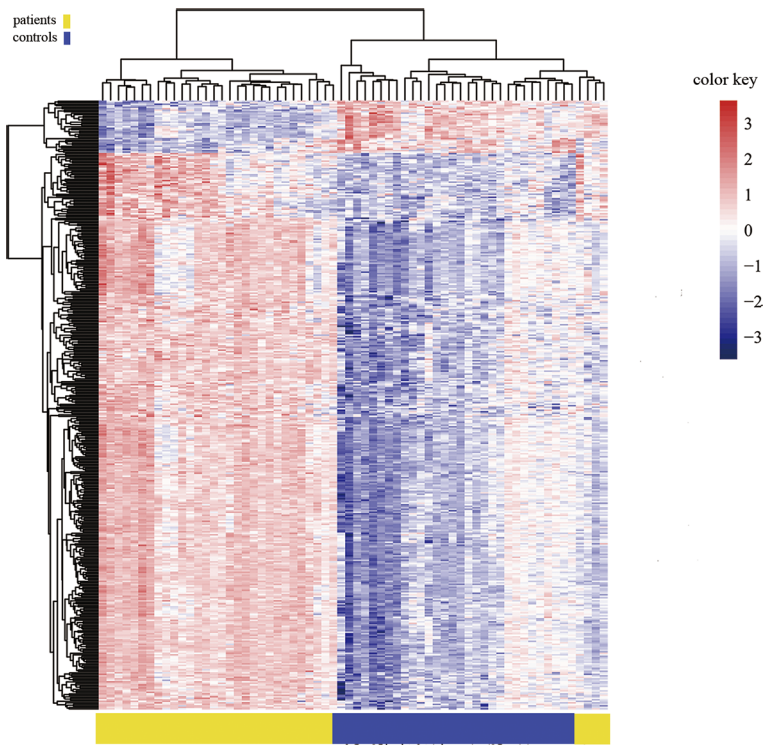

FIGURE 5 | Heat map generated from clustering-analysis of microarray data illustrating differentially methylated DNA sites in the promoter region.

Ontological Profiling of Differentially Methylated Genes in the Blood of Patients With ICH

The 1157 sites with available biological data corresponded to 949 genes. The corresponding biological functions of these genes were obtained from the Database for Annotation, Visualization, and Integrated Discovery (DAVID) database. All genes were enriched in 69 cellular component (CC) terms, and gene enrichment in the following 7 terms was significant (Bonferroni corrected p-value<0.05): (1) GO:0005829, cytosol; (2) GO:0005925, focal adhesion; (3) GO:0015629, actin cytoskeleton; (4) GO:0016020, membrane; (5) GO:0005737, cytoplasm; (6) GO:0005886, plasma membrane; and (7) GO:0016023, cytoplasmic, membrane-bounded vesicle. Among 179 biological process (BP) terms, the following 4 terms were significantly enriched in differentially methylated genes (Bonferroni corrected p-value<0.05): (1) GO:0007165, signal transduction; (2) GO:0043547, positive regulation of GTPase activity; (3) GO:0035556, intracellular signal transduction; and (4) GO:0016477, cell migration. Among the molecular function (MF) terms, 63 terms were enriched in the differentially methylated genes, and 1 of these terms was significantly enriched (Bonferroni corrected *p*-value<0.05): GO:0005515, protein binding (**Figure 7**).

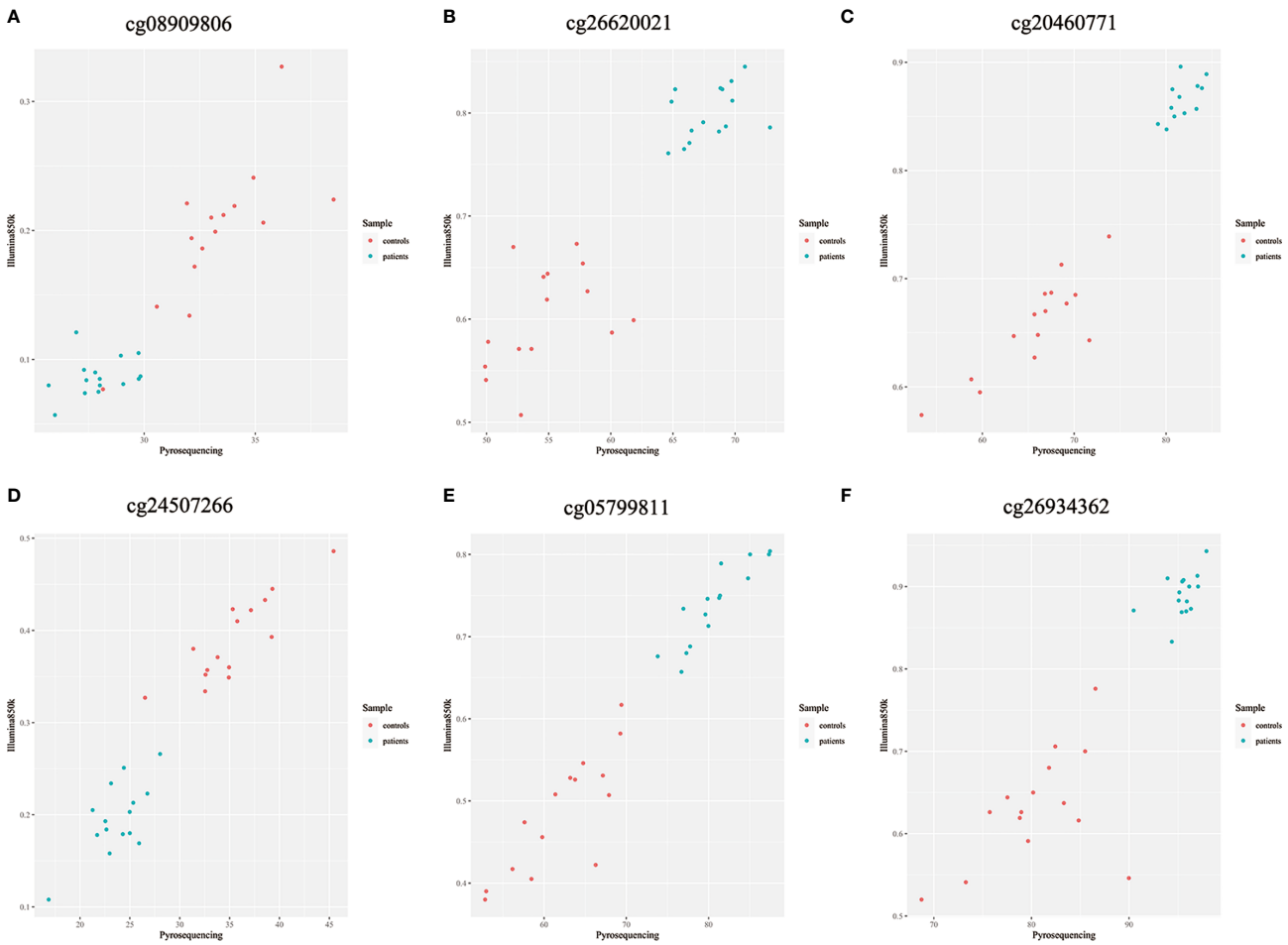

FIGURE 6 | **(A–F)** Methylation chip and pyrosequencing correlation scatter plot Shown are degrees of methylation in 6 CpG loci (cg08909806, cg26620021, cg20460771, cg24507266, cg05799811, cg26934362) reported by Illumina Infinium Human Methylation 850k BeadChip (Y axis, ratio) and pyrosequencing (X axis, percentage) assays. Blue and red dots in each panel plot values of methylation at a given site among individual patients with ICH (n=15) and controls (n=15).

Genomic Network Profiling of Differential Methylated Genes in the Blood of Patients With ICH

Through bioinformatics assessment against the Kyoto Encyclopedia of Genes and Genomes (KEGG) database (http://www.genome.jp/kegg/), a total of 90 genomic networks/pathways were predicted to exhibit biological interplay between/among differentially methylated genes in ICH, and the 5 following networks/pathways were significant (Bonferroni corrected p-value<0.05): (1) hsa04660, T cell receptor signaling pathway; (2) hsa04650, natural killer (NK) cell-mediated cytotoxicity; (3) hsa04662, B cell receptor signaling pathway; (4) hsa04071, sphingolipid signaling pathway; and (5) hsa05205, proteoglycans in cancer (**Table 3**).

The Relationship Between DNA Methylation Patterns and Clinical Outcomes, Hematoma Volumes, Immunological Homeostasis

The top 10 methylation sites correlated with clinical outcomes and hematoma volumes were showed in the **Table 4**. In order to explore the role of immunological homeostasis in the ICH methylation pattern, we screened out the DNA methylation sites in the promoter region related to clinical prognosis, and found the DNA methylation sites involved in immunological homeostasis, including cg24270157(*IL15*), cg23343408 (*TLR5*), which are negatively correlated with the mRS scores (**Figure 8**).

DISCUSSION

This is the first report to identify an altered DNA methylation pattern in the whole blood of ICH patients. Using the Illumina Infinium Human Methylation 850k BeadChip, 844668 DNA methylation sites were tested. Differentially methylated sites with a Bonferroni corrected p-value < 0.05 were considered significant. We identified 1530 differential DNA methylation sites, among which 1377 sites were significantly hypermethylated, and 153 sites were hypomethylated (yielding a ratio of 9) in ICH patients relative to their methylation in the healthy control group.

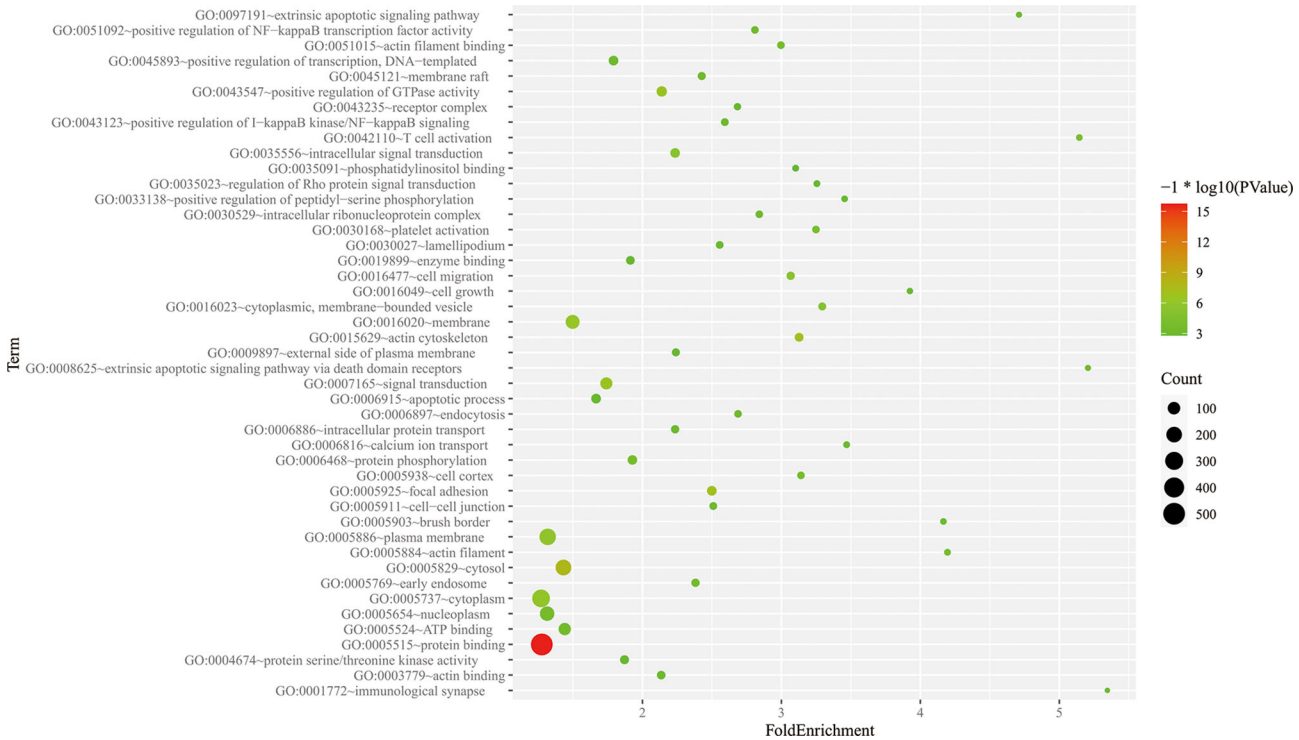

FIGURE 7 | Partial GO pathway enrichment analysis bubble chart. The vertical axis indicates the name of the GO pathway, the horizontal axis is the enrichment factor, and the size of the circle indicates the number of differential methylation-related genes involved in the pathway, The color response of each channel takes p value of – log10.

The methylation of sites around promoters has the strongest inhibitory effect on transcription (24). In this study, among the 1530 positive sites, 406 were located in promoter regions; among these 406 sites, 371 were hypermethylated, and 35 were hypomethylated in patients with ICH, suggesting predominantly increased methylation at these sites. Such changes could enhance the expression of the corresponding genes. This study identified the genome-wide DNA methylation pattern of peripheral blood from patients with ICH and found that the main differences in methylation between ICH patients and normal controls are hypermethylation.

The bioinformatics profile of our data indicates that the differentially methylated regions are correlated to 949 known functional genes. The top ten hypermethylated and top ten hypomethylated genes (**Table 2**), such as *S1PR1* (sphingosine-1-phosphate receptor), the expression of which can improve the

TABLE 3 | Differential methylation-associated gene KEGG pathway TOP5 in ICH.

Category	Term	Count	Bonferroni *P* value	Genes	Fold Enrichment
KEGG_PATHWAY	hsa04660:T cell receptor signaling pathway	23	6.05E-07	*PTPRC, PTPN6, ITK, TNF, VAV3, CD8A, MAP2K2, NFKBIB, PIK3CD, CD247, RAF1, IL10, NCK2, PRKCQ, MAPK1, FYN, GSK3B, PAK4, ZAP70, PIK3R5, PPP3CA, NFATC2, AKT2*	4.5922908
KEGG_PATHWAY	hsa04650:Natural killer cell mediated cytotoxicity	24	3.33E-06	*PRKCA, PRF1, ITGAL, PTPN6, TNF, VAV3, MAP2K2, CD247, PIK3CD, KLRK1, RAF1, FASLG, GZMB, MAPK1, TNFRSF10D, FYN, ZAP70, KLRC4-KLRK1, PIK3R5, PPP3CA, NFATC2, KLRD1, TYROBP, SH3BP2*	4.045667447
KEGG_PATHWAY	hsa04662:B cell receptor signaling pathway	15	9.76E-04	*PTPN6, VAV3, MAP2K2, NFKBIB, PIK3CD, RAF1, MAPK1, GSK3B, CD81, PIK3AP1, PIK3R5, CD79B, PPP3CA, NFATC2, AKT2*	4.470755694
KEGG_PATHWAY	hsa04071: Sphingolipid signaling pathway	20	9.93E-04	*PRKCA, TNF, SGPP1, MAP2K2, PPP2R5C, PIK3CD, RAF1, MAPK10, SGMS1, ADORA1, TRADD, TNFRSF1A, MAPK1, S1PR1, FYN, S1PR5, PIK3R5, PPP2R5E, PPP2R2C, AKT2*	3.427579365
KEGG_PATHWAY	hsa05205: Proteoglycans in cancer	25	0.007635914	*TNF, CAMK2G, RPS6KB2, FASLG, TGFB1, CTNNB1, IGF1R, CD44, PRKACA, PIK3R5, GPC1, CAMK2A, AKT2, PRKCA, PTPN6, ARHGEF1, MAP2K2, PIK3CD, HSPG2, RAF1, DDX5, ITPR1, MAPK1, SMO, RRAS2*	2.570684524

TABLE 4 | Top 10 methylation sites correlated with clinical outcomes and hematoma volumes.

	TargetID	*R*	*P* value	CHR	GROUP	GENE_NAME
Top 10 methylation sites correlated with clinical outcomes	cg04128563	0.759939	1.1E-06	6	TSS1500	*AMD1*
	cg21112259	-0.73267	4.2E-06	12	5'UTR;Body	*CSAD*
	cg07624428	-0.72344	6.3E-06	16		
	cg13749939	0.721965	6.7E-06	11	TSS1500	*SLC25A22*
	cg10843426	0.714226	9.3E-06	1		
	cg03770703	-0.71011	1.1E-05	1	TSS1500	*NMNAT2*
	cg27084073	-0.70993	1.1E-05	18		
	cg24764979	-0.70484	1.4E-05	16	TSS1500;5'UTR;1stExon	*GRIN2A*
	cg21669653	0.703948	1.4E-05	12		
	cg13110300	-0.70106	1.6E-05	6		
Top 10 methylation sites correlated with hematoma volumes	cg07877097	-0.80207	9.9E-08	6		
	cg01174235	-0.73588	3.6E-06	7	Body	*WBSCR17*
	cg16909124	0.727268	5.3E-06	12	TSS200	*NR2C1*
	cg20342930	-0.72361	6.2E-06	3	Body	*SPATA16*
	cg08049060	0.720711	7.1E-06	3	TSS200	*TMEM115*
	cg23684711	0.717926	8.0E-06	1	1stExon;5'UTR	*ISG15*
	cg22716633	-0.71382	9.5E-06	4	Body	*PPP2R2C*
	cg00617889	-0.71257	1.0E-05	5		
	cg04662567	-0.71024	1.1E-05	6		
	cg26260819	-0.70911	1.2E-05	11	Body;1stExon	*CRY2*

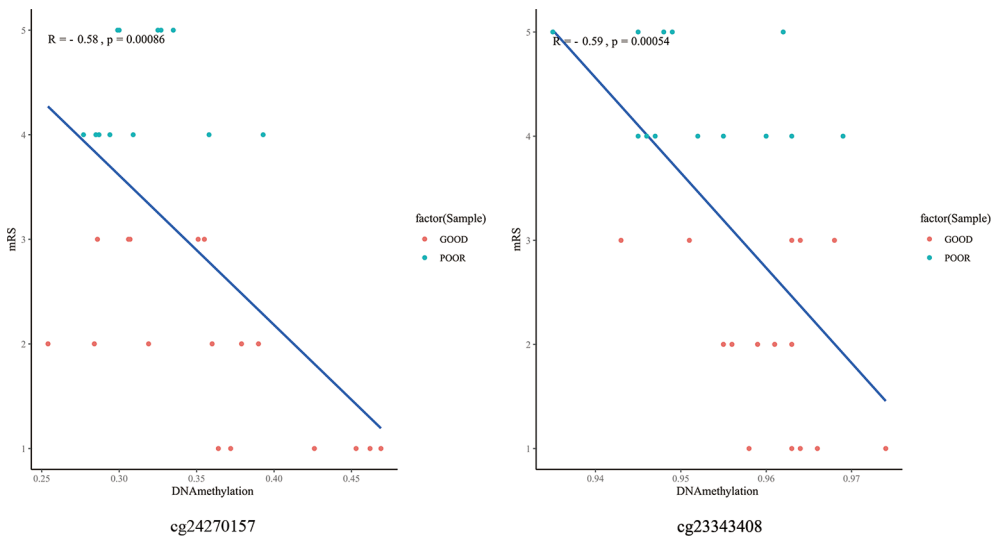

FIGURE 8 | The DNA methylation sites involved in immunological homeostasis and mRS correlation scatter plot. degrees of methylation in cg24270157, cg23343408 are negatively correlated with the 3 months mRS score (R=-0.58, R=-0.59), red dots indicate the favorable outcome patients and the blue means poor outcome.

clinical outcome of ICH, are related to the pathophysiology of ICH (25). The levels of 5-hydroxymethylcytosine in the CpG-rich regions of the *AKT2*(serine/threonine kinase 2), *PDPK1* (3-phosphoinositide dependent protein kinase 1)and *VEGF* (ascular endothelial growth factor) genes were significantly decreased and at their minimum levels, suggesting the coordinated upregulation of proinflammatory/anti-inflammatory signaling pathways and neuronal signaling systems in ICH mouse brains; furthermore, changes in the expression of these genes contribute to cell death after ICH (15). This confirms the involvement of epigenetic mechanisms such as DNA hydroxymethylation in pathological changes following ICH. Our current data revealed the hypermethylation of the promoters of the *AKT2* and *PDPK1* genes in ICH patients relative to their methylation in the control group. Studies have shown that increased expression of the *TSPO* (translocator protein) gene after ICH may be an intrinsic mechanism that prevents an increase in the inflammatory response (26). The polymorphism rs10940495 in the *IL6ST* (interleukin 6 signal transducer) gene is associated with functional outcome 6 months after ICH (27), transforming growth factor beta 1(*TGF-β1*) modulates microglia-mediated neuroinflammation after ICH and promotes functional recovery (28). The relationship between these genes and ICH needs further research.

KEGG pathway analysis showed that these genes form interconnected networks involved in the T cell receptor signaling pathway, NK cell (natural killer cell)-mediated cytotoxicity, the B cell receptor signaling pathway, the sphingolipid signaling pathway and other networks. The T cell receptor signaling network, which is a proinflammatory signaling pathway, contains three major signaling pathways, the Ca^{2+}, mitogen-activated protein kinase (MAPK) kinase and nuclear factor-κB (NF-κB) signaling pathways, that mobilize transcription factors that are critical for gene expression and for T cell growth and differentiation (29). The MAPK family is divided into three subfamilies: p38 MAPKs, extracellular signal-regulated kinases (ERK1/2) and c-Jun amino-terminal kinases (JNKs). Activation of the MAPK pathway protects against ICH-induced secondary brain injury (30). In the present study, genes in the MAPK pathway (*RAF1, MAPK1* and *MAP2K2*) were differentially methylated in ICH patients relative to their methylation status in the control group.

NF-κB signaling pathways plays a key role in immunological homeostasis (31). Previous research indicated a relationship between NF-kB and the pathobiology of perilesional cell death after ICH. In our study, it was found that the methylation pattern of partially DNA methylation sites located in the promoter region was negatively correlated with the follow-up mRS scores of ICH. And these methylation site-associated genes (*IL15, TLR5*) are related to NF-kB signaling pathways (32, 33). We speculate that hypomethylation of the promoter region of these genes may affect their expression and participate in immunological homeostasis of ICH, which is worth-study in the future.

The PI3K/Akt signaling pathway can suppress the Ca^{2+} signaling pathway by glycogen synthase kinase-3β (GSK-3β) in the T cell receptor signaling networks, and statins can increase brain-derived neurotrophic factor (BDNF) and VEGF expression, which activated the PI3K/Akt-mediated signaling signaling pathway and improved neurological function in an autologous ICH model (34). Among the various cytokines that mediate inflammatory reactions in ICH, the proinflammatory cytokines IL, tumor necrosis factor-α (TNF-α) and VEGF play important roles (35–37). In addition, altered methylation in the T cell receptor signaling networks may change the corresponding inflammatory pathways in ICH.

In the present study, genes connected with the NK pathway (*KLRK1, TGFβ1, ITGAL*) were differentially methylated in ICH patients relative to their methylation status in the control group. KLRK1, the receptor for UL16-binding proteins, is expressed on primary NK cells (38), and TGFβ1 expression dramatic reduces surface KLRK1 expression associated with impaired NK cytotoxicity (39). Previous studies suggest that polymorphisms and haplotypes in the *TGFβ1* gene are associated with cerebral infarction and ICH (40, 41). Therefore, far more research on the relationship between changes in the methylation of *KLRK1* and *TGFβ1* with ICH are needed. *ITGAL* gene, which encodes CD11a, is important in adhesive interactions between T cells and other cells of the immune system in the NK pathway. Furthermore, *ITGAL* gene promoter methylation and chromatin structure may contribute to the tissue-specific expression of CD11a (42). However, the relationship between changes in *ITGAL* methylation and ICH is unclear.

There are several limitations to this study. First, we used DNA from peripheral blood leukocytes, representing groups of different cells with different epigenetic profiles. The purpose of this study is to find out some potential epigenetic bio-marks of ICH, future research on more specific types of samples (such as NK-cells, CD8+ T-cells, Neutrophils), which by sorting of subsets by flow cytometry, may provide us with more detailed results. Secondly, the sample size needs to be increased to improve the reliability of the research in the future. Studies have found that primary damage following ICH is mainly the result of the mass effect of hematoma (43). Secondary damage in the brain following ICH occurs through the induction of hematoma toxicity, oxidative stress, cerebral edema and inflammation. Genes associated with the differentially methylated sites identified in this study are primarily involved in inflammatory pathways. DNA methylation is speculated to be involved in the inflammatory response-related mechanism of ICH, which provides new ideas for epigenetic research on ICH. Therefore, further evidence to support proteomics-related studies is still needed.

CONCLUSION

We identified 1530 differentially methylated sites between patients with ICH and normal controls for the first time with the Human Methylation 850k BeadChip. Some of the differentially methylated sites identified in the present study are associated with promoters and genes (such as *RAF1*, *MAPK1*, *MAP2K2*, *AKT2*, *KLRK1, TGFβ1, ITGAL*) important for the biological and metabolic regulation of many different inflammatory pathways. Therefore, DNA methylation may play an important role in the pathogenesis of ICH. We hope that future research will combine genomics and proteomics studies to further elucidate the mechanism of DNA methylation in ICH.

DATA AVAILABILITY STATEMENT

The datasets presented in this study can be found in online repositories. The names of the repository/repositories and accession number(s) can be found below: NCBI GEO GSE179759.

ETHICS STATEMENT

The studies involving human participants were reviewed and approved by Medical Ethics Committee of Xiangya Hospital Central South University (201503225). The patients/participants provided their written informed consent to participate in this study.

AUTHOR CONTRIBUTIONS

The co-authors YuZ and HL contributed equally to this article in clinical recruitment,drafted the manuscript and statistical analysis. LZ and YiZ designed the study. SW, MX, JL and LC

collected the samples. RC, XW and LW contributed to the reagents, materials, and analysis tools. SW, YS and WX provided technical assistance. All authors contributed to the article and approved the submitted version.

FUNDING

This study is funded by the National Science & Technology Foundational Resource Investigation Program of China (Grant No. 2018FY100900), the National Natural Science Foundation of China (Grant No.81571151), the Natural Science Foundation of Hunan Province, China (Grant No. 2016JJ2164) and the Natural Science Foundation of Hunan Province, China (Grant No. 2017JJ2356).

ACKNOWLEDGMENTS

The authors thank the patients and their caregivers who took part in the study, as well as the staff at Neurology Department of Xiangya Hospital.

REFERENCES

1. Zia E, Engstr MG, Svensson PJ, Norrving B, Pessah-Rasmussen H. Three-Year Survival and Stroke Recurrence Rates in Patients With Primary Intracerebral Hemorrhage. *Stroke* (2009) 40:3567–73. doi: 10.1161/STROKEAHA.109.556324
2. Yang QD, Niu Q, Zhou YH, Liu YH, Xu HW, Gu WP, et al. Incidence of Cerebral Hemorrhage in the Changsha Community. A Prospective Study From 1986 to 2000. *Cerebrovasc Dis* (2004) 17:303–13. doi: 10.1159/000077341
3. Liu B, Zhang L, Yang Q. Genetics of Intracerebral Hemorrhage: Insights From Candidate Gene Approaches. *Neurol India* (2012) 60:3–8. doi: 10.4103/0028-3886.93581
4. Carmichael ST, Vespa PM, Saver JL, Coppola G, Geschwind DH, Starkman S, et al. Genomic Profiles of Damage and Protection in Human Intracerebral Hemorrhage. *J Cereb Blood Flow Metab* (2008) 28:1860–75. doi: 10.1038/jcbfm.2008.77
5. Rosell A, Vilalta A, García-Berrocoso T, Fernández-Cadenas I, Montaner J. Brain Perihematoma Genomic Profile Following Spontaneous Human Intracerebral Hemorrhage. *PloS One* (2012) 6:e16750. doi: 10.1371/journal.pone.0016750
6. Portela A, Esteller M. Epigenetic Modifications and Human Disease. *Nat Biotechnol* (2010) 28:1057–68. doi: 10.1038/nbt.1685
7. Carpenter AM, Singh IP, Gandhi CD, Prestigiacomo CJ. Genetic Risk Factors for Spontaneous Intracerebral Haemorrhage. *Nat Rev Neurol* (2015) 12:40–9. doi: 10.1038/nrneurol.2015.226
8. Attwood JT, Yung RL, Richardson BC. DNA Methylation and the Regulation of Gene Transcription. *Cell Mol Life Sci Cmls* (2002) . 59:241–57. doi: 10.1007/s00018-002-8420-z
9. Qureshi IA, Mehler MF. Epigenetic Mechanisms Underlying Human Epileptic Disorders and the Process of Epileptogenesis. *Neurobiol Dis* (2010) 39:53–60. doi: 10.1016/j.nbd.2010.02.005
10. Sharma P, Kumar J, Garg G, Kumar A, Patowary A, Karthikeyan G, et al. Detection of Altered Global DNA Methylation in Coronary Artery Disease Patients. *DNA Cell Biol* (2008) 27:357–65. doi: 10.1089/dna.2007.0694
11. Lee J, Park JH, Yan BC, Kim IH, Cho G, Jeoung D, et al. Effects of Transient Cerebral Ischemia on the Expression of DNA Methyltransferase 1 in the Gerbil Hippocampal CA1 Region. *Neurochemical Res* (2013) 38:74–81. doi: 10.1007/s11064-012-0890-2
12. Zaina S, Heyn H, Carmona FJ, Varol N, Sayols S, Condom E, et al. DNA Methylation Map of Human Atherosclerosis. *Circ: Cardiovasc Genet* (2014) 7:692–700. doi: 10.1161/CIRCGENETICS.113.000441
13. O'Donnell MJ, Chin SL, Rangarajan S, Xavier D, Liu L, Zhang H, et al. Global and Regional Effects of Potentially Modifiable Risk Factors Associated With Acute Stroke in 32 Countries (INTERSTROKE): A Case-Control Study. *Lancet* (2016) 388:761–75. doi: 10.1016/S0140-6736(16)30506-2
14. Smolarek I, Wyszko E, Barciszewska AM. Global DNA Methylation Changes in Blood of Patients With Essential Hypertension. *Med Sci Monitor* (2010) 16:R149–55. doi: 10.1016/j.mehy.2009.07.026
15. Tang Y, Han S, Asakawa T, Luo Y, Han X, Xiao B, et al. Effects of Intracerebral Hemorrhage on 5-Hydroxymethylcytosine Modification in Mouse Brains. *Neuropsychiatr Dis Treat* (2016) 12:617–24. doi: 10.2147/NDT.S97456
16. Ficz G, Branco MR, Seisenberger S, Santos F, Krueger F, Hore TA, et al. Dynamic Regulation of 5-Hydroxymethylcytosine in Mouse ES Cells and During Differentiation. *Nature* (2011) 473:398–402. doi: 10.1038/nature10008
17. Bacalini MG, Gentilini D, Boattini A, Giampieri E, Pirazzini C, Giuliani C, et al. Identification of a DNA Methylation Signature in Blood Cells From Persons With Down Syndrome. *Aging* (2015) 7:82–93. doi: 10.18632/aging.100715
18. Masliah E, Dumaop W, Galasko D, Desplats P. Distinctive Patterns of DNA Methylation Associated With Parkinson Disease. *Epigenetics: Off J DNA Methylation Soc* (2013) 8:1030–8. doi: 10.4161/epi.25865
19. Woo D, Sauerbeck LR, Kissela BM, Khoury JC, Szaflarski JP, Gebel J, et al. Genetic and Environmental Risk Factors for Intracerebral Hemorrhage: Preliminary Results of a Population-Based Study * Editorial Comment: Preliminary Results of a Population-Based Study. *Stroke* (2002) 33:1190–6. doi: 10.1161/01.STR.0000014774.88027.22
20. Zeng Y, Ma M, Liu B, Xia J, Xu H, Liu Y, et al. Association Between ECE1 Gene Polymorphisms and Risk of Intracerebral Haemorrhage. *J Int Med Res* (2016) 44:444–52. doi: 10.1177/0300060516635385
21. Long HY, Feng L, Kang J, Luo ZH, Xiao WB, Long LL, et al. Blood DNA Methylation Pattern Is Altered in Mesial Temporal Lobe Epilepsy. *Sci Rep* (2017) 7:43810. doi: 10.1038/srep43810
22. Pidsley R, Zotenko E, Peters TJ, Lawrence MG, Clark SJ. Critical Evaluation of the Illumina Methylationepic Beadchip Microarray for Whole-Genome Dna Methylation Profiling. *Genome Biol* (2016) 17:208. doi: 10.1186/s13059-016-1066-1
23. Rajendram R, Ferreira JC, Grafodatskaya D, Choufani S, Chiang T, Pu S, et al. Assessment of Methylation Level Prediction Accuracy in Methyl-DNA Immunoprecipitation and Sodium Bisulfite Based Microarray Platforms. *Epigenetics* (2011) 6:410–5. doi: 10.4161/epi.6.4.14763
24. Smith ZD, Chan MM, Mikkelsen TS, Gu H, Gnirke A, Regev A, et al. A Unique Regulatory Phase of DNA Methylation in the Early Mammalian Embryo. *Nature* (2012) 484:339–44. doi: 10.1038/nature10960
25. Sun N, Shen Y, Han W, Shi K, Wood K, Fu Y, et al. Selective Sphingosine-1-Phosphate Receptor 1 Modulation Attenuates Experimental Intracerebral Hemorrhage. *Stroke* (2016) 47:1899–906. doi: 10.1161/STROKEAHA.115.012236
26. Bonsack F, Alleyne CH, Sukumari-Ramesh S. Augmented Expression of TSPO After Intracerebral Hemorrhage: A Role in Inflammation? *J Neuroinflamm* (2016) 13:151. doi: 10.1186/s12974-016-0619-2
27. El Husseini N, Hoffman BM, Bennett ER, Li Y, Williamson Taylor RA, Hailey CE, et al. Association of IL6ST (Gp130) Polymorphism With Functional Outcome Following Spontaneous Intracerebral Hemorrhage. *J Stroke Cerebrovascular Dis* (2018) 27:125–31. doi: 10.1016/j.jstrokecerebrovasdis.2017.08.017
28. Taylor RA, Chang CF, Goods BA, Hammond MD, Grory BM, Ai Y, et al. TGF-β1 Modulates Microglial Phenotype and Promotes Recovery After Intracerebral Hemorrhage. *J Clin Invest* (2016) 1:280–92. doi: 10.1172/JCI88647
29. Brownlie RJ, Zamoyska R. T Cell Receptor Signalling Networks: Branched, Diversified and Bounded. *Nat Rev Immunol* (2013) 13:257–69. doi: 10.1038/nri3403
30. Wen Z, Mei B, Li H, Dou Y, Tian X, Shen M, et al. P2X7 Participates in Intracerebral Hemorrhage-Induced Secondary Brain Injury in Rats *via* MAPKs Signaling Pathways. *Neurochemical Res* (2017) 42:2372–83. doi: 10.1007/s11064-017-2257-1
31. Andersson U, Tracey KJ. Reflex Principles of Immunological Homeostasis. *Annu Rev Immunol* (2012) 30:313–35. doi: 10.1146/annurev-immunol-020711-075015
32. Smith MF, Mitchell A, Li G, Ding S, Fitzmaurice AM, Ryan K, et al. TLR2 and TLR5, But Not TLR4, Are Required for Helicobacter Pylori-Induced NF-kB Activation and Chemokine Expression by Epithelial Cells. *J Biol Chem* (2003) 35:33552–60. doi: 10.1074/jbc.M305536200

33. Yan W, Fan W, Chen C, Wu Y, Fan Z, Chen J, et al. IL-15 Up-Regulates the MMP-9 Expression Levels and Induces Inflammatory Infiltration of Macrophages in Polymyositis Through Regulating the NF-kB Pathway. *Gene* (2016) 1:137–47. doi: 10.1016/j.gene.2016.06.055
34. Yang D, Han Y, Zhang J, Chopp M, Seyfried DM. Statins Enhance Expression of Growth Factors and Activate the PI3K/Akt-Mediated Signaling Pathway After Experimental Intracerebral Hemorrhage. *World J Neurosci* (2012) 02:74–80. doi: 10.4236/wjns.2012.22011
35. Mracsko E, Veltkamp R. Neuroinflammation After Intracerebral Hemorrhage. *Front Cell Neurosci* (2014) 8:388. doi: 10.3389/fncel.2014.00388
36. Yang G, Shao G. Elevated Serum IL-11, TNF α, and VEGF Expressions Contribute to the Pathophysiology of Hypertensive Intracerebral Hemorrhage (HICH). *Neurological Sci* (2016) 37:1253–9. doi: 10.1007/s10072-016-2576-z
37. Zheng J, Sun J, Yang L, Zhao B, Fan Z. The Potential Role of Vascular Endothelial Growth Factor as a New Biomarker in Severe Intracerebral Hemorrhage. *J Clin Lab Anal* (2017) 31:e22076. doi: 10.1002/jcla.22076
38. Sutherland CL, Chalupny NJ, Schooley K, VandenBos T, Kubin M, Cosman D. UL16-Binding Proteins, Novel MHC Class I-Related Proteins, Bind to NKG2D and Activate Multiple Signaling Pathways in Primary NK Cells. *J Immunol* (2002) 2:671–9. doi: 10.4049/jimmunol.168.2.671
39. Lee JC, Lee KM, Kim DW, Heo DS. Elevated TGF-Beta1 Secretion and Down-Modulation of NKG2D Underlies Impaired NK Cytotoxicity in Cancer Patients. *J Immunol* (2004) 172:7335–40. doi: 10.4049/jimmunol.172.12.7335
40. Tao H, Chen G, Cheng G, Shan X. The Haplotype of the Tgfβ1 Gene Associated With Cerebral Infarction in Chinese. *Can J Neurological Sci* (2012) 39:626–31. doi: 10.1017/S0317167100015365
41. Kumar P, Kumar A, Misra S, Sagar R, Farooq M, Kumari R, et al. Association of Transforming Growth Factor-β1 Gene C509T, G800A and T869C Polymorphisms With Intracerebral Hemorrhage in North Indian Population: A Case–Control Study. *Neurological Sci* (2016) 37:353–9. doi: 10.1007/s10072-015-2426-4
42. Lu Q, Ray D, Gutsch D, Richardson B. Effect of DNA Methylation and Chromatin Structure on ITGAL Expression. *Blood* (2002) 99:4503–8. doi: 10.1182/blood.v99.12.4503
43. Qureshi AI, Mendelow AD, Hanley DF. Intracerebral Haemorrhage. *Lancet* (2009) 373:1632–44. doi: 10.1016/S0140-6736(09)60371-8

Conflict of Interest: The authors declare that the research was conducted in the absence of any commercial or financial relationships that could be construed as a potential conflict of interest.

The handling editor declared a shared affiliation with the authors at time of review.

Publisher's Note: All claims expressed in this article are solely those of the authors and do not necessarily represent those of their affiliated organizations, or those of the publisher, the editors and the reviewers. Any product that may be evaluated in this article, or claim that may be made by its manufacturer, is not guaranteed or endorsed by the publisher.

frontiers in Immunology

ORIGINAL RESEARCH
published: 09 September 2021
doi: 10.3389/fimmu.2021.722479

Human Mitochondrial Ribosomal RNA Modification-Based Classification Contributes to Discriminate the Prognosis and Immunotherapy Response of Glioma Patients

Peng Wang[1,2], *Jingying Li*[3], *Miaojing Wu*[1], *Minghua Ye*[1], *Kai Huang*[1,3,4*] *and Xingen Zhu*[1,2*]

[1] Department of Neurosurgery, The Second Affiliated Hospital of Nanchang University, Nanchang, China, [2] Institute of Neuroscience, Nanchang University, Nanchang, China, [3] Comprehensive Intensive Care Unit, Second Affiliated Hospital of Nanchang University, Nanchang, China, [4] East China Institute of Digital Medical Engineering, Shangrao, China

OPEN ACCESS

Edited by:
Mingzhu Yin,
Central South University, China

Reviewed by:
Bing Feng,
École Polytechnique Fédérale de Lausanne, Switzerland
Xiuping Zhou,
Xuzhou Medical University, China

***Correspondence:**
Xingen Zhu
ndefy89006@ncu.edu.cn
Kai Huang
kaihuang@ncu.edu.cn

Specialty section:
This article was submitted to Cancer Immunity and Immunotherapy, a section of the journal Frontiers in Immunology

Received: 08 June 2021
Accepted: 24 August 2021
Published: 09 September 2021

Citation:
Wang P, Li J, Wu M, Ye M, Huang K and Zhu X (2021) Human Mitochondrial Ribosomal RNA Modification-Based Classification Contributes to Discriminate the Prognosis and Immunotherapy Response of Glioma Patients. Front. Immunol. 12:722479. doi: 10.3389/fimmu.2021.722479

Background: Epigenetic regulations of the tumor microenvironment (TME) and immunotherapy have been investigated in recent years. Nevertheless, the potential value of mitochondrial ribosomal RNA (mt-rRNA) modification in regulation of the TME and immunotherapy remains unknown.

Methods: We comprehensively investigated the mt-rRNA-modification patterns in glioma patients based on nine regulators of mt-rRNA. Subsequently, these modification patterns were correlated systematically with immunologic characteristics and immunotherapy. An "mt-rRNA predictor" was constructed and validated in multiple publicly available cohorts to provide guidance for prognosis prediction and immunotherapy of glioma patients.

Results: Two distinct patterns of mt-rRNA modification were determined based on the evidence that nine regulators of mt-rRNA correlated significantly with most clinicopathologic characteristics, immunomodulators, TME, immune-checkpoint blockers (ICBs), and prognosis. Patients with mt-rRNA subtype II presented significantly poorer overall survival/progression-free survival (OS/PFS), but higher tumor mutational burden (TMB), more somatic mutations, and copy number variation (CNV). These two mt-rRNA subtypes had distinct TME patterns and responses to ICB therapy. An mt-rRNA predictor was constructed and validated in four glioma cohorts. The subtype with high mt-rRNA score, characterized by increased TMB, infiltration of immune cells, and activation of immunity, suggested an immune-activated phenotype, and was also linked to greater sensitivity to immunotherapy using anti-programmed cell death protein 1 (PD-1) but resistance to temozolomide.

Conclusions: Regulators of mt-rRNA modification have indispensable roles in the complexity and diversity of the TME and prognosis. This novel classification based on

patterns of mt-rRNA modification could provide an effective prognostic predictor and guide more appropriate immunotherapy/chemotherapy strategies for glioma patients.

Keywords: mt-rRNA, tumor microenvironment, genomic variation, immunotherapy, temozolomide, glioma

INTRODUCTION

Gliomas are the most common primary intracranial tumors of the central nervous system. Of the subtypes of gliomas, glioblastomas are the most malignant and deadliest (1–3). The previous treatment options for gliomas (maximal resection, adjuvant chemotherapy with temozolomide, and radiotherapy) have failed to achieve satisfactory results (4). Developments in epigenetics and immunology have enabled molecular-targeted therapies and immunotherapies for gliomas. However, most of these potential new therapies are being tested in clinical trials and have not been found to significantly lengthen the survival of patients suffering from glioma (5, 6). Therefore, the exploration of novel therapeutic strategies on glioma is a long-term and arduous task.

More than 170 types of RNA modifications have been reported. These modifications are present in all living organisms and have indispensable roles in biological activities, with post-transcriptional modifications of ribosomal RNA accounting for a large proportion (7). Mammalian mitochondria possess their ribosomes. The latter consist of two subunits (large and small), which synthesize the 13 key proteins of the oxidative-phosphorylation system (8–10). Hence, homeostasis of the biogenesis and modification of mitochondrial ribosomes are essential for cellular metabolism and mitochondrial translation. Abnormal mitochondrial ribosome modification can lead to the interruption of mitochondrial protein synthesis and impedes assembly of the components of the mitochondrial respiratory chain, which usually leads to metabolic-related diseases (11, 12). With the development of cryo-electron microscopy, nine modifications of mt-rRNA have been identified. All corresponding modifying enzymes have been described to explore their effects on the biogenesis and function of mitochondria (9, 10, 12, 13). The prominent modification of mammalian mt-rRNA involves catalysis by methyltransferases consisting of TRMT2B (modifies the nucleotide m^5U429), METTL15 (modifies the nucleotide m^4C839), NSUN4 (modifies the nucleotide m^5C841), TFB1M (modifies the nucleotide $m^6_2A936/7$), TRMT61B (modifies the nucleotide m^1A947), MRM1 (modifies the nucleotide Gm1145), MRM2/FTSJ2 (modifies the nucleotide Um1369), MRM3/RNMTL1 (modifies the nucleotide Gm1370) and RPUSD4 (modifies the nucleotide Ψ1397) (11, 12, 14–16). Deeper understanding of these regulators could aid the determination of the function and mechanism of mt-rRNA modification in post-transcriptional regulation. Accumulating evidence indicates that expression disorders and genetic variations of mt-rRNA regulators are associated with developmental defects, apoptosis, cardiomyopathy, metabolic disorders, progression of malignant tumors, and immunomodulatory abnormalities (17–19).

Immunotherapy is represented by immune-checkpoint blockade. It has been studied extensively in recent years as novel and satisfactory therapy for malignant tumors. Unfortunately, immunotherapy cannot extend the survival of patients (20, 21). Numerous studies have revealed that the microenvironment of tumor cells, rather than the genetic and epigenetic variations of tumor cells, plays an essential part in the occurrence and malignant progression of tumors (22). Further study of the tumor microenvironment (TME) has revealed its important role in tumor progression, immune escape, and immunotherapy response. Anti-programmed cell death protein 1 (PD-1) and its ligand (PD-L1) are the most studied and most efficacious immune-checkpoint blockers (ICBs). They mainly regulate the immune response of T cells in the TME so as to avoid anti-tumor immune reactions, and then attack the tumor (21, 23). Anti-PD-1 has been used in the treatment of melanoma, non-small-cell lung cancer, and colon cancer, but its clinical efficacy against glioma is not high. Several studies have revealed that the relatively high immunosuppressive microenvironment and low tumor mutational burden (TMB) may lead to immunotherapy failure (24–26). Therefore, the selection of suitable immunotherapy for glioma patients through comprehensive analyses of transcriptional regulations, genetic variations, and the immune microenvironment of gliomas may be challenging.

In this study, we analyzed the expression patterns and immunological value of the regulators of mt-rRNA modification. Based on the features of nine mt-rRNA regulators, we identified two patterns of mt-rRNA modification in glioma patients which had distinct functional annotations, clinicopathologic characteristics, and survival outcomes. Subsequently, integrated analyses revealed significant differences in genomic variation, the TME, and ICB expression levels between the two subtypes of patients, and determined the different responses to immunotherapy. Therefore, we constructed an "mt-rRNA predictor" that could distinguish the two mt-rRNA subtypes of glioma patients and verified it in four independent cohorts of glioma patients. This mt-rRNA predictor could provide a selection strategy for screening glioma patients who elicit a positive response to immunotherapy or temozolomide therapy. In this way, we aimed to provide novel ideas for survival prediction and better targeted therapy for glioma patients according to the classification of mt-rRNA modification patterns.

MATERIALS AND METHODS

The flowchart of this work is shown as **Figure 1**.

Acquisition and Preprocessing of Datasets From Glioma Patients

Data on RNA-sequencing, somatic mutations, and copy number, as well as the matched clinical data of glioma patients, were

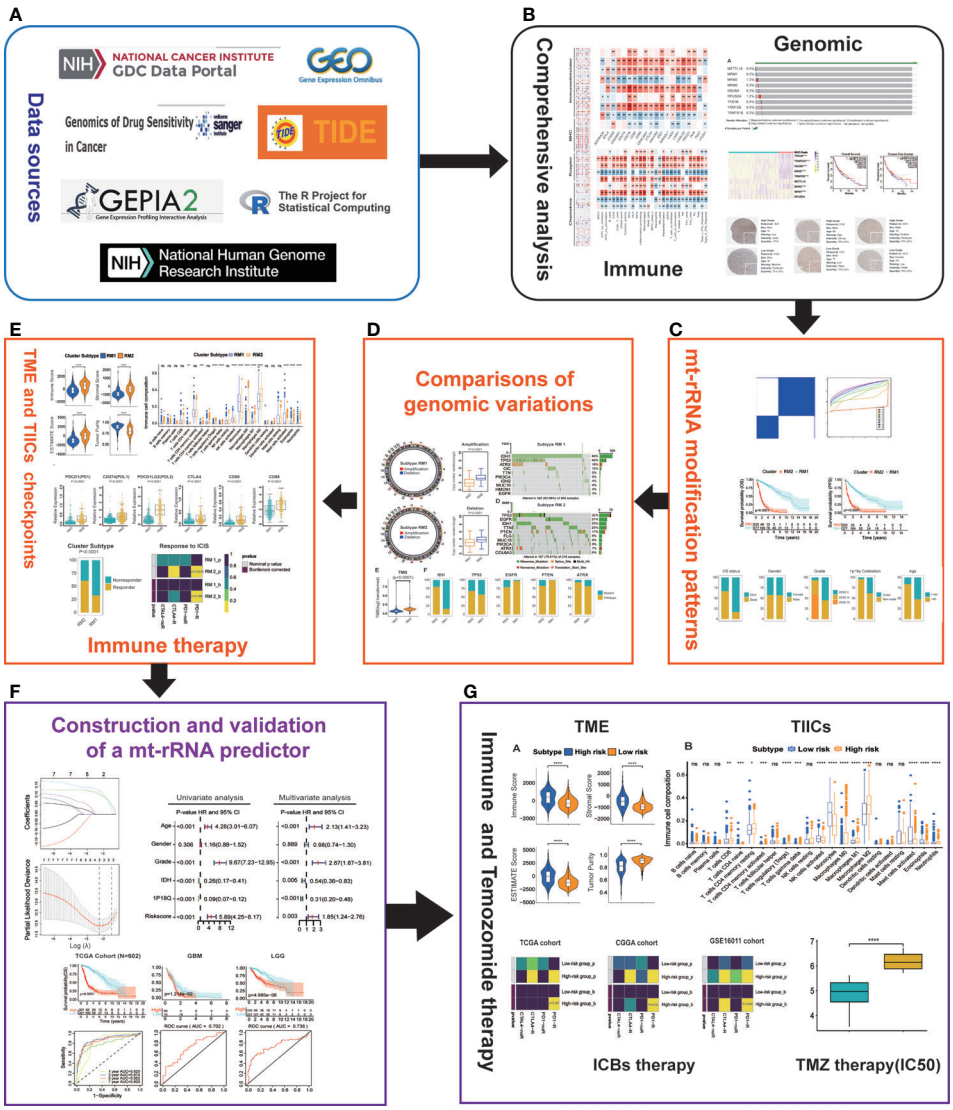

FIGURE 1 | Overview of this study. **(A)** Data sources and analytic software used in this study. **(B)** Comprehensive analyses of nine regulators of mt-rRNA modification. **(C)** Identification of the patterns of mt-rRNA modification. **(D)** Comparisons of genomic variations between two patterns of mt-rRNA modification. **(E)** Correlations between the patterns of mt-rRNA modification and immunologic elements and immunotherapy. **(F)** Construction and validation of a mt-rRNA predictor and the prognostic role of this mt-rRNA predictor in glioma. **(G)** Role of this mt-rRNA predictor in predicting the response to ICB immunotherapy and temozolomide chemotherapy. Significance: ns, $P > 0.05$, $^{*}P < 0.05$, $^{**}P < 0.01$, $^{***}P < 0.001$, $^{****}P < 0.0001$.

obtained from The Cancer Genome Atlas (TCGA; https://portal.gdc.cancer.gov/), Chinese Glioma Genome Atlas (CGGA; www.cgga.org.cn/) and Gene Expression Omnibus (GEO; www.ncbi.nlm.nih.gov/geo/) databases. After excluding patients with incomplete clinical information, 1136 glioma samples (TCGA, n = 602; CGGA, n = 286; microarray data (GSE16011), n = 248) were gathered for further analyses. Subsequently, transcripts per kilobase million (TPM) values of RNA-sequencing data, robust multichip averaging analysis (RMA)-processed values of microarray data (GSE16011), RNA-sequencing data (RSEM value), and real-time reverse transcription-quantitative polymerase chain reaction (RT-qPCR) data (SAHNU cohort) of clinical samples were log2-transformed and normalized to make the gene-expression profiles of different platforms comparable. The clinical information of the 1136 public glioma patients is displayed in **Supplementary Table S1**. Furthermore, the somatic-mutation data and frequencies of genes (in mutation annotation format) were analyzed using "maftools" within R (R Institute for Statistical Computing, Vienna, Austria; www.r-project.org/). Amplification or deletion of copy number variation (CNV) data were identified using the GISTIC algorithm (27). Moreover, the half-maximal inhibitory concentration (IC50) of Temozolomide in glioma patients and matched RNA-sequencing data were downloaded from the

Genomics of Drug Sensitivity in Cancer (GDSC) database (www.cancerrxgene.org/) (28).

Frozen specimens of glioma used in the present study were obtained from patients who underwent surgery at The Second Affiliated Hospital of Nanchang University (SAHNU) from 2015 to 2020. Clinical information was obtained through electronic medical records. Overall survival (OS) data were not available because information based on telephone follow-up were missing. Thirteen samples of high-grade glioma (World Health Organization (WHO) grade III, IV), 12 samples of low-grade glioma (WHO grade II), and eight samples of non-neoplastic brain tissue (NBT; collected from surgery of people with intractable epilepsy, and which were used as controls) were employed. The clinical information of these 33 patients is also displayed in **Supplementary Table S1**.

Ethical Approval of the Study Protocol

The study protocol was approved by the medical ethics committee of the Second Affiliated Hospital of Nanchang University (Nanchang, China) and was undertaken in accordance with the Helsinki Declaration 1964 and its later amendments. Written informed consent was acquired from each glioma patient.

Immunohistochemistry

The immunohistochemistry of pathologic specimens of the nine regulators of mt-rRNA modification were downloaded from The Human Protein Atlas (www.proteinatlas.org/). Meanwhile, the quantity and intensity of Staining as well as the information of patients were acquired online.

Immunological Features of the TME in Glioma

The immunological features of the TME in glioma were evaluated: expression of immunomodulators; abundances of immune cells and stromal cells; infiltration level of tumor-infiltrating immune cells (TIICs); ICBs expression level. First, we obtained the composition of 122 immunomodulators (immune stimulators, major histocompatibility complex molecules, chemokines, and receptors) from the research of Charoentong et al., and collected 28 ICBs with therapeutic potential from the work of Auslander and colleagues (29, 30). The ESTIMATE algorithm was utilized to evaluate the abundance of immune cells and stromal cells, as well as the tumor purity based on the expression profiles of glioma patients (31). Four types of scores were generated by the ESTIMATE algorithm: positively reflecting the abundance of stromal cells (stromal score), positively reflecting the abundance of immune cells (immune score), positively reflecting nontumor composites (ESTIMATE score), and tumor purity. We also calculated the infiltration level of 22 types of TIICs in the TME based on the expression profiles of glioma samples using a deconvolution method according to linear support vector regression (CIBERSORT) (32). Thereafter, the enrichment score of 29 "immune signatures" (including the types, functions, and molecular pathways of TIICs and the immune activity of tumors) were quantified using single-sample gene-set enrichment analysis (ssGSEA) according to the method described by Xu and colleagues (33).

Unsupervised Clustering of mt-rRNA Regulator-Based Classification of Glioma Patients

The expression levels of nine regulators of mt-rRNA modification were extracted from the TCGA dataset for further classifying (34). Unsupervised clustering analysis based on a machine-learning algorithm (k-means) was undertaken to identify distinct patterns of mt-rRNA modification according to the expression profiles of nine mt-rRNA regulators, and we classified glioma patients for further evaluation. The number of clusters and their stability was determined comprehensively by the steps mentioned above as well as 1000-times repetitions, the relative change in the area under the cumulative distribution function (CDF) curve, and the consensus "heatmap" based on the "ConsensusClusterPlus" package in R (35). We further explored the correlation between clinicopathologic features and mt-rRNA subtypes of glioma patients. Survival analyses using the Kaplan–Meier method were used to investigate the prognosis of glioma patients with different mt-rRNA subtypes: OS and PFS.

TMB and CNV Between Two mt-rRNA Subtypes

Maftools and GenVisR were run to analyze and visualize the mutation types and frequencies of genes between two mt-rRNA subtypes (36, 37). The TMB is the total number of nonsynonymous mutations and is an emerging biomarker for the response to immunotherapy. The TMB was compared among different subtypes of mt-rRNA-modification patterns. In addition, significant amplifications and deletions in the whole genome were identified and visualized further using "RCircos" within R (38).

Functional Annotation and Gene Set Variation Analysis

We wished to explore the significantly enriched molecular pathways of the different subtypes of mt-rRNA-modification patterns. Hence, we undertook GSVA (a non-parametric and unsupervised method) using the R package "GSVA "based on the gene sets of "c2.cp.kegg.v6.2.symbols", which we downloaded from the Molecular Signatures Database (MSigDB) database (www.gsea-msigdb.org/gsea/msigdb/) (39). The KEGG pathways with an adjusted $P < 0.05$, $|\log2 \text{ fold change (FC)}| > 0.1$ and false discovery rate (FDR) < 0.05 were considered significant between the two mt-rRNA subtypes.

Prediction of ICB Therapy Response

Tumor Immune Dysfunction and Exclusion (TIDE; http://tide.dfci.harvard.edu/) is an algorithm used to determine the characteristics of T-cell dysfunction by testing how the expression of each gene in a tumor interacts with the level of cytotoxic T lymphocyte (CTL) invasion to affect the survival of patients and response to immunotherapy (40). We predicted the clinical response of glioma patients to immunotherapy using the TIDE algorithm based on the expression profiles in each cohort.

Subsequently, the clinical response to ICB therapy was also predicted with the subclass mapping (https://cloud.genepattern.org/gp/) method (41). Bonferroni-corrected $P < 0.05$ was considered to be a significant response or non-response to therapy using anti-PD1 or anti-CTLA4 with the cutoff FDR < 0.05.

Construction and Validation of the mt-rRNA Predictor

The total of 1136 glioma patients were classified into a training set (TCGA) and three validation sets (CGGA, GSE16011, SAHNU). First, in the training set, we undertook univariate Cox analysis of these mt-rRNA regulators using the R package "survival". Subsequently, the least absolute shrinkage and selector operation (LASSO) algorithm was utilized to select optimal-candidate differentially expressed mt-rRNA regulators with the best discriminative capability in the training set. Then, we constructed an mt-rRNA predictor based on the expression profiles of mt-rRNA regulators weighted using the multivariate Cox regression coefficient as follows:

$$mt - rRNA\ score = \sum_{i=1}^{n}(Coef_i + Exp_i)$$

where $Coef_i$ is the coefficient and Exp_i is the expression of mt-rRNA-modification regulators. The coefficient of each regulator was also obtained to calculate the mt-rRNA score in the validation sets. Specifically, glioma patients were classified into low-score and high-score subtypes based on the median mt-rRNA score. The prognostic importance of the mt-rRNA predictor was assessed between the two subtypes using the Kaplan–Meier method, and the prediction efficiency was tested further with receiver operating characteristic (ROC) curves. Moreover, univariate and multivariate Cox regression analyses were carried out to explore the prognostic value of the mt-rRNA predictor with multiple clinical and molecular pathologic characteristics. Similar methods were used to verify the predictive performance of mt-rRNA predictor in the validation sets.

Chemotherapeutic Response to TMZ

Temozolomide is first-line chemotherapy for glioma patients. We obtained the IC50 of temozolomide in glioma specimens and RNA-sequencing data from the largest publicly available pharmacogenomics database (GDSC) and normalized them by log2-transformation for further analyses. Glioma specimens treated with temozolomide were divided into two groups according to the median mt-rRNA score.

Quantitative Real-Time Polymerase Chain Reaction of the SAHNU Cohort

We used methods we described previously to measure mRNA expression of regulators of mt-rRNA modification in glioma specimens (42). Briefly, total RNA was extracted from brain tissue and reverse-transcribed into complimentary-DNA. Next, relative mRNA expression of genes was normalized to that of GAPDH, and we evaluated the fold change using the $2^{-\Delta\Delta CT}$ method. The primer sequences used for RT-qPCR were obtained from RiboBio (Guangzhou, China) and were as follows: MRM2 forward 5'-GTGATTCTGAGCGACATGGC-3', reverse 5'-ATGACTCTTTCCTGCTGGCT-3'; TRMT2B forward 5′-TCAAGAGTCCTAAATGCACAACC-3′, reverse 5′-CCAG GAGTCATCTCTACAATGC –3′.

Statistical Analyses

Correlations between variables were assessed using Spearman or Pearson correlation analyses. Variables with a normal distribution were analyzed by the unpaired Student's t-test. Variables with a non-normal distribution were analyzed by the Mann–Whitney U-test. For comparisons of categorical variables, the Kruskal–Wallis test and one-way ANOVA were used for non-parametric and parametric methods, respectively. The Kaplan–Meier method was employed to calculate the survival curve of categorical variables, whereas the log-rank test was used to estimate significance. According to the method of Hoshida and colleagues, the Bonferroni correction was applied to correct nominal P-values in the subgroup analysis of ICB immunotherapy. Statistical analyses were carried out using R 3.6.5, and $P < 0.05$ (two-sided) was considered significant.

RESULTS

The Value of Nine mt-rRNA Modification Regulators in Gliomas

Considering the possible biological functions of mt-rRNA-modification enzymes in gliomas, we conducted a comprehensive study on these regulators in TCGA cohort. As shown in a heatmap, the expression of most regulators of mt-rRNA modification was associated significantly with the WHO grade (**Supplementary Figure S1A**). Measurement of expression of each dysregulated mt-rRNA-modification regulator showed MRM1, TRMT2B, TFB1M, MRM3, NSUN4, TRMT61B, and MRM3 to be correlated significantly with each WHO grade (**Figure 2B**). Moreover, we observed protein expression of MRM1, MRM3, TRMT2B, and NSUN4 to be significantly different between low- and high-grade gliomas, whereas other regulators could not be obtained due to lack of data (**Supplementary Figures S1B–D**). Afterwards, we undertook survival analyses (OS and PFS) using the GEPIA2 website. Glioma patients were stratified into low- and high-expression groups based on the median expression of each regulator of mt-rRNA modification, respectively. Survival analyses using the Kaplan–Meier method indicated that these regulators of mt-rRNA modification were prognostic biomarkers in OS and PFS ($P < 0.01$ for all) (**Supplementary Figure S2A**), except for METTL15 (**Supplementary Figure S2B**). Furthermore, we observed that the genomic alterations (somatic mutations and CNVs) of the nine regulators of mt-rRNA modification were very rare (≤1.2% for all) (**Supplementary Figure S3A**) in gliomas using the "cBioPortal" of TCGA. All these results suggested that the aberrant expression of mt-rRNA regulators has the potential to be a prognostic biomarker, which is not generated by genetic mutations.

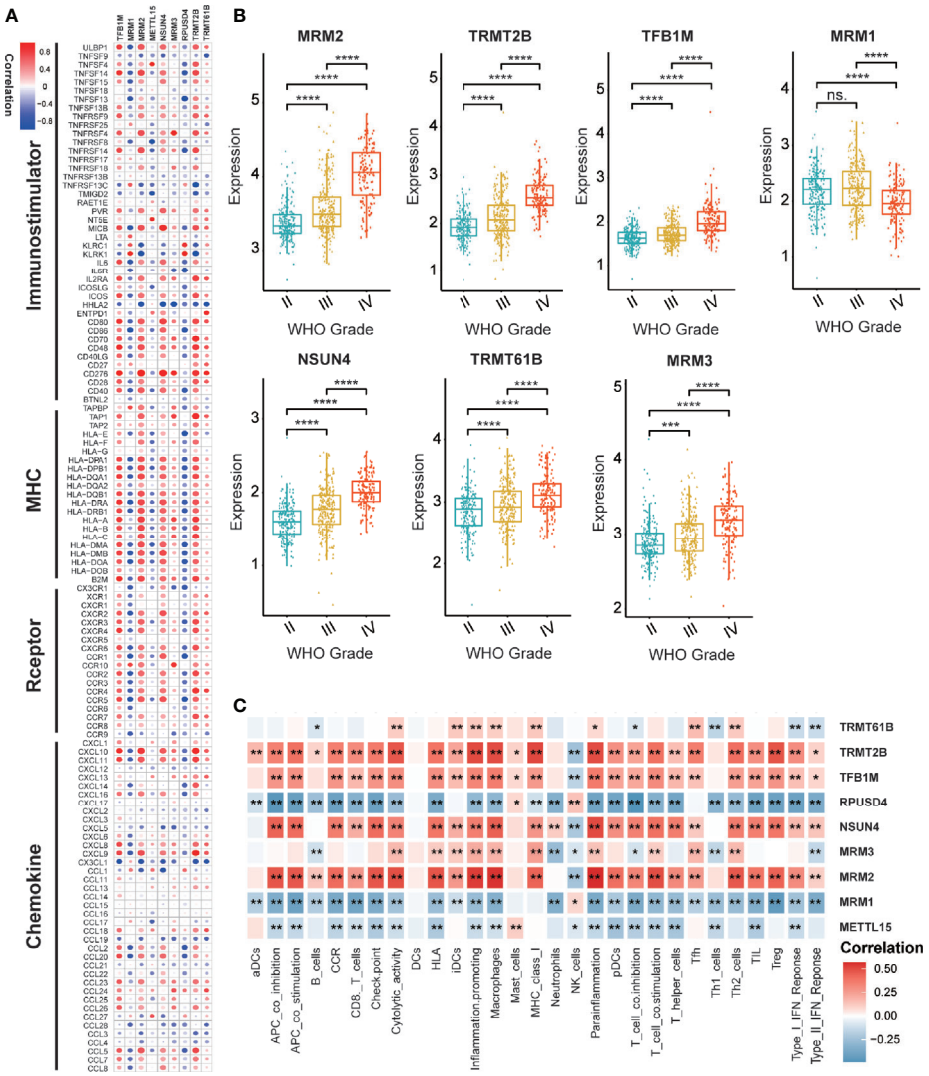

FIGURE 2 | Value of regulators of mt-rRNA modification in gliomas. **(A)** Correlation between nine regulators of mt-rRNA modification and 122 immunomodulators. **(B)** Expression of each dysregulated mt-rRNA-modification regulator. **(C)** Correlation between nine mt-rRNA-modification regulators and 29 immune signatures. Significance: ns P > 0.05, *P < 0.05, **P < 0.01, ***P < 0.001, ****P < 0.0001.

Correlation analyses aimed at exploring the immunological value of regulators of mt-rRNA modification are critical in determining the potential of immunotherapy. Our findings revealed that MRM2, NSUN4, TFB1M, and TRMT2B were correlated significantly with most immunomodulators in glioma, whereas MRM1 and RPUSD4 were correlated negatively (**Figure 2A**). Enrichment of immune signatures in the TME of glioma was also estimated using the ssGSEA algorithm, and the appearance of most of the regulators of mt-rRNA modification was correlated with levels of TIIC infiltration (**Figure 2C**). Furthermore, expression of regulators of mt-rRNA modification was associated with major moieties associated with immune checkpoints in glioma, especially PD-L1, PD-1, CD80, CD274, TIM3, and IDO1 (**Supplementary Figure S3B**). In summary, the above results suggested that the aberrant expression of mt-rRNA regulators in gliomas was TME-specific, which indicates the potential value of mt-rRNA regulators as targets for tumor immunotherapy.

Identification of Two Subtypes With Distinct Functional Annotations, Clinicopathological Features, and Clinical Outcomes

Glioma patients were classified into qualitatively different patterns of mt-rRNA modification based on the expression levels of nine regulators of mt-rRNA modification using the ConsensusClusterPlus algorithm. According to the relative change in the area under the CDF curve and the consensus heatmap, k = 2

seemed to be an adequate selection (**Figure 3A** and **Supplementary Figures S3C, D**). Hence, two distinct subtypes were identified: mt-rRNA modification 1 (RM1, n = 377, 62.6%) and mt-rRNA modification 2 (RM2, n = 225, 37.4%). Prognostic analysis for the two subtypes revealed that RM1 had a particularly significant survival advantage over RM2 in OS and PFS (**Figures 3B, C**). Subsequently, the clinicopathologic features of glioma patients with the two subtypes were compared (**Figure 3D** and **Supplementary Table S2**). The proportion of surviving patients (83%), younger in age at the diagnosis (53%), and 1p19q-codeletion status (38%) in RM1 were significantly higher than that for RM2 (surviving patients, 33%; younger in age at the diagnosis, 16%; 1p19q-codeletion status, 4%). Moreover, patients with the RM2 subtype had a higher WHO grade ($P < 0.0001$). However, there was no difference in gender between the two subtypes (**Figure 3E**).

GSVA was conducted to explore the molecular pathways and potential mechanisms related to the two subtypes of mt-rRNA modification of glioma patients. We identified 135 differentially enriched molecular pathways: 36 pathways enriched in RM1 and 99 pathways enriched in RM2 (**Supplementary Table S3**). RM1-subtype tumors were correlated mainly with the tumor metabolism-related mechanisms (e.g., PROPANOATE_METABOLISM and BUTANOATE_METABOLISM) and pathway (e.g., "MTOR_SIGNALING_PATHWAY"). RM2-subtype tumors were correlated mainly with the genesis and development of tumors (e.g., "focal adhesion and apoptosis"), cancer-related signaling pathways (e.g., "P53 signaling pathway", "cell cycle and chemokine signaling pathway"), and immune responses (e.g., "T and B cell receptor signaling pathway", "antigen processing and presentation", and "natural killer cell-mediated cytotoxicity") (**Figure 4A**).

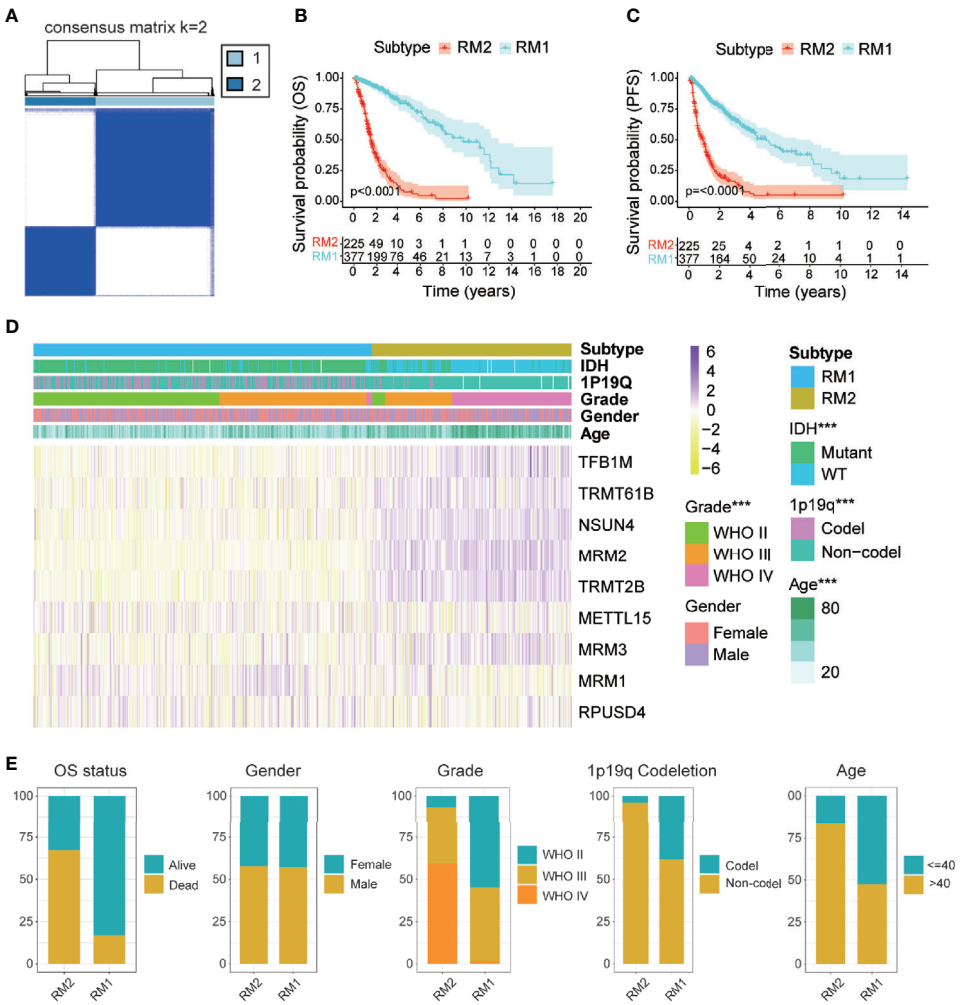

FIGURE 3 | Comparisons of clinicopathologic features between two subtypes of mt-rRNA modification in TCGA cohort. **(A)** Consensus clustering matrix for the optimal number, k = 3. **(B, C)** Kaplan–Meier analyses for patients with the two subtypes of mt-rRNA modification. **(D)** Correlation between subtypes of mt-rRNA modification and clinicopathologic features. **(E)** Comparisons of OS status, gender, WHO grade, 1p19q codeletion, and age between two types of mt-rRNA modification. Significance: ***$P < 0.001$.

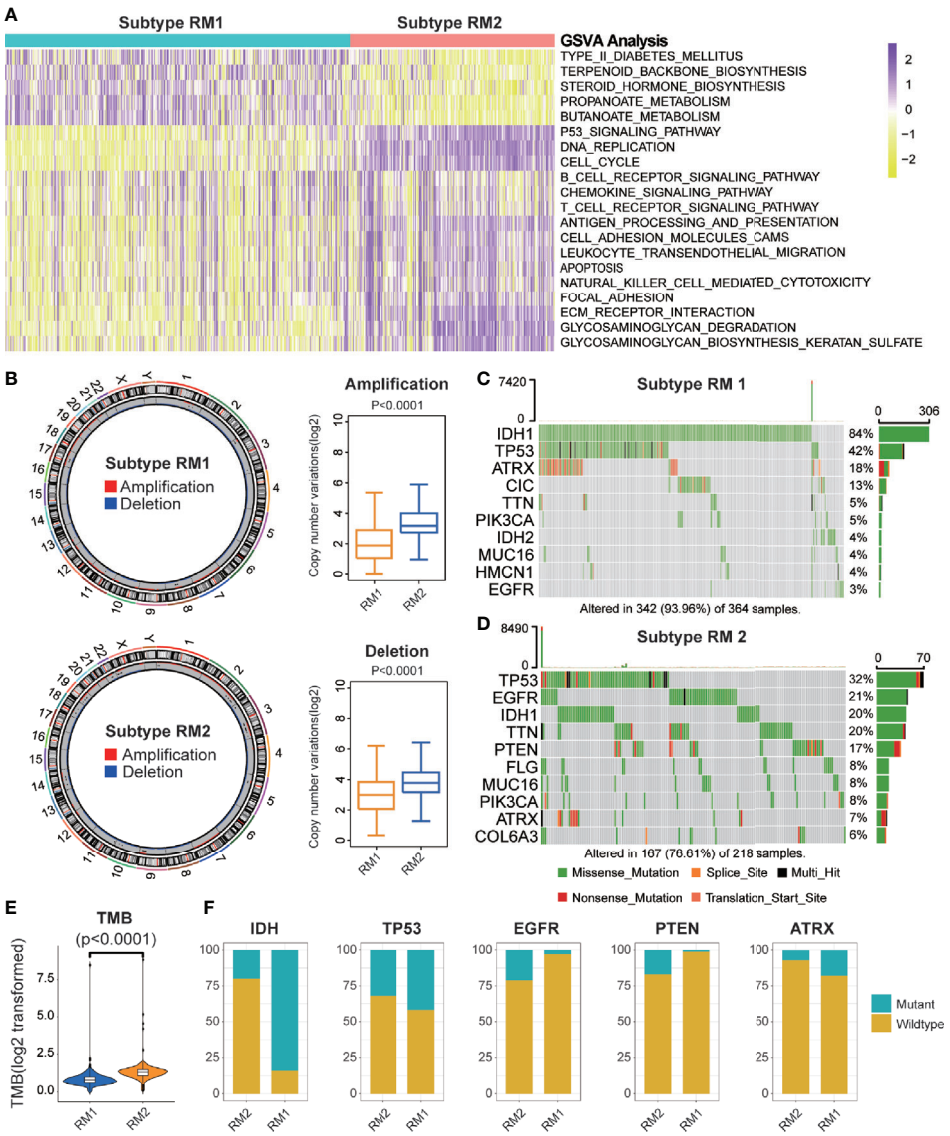

FIGURE 4 | Functional annotation and genomic variations of two subtypes of mt-rRNA modification. **(A)** Heatmap of the top-20 differentially enriched molecular pathways between two types of mt-rRNA modification (yellow = high score and purple = low score). **(B)** Left: Circos plots illustrating the amplification and deletion of two subtypes. Right: Significant difference in CNV frequencies between two subtypes. **(C, D)** The waterfall plots illustrate the top-10 somatic mutations in tumors for two subtypes. **(E)** The different TMB between the two subtypes. **(F)** Comparisons of IDH, TP53, EGFR, PTEN, and ATRX mutations between two subtypes.

Differences in Genomic Variation Between the Two Subtypes

Considering the indispensable role of genomic variation in the infiltration pattern of immune cells and regulation of tumor immunity, we undertook analyses of CNV and somatic mutation to explore the distinct genomic alterations in the different subtypes of mt-rRNA modification. The frequency of CNV, both amplification ($P < 0.001$) and deletion ($P < 0.001$), in patients with RM2, was significantly higher than that in patients with RM1 (**Figure 4B**). Afterwards, a "waterfall" map of somatic mutations showed that each subtype of mt-rRNA modification had specific mutated genes (**Figures 4C, D**). The proportion of RM2-subtype patients with mutations of IDH1 (20%), ATRX (7%), EGFR (21%), and PTEN (17%) was significantly different from those with the RM1 subtype ($P < 0.01$ for all), whereas there was no significant difference in the mutation frequency of TP53 (**Figure 4F**). Moreover, patients tended to bear a higher TMB in the RM2 subtype than that in the RM1 subtype ($P < 0.0001$) (**Figure 4E**). Taken together, these findings suggested that glioma patients with a different subtype of mt-rRNA modification could have differences in response to immunotherapy.

Distinct Immunological Characteristics and Immunotherapy of the Two mt-rRNA Modification Subtypes

To investigate the immunologic characteristics of glioma patients, we first used the ESTIMATE algorithm to reveal the TME compositions of the two subtypes of mt-rRNA modification. Compared with patients with the RM1 subtype, patients with the RM2 subtype possessed higher stromal, immune, and ESTIMATE scores, accompanied by lower tumor purity ($P < 0.0001$ for all) (**Figure 5A**). Afterwards, the CIBESORT algorithm was used to quantify the TIIC abundance of glioma patients. Most subsets of CD4+T cells and macrophages as well as neutrophils infiltrated in the RM2 subtype, whereas activated natural killer (NK) cells, mast cells, monocytes, and eosinophils infiltrated in the RM1 subtype (**Figure 5B**). These analyses suggested that the RM2 subtype was associated with higher levels of TIIC infiltration and lower tumor purity, which could have implications for immunotherapy.

Most immune-checkpoint molecules were significantly different between the two subtypes, among which expression of PD1, CTLA, and their ligands (PD-L1, PD-L2, CD80 and CD86, $P < 0.0001$ for all) was significantly higher in the RM2 subtype (**Figure 5C**). Moreover, we also investigated the correlation between the marker of M2-type (MRC1/CD206 and CSF1R/CD115) and different mt-rRNA subtypes. It revealed that the expression of MRC1 was significantly lower in the RM2 subtype, while CSF1R represented no difference (**Figure 5D**). The results indicated that macrophages were mainly polarization toward the M1-type state (which markers are CD80 and CD86) in the RM2 subtype. Based on these results, we used the TIDE algorithm to predict the potential response to immunotherapy in glioma patients. The number of immunotherapy responders with the RM2 subtype was nearly twice that of immunotherapy responders with the RM1 subtype (61% vs. 32%, $P < 0.01$) (**Figure 5E**). Then, subclass mapping was utilized to predict the response of the two subtypes of mt-rRNA modification to ICB therapy (anti-PD1 and anti-CTLA4). Patients with the RM2 subtype were more sensitive to anti-PD1 treatment (Bonferroni $P = 0.0096$) (**Figure 5F**).

Identification and Validation of a mt-rRNA Regulator Predictor

We used bulk RNA-sequencing data from four independent glioma cohorts (TCGA, CGGA, GSE16011, and SAHNU databases) to explore the value of these mt-rRNA regulators for clinical application. First, in the training set, we found eight mt-rRNA regulators to be correlated significantly with OS ($P < 0.01$), which was consistent with our predictions using the GEPIA2 website (**Figure 6A**). Among these genes, MRM2, MRM3, NUSN4, TFB1M, TRMT2B, and TRMT61B acted as protective factors, whereas MRM1 and RPUSD4 acted as risk factors. Hence, the LASSO Cox regression algorithm was employed to the relevant patterns of mt-rRNA modification *via* expression of the most critical eight regulators in the TCGA cohort, which acted as the training set (**Supplementary Figures S3E, F**). Two regulators of mt-rRNA modification (MRM2 and TRMT2B) were selected to construct the model of risk prediction. The formula used for calculation of the mt-rRNA score was: mt-rRNA score = 0.108 × (MRM2 expression) + 0.125 × (TRMT2B expression). According to the median mt-rRNA score, glioma patients were divided into a low-risk subtype and a high-risk subtype in TCGA, CGGA, GSE16011, and SAHNU cohorts. Afterwards, we explored the association and demographic features between the mt-rRNA score and each clinicopathologic feature (**Figure 6B** and **Supplementary Table S4**). The mt-rRNA score was significantly different between glioma patients stratified by OS status, WHO grade, 1p19q codeletion, and IDH status, but not by gender in the training set (**Figure 6C**). Similar results were observed in the validation sets, CGGA cohort, and GSE16011 cohort (**Supplementary Figures 4A, B**). In addition, we explored relative mRNA expression of MRM2 and TRMT2B using RT-qPCR. Results revealed that MRM2 and TRMT2B were differentially expressed between NBTs, low-grade glioma tissues, and high-grade glioma tissues (**Supplementary Figure 5B**). We also found the mt-rRNA score to be correlated significantly with WHO grade ($P = 0.004$) and age ($P = 0.008$) in the SAHNU cohort (**Supplementary Figure 5A, C**).

Moreover, glioma patients with the low-risk subtype presented significantly better OS ($P < 0.0001$) (**Figure 6D**) and PFS ($P < 0.0001$; **Supplementary Figure 5D**) in the training set. ROC analyses revealed the predictive efficiency at 1, 3, 5, and 7 years (area under the ROC curve (AUC >0.75 for all) for distinguishing the low-risk subtype and high-risk subtype in the training set (**Figure 6G** and **Supplementary Figure S5E**). Consistently, the mt-rRNA predictor had excellent performance in discriminating the outcomes (**Figures 6E, F**) for glioma patients as evaluated in the two validation sets, with powerful predictive efficiency (AUC >0.7 for both) (**Figures 6H, I**). We also explored the prognostic value of the mt-rRNA predictor for different WHO grades. Survival analyses using the Kaplan–Meier method demonstrated that patients with lower-grade glioma and glioblastoma (GBM) patients with low-risk scores presented significantly better OS in the CGGA and GSE16011 cohorts (**Supplementary Figures S6C, D**), data which were consistent with the results in TCGA cohort (**Supplementary Figure S6A**). However, there was no difference in PFS between glioblastoma patients stratified by the mt-rRNA score in the TCGA cohort (**Supplementary Figure S6B**). Univariate and multivariate Cox regression analyses for the three cohorts revealed significant associations between the mt-rRNA predictor and OS/PFS in TCGA, CGGA, and GSE16011 cohorts ($P < 0.05$ for all) (**Supplementary Figure S7A–D**), which indicated that the mt-rRNA predictor was an independent prognostic indicator. Taken together, these results indicated that the mt-rRNA predictor calculated using the mt-rRNA score could predict the prognosis and clinicopathologic features of glioma patients accurately.

The High-Risk Subtype Exhibited Greater Sensitivity to Immunotherapy but Was Resistant to Temozolomide

First, TME patterns were also estimated in the CGGA and GSE16011 cohorts using the same method. Similar to the results of TCGA (**Figure 7A**), the stromal, immune, and

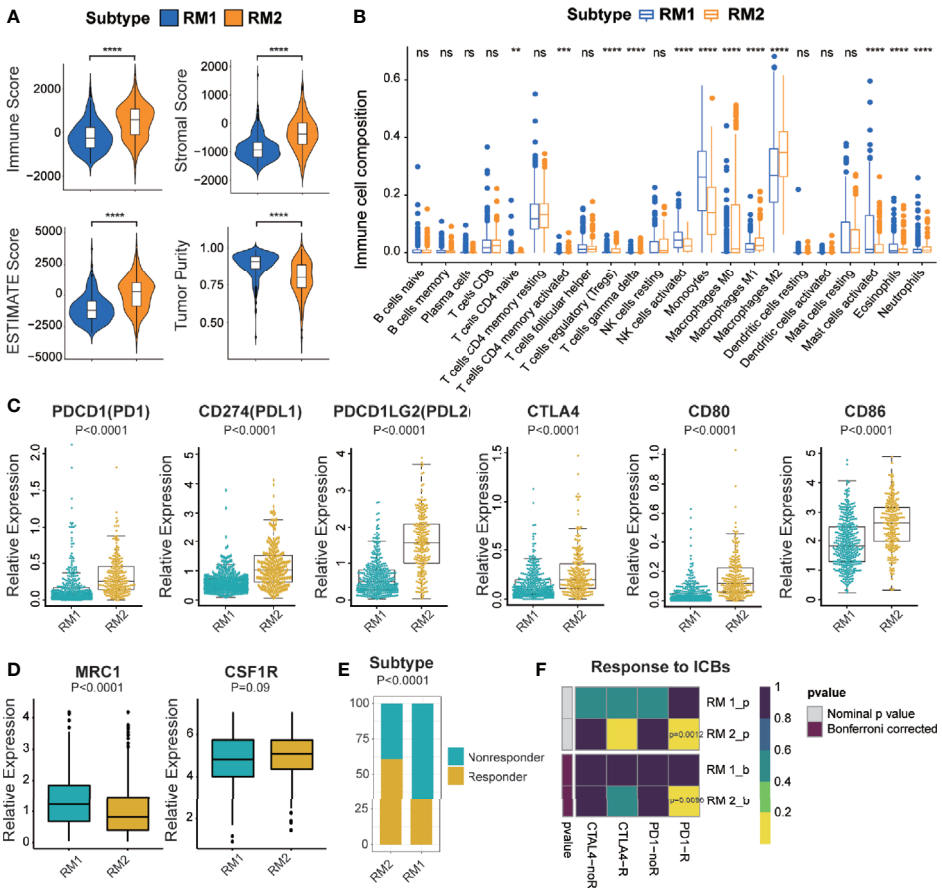

FIGURE 5 | Different TME characteristics and response to immunotherapy of two subtypes in TCGA cohort. **(A)** Comparisons of immune score, stromal score, tumor purity, and ESTIMATE score between two subtypes. **(B)** Difference in the abundance of TIICs between two subtypes. **(C, D)** Different levels of ICBs between two subtypes. **(E)** Different proportions of responders and non-responders to immunotherapy between two subtypes. **(F)** Prediction of response to ICBs (PD1 and CTLA4) therapy in different subtypes. Significance: ns $P > 0.05$, < 0.05, $^{**}P < 0.01$, $^{***}P < 0.001$, $^{****}P < 0.0001$.

ESTIMATE scores were significantly higher and the tumor purity was lower in the high-risk subtype (P < 0.05 for all), which indicated the high abundance of stromal cells and immune cells and low tumor purity in the high-risk subtype (**Supplementary Figures S8A, C**). CIBERSORT analyses further revealed that memory resting T cell CD4, resting NK cells, and most macrophage subsets were infiltrated significantly in the high-risk subtype, whereas activated NK cells and mast cells were abundant in the low-risk subtype. (**Figure 7B** and **Supplementary Figures S8B, D**). Subsequently, we also investigated the relationship between the expression of immune-checkpoint molecules and mt-rRNA score in the three cohorts. We found most of the immune-checkpoint molecules were associated with the mt-rRNA score (**Supplementary Figures S7A–C**). For the well-known ICBs, the expression of PD1 and its ligands PD-L1 and PD-L2 was correlated significantly with the mt-rRNA score, but the correlation between CTLA4 and the mt-rRNA score was poor (**Figure 7C**). These ICBs were also expressed differently between the two subtypes in the validation sets (**Supplementary Figures S9D, E**), with the exception of the ligands of CTLA4 in the GSE16011 cohort (**Supplementary Figure S9E**). Moreover, patients tended to bear a higher TMB in the high-risk subtype than that in the low-risk subtype (P < 0.0001, **Figure 7D**).

On the basis of the above findings, the TIDE algorithm was employed to predict the response to ICB therapy of glioma patients in the three cohorts. The mt-rRNA score of responders and non-responders was significantly different (P < 0.0001 for all) (**Figure 7F** and **Supplementary Figures S10A, D**). Moreover, the proportion of responders to ICB therapy who had the high-risk subtype was significantly higher than the proportion of responders to ICB therapy who had the low-risk subtype (P < 0.0001 for all) (**Figure 7G** and **Supplementary Figures S10B, E**). Subclass mapping demonstrated that glioma patients with the high-risk subtype were more sensitive to anti-PD1 therapy in the TCGA, CGGA, GSE16011 cohort, with Bonferroni P = 0.007, 0.032, and 0.046, respectively (**Figure 7H** and **Supplementary Figures S10C, F**).

Considering that temozolomide chemotherapy is the first-line treatment for glioma, we explored the response of patients with

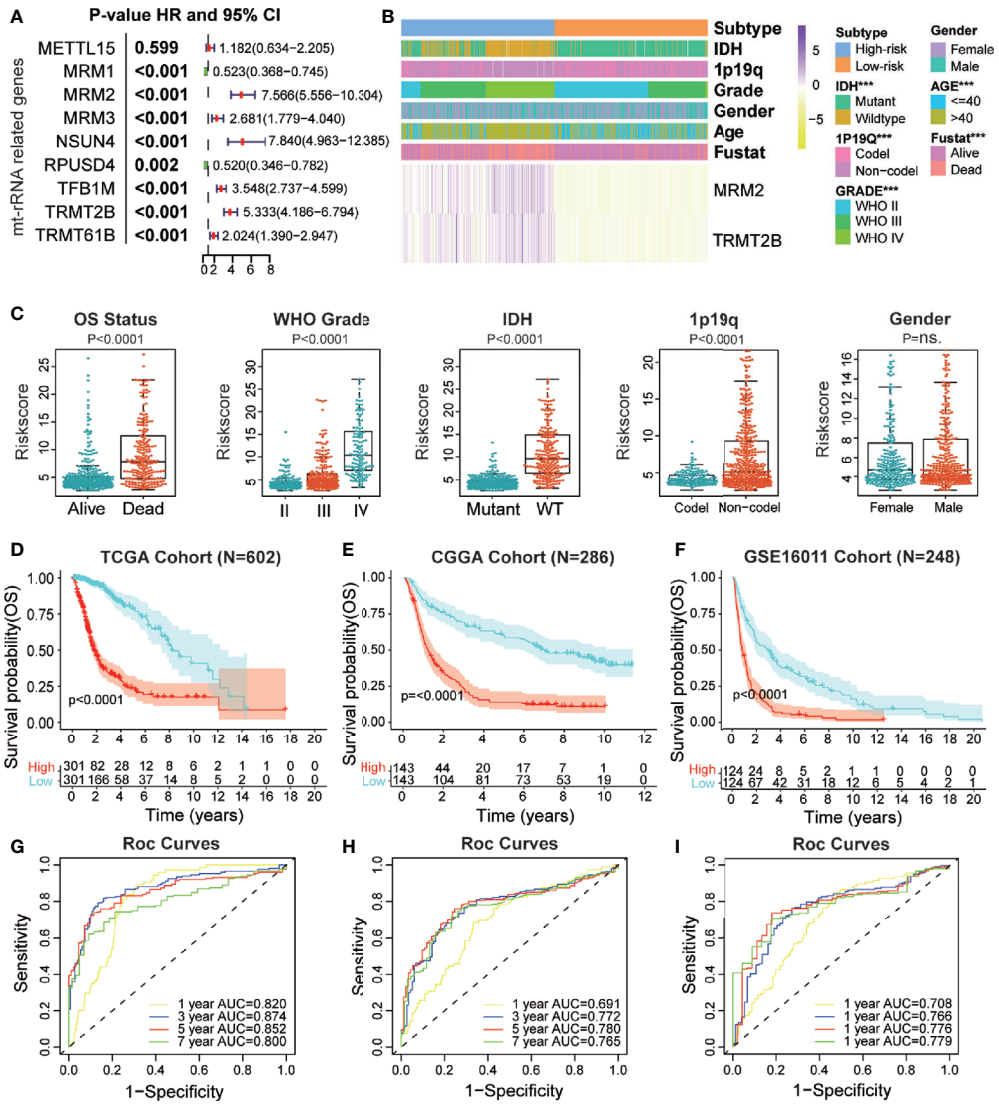

FIGURE 6 | Prognostic value of a mt-rRNA predictor in gliomas. **(A)** Prognostic value of nine regulators of mt-rRNA modification in TCGA cohort. **(B)** Correlation between the mt-rRNA predictor and clinicopathologic features. **(C)** Comparisons of OS, WHO grade, 1p19q codeletion, IDH mutation, and gender between two risk subtypes of mt-rRNA. **(D–F)** Kaplan–Meier analyses of the mt-rRNA predictor with OS in TCGA, CGGA, and GSE16011 cohorts. **(G–I)** AUC of ROC curves for predicting 1-, 3-, 5-, and 7-year OS in TCGA, CGGA, and GSE16011 cohorts, respectively. Significance: ns $P > 0.05$, $^{***}P < 0.001$.

the two subtypes of mt-rRNA risk to temozolomide therapy based on the GDSC database. The log-IC50 of temozolomide in patients with the low-risk subtype was significantly lower than that of cases with the high-risk subtype. Hence, glioma patients with the high-risk subtype were more resistant to temozolomide than those with the low-risk subtype (**Figure 7E**).

DISCUSSION

In this study, we conducted comprehensive analyses of the correlation between the patterns of mt-rRNA modification and efficacy of immunotherapy and chemotherapy in glioma, proposed a predictor to distinguish subtypes based on the mt-rRNA regulator, and verified this predictor with available RNA-sequencing data and related clinical information from four independent cohorts. First, we integrated the expression of 122 immunomodulators, 29 immune signatures calculated with the ssGSEA, clinical outcomes, clinicopathologic characteristics, genomic variations, and the nine mt-rRNA regulators of glioma patients in the TCGA database, and studied the relationship between them. Then, the TME and composition of TIICs were evaluated by ESTIMATE and CIBERSORT algorithms, respectively. We divided glioma patients into two subtypes of mt-rRNA-modification patterns based on the expression profiles of nine mt-rRNA regulators and clarified

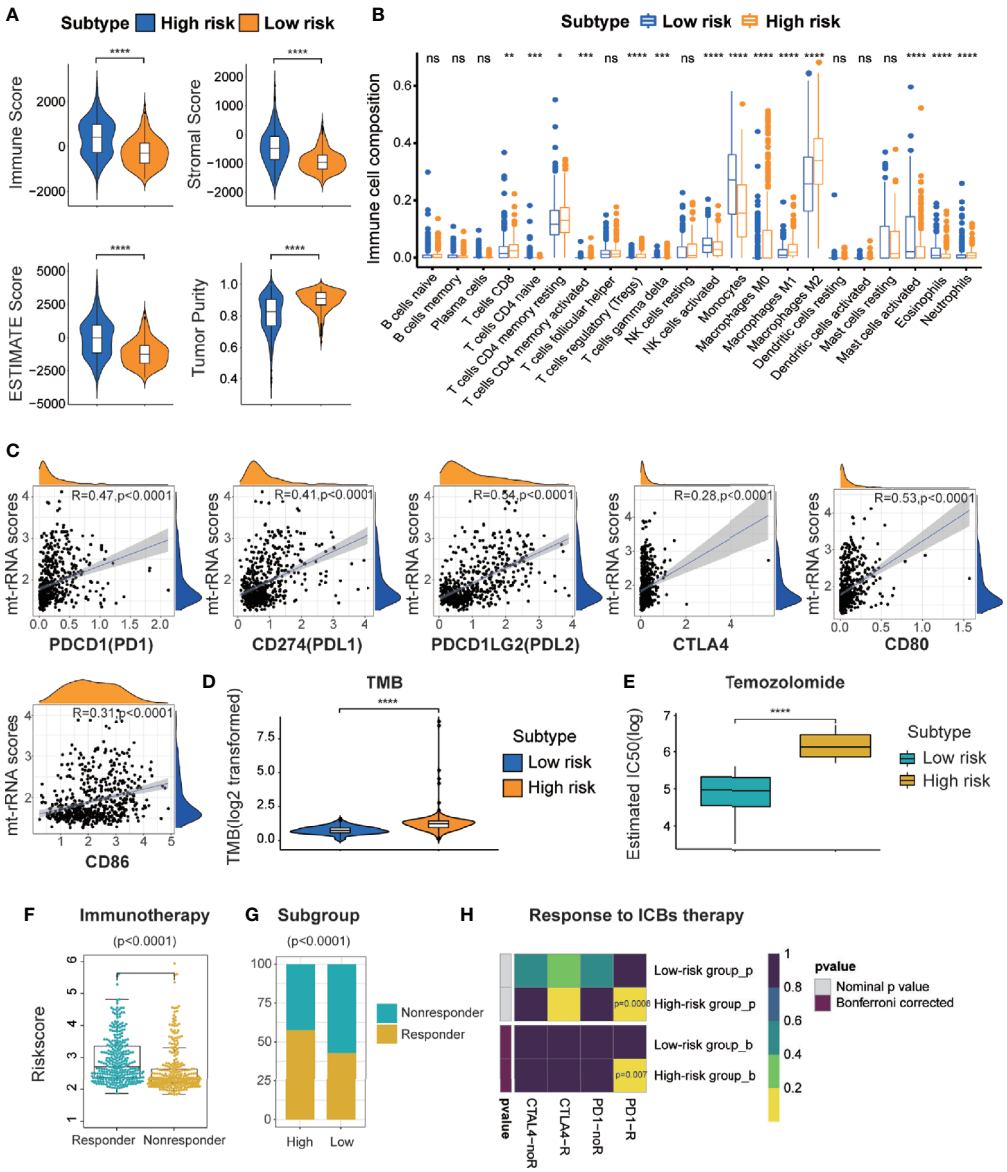

FIGURE 7 | Different TME characteristics, immunotherapy, and response to temozolomide therapy of two risk subtypes of mt-rRNA in TCGA cohort. **(A)** Comparisons of immune score, stromal score, tumor purity, and ESTIMATE score between high-risk and low-risk subtypes. **(B)** Different abundance of TIICs between high-risk and low-risk subtypes. **(C)** Correlation analyses between the mt-rRNA score and ICBs. **(D)** Comparison of the TMB between high-risk and low-risk subtypes. **(E)** Different IC50 of temozolomide between two subtypes in the GDSC database. **(F)** Comparison of the mt-rRNA score between the responder group and non-responder group. **(G)** Different proportions of responders and non-responders to immunotherapy between two subtypes. **(H)** Prediction of response to ICBs (PD1 and CTLA4) therapy in high-risk and low-risk subtypes. Significance: ns $P > 0.05$, $^{*}P < 0.05$, $^{**}P < 0.01$, $^{***}P < 0.001$, $^{****}P < 0.0001$.

the association between the two subtypes and clinicopathologic parameters. Glioma patients with RM2 could achieve better therapeutic effects through immunotherapy (especially anti-PD-1 therapy) as predicted by the TIDE algorithm. In addition, patients in this group had longer OS and PFS. To make the method more clinically practical for glioma patients, the two most critical prognostic genes for mt-rRNA regulation were identified and defined as mt-rRNA predictors to distinguish different mt-rRNA subtypes by using the LASSO algorithm. The forecasted effect of this predictor was verified further in the CGGA, GSE16011, and SAHNC cohorts.

In recent years, immunotherapy for tumors has been studied extensively using ICBs, tumor-cell immunotherapy, and antitumor vaccines. However, the immunotherapy effect in phase-III clinical trials for glioblastoma has not been satisfactory (24, 43). Several factors can determine the efficacy of immunotherapy in glioma patients. Taking anti-PD-1/PD-L1 treatment as an example, the TMB, mismatch repair, expression

of PD-L1 (CD274), and TICC composition can affect efficacy (25, 44, 45). When investigating immunotherapy in phase-III clinical trials for glioblastoma, patients are not screened for these parameters, and such undifferentiated treatment may be the reason for the poor efficacy of immunotherapy. Hence, comprehensive analyses of the role of these factors will help to enhance understanding of the immune response to gliomas and guide more efficacious immunotherapy strategies.

Increasing evidence has demonstrated that RNA modifications have indispensable roles in inflammation, innate immunity, and anti-tumor activities, among which the most extensive and in-depth research has been on m6A. Bo Zhang and colleagues demonstrated that modification of m6A methylation is involved in the regulation of the microenvironment of gastric cancer, and has a guiding role in immunotherapy (46). Jianyang Du and coworkers revealed that m6A regulators had different modification patterns and characteristics of immunity in low-grade glioma (47). Most studies have focused on m6A modification, the overall TME characterization mediated by mt-rRNA modification and its regulators is not recognized.

In this work, based on nine mt-rRNA regulators, we revealed two distinct subtypes of mt-rRNA modification with significantly different TME characterization. RM2 was characterized by the activation of immunity and related enriched pathways, which corresponded to an immune-activated phenotype. RM1 was characterized by infiltration of innate immune cells (eosinophils, NK cells, and mast cells), which corresponded to an immune-excluded phenotype (48, 49). Meanwhile, patients with this pattern of mt-rRNA modification showed a matching survival advantage. Recent studies have suggested that tumors with immune-excluded phenotype also show infiltration of immune cells because the latter remain in the matrix around the tumor cell "nests" rather than penetrating the parenchyma of tumor cells (50, 51). Moreover, we revealed a significant correlation between the subtypes and TMB, including several common somatic mutations (TP53, PTEN, and EGFR) in gliomas (52). mt-rRNA modification played an important part in formation of the "immune landscape" of the TME, which suggests that mt-rRNA modification may affect the therapeutic efficacy of ICBs. Glioma patients with the RM2 subtype had a significantly better response to anti-PD-1 immunotherapy. We created an mt-rRNA predictor that could be used to characterize cell infiltration in the TME, TMB, and clinicopathologic features of glioma patients. This mt-rRNA predictor could act as an independent prognostic biomarker for predicting clinical outcomes as well as the efficacy of PD-1 immunotherapy and temozolomide chemotherapy through the mt-rRNA score.

However, our study still had two main limitations. First, we obtained only 33 glioma specimens with pathologic data, but no clinical outcomes, to verify the results of our study. We need to collect more glioma samples and obtain the corresponding clinical outcomes from our center in the future. Second, our conclusions are based only on the analysis and prediction of transcriptome data in publicly available databases, the relationship between mt-rRNA modification and immunotherapy responsiveness needs to be tested in the future immunotherapy cohort.

CONCLUSIONS

In conclusion, according to patterns of mt-rRNA modification, glioma patients can be divided into two distinct subtypes which have a notably different prognosis and response to immunotherapy. Our study provides a potential strategy for "individualized" tumor immunotherapy in the future. We constructed a mt-rRNA predictor which made subgrouping based on mt-rRNA regulators and precision immunotherapy clinically feasible.

DATA AVAILABILITY STATEMENT

The datasets presented in this study can be found in online repositories. The names of the repository/repositories and accession number(s) can be found in the article/ **Supplementary Material**.

ETHICS STATEMENT

The studies involving human participants were reviewed and approved by The medical ethics committee of the Second Affiliated Hospital of Nanchang University. The patients/ participants provided their written informed consent to participate in this study.

AUTHOR CONTRIBUTIONS

XZ and KH designed the research. JL, MW, and MY contributed to the collect the brain tissue samples and matching clinical data. PW contributed to the public data collection and analysis, figures and tables, complete the experiments, and were involved in manuscript writing. XZ and KH performed the correction of the language and revision. All authors contributed to the article and approved the submitted version.

FUNDING

The present study was supported by the National Natural Science Foundation of China (grant nos. 81960456, 82002660, 81760445, and 81760446).

ACKNOWLEDGMENTS

We thank all the participants who were involved in this study.

SUPPLEMENTARY MATERIAL

The Supplementary Material for this article can be found online at: https://www.frontiersin.org/articles/10.3389/fimmu.2021.722479/full#supplementary-material

REFERENCES

1. Weller M, Wick W, Aldape K, Brada M, Berger M, Pfister SM, et al. Glioma. *Nat Rev Dis Primers* (2015) 1:15017. doi: 10.1038/nrdp.2015.17
2. Zhang H, Wang R, Yu Y, Liu J, Luo T, Fan F. Glioblastoma Treatment Modalities Besides Surgery. *J Cancer* (2019) 10:4793–806. doi: 10.7150/jca.32475
3. Jiang T, Mao Y, Ma W, Mao Q, You Y, Yang X, et al. CGCG Clinical Practice Guidelines for the Management of Adult Diffuse Gliomas. *Cancer Lett* (2016) 375:263–73. doi: 10.1016/j.canlet.2016.01.024
4. Stupp R, Taillibert S, Kanner A, Read W, Steinberg D, Lhermitte B, et al. Effect of Tumor-Treating Fields Plus Maintenance Temozolomide vs Maintenance Temozolomide Alone on Survival in Patients With Glioblastoma: A Randomized Clinical Trial. *JAMA* (2017) 318:2306–16. doi: 10.1001/jama.2017.18718
5. Gilbert MR, Dignam JJ, Armstrong TS, Wefel JS, Blumenthal DT, Vogelbaum MA, et al. A Randomized Trial of Bevacizumab for Newly Diagnosed Glioblastoma. *N Engl J Med* (2014) 370:699–708. doi: 10.1056/NEJMoa1308573
6. Sandmann T, Bourgon R, Garcia J, Li C, Cloughesy T, Chinot OL, et al. Patients With Proneural Glioblastoma May Derive Overall Survival Benefit From the Addition of Bevacizumab to First-Line Radiotherapy and Temozolomide: Retrospective Analysis of the AVAglio Trial. *J Clin Oncol* (2015) 33:2735–44. doi: 10.1200/JCO.2015.61.5005
7. Boccaletto P, Baginski B. MODOMICS: An Operational Guide to the Use of the RNA Modification Pathways Database. *Methods Mol Biol* (2021) 2284:481–505. doi: 10.1007/978-1-0716-1307-8_26
8. Greber BJ, Boehringer D, Leibundgut M, Bieri P, Leitner A, Schmitz N, et al. The Complete Structure of the Large Subunit of the Mammalian Mitochondrial Ribosome. *Nature* (2014) 515:283–6. doi: 10.1038/nature13895
9. Greber BJ, Bieri P, Leibundgut M, Leitner A, Aebersold R, Boehringer D, et al. Ribosome. The Complete Structure of the 55S Mammalian Mitochondrial Ribosome. *Science* (2015) 348:303–8. doi: 10.1126/science.aaa3872
10. Brown A, Amunts A, Bai XC, Sugimoto Y, Edwards PC, Murshudov G, et al. Structure of the Large Ribosomal Subunit From Human Mitochondria. *Science* (2014) 346:718–22. doi: 10.1126/science.1258026
11. Bohnsack MT, Sloan KE. The Mitochondrial Epitranscriptome: The Roles of RNA Modifications in Mitochondrial Translation and Human Disease. *Cell Mol Life Sci* (2018) 75:241–60. doi: 10.1007/s00018-017-2598-6
12. Lopez Sanchez MIG, Cipullo M, Gopalakrishna S, Khawaja A, Rorbach J. Methylation of Ribosomal RNA: A Mitochondrial Perspective. *Front Genet* (2020) 11:761. doi: 10.3389/fgene.2020.00761
13. Rorbach J, Minczuk M. The Post-Transcriptional Life of Mammalian Mitochondrial RNA. *Biochem J* (2012) 444:357–73. doi: 10.1042/BJ20112208
14. Rebelo-Guiomar P, Powell CA, Van Haute L, Minczuk M. The Mammalian Mitochondrial Epitranscriptome. *Biochim Biophys Acta Gene Regul Mech* (2019) 1862:429–46. doi: 10.1016/j.bbagrm.2018.11.005
15. Chen H, Shi Z, Guo J, Chang KJ, Chen Q, Yao CH, et al. The Human Mitochondrial 12S rRNA M(4)C Methyltransferase METTL15 Is Required for Mitochondrial Function. *J Biol Chem* (2020) 295:8505–13. doi: 10.1074/jbc.RA119.012127
16. Powell CA, Minczuk M. TRMT2B is Responsible for Both tRNA and rRNA M (5)U-Methylation in Human Mitochondria. *RNA Biol* (2020) 17:451–62. doi: 10.1080/15476286.2020.1712544
17. Marcel V, Ghayad SE, Belin S, Therizols G, Morel AP, Solano-Gonzalez E, et al. P53 Acts as a Safeguard of Translational Control by Regulating Fibrillarin and rRNA Methylation in Cancer. *Cancer Cell* (2013) 24:318–30. doi: 10.1016/j.ccr.2013.08.013
18. Blanco S, Frye M. Role of RNA Methyltransferases in Tissue Renewal and Pathology. *Curr Opin Cell Biol* (2014) 31:1–7. doi: 10.1016/j.ceb.2014.06.006
19. Garone C, D'Souza AR, Dallabona C, Lodi T, Rebelo-Guiomar P, Rorbach J, et al. Defective Mitochondrial rRNA Methyltransferase MRM2 Causes MELAS-Like Clinical Syndrome. *Hum Mol Genet* (2017) 26:4257–66. doi: 10.1093/hmg/ddx314
20. Topalian SL, Hodi FS, Brahmer JR, Gettinger SN, Smith DC, McDermott DF, et al. Safety, Activity, and Immune Correlates of Anti-PD-1 Antibody in Cancer. *N Engl J Med* (2012) 366:2443–54. doi: 10.1056/NEJMoa1200690
21. Rizvi NA, Hellmann MD, Snyder A, Kvistborg P, Makarov V, Havel JJ, et al. Cancer Immunology. Mutational Landscape Determines Sensitivity to PD-1 Blockade in Non-Small Cell Lung Cancer. *Science* (2015) 348:124–8. doi: 10.1126/science.aaa1348
22. Pitt JM, Marabelle A, Eggermont A, Soria JC, Kroemer G, Zitvogel L. Targeting the Tumor Microenvironment: Removing Obstruction to Anticancer Immune Responses and Immunotherapy. *Ann Oncol* (2016) 27:1482–92. doi: 10.1093/annonc/mdw168
23. Patrick M, Forde MB, Yang X, Yin R, Xu L, Wolchok JD, et al. Neoadjuvant PD-1 Blockade in Resectable Lung Cancer; Nivolumab and Ipilimumab in Advanced Melanoma; Overall Survival With Combined Nivolumab and Ipilimumab in Advanced Melanoma; Prolonged Survival in Stage III Melanoma With Ipilimumab Adjuvant Therapy; Combined Nivolumab and Ipilimumab or Monotherapy in Untreated Melanoma; Combined Nivolumab and Ipilimumab or Monotherapy in Untreated Melanoma; Nivolumab and Ipilimumab Versus Ipilimumab in Untreated Melanoma; Rapid Eradication of a Bulky Melanoma Mass With One Dose of Immunotherapy; Genetic Basis for Clinical Response to CTLA-4 Blockade; Genetic Basis for Clinical Response to CTLA-4 Blockade in Melanoma; Nivolumab Plus Ipilimumab in Advanced Melanoma; Safety and Tumor Responses With Lambrolizumab (Anti-PD-1) in Melanoma; Hepatotoxicity With Combination of Vemurafenib and Ipilimumab. *N Engl J Med* (2018) 379:2185. doi: 10.1056/NEJMx180040
24. Reardon DA, Brandes AA, Omuro A, Mulholland P, Lim M, Wick A, et al. Effect of Nivolumab vs Bevacizumab in Patients With Recurrent Glioblastoma: The CheckMate 143 Phase 3 Randomized Clinical Trial. *JAMA Oncol* (2020) 6:1003–10. doi: 10.1001/jamaoncol.2020.1024
25. Yang T, Kong Z, Ma W. PD-1/PD-L1 Immune Checkpoint Inhibitors in Glioblastoma: Clinical Studies, Challenges and Potential. *Hum Vaccin Immunother* (2021) 17:546–53. doi: 10.1080/21645515.2020.1782692
26. Touat M, Li YY, Boynton AN, Spurr LF, Iorgulescu JB, Bohrson CL, et al. Mechanisms and Therapeutic Implications of Hypermutation in Gliomas. *Nature* (2020) 580:517–23. doi: 10.1038/s41586-020-2209-9
27. Mermel CH, Schumacher SE, Hill B, Meyerson ML, Beroukhim R, Getz G. GISTIC2.0 Facilitates Sensitive and Confident Localization of the Targets of Focal Somatic Copy-Number Alteration in Human Cancers. *Genome Biol* (2011) 12:R41. doi: 10.1186/gb-2011-12-4-r41
28. Geeleher P, Cox NJ, Huang RS. Clinical Drug Response can be Predicted Using Baseline Gene Expression Levels and *In Vitro* Drug Sensitivity in Cell Lines. *Genome Biol* (2014) 15:R47. doi: 10.1186/gb-2014-15-3-r47
29. Charoentong P, Finotello F, Angelova M, Mayer C, Efremova M, Rieder D, et al. Pan-Cancer Immunogenomic Analyses Reveal Genotype-Immunophenotype Relationships and Predictors of Response to Checkpoint Blockade. *Cell Rep* (2017) 18:248–62. doi: 10.1016/j.celrep.2016.12.019
30. Auslander N, Zhang G, Lee JS, Frederick DT, Miao B, Moll T, et al. Robust Prediction of Response to Immune Checkpoint Blockade Therapy in Metastatic Melanoma. *Nat Med* (2018) 24:1545–9. doi: 10.1038/s41591-018-0157-9
31. Yoshihara K, Shahmoradgoli M, Martinez E, Vegesna R, Kim H, Torres-Garcia W, et al. Inferring Tumour Purity and Stromal and Immune Cell Admixture From Expression Data. *Nat Commun* (2013) 4:2612. doi: 10.1038/ncomms3612
32. Newman AM, Liu CL, Green MR, Gentles AJ, Feng W, Xu Y, et al. Robust Enumeration of Cell Subsets From Tissue Expression Profiles. *Nat Methods* (2015) 12:453–7. doi: 10.1038/nmeth.3337
33. He Y, Jiang Z, Chen C, Wang X. Classification of Triple-Negative Breast Cancers Based on Immunogenomic Profiling. *J Exp Clin Cancer Res* (2018) 37:327. doi: 10.1186/s13046-018-1002-1
34. Wilkerson MD, Hayes DN. ConsensusClusterPlus: A Class Discovery Tool With Confidence Assessments and Item Tracking. *Bioinformatics* (2010) 26:1572–3. doi: 10.1093/bioinformatics/btq170
35. Senbabaoglu Y, Michailidis G, Li JZ. Critical Limitations of Consensus Clustering in Class Discovery. *Sci Rep* (2014) 4:6207. doi: 10.1038/srep06207
36. Mayakonda A, Lin DC, Assenov Y, Plass C, Koeffler HP. Maftools: Efficient and Comprehensive Analysis of Somatic Variants in Cancer. *Genome Res* (2018) 28:1747–56. doi: 10.1101/gr.239244.118
37. Skidmore ZL, Wagner AH, Lesurf R, Campbell KM, Kunisaki J, Griffith OL, et al. GenVisR: Genomic Visualizations in R. *Bioinformatics* (2016) 32:3012–4. doi: 10.1093/bioinformatics/btw325

38. Zhang H, Meltzer P, Davis S. RCircos: An R Package for Circos 2D Track Plots. *BMC Bioinf* (2013) 14:244. doi: 10.1186/1471-2105-14-244
39. Hanzelmann S, Castelo R, Guinney J. GSVA: Gene Set Variation Analysis for Microarray and RNA-Seq Data. *BMC Bioinf* (2013) 14:7. doi: 10.1186/1471-2105-14-7
40. Jiang P, Gu S, Pan D, Fu J, Sahu A, Hu X, et al. Signatures of T Cell Dysfunction and Exclusion Predict Cancer Immunotherapy Response. *Nat Med* (2018) 24:1550–8. doi: 10.1038/s41591-018-0136-1
41. Hoshida Y, Brunet JP, Tamayo P, Golub TR, Mesirov JP. Subclass Mapping: Identifying Common Subtypes in Independent Disease Data Sets. *PloS One* (2007) 2:e1195. doi: 10.1371/journal.pone.0001195
42. Wang P, Wu M, Tu Z, Tao C, Hu Q, Li K, et al. Identification of RNA: 5-Methylcytosine Methyltransferases-Related Signature for Predicting Prognosis in Glioma. *Front Oncol* (2020) 10:1119. doi: 10.3389/fonc.2020.01119
43. Weller M, Butowski N, Tran DD, Recht LD, Lim M, Hirte H, et al. Rindopepimut With Temozolomide for Patients With Newly Diagnosed, EGFRvIII-Expressing Glioblastoma (ACT IV): A Randomised, Double-Blind, International Phase 3 Trial. *Lancet Oncol* (2017) 18:1373–85. doi: 10.1016/S1470-2045(17)30517-X
44. Wang X, Guo G, Guan H, Yu Y, Lu J, Yu J. Challenges and Potential of PD-1/PD-L1 Checkpoint Blockade Immunotherapy for Glioblastoma. *J Exp Clin Cancer Res* (2019) 38:87. doi: 10.1186/s13046-019-1085-3
45. Khasraw M, Reardon DA, Weller M, Sampson JH. PD-1 Inhibitors: Do They Have a Future in the Treatment of Glioblastoma? *Clin Cancer Res* (2020) 26:5287–96. doi: 10.1158/1078-0432.CCR-20-1135
46. Zhang B, Wu Q, Li B, Wang D, Wang L, Zhou YL. M(6)A Regulator-Mediated Methylation Modification Patterns and Tumor Microenvironment Infiltration Characterization in Gastric Cancer. *Mol Cancer* (2020) 19:53. doi: 10.1186/s12943-020-01170-0
47. Du J, Ji H, Ma S, Jin J, Mi S, Hou K, et al. M6a Regulator-Mediated Methylation Modification Patterns and Characteristics of Immunity and Stemness in Low-Grade Glioma. *Brief Bioinform* (2021) bbab013. doi: 10.1093/bib/bbab013
48. Turley SJ, Cremasco V, Astarita JL. Immunological Hallmarks of Stromal Cells in the Tumour Microenvironment. *Nat Rev Immunol* (2015) 15:669–82. doi: 10.1038/nri3902
49. Chen DS, Mellman I. Elements of Cancer Immunity and the Cancer-Immune Set Point. *Nature* (2017) 541:321–30. doi: 10.1038/nature21349
50. Gajewski TF. The Next Hurdle in Cancer Immunotherapy: Overcoming the Non-T-Cell-Inflamed Tumor Microenvironment. *Semin Oncol* (2015) 42:663–71. doi: 10.1053/j.seminoncol.2015.05.011
51. Joyce JA, Fearon DT. T Cell Exclusion, Immune Privilege, and the Tumor Microenvironment. *Science* (2015) 348:74–80. doi: 10.1126/science.aaa6204
52. Segura-Collar B, Gargini R, Tovar-Ambel E, Hernandez-SanMiguel E, Epifano C, Perez de Castro I, et al. The EGFR-TMEM167A-P53 Axis Defines the Aggressiveness of Gliomas. *Cancers (Basel)* (2020) 12(1):208. doi: 10.3390/cancers12010208

Conflict of Interest: The authors declare that the research was conducted in the absence of any commercial or financial relationships that could be construed as a potential conflict of interest.

Publisher's Note: All claims expressed in this article are solely those of the authors and do not necessarily represent those of their affiliated organizations, or those of the publisher, the editors and the reviewers. Any product that may be evaluated in this article, or claim that may be made by its manufacturer, is not guaranteed or endorsed by the publisher.

frontiers in Immunology

ORIGINAL RESEARCH
published: 30 September 2021
doi: 10.3389/fimmu.2021.731048

Hypoxia-Related lncRNA Correlates With Prognosis and Immune Microenvironment in Lower-Grade Glioma

Shengchao Xu[1], Lu Tang[2], Zhixiong Liu[1], Chengke Luo[1] and Quan Cheng[1,3]**

[1] Department of Neurosurgery, Xiangya Hospital, Central South University, Changsha, China, [2] Department of Thoracic Surgery, Xiangya Hospital, Central South University, Changsha, China, [3] National Clinical Research Center for Geriatric Disorders, Xiangya Hospital, Central South University, Changsha, China

OPEN ACCESS

Edited by:
Peng Qu,
National Institutes of Health (NIH), United States

Reviewed by:
Markus Biburger, Friedrich-Alexander-University Erlangen-Nürnberg, Germany
Lele Song, University of Pennsylvania, United States

***Correspondence:**
Quan Cheng
chengquan@csu.edu.cn
Chengke Luo
ck_luo@csu.edu.cn

Specialty section:
This article was submitted to Cancer Immunity and Immunotherapy, a section of the journal Frontiers in Immunology

Received: *26 June 2021*
Accepted: *09 September 2021*
Published: *30 September 2021*

Citation:
Xu S, Tang L, Liu Z, Luo C and Cheng Q (2021) Hypoxia-Related lncRNA Correlates With Prognosis and Immune Microenvironment in Lower-Grade Glioma. Front. Immunol. 12:731048. doi: 10.3389/fimmu.2021.731048

Background: Hypoxia-related genes are demonstrated to correlate with the prognosis of various cancers. However, the role of hypoxia-related long non-coding RNAs (HRLs) in lower-grade glioma (LGG) remains unclear.

Methods: A total of 700 LGG samples were extracted from TCGA and CGGA databases. Pearson correlation analysis was used to identify HRLs. Lasso analysis was adopted to construct the HRL signature. TIDE algorithm was used to predict responses to immune checkpoint inhibitors. Cell proliferation was estimated by cell counting kit-8 assay, colony formation assay, and EdU assay.

Results: We identified 340 HRLs and constructed a novel risk signature composed of 19 HRLs. The risk score exhibited potent value in predicting the prognosis of LGG patients and was significantly associated with the prognosis of LGG patients. Moreover, HRL signature could distinguish patients with similar expression levels of immune checkpoints and might predict the efficacy of immune checkpoint inhibitors. Additionally, hypoxia-related pathways and immune pathways were enriched in high-risk group, and high risk score indicated low tumor purity and high immune infiltration. Two major HRLs, LINC00941 and BASP1-AS1, could significantly affect the proliferation of glioma cells.

Conclusions: Our study constructed a novel HRL signature that could predict the prognosis and immunotherapy response of LGG patients. HRLs could be novel biomarkers to predict the prognosis of LGG patients and potential targets for LGG treatment.

Keywords: lower-grade glioma, hypoxia, long non-coding RNA, immune microenvironment, immune infiltration

INTRODUCTION

Glioma is the most common type of brain cancer (1). The World Health Organization (WHO) has classified gliomas into four grades, in which the higher grade indicates the higher malignancy. Patients with grade II glioma have a median overall survival (OS) of about 11 years, and those with grade III glioma have a median OS of approximately 3 years (2, 3). Since glioblastoma (grade IV glioma) has a superior malignancy and a poor prognosis, the Cancer Genome Atlas (TCGA) classified grade II and III gliomas as lower-grade glioma (LGG). Although great progress has been made to develop novel therapeutics against cancer, few drugs have been approved for LGG treatment, and the prognosis of LGG patients remains poor (4). Therefore, there is a clear urgent to develop novel biomarkers to predict the prognosis of LGG patients and find potential targets for the treatment of LGG.

Hypoxia has been implicated to promote the progression of tumors with the induction of hypoxic tumor context (5). The occurrence and development of tumors often accompanies with several adaptive alternations such as angiogenesis, proliferation, and so on, where hypoxia can promote the aggressiveness of tumors (6). In glioblastoma, extensive tissue hypoxia is commonly detected, and it can facilitate the formation of glioma stem-like cells, which is closely associated with tumor recurrence (7). Besides, hypoxia-related genes are demonstrated to correlate with the prognosis of glioma patients (8, 9). Therefore, hypoxia is crucial for glioma development.

In recent years, long non-coding RNA (lncRNA) have emerged to play diverse roles in various biological processes (10). These lncRNAs can modulate transcriptional and post-transcriptional of genes and regulate the expression of tumor suppressors or initiators, which confers the occurrence and progression of cancer (11). In gliomas, lncRNA has been implicated to be associated with the proliferation, invasion, and prognosis of glioma cells (12–15). However, no research has comprehensively revealed the role of hypoxia-related lncRNAs (HRLs) in LGG.

A previous study indicated that hypoxia-related signature was associated with the prognosis and immune microenvironment of glioma patients (8). However, the role of HRLs in LGG remained unclear. Herein, our study extracted data from TCGA and Chinese Glioma Genome Atlas (CGGA) databases to identify candidate HRLs and constructed related signature, aiming to explore its prognostic value in LGG patients and its association with LGG immune microenvironment.

MATERIALS AND METHODS

Data Extraction

A total of 700 grade II and III glioma samples were included in our study. The RNA-seq and clinical data were extracted from CGGA (http://www.cgga.org.cn/) and TCGA (https://portal.gdc.cancer.gov/) databases. In this study, TCGA-LGG dataset (n=522) was defined as the training cohort, whereas CGGA dataset (n=178) was the validation cohort. The characteristics of glioma samples in this study were summarized in **Table 1**.

TABLE 1 | Characteristics of the training cohort and validation cohort.

Features	Training cohort	Validation cohort
	TCGA (n=522)	CGGA (n=178)
Age		
≤ 45	320	135
> 45	202	43
Gender		
Male	289	107
Female	233	71
Grade		
II	256	102
III	265	76
NA	1	0
IDH status		
Mutant	423	131
Wildtype	96	47
NA	3	0
1p/19q status		
Codel	171	60
Non-codel	351	118
MGMT status		
Unmethylated	91	86
Methylated	431	76
NA	0	16

IDH, isocitrate dehydrogenase; MGMT, O6 -methylguanine-DNA methyltransferase.

Moreover, IMvigor210 dataset, a cohort of atezolizumab (anti-PD-L1 monoclonal antibody) for the treatment of urothelial carcinoma, was extracted to evaluate the predictive value of HRL signature for the efficacy of immunotherapy (16).

Identification of HRLs

The 26 hypoxia-related genes were reported by previous studies (17, 18). A total of 14,488 and 13,895 lncRNAs were identified in the TCGA and CGGA datasets, respectively. Those lncRNAs whose expressions closely corelated with the expression of 26 hypoxia-related genes ($|R|>0.5$ and $p<0.01$) were identified as HRLs.

Bioinformatic Analyses

To evaluate the involvement of biological processes of each sample, gene set variation analysis (GSVA) was conducted to quantify the involvement of Gene Ontology pathways in each LGG sample (19). As for gene set enrichment analysis (GSEA), differentially expressed genes between two groups were identified. Those with false discovery rate (FDR) ≤0.05 were selected for GSEA analysis. Gene sets of hallmarks were obtained from the Molecular Signatures Database (MSigDB). Gene Ontology (GO) and Kyoto Encyclopedia of Genes and Genomes (KEGG) enrichment analyses were conducted by "clusterprofiler" R package. The nomogram and calibration curves were constructed and visualized using "rms" and "regplot" R packages. Tumor Immune Dysfunction and Exclusion (TIDE) algorithm was used to predict the responses of glioma patients to immune checkpoint inhibitors (ICIs) (20).

Estimation of Immune Microenvironment

Estimation of Stromal and Immune cells in Malignant Tumor tissues using Expression data (ESTIMATE) analysis was

conducted to calculate the tumor purity of each sample by "estimate" R package (21). The infiltration of immune cells was estimated by single-sample Gene Set Enrichment Analysis (ssGSEA) and Tumor Immune Estimation Resource (TIMER), and Cell-type Identification by Estimating Relative Subsets of RNA Transcripts (CIBERSORT) algorithms (22–24).

Construction of Risk Signature

The risk signature was constructed using the least absolute shrinkage and selection operator (LASSO) analysis. The risk score was calculated by the following algorithm:

$$\text{Risk Score} = \Sigma_{i=1}^{n} Coefficient_i * Gene_i$$

Subgroup Analysis

For subgroup analysis, LGG patients were divided into different groups based on the following variables: grade (grades II or III), age (≤45 years old or >45 years old), and IDH status (mutant or wildtype).

Construction of Competing Endogenous RNA Network

The potential target miRNAs of LINC00941 and BASP1-AS1 were predicted using ENCORI online webtool (http://starbase.sysu.edu.cn/). Then, the potential target mRNAs of these miRNAs were predicted using microT-CDS (http://diana.imis.athena-innovation.gr/DianaTools/index.php?r=microT_CDS/index) and mirDIP online webtools (http://ophid.utoronto.ca/mirDIP/). Pearson correlation analysis was conducted to screen genes co-expressed with LINC00941 or BASP1-AS1 in the TCGA dataset with r>0.4 and p<0.001. These genes were intersected with predicted mRNAs to define potential mRNA targets of LINC00941 or BASP1-AS1. Finally, the lncRNA-miRNA-mRNA network was constructed using Cytoscape 3.8.0.

Cell Culture and Cell Transfection

Given the fact that there were no widely used LGG cell lines, and glioblastoma and LGG belonged to gliomas, we used two glioblastoma cells (DBTRG-05MG and U251 MG) in this study to explore the effect of HRLs on gliomas. DBTRG was cultured in RPMI-1640 medium with 10% fetal bovine serum (FBS, ExCell Bio, China), and U251 was cultured in DMEM medium with 10% FBS (ExCell Bio, China). Specific siRNAs targeting LINC00941 and BASP1-AS1 were designed and synthesized by GenePharma. Lipofectamine 3000 (Invitrogen, USA) was used for cell transfection.

Extraction of Total RNA and Quantitative Real-Time PCR

Total RNA was extracted using TRIzol reagent (Invitrogen, USA). The PrimeScript RT reagent Kit (RR047A, Takara) was used to synthesize cDNA. The TB Green Fast qPCR Mix (RR430S, Takara) was used for qPCR. GAPDH was used as the reference gene. Primers used in this study were as follows: GAPDH: F, CAGGAGGCATTGCTGATGAT; R, GAAGGCTGGGGCTCATTT. LINC00941: F, ACCACTACACTCAGCCAAATAC; R, GGCTATCAACTGTCTCCTTTAGAC. BASP1-AS1: F, AGCACCGGGACACAGAATAG; R, TTTGCGGGAAGGTAAAATTG.

Cell Counting Kit-8 Assay

In each well of 96-well plate, 2×10^3 cells were inoculated and maintained in culture medium for 0, 24, 48, and 72 h. Then, 10 μl CCK-8 reagent (DOJINDO, Japan) was added into each well, and the optical density of 450 nm was estimated.

Colony Formation Assay

In each well of six-well plate, 800 cells were seeded and maintained in culture medium for 14 days. After the fix with 4% paraformaldehyde, cells were stained with 0.1% crystal violet.

5-Ethynyl-2'-Deoxyuridine Assay

A total of 1×10^5 cells was seeded in 20 mm round coverslip. The EdU Cell Proliferation Assay Kit (Ribobio, China) was used for EdU assay and the processes were conducted according to the manufacturer's instructions.

Statistical Analysis

Statistical analyses and visualization were mainly performed using R version 3.6.0 and GraphPad Prism version 8.0.1. Student's t test and one-way ANOVA analysis were used to estimate the differences between two groups and more than two groups. Kaplan-Meier analysis was conducted to compare the survival differences between two groups of patients. Multivariate Cox analysis was used to evaluate the prognostic value of risk score. The correlation of gene expression was determined by Pearson correlation analysis. Time-dependent receiver operating characteristic (ROC) curve analysis was adopted to estimate the predictive value of risk score. Two-sided $p \leq 0.05$ was regarded as statistically significant.

RESULTS

Identification of HRLs in the TCGA and CGGA Datasets

To preliminarily explore the role of hypoxia and lncRNAs in LGG, we screened HRLs in the TCGA dataset. A total of 14,488 lncRNAs and 26 hypoxia-related genes were identified and selected for our study (**Figure 1A**). Pearson correlation analysis identified 399 HRLs (|R|>0.5 and p<0.01) in the TCGA dataset (**Table S1**). After the intersection with lncRNAs in the CGGA dataset, 340 HRLs were identified. With the application of univariate Cox analysis and Lasso analysis, 19 HRLs were selected for further analysis (**Figure 1B**). Among these lncRNAs, four lncRNAs (AL391834.1, LINC00836, BASP1-AS1, and AL023806.1) played protective roles in LGG, whereas the other 15 lncRNAs were risk factors (p<0.05) (**Figure 1C**). Kaplan-Meier analysis further validated the prognostic values of these lncRNAs in the two datasets (p<0.05) (**Figure S1**). The correlation between 19 selected HRLs and 26 hypoxia-related genes were shown by the

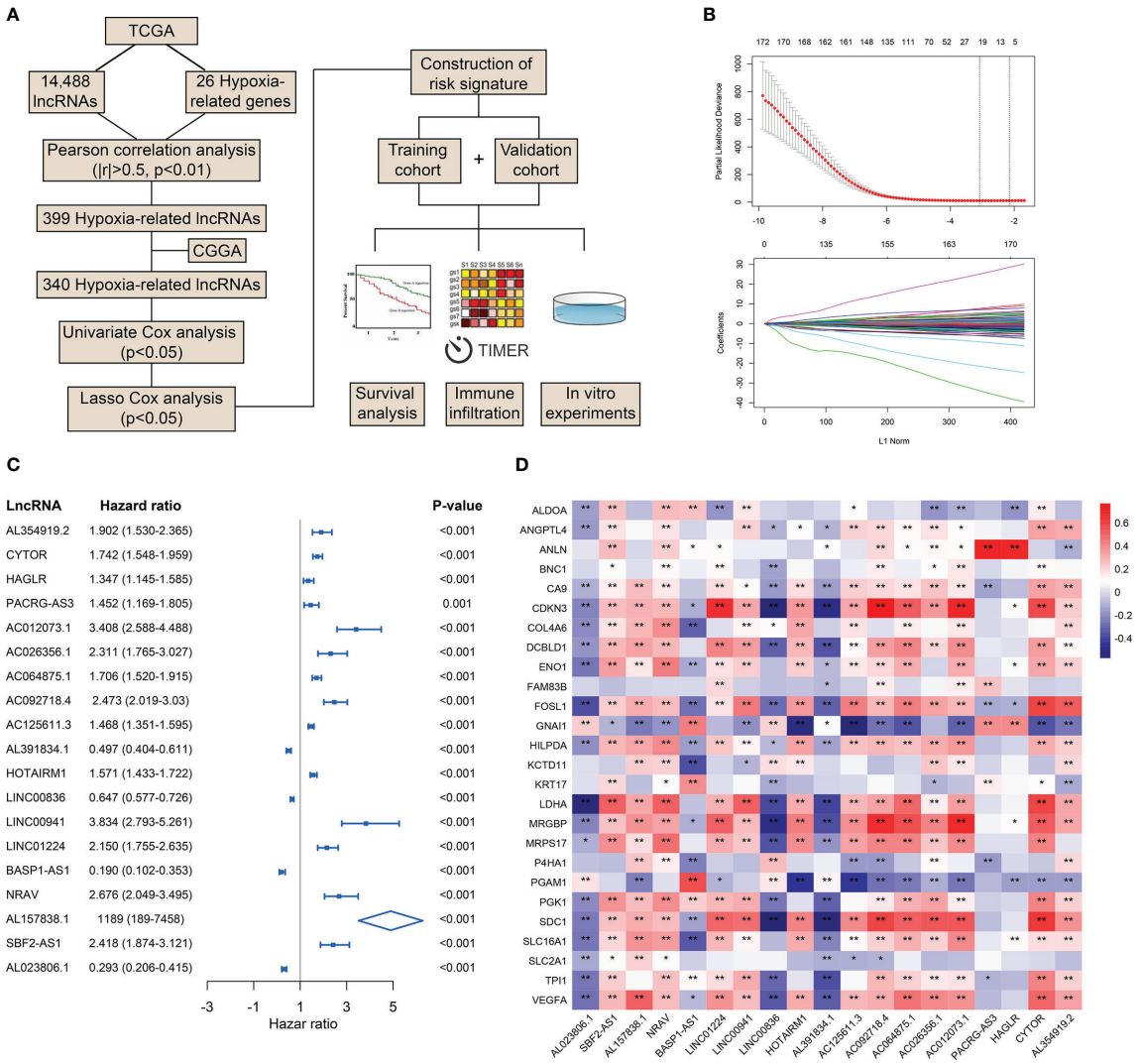

FIGURE 1 | Identification of HRLs in the TCGA and CGGA datasets. **(A)** Flow chart of the whole study. **(B)** Lasso analysis of prognostic HRLs with minimum lambda value. **(C)** Univariate Cox analysis of 19 selected HRLs. **(D)** Heatmap of the correlation between hypoxia-related genes and HRLs. *p < 0.05, **p < 0.01.

heatmap (**Figure 1D**). These results indicated that identified lncRNAs were correlated with hypoxia and were prognostic biomarkers of LGG.

Risk Signature Based on HRL Correlated With the Prognosis and Clinical Features in LGG

Then we constructed the HRL signature to further characterize the role of HRLs in LGG. With the application of Lasso analysis, the coefficient of 19 HRLs was determined, in which the coefficient of four lncRNAs (AL391834.1, LINC00836, BASP1-AS1, and AL023806.1) was negative and that of the other lncRNAs was positive (**Figure 2A**). The risk score of each LGG patients was calculated according to the coefficient and expression of 19 HRLs. Risk score was significantly associated with the expression of hypoxia-related genes (**Figure S2**). Then, LGG patients were divided into high-risk and low-risk groups based on the medium value of risk score (**Figures 2B, C**). Patients whose survival time was relatively short and status was censored were enriched in high-risk group (**Figures 2B, C**). The area under curve (AUC) of risk score in predicting 1-, 3-, and 5-year survival of LGG patients was 0.862, 0.874, and 0.805, respectively, in the TCGA dataset, whereas those were 0.835, 0.860, and 0.845, respectively, in the CGGA dataset (**Figure 2D**). Four protective lncRNAs (AL391834.1, LINC00836, BASP1-AS1, and AL023806.1) were highly expressed in low-risk group, whereas other lncRNAs were highly expressed in high-risk group (**Figures 2E, F**). Regarding several well-known biomarkers of glioma, risk score was significantly elevated in grade III glioma compared with grade II one (p<0.05) (**Figure 2G**). In the meantime, risk score was significantly lower in IDH mutant and 1p19q co-deleted gliomas (p<0.05) (**Figures 2H, I**). However, as

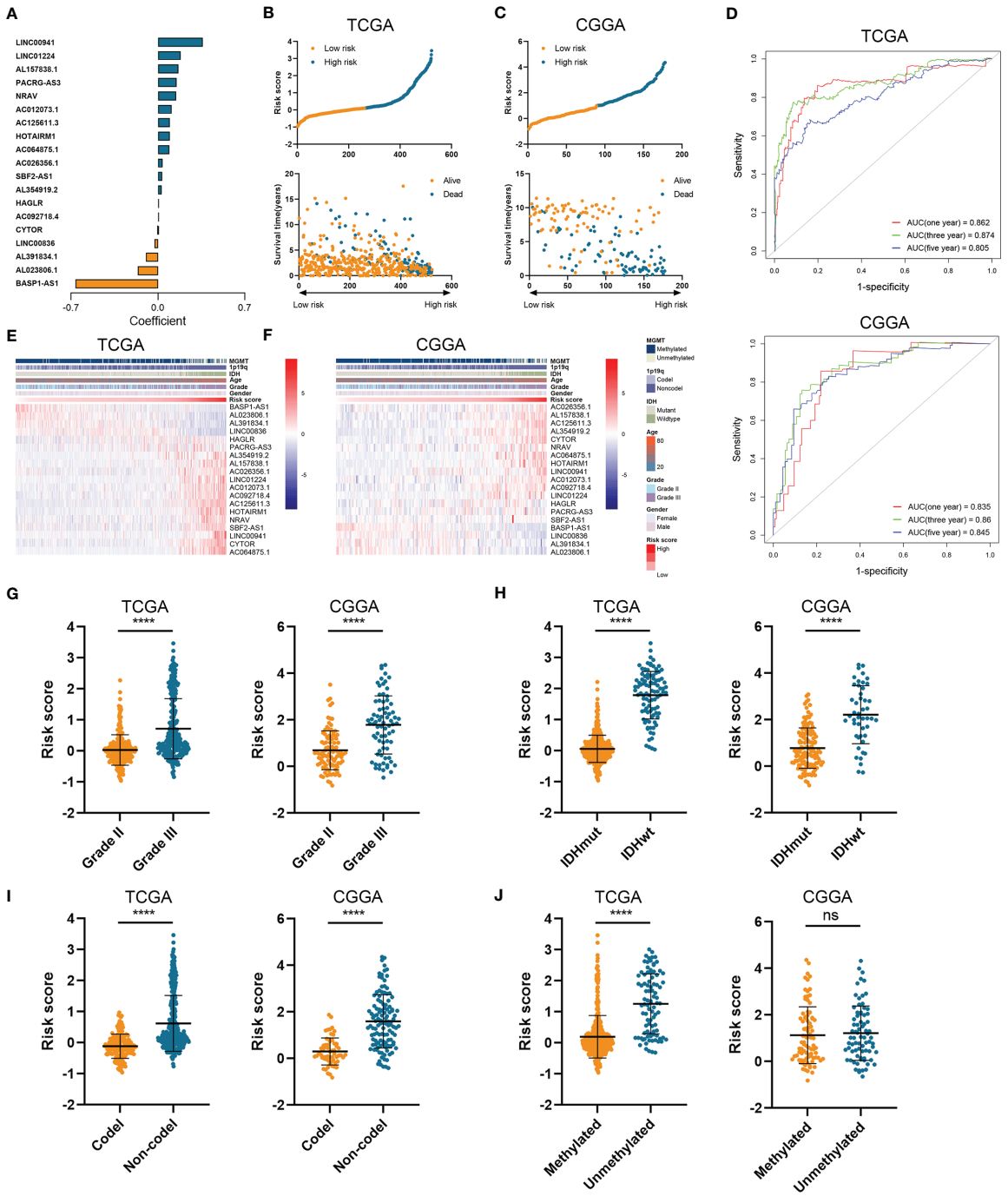

FIGURE 2 | Construction of risk signature based on the expression of HRLs. **(A)** The coefficient of 19 HRLs for the construction of risk signature. **(B, C)** The risk score and survival time of each sample in the TCGA **(B)** and CGGA **(C)** datasets. **(D)** Time-dependent ROC analysis of risk score in predicting 1-, 3-, and 5-year survival. **(E, F)** The expression of 19 HRLs in each sample from low risk to high risk in the TCGA **(E)** and CGGA **(F)** datasets. **(G–J)** The risk score in different grades **(G)**, IDH status **(H)**, 1p19q status **(I)**, and MGMT status **(J)** of gliomas in the two datasets. ****p < 0.0001; ns, no significance.

for the methylation of MGMT promoter, risk score did not share the consistent trend in the TCGA and CCGA dataset, where risk score was significantly elevated in MGMT unmethylated glioma in the TCGA dataset ($p<0.05$) but not in CCGA dataset ($p>0.05$) (**Figure 2J**). These findings suggested that the constructed risk signature based on the expression of HRLs was associated with clinical features of LGG and could predict the survival time of LGG patients.

Risk Score Was an Independent Risk Factor for LGG Patients

To further verify the prognostic value of risk signature, we constructed a nomogram model, whose C-indexes were 0.857 and 0.772 in the TCGA and CGGA datasets, respectively (**Figure 3A**). Moreover, a calibration plot for probability of survival exhibited satisfactory concordance with the prediction of 3-year and 5-year OS in the TCGA dataset (**Figure 3B**). Then we conducted a subgroup analysis to verify the prognostic value of HRL signature in different subgroups of LGG patients. Results showed that LGG patients with high risk score had poor prognosis ($p<0.05$) (**Figure 3C**). As for grade II and III gliomas, high risk score indicated worse prognosis ($p<0.05$) (**Figures 3D, E**). Similarly, in IDH mutant or wildtype LGG patients, those in low-risk group had longer survival time ($p<0.05$) (**Figures 3F, G**). Moreover, when patients were divided into young (age ≤45 years old) and old (age >45 years old) groups, the prognostic value of risk score was consistent ($p<0.05$) (**Figures 3H, I**). Furthermore, multivariate Cox analysis revealed that risk score and grade were independent risk factors for LGG patients in the TCGA and CGGA datasets ($p<0.05$) (**Table 2**). These results indicated that risk score was a potent marker to predict the prognosis of LGG patients.

Risk Stratification Correlated With the Efficacy of Immunotherapy

Since immunotherapy was a promising therapeutic approach in cancer treatment, we explored the association between risk stratification and the efficacy of ICIs. The expression of several immune checkpoints including PD-1, PD-L1, CTLA-4, TIM-3, B7-H3, IDO1, and LAG3 was significantly elevated in high-risk group compared with the low-risk group in the TCGA and CGGA datasets ($p<0.05$) (**Figures 4A, B**). Patients with low risk score and low PD-1 expression had significantly better prognosis than those with high risk score and low PD-1 expression ($p<0.05$) (**Figure 4C**), and patients with low risk score and high PD-1 had prolonged survival than those with high risk score and high PD-1 ($p<0.05$) (**Figure 4C**). Similarly, the stratification based on HRL signature and immune checkpoints was associated with significant survival difference in LGG patients. Patients with low risk score tended to have better prognosis no matter when the immune checkpoints (PD-L1 and CTLA-4) were highly or lowly expressed ($p<0.05$) (**Figures 4D, E**). With the application of TIDE algorithm, we found that TIDE score was significantly elevated in high-risk group, which indicated that patients in high-risk group had worse responses to immunotherapy compared with low-risk group ($p<0.05$) (**Figure 4F**). Thereafter, we extracted the data from IMvigor210 dataset, a cohort of atezolizumab for the treatment of urothelial carcinoma, to investigate the correlation between HRL signature and immunotherapeutic efficacy. Due to the limited number of lncRNA in IMvigor210 dataset, only 11 out of 19 HRLs were identified, and risk score was calculated based on the coefficient and expression of 11 HRLs. Results showed that HRL signature was significantly correlated with the survival of urothelial carcinoma patients receiving atezolizumab treatment ($p<0.05$) (**Figure 4G**). However, in the IMvigor210 cohort, patients with high risk score had a better prognosis, which might be due to the different roles of HRLs in different types of cancer. Nevertheless, these findings suggested that HRL signature might be a potential biomarker to predict the therapeutic response of immune checkpoint inhibitors.

High-Risk Group Exhibited Distinct Immune Characteristics

Further we explored the potential pathways that were associated with the prognosis of patients in high-risk and low-risk groups. GSVA analysis revealed that hypoxia inducible factor 1 (HIF-1) signaling pathway and immune-related pathways including lymphocyte activation, interleukin-mediated signaling pathway, and antigen processing and presentation were highly enriched in high-risk group (**Figures 5A, B**). Differentially expressed genes between high-risk and low-risk groups were screened in the TCGA and CGGA datasets (**Figure S3**). GSEA analysis showed that genes highly expressed in the high-risk group were enriched in hypoxia-related pathway (**Figure 5C**). Meanwhile, these genes were involved in antigen processing and presentation as well as interleukin secretion in GO pathways (**Figure 5D**); in KEGG terms, these genes were associated with antigen processing and presentation, T cell differentiation, and B cell receptor signaling pathway (**Figure 5E**). Therefore, risk stratification based on risk scores was associated with hypoxia-related pathways, and the high-risk group exhibited highly activated immune characteristics.

High Risk Score Indicated Low Tumor Purity and High Immune Infiltration

Since tumor immune microenvironment was implicated to be associated with the prognosis of LGG patients (25, 26), we also explored the correlation between risk signature and immune microenvironment in LGG. The risk score was significantly positively associated with the stromal score, immune score, and ESTIMATE score ($p<0.05$) (**Figures 6A–C**). Then tumor purity was calculated according to the algorithm based on ESTIMATE score (21), and high risk score notably indicated low tumor purity ($p<0.05$) (**Figure 6D**). The infiltration of immune cells was estimated by the conduct of ssGSEA and TIMER algorithms, which contained 28 and six immune cells, respectively. Immune cells such as macrophages, activated T cells, activated B cells, and activated dendritic cells were enriched in high-risk group of samples (**Figures 6E, F**). Besides, risk score was significantly correlated with the abundance of dendritic cell, macrophage, and CD4+ T cells ($p<0.05$) (**Figures 6G, H**). In addition, CIBERSORT algorithm revealed that the abundance of B cells, macrophages (M1 and M2 subtypes), and naïve CD4+ T cells were highly infiltrated in high-risk group ($p<0.05$) (**Figures 6I, J**). These results suggested that risk signature was associated with immune infiltration, and high risk score implied low tumor purity, which might account for its risk role in the prognosis of LGG patients.

Two Prognostic HRLs Were Associated With Prognosis and Immune Infiltration

To investigate the role of HRLs in LGG, we selected two HRLs (LINC00941 and BASP1-AS1), which had the largest absolute

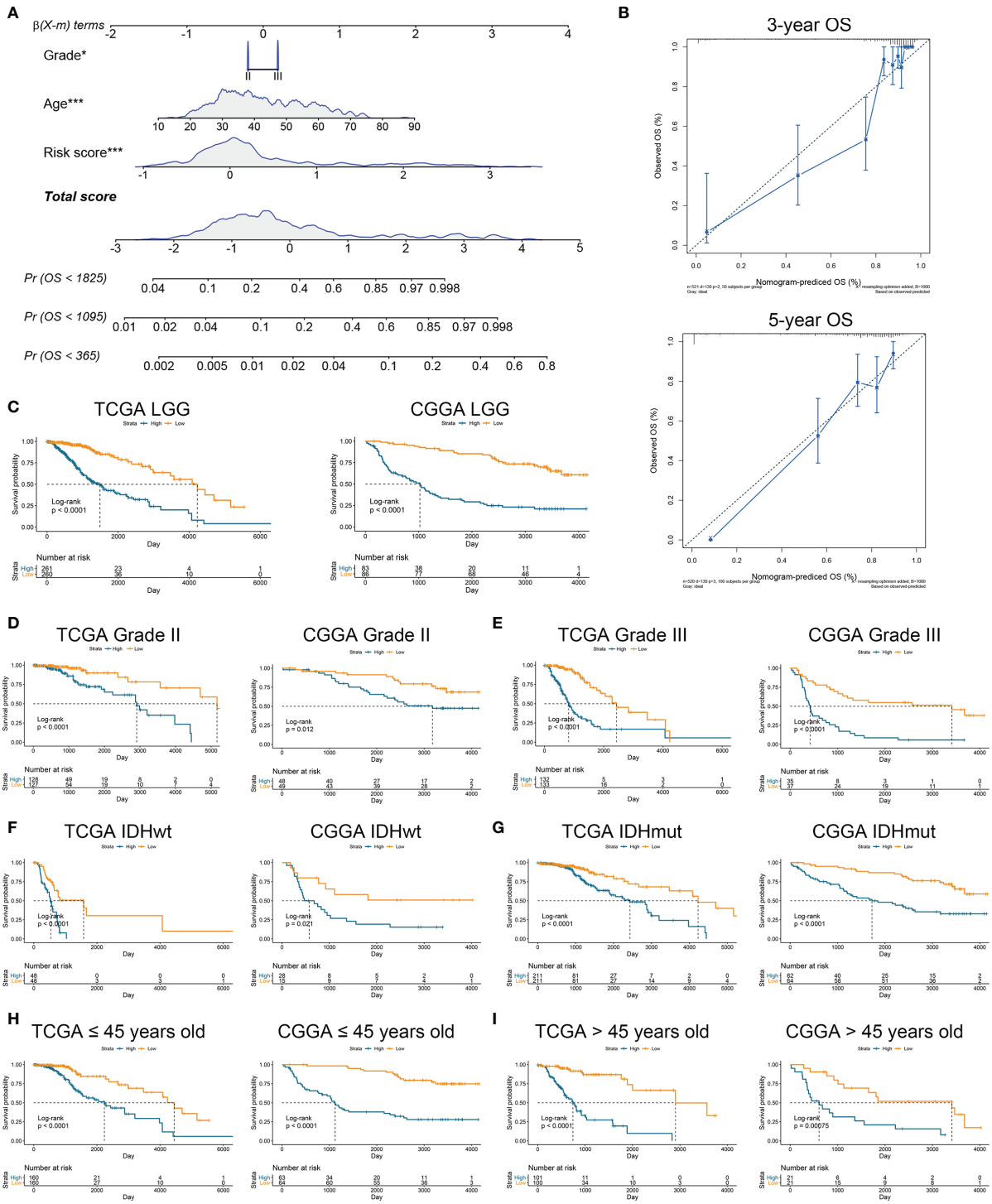

FIGURE 3 | Risk signature was associated with the prognosis of LGG patients. **(A)** Nomogram model of grade, age, and risk score in the TCGA dataset. **(B)** Calibration curve model to verify the predictive value of risk score regarding 3-year and 5-year survival. **(C)** Kaplan-Meier analysis of high-score and low-score in LGG patients. **(D, E)** Kaplan-Meier analysis of high-score and low-score patients in grade II **(D)** and grade III **(E)** gliomas. **(F, G)** Kaplan-Meier analysis of high-score and low-score patients in IDH wildtype **(F)** and IDH mutant **(G)** gliomas. **(H, I)** Kaplan-Meier analysis of high-score and low-score patients ≤45 years old **(H)** or >45 years old **(I)** in diffuse gliomas.

TABLE 2 | Multivariate analysis of risk signature in the training and validation cohorts.

Variables	TCGA (n=522)		CGGA (n=178)	
	HR (95% CI)	P value	HR (95% CI)	P value
Risk score	4.093 (2.884–5.810)	<0.001	1.554 (1.197–2.018)	0.001
Age	1.051 (1.033–1.068)	<0.001	1.011 (0.988–1.034)	0.351
Gender	1.221 (0.850–1.756)	0.280	0.595 (0.370–0.956)	0.032
Grade	1.491 (0.962–2.312)	0.004	2.755 (1.640–4.628)	<0.001
IDH	0.405 (0.193–0.852)	0.017	0.656 (0.353–1.220)	0.183
1p19q	1.574 (0.919–2.695)	0.099	3.825 (1.835–7.972)	<0.001
MGMT	1.028 (0.640–1.649)	0.910	1.325 (0.802–2.190)	0.272

HR, hazard ratio; CI, confidence interval; IDH, isocitrate dehydrogenase; MGMT, O6 -methylguanine-DNA methyltransferase.

coefficient in risk signature, for further analysis. In the TCGA and CGGA datasets, low expression of LINC00941 and high expression of BASP1-AS1 indicated favorable prognosis in LGG patients ($p<0.05$) (**Figures 7A, B**). Moreover, the expression of LINC00941 was significantly elevated in grade III glioma than grade II one, whereas that of BASP1-AS1 exhibited opposite expression pattern ($p<0.05$) (**Figures 7C, D**). Similarly, LINC00941 was highly expressed in IDH wildtype glioma, and BASP1-AS1 was highly expressed in IDH mutant glioma ($p<0.05$) (**Figures 7E, F**). Therefore, LINC00941 and BASP1-AS1 were significantly associated with the prognosis and clinical features of LGG patients. Besides, we found that LINC00941 was significantly negatively correlated with tumor purity ($r=-0.19$, $p<0.05$) whereas BASP1-AS1 was positively associated with tumor purity ($r=0.51$, $p<0.05$) (**Figure 7G**). LINC00941 was significantly positively associated with the infiltration of B cell, CD8+ T cell, neutrophil, macrophage, and dendritic cell ($|r|>0.1$, $p<0.05$), whereas BASP1-AS1 was negatively associated with the infiltration of B cell, CD4+ T cell, neutrophil, macrophage, and dendritic cell ($|r|>0.25$, $p<0.05$) (**Figures 7H–M**). Therefore, LINC00941 and BASP1-AS1 were significantly associated with the prognosis and immune infiltration in LGG.

LINC00941 and BASP-AS1 Exerted Diverse Effects on the Proliferation of Glioma Cells

Then we performed *in vitro* experiments to verify the pathogenic role of LINC00941 and BASP1-AS1 in glioma cells. Three siRNAs were transfected in U251 and DBTRG cells to inhibit the expression of LINC00941 and BASP1-AS1, in which si-LINC00941#1 and si-LINC00941#2 as well as si-BASP1-AS1#1 and si-BASP1-AS1#3 were selected with the relatively high efficiency ($p<0.05$) (**Figures 8A, B**). The inhibition of LINC00941 significantly reduced the proliferation of glioma cells, whereas the inhibition of BASP1-AS1 significantly promoted their proliferation rates ($p<0.05$) (**Figures 8C, D**). Colony formation assay indicated that the knockdown of LINC00941 markedly decreased the colony number, whereas the knockdown of BASP1-AS1 exerted reversed effects ($p<0.05$) (**Figures 8E, F**). Moreover, EdU assay revealed that the proliferation of glioma cells was suppressed by the inhibition of LINC00941 and promoted by the inhibition of BASP1-AS1 (**Figures 8G, H**). Therefore, two prognostic HRLs, LINC00941 and BASP1-AS1, were associated with the proliferation of glioma cells and were potential therapeutic targets for glioma.

Bioinformatic Analysis of Molecular Mechanisms Underlying LINC00941 and BASP1-AS1

The discovery of ceRNA provided a novel insight into the pathogenic role of lncRNA in cancers. Therefore, we applied bioinformatic analyses to explore the potential miRNA and mRNA targets of LINC00941 and BASP1-AS1. Since lncRNA tended to elevate the expression of mRNA by acting as ceRNA, we screened co-expressed mRNAs of LINC00941 and BASP1-AS1 in the TCGA dataset. After the intersect with predicted miRNA and mRNA targets, the ceRNA network of LINC00941 and BASP1-AS1 was constructed (**Figures 9A, B**). Enrichment analysis revealed that LINC00941-targeting mRNAs were associated with cellular senescence and ion channel activity, whereas BASP1-AS1-targeting mRNAs were enriched in membrane potential, synaptic activity, and ion channel activity (**Figures 9C, D**). Differentially expressed genes were screened between high and low expression of LINC00941 or BASP1-AS1 groups (**Figures S3C, D**). GSEA revealed that epithelial mesenchymal transition (EMT), K-ras signaling, reactive oxygen species pathway, and TNF-α signaling pathway were highly enriched in high-LINC00941 group, whereas myc and Wnt/β-catenin were enriched in low-LINC00941 group (**Figure 9E**). Meanwhile, Hedgehog and K-ras signaling pathways were enriched in high-BASP1-AS1 group, and EMT, IL-6/JAK/STAT3, Interferon-α, and TNF-α signaling pathways were enriched in low-BASP1-AS1 group (**Figure 9F**). Therefore, these results indicated that LINC00941 and BASP1-AS1 might affect the proliferation of glioma cells by regulating ion channel activity *via* modulating EMT and TNF-α signaling pathway.

DISCUSSION

Hypoxia and lncRNA have been implicated to be critical factors to promote the progression of glioma (27, 28). In our study, we identified 340 HRLs and constructed a novel risk signature composed of 19 HRLs. The risk score exhibited potent value in predicting the prognosis of LGG patients and was significantly associated with the prognosis of LGG patients. Moreover, HRL signature could distinguish patients with similar expression levels of immune checkpoints and might predict the efficacy of ICIs. Additionally, hypoxia-related pathways and immune pathways were enriched in high-risk group, and high risk score indicated

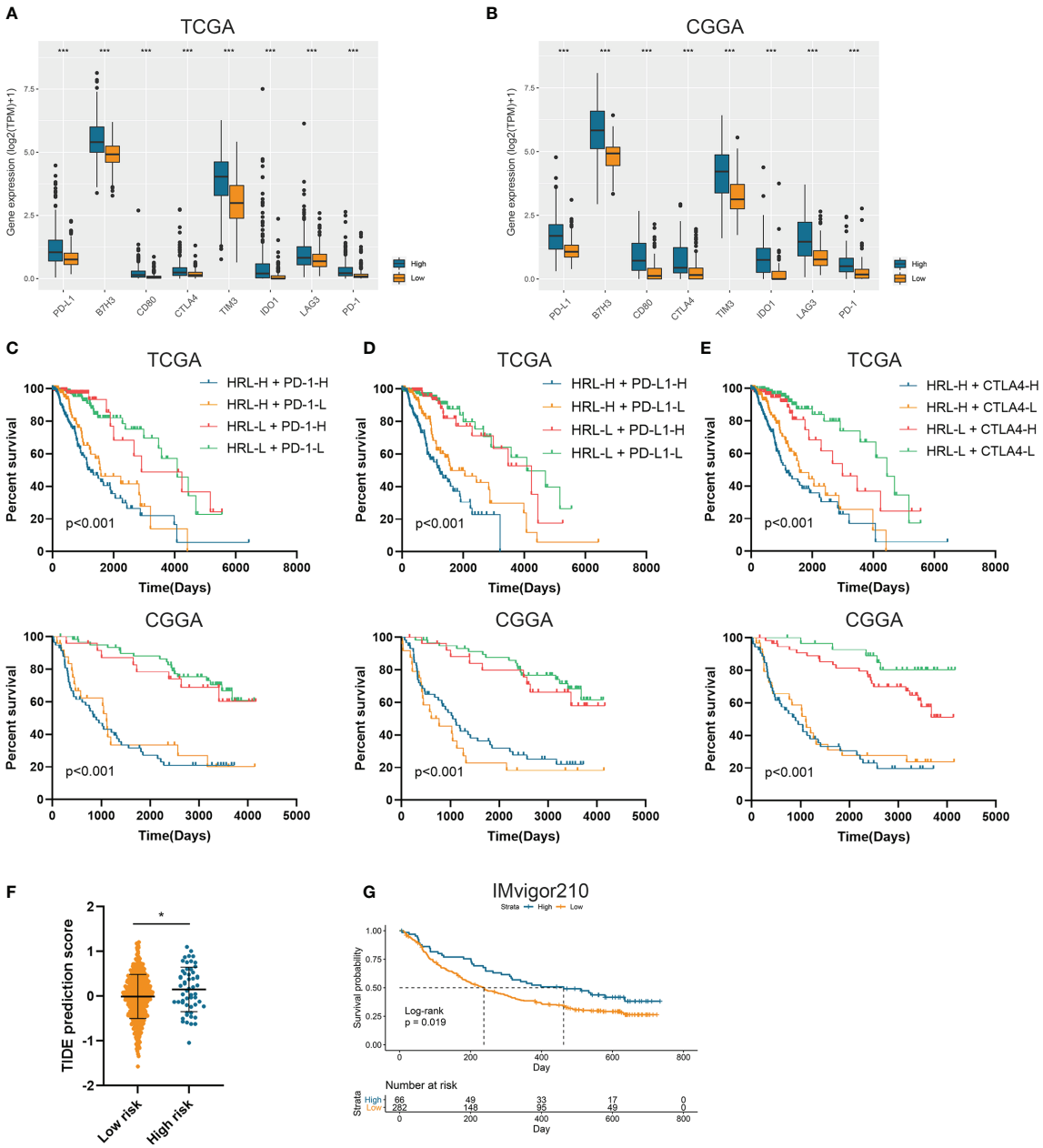

FIGURE 4 | Risk stratification correlated with the efficacy of immunotherapy. **(A, B)** The expression of several immune checkpoints in high-risk and low-risk groups in the TCGA **(A)** and CGGA **(B)** datasets. **(C–E)** Kaplan-Meier analyses of overall survival among four patient groups stratified by the HRL signature and PD-1 **(C)**, PD-L1 **(D)**, and CTLA-4 **(E)**. **(F)** TIDE score of high-risk and low-risk groups in TCGA dataset. **(G)** Kaplan-Meier analysis of urothelial carcinoma patients stratified by HRL signature in IMvigor210 cohort. *p < 0.05, ***p < 0.001.

low tumor purity and high immune infiltration. *In vitro* experiments revealed that two major HRLs, LINC00941 and BASP1-AS1, could significantly affect the proliferation of glioma cells, in which EMT and TNF-α signaling pathway might be the underlying mechanism. Our study revealed a novel HRL signature to predict the prognosis of LGG patients. LINC00941 and BASP1-AS1 could be potential targets for LGG treatment.

Hypoxia microenvironment induced by tumor cells could facilitate the progression of tumors. Multiple studies revealed that hypoxia-related genes were associated with the prognosis of patients with pancreatic cancer, lung adenocarcinoma, head and neck cancer, bladder cancer, and other malignancies (18, 29–31). In high-risk bladder cancer, a signature composed of 24 hypoxia-related genes could significantly predict the prognosis and

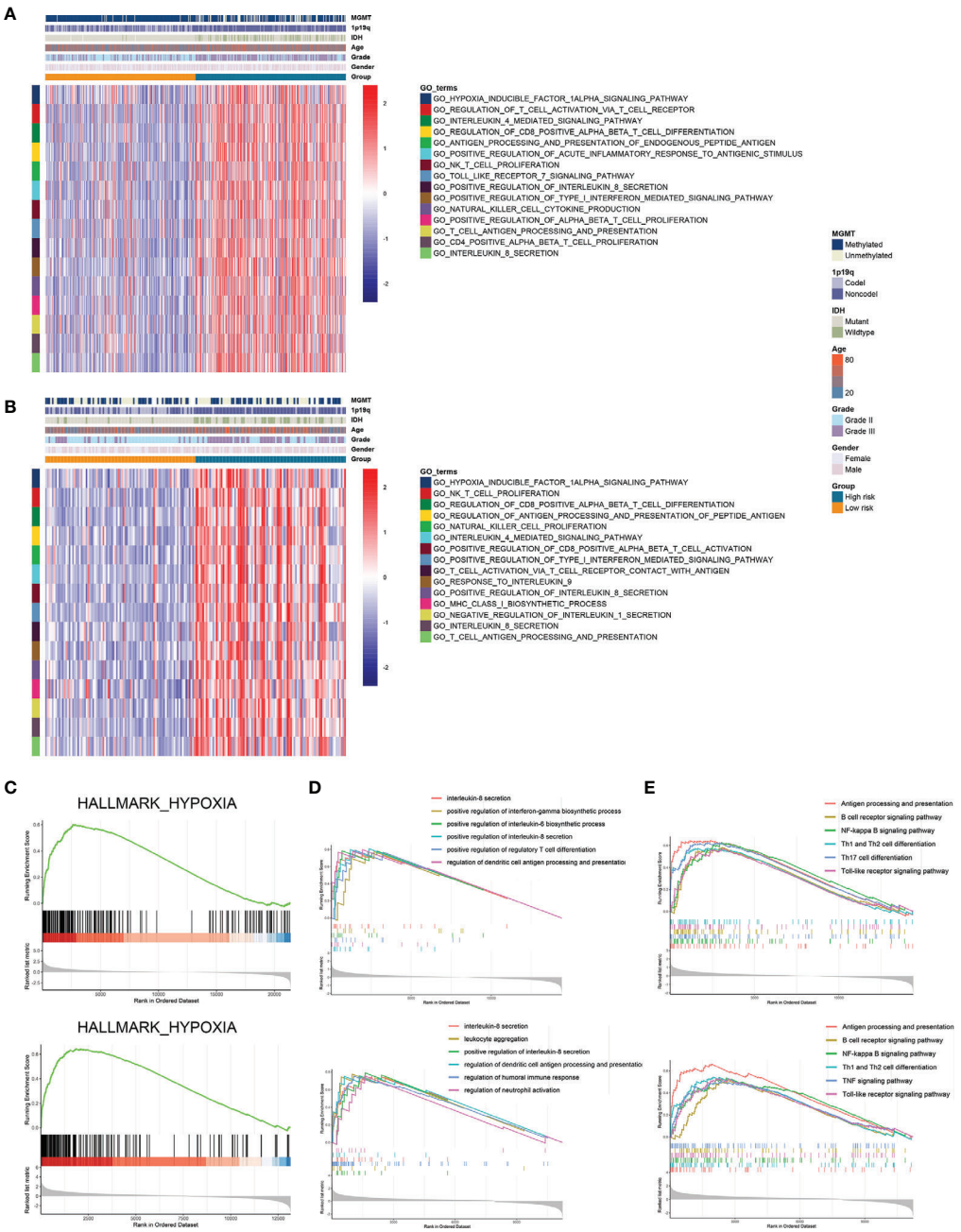

FIGURE 5 | Risk stratification exhibited distinct immune characteristics. **(A, B)** GSVA analysis of hypoxia and immune pathways in high-risk and low-risk groups in the TCGA **(A)** and CGGA **(B)** datasets. **(C)** Differentially expressed genes between high-risk and low-risk groups were enriched in hypoxia-related pathways. **(D, E)** GSEA analysis of differentially expressed genes between high-risk and low-risk groups in GO **(D)** and KEGG **(E)** terms.

benefit from radiotherapy (31). Another 28-gene hypoxia signature also exhibited potent ability to predict the prognosis of bladder cancer patients (32). Moreover, a 26-gene hypoxia signature was shown to predict the benefit from hypoxia-modifying treatment in laryngeal cancer (17). When combination with immune genes, head and neck cancer patients were classified into three groups, in which those with low-hypoxia and high-immune characteristics had relatively favorable prognosis (18). In our study, 26 hypoxia-related genes were selected to screen HRLs, in which GNAI1 and PGAM1 were significantly associated with almost all HRLs. Kaplan-Meier analysis revealed that GNAI1 and PGAM1 were protective factors for LGG patients. Besides, GNAI1 and PGAM1 were positively associated with the expression of BASP1-AS1,

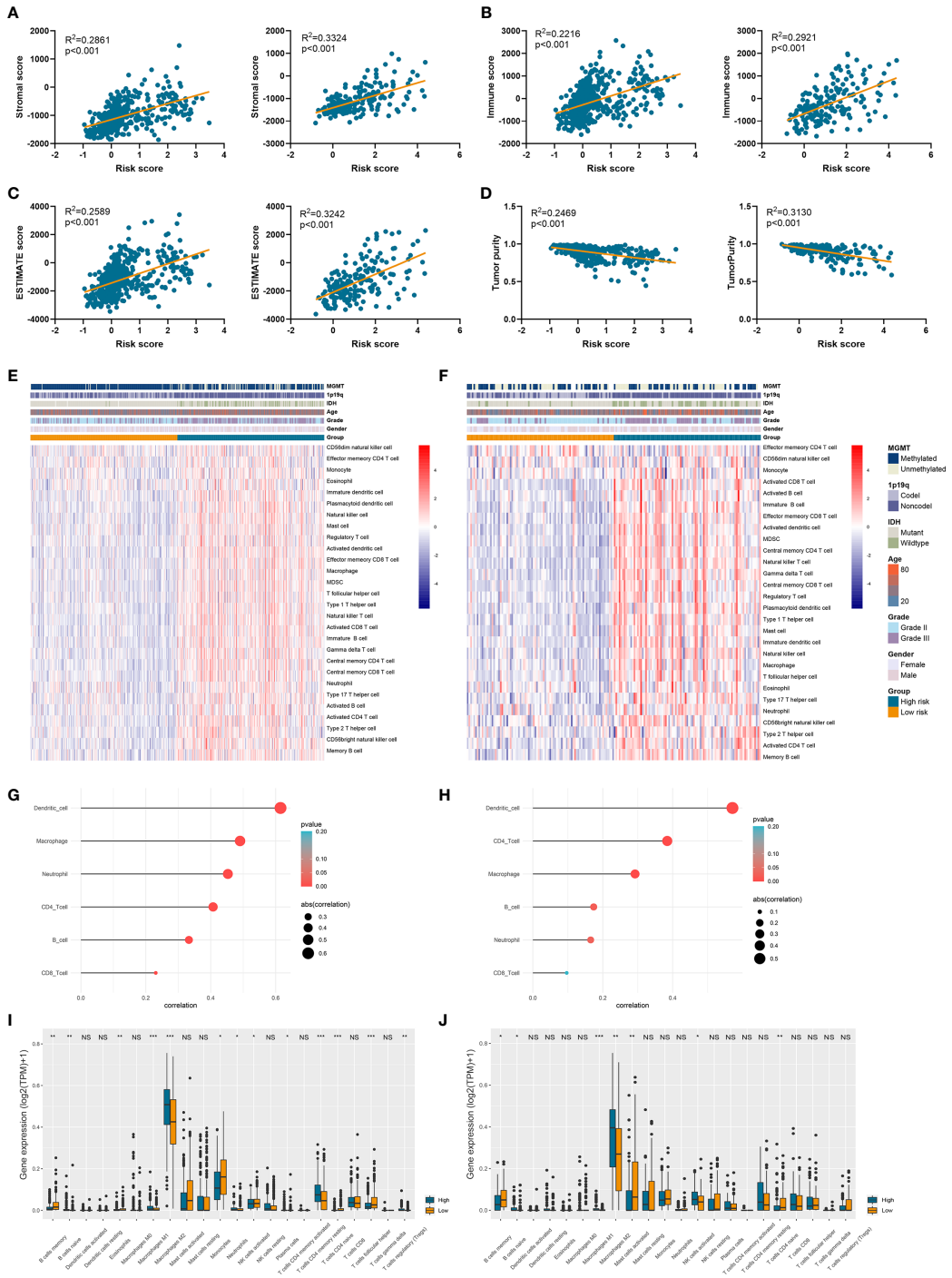

FIGURE 6 | Risk signature was associated with tumor purity and immune infiltration. **(A–D)** The association between risk score and stromal score **(A)**, immune score **(B)**, ESTIMATE score **(C)**, and tumor purity **(D)**. **(E, F)** The abundance of 28 immune cells estimated by ssGSEA algorithm in high-risk and low-risk groups in TCGA **(E)** and CGGA **(F)** datasets. **(G, H)** The correlation between risk score and six immune cells estimated by TIMER algorithm in TCGA **(G)** and CGGA **(H)** datasets. **(I, J)** The abundance of 22 immune cells estimated by CIBERSORT algorithm in high-risk and low-risk groups in TCGA **(I)** and CGGA **(J)** datasets. *p < 0.05, **p < 0.01, ***p < 0.001, ns, no significance.

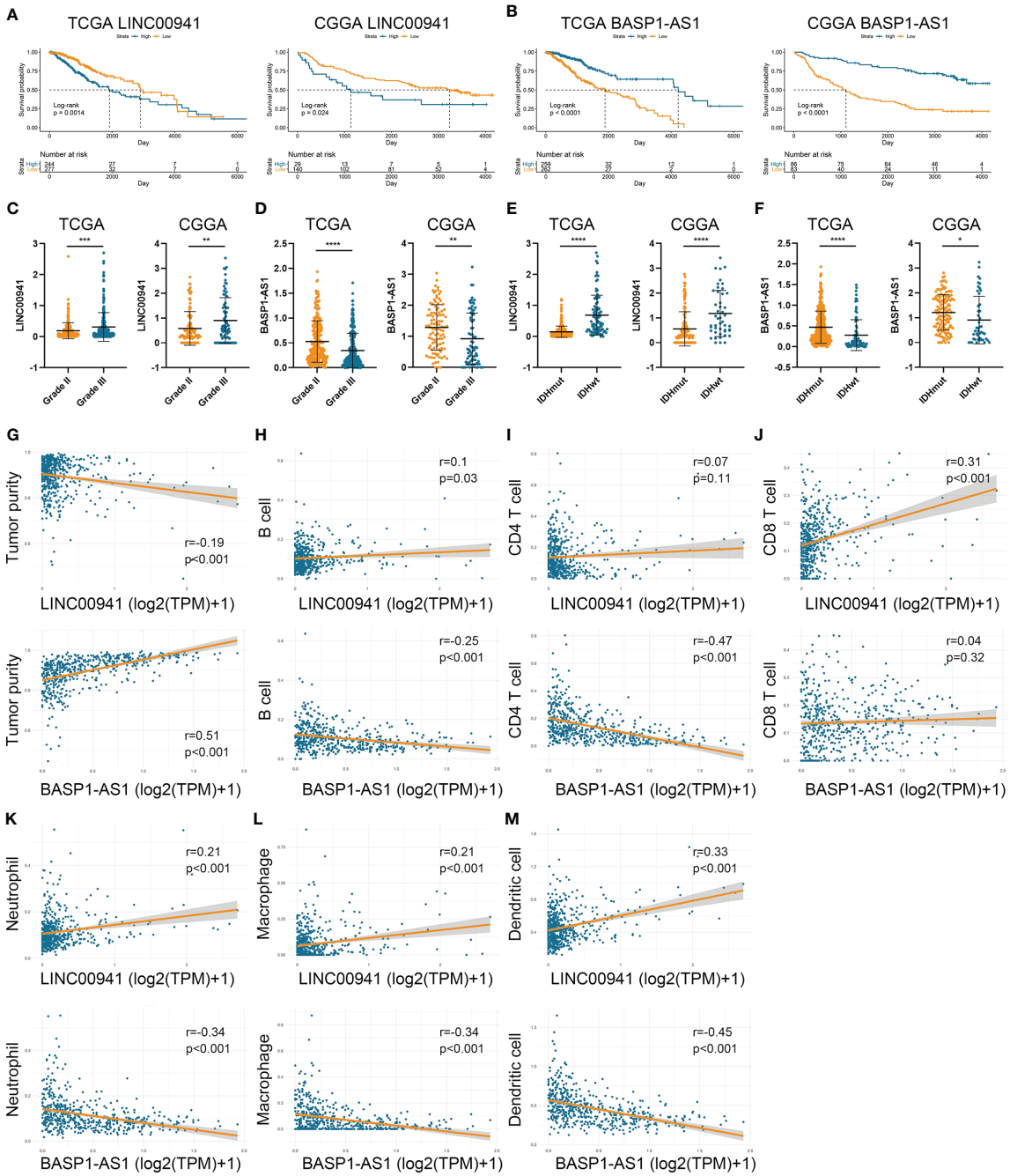

FIGURE 7 | LINC00941 and BASP1-AS1 were associated with the prognosis and immune infiltration in LGG. **(A, B)** Kaplan-Meier analysis of LINC00941 and BASP1-AS1 in LGG patients of TCGA **(A)** and CGGA **(B)** datasets. **(C, D)** The expression of LINC00941 **(C)** and BASP1-AS1 **(D)** in grade II and III gliomas. **(E, F)** The expression of LINC00941 **(E)** and BASP1-AS1 **(F)** in IDH wildtype and IDH mutant gliomas. **(G)** The correlation between LINC00941 and BASP1-AS1 with tumor purity. **(H–M)** The correlation between LINC00941 and BASP1-AS1 with the abundance of B cell **(H)**, CD4+ T cell **(I)**, CD8+ T cell **(J)**, neutrophil **(K)**, macrophage **(L)**, and dendritic cell **(M)**. *p < 0.05, **p < 0.01, ***p < 0.001, ****p < 0.0001.

whose high expression indicated favorable prognosis in LGG. Meanwhile, the expression of GNAI1 and PGAM1 was negatively associated with that of LINC00941 or LINC01224, which were risk factors for LGG patients. Therefore, GNAI1 and PCAM1 might be potential tumor suppressor in LGG. Further, we constructed a 19-lncRNA hypoxia signature and calculated risk score of LGG patients. Further analyses revealed that risk score had a potent accuracy in predicting the survival of LGG

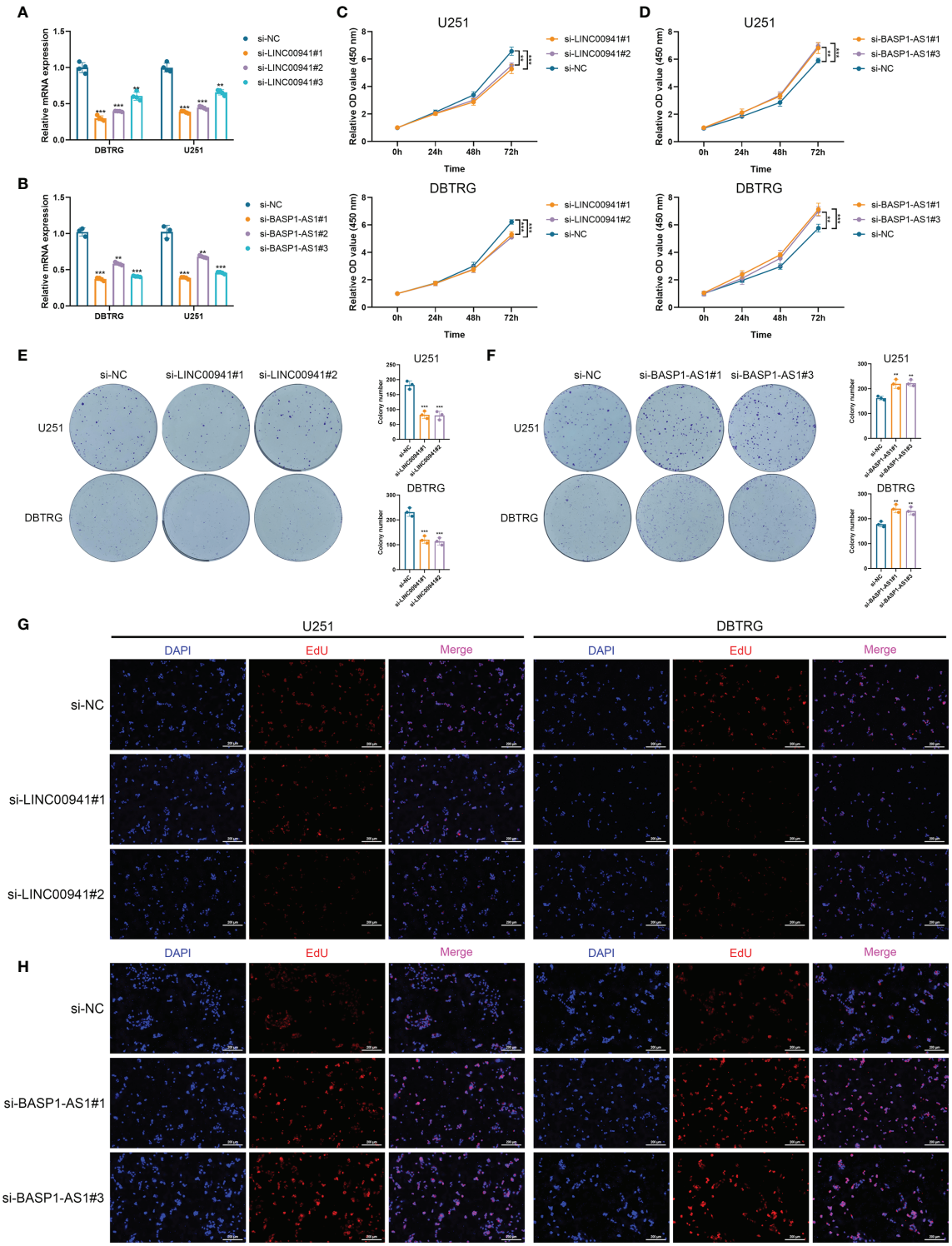

FIGURE 8 | LINC00941 and BASP1-AS1 exerted opposite effects on the proliferation of glioma cells. **(A, B)** The expression of LINC00941 **(A)** and BASP1-AS1 **(B)** after the transfection of three specific siRNAs. **(C, D)** CCK-8 assay of U251 and DBTRG cells after the knockdown of LINC00941 **(C)** and BASP1-AS1 **(D)**. **(E, F)** Colony formation assay of U251 and DBTRG cells after the knockdown of LINC00941 **(E)** and BASP1-AS1 **(F)**. **(G, H)** EdU assay of U251 and DBTRG cells after the knockdown of LINC00941 **(G)** and BASP1-AS1 **(H)**. $^{**}p < 0.01$, $^{***}p < 0.001$.

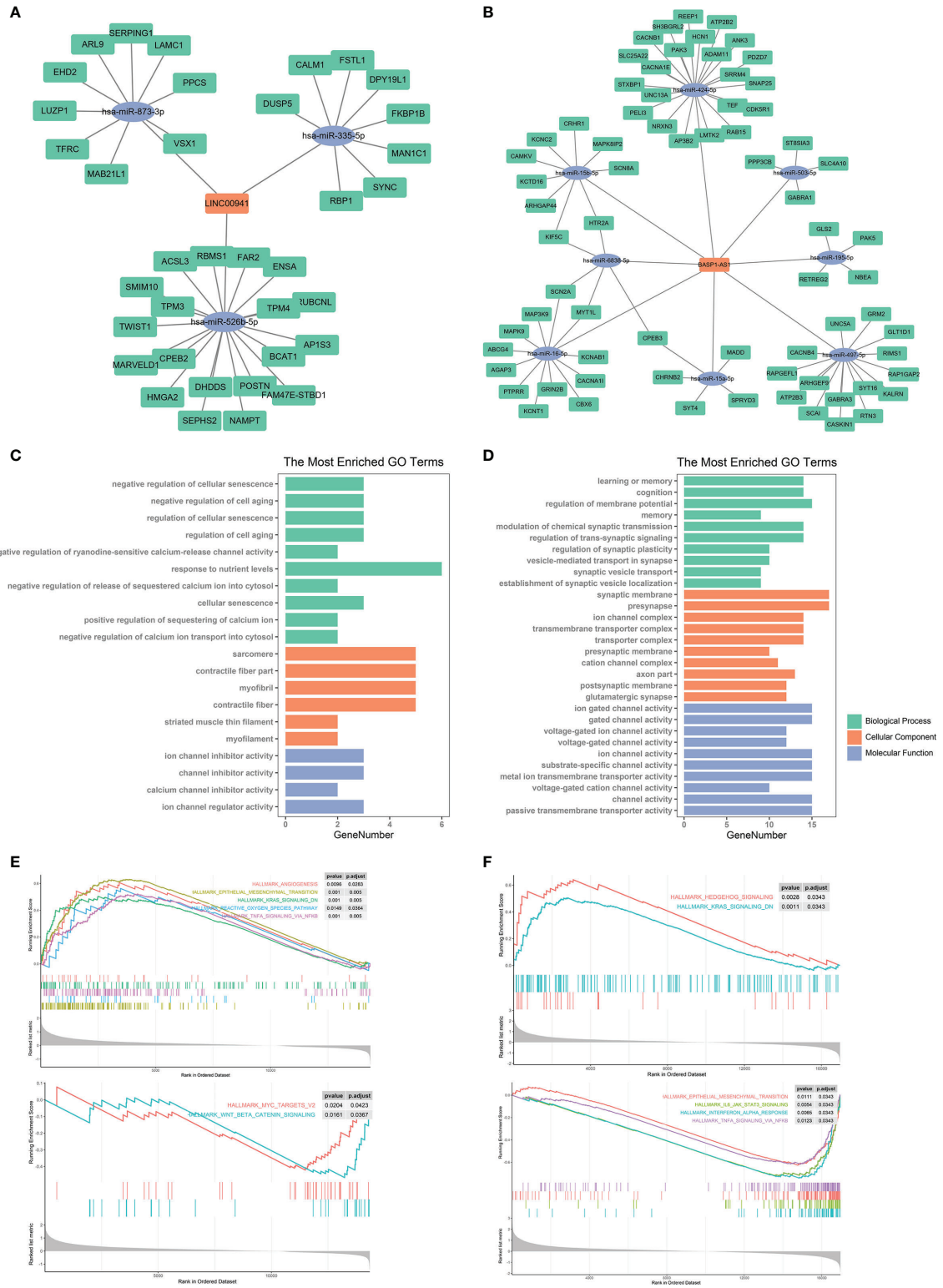

FIGURE 9 | Bioinformatic analysis of molecular mechanisms underlying LINC00941 and BASP1-AS1. **(A, B)** Competing endogenous RNA network of LINC00941 **(A)** and BASP1-AS1 **(B)**. **(C, D)** Enrichment analysis of targeting mRNAs of LINC00941 **(C)** and BASP1-AS1 **(D)**. **(E, F)** Gene set enrichment analysis of differentially expressed genes between high- and low-expression of LINC00941 **(E)** and BASP1-AS1 **(F)**.

patients. Besides, high risk score indicated poor prognosis in different subgroups of LGG patients. When other clinical features were taken into consideration, risk score remained to be an independent risk factor for LGG patients. Therefore, our study revealed a novel HRL signature that could be used to predict the prognosis of LGG patients.

ICIs have shown promising efficacy in clinical care of various cancers (33, 34). However, since different patients exhibited diverse responses to ICIs, the discovery of predictive biomarkers would benefit cancer patients receiving ICIs. Although PD-L1 has been proposed to be a biomarker that is positively associated with the efficacy of ICI, the single biomarker is insufficient for cancer patients (35, 36). TIDE algorithm was developed by Jiang et al. to predict the responses to ICIs through characterizing dysfunctional T cells and infiltrated cytotoxic T lymphocytes (CTLs) level (20). In our study, we found that immune checkpoints were highly expressed in high-risk group stratified by HRL signature. HRL signature could distinguish patients with similar expression levels of immune checkpoints. Moreover, patients with low risk score and low immune checkpoints expression had significantly prolonged survival, which indicated that low risk score was associated with better response to ICIs. Since high TIDE score indicated poor response to ICI, our study revealed that the TIDE score was significantly decreased in the low-risk group, which was consistent with our hypothesis. Therefore, HRL signature might facilitate the application of ICI for the treatment of glioma. In IMvigor210 cohort, HRL signature was significantly associated with the prognosis of urothelial carcinoma patients, and high risk score indicated favorable prognosis. According to our results, the high-risk group had high immune infiltration and well responses to immunotherapy, which might account for the favorable prognosis of high-risk group in IMvigor210 cohort.

Recently, immune microenvironment was shown to play a critical role in cancer development (37–40). Multiple studies have demonstrated the immunosuppressive context surrounding glioma cell (41). Glioma cells would promote the expression of immune checkpoints such as programmed cell death 1 ligand (PD-L1) to induce immune escape (42). Besides, glioma cells would activate tumor-associated macrophages and regulatory T (Treg) cells, which suppressed the activities of cytotoxic T cells (43). HIF-1α was reported to regulate the functions and differentiations of myeloid-derived suppressor cells (44), which were a major component of immune-suppressive network. Besides, HIF-1α could increase the expression of PD-L1 by binding to its hypoxia response elements (45). Therefore, hypoxia microenvironment would mediate immune-suppressive effects and facilitate the progression of tumor cells. In this study, we found that high-risk group was associated with HIF-1α and immune-related pathways. Genes highly expressed in high-risk group was enriched in hypoxia and immune processes. Besides, high-risk group had a high infiltration of dendritic cell, macrophage, and T cells, which might be due to its hypoxia characteristics. However, it should be noted that the direct effect of HRLs on immune infiltration required additional experiments, and high immune infiltration was a characteristic of high-risk group rather than a result caused by HRLs. It seemed to be contradictory that the high immune infiltration indicated favorable prognosis in head and neck cancer whereas it indicated poor prognosis in LGG (18, 25, 26). Nevertheless, high infiltration of cytotoxic immune cells could suppress the development of tumor cells and result in favorable prognosis. In contrast, high infiltration of immunosuppressive immune cells such as M2 subtype macrophage and myeloid-derived suppressor cell would promote the progression of tumor and lead to poor prognosis. Therefore, immune-activating strategies such as ICIs remain to be promising therapeutics for glioma.

A previous study reported that immune infiltration-related lncRNA signature could predict responses to ICIs in non-small cell lung cancer patients, indicating the potential crosstalk between immune infiltration and immunotherapy response (46). Jiang et al. suggested that CTL-high tumors tended to evade from immune surveillance through inducing T cell dysfunction, which was defined as "non-responders" in TIDE algorithm (20). In our study, ssGSEA algorithm revealed that activated CD8+ T cell was highly enriched in high-risk group, which indicated a poor response to ICIs and was consistent with the elevated TIDE score in high-risk group.

Numerous studies have reported the role of lncRNA as biomarkers or potential therapeutic targets in cancers and other diseases (47, 48). Signatures composed on lncRNAs also exhibited promising value in predicting the prognosis and recurrence of cancers. Zhou et al. identified a six-lncRNA signature that could efficiently predict the risk of tumor recurrence in patients with colon cancer (49). Besides, signatures composed of immune-related lncRNA was shown to indicate the prognosis of patients with hepatocellular carcinoma, breast cancer, lung adenocarcinoma, and esophageal squamous cell carcinoma (50–53). In glioma, lncRNA signature was implicated to be a promising biomarker of tumor progression (54). However, to our limited knowledge, no study had reported the role of HRLs in the prognosis and immune microenvironment of gliomas. Our study constructed a 19-HRL signature that was associated with the prognosis the LGG patients. Besides, two major HRLs of the risk signature, LINC00941 and BASP1-AS1, were selected as the representation of HRL signature. Bioinformatic analyses indicated that LINC00941 and BASP1-AS1 were significantly associated with the prognosis and immune infiltration in LGG. *In vitro* experiments revealed that the inhibition of LINC00941 could significantly suppress the proliferation of glioma cells, whereas the inhibition of BASP1-AS1 exerted reversed effects. Previous studies indicated that ion channel was associated with the progression and prognosis of glioma (55, 56). Moreover, cell senescence was reported to correlate with the proliferation and migration of glioma (57, 58). Through the construction of ceRNA network, we found that LINC00941 and BASP1-AS1 might affect the proliferation of glioma cells *via* regulating ion channel activities and cell senescence. In addition, in high-LINC00941 and low-BASP1-AS1 group, EMT and TNF-α signaling pathways were highly enriched. Since EMT and TNF-α were found to be highly involved in the progression of glioma

(59, 60), the increased level of LINC00941 and the decreased level of BASP1-AS1 might account for the promoted proliferation of glioma cells through activating EMT and TNF-α signaling pathway. Therefore, LINC00941 and BASP1-AS1 could be potential targets for glioma treatment.

CONCLUSIONS

To sum up, our study constructed a novel HRL signature that could predict the prognosis and was associated with immune infiltration of LGG. HRLs could be novel biomarkers to predict the prognosis and potential targets for LGG treatment.

DATA AVAILABILITY STATEMENT

The original contributions presented in the study are included in the article/**Supplementary Material**. Further inquiries can be directed to the corresponding authors.

AUTHOR CONTRIBUTIONS

QC and CL conceived, designed, and supervised the study. SX drafted the manuscript. SX, LT, and ZL collected the data. SX performed data analysis and visualization. All authors contributed to the article and approved the submitted version.

FUNDING

This work was supported by National Natural Science Foundation of China (81703622, 81873635, 81902553, 82073893), Natural Science Foundation of Hunan Province (2018JJ3838, 2019JJ50942), Key Research and Development Program of Hunan Province (2018SK2101), China Postdoctoral Science Foundation (2018M633002, 2021T140750), Hunan Provincial Health Committee Foundation of China (C2019186), and Xiangya Hospital Central South University postdoctoral foundation.

SUPPLEMENTARY MATERIAL

The Supplementary Material for this article can be found online at: https://www.frontiersin.org/articles/10.3389/fimmu.2021.731048/full#supplementary-material

Supplementary Figure S1 | Kaplan-Meier analysis of randomly selected eight HRLs in LGG patients.

Supplementary Figure S2 | The correlation between risk score and hypoxia-related genes.

Supplementary Figure S3 | Volcano plot of differentially expressed genes. **(A, B)** Differentially expressed genes between high-risk and low-risk groups in the TCGA **(A)** and CGGA **(B)** datasets. **(C, D)** Differentially expressed genes between high or low expression of LINC00941 **(C)** and BASP1-AS1 **(D)** groups.

Supplementary Figure S4 | Kaplan-Meier analysis of GNAI1 and PGAM1 in TCGA dataset.

REFERENCES

1. Ostrom QT, Cioffi G, Gittleman H, Patil N, Waite K, Kruchko C, et al. CBTRUS Statistical Report: Primary Brain and Other Central Nervous System Tumors Diagnosed in the United States in 2012-2016. *Neuro Oncol* (2019) 21 (Supplement_5):v1–v100. doi: 10.1093/neuonc/noz150
2. Smoll NR, Gautschi OP, Schatlo B, Schaller K, Weber DC. Relative Survival of Patients With Supratentorial Low-Grade Gliomas. *Neuro Oncol* (2012) 14 (8):1062–9. doi: 10.1093/neuonc/nos144
3. Ohgaki H, Kleihues P. Population-Based Studies on Incidence, Survival Rates, and Genetic Alterations in Astrocytic and Oligodendroglial Gliomas. *J Neuropathol Exp Neurol* (2005) 64(6):479–89. doi: 10.1093/jnen/64.6.479
4. Jiang T, Nam DH, Ram Z, Poon WS, Wang J, Boldbaatar D, et al. Clinical Practice Guidelines for the Management of Adult Diffuse Gliomas. *Cancer Lett* (2021) 499:60–72. doi: 10.1016/j.canlet.2020.10.050
5. Petrova V, Annicchiarico-Petruzzelli M, Melino G, Amelio I. The Hypoxic Tumour Microenvironment. *Oncogenesis* (2018) 7(1):10. doi: 10.1038/s41389-017-0011-9
6. Jing X, Yang F, Shao C, Wei K, Xie M, Shen H, et al. Role of Hypoxia in Cancer Therapy by Regulating the Tumor Microenvironment. *Mol Cancer* (2019) 18(1):157. doi: 10.1186/s12943-019-1089-9
7. Colwell N, Larion M, Giles AJ, Seldomridge AN, Sizdahkhani S, Gilbert MR, et al. Hypoxia in the Glioblastoma Microenvironment: Shaping the Phenotype of Cancer Stem-Like Cells. *Neuro Oncol* (2017) 19(7):887–96. doi: 10.1093/neuonc/now258
8. Lin W, Wu S, Chen X, Ye Y, Weng Y, Pan Y, et al. Characterization of Hypoxia Signature to Evaluate the Tumor Immune Microenvironment and Predict Prognosis in Glioma Groups. *Front Oncol* (2020) 10:796. doi: 10.3389/fonc.2020.00796
9. Xiao K, Tan J, Yuan J, Peng G, Long W, Su J, et al. Prognostic Value and Immune Cell Infiltration of Hypoxic Phenotype-Related Gene Signatures in Glioblastoma Microenvironment. *J Cell Mol Med* (2020) 24(22):13235–47. doi: 10.1111/jcmm.15939
10. Peng WX, Koirala P, Mo YY. LncRNA-Mediated Regulation of Cell Signaling in Cancer. *Oncogene* (2017) 36(41):5661–7. doi: 10.1038/onc.2017.184
11. Yang G, Lu X, Yuan L. LncRNA: A Link Between RNA and Cancer. *Biochim Biophys Acta* (2014) 1839(11):1097–109. doi: 10.1016/j.bbagrm.2014.08.012
12. Liu C, Peng Z, Li P, Fu H, Feng J, Zhang Y, et al. lncRNA RMST Suppressed GBM Cell Mitophagy Through Enhancing FUS SUMOylation. *Mol Ther Nucleic Acids* (2020) 19:1198–208. doi: 10.1016/j.omtn.2020.01.008
13. Xin J, Zhao YH, Zhang XY, Tian LQ. LncRNA NFIA-AS2 Promotes Glioma Progression Through Modulating the miR-655-3p/ZFX Axis. *Hum Cell* (2020) 33(4):1273–80. doi: 10.1007/s13577-020-00408-9
14. Deng Y, Zhou L, Yao J, Liu Y, Zheng Y, Yang S, et al. Associations of lncRNA H19 Polymorphisms at MicroRNA Binding Sites With Glioma Susceptibility and Prognosis. *Mol Ther Nucleic Acids* (2020) 20:86–96. doi: 10.1016/j.omtn.2020.02.003
15. Ruan X, Zheng J, Liu X, Liu Y, Liu L, Ma J, et al. lncRNA LINC00665 Stabilized by TAF15 Impeded the Malignant Biological Behaviors of Glioma Cells *via* STAU1-Mediated mRNA Degradation. *Mol Ther Nucleic Acids* (2020) 20:823–40. doi: 10.1016/j.omtn.2020.05.003
16. Rosenberg JE, Hoffman-Censits J, Powles T, van der Heijden MS, Balar AV, Necchi A, et al. Atezolizumab in Patients With Locally Advanced and Metastatic Urothelial Carcinoma Who Have Progressed Following Treatment With Platinum-Based Chemotherapy: A Single-Arm, Multicentre, Phase 2 Trial. *Lancet (London England)* (2016) 387 (10031):1909–20. doi: 10.1016/S0140-6736(16)00561-4
17. Eustace A, Mani N, Span PN, Irlam JJ, Taylor J, Betts GN, et al. A 26-Gene Hypoxia Signature Predicts Benefit From Hypoxia-Modifying Therapy in Laryngeal Cancer But Not Bladder Cancer. *Clin Cancer Res* (2013) 19 (17):4879–88. doi: 10.1158/1078-0432.CCR-13-0542
18. Brooks JM, Menezes AN, Ibrahim M, Archer L, Lal N, Bagnall CJ, et al. Development and Validation of a Combined Hypoxia and Immune Prognostic Classifier for Head and Neck Cancer. *Clin Cancer Res* (2019) 25 (17):5315–28. doi: 10.1158/1078-0432.CCR-18-3314
19. Hanzelmann S, Castelo R, Guinney J. GSVA: Gene Set Variation Analysis for Microarray and RNA-Seq Data. *BMC Bioinf* (2013) 14:7. doi: 10.1186/1471-2105-14-7

20. Jiang P, Gu S, Pan D, Fu J, Sahu A, Hu X, et al. Signatures of T Cell Dysfunction and Exclusion Predict Cancer Immunotherapy Response. *Nat Med* (2018) 24(10):1550–8. doi: 10.1038/s41591-018-0136-1
21. Yoshihara K, Shahmoradgoli M, Martinez E, Vegesna R, Kim H, Torres-Garcia W, et al. Inferring Tumour Purity and Stromal and Immune Cell Admixture From Expression Data. *Nat Commun* (2013) 4:2612. doi: 10.1038/ncomms3612
22. Li T, Fu J, Zeng Z, Cohen D, Li J, Chen Q, et al. TIMER2.0 for Analysis of Tumor-Infiltrating Immune Cells. *Nucleic Acids Res* (2020) 48(W1):W509–W14. doi: 10.1093/nar/gkaa407
23. Newman AM, Liu CL, Green MR, Gentles AJ, Feng W, Xu Y, et al. Robust Enumeration of Cell Subsets From Tissue Expression Profiles. *Nat Methods* (2015) 12(5):453–7. doi: 10.1038/nmeth.3337
24. Barbie DA, Tamayo P, Boehm JS, Kim SY, Moody SE, Dunn IF, et al. Systematic RNA Interference Reveals That Oncogenic KRAS-Driven Cancers Require TBK1. *Nature* (2009) 462(7269):108–12. doi: 10.1038/nature08460
25. Zhang C, Cheng W, Ren X, Wang Z, Liu X, Li G, et al. Tumor Purity as an Underlying Key Factor in Glioma. *Clin Cancer Res* (2017) 23(20):6279–91. doi: 10.1158/1078-0432.CCR-16-2598
26. Xu S, Tang L, Dai G, Luo C, Liu Z. Immune-Related Genes With APA in Microenvironment Indicate Risk Stratification and Clinical Prognosis in Grade II/III Gliomas. *Mol Ther Nucleic Acids* (2021) 23:1229–42. doi: 10.1016/j.omtn.2021.01.033
27. Wang S, Qi Y, Gao X, Qiu W, Liu Q, Guo X, et al. Hypoxia-Induced lncRNA PDIA3P1 Promotes Mesenchymal Transition *via* Sponging of miR-124-3p in Glioma. *Cell Death Dis* (2020) 11(3):168. doi: 10.1038/s41419-020-2345-z
28. Li J, Liao T, Liu H, Yuan H, Ouyang T, Wang J, et al. Hypoxic Glioma Stem Cell-Derived Exosomes Containing Linc01060 Promote Progression of Glioma by Regulating the MZF1/c-Myc/HIF1alpha Axis. *Cancer Res* (2021) 81(1):114–28. doi: 10.1158/0008-5472.CAN-20-2270
29. Ding J, He X, Cheng X, Cao G, Chen B, Chen S, et al. A 4-Gene-Based Hypoxia Signature is Associated With Tumor Immune Microenvironment and Predicts the Prognosis of Pancreatic Cancer Patients. *World J Surg Oncol* (2021) 19(1):123. doi: 10.1186/s12957-021-02204-7
30. Mo Z, Yu L, Cao Z, Hu H, Luo S, Zhang S. Identification of a Hypoxia-Associated Signature for Lung Adenocarcinoma. *Front Genet* (2020) 11:647. doi: 10.3389/fgene.2020.00647
31. Yang L, Taylor J, Eustace A, Irlam JJ, Denley H, Hoskin PJ, et al. A Gene Signature for Selecting Benefit From Hypoxia Modification of Radiotherapy for High-Risk Bladder Cancer Patients. *Clin Cancer Res* (2017) 23(16):4761–8. doi: 10.1158/1078-0432.CCR-17-0038
32. Yang L, Roberts D, Takhar M, Erho N, Bibby BAS, Thiruthaneeswaran N, et al. Development and Validation of a 28-Gene Hypoxia-Related Prognostic Signature for Localized Prostate Cancer. *EBioMedicine* (2018) 31:182–9. doi: 10.1016/j.ebiom.2018.04.019
33. Havel JJ, Chowell D, Chan TA. The Evolving Landscape of Biomarkers for Checkpoint Inhibitor Immunotherapy. *Nat Rev Cancer* (2019) 19(3):133–50. doi: 10.1038/s41568-019-0116-x
34. Zhang H, Dai Z, Wu W, Wang Z, Zhang N, Zhang L, et al. Regulatory Mechanisms of Immune Checkpoints PD-L1 and CTLA-4 in Cancer. *J Exp Clin Cancer Res* (2021) 40(1):184. doi: 10.1186/s13046-021-01987-7
35. Gibney GT, Weiner LM, Atkins MB. Predictive Biomarkers for Checkpoint Inhibitor-Based Immunotherapy. *Lancet Oncol* (2016) 17(12):e542–e51. doi: 10.1016/S1470-2045(16)30406-5
36. Patel SP, Kurzrock R. PD-L1 Expression as a Predictive Biomarker in Cancer Immunotherapy. *Mol Cancer Ther* (2015) 14(4):847–56. doi: 10.1158/1535-7163.MCT-14-0983
37. Quail DF, Joyce JA. The Microenvironmental Landscape of Brain Tumors. *Cancer Cell* (2017) 31(3):326–41. doi: 10.1016/j.ccell.2017.02.009
38. Wang Y, Wang Y, Xu C, Liu Y, Huang Z. Identification of Novel Tumor-Microenvironment-Regulating Factor That Facilitates Tumor Immune Infiltration in Colon Cancer. *Mol Ther Nucleic Acids* (2020) 22:236–50. doi: 10.1016/j.omtn.2020.08.029
39. Zhang X, Shi M, Chen T, Zhang B. Characterization of the Immune Cell Infiltration Landscape in Head and Neck Squamous Cell Carcinoma to Aid Immunotherapy. *Mol Ther Nucleic Acids* (2020) 22:298–309. doi: 10.1016/j.omtn.2020.08.030
40. Zhang Y, Yang M, Ng DM, Haleem M, Yi T, Hu S, et al. Multi-Omics Data Analyses Construct TME and Identify the Immune-Related Prognosis Signatures in Human LUAD. *Mol Ther Nucleic Acids* (2020) 21:860–73. doi: 10.1016/j.omtn.2020.07.024
41. Colombo MP, Piconese S. Regulatory-T-Cell Inhibition Versus Depletion: The Right Choice in Cancer Immunotherapy. *Nat Rev Cancer* (2007) 7 (11):880–7. doi: 10.1038/nrc2250
42. Bloch O, Crane CA, Kaur R, Safaee M, Rutkowski MJ, Parsa AT. Gliomas Promote Immunosuppression Through Induction of B7-H1 Expression in Tumor-Associated Macrophages. *Clin Cancer Res* (2013) 19(12):3165–75. doi: 10.1158/1078-0432.CCR-12-3314
43. Xu S, Tang L, Li X, Fan F, Liu Z. Immunotherapy for Glioma: Current Management and Future Application. *Cancer Lett* (2020) 476:1–12. doi: 10.1016/j.canlet.2020.02.002
44. Corzo CA, Condamine T, Lu L, Cotter MJ, Youn JI, Cheng P, et al. HIF-1alpha Regulates Function and Differentiation of Myeloid-Derived Suppressor Cells in the Tumor Microenvironment. *J Exp Med* (2010) 207(11):2439–53. doi: 10.1084/jem.20100587
45. Noman MZ, Desantis G, Janji B, Hasmim M, Karray S, Dessen P, et al. PD-L1 is a Novel Direct Target of HIF-1alpha, and its Blockade Under Hypoxia Enhanced MDSC-Mediated T Cell Activation. *J Exp Med* (2014) 211(5):781–90. doi: 10.1084/jem.20131916
46. Sun J, Zhang Z, Bao S, Yan C, Hou P, Wu N, et al. Identification of Tumor Immune Infiltration-Associated lncRNAs for Improving Prognosis and Immunotherapy Response of Patients With non-Small Cell Lung Cancer. *J Immunother Cancer* (2020) 8(1):e000110. doi: 10.1136/jitc-2019-000110
47. Bhan A, Soleimani M, Mandal SS. Long Noncoding RNA and Cancer: A New Paradigm. *Cancer Res* (2017) 77(15):3965–81. doi: 10.1158/0008-5472.CAN-16-2634
48. Dai C, Zhao C, Xu M, Sui X, Sun L, Liu Y, et al. Serum lncRNAs in Early Pregnancy as Potential Biomarkers for the Prediction of Pregnancy-Induced Hypertension, Including Preeclampsia. *Mol Ther Nucleic Acids* (2021) 24:416–25. doi: 10.1016/j.omtn.2021.03.010
49. Zhou M, Hu L, Zhang Z, Wu N, Sun J, Su J. Recurrence-Associated Long Non-Coding RNA Signature for Determining the Risk of Recurrence in Patients With Colon Cancer. *Mol Ther Nucleic Acids* (2018) 12:518–29. doi: 10.1016/j.omtn.2018.06.007
50. Hong W, Liang L, Gu Y, Qi Z, Qiu H, Yang X, et al. Immune-Related lncRNA to Construct Novel Signature and Predict the Immune Landscape of Human Hepatocellular Carcinoma. *Mol Ther Nucleic Acids* (2020) 22:937–47. doi: 10.1016/j.omtn.2020.10.002
51. Shen Y, Peng X, Shen C. Identification and Validation of Immune-Related lncRNA Prognostic Signature for Breast Cancer. *Genomics* (2020) 112 (3):2640–6. doi: 10.1016/j.ygeno.2020.02.015
52. Li Y, Shen R, Wang A, Zhao J, Zhou J, Zhang W, et al. Construction of a Prognostic Immune-Related LncRNA Risk Model for Lung Adenocarcinoma. *Front Cell Dev Biol* (2021) 9:648806. doi: 10.3389/fcell.2021.648806
53. Zhu T, Ma Z, Wang H, Wei D, Wang B, Zhang C, et al. Immune-Related Long Non-Coding RNA Signature and Clinical Nomogram to Evaluate Survival of Patients Suffering Esophageal Squamous Cell Carcinoma. *Front Cell Dev Biol* (2021) 9:641960. doi: 10.3389/fcell.2021.641960
54. Lin X, Jiang T, Bai J, Li J, Wang T, Xiao J, et al. Characterization of Transcriptome Transition Associates Long Noncoding RNAs With Glioma Progression. *Mol Ther Nucleic Acids* (2018) 13:620–32. doi: 10.1016/j.omtn.2018.10.009
55. Chen X, Wanggou S, Bodalia A, Zhu M, Dong W, Fan JJ, et al. A Feedforward Mechanism Mediated by Mechanosensitive Ion Channel PIEZO1 and Tissue Mechanics Promotes Glioma Aggression. *Neuron* (2018) 100(4):799–815 e7. doi: 10.1016/j.neuron.2018.09.046
56. Wang R, Gurguis CI, Gu W, Ko EA, Lim I, Bang H, et al. Ion Channel Gene Expression Predicts Survival in Glioma Patients. *Sci Rep* (2015) 5:11593. doi: 10.1038/srep11593
57. Zhao Z, Wang Y, Yun D, Huang Q, Meng D, Li Q, et al. TRIM21 Overexpression Promotes Tumor Progression by Regulating Cell Proliferation, Cell Migration and Cell Senescence in Human Glioma. *Am J Cancer Res* (2020) 10(1):114–30.
58. Wu J, Su HK, Yu ZH, Xi SY, Guo CC, Hu ZY, et al. Skp2 Modulates Proliferation, Senescence and Tumorigenesis of Glioma. *Cancer Cell Int* (2020) 20:71. doi: 10.1186/s12935-020-1144-z
59. Lah TT, Novak M, Breznik B. Brain Malignancies: Glioblastoma and Brain Metastases. *Semin Cancer Biol* (2020) 60:262–73. doi: 10.1016/j.semcancer.2019.10.010

60. Lei Q, Gu H, Li L, Wu T, Xie W, Li M, et al. TNIP1-Mediated TNF-Alpha/NF-kappaB Signalling Cascade Sustains Glioma Cell Proliferation. *J Cell Mol Med* (2020) 24(1):530–8. doi: 10.1111/jcmm.14760

Conflict of Interest: The authors declare that the research was conducted in the absence of any commercial or financial relationships that could be construed as a potential conflict of interest.

Publisher's Note: All claims expressed in this article are solely those of the authors and do not necessarily represent those of their affiliated organizations, or those of the publisher, the editors and the reviewers. Any product that may be evaluated in this article, or claim that may be made by its manufacturer, is not guaranteed or endorsed by the publisher.

frontiers in Immunology

ORIGINAL RESEARCH
published: 26 October 2021
doi: 10.3389/fimmu.2021.724276

Single-Cell Sequencing Reveals the Novel Role of Ezh2 in NK Cell Maturation and Function

Minghang Yu[1,2†], *Ziyang Su*[2†], *Xuefeng Huang*[1,2] *and Xi Wang*[1,2*]

[1] Beijing Key Laboratory of Emerging Infectious Diseases, Institute of Infectious Diseases, Beijing Ditan Hospital, Capital Medical University, Beijing, China, [2] Department of Immunology, School of Basic Medical Sciences; Advanced Innovation Center for Human Brain Protection, Beijing Key Laboratory for Cancer Invasion and Metastasis, Department of Oncology, Capital Medical University, Beijing, China

OPEN ACCESS

Edited by:
Qin Yan,
Yale University, United States

Reviewed by:
Xianxiao Zhou,
Icahn School of Medicine at Mount Sinai, United States
Harvey Cantor,
Dana–Farber Cancer Institute, United States

***Correspondence:**
Xi Wang
xiwang@ccmu.edu.cn

[†]These authors have contributed equally to this work

Specialty section:
This article was submitted to Cancer Immunity and Immunotherapy, a section of the journal Frontiers in Immunology

Received: 12 June 2021
Accepted: 04 October 2021
Published: 26 October 2021

Citation:
Yu M, Su Z, Huang X and Wang X (2021) Single-Cell Sequencing Reveals the Novel Role of Ezh2 in NK Cell Maturation and Function. Front. Immunol. 12:724276. doi: 10.3389/fimmu.2021.724276

Natural killer (NK) cells are lymphocytes primarily involved in innate immunity and exhibit important functional properties in antimicrobial and antitumoral responses. Our previous work indicated that the enhancer of zeste homolog 2 (Ezh2) is a negative regulator of early NK cell differentiation and function through trimethylation of histone H3 lysine 27 (H3K27me3). Here, we deleted Ezh2 from immature NK cells and downstream progeny to explore its role in NK cell maturation by single-cell RNA sequencing (scRNA-seq). We identified six distinct NK stages based on the transcriptional signature during NK cell maturation. Conditional deletion of Ezh2 in NK cells resulted in a maturation trajectory toward NK cell arrest in CD11b SP stage 5, which was clustered with genes related to the activating function of NK cells. Mechanistically, we speculated that Ezh2 plays a critical role in NK development by activating AP-1 family gene expression independent of PRC2 function. Our results implied a novel role for the Ezh2-AP-1-Klrg1 axis in altering the NK cell maturation trajectory and NK cell-mediated cytotoxicity.

Keywords: NK cell, Ezh2, maturation trajectory, cytotoxic function, AP-1, scRNA-seq

INTRODUCTION

Natural killer (NK) cells are lymphocytes belonging to innate immunity with effector functions, including roles as cytolytic effectors and potent producers of cytokines (1–3). In the bone marrow (BM) of mice, the NK cell lineage derives from common lymphoid progenitors (CLPs) through the acquisition of CD122 expression (4). After acquiring NK1.1 and CD49b surface expression, murine NK cells can further develop to maturity (4, 5). NK cell maturation *in vivo* follows the pathway $CD11b^{low}CD27^{high}$ (CD27 single positive, CD27 SP) → $CD11b^{high}CD27^{high}$ (CD11b CD27 double positive, DP) → $CD11b^{high}CD27^{low}$ (CD11b single positive, CD11b SP) (6). $CD11b^{high}$ NK cells display potent effector functions compared with $CD27^{high}$ NK cells (6). Klrg1 is a marker of terminal maturation acquired by NK cells (7, 8). Interestingly, Scott *et al.* found that Klrg1 is a C-type lectin-like inhibitory receptor with an immune receptor tyrosine-based inhibitory motif in its cytoplasmic domain during the activation of mouse NK cells (9). Masayuki *et al.* found that *Klrg1* binds to

members of the classical cadherin family and inhibits NK cell cytotoxicity (10). The Klrg1$^+$ ILC2 pool has recently been shown to be impaired in mice deficient in BATF, a member of the AP-1 superfamily (11), implying a potential role of the AP-1 superfamily in the regulation of the Klrg1$^+$ lymphocyte population.

Ezh2 is the catalytic subunit of polycomb repressive complex 2 (PRC2) (12) and has been traditionally known to mediate histone H3K27 trimethylation, a hallmark of silent chromatin (13). However, Ezh2 also promotes gene expression in cancer cells without being dependent on its methyltransferase activity. Ezh2 activates gene expression based on a transactivation domain (TAD) capable of interacting with components of the active transcription machinery (14). Shi B et al. found that Ezh2 physically binds to estrogen receptor α (ERα), β-catenin, and mediators to transactivate promoters of downstream genes in MCF-7 ER-positive breast cancer cells (15). In addition, Jung et al. also showed that the PRC2-independent interaction between Ezh2 and PAF (PCNA-associated factor) mediates activation of β-catenin target genes in colon cancer cells (16). We previously reported that deletion or inhibition of Ezh2 in hematopoietic stem and progenitor cells (HSPCs) enhanced NK cell commitment and cytotoxicity against tumor cells (17). However, whether Ezh2 regulates NK cell development and function at a later stage and how Ezh2 exerts its biological activity remain elusive.

In this study, NK cell maturation was divided into six detailed stages at the transcriptome level from early CD27 SP stage 1 to Klrg1 high stage 6. We further showed that altered NK-mediated cytotoxic function is intrinsically associated with altered developmental processes. Furthermore, *Ezh2*$^{-/-}$ NK cells followed a maturation trajectory toward arrest in CD11b SP stage 5. We found that the Klrg1 high stage corresponded to a late population to the CD11b SP stage. *Itgam* is clustered with genes known to enhance NK cell cytotoxic function through a pseudotemporal expression pattern (18–20), while *Klrg1* shows the opposite orientation (21–24). Furthermore, we found that the transcriptional levels of AP-1 family members were consistently downregulated in *Ezh2*-deficient NK cells. Motifs distributed across promoters of genes from the AP-1 superfamily are most similar to the estrogen-related receptor (ERR) family binding site. In conclusion, our results implied a novel role for the Ezh2-AP-1-Klgr1 axis in altering the NK cell maturation trajectory and enhancing NK cell-mediated cytotoxicity.

MATERIALS AND METHODS

Mice

Ezh2$^{fl/fl}$ mice were purchased from the Jackson Laboratory (Bar Harbor, ME, USA). *Ncr1*^{iCre} mice were purchased from Beijing Biocytogen (Beijing, China). To generate Ezh2 deletion in NK cells, *Ezh2*$^{fl/fl}$ mice were crossed with *Ncr1*^{iCre} mice to obtain *Ezh2*$^{fl/fl}$;*Ncr1*^{iCre} mice (*Ezh2*$^{\Delta NK}$). All mice were housed in a specific pathogen-free facility for use according to the guidelines for experimental animals at Capital Medical University. All animals used were C57BL/6 mice aged 6 to 8 weeks.

NK Cell Separation, Library Construction, and Sequencing

Spleens were mechanically disrupted in PBS, and single-cell suspensions were prepared as described previously (17). For cell sorting, bulk spleen cells were used to isolate CD45$^+$CD3$^-$CD19$^-$NKp46$^+$NK1.1$^+$ cells for scRNA-seq experiments by the BD FACSAria III instrument, and the purity was generally above 95%. Library construction was performed using a BD Rhapsody™ Single-Cell Analysis System following a standard protocol provided by the manufacturer (BD Biosciences) (25). RNA sequencing was performed on an Illumina HiSeq 2500 machine with a sequencing depth of at least 50,000 reads per cell.

ScRNA-seq Data Analysis

Sequenced reads were aligned to the GRCm38 murine transcriptome, and then the expression of transcripts in each cell was quantified using the BD™ Rhapsody Whole Transcriptome Assay Analysis Pipeline. Downstream analyses were implemented using R (v4.0.2) and the package iCellR. Low-quality cells were excluded in the initial quality control (QC) step by removing cells with fewer than 500 genes expressed or more than 2,400 genes. We also removed cells with mitochondrial transcript contents greater than 5%. As a result, 2,584 *Ezh2*$^{-/-}$ NK cells and 2,612 WT NK cells were retained, and 2,584 WT NK cells were selected to achieve equal group numbers for further analysis. The function norm.date (norm.method = "ranked.glsf", top.rank = 500) was applied for data normalization.

Dimension Reduction, Unsupervised Clustering, Cell Type Prediction, and Developmental Trajectory Inference

Variable genes were selected by the make.gene.model function (dispersion.limit = 1.5, base.mean.rank = 500, no.mito.model = T, mark.mito = T, interactive = F). Ribosomal genes were removed. Then, the variable genes were used for PCA implemented with the run.pca function. Next, we selected PCs 1–10 as input for tSNE and UMAP analyses or 1–20 for KnetL analysis. Cells were clustered with iCellR's iclust function. Marker genes were identified by the findMarkers function (fold.change = 1.5, padjval = 0.1), and then top markers were determined (marker.genes, topde = 10, min.base.mean = 0.05, filt.ambig = F). Cell type prediction was performed by the cell.type.pred function (immgen.data = "uli.rna", gene = maerker.genes, plot.type = "point.plot", top.cell.types =10) based on the ImmGen Ultra Low Input (ULI) RNA-seq dataset. Pseudotime was generated with Monocle v2 to infer the potential lineage differentiation trajectory based on the iCellR object.

Identification of DEGs, Pathway Enrichment, Network Construction, and Molecular Complex Detection

DEG analysis was carried out in iCellR. We used the iCellR function run.diff.exp to identify DEGs between *Ezh2*$^{fl/fl}$ and *Ezh2*$^{\Delta NK}$ cells within each stage. DEGs with padj < 0.05 were taken for further analysis. Identification of pathway and network

enrichment and the MCODE algorithm were executed using Metascape (26) (http://metascape.org/). Accordingly, p-values were calculated based on the accumulative hypergeometric distribution, and q-values were calculated using the Banjamini–Hochberg procedure to account for multiple comparisons. Kappa scores were used as the similarity metric when performing hierarchical clustering on the enriched terms, and subtrees with a similarity > 0.3 were considered a cluster.

Gene Motif Analysis

The putative promoter sequence was obtained from mm10 of the UCSC genome and then submitted to the Multiple Expectation Maximization for Motif Elicitation (MEME) *de novo* motif detection tool (meme mocular_complex.txt -dna -oc. -nostatus -time 14400 -mod zoops -nmotifs 10 -minw 6 -maxw 50 -objfun classic -revcomp -markov_order 0) and the Tool for Motif to Motif comparison (TOMTOM) (tomtom -no-ssc -oc. -verbosity 1 -min-overlap 5 -mi 1 -dist pearson -evalue -thresh 10.0 -time 300 query_motifs db/JASPAR/JASPAR2018_CORE_vertebrates_nonredundant.memedb/MOUSE/uniprobe_mouse.meme) for comparison with known motifs.

Coexpression Network Construction

The WGCNA package of R software was applied to uncover correlations among genes. The gene expression matrix for each condition was extracted from iCellR. The power of β was set with the pickSoftThreshold function. The following analysis proceeded according to the official document provided by Dr. Jeremy Miller (https://horvath.genetics.ucla.edu/html/CoexpressionNetwork/JMiller/).

RESULTS

NK Cells Were Separated Into Six Developmental Stages

Our previous research showed that Ezh2 is a negative regulator of NK cell differentiation and function (17). However, the role of Ezh2 in regulating NK cell maturation remains unclear. To determine the role of Ezh2 in NK cell maturation, we sorted NK cells from the spleens of *Ezh2*$^{fl/fl}$ and *Ezh2*$^{\Delta NK}$ mice to study the developmental heterogeneity of NK cells at the single-cell level using the BD Rhapsody single-cell gene expression system. A mean of 1,446 genes per cell among WT NK cells and 1,333 among *Ezh2*$^{-/-}$ NK cells were detected from 5,168 cells (2,584 in each condition). The KNN-based network graph drawing layout (KNetL) analysis showed higher resolution in unbiased clustering than t-distributed stochastic neighbor embedding (t-SNE) or uniform manifold approximation and projection (UMAP) analyses (**Figure S1**). KNteL analysis showed 13 distinct clusters from both mouse strains based on transcript signatures of WT and *Ezh2*$^{-/-}$ NK cells (**Figure 1** and **Figure S2**). The distributions of *Cd27*, *Itgam*, and *Klrg1* followed a counterclockwise pattern in the KNetL plot. Each cluster was independently compared to the ImmGen Ultra Low Input (ULI) RNA-seq dataset, which contained a total of 157 cell types, using a hypergeometric test. The top 10 predicted cell type for each cluster was then exhibited (**Figure S3**). All clusters were predicted to be likely NK cells and retained for further analysis. We found that Cluster 1 showed the highest *Cd27* expression and little *Itgam* expression; thus, this cluster was considered indicative of stage 1 (early CD27 SP NK cells). CD11b expression was initiated in Cluster 2 and Cluster 5 and then defined as corresponding to stage 2 (late CD27 SP NK cells). Stage 3 (early DP NK cells) and stage 4 (late DP NK cells) NK cells were identified based on the expression densities of *Itgam* and *Cd27* (**Figure S4**). Initiation of *Klrg1* expression occurred in stage 4. *Cd27* expression was mostly lost since stage 5 (CD11b SP NK cells), which consisted of Clusters 6, 8, and 10. Clusters within stage 5 undergo a process of diminishing *Cd27* expression, increasing *Itgam* expression, and steady but relatively moderate expression of *Klrg1* in the order of Cluster 10 → Cluster 6 → Cluster 8 (**Figure S4**). Clusters 11, 12, and 13 corresponded to stage 6 terminal CD27^{-}CD11b^{high}Klrg1^{high} NK cells (Klrg1 high NK) (**Figure 1B** and **Figure S4**). We identified 57 marker genes across stages, and these genes separated the stages into two tendencies (**Figure 1C**). Stages 1–3 demonstrated higher transcriptional levels of *Ltb, Emb, Thy1, Xcl1, Tcf7, Cxcr3, Ccr2*, and *Ctla2a*, while stages 3–6 showed augmented levels of *Ly6c2, Cma1, Gzma, Itgam, Klrg1, Rap1b*, and *Klra9*. (**Figure 1C**). Of note, we found that initiation of *Klrg1* transcription might be a late molecular event for *Itgam* (**Figure 1D**). In conclusion, we merged unbiased clusters into six stages—early CD27 SP, late CD 27 SP, early DP, late DP, CD11b SP, and Klrg1 high—based on the transcriptional levels of the conventional surface markers of NK cell development.

Differential Cytotoxic Functions in *Ezh2*-Deficient NK Cells Were Intrinsically Associated With Alteration in the Developmental Process

To understand the differential gene expression pattern between WT and *Ezh2*$^{-/-}$ NK cells across six stages, we first determined the DEGs in two conditions within each stage (**Table S1**). A meta-analysis workflow (27) was used to combine DEGs between WT and *Ezh2*-deficient NK cells (**Figure 2A**). Interestingly, stage 2 and stage 5/6 shared many genes, implying that transcriptional alterations in stage 2 may have a cumulative effect in later stages. DEGs of CD11b SP stage 5 were enriched for terms related to natural killer cell-mediated cytotoxicity (ko34650) (**Figure 2B**). To further understand the biological processes that may influence NK cell cytotoxic function, a subset of enriched terms was selected and rendered as a network plot, where terms with a similarity > 0.3 were connected by edges. We selected the terms with the best p-values from each of the 20 clusters under a constraint of no more than 15 terms per cluster and no more than 250 terms in total. The enrichment network showed that the natural killer cell-mediated cytotoxicity term shared a close relationship with terms related to positive regulation of tumor necrosis factor production and osteoclast differentiation (**Figure 2C**). Of note, genes enriched in the

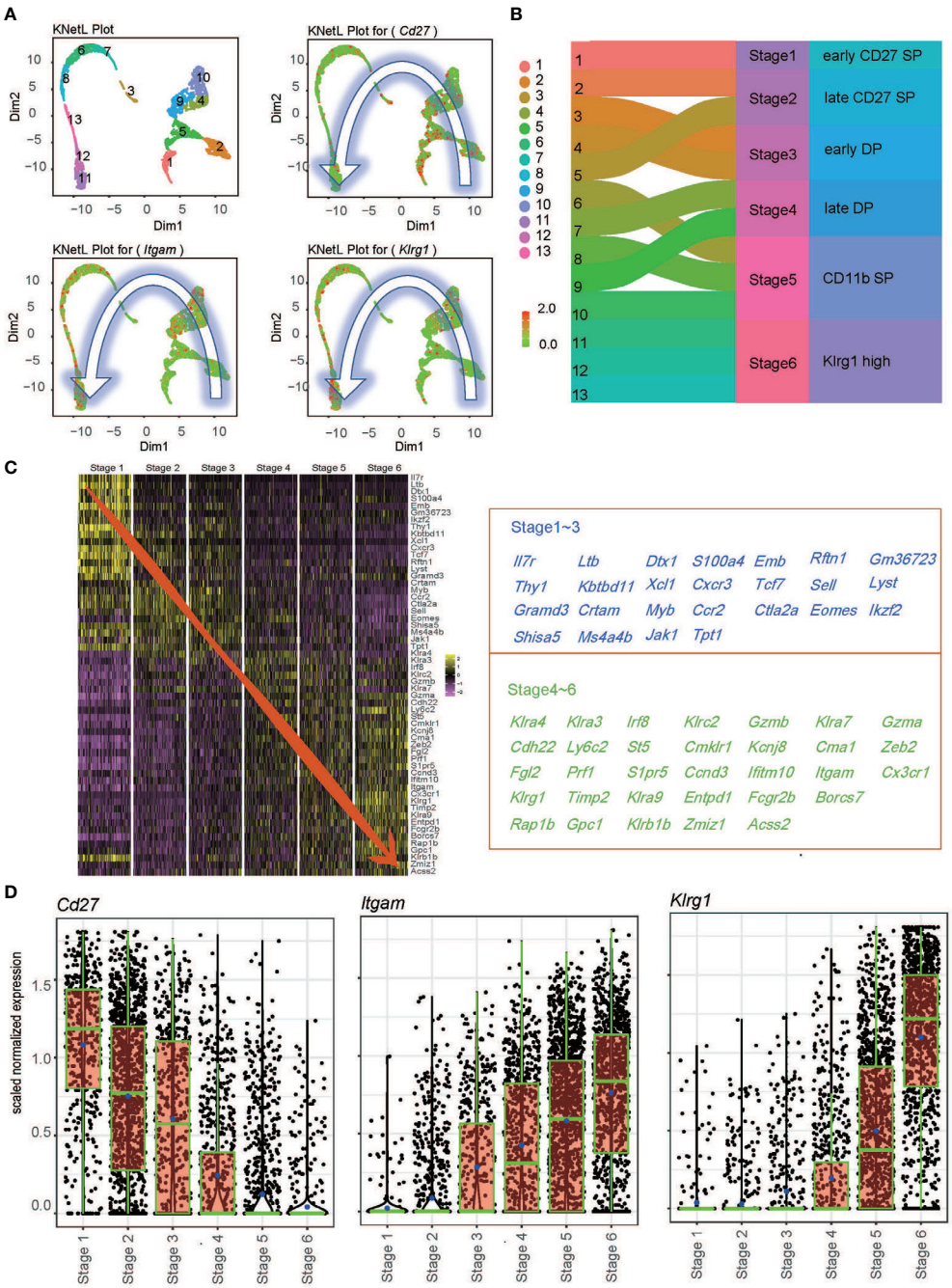

FIGURE 1 | Transcriptional levels of conventional surface markers across the single-cell transcriptional profile. **(A)** Expression of Cd27, Itgam, and Klrg1 across 13 clusters defined by KnetL. The color key indicates iCellR imputed gene expression values. **(B)** Merging strategy based on the expression of Cd27, Itgam, and Klrg1 across 13 clusters. **(C)** Heatmap of the top 10 marker genes within the six stages (left) and gene list (right). **(D)** Boxplots demonstrate the expression of Cd27 and Klrg1 in each newly merged NK stage.

osteoclast differentiation term, such as *Id2* (28), *Ccl3* (24), and *Tyrobp* (29), have been reported to also promote NK cell development (**Figure 2D**). These results suggested that the differential cytotoxic functions of NK cells may share intrinsic connections with an altered development process.

Maturation Trajectory of *Ezh2*$^{-/-}$ NK Cells Arresting in CD11b SP Stage 5

To explore the differential development process between WT NK cells and *Ezh2*-deficient NK cells, we used Monocle2 pseudotime analysis to simulate the maturation trajectory based on the marker

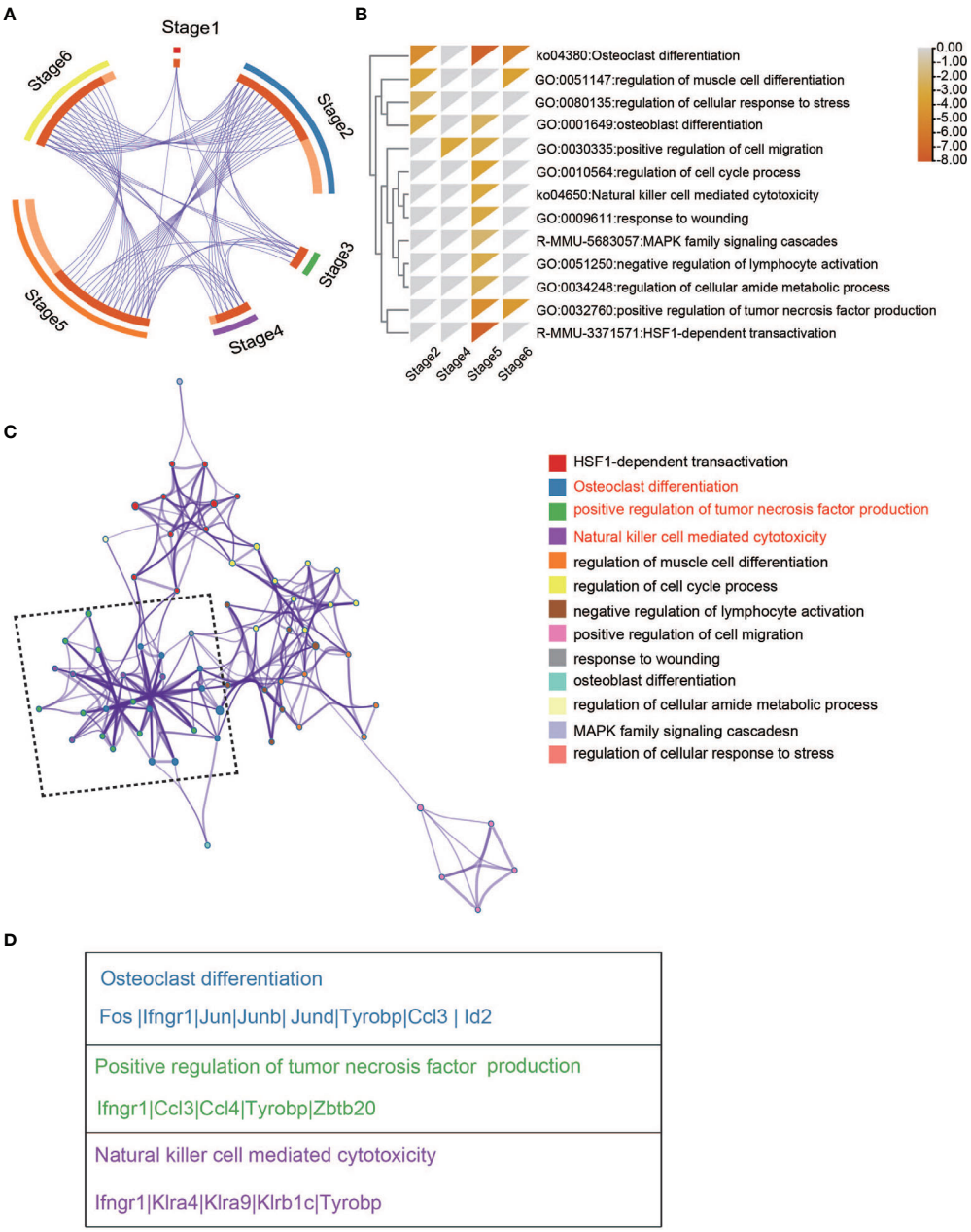

FIGURE 2 | Enriched pathway network of DEGs between WT and Ezh2-/-NK cells. **(A)** Overlap between gene lists, where purple curves link identical genes. **(B)** Heatmap of enriched terms across input gene lists colored by p-values. **(C)** Network of enriched terms colored by cluster ID, where nodes sharing the same cluster ID are typically close to each other. **(D)** Gene lists of indicated pathways and processes.

gene in **Figure 1**. Cells from each of the six stages were assigned to the pseudotime trajectory with five states and two trajectories (**Figure 3A**). The pseudotime progression indicated the maturation order (**Figure 3B**). WT NK cells took advantage in trajectory 1, and *Ezh2*$^{-/-}$ NK cells dominated trajectory 2 (**Figures 3C, F**). The root point of trajectory 1 (up, state 1,5) is obvious upright as stage 1 mostly resided here. Based on this root point, the pseudotime dictated that the up-left side of trajectory 1 corresponded to the most mature population, which was dominated by stage 6. The cells in stage 2 to stage 5 spread across the trajectory from right to left. Trajectory 1 shows a classical process of NK cell maturation (**Figures 3D, E**). However, trajectory 2 (down, state 3, 4) seemed to skip stage 1 in the down-right. Interestingly, while stages 2, 3, 4, and 5 also spread from down-right state 4 to down-left state 3 in trajectory 2, stage 6 (Klrg1 high) was likely to be aborted in down-left side state 3 since stage 5 (CD11b SP) dominated this root (**Figures 3D, E**).

Differential cytotoxic functions in *Ezh2*-deficient NK cells shared intrinsic connections with altered development processes

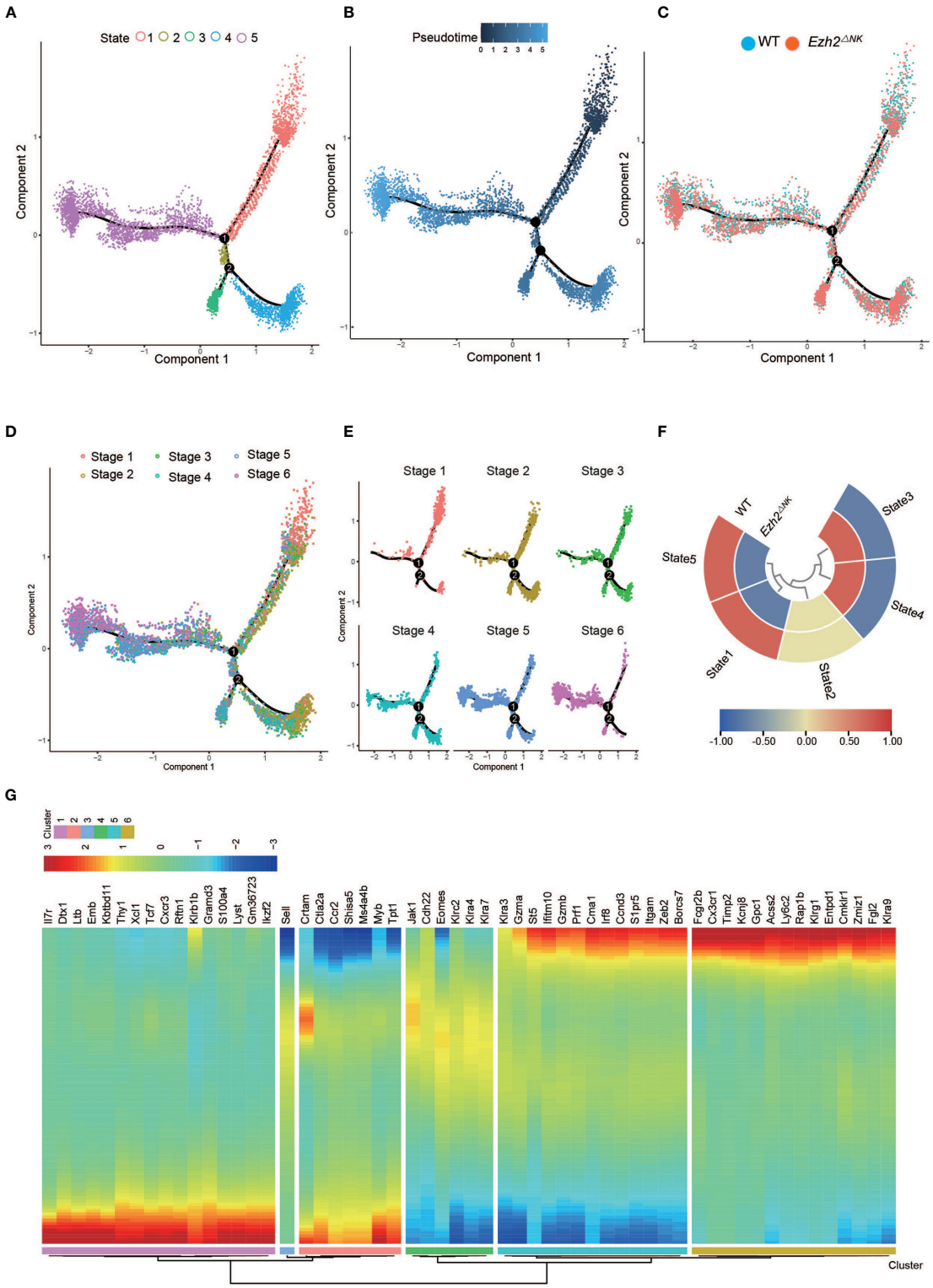

FIGURE 3 | The heterogeneity of relative maturity between WT and Ezh2$^{\Delta NK}$ mice. **(A)** The relative maturity along the developmental trajectory is displayed across pseudotime. **(B)** Distribution of five developmental states defined by monocle along the pseudotime trajectory. **(C)** Distribution of all conditions along the pseudotime trajectory. **(D)** Distribution of all NK stages along the pseudotime trajectory. **(E)** Heatmap of normalized cell numbers of each NK stage in the pseudotime trajectory states. **(F)** The compositions of WT and Ezh2$^{-/-}$ NK cells in five states. **(G)** Heatmap showing clustering genes by pseudotemporal expression pattern.

(**Figure 2**). Thus, pseudotime-dependent genes were clustered by pseudotemporal expression patterns. *Itgam* and *Klrg1* were separately grouped into Cluster 5 and Cluster 6, indicating that they followed differential kinetic trends. Of note, *Gzma, Gzmb, Prf1*, and *Irf8* were clustered with *Itgam* (**Figure 2**), which is associated with NK cell antitumor function (18–20). *Fcgr2b, Fgl2, Cx3cr1*, and *Klra9* (Ly49C) were grouped into Cluster 6 with *Klrg1* (**Figure 2**). The expression of Fcgr2b, Fgl2, and Ly49C is known to impair the cytotoxic function of NK cells (21–23). $Cx3cr1^+$ NK cells have been reported to show less proliferation potential than $Cx3cr1^-$ NK cells (30). These results indicate that CD11b SP NK cells may gain a cytotoxic capacity exceeding that of Klrg1-high NK cells. Therefore, these results suggested that deletion of *Ezh2* may restrain the terminal Klrg1-high NK cell pool and lead to enhanced cytotoxicity.

Ezh2-Deficient NK Cells Exhibited a Lower Transcriptional Level of Members of the AP-1 Family

Interestingly, the frequencies of $Klrg1^+$ NK cells were the same in $Ezh2^{\Delta NK}$ mice compared with WT mice by flow cytometry (data not shown), although robust expansion of the $CD27^-CD11b^+$ NK pool was observed. To further explain this phenomenon, we identified a densely connected network of protein–protein interactions in DEGs using MCODE. Two key modes of densely connected network components were identified. MCODE1 is composed of *Fos, Junb, Jund*, and *Jun* (AP-1 superfamily), while *Dusp1, Hspa1a*, and *Hspa1b* (HSF-1 family) constitute MCODE2 (**Figure 4A**). The expression patterns of the indicated genes across stages between conditions were described. The genes were mostly downregulated in $Ezh2^{-/-}$ NK cells across six stages compared with WT NK cells (**Figure 4B**), which seems to contradict reports indicating that Ezh2 is a negative regulator of chromatin activation (31). To further explore the underlying mechanism, the promoter sequences of these genes were obtained from the UCSC Genome Browser (**Table S2**). Analysis of conserved motif distributions was performed using the motif analysis online program MEME (32). Motif 1 and Motif 2 were distributed across promoters of all genes (**Figure 4C**). Submission of the position weight matrix of motifs to TOMTOM (33) revealed that Motif 1 recognizes DNA and is most similar to the estrogen-related receptor family binding motif (**Figure 4D**).

We also performed the WGCNA. The most preserved module between the two conditions is turquoise (**Figure S5A** and **Table S3**). As expected, most of the regulators of NK cell maturation and function were in turquoise (**Table S4**), such as Il2rb, Cd27, Ifng, Nfkb1, Smad3, Tcf7, Bcl2, Foxo1, Gata3, Stat2, and Stat4 (5). Venn diagram showed the overlap between the Turquoise module genes and DEGs. Interestingly, members of AP-1 family Junb, Jund, and Fos belong to both DEGs and the turquoise module (**Figure S5B**). This agrees with our conclusion that the AP-1 family plays an important role in regulating the maturation and function of Ezh2-deficiency NK cells. Overall, our results suggested that deletion of Ezh2 may alter the NK maturation trajectory and enhance cytotoxic function by attenuating the AP-1 superfamily.

DISCUSSION

The role of NK cells in the development and function of epigenetic modifications remains poorly understood. Specifically, histone modification during NK cell ontology is only partially defined. Li et al. found that the histone modification state has a profound impact on NK cell activation (34). During acute NK cell activation, the epigenetic and transcriptional profiles are altered, and p300 enhancer modifications are also involved in high-level transcriptional induction of T-bet and STATs to facilitate the rapid immune response (35). Kdm5a, an H3K4me3 demethylase, is a positive modifier of NK cell activation and is recruited to the SOCS1 promoter by p50 to maintain a repressive chromatin configuration, which promotes NK cell production of interferon-γ (IFN-γ) (36). Adam et al. identified histone H3K27 demethylases as key regulators of cytokine production using small-molecule inhibitors of chromatin methylation and acetylation screens in human NK cells, and GSK-J4 is an H3K27 demethylase inhibitor that can increase global levels of the repressive H3K27me3 chromatin marker and lead to suppression of the anti-inflammatory response (37). Interestingly, in our previous research, we found that Ezh2 deletion in *Vav-iCre* mice led to alterations in differentiation and enhanced function following Vav expression (17). Here, we found that loss of Ezh2 is required to constrain terminal and functionally impaired Klrg1-high NK cells.

ScRNA-seq is a powerful technique allowing unbiased identification of cellular diversity and heterogeneous transcriptional signatures within one cell population (38, 39). Our results provide a transcriptional landscape of individual NK cells from the mouse spleen and a clustered subpopulation of NK cells based on the distribution of surface markers. We identified six stages based on the transcriptional levels of *Cd27*, *Itgam*, and *Klrg1*: early CD27 SP stage 1, late CD27 SP stage 2, early DP stage 3, late DP stage 4, CD11b SP stage 5, and Klrg1 high stage 6 (**Figure 1B**). Trends in marker gene expression were basically consistent with those reported in previous research by Adeline Crinier et al. (40), as shown in **Figure 1C**. We noticed that differential NK cytotoxicity was intrinsically connected with altered developmental processes (**Figures 2C, D**). Furthermore, we found that Ezh2-deficient NK cells follow a maturation trajectory toward arrest before Klrg1 high stage 6 (**Figure 3C**). NK cells have been reported to acquire the terminal marker Klrg1 and become less responsive to proliferative signals following a decrease in the turnover rate and homeostatic expansion *in vivo* (8). Several studies have shown that Klrg1 inhibits NK cell activation (9) and cytotoxicity (10). Consistent with this, we found that *Klrg1* was clustered with genes that are known to impair NK cell proliferation and cytotoxicity by a pseudotemporal expression pattern (**Figure 3G**). Thus, we speculated that enhanced cytotoxicity is due to a distinct maturation trajectory in *Ezh2*-deficient NK cells.

The AP-1 family is a pioneer transcription factor (TF) family with an important role in establishing new cell fate competence by granting long-term chromatin access to nonpioneer factors and is also a crucial determinant of cell identity through opening and licensing of the enhancer landscape (41, 42). In particular, AP-1

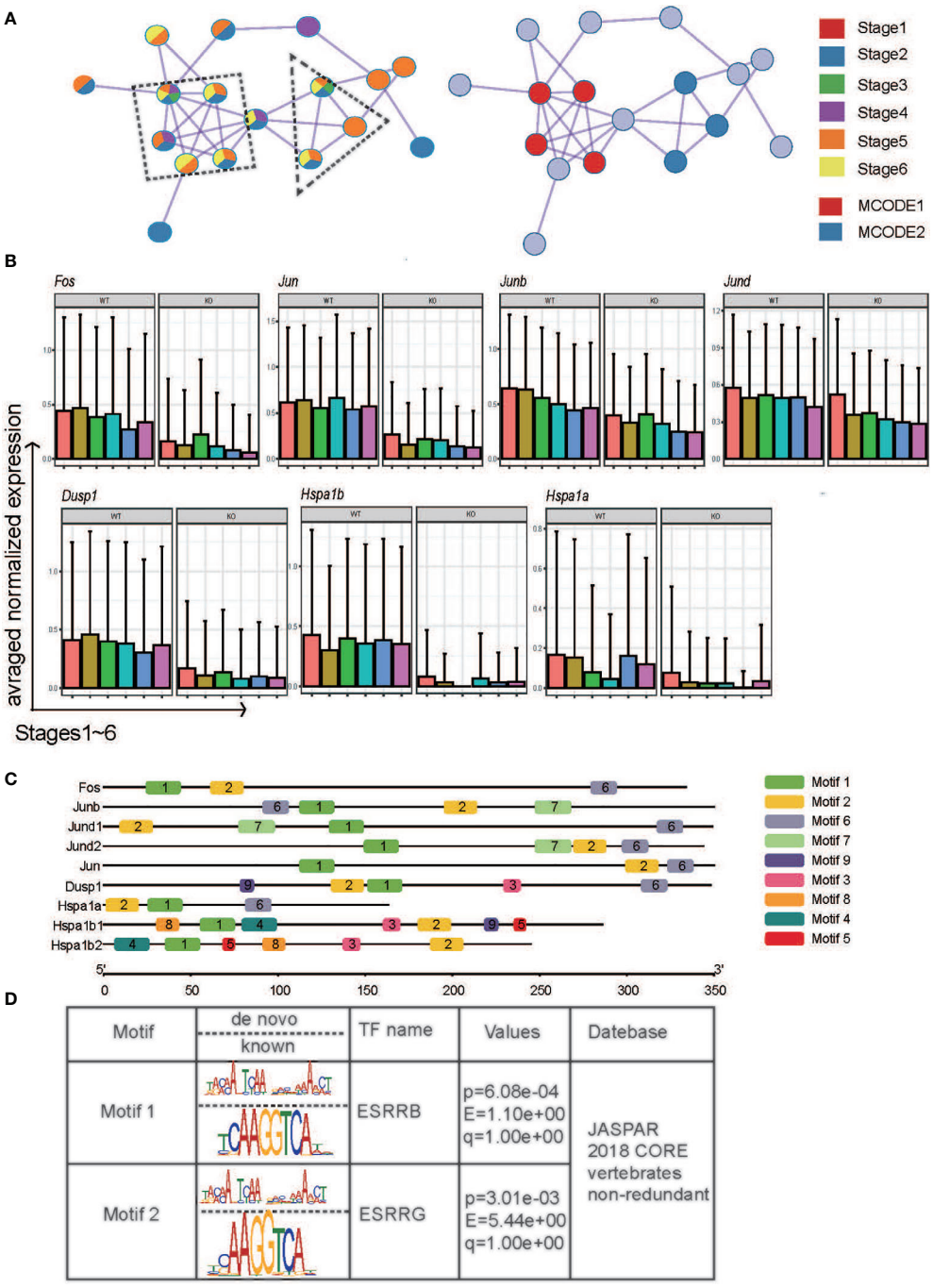

FIGURE 4 | The potential mechanism by which Ezh2 regulates the expression of the indicated genes. **(A)** Components identified by the MCODE algorithm of Metascape analysis. **(B)** Boxplot of the indicated genes at different stages under the two conditions. **(C)** Distribution of PWM generated by the meme suite across promoters of the indicated genes. **(D)** The transcription factors predicted by TOMTOM.

TFs recruit the SWI/SNF (BAF) complex to enhancers to establish accessible chromatin in fibroblasts (43). Jeong SM et al. found that the SWI/SNF chromatin-remodeling complex modulates peripheral T cell activation and proliferation by controlling AP-1 expression. Our previous research confirmed that tumor formation following SNF5 loss leads to elevated expression of EZH2 (44). Stefaniewe et al. found that Fra-2/AP-1 is regulated through lysine methylation by Ezh2 in terminal epidermal differentiation (45). Thus, we speculate that the AP-1 family plays an important role in EZH2-mediated chromatin remodeling.

Recently, the role of the AP-1 family in the immune response has also been explored (46, 47). BATF constitutes an important

subset of the AP-1 superfamily (48) and forms a heterodimer complex containing AP-1 and JUN proteins to promote transcriptional activation (47). For example, Miller et al. found that the numbers and function of Klrg1-high ILC2 cells are impaired in the IL-25-mediated helminth clearance model in BATF-deficient mice (11). Consistently, as shown in **Figure 4A**, we found differential expression patterns of the AP-1 superfamily between the two mouse strains by MCODE. We further confirmed that AP-1 superfamily members were downregulated in Ezh2$^{-/-}$ NK cells compared to WT NK cells at each stage (**Figure 4B**). In our WGCNA, the AP-1 family was found to contain modules with many important regulators of NK cell maturation and function. Thus, we speculate that the AP-1 family plays an important role in Ezh2-mediated regulation of NK cell maturation and cytotoxicity. Lau et al. found that *Klrg1* was within regions with the most variable chromatin accessibility during MCMV infection. Of note, members of the AP-1 transcription factor family, especially Junb and Jund, are found in regions that become more accessible to memory NK cells than to naïve NK cells (49). Our results supported that the members of AP-1 superfamily skew the Klrg1^{+} NK population.

A nonclassical regulatory mechanism of Ezh2 exists in cancer cells. For example, Ezh2 can activate the transcription of downstream target genes through methylation of nonhistone proteins (50, 51) or directly form transcription complexes with other factors independent of PRC2 (15, 16, 52). Jiao L et al. reported that Ezh2 contains a hidden, partially disordered transactivation domain (TAD), which directly binds to the transcriptional coactivator p300 and activates gene expression (14). Specifically, Shi B et al. reported that Ezh2 physically interacts directly with estrogen receptor alpha and functionally enhances gene transactivation (15). We found that motifs enriched in promoters of the indicated genes are most likely to be the binding site of ERRs, which are structurally similar to the ER (53, 54). Our study implied that Ezh2 may act as a transcriptional activator in the regulation of AP-1 superfamily gene expression by interacting with ERRs. In conclusion, our results implied a novel role for the Ezh2-AP-1-Klgr1 axis in altering the NK cell maturation trajectory and NK cell-mediated cytotoxicity.

DATA AVAILABILITY STATEMENT

The sequencing data has been deposited in the NCBI GEO database (https://www.ncbi.nlm.nih.gov/geo/; accession number: GSE179186).

ETHICS STATEMENT

The animal study was reviewed and approved by Capital Medical University.

AUTHOR CONTRIBUTIONS

XW conceived and supervised the study as well as revised the manuscript. MY and ZS designed the research, exported the figures, wrote the first draft of the manuscript, and performed the verification experiment.XH helped in performing the experiments. All authors contributed to the article and approved the submitted version.

FUNDING

This work was supported by grants from the Ministry of Science and Technology of People's Republic of China (grant# 2014CB910100 to XW), the Support Project of High-level Teachers in Beijing Municipal Universities in the Period of 13th Five-year Plan (IDHT20190510 to XW), and the National Natural Science Foundation of China (81972652 to XW).

SUPPLEMENTARY MATERIAL

The Supplementary Material for this article can be found online at: https://www.frontiersin.org/articles/10.3389/fimmu.2021.724276/full#supplementary-material

Supplementary Figure 1 | PCA, UMAP, tSNE and KnetL plots of clusters.

Supplementary Figure 2 | Percentages of NK cells from the indicated conditions across thirteen clusters.

Supplementary Figure 3 | Top 10 cell types identified using the ImmGen Ultra Low Input (ULI) RNA-seq dataset against the genes within each cluster by a hypergeometric test.

Supplementary Figure 4 | Boxplots of Cd27, Itgam, and Klrg1 across the original 13 clusters in **(A)**, WT mice and Ezh2$^{\Delta NK}$ mice or across 6 newly merged stages in WT mice and Ezh2$^{\Delta NK}$ mice.

Supplementary Figure 5 | (A) Hierarchical cluster tree showing coexpression modules of WT NK cells (left) identified by WGCNA and their preservation in Ezh2-deficient NK cells (right). **(B)** Venn diagram showing the overlap between the Turquoise module genes and DEGs.

REFERENCES

1. Lodoen MB, Lanier LL. Natural Killer Cells as an Initial Defense Against Pathogens. *Curr Opin Immunol* (2006) 18:391–8. doi: 10.1016/j.coi.2006.05.002
2. Wang D, Malarkannan S. Transcriptional Regulation of Natural Killer Cell Development and Functions. *Cancers* (2020) 12:1591. doi: 10.3390/cancers12061591
3. Vivier E, Ugolini S, Blaise D, Chabannon C, Brossay L. Targeting Natural Killer Cells and Natural Killer T Cells in Cancer. *Nat Rev Immunol* (2012) 12:239–52. doi: 10.1038/nri3174
4. Yu J, Freud AG, Caligiuri MA. Location and Cellular Stages of Natural Killer Cell Development. *Trends Immunol* (2013) 34:573–82. doi: 10.1016/j.it.2013.07.005
5. Abel AM, Yang C, Thakar MS, Malarkannan S. Natural Killer Cells: Development, Maturation, and Clinical Utilization. *Front Immunol* (2018) 9:1869. doi: 10.3389/fimmu.2018.01869

6. Kim S, Iizuka K, Kang HS, Dokun A, French AR, Greco S, et al. *In Vivo* Developmental Stages in Murine Natural Killer Cell Maturation. *Nat Immunol* (2002) 3:523–8. doi: 10.1038/ni796
7. Narni-Mancinelli E, Chaix J, Fenis A, Kerdiles YM, Yessaad N, Reynders A, et al. Fate Mapping Analysis of Lymphoid Cells Expressing the NKp46 Cell Surface Receptor. *Proc Natl Acad Sci USA* (2011) 108:18324–9. doi: 10.1073/pnas.1112064108
8. Huntington ND, Tabarias H, Fairfax K, Brady J, Hayakawa Y, Degli-Esposti MA, et al. NK Cell Maturation and Peripheral Homeostasis Is Associated With KLRG1 Up-Regulation. *J Immunol* (2007) 178:4764–70. doi: 10.4049/jimmunol.178.8.4764
9. Robbins SH, Nguyen KB, Takahashi N, Mikayama T, Biron CA, Brossay L. Cutting Edge: Inhibitory Functions of the Killer Cell Lectin-Like Receptor G1 Molecule During the Activation of Mouse NK Cells. *J Immunol* (2002) 168:2585–9. doi: 10.4049/jimmunol.168.6.2585
10. Ito M, Maruyama T, Saito N, Koganei S, Yamamoto K, Matsumoto N. Killer Cell Lectin-Like Receptor G1 Binds Three Members of the Classical Cadherin Family to Inhibit NK Cell Cytotoxicity. *J Exp Med* (2006) 203:289–95. doi: 10.1084/jem.20051986
11. Miller MM, Patel PS, Bao K, Danhorn T, O'Connor BP, Reinhardt RL. BATF Acts as an Essential Regulator of IL-25-Responsive Migratory ILC2 Cell Fate and Function. *Sci Immunol* (2020) 5:eaay3994. doi: 10.1126/sciimmunol.aay3994
12. Jiao L, Liu X. Structural Basis of Histone H3K27 Trimethylation by an Active Polycomb Repressive Complex 2. *Science* (2015) 350:aac4383. doi: 10.1126/science.aac4383
13. Cao R, Wang L, Wang H, Xia L, Erdjument-Bromage H, Tempst P, et al. Role of Histone H3 Lysine 27 Methylation in Polycomb-Group Silencing. *Science* (2002) 298:1039–43. doi: 10.1126/science.1076997
14. Jiao L, Shubbar M, Yang X, Zhang Q, Chen S, Wu Q, et al. A Partially Disordered Region Connects Gene Repression and Activation Functions of EZH2. *Proc Natl Acad Sci USA* (2020) 117:16992–7002. doi: 10.1073/pnas.1914866117
15. Shi B, Liang J, Yang X, Wang Y, Zhao Y, Wu H, et al. Integration of Estrogen and Wnt Signaling Circuits by the Polycomb Group Protein EZH2 in Breast Cancer Cells. *Mol Cell Biol* (2007) 27:5105–19. doi: 10.1128/MCB.00162-07
16. Jung HY, Jun S, Lee M, Kim HC, Wang X, Ji H, et al. PAF and EZH2 Induce Wnt/beta-Catenin Signaling Hyperactivation. *Mol Cell* (2013) 52:193–205. doi: 10.1016/j.molcel.2013.08.028
17. Yin J, Leavenworth JW, Li Y, Luo Q, Xie H, Liu X, et al. Ezh2 Regulates Differentiation and Function of Natural Killer Cells Through Histone Methyltransferase Activity. *Proc Natl Acad Sci United States America* (2015) 112:15988–93. doi: 10.1073/pnas.1521740112
18. Lieberman J. Granzyme A Activates Another Way to Die. *Immunol Rev* (2010) 235:93–104. doi: 10.1111/j.0105-2896.2010.00902.x
19. Fehniger TA, Cai SF, Cao X, Bredemeyer AJ, Presti RM, French AR, et al. Acquisition of Murine NK Cell Cytotoxicity Requires the Translation of a Pre-Existing Pool of Granzyme B and Perforin mRNAs. *Immunity* (2007) 26:798–811. doi: 10.1016/j.immuni.2007.04.010
20. Adams NM, Lau CM, Fan X, Rapp M, Geary CD, Weizman OE, et al. Transcription Factor IRF8 Orchestrates the Adaptive Natural Killer Cell Response. *Immunity* (2018) 48:1172–82.e6. doi: 10.1016/j.immuni.2018.04.018
21. Bhatnagar N, Ahmad F, Hong HS, Eberhard J, Lu IN, Ballmaier M, et al. FcgammaRIII (CD16)-Mediated ADCC by NK Cells Is Regulated by Monocytes and FcgammaRII (Cd32). *Eur J Immunol* (2014) 44:3368–79. doi: 10.1002/eji.201444515
22. Ostapchuk YO, Perfilyeva YV, Kali A, Tleulieva R, Yurikova OY, Stanbekova GE, et al. Fc Receptor Is Involved in Nk Cell Functional Anergy Induced by Miapaca2 Tumor Cell Line. *Immunol Invest* (2020) 30:1–16. doi: 10.1080/08820139.2020.1813757
23. Forbes CA, Scalzo AA, Degli-Esposti MA, Coudert JD. Ly49C Impairs NK Cell Memory in Mouse Cytomegalovirus Infection. *J Immunol* (2016) 197:128–40. doi: 10.4049/jimmunol.1600199
24. Bernardini G, Sciume G, Bosisio D, Morrone S, Sozzani S, Santoni A. CCL3 and CXCL12 Regulate Trafficking of Mouse Bone Marrow NK Cell Subsets. *Blood* (2008) 111:3626–34. doi: 10.1182/blood-2007-08-106203
25. Shum EY, Walczak EM, Chang C, Christina Fan H. Quantitation of mRNA Transcripts and Proteins Using the BD Rhapsody Single-Cell Analysis System. *Adv Exp Med Biol* (2019) 1129:63–79. doi: 10.1007/978-981-13-6037-4_5
26. Zhou Y, Zhou B, Pache L, Chang M, Khodabakhshi AH, Tanaseichuk O, et al. Metascape Provides a Biologist-Oriented Resource for the Analysis of Systems-Level Datasets. *Nat Commun* (2019) 10:1523. doi: 10.1038/s41467-019-09234-6
27. Tripathi S, Pohl MO, Zhou Y, Rodriguez-Frandsen A, Wang G, Stein DA, et al. Meta- and Orthogonal Integration of Influenza "OMICs" Data Defines a Role for UBR4 in Virus Budding. *Cell Host Microbe* (2015) 18:723–35. doi: 10.1016/j.chom.2015.11.002
28. Hesslein DG, Lanier LL. Transcriptional Control of Natural Killer Cell Development and Function. *Adv Immunol* (2011) 109:45–85. doi: 10.1016/B978-0-12-387664-5.00002-9
29. Tomasello E, Vivier E. KARAP/DAP12/TYROBP: Three Names and a Multiplicity of Biological Functions. *Eur J Immunol* (2005) 35:1670–7. doi: 10.1002/eji.200425932
30. Bari R, Granzin M, Tsang KS, Roy A, Krueger W, Orentas R, et al. A Distinct Subset of Highly Proliferative and Lentiviral Vector (LV)-Transducible NK Cells Define a Readily Engineered Subset for Adoptive Cellular Therapy. *Front Immunol* (2019) 10:2001. doi: 10.3389/fimmu.2019.02001
31. Sauvageau M, Sauvageau G. Polycomb Group Proteins: Multi-Faceted Regulators of Somatic Stem Cells and Cancer. *Cell Stem Cell* (2010) 7:299–313. doi: 10.1016/j.stem.2010.08.002
32. Bailey TL, Elkan C. Fitting a Mixture Model by Expectation Maximization to Discover Motifs in Biopolymers. *Proc Int Conf Intell Syst Mol Biol* (1994) 2:28–36.
33. Gupta S, Stamatoyannopoulos JA, Bailey TL, Noble WS. Quantifying Similarity Between Motifs. *Genome Biol* (2007) 8:R24. doi: 10.1186/gb-2007-8-2-r24
34. Li Y, Wang J, Yin J, Liu X, Yu M, Li T, et al. Chromatin State Dynamics During NK Cell Activation. *Oncotarget* (2017) 8:41854–65. doi: 10.18632/oncotarget.16688
35. Sciume G, Mikami Y, Jankovic D, Nagashima H, Villarino AV, Morrison T, et al. Rapid Enhancer Remodeling and Transcription Factor Repurposing Enable High Magnitude Gene Induction Upon Acute Activation of NK Cells. *Immunity* (2020) 53:745–58.e4. doi: 10.1016/j.immuni.2020.09.008
36. Zhao D, Zhang Q, Liu Y, Li X, Zhao K, Ding Y, et al. H3K4me3 Demethylase Kdm5a Is Required for NK Cell Activation by Associating With P50 to Suppress Socs1. *Cell Rep* (2016) 15:288–99. doi: 10.1016/j.celrep.2016.03.035
37. Cribbs A, Hookway ES, Wells G, Lindow M, Obad S, Oerum H, et al. Inhibition of Histone H3K27 Demethylases Selectively Modulates Inflammatory Phenotypes of Natural Killer Cells. *J Biol Chem* (2018) 293:2422–37. doi: 10.1074/jbc.RA117.000698
38. Kolodziejczyk AA, Kim JK, Svensson V, Marioni JC, Teichmann SA. The Technology and Biology of Single-Cell RNA Sequencing. *Mol Cell* (2015) 58:610–20. doi: 10.1016/j.molcel.2015.04.005
39. Stubbington MJT, Rozenblatt-Rosen O, Regev A, Teichmann SA. Single-Cell Transcriptomics to Explore the Immune System in Health and Disease. *Science* (2017) 358:58–63. doi: 10.1126/science.aan6828
40. Crinier A, Milpied P, Escaliere B, Piperoglou C, Galluso J, Balsamo A, et al. High-Dimensional Single-Cell Analysis Identifies Organ-Specific Signatures and Conserved NK Cell Subsets in Humans and Mice. *Immunity* (2018) 49:971–86.e5. doi: 10.1016/j.immuni.2018.09.009
41. Martinez-Zamudio RI, Roux PF, de Freitas J, Robinson L, Dore G, Sun B, et al. AP-1 Imprints a Reversible Transcriptional Programme of Senescent Cells. *Nat Cell Biol* (2020) 22:842–55. doi: 10.1038/s41556-020-0529-5
42. Soufi A, Garcia MF, Jaroszewicz A, Osman N, Pellegrini M, Zaret KS. Pioneer Transcription Factors Target Partial DNA Motifs on Nucleosomes to Initiate Reprogramming. *Cell* (2015) 161:555–68. doi: 10.1016/j.cell.2015.03.017
43. Vierbuchen T, Ling E, Cowley CJ, Couch CH, Wang X, Harmin DA, et al. AP-1 Transcription Factors and the BAF Complex Mediate Signal-Dependent Enhancer Selection. *Mol Cell* (2017) 68:1067–1082 e12. doi: 10.1016/j.molcel.2017.11.026
44. Wilson BG, Wang X, Shen X, McKenna ES, Lemieux ME, Cho YJ, et al. Epigenetic Antagonism Between Polycomb and SWI/SNF Complexes During Oncogenic Transformation. *Cancer Cell* (2010) 18:316–28. doi: 10.1016/j.ccr.2010.09.006
45. Wurm S, Zhang J, Guinea-Viniegra J, Garcia F, Munoz J, Bakiri L, et al. Terminal Epidermal Differentiation Is Regulated by the Interaction of Fra-2/AP-1 With Ezh2 and ERK1/2. *Genes Dev* (2015) 29:144–56. doi: 10.1101/gad.249748.114

46. Zenz R, Eferl R, Scheinecker C, Redlich K, Smolen J, Schonthaler HB, et al. Activator Protein 1 (Fos/Jun) Functions in Inflammatory Bone and Skin Disease. *Arthritis Res Ther* (2008) 10:201. doi: 10.1186/ar2338
47. Murphy TL, Tussiwand R, Murphy KM. Specificity Through Cooperation: BATF-IRF Interactions Control Immune-Regulatory Networks. *Nat Rev Immunol* (2013) 13:499–509. doi: 10.1038/nri3470
48. Dorsey MJ, Tae HJ, Sollenberger KG, Mascarenhas NT, Johansen LM, Taparowsky EJ. B-ATF: A Novel Human bZIP Protein That Associates With Members of the AP-1 Transcription Factor Family. *Oncogene* (1995) 11:2255–65.
49. Lau CM, Adams NM, Geary CD, Weizman OE, Rapp M, Pritykin Y, et al. Epigenetic Control of Innate and Adaptive Immune Memory. *Nat Immunol* (2018) 19:963–72. doi: 10.1038/s41590-018-0176-1
50. Kim E, Kim M, Woo DH, Shin Y, Shin J, Chang N, et al. Phosphorylation of EZH2 Activates STAT3 Signaling via STAT3 Methylation and Promotes Tumorigenicity of Glioblastoma Stem-Like Cells. *Cancer Cell* (2013) 23:839–52. doi: 10.1016/j.ccr.2013.04.008
51. Xu K, Wu ZJ, Groner AC, He HH, Cai C, Lis RT, et al. EZH2 Oncogenic Activity in Castration-Resistant Prostate Cancer Cells Is Polycomb-Independent. *Science* (2012) 338:1465–9. doi: 10.1126/science.1227604
52. Lee ST, Li Z, Wu Z, Aau M, Guan P, Karuturi RK, et al. Context-Specific Regulation of NF-kappaB Target Gene Expression by EZH2 in Breast Cancers. *Mol Cell* (2011) 43:798–810. doi: 10.1016/j.molcel.2011.08.011
53. Giguere V, Yang N, Segui P, Evans RM. Identification of a New Class of Steroid Hormone Receptors. *Nature* (1988) 331:91–4. doi: 10.1038/331091a0
54. Hong H, Yang L, Stallcup MR. Hormone-Independent Transcriptional Activation and Coactivator Binding by Novel Orphan Nuclear Receptor ERR3. *J Biol Chem* (1999) 274:22618–26. doi: 10.1074/jbc.274.32.22618

Conflict of Interest: The authors declare that the research was conducted in the absence of any commercial or financial relationships that could be construed as a potential conflict of interest.

Publisher's Note: All claims expressed in this article are solely those of the authors and do not necessarily represent those of their affiliated organizations, or those of the publisher, the editors and the reviewers. Any product that may be evaluated in this article, or claim that may be made by its manufacturer, is not guaranteed or endorsed by the publisher.

frontiers in Immunology

ORIGINAL RESEARCH
published: 29 October 2021
doi: 10.3389/fimmu.2021.746647

Comprehensive of N1-Methyladenosine Modifications Patterns and Immunological Characteristics in Ovarian Cancer

Jinhui Liu[1†], Can Chen[2†], Yichun Wang[3†], Cheng Qian[1†], Junting Wei[4], Yan Xing[1] and Jianling Bai[5*]*

[1] Department of Gynecology, The First Affiliated Hospital of Nanjing Medical University, Nanjing, China, [2] Department of Laboratory Medicine, The First Affiliated Hospital, Nanjing Medical University, Nanjing, China, [3] Department of Urology, The First Affiliated Hospital of Nanjing Medical University, Nanjing, China, [4] The Second Clinical School of Nanjing Medical University, Nanjing, China, [5] Department of Biostatistics, School of Public Heath, Nanjing Medical University, Nanjing, China

Background: recently, many researches have concentrated on the relevance between N1-methyladenosine (m1A) methylation modifications and tumor progression and prognosis. However, it remains unknown whether m1A modification has an effect in the prognosis of ovarian cancer (OC) and its immune infiltration.

Methods: Based on 10 m1A modulators, we comprehensively assessed m1A modification patterns in 474 OC patients and linked them to TME immune infiltration characteristics. m1Ascore computed with principal component analysis algorithm was applied to quantify m1A modification pattern in OC patients. m1A regulators protein and mRNA expression were respectively obtained by HPA website and RT-PCR in clinical OC and normal samples.

Results: We finally identified three different m1A modification patterns. The immune infiltration features of these m1A modification patterns correspond to three tumor immune phenotypes, including immune-desert, immune-inflamed and immune-excluded phenotypes. The results demonstrate individual tumor m1A modification patterns can predict patient survival, stage and grade. The m1Ascore was calculated to quantify individual OC patient's m1A modification pattern. A high m1Ascore is usually accompanied by a better survival advantage and a lower mutational load. Research on m1Ascore in the treatment of OC patients showed that patients with high m1Ascore showed marked therapeutic benefits and clinical outcomes in terms of chemotherapy and immunotherapy. Lastly, we obtained four small molecule drugs that may potentially ameliorate prognosis.

OPEN ACCESS

Edited by:
Mingzhu Yin,
Central South University, China

Reviewed by:
Yifei Liu,
Affiliated Hospital of Nantong University, China
Fangrong Yan,
China Pharmaceutical University, China

****Correspondence:***
Jianling Bai
baijianling@njmu.edu.cn
Yan Xing
13951891712@163.com

†These authors have contributed equally to this work

Specialty section:
This article was submitted to Cancer Immunity and Immunotherapy, a section of the journal Frontiers in Immunology

Received: *24 July 2021*
Accepted: *14 October 2021*
Published: *29 October 2021*

Citation:
Liu J, Chen C, Wang Y, Qian C, Wei J, Xing Y and Bai J (2021) Comprehensive of N1-Methyladenosine Modifications Patterns and Immunological Characteristics in Ovarian Cancer. Front. Immunol. 12:746647. doi: 10.3389/fimmu.2021.746647

Conclusion: This research demonstrates that m1A methylation modification makes an essential function in the prognosis of OC and in shaping the immune microenvironment. Comprehensive evaluation of m1A modifications improves our knowledge of immune infiltration profile and provides a more efficient individualized immunotherapy strategy for OC patients.

Keywords: ovarian cancer, m1A modification, tumor microenvironment, prognosis, immune checkpoint blockade

INTRODUCTION

Most scientists have focused on the critical effect on RNA methylation modifications in regulating genetic function. Different from DNA methylation, RNA methylation modifications, including N6-methyladenosine (m6A), 5-methylcytosine (m5C) and N1-methyladenosine (m1A), mainly regulate genetic expression at the post-transcriptional level (1–4). Among them, m1A methylation modification refers to inserting a methyl ester to its nitrogen atom at the adenine 1 position of RNA molecules such as mRNA, tRNA, and rRNA (5, 6), and m1A methylation modification is mainly enriched in mRNA 5'-untranslated region (UTR), which is different from most common m6A RNA modification (5, 7). m1A methylation modification maintains the structure and function of non-coding RNAs (ncRNAs), a process that is dynamically reversible and involves three classes of molecules: methyltransferases, demethylases and binding proteins (8). TRMT10C, Trmt61B and TRMT6/61A (methyltransferases) mediate the methylation modification process, as TRMT10C catalyzes m1A at site 9, Whereas the remaining two were catalyzed at site 58 (9–11). Demethylases including ALKBH1 and ALKBH3 can scrub the methylation modification signal from single-stranded DNA and RNA (12–15). The m1A binding proteins comprising YTHDF1, YTHDF2, YTHDF3 and YTHDC1 can read m1A methylation modification information and recognize and bind m1A methylation sites (16). These regulatory genes make an essential function in the process of modifying m1A. More researches have shown that abnormal expression or mutations of m1A regulatory molecules can affect transcription and translation processes, leading to abnormal pathological processes such as abnormal cell proliferation, retarded organismal development and tumorigenesis (17–20).

Using immune checkpoint inhibitors (ICIs), particularly PD-1, PD-L1 and CTLA-4 have become pivotal drugs in tumor-targeted molecular therapy with a brighter therapeutic future (21, 22). Ovarian cancer (OC) is a common malignant carcinoma of female reproductive organs, which seriously threatens women's lives. Currently, some scholars believe that the application of ICIs can restore T cell function and achieve therapeutic effects (23). However, in clinical practice, most OC patients show resistance to ICIs or the clinical benefits are not as expected (24). The application of ICIs therapy in OC is still controversial (25, 26). Positive response to immunotherapy usually depends on tumor cell interactions (27, 28) and immune regulation within tumor microenvironment (TME) (29, 30). TME consists of tumor cells, neighboring cells, vasculature and the extracellular matrix (ECM). The interaction between tumor cells and other components of TME can induce physiological or pathological changes (31). For example, the immunosuppressive microenvironment in epithelial ovarian cancer (EOC) makes it ineffective for immunotherapy. However, the use of 5-azacytidine has been clinically found to not only increase $CD8^+$ T cells and NK cells, but also decrease the macrophage and myeloid suppressor cell in TME. At this point, the tumor immunosuppressive microenvironment is weakened and the efficacy of immune checkpoint therapy is improved (32). Therefore, understanding the interactions and detailed mechanisms between immunotherapy and TME is a priority to improve the efficacy of immunotherapy.

Recently, some researches have concentrated on exploring the relationship between m1A regulators and TME. For example, woo et al. believe that the cytokine CSF-1 has an adverse effect on the prognosis of OC, and m1A methylation is engaged in the degradation of CSF-1 mRNA. Among them, ALKBH3 overexpression increase the stability of CSF-1 and increase CSF-1 expression (18). Wang et al. found that the silencing of TRMT10C suppresses OC proliferation and migration (33). However, the influence of m1A regulators on the development and progression of OC depends on the interaction of multiple regulators, rather than the influence of a single molecule. Thence, a complete assessment of the immune status mediated by multiple m1A regulators will facilitate our insight into the regulatory role of m1A regulators in OC TME.

In this research, we compiled the genetic and clinical information of 474 OC patients to synthetically assess m1A modification modes and correlate them with TME. Ultimately, we identified three m1A modification modes and observed different immune status and prognosis among the modes, which indicates that m1A modification in OC patients makes a critical function in establishing a single TME. Therefore, we developed a scoring system on the basis of genetic profile of the m1A regulators to quantify the m1A modification pattern of each OV patient.

METHODS

Ovarian Cancer Data Source and Preprocessing

Public RNA-seq expressed data and full clinical annotations are available from The Cancer Genome Atlas (TCGA) and Gene Expression Omnibus (GEO) databases. The exclusion criteria include removing all samples without clinical follow-up information, removing all samples with unknown survival time < 30 days and removing all samples without survival

status. After excluding samples with incomplete survival data, a total of 3 eligible OC cohorts, including GSE9891, GSE29691 and TCGA-OV, were collected to be processed. RNA sequencing data of gene expression (FPKM values) and clinical information in TCGA dataset were accessed directly from GDC website (https://portal.gdc.cancer.gov/). FPKM data were converted to transcripts per kilobase million (TPM) data. Normalized RNA sequencing data and corresponded clinical information for GSE9891, GSE29691 microarray dataset were accessed directly from GEO website (http://www.ncbi.nlm.nih.gov/geo). Batch effects between these cohorts were removed using "sva" R package (34). OC patients with mutational data were obtained from TCGA database. A total of 16 OC specimens and 16 normal tissues were obtained from the first affiliated hospital of Nanjing medical university. We obtain all the written informed consent from patients.

Unsupervised Clustering Analysis of 10 m1A Regulators

Total 10 regulators were selected from TCGA and GEO datasets for determining m1A modification patterns. On the basis of expression of 10 m1A regulators, we used the ConsensuClusterPlus package to apply unsupervised clustering analysis in order to facilitate the identification of different m1A modification patterns and the classification of patients. The consensus clustering algorithm determines how many clusters there are, and the process is repeated a thousand times to ensure reliability (35, 36).

Gene Set Variation Analysis (GSVA)

GSVA, a non-parametric unsupervised method, can be applied to assess the difference gene set enrichment between different m1A modification modes (37). Download the gene set "c2.cp.kegg.v6.2.symbols" from MSigDB database and use it for running GSVA. An adjusted $P<0.05$ was regarded as statistically significant.

TME Immune Cell Infiltration Analysis

CIBERSORT provides expression data for 22 common immune cells LM22. Based on these data, we calculated the association between m1Ascore and immune cell infiltration (38, 39). We utilized the ssGSEA (single sample gene set enrichment analysis) algorithm to assess the degree on immune infiltration. ESTIMATE algorithm was utilized to score stromal and immune gene sets and calculate tumor purity (40).

Identify Differentially Expressed Genes (DEGs) Between Different Phenotypes of m1A

We applied the empirical Bayesian approach of the limma package to find out DEGs of the three m1A modification patterns (41). The adjusted p for these genes is less than 0.05.

Construction of m1A Gene Signature

In order to quantify m1A modification pattern of single OC patients, we built a score scheme to assess m1A modification patterns, which we termed as m1Ascore. The m1Ascore was built in the following steps: first, we normalized the DEGs extracted from the different m1Aclusters and extracted overlapping DEGs. overlapping DEGs were analyzed using unsupervised clustering to classify OC patients into several groups. Consensus clustering algorithms were used to determine the count of gene clusters and their stabilization. We conducted prognostic analysis for each overlapping DEG with Cox regression method and screened genes with $P<0.05$. Principal component analysis (PCA) was used for building m1A-associated gene signature. Principal components 1 and 2 were both chosen for feature scores. m1Ascore = $\sum$ (PC1i + PC2i). Where i is m1A phenotype-related genes' expression (42, 43).

IPS Analysis

IPS is a representative gene associated with immunogenicity calculated using z-score. It uses PD-L1 expression of the four tumor-associated immune cells individually as an evaluation metric to distinguish the beneficiary population. Higher scores were linked to high immunogenicity (44). OC patients' IPS comes from the Cancer Immunome Atlas (TCIA) (https://tcia.at/home).

Connectivity Map (CMap) Dataset

CMap, as a gene expression profile database, allows the comparison of differentially expressed gene profiles with database reference datasets to obtain highly correlated agents with diseases (45). We utilized the CMap database to obtain the linkage between m1Ascore, OC and drugs. The 3D structures of the obtained agents can be accessed from Pubchem website.

External Validation of 10 m1A Regulators Protein Levels

The Human Protein Atlas (HPA) (https://www.proteinatlas.org) includes tissue and cellular protein distribution data from 44 different normal tissue categories and 17 major cancer categories. Immunohistochemical staining intensity, number, location and patient information are available online. After exploring 10 m1A-related genes in HPA database, seven m1A regulators expression (ALKBH1, ALKBH3, TRMT6, TRMT10C, TRMT61B, YTHDC1 and YTHDF2) in normal and OC tissues was obtained.

Quantitative Real Time PCR

Trizol reagent (Thermo Fisher Scientific, USA) was utilized to isolate and extract RNA from tissue samples. NanoDrop 2000 spectrophotometer (Thermo Scientific, USA) was designed to assess RNA quantity control and concentration. A high-capacity reverse transcription kit (Takara, Japan) was designed for reverse transcription of total RNA to cDNA. qRT-PCR was conducted in a Light Cycler 480II (Roche) using SYBR Green technology (Takara). Record the cycling threshold (Ct) for each gene and calculate the target gene mRNA expression with the $2^{-\Delta\Delta Ct}$ method. All steps of the qRT PCR were performed according to the reagent instructions and all experiments were repeated 3 times. PCR primers are showed in **Table S1**.

Statistical Analysis

Correlation coefficients between immune cells and m1A regulators expression were calculated by Spearman correlation analysis. Differences between three groups were compared with Kruskal-Wallis test, and associations among categorical covariates were tested with $\chi 2$ test (46). Based on the relevance of m1Ascore to patient prognosis, the optimal cut-off value for each dataset subgroup was defined using the survminer R package. This value dichotomizes the patients into high and low m1Ascore subgroups. Log-rank statistics were used for reducing the batch effect of calculations. Kaplan-Meier method was applied for drawing OS plots and log-rank test was utilized to identify statistics differences. Univariate Cox regression were used to compute risk ratios for m1A regulators and genes associated with m1A phenotype. Multivariate Cox regression was applied for identifying independent survival factors as well as the "forestplot" R package to visualize the results. The Maftools package and its "oncoplot" feature are used to present mutational differences. $P < 0.05$ is considered statistically significant. All data were processed in R 3.6.1 software.

RESULTS

m1A Regulators Mutation and Expression Difference and Its Clinical Relevance in OC

The total workflow is as shown in the following figure (**Supplementary Figure 1**). According to previous literature reports, we identified 10 m1A methylated genes. First, we integrated somatic mutations and copy number variants (CNVs) of these genes to characterize the mutations. As can be seen in **Supplementary Figure 2**, the mean mutation rate of m1A regulators is very low, and only 7 of 436 specimens have m1A regulator mutations, with a frequency of 1.61%. Subsequently, we analyzed the change frequency of the CNV in m1A regulators. **Figure 1A** shows that copy number variation was present in all 10 regulators, of which, most were dominated by copy number amplification, with only YTHDF2 exhibiting a copy number deletion. **Figure 1B** further visualizes the location of CNV alterations in the m1A regulators on the chromosome. By analyzing the expression of these 10 m1A regulators, we identified two subgroups that did not cross over, which demonstrated that we could completely distinguish between OC and normal samples based on m1A regulators expression levels (**Figure 1C**).

For searching the link between m1A methylation regulators and OC, we compared m1A regulator mRNA expression in OC and normal tissues from two databases, TCGA and GEO, respectively. TCGA data showed aberrant expression of all m1A regulators in OC. The expression of all genes in OC was greater than that in normal ($p<0.001$, **Figure 1D**). However, the different expression of these m1A regulators was not the same as that in GSE27651 database. In GSE27651 dataset, there was no statistical difference in ALKBH3 and TRMT61A expression between OC and normal samples. And compared with normal tissues, ALKBH1 expression ($P<0.01$) was significantly decreased in OC, while the expression of YTHDC1 increased ($P<0.05$, **Figure 1E**). Furthermore, we compared the differences in m1A regulator expression at the protein level between two tissues.

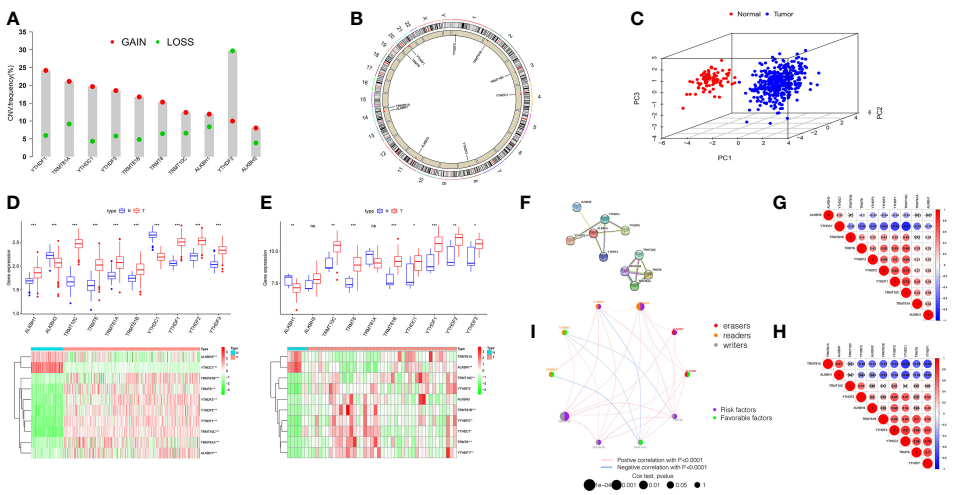

FIGURE 1 | Landscape of genetic and expression variation of m1A regulators in ovarian cancer. **(A)** The CNV variation frequency of m1A regulators in TCGA-OV cohort. The deletion frequency, green dot; The amplification frequency, red dot. **(B)** The location of CNV alteration of m1A regulators on 23 chromosomes using TCGA cohort. **(C)** Principal component analysis for the expression profiles of 10 m1A regulators to distinguish tumors from normal samples in TCGA cohort. **(D, E)** Boxplot and differential expression heatmap of m1A RNA methylation regulators in OC and normal tissues from **(D)** TCGA and **(E)** GEO datasets. **(F)** The PPI network of m1A RNA methylation regulators. **(G)** Spearman correlation analysis of m1A RNA methylation regulators in TCGA cohort. **(H)** Spearman correlation analysis of m1A RNA methylation regulators in GSE27651 cohort. **(I)** The interaction among m1A regulators in ovarian cancer. Violet dots in the circle, risk factors of prognosis; green dots in the circle, favorable factors of prognosis. The lines linking regulators showed their interactions, and thickness showed the correlation strength between regulators. *P < 0.05; **P < 0.01; ***P < 0.001. ns, not significant.

The results proved that ALKBH3 expression was lower in tumor compared to normal tissues, TRMT61A expression differences were not meaningful and the rest were expressed higher in OC (**Supplementary Figure 3A**). The above analysis indicates a high degree of heterogeneity in genetic variation and expression differences between normal and OC tissues, which indicates that the imbalance in the expression of m1A regulators makes a critical function in the development of OC and that genetic variation may interfere with their expression levels.

Next, we tried to clarify the relationship among the 10 m1A RNA methylation regulators. Analysis of the String database (**Figure 1F**) showed that ALKBH1 may be a central gene of the m1A RNA methylation regulator. However, further analysis did not display an expression correlation between ALKBH1 and other regulators. Interestingly, in TCGA cohort, we found that TRMT10C was positively related with seven m1A regulators, particularly YTHDF1 and YTHDF2. In contrast, YTHDC1 was negatively correlated with other eight regulators, particularly YTHDF1 and TRMT10C (**Figure 1G**). This suggests that TRMT10C and YTHDC1 may be key genes in m1A RNA methylation regulators affecting OC occurrence and development. However, in the GSE27691 cohort, we found that TRMT61A was negatively correlated with the expression of seven m1A regulators, particularly YTHDC1 and YTHDF1. In contrast, YTHDF1 was positively correlated with six other regulators, particularly YTHDC1 (**Figure 1H**). Broadly speaking, the correlation trends between the regulators in the TCGA and GEO databases were generally consistent.

We discuss the prognostic relevance of m1A regulators in patients with OC (**Supplementary Figure 3B**). We found that some m1A regulators, including ALKBH1, ALKBH3, TRMT6, TRMT10C, YTHDF1 and YTHDF2 are oncogenic and that overexpression of these genes results in worse prognosis for OC patients. The m1A regulator network diagram further describes the connections and interactions between m1A regulators and their prognostic significance for OV patients (**Figure 1I**). We revealed that m1A regulators expression showed significant correlations both within the same category and between different categories.

m1A Regulators-Mediated m1A Modification Patterns

According to 10 m1A regulator expression, we used R program to classify OC patients with different m1A modification patterns and eventually identified three different modification patterns by using an unsupervised clustering approach, namely m1A cluster-A (227 patients), B (148 patients), and C (236 patients) (**Figure 2A** and **Supplementary Figures 4A–C**). To discover the prognostic worth of the three m1A modification patterns, we concluded Kaplan-Meier analysis, the survival curves showed that the m1A cluster-B modification pattern was more pronounced among the three m1A modification subtypes (P = 0.009, **Figure 2B**). We also plotted heat maps to discuss the correlation between clinicopathological characteristics of OC patients and m1A modification patterns (**Figure 2C**).

Subsequently, we performed GSVA enrichment analysis of the three m1A modification patterns to investigate the associated pathways and biological significance. As shown in **Figures 2D, E**, m1A cluster-A and m1A cluster-C are similar in that both are significantly enriched for a number of gene replication and repair-related pathways, including homologous recombination, mismatch repair, and DNA replication. Differently, ECM-

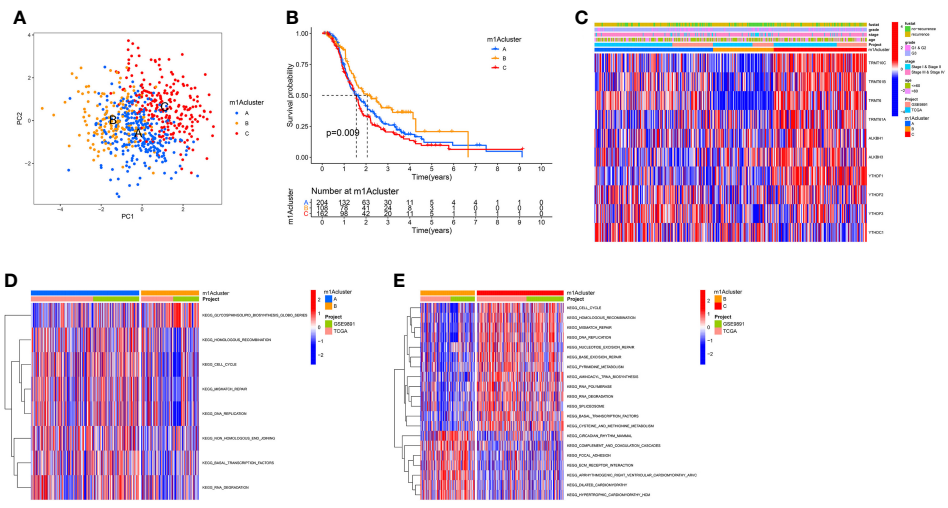

FIGURE 2 | The m1A modification patterns in OC and biological characteristics of m1A subtypes. **(A)** The principal component analysis for the transcriptome profiles of three m1A modification patterns. **(B)** Survival analyses of the three m1A modification patterns based on 611 OC patients. **(C)** Unsupervised clustering of 10 m1A regulators in two independent ovarian cancer cohorts. **(D, E)** GSVA enrichment analysis showing the activation states of biological pathways in distinct m1A modification patterns. The red represented activated pathways and blue represented inhibited pathways. **(D)** The m1A cluster A *vs* m1A cluster B; **(E)** The m1A cluster B *vs* m1A cluster C.

receptor interaction and focal adhesion were heavily abundant in m1Acluster-B, which may be related to the cellular matrix and its role in TME.

Immune Characteristics in Different m1A Modification Patterns

To better understand the relationship between m1A modification patterns and immunity, we explored immune characteristics of different m1A modification patterns. Analysis of cellular infiltration in the TME showed that the three m1A modification patterns had distinctly different TME cellular infiltration characteristics, with the most abundant immune cellular infiltration in m1A cluster-B, including many CD4+ T cells, plasmacytoid dendritic cells, monocyte, NK cells, MDSC, etc. (**Figure 3A**). This immunological profile corresponds to a tumor immune-inflamed phenotype (47), and tumor patients with this profile are the most responsive to immunotherapy, and m1A cluster-B patients do show a matched survival advantage (**Figure 2B**).

Furthermore, the results of GSVA analysis showed (**Figure 2E**) that the cluster B modification pattern significantly correlated with intrastromal interactions. Therefore, we hypothesized that the matrix in cluster B activates the anti-tumor effects of immune cells. We then employed ESTIMATE algorithm to calculate the proportion of the immune matrix component of each m1A modification pattern in the TME and presented it as immune score, stromal score and estimate score, which were positively correlated with immunity, stroma and the sum of both. We found that clusters-A and B had significantly more immune and stromal components in TME than cluster-C ($p<0.05$, **Figure 3B**).

In clinical tumor immunotherapy, the main immune checkpoint inhibitors currently in use include CTLA-4 inhibitors and PD-1 inhibitors. In order to advance the study of ICIs, understanding immune checkpoints expression in three m1A modification patterns is necessary. Therefore, we explored immune checkpoints expression in different m1A modification patterns. As seen in **Figure 3C**, immune checkpoint expression was slightly different in m1A subtypes, with slightly higher immune checkpoint expression in cluster A compared to cluster C ($p < 0.05$).

Construction of m1A Gene Signature and Its Immunological and Clinical Characterization

To explore the biology of each m1A modification pattern, we identified 527 m1A-associated DEGs (**Figure 4A**) and conducted GO and KEGG analysis on these genes (**Supplementary Figure 4D**). Based on 527 m1A phenotype-related genes, an unsupervised cluster analysis was then performed, and the patients were divided into different genomic groups. Similarly, unsupervised clustering algorithm exhibited three m1A modification genomic phenotypes, which termed as m1A gene clusters A, B, C (**Figure 4B** and **Supplementary Figures 4E–G**). This demonstrates that there are indeed three distinct patterns of m1A modification in OC. We observed that the three different gene clusters have different clinical characteristics (**Figure 4B**). Compared with m1A gene cluster-A and cluster-C, OC patients in m1A gene cluster-B displayed poor differentiation and higher frequency of recurrence (**Figure 4B**); and of the three m1A gene clusters, patients in gene cluster-C had longer survival times (p=0.001, **Figure 4C**). Moreover, m1A regulators' expression in the three m1A gene clusters also had significant differences (**Figure 4D**). In addition, we performed immune correlation analysis on the m1A gene cluster A-C. As shown in **Figure 4E**, the three m1A gene modification patterns have different TME cell infiltration characteristics. Unlike the m1A modification pattern, the m1A gene modification pattern has the most abundant immune cell infiltration in m1A gene cluster-A, such as activated

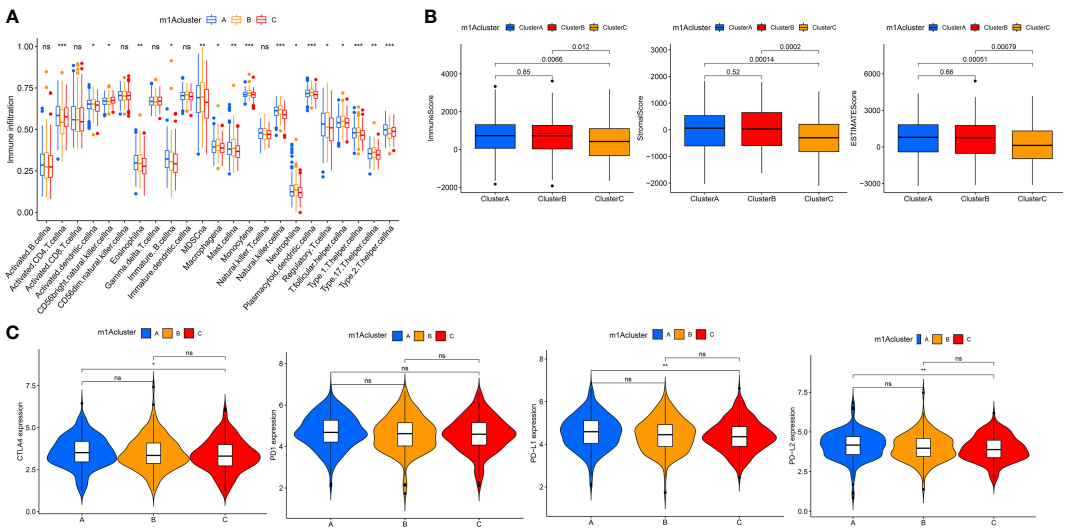

FIGURE 3 | TME cell infiltration characteristics and immune checkpoints in distinct m1A modification patterns. **(A)** The abundance of each TME infiltrating cell in three m1A modification patterns. **(B)** The box plot indicated the correlation between different m1A modification patterns and immune scores, stromal scores and estimate score. **(C)** The expression of CTLA-4, PD1, PD-L1 and PD-L2 among distinct m1A modification patterns. *P < 0.05; **P < 0.01; ***P < 0.001. ns, not significant.

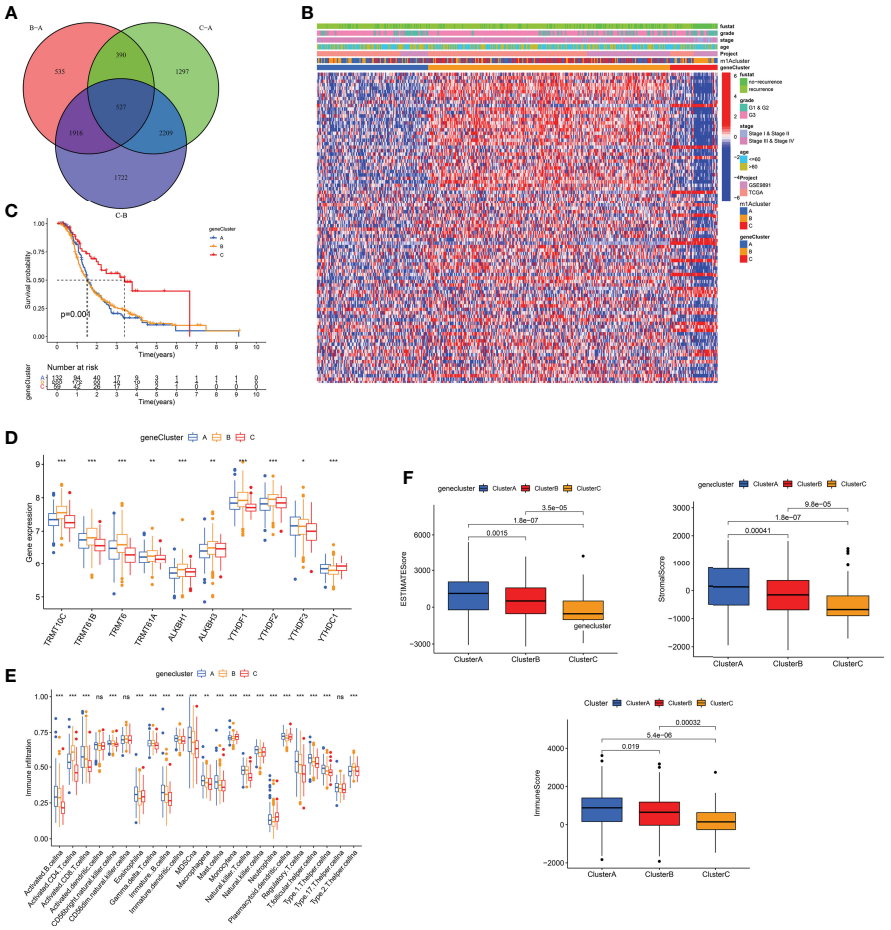

FIGURE 4 | The m1A gene clusters in OC and biological characteristics of m1A gene subtypes. **(A)** 527 m1A phenotype-related genes shown in venn diagram. **(B)** Unsupervised clustering of overlapping m1A phenotype-related genes in TCGA and GEO cohorts to classify patients into different genomic subtypes, termed as m1A gene cluster A-C, respectively. The gene clusters, m1A clusters, tumor stage, grade, survival status and age were used as patient annotations. **(C)** Kaplan-Meier curves indicated m1A modification genomic phenotypes were markedly related to overall survival of OC patients. **(D)** The expression of 10 m1A regulators in three m1A gene clusters. **(E)** The abundance of each TME infiltrating cell in three m1A gene clusters. **(F)** The box plot indicated difference in immune scores, stromal scores and estimate score between three m1A gene clusters. *P < 0.05; **P < 0.01; ***P < 0.001. ns, not significant.

CD8+T cell, MDSC, immature DC, monocyte, plasmacytoid DC, etc. After applying ESTIMATE algorithm, we found that gene cluster-A has the most immune and matrix components in TME, followed by gene cluster-B (P<0.05, **Figure 4F**). These findings demonstrate that m1A methylation modifications play an important regulatory effect on building of different TME landscapes.

Due to individual differences in m1A modification, based on 527 DEGs, we built a score system to accurately assess m1A modification pattern of single OC patients, and termed it the m1Ascore. First, the alluvial map visually displays the attribute changes of a single OC patient (**Figure 5A**). To better characterize the immunological profile of m1A feature, we analyzed the association between immune cells and m1Ascore (**Figure 5B**). Kruskal-Wallis test showed significant differences in m1Ascore between m1A gene clusters. Gene cluster-C scored highest median value and the lowest was for gene cluster-B (**Figure 5C**). In contrast, the highest median value was observed in m1A cluster B, while the lowest median value was observed in m1A cluster C (**Figure 5D**). Combining previous survival analysis in different clusters (**Figures 2B** and **4C**), this indicates that the m1Ascore may be positively correlated with the survival of OC patients.

Until we determined the prognostic value of m1Ascore, we evaluated the significance of the m1Ascore in immunological terms. First, we examined the correlation between immune cells and m1Ascore, and found that M1 macrophages, $CD8^+$ T cells, gamma delta T cells, T follicular helper cells decreased as m1Ascore increased, with a negative correlation between the two; in contrast DCs and resting CD4 memory T cells were positively related to m1Ascore, and cell infiltration increased with increasing score (**Figure 5E**). Subsequently, following the optimal cutoff values defined from survminer package, we dichotomized OC specimens into high- and low-m1Ascore groups and initially assessed the TME immune infiltration in these two groups. **Figure 5F** shows that intrinsic immune cells, including monocyte, NK cells and

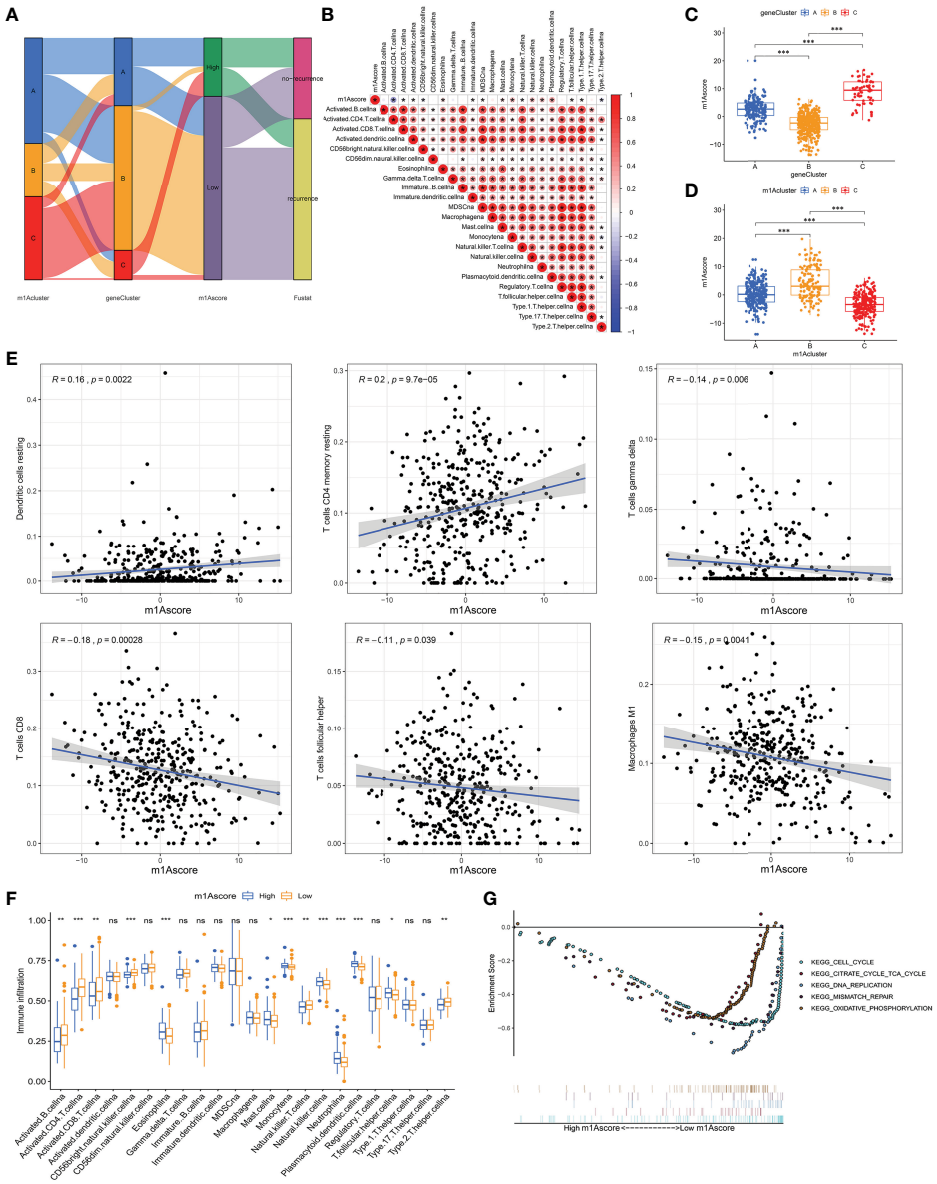

FIGURE 5 | Construction of m1A signatures. **(A)** Alluvial diagram showing the changes of m1Aclusters, gene cluster, m1Ascore and patient survival status. **(B)** Correlations between m1Ascore and the known gene signatures using Spearman analysis. Negative correlation was marked with blue and positive correlation with red. **(C)** Differences in m1Ascore among three gene clusters. **(D)** Differences in m1Ascore among three m1A modification patterns. **(E)** The correlation between m1Ascore and several immune cell, including resting dendritic cells, macrophages M1, resting memory CD4+ T cells, CD8+ T cells, follicular helper T cells and gamma delta T cells. **(F)** The abundance of each TME infiltrating cell in low- and high-m1Ascore group. **(G)** Enrichment plots showing cell cycle, citrate cycle TCA cycle, DNA replication, mismatch repair, and oxidative phosphorylation pathways were enriched in the low m1Ascore subgroup. *P < 0.05; **P < 0.01; ***P < 0.001. ns, not significant.

plasmacytoid DCs, were predominantly increased in high m1Ascore subgroup. On the contrary, there are more adaptive immune cells, consisting of B cells, CD4+ T cells and CD8+ T cells in low m1Ascore subgroup. Similarly, we apply the ESTIMATE algorithm between the two groups, and noticed no significant difference in infiltrating components in TME between the two groups (**Supplementary Figure 4H**). Furthermore, GSEA revealed that the low m1Ascore group mainly enriched some metabolic pathways and gene replication and repair-related pathways, including DNA replication and oxidative phosphorylation signaling. These are all tumor-related pathways, suggesting a poor prognosis for the low m1Ascore group (**Figure 5G**).

Next, we deeply analyze the value of m1Ascore in the prognosis of OC patients. High m1Ascore group patients showed better survival benefits (**Figure 6A**). Similarly, the high m1Ascore group consistently showed a marked survival advantage in patients stratified by different clinical characteristics (**Figure 6B**). Moreover, high m1Ascore group had a significantly greater

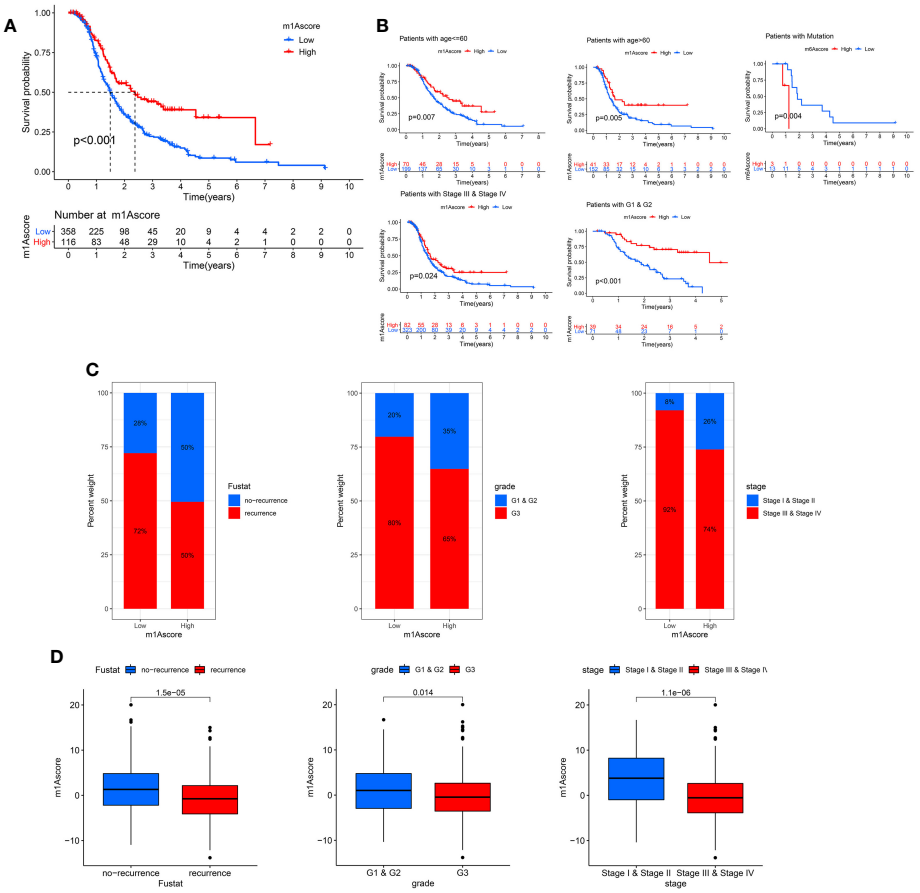

FIGURE 6 | Characteristics of m1A modification in OC patient subtypes. **(A)** Survival analyses of low and high m1Ascore patient groups in OC cohort using Kaplan-Meier curves. **(B)** Kaplan-Meier curves depicted the survival difference between low and high m1Ascore in the stratified analysis of OC patients, including age, grade, stage, and BRCA mutation. **(C)** The proportion of patient survival status, stage and grade in high and low m1Ascore groups. **(D)** Boxplots for m1Ascore between different characteristics OC patients, including patient survival status, stage and grade.

proportion of early-stage patients and recurrence-free population (**Figure 6C**), and these patients had higher m1Ascore (P<0.05, **Figure 6D**). This means that high scoring populations characterized by m1Acluster-B modification modes and immune activation phenotypes have a more favorable prognostic outlook. The above outcomes indicate that m1Ascore can also be employed to assess several clinical features of OC patients, including clinical stage, grade, and survival status.

Correlation Between m1A Score and Tumor Burden Mutation

There is a statistics association between tumor burden mutations (TMB) and tumor stage, grade, residual tumor size, and immune infiltrating cells in TME, which indicates that TMB has a major role in predicting OC survival and guiding immunotherapy in OC patients (48). Given TMB's clinically important nature, we attempted to probe the inherent relevance between TMB and m1Ascore to clarify genuine markings of the two groups. First, as shown in **Figure 7A**, although not statistically significant, low m1Ascore subgroup patients showed greater TMB than high m1Ascore group. Correlation analysis also confirmed that m1Ascore is significantly negatively associated with TMB (Spearman coefficient: R = -0.18, p = 0.0051; **Figure 7B**). Then, patients were dichotomized into high and low TMB groups. As shown in **Figure 7C**, we observed that OS was better in high-TMB patients (p=0.016). Collectively, these findings indicate that m1Ascore can be treated a predictor independent of TMB. Besides, we use maftools package to compare the distribution of somatic variation between low and high m1Ascore groups in TCGA. **Figure 7D** illustrates that low m1Ascore group exhibited a more extensive TMB than the high m1Ascore subgroup. These results provide new insights into the mechanisms underlying tumor m1Ascore composition and gene mutation, and indirectly confirm the value of m1Ascore in predicting the outcome of immunotherapy

The Role of m1A Modification Patterns in Ovarian Cancer Treatment

In recent years, platinum-based drugs and paclitaxel have been used as representative drugs for chemotherapy of OC (49). For

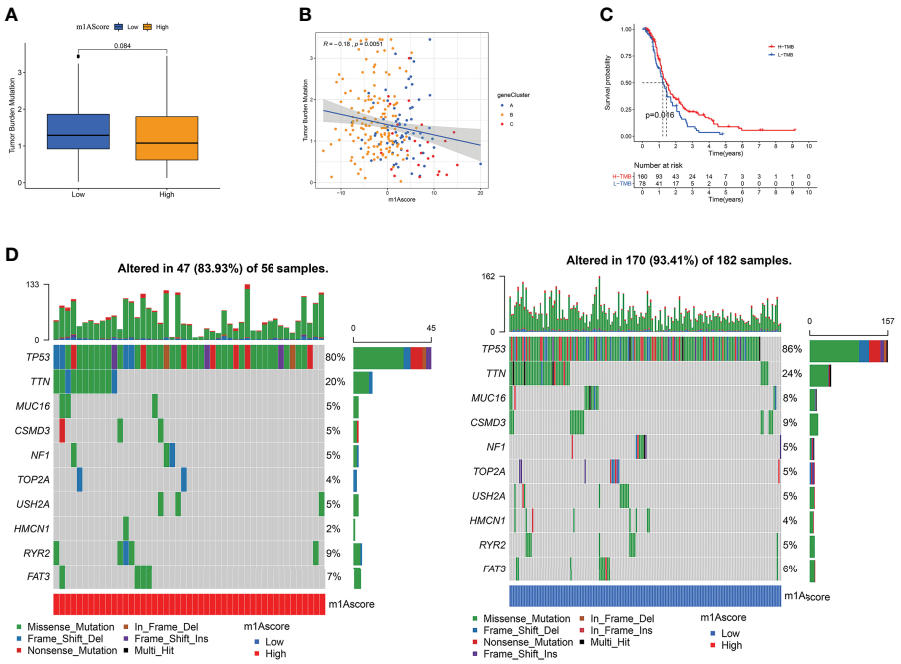

FIGURE 7 | The Correlation between the m1Ascore and somatic variants. **(A)** TMB difference in the high and low m1Ascore subgroups. **(B)** Scatterplots depicting the positive correlation between m1Ascores and tumor mutation load. **(C)** Kaplan-Meier curves for high and low TMB groups of the TCGA-OV patient. **(D)** The single-nucleotide variant was constructed using high m1Ascores on the left (red) and low m1Ascores on the right (blue). Individual patients are represented in each column.

this reason, based on the two treatment cohorts of TCGA and GSE9891, we explored whether m1A modification characteristics can predict the response of patients to these two first-line chemotherapeutic agents, including cisplatin and paclitaxel. It can be seen from **Figure 8A** that patients with low m1Ascore showed significant treatment sensitivity to both groups of drugs, which indicates that the m1Ascore facilitates the forecasting of patient reaction to chemotherapy.

Moreover, we utilized CMap database to examine the potential role of m1Ascore in the development of new drugs for OC. First, we screened for differentially expressed genes between the groups with high and low m1Ascore (**Supplementary Figures 5A, B**) and conducted GO and KEGG enrichment analysis on these genes (**Supplementary Figures 5C, D**). Subsequently, we utilized CMap database to analyze these genes and find drugs with high association with OC. The top 10 small molecule drugs highly correlated with OC are shown in **Table 1**. Among these agents, we obtained chemical structure information from PubChem for 4 most important small molecule agents (**Figures 9A–D**).

ICI has emerged as a key drug for immunotherapy (23). However, there is still several patients who do not respond to immunotherapy, which to some extent limits the application of ICIs. Therefore, Charoentong et al. developed a quantitative scoring scheme called immune phenotype score (IPS) to ascertain the determinants that influence tumor immunogenicity. In this scoring scheme, IPS is an excellent predictor for detecting anti PD-1 and anti CTLA-4 antibody responses (44). Here, we completely analyzed the link that exists between IPS and immune characteristics. The IPS-CTLA4-neg-PD-1-neg, IPS-CTLA4-neg-PD-1-pos, IPS-CTLA4-pos-PD-1-neg, IPS-CTLA4-pos-PD-1-pos scores were designed to assess the likelihood of patients receiving ICIs therapies. The results proved that the score increased significantly in the high m1Ascore group (**Figure 8B**): IPS-CTLA4-neg-PD-1-neg, P = 0.023; IPS-CTLA4-neg-PD-1-pos, P = 0.036. This indicates that the high m1Ascore group shows higher IPS and appears to have more immunogenic phenotypes. These results suggest that the effectiveness of ICIs may be better in patients with high m1Ascore.

Besides, we also investigated some common immune molecules expressions in different m1Ascore groups, including CD274, PDCD1, CD40, CXCL9 and so on. We observed that most genes, except CD70, showed higher expression levels in the low m1Ascore group (**Figure 8C**). This may also be a major factor in the lower survival rate of low m1Ascore patients (**Figure 6A**). These results above imply that quantification of m1A modification patterns might be used as a prospective and stable biomarker for chemotherapeutic response and immunotherapy evaluation.

Clinical Validation of Proteins, mRNA Expression of m1A Regulators

We used the HPA database to analyze m1A regulator protein expression. Since immunohistochemical data for TRMT61A, YTHDF and YTHDF3 were missing from the HPA data, we only analyzed the remaining seven m1A regulators. Compared to the normal tissue, TRMT10C, TRMT6 and YTHDF2 were

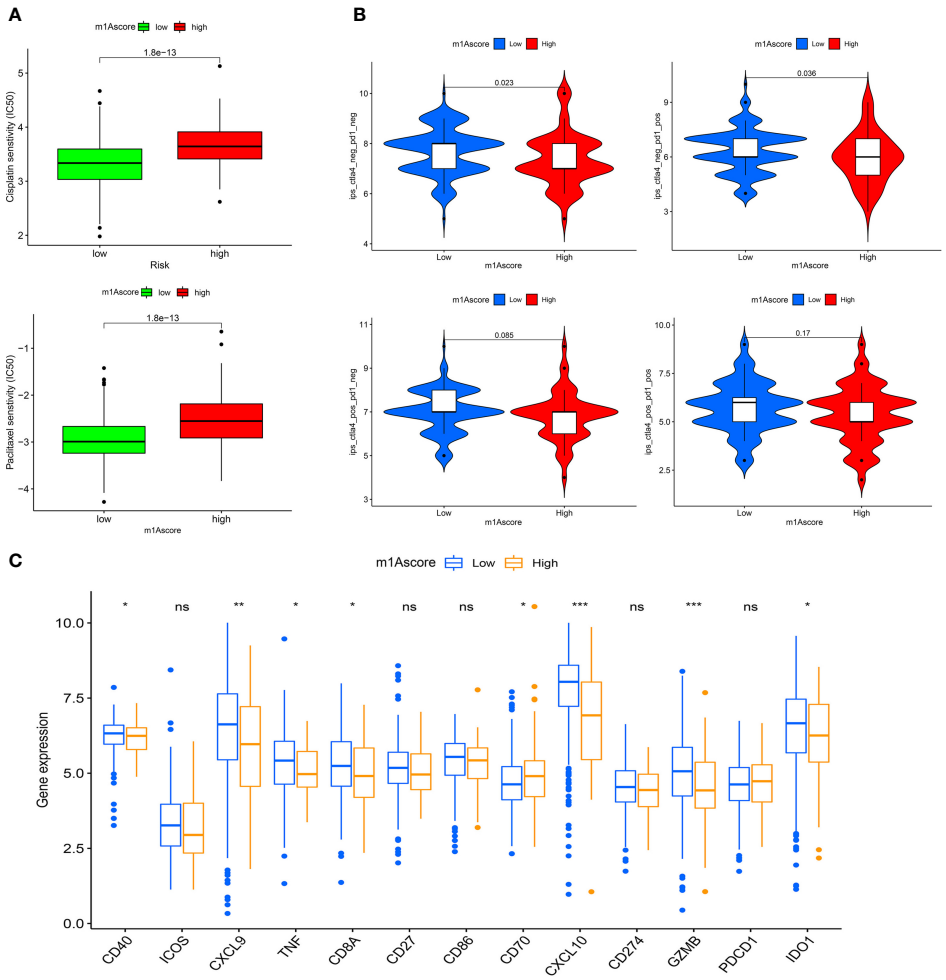

FIGURE 8 | m1A modification patterns in the role of OC clinical therapies **(A)** Box plot showing the sensitivity of patients with high and low m1Ascore subgroups to chemotherapy drugs, including cisplatin and paclitaxel. **(B)** The association between IPS and immune checkpoints in OC patients with different m1Asocre. **(C)** The expression of immune-relevant genes in high and low m1Ascore subgroups. *P < 0.05; **P < 0.01; ***P < 0.001; ns, not significant.

TABLE 1 | Results of CMap analysis.

cmap name	mean	n	enrichment	p-value	specificity	percent non-null
resveratrol	0.520	9	0.700	0.00006	0.0931	66
guanabenz	-0.440	5	-0.859	0.00008	0	60
amodiaquine	0.708	4	0.900	0.0001	0	100
indoprofen	-0.673	4	-0.910	0.0001	0	100
oxybenzone	-0.584	4	-0.851	0.00092	0.0141	75
pyrvinium	0.543	6	0.730	0.00103	0.0884	66
pyridoxine	0.386	4	0.836	0.00111	0	50
natamycin	0.367	4	0.808	0.00253	0	50
aciclovir	-0.352	6	-0.679	0.00294	0.0199	50
antimycin A	0.464	5	0.715	0.00439	0.0281	60

relatively highly expressed in the tumor tissue, while YTHDC1 was relatively less expressed. TRMT61B was moderately expressed in both tumor and normal samples. ALKBH1 and ALKBH3 were both lowly expressed in tumor and normal samples (**Figures 10A–G**).

In terms of mRNA levels, TRMT6, TRMT61A, TRMT61B, TRMT10C, YTHDF1 and YTHDF2 YTHDF3 were overexpressed in tumor sample. While ALKBH1 and YTHDC1 were overexpressed in normal sample. ALKBH3 expression had no difference between the tumor and normal sample

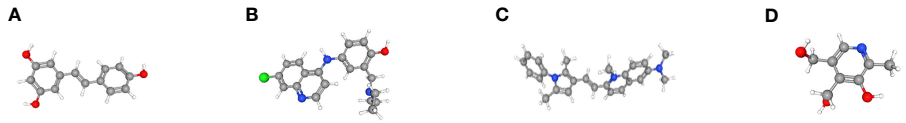

FIGURE 9 | The 3D structure of the four small molecule drugs for OC. **(A)** resveratrol, **(B)** amodiaquine, **(C)** pyrvinium, and **(D)** pyridoxine.

(**Figures 11A–J**). The mRNA expression detected by PCR was in general agreement with the TCGA database (**Figure 1D**).

DISCUSSION

More and more evidences show that under the interaction between multiple m1A regulators, m1A modification makes a critical function in inflammation, immune response, and tumorigenesis (50, 51). Most previous researches have focused on a single cell or a single regulator (51, 52), and thus a comprehensive understanding of the overall infiltration characteristics of the immune microenvironment mediated by the co-regulation of multiple m1A regulators is still lacking. Lately, m6 A modification has been fully explored in the tumor immune infiltration of OC (53). In this research, we highlighted the effect of m1A modifications in TME cell infiltration to enhance the knowledge of anti-tumor immune response and allow for targeted immunotherapy regimens to be proposed.

In our research, on the basis of 10 m1A regulators, we identified three different m1A modification patterns. Each of the three modification patterns has a different TME immune cell infiltration profile, where the ESTIMATE algorithm showed substantial innate immunity and matrix activation in both cluster-A and B. Combined with immune cell infiltration profile, we observed that cluster-B

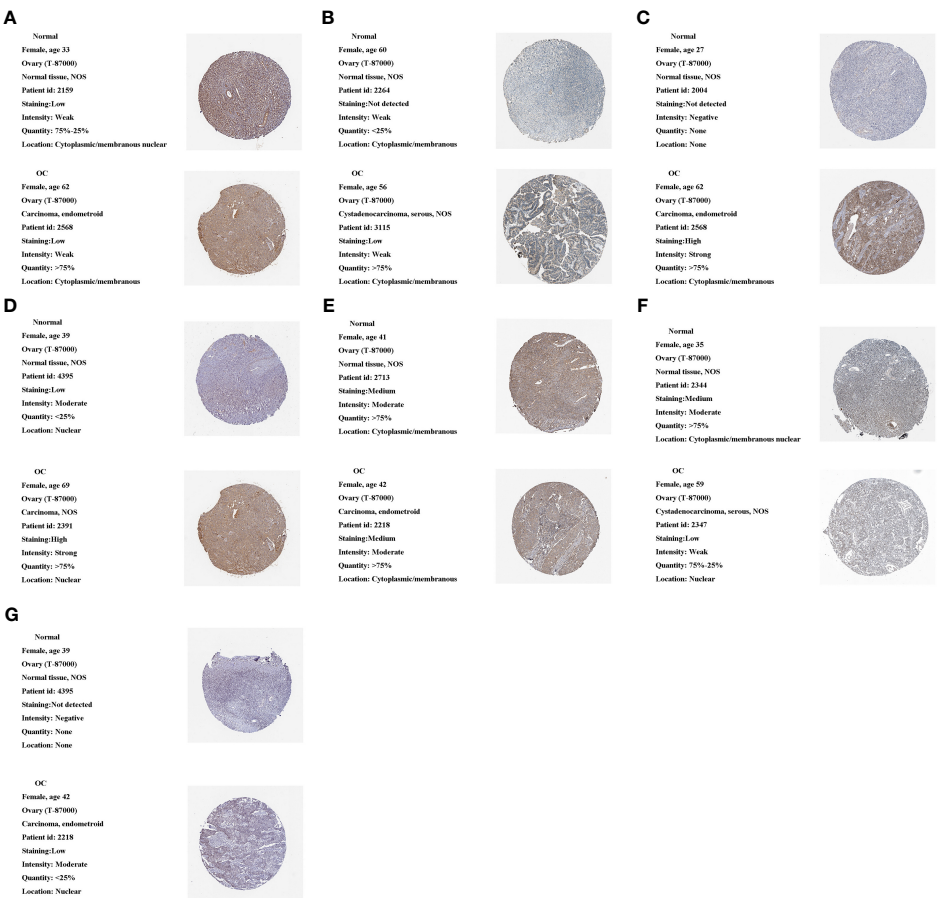

FIGURE 10 | Protein expression of 10 m1A regulators in the tumor and normal tissues in the HPA database. **(A)** ALKBH1 expression. **(B)** ALKBH3 expression. **(C)** TRMT10C expression. **(D)** TRMT6 expression. **(E)** TRMT61B expression. **(F)** YTHDC1 expression. **(G)** YTHDF2 expression.

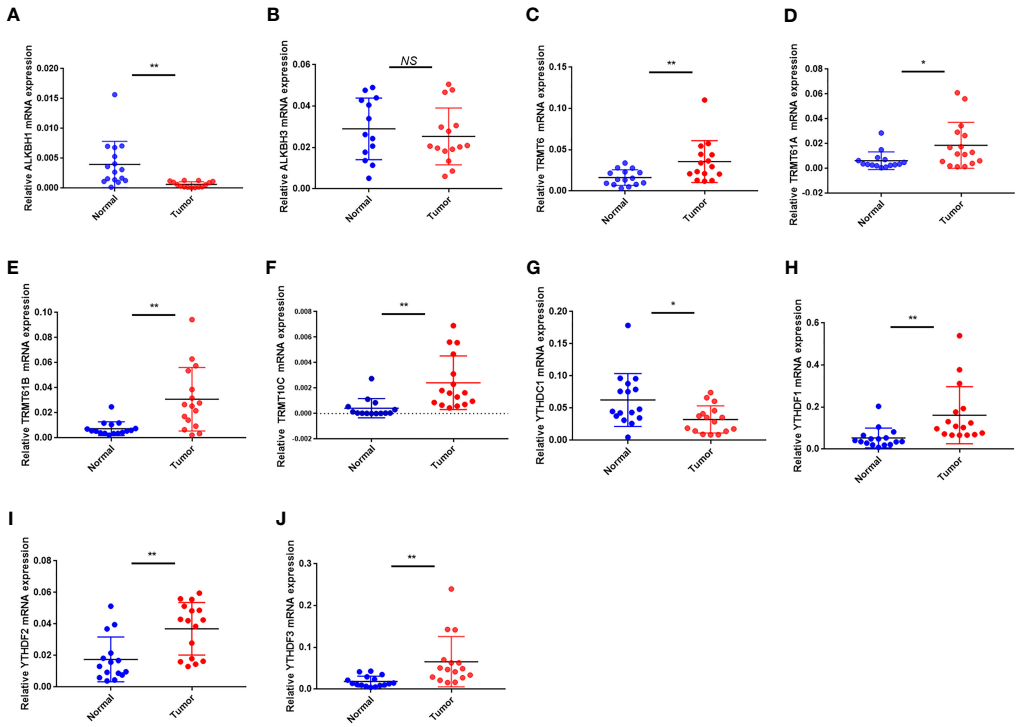

FIGURE 11 | The mRNA expression of the 10 m1A regulators in tumor and normal samples. **(A–J)** The mRNA expression of **(A)** ALKBH1, **(B)** ALKBH3, **(C)** TRMT6, **(D)** TRMT61A, **(E)** TRMT61B, **(F)** TRMT10C, **(G)** YTHDC1, **(H)** YTHDF1, **(I)** YTHDF2 and **(J)** YTHDF3. *P < 0.05; **P < 0.01; ns, not significant.

corresponds to immune-inflamed phenotype, which contains many $CD4^+$ T cells accompanied by myeloid cells and monocytes infiltration that activates an adaptive immune response. Cluster-A corresponds to the immune-excluded phenotype. Although there is also a large infiltration of immune cells within this tumor phenotype, most immune cells are present in the matrix that surrounds the nests of tumor cells, instead of penetrating the parenchyma. This limits tumor entry for immune cells to exert their immune effects. The characteristics of cluster-C correspond to an immune-desert phenotype. The immune-desert phenotype is related to immune tolerance and absence of T cell activation (47). By combining the immune cell infiltration profiles of individual clusters, this confirms the validity of the immunophenotypic categorization of the various m1A modification patterns. Thus, having thoroughly explored TME cell infiltration profiles induced by different m1A modification patterns, improves the future application of precision-focused, personalized therapy against OC. Furthermore, in this research, differences in the mRNA transcriptome between different m1A modification patterns have been demonstrated to be markedly linked to m1A and cellular matrix-related biological pathways. These DEGs are considered to be m1A-associated signature genes. In agreement with the clustering of m1A-modified phenotypes, three genomic clusters were defined on the basis of DEGs that were likewise associated with matrix and immune activation. This reaffirms important role of m1A modifications in structuring the diverse TME landscape. Hence, a comprehensive evaluation of m1A modification patterns will strengthen our visibility into the infiltration features of TME cells.

Given individual differences in m1A modification, a scoring system was developed to precisely assess the pattern of m1A modification in single OC patients, referred to as the m1Ascore. m1Acluster B, characterized by an immune-inflamed phenotype, showed the highest m1Ascore and the best prognostic outcome, whereas the immune-desert phenotype, characterized by m1Acluster C was the exact opposite. These results were also fully validated in the m1A genomic clusters. This suggests that m1Ascore is a reliable prognostic factor in OC and can be used to comprehensively assess individual tumor m1A modification patterns.

ICTs, including anti-PD-1 and CTLA-4 therapies have completely improved therapeutic and prognostic profile for a variety of advanced cancers, including OC (54). Although the survival of OC patients receiving immunotherapy has been significantly improved, there are obvious individual differences in the response of patients to immunotherapy. Therefore, finding markers that predict the results of immunotherapy is of clinical relevance. Earlier studies indicated that large CD8+ T cell infiltration plus the presence of nonsynonymous mutations propel the reaction to anti-PD-1 therapy. Furthermore, by confirming the predictive worth of m1Ascore in two anti-PD-1 and anti-CTLA-4 immunotherapy cohorts, we discovered that high m1Ascore patients were more likely to be treated with ICIs. Thus, we prove that m1A modification patterns play a nontrivial

part in molding distinct immune TME landscapes, meaning that m1A modification influences ICI treatment efficacy.

Luckily, we have found several small molecule medicines, such as resveratrol, amodiaquine, pyrvinium and pyridoxine, that can improve ovarian cancer treatment outcomes. Among them, resveratrol, as a natural polyphenolic organic compound, has antioxidant, anti-inflammatory, anti-cancer and cardiovascular protective functions. In a variety of tumor models, including ovarian cancer and pancreatic cancer, resveratrol was proven to be potent in controlling tumor cell proliferation and cancer development. Nevertheless, resveratrol is impacted by several factors during cancer treatment and further clinical studies are needed to confirm its role (55, 56). Usually, amodiaquine is applied to treat various types of malaria, acting in the intra-erythrocytic phase, mainly controlling symptoms quickly and with good tolerability (57). Currently, some studies have revealed that amodiaquine has potential anticancer effects in some cancers and has a wide range of applications (58, 59). Pyrvinium, as a cyanamide dye-like compound, has a significant anti-pinworm effect, interfering with the respiratory enzyme system of the worm and inhibiting oxygen uptake. In clinical trials, pyrvinium pamoate is considered to be an anthelmintic with anticancer effects. It kills tumor cells and restrains cancer cell metastasis by suppressing lipid anabolic metabolism (60, 61). Pyridoxine, also known as vitamin B6, is an essential trace element for maintaining the metabolic and regulatory processes of the body. Some studies have proven that pyridoxine intake is negatively associated with breast cancer risk, which means that pyridoxine has a potential protective function on the risk of breast cancer (62, 63). The above-mentioned agents have their own different effects in the anti-tumor field. However, clinical trials are still needed to validate the application of these drugs in OC patients.

Finally, we measured mRNA and protein expression levels of m1A regulators in OC and normal samples. We found higher protein and mRNA expression of TRMT6, TRMT10C and YTHDF2 in tumor samples. TRMT61A, TRMT61B, YTHDF1 and YTHDF3 mRNAs were higher in tumor tissues, but protein expression was weaker or not apparently distinct between tumor and normal samples. ALKBH1 and ALKBH3 mRNAs were higher in normal samples, but protein expression did not differ markedly between tumor and normal samples. YTHDC1 protein mRNA and mRNA expression were higher in normal tissues. mRNA and protein expression were broadly in agreement with TCGA and GEO databases.

However, our study also has some deficiencies. Our research materials are all derived from databases, and the results are obtained on the basis of bioinformatics. There is a lack of clinical cohorts and prospective clinical trials to validate the correlation between m1A modification and tumor immunity.

In clinical applications, m1Ascore can be applied to synthetically assess the m1A methylation modification pattern and the corresponding immune cell infiltration characteristics in individual patients, so as to facilitate the determination of tumor immunophenotypes and guide more effective clinical medications. We also proved that m1Ascore can be used not only to assess the clinicopathological characteristics of patients, including clinical stage and tumor mutation burden, but also as an independent prognostic biomarker. Furthermore, we validated that m1Ascore predicts the effectiveness of adjuvant chemotherapy and the clinical response of patients to anti-PD-1/CTLA-4 therapy. Thus, we herein provide clinicians with new ideas for immuno-oncology and individualized immunotherapy in OC.

CONCLUSION

In conclusion, this research investigated the regulatory role of m1A methylation modifications in the immune microenvironment of OC. m1A methylation modifications are one of the critical factors contributing to the heterogeneity of individual tumor immune infiltration. A thorough evaluation of m1A modification patterns in single OC patients may facilitates our comprehension of tumor immune landscape and provide more efficacious therapeutic approaches for OC patients.

DATA AVAILABILITY STATEMENT

The datasets presented in this study can be found in online repositories. The names of the repository/repositories and accession number(s) can be found in the article/**Supplementary Material**.

ETHICS STATEMENT

The studies involving human participants were reviewed and approved by Nanjing Medical University. The patients/participants provided their written informed consent to participate in this study. Written informed consent was obtained from the individual(s) for the publication of any potentially identifiable images or data included in this article.

AUTHOR CONTRIBUTIONS

YX and JB conceived the study and participated in the study design, performance, and manuscript writing. JL and CC conducted the bioinformatics analysis. YW, CQ, and JW revised the manuscript. All authors contributed to the article and approved the submitted version.

ACKNOWLEDGMENTS

We would like to thank the researchers and study participants for their contributions.

SUPPLEMENTARY MATERIAL

The Supplementary Material for this article can be found online at: https://www.frontiersin.org/articles/10.3389/fimmu.2021.746647/full#supplementary-material

Supplementary Figure 1 | The workflow employed in the development of the m1Ascore.

Supplementary Figure 2 | The mutation frequency of 10 m1A regulators in 436 patients with ovarian cancer. Each column represented individual patients. The upper barplot showed TMB and the number on the right indicated the mutation frequency in each regulator. The right barplot showed the proportion of each variant type. The stacked barplot below showed fraction of conversions in each sample.

Supplementary Figure 3 | (A) Differential expression of the m1A methylation regulators at the protein level. **(B)** Kaplan-Meier curves demonstrate the prognostic relevance of m1A methylation regulator expression to OC patients.**(A)**

Supplementary Figure 4 | (A) Cumulative distribution function curves for unsupervised clustering of 10 m1A regulators, k = 2-9. **(B)** Relative change in area under the CDF curve for unsupervised clustering of 10 m1A regulators, k = 2-9. **(C)** Heat map of the consensus matrix for the OC sample at k = 3. **(D)** Gene Ontology (left) and Kyoto Encyclopedia of Genes and Genomes (right) enrichment analyses of 527 m1A phenotype-related DEGs. **(E)** Cumulative distribution function curves for unsupervised clustering of 527 m1A phenotype-related genes in OC cohort, k = 2-9. **(F)** Relative change in area under the CDF curve for unsupervised clustering of 527 m1A phenotype-associated genes, k = 2-9. **(G)** Heat map of the consensus matrix for k = 3. **(H)** The box plot indicated difference in immune scores, stromal scores and estimate score between low and high m1Ascore subgroup

Supplementary Figure 5 | (A) Volcano plot of differentially expressed genes between high and low m1Ascore groups. **(B)** heatmap of differentially expressed genes between high and low m1Ascore groups. **(C)** Kyoto Encyclopedia of Genes and Genomes and **(D)** Gene Ontology enrichment analyses of differentially expressed genes between groupings of high and low m1Ascore.

REFERENCES

1. Zhao BS, Roundtree IA, He C. Post-Transcriptional Gene Regulation by mRNA Modifications. *Nat Rev Mol Cell Biol* (2017) 18(1):31–42. doi: 10.1038/nrm.2016.132
2. Boccaletto P, Machnicka MA, Purta E, Piatkowski P, Baginski B, Wirecki TK, et al. MODOMICS: A Database of RNA Modification Pathways. 2017 Update. *Nucleic Acids Res* (2018) 46(D1):D303–d307. doi: 10.1093/nar/gkx1030
3. Wang X, Lu Z, Gomez A, Hon GC, Yue Y, Han D, et al. N6-Methyladenosine-Dependent Regulation of Messenger RNA Stability. *Nature* (2014) 505 (7481):117–20. doi: 10.1038/nature12730
4. Squires JE, Patel HR, Nousch M, Sibbritt T, Humphreys DT, Parker BJ, et al. Widespread Occurrence of 5-Methylcytosine in Human Coding and Non-Coding RNA. *Nucleic Acids Res* (2012) 40(11):5023–33. doi: 10.1093/nar/gks144
5. Dominissini D, Nachtergaele S, Moshitch-Moshkovitz S, Peer E, Kol N, Ben-Haim MS, et al. The Dynamic N(1)-Methyladenosine Methylome in Eukaryotic Messenger RNA. *Nature* (2016) 530(7591):441–6. doi: 10.1038/nature16998
6. Zhang C, Jia G. Reversible RNA Modification N(1)-Methyladenosine (M(1)A) in mRNA and tRNA. *Genomics Proteomics Bioinformatics* (2018) 16 (3):155–61. doi: 10.1016/j.gpb.2018.03.003
7. Li X, Xiong X, Wang K, Wang L, Shu X, Ma S, et al. Transcriptome-Wide Mapping Reveals Reversible and Dynamic N(1)-Methyladenosine Methylome. *Nat Chem Biol* (2016) 12(5):311–6. doi: 10.1038/nchembio.2040
8. Roundtree IA, Evans ME, Pan T, He C. Dynamic RNA Modifications in Gene Expression Regulation. *Cell* (2017) 169(7):1187–200. doi: 10.1016/j.cell.2017.05.045
9. Chujo T, Suzuki T. Trmt61B Is a Methyltransferase Responsible for 1-Methyladenosine at Position 58 of Human Mitochondrial tRNAs. *Rna* (2012) 18(12):2269–76. doi: 10.1261/rna.035600.112
10. Safra M, Sas-Chen A, Nir R, Winkler R, Nachshon A, Bar-Yaacov D, et al. The M1a Landscape on Cytosolic and Mitochondrial mRNA at Single-Base Resolution. *Nature* (2017) 551(7679):251–5. doi: 10.1038/nature24456
11. Vilardo E, Rossmanith W. Molecular Insights Into HSD10 Disease: Impact of SDR5C1 Mutations on the Human Mitochondrial RNase P Complex. *Nucleic Acids Res* (2015) 43(10):5112–9. doi: 10.1093/nar/gkv408
12. Duncan T, Trewick SC, Koivisto P, Bates PA, Lindahl T, Sedgwick B. Reversal of DNA Alkylation Damage by Two Human Dioxygenases. *Proc Natl Acad Sci USA* (2002) 99(26):16660–5. doi: 10.1073/pnas.262589799
13. Aas PA, Otterlei M, Falnes PO, Vågbø CB, Skorpen F, Akbari M, et al. Human and Bacterial Oxidative Demethylases Repair Alkylation Damage in Both RNA and DNA. *Nature* (2003) 421(6925):859–63. doi: 10.1038/nature01363
14. Trewick SC, Henshaw TF, Hausinger RP, Lindahl T, Sedgwick B. Oxidative Demethylation by Escherichia Coli AlkB Directly Reverts DNA Base Damage. *Nature* (2002) 419(6903):174–8. doi: 10.1038/nature00908
15. Chen Z, Qi M, Shen B, Luo G, Wu Y, Li J, et al. Transfer RNA Demethylase ALKBH3 Promotes Cancer Progression *via* Induction of tRNA-Derived Small RNAs. *Nucleic Acids Res* (2019) 47(5):2533–45. doi: 10.1093/nar/gky1250
16. Dai X, Wang T, Gonzalez G, Wang Y. Identification of YTH Domain-Containing Proteins as the Readers for N1-Methyladenosine in RNA. *Anal Chem* (2018) 90(11):6380–4. doi: 10.1021/acs.analchem.8b01703
17. Shi Q, Xue C, Yuan X, He Y, Yu Z. Gene Signatures and Prognostic Values of M1a-Related Regulatory Genes in Hepatocellular Carcinoma. *Sci Rep* (2020) 10(1):15083. doi: 10.1038/s41598-020-72178-1
18. Woo HH, Chambers SK. Human ALKBH3-Induced M(1)A Demethylation Increases the CSF-1 mRNA Stability in Breast and Ovarian Cancer Cells. *Biochim Biophys Acta Gene Regul Mech* (2019) 1862(1):35–46. doi: 10.1016/j.bbagrm.2018.10.008
19. Waku T, Nakajima Y, Yokoyama W, Nomura N, Kako K, Kobayashi A, et al. NML-Mediated rRNA Base Methylation Links Ribosomal Subunit Formation to Cell Proliferation in a P53-Dependent Manner. *J Cell Sci* (2016) 129 (12):2382–93. doi: 10.1242/jcs.183723
20. Engel M, Chen A. The Emerging Role of mRNA Methylation in Normal and Pathological Behavior. *Genes Brain Behav* (2018) 17(3):e12428. doi: 10.1111/gbb.12428
21. Qin S, Xu L, Yi M, Yu S, Wu K, Luo S. Novel Immune Checkpoint Targets: Moving Beyond PD-1 and CTLA-4. *Mol Cancer* (2019) 18(1):155. doi: 10.1186/s12943-019-1091-2
22. Tu L, Guan R, Yang H, Zhou Y, Hong W, Ma L, et al. Assessment of the Expression of the Immune Checkpoint Molecules PD-1, CTLA4, TIM-3 and LAG-3 Across Different Cancers in Relation to Treatment Response, Tumor-Infiltrating Immune Cells and Survival. *Int J Cancer* (2020) 147(2):423–39. doi: 10.1002/ijc.32785
23. Brahmer JR, Tykodi SS, Chow LQ, Hwu WJ, Topalian SL, Hwu P, et al. Safety and Activity of Anti-PD-L1 Antibody in Patients With Advanced Cancer. *N Engl J Med* (2012) 366(26):2455–65. doi: 10.1056/NEJMoa1200694
24. Yi M, Yu S, Qin S, Liu Q, Xu H, Zhao W, et al. Gut Microbiome Modulates Efficacy of Immune Checkpoint Inhibitors. *J Hematol Oncol* (2018) 11(1):47. doi: 10.1186/s13045-018-0592-6
25. Ghisoni E, Imbimbo M, Zimmermann S, Valabrega G. Ovarian Cancer Immunotherapy: Turning Up the Heat. *Int J Mol Sci* (2019) 20(12):2927. doi: 10.3390/ijms20122927
26. Odunsi K. Immunotherapy in Ovarian Cancer. *Ann Oncol* (2017) 28 (suppl_8):viii1–7. doi: 10.1093/annonc/mdx444
27. Rizvi NA, Hellmann MD, Snyder A, Kvistborg P, Makarov V, Havel JJ, et al. Cancer Immunology. Mutational Landscape Determines Sensitivity to PD-1 Blockade in Non-Small Cell Lung Cancer. *Science* (2015) 348(6230):124–8. doi: 10.1126/science.aaa1348
28. Yarchoan M, Hopkins A, Jaffee EM. Tumor Mutational Burden and Response Rate to PD-1 Inhibition. *N Engl J Med* (2017) 377(25):2500–1. doi: 10.1056/NEJMc1713444
29. Cristescu R, Mogg R, Ayers M, Albright A, Murphy E, Yearley J, et al. Pan-Tumor Genomic Biomarkers for PD-1 Checkpoint Blockade-Based Immunotherapy. *Science* (2018) 362(6411):eaar3593. doi: 10.1126/science.aar3593
30. Mariathasan S, Turley SJ, Nickles D, Castiglioni A, Yuen K, Wang Y, et al. TGFβ Attenuates Tumour Response to PD-L1 Blockade by Contributing to Exclusion of T Cells. *Nature* (2018) 554(7693):544–8. doi: 10.1038/nature25501
31. Hanahan D, Coussens LM. Accessories to the Crime: Functions of Cells Recruited to the Tumor Microenvironment. *Cancer Cell* (2012) 21(3):309–22. doi: 10.1016/j.ccr.2012.02.022
32. Stone ML, Chiappinelli KB, Li H, Murphy LM, Travers ME, Topper MJ, et al. Epigenetic Therapy Activates Type I Interferon Signaling in Murine Ovarian

Cancer to Reduce Immunosuppression and Tumor Burden. *Proc Natl Acad Sci USA* (2017) 114(51):E10981–90. doi: 10.1073/pnas.1712514114
33. Wang Q, Zhang Q, Huang Y, Zhang J. M(1)A Regulator TRMT10C Predicts Poorer Survival and Contributes to Malignant Behavior in Gynecological Cancers. *DNA Cell Biol* (2020) 39(10):1767–78. doi: 10.1089/dna.2020.5624
34. Leek JT, Storey JD. Capturing Heterogeneity in Gene Expression Studies by Surrogate Variable Analysis. *PloS Genet* (2007) 3(9):1724–35. doi: 10.1371/journal.pgen.0030161
35. Yu G, Wang LG, Han Y, He QY. Clusterprofiler: An R Package for Comparing Biological Themes Among Gene Clusters. *Omics* (2012) 16(5):284–7. doi: 10.1089/omi.2011.0118
36. Wilkerson MD, Hayes DN. ConsensusClusterPlus: A Class Discovery Tool With Confidence Assessments and Item Tracking. *Bioinformatics* (2010) 26 (12):1572–3. doi: 10.1093/bioinformatics/btq170
37. Hänzelmann S, Castelo R, Guinney J. GSVA: Gene Set Variation Analysis for Microarray and RNA-Seq Data. *BMC Bioinformatics* (2013) 14:7. doi: 10.1186/1471-2105-14-7
38. Newman AM, Liu CL, Green MR, Gentles AJ, Feng W, Xu Y, et al. Robust Enumeration of Cell Subsets From Tissue Expression Profiles. *Nat Methods* (2015) 12(5):453–7. doi: 10.1038/nmeth.3337
39. Thorsson V, Gibbs DL, Brown SD, Wolf D, Bortone DS, Ou Yang TH, et al. The Immune Landscape of Cancer. *Immunity* (2018) 48(4):812–30.e814. doi: 10.1016/j.immuni.2018.03.023
40. Yoshihara K, Shahmoradgoli M, Martínez E, Vegesna R, Kim H, Torres-Garcia W, et al. Inferring Tumour Purity and Stromal and Immune Cell Admixture From Expression Data. *Nat Commun* (2013) 4:2612. doi: 10.1038/ncomms3612
41. Ritchie ME, Phipson B, Wu D, Hu Y, Law CW, Shi W, et al. Limma Powers Differential Expression Analyses for RNA-Sequencing and Microarray Studies. *Nucleic Acids Res* (2015) 43(7):e47. doi: 10.1093/nar/gkv007
42. Sotiriou C, Wirapati P, Loi S, Harris A, Fox S, Smeds J, et al. Gene Expression Profiling in Breast Cancer: Understanding the Molecular Basis of Histologic Grade to Improve Prognosis. *J Natl Cancer Inst* (2006) 98(4):262–72. doi: 10.1093/jnci/djj052
43. Zeng D, Li M, Zhou R, Zhang J, Sun H, Shi M, et al. Tumor Microenvironment Characterization in Gastric Cancer Identifies Prognostic and Immunotherapeutically Relevant Gene Signatures. *Cancer Immunol Res* (2019) 7(5):737–50. doi: 10.1158/2326-6066.CIR-18-0436
44. Charoentong P, Finotello F, Angelova M, Mayer C, Efremova M, Rieder D, et al. Pan-Cancer Immunogenomic Analyses Reveal Genotype-Immunophenotype Relationships and Predictors of Response to Checkpoint Blockade. *Cell Rep* (2017) 18(1):248–62. doi: 10.1016/j.celrep.2016.12.019
45. Lamb J, Crawford ED, Peck D, Modell JW, Blat IC, Wrobel MJ, et al. The Connectivity Map: Using Gene-Expression Signatures to Connect Small Molecules, Genes, and Disease. *Science* (2006) 313(5795):1929–35. doi: 10.1126/science.1132939
46. Hazra A, Gogtay N. Biostatistics Series Module 3: Comparing Groups: Numerical Variables. *Indian J Dermatol* (2016) 61(3):251–60. doi: 10.4103/0019-5154.182416
47. Chen DS, Mellman I. Elements of Cancer Immunity and the Cancer-Immune Set Point. *Nature* (2017) 541(7637):321–30. doi: 10.1038/nature21349
48. Bi F, Chen Y, Yang Q. Significance of Tumor Mutation Burden Combined With Immune Infiltrates in the Progression and Prognosis of Ovarian Cancer. *Cancer Cell Int* (2020) 20:373. doi: 10.1186/s12935-020-01472-9
49. Armstrong DK, Bundy B, Wenzel L, Huang HQ, Baergen R, Lele S, et al. Intraperitoneal Cisplatin and Paclitaxel in Ovarian Cancer. *N Engl J Med* (2006) 354(1):34–43. doi: 10.1056/NEJMoa052985
50. Han X, Wang M, Zhao YL, Yang Y, Yang YG. RNA Methylations in Human Cancers. *Semin Cancer Biol* (2020) 18(20):30241–8. doi: 10.1016/j.semcancer.2020.11.007
51. Liu F, Clark W, Luo G, Wang X, Fu Y, Wei J, et al. ALKBH1-Mediated tRNA Demethylation Regulates Translation. *Cell* (2016) 167(3):816–28.e816. doi: 10.1016/j.cell.2016.09.038
52. Kawarada L, Suzuki T, Ohira T, Hirata S, Miyauchi K, Suzuki T. ALKBH1 Is an RNA Dioxygenase Responsible for Cytoplasmic and Mitochondrial tRNA Modifications. *Nucleic Acids Res* (2017) 45(12):7401–15. doi: 10.1093/nar/gkx354
53. Fan L, Lin Y, Lei H, Shu G, He L, Yan Z, et al. A Newly Defined Risk Signature, Consisting of Three M(6)A RNA Methylation Regulators, Predicts the Prognosis of Ovarian Cancer. *Aging (Albany NY)* (2020) 12(18):18453–75. doi: 10.2139/ssrn.3514606
54. Hamanishi J, Mandai M, Ikeda T, Minami M, Kawaguchi A, Murayama T, et al. Safety and Antitumor Activity of Anti-PD-1 Antibody, Nivolumab, in Patients With Platinum-Resistant Ovarian Cancer. *J Clin Oncol* (2015) 33 (34):4015–22. doi: 10.1200/JCO.2015.62.3397
55. Carter LG, D'Orazio JA, Pearson KJ. Resveratrol and Cancer: Focus on *In Vivo* Evidence. *Endocr Relat Cancer* (2014) 21(3):R209–25. doi: 10.1530/ERC-13-0171
56. Rauf A, Imran M, Butt MS, Nadeem M, Peters DG, Mubarak MS. Resveratrol as an Anti-Cancer Agent: A Review. *Crit Rev Food Sci Nutr* (2018) 58 (9):1428–47. doi: 10.1080/10408398.2016.1263597
57. Olliaro P, Nevill C, LeBras J, Ringwald P, Mussano P, Garner P, et al. Systematic Review of Amodiaquine Treatment in Uncomplicated Malaria. *Lancet* (1996) 348(9036):1196–201. doi: 10.1016/S0140-6736(96)06217-4
58. Parvathaneni V, Kulkarni NS, Chauhan G, Shukla SK, Elbatanony R, Patel B, et al. Development of Pharmaceutically Scalable Inhaled Anti-Cancer Nanotherapy - Repurposing Amodiaquine for Non-Small Cell Lung Cancer (NSCLC). *Mater Sci Eng C Mater Biol Appl* (2020) 115:111139. doi: 10.1016/j.msec.2020.111139
59. Salentin S, Adasme MF, Heinrich JC, Haupt VJ, Daminelli S, Zhang Y, et al. From Malaria to Cancer: Computational Drug Repositioning of Amodiaquine Using PLIP Interaction Patterns. *Sci Rep* (2017) 7(1):11401. doi: 10.1038/s41598-017-11924-4
60. Dattilo R, Mottini C, Camera E, Lamolinara A, Auslander N, Doglioni G, et al. Pyrvinium Pamoate Induces Death of Triple-Negative Breast Cancer Stem-Like Cells and Reduces Metastases Through Effects on Lipid Anabolism. *Cancer Res* (2020) 80(19):4087–102. doi: 10.1158/0008-5472.CAN-19-1184
61. Momtazi-Borojeni AA, Abdollahi E, Ghasemi F, Caraglia M, Sahebkar A. The Novel Role of Pyrvinium in Cancer Therapy. *J Cell Physiol* (2018) 233 (4):2871–81. doi: 10.1002/jcp.26006
62. Egnell M, Fassier P, Lécuyer L, Zelek L, Vasson MP, Hercberg S, et al. B-Vitamin Intake From Diet and Supplements and Breast Cancer Risk in Middle-Aged Women: Results From the Prospective NutriNet-Santé Cohort. *Nutrients* (2017) 9(5):488. doi: 10.3390/nu9050488
63. Zhang L, Zhou D, Guan W, Ren W, Sun W, Shi J, et al. Pyridoxine 5'-Phosphate Oxidase Is a Novel Therapeutic Target and Regulated by the TGF-β Signalling Pathway in Epithelial Ovarian Cancer. *Cell Death Dis* (2017) 8 (12):3214. doi: 10.1038/s41419-017-0050-3.

Conflict of Interest: The authors declare that the research was conducted in the absence of any commercial or financial relationships that could be construed as a potential conflict of interest.

Publisher's Note: All claims expressed in this article are solely those of the authors and do not necessarily represent those of their affiliated organizations, or those of the publisher, the editors and the reviewers. Any product that may be evaluated in this article, or claim that may be made by its manufacturer, is not guaranteed or endorsed by the publisher.

frontiers in Immunology

ORIGINAL RESEARCH
published: 02 November 2021
doi: 10.3389/fimmu.2021.734646

Comprehensive Multi-Omics Identification of Interferon-γ Response Characteristics Reveals That RBCK1 Regulates the Immunosuppressive Microenvironment of Renal Cell Carcinoma

Wenhao Xu[1†], Juli Tao[2†], Wenkai Zhu[1†], Wangrui Liu[3†], Aihetaimujiang Anwaier[1], Xi Tian[1], Jiaqi Su[1], Guohai Shi[1], Haineng Huang[2,3], Gaomeng Wei[4], Chuanyu Li[3], Yuanyuan Qu[1*], Hailiang Zhang[1*] and Dingwei Ye[1*]*

[1] Department of Urology, Fudan University Shanghai Cancer Center, Shanghai, China, [2] Department of Hematology and Rheumatology, Affiliated Hospital of Youjiang Medical University for Nationalities, Baise, China, [3] Department of Neurosurgery, Affiliated Hospital of Youjiang Medical University for Nationalities, Baise, China, [4] Department of Urology, Affiliated Hospital of Youjiang Medical University for Nationalities, Baise, China

Interferon-gamma (IFN-γ) has a complex role in modulating the tumor microenvironment (TME) during renal cell carcinoma (RCC) development. To define the role of IFN-γ response genes in RCC progression, we characterized the differential gene expression, prognostic implications, and DNA variation profiles of selected IFN-γ response signatures, which exhibited a significant hazard ratio for the overall survival (OS) and progression-free survival (PFS) of papillary, chromophobia, and clear cell RCC (ccRCC) patients (n = 944). Prognostic nomograms were constructed to predict the outcomes for ccRCC patients, highlighting the prognostic implications of RANBP2-type and C3HC4-type zinc finger containing 1 (RBCK1). Interestingly, large-scale pan-cancer samples (n = 12,521) and three single-cell RNA datasets revealed that RBCK1 showed markedly differential expression between cancer and normal tissues and significantly correlated with tumor-infiltrating immune cells, tumor purity, and immune checkpoint molecules, such as PD-L1, CTLA-4, LAG-3, and TIGIT in pan-cancer samples. Notably, the TIDE score was significantly higher in the RBCK1^{high} group compared with the RBCK1^{low} group in both ccRCC and RCC cohorts. Besides, immunohistochemistry staining showed significantly elevated RBCK1 expression in tumors (n = 50) compared with kidney samples (n = 40) from a real-world cohort, Fudan University Shanghai Cancer Center (FUSCC, Shanghai). After RBCK1 expression was confirmed in ccRCC, we found a significantly decreased number of infiltrating CD4$^+$ T cells, CD4$^+$ FOXP3$^+$ Treg cells, M1 macrophages, and CD56$^{bight/dim}$ NK cells in the immune-cold RBCK1^{high} group. In addition to the distinct heterogeneous immune microenvironment, the increased expression of RBCK1 predicted

OPEN ACCESS

Edited by:
Mingzhu Yin,
Central South University, China

Reviewed by:
Hongkai Wang,
Shanghai Medical College of Fudan University, China
Jian-Yuan Zhao,
Fudan University, China
Jun Wang,
Sun Yat-sen University Cancer Center (SYSUCC), China
Jianfeng Yang,
Shanghai University of Traditional Chinese Medicine, China
Zhihong Liu,
Shanghai First People's Hospital, China

***Correspondence:**
Chuanyu Li
lcy1983162008@163.com
Yuanyuan Qu
quyy1987@163.com
Hailiang Zhang
zhanghl918@163.com
Dingwei Ye
dwyelie@163.com

[†]These authors have contributed equally to this work

Specialty section:
This article was submitted to Cancer Immunity and Immunotherapy, a section of the journal Frontiers in Immunology

Received: *01 July 2021*
Accepted: *11 October 2021*
Published: *02 November 2021*

a prominently worse prognosis than the RBCK1^{low} group for 232 ccRCC patients in the FUSCC proteomic cohort. Furthermore, after transfected with siRNA in human ccRCC cells, extraordinarily decreased cell proliferation, migration capacities, and prominently elevated apoptosis tumor cell proportion were found in the siRNA groups compared with the negative control group. In conclusion, this study identified IFN-γ response clusters, which might be used to improve the prognostic accuracy of immune contexture in the ccRCC microenvironment. Immune-cold RBCK1^{high} patients have pro-tumorigenic immune infiltration and significantly worse outcomes than RBCK1^{low} patients based on results from multi-omics to real-world data. Our discovery of novel independent prognostic indicators for RCC highlights the association between tumor alterations and immune phenotype.

Keywords: renal cell carcinoma, ccRCC kidney cancer, IFN-γ, immune checkpoint therapies, tumor microenvironment, RBCK1, bioinformatics, machine learning algorithm

INTRODUCTION

Although the diagnosis and treatment of renal cell carcinoma (RCC) have improved over the past 20 years, RCC is still one of the most fatal urinary malignancies. There were approximately 400,000 new RCC cases and 175,000 estimated deaths caused by RCC worldwide in 2018 (1). RCC can be classified as papillary RCC (pRCC), chromophobia RCC (chRCC), or clear cell RCC (ccRCC), which arise from the renal cortex or renal tubular epithelial cells and accounts for approximately 85% of all primary renal cancers (2).

Interferon (IFN) therapy, the first effective immunotherapy, has an important role in the treatment of RCC. In the era of targeted therapy, IFN is used to treat high-risk metastatic renal cell carcinoma patients in Japan and improve their survival (3). RCC patients with lung metastasis can benefit from combination therapy with IFN-α and IL-2 (4, 5). Currently, there are many strategies for the treatment of RCC including targeted therapies such as sorafenib and sunitinib or immunotherapies such as PD-L1 or PD-1 inhibitors. These new treatment regimens have important implications for the management of RCC. However, RCC is a highly heterogeneous cancer that lacks effective markers to guide prognosis and treatment (6). Furthermore, activation of tumor cell pro-cancer signals not only affects its own malignant biological behavior to promote tumor occurrence and development but also changes the metabolism and secretion of tumor cells and the tumor microenvironment, which alters the functional phenotype of tumor-infiltrating immune cells that aid in tumor immune escape (7, 8).

IFN-γ-signaling-related genes have an important role in the prognosis of RCC. Some IFN-γ-signaling-related genes, such as the IRF family genes, regulate the cell cycle and induce apoptosis in RCC cells (9). *RBCK1*, an IFN-γ-signaling-related gene, promoted p53 degradation *via* ubiquitination in RCC. The signature of IFN-γ-signaling-related genes may provide strategies to identify cancer-specific diagnosis and prognosis (10). A recent study found that PD-L1 was induced in ccRCC-like cell lines by canonical IFN-γ signaling and high levels of PD-L1 mRNA in tumor tissues were positively correlated with an IFN-γ signature that favorably affected prognosis (11). These findings suggest that interferon-related genes can be used to guide the treatment of immune checkpoint inhibitors.

The rapid development of bioinformatics has improved disease diagnosis, prognosis, treatment, phenotypes, and human phenomics (12–14). Different machine learning algorithms require rigorous statistics and real-world *in vitro* or clinical verification to determine tumor heterogeneity and the tumor microenvironment (15). This study hypothesized that IFN-related genes can be used to monitor the progression and long-term prognosis of renal cell carcinoma including clear cell RCC, chromophobe RCC, and papillary RCC and that these key genes can be used as simple biomarkers in a prediction model to predict the tumor-suppressive immune microenvironment and determine the poor prognosis of renal cell carcinoma.

METHODS

Ethical Approval and Consent to Participate

All of the study designs and test procedures were performed in accordance with the Helsinki Declaration II. Ethical approval and participation consent of this study was reviewed and agreed upon by the Fudan University Shanghai Cancer Center (FUSCC) Institutional Review Board (No. 2008222-Exp49).

Data Download and Sample Collection

The RNA-seq, copy number variation, mutation, and clinical and survival data of 530 ccRCC, 323 pRCC, and 91 chRCC patients were obtained from The Cancer Genome Atlas (TCGA, https://portal.gdc.cancer.gov) database with gene IDs converted from Ensembl ID to gene symbol matrix. The phenotypic and clinical data of large-scale pan-cancer samples (n = 12,521) were enrolled from the TCGA database. In addition, 232 ccRCC patients with proteomics sequencing and clinical data and 50 ccRCC together with 40 normal kidney FFPE samples were enrolled from the FUSCC cohort. The clinicopathological characteristics of 765

ccRCC patients from the TCGA and FUSCC cohort are described in **Supplementary Table 1**.

Clinicopathological Characteristics and Survival Analysis

Student's *t*-test was used to compare the expression levels of targeted genes in tumor and normal samples. Association between gene expression and clinicopathological characteristics was evaluated using Wilcoxon rank sum test and visualized using ggplot2 R package. The Kaplan–Meier survival with log-rank test was implemented to compare the survival benefit difference between groups. *p*-values and hazard ratio (HR) with 95% confidence interval (95% CI) were obtained using log-rank tests and univariate Cox proportional hazards regression. All the above analysis methods and R packages (ggrisk, survival, survminer, timeROC) were implemented by R Foundation for Statistical Computing version 4.0.3.

DNA Variation Distribution Analysis

We downloaded the single nucleotide variation (SNV), copy number variation (CNV), genetic mutation data, transcriptome data, and clinical data from the TCGA database. To identify the somatic mutations of the patients with ccRCC, pRCC, and chRCC, mutation data were downloaded and visualized using the "maftools" package in R software. The profiles of SNV, CNV, and heterozygous CNV and the survival difference between CNV and the wide type of the IFN-γ response genes in RCC were analyzed based on Gene Set Cancer Analysis (GSCA, http://bioinfo.life.hust.edu.cn/GSCA), an integrated database for genomic and immunogenomic gene set cancer analysis.

Construction of IFN-γ Response Gene Prediction Models and Nomogram

The least absolute shrinkage and selection operator (LASSO) Cox regression algorithm was used for the selection of independent indicators with 10-fold cross-validation using the R software package glmnet. The IFN-γ response gene prediction models (IPMs) for prognosis were constructed based on derived hub genes and corresponding assignment value. Besides, univariate and multivariate Cox regression analyses were performed to construct the nomogram enrolling IFN-γ response genes with the most prognostic implications and clinical features, such as age, pathological TNM stage, and ISUP grade using forestplot R package. The nomogram was developed based on the results of multivariate Cox proportional hazards analysis to predict the 1-, 3-, and 5-year survival recurrence.

Assessment of Immune Cell Infiltration and Immune Checkpoint Expression

To develop reliable immune cell infiltration calculations, we implemented the immunedeconv R package which integrates xCell and CIBERSORT algorithms. Siglec-15, IDO-1, CD274, HAVCR2, PDCD1, CTLA-4, LAG-3, and PDCD1LG2 were selected to be immune checkpoints, and the expression level was extracted in pan-cancers. The association between target gene expression and immune cell infiltration of immune checkpoint expression level was assessed using Spearman's test.

Evaluation of Immunotherapy Efficacy in Patients With RCC

The Tumor Immune Dysfunction and Exclusion (TIDE) algorithm based on expression profile data has been used to predict the responsiveness of ccRCC and RCC patients receiving immune checkpoint inhibitors (ICIs) (16). Differentially expressed immune checkpoints between tumor groups and normal samples were assessed.

Immunohistochemistry Staining and Tumor Immune Microenvironment Characterizations of ccRCC

Immunohistochemistry (IHC) was utilized to evaluate the expression level of RBCK1 (ab219955; Abcam) in 50 ccRCC and 40 adjacent normal tissues from the FUSCC Tissue Bank according to procedures previously described (17). Then, opal multispectral imaging was used to identify differential immune cell infiltration. CD3 (Kit-0003, Maxim, China), CD4 (RMA-0620, Maxim, China), CD8 (RMA-0514, Maxim, China), FOXP3 (98377, CST), CD20 (MAB-0669, Maxim, China), CD56 (99746, CST), CD68 (76437, CST), CD163 (MAB-0206, Maxim, China), PD-1 (84651, CST), and PD-L1 (13684, CST) antibodies were added to the slide and incubated overnight in a humidified chamber at 4°C. HRP-labeled goat anti-rabbit/mouse secondary antibody was added dropwise and incubated at room temperature. Finally, the slices are imaged and quantitatively analyzed on a multispectral imaging system (Vectra® Polaris™, Shanghai).

Assessment of RBCK1 Expression in Single-Cell RNA-Seq Datasets

Tumor Immune Single-Cell Hub (TISCH, http://tisch.comp-genomics.org/home/) was implemented to screen for scRNA-seq datasets with detailed cell-type annotation at the single-cell expression focusing on the tumor microenvironment in cancers. GSE111360 ($n = 2$, number of cells = 23,130), GSE139555 ($n = 3$, number of cells = 49,907), and GSE145281_PDL1 ($n = 4$, number of cells = 44,220) were included with correlation analyzed between RBCK1 expression and the abundance of immune cell infiltrations.

Human ccRCC Cell Culture and Cell Transfection

The human ccRCC cell line, 786-O, was obtained from the National Collection of Authenticated Cell Cultures of China (No. TCHu186). The 786-O cells were cultured in culture medium RPMI-1640 (C11875500BT, GIBCO by Life Technologies, USA), supplemented with 10% fetal bovine serum (Hyclone, Life Sciences, Shanghai, China). Cells were incubated in a humidified atmosphere incubator of 5% CO_2 at 37°C. 786-O cells have been transfected with double-stranded siRNA according to the protocol of the manufacturer using plasmid using Lipofectamine 3000 reagent (RiboBio) in a six-well

plate, as previously described (17). The transfection dose for each well was 15 μl of siRNA1 (sequences: GGTGCACCTT CATCAACAA), siRNA2 (sequences: GGATTACCAGCGA TTTCTA), or non-targeting siRNA (negative control) at a concentration of 10 nmol/L after incubated using RPMI-1640 for 20 min. 786-O cells were harvested for at least 24 h after transfection for further experimental analysis.

Total mRNA Extraction and Real-Time Quantitative PCR

Total RNA sequence was isolated using TRIzol reagent (Invitrogen, Carlsbad, CA) from transfected and control cells. SYBR® Premix Ex Taq™ (TaKaRa) was used to perform qRT-PCR reactions in triplicate according to the protocols of the manufacturer. The primers of RBCK1 were as follows: forward—5′-GCA GAT GAA CTG CAA GGA GTA TCA-3′ and reverse—5′-TGC AGC ATC ACC TTC AGC AT-3′. The relative RBCK1 expression quantity was measured after the $2^{-\Delta\Delta Ct}$ calculation using beta-actin as the internal standard.

Cell Counting Kit-8 Assay

For viability assays, the transfected 786-O cells were seeded into 96-well plates at a density of 2,000 cells/well. Next, a 10-μl Cell Counting Kit (CCK)-8 solution (KeyGen Biotech, Nanjing, China) was added to each well, and cells were incubated at 37°C for an additional 2 h. The absorbance of each well at 450 nm was measured at 0, 1, 2, 3, 4, and 5 days after inoculation using an automatic microplate reader (Tecan, Switzerland) at 490 nm wavelength optical density. Three replicate analyses were performed for each sample.

Flow Cytometry Assays for Cell Apoptosis

Apoptosis detection assay was performed using Annexin V-FITC Apoptosis Detection Kits (BD, USA) in accordance with the procedures of the manufacturer. Propidium iodide (PI) is a fluorescent dye that stains DNA and RNA and is used to analyze cell cycle by flow cytometry. Briefly, 786-O cells were seeded, triple washed with PBS, and then treated with 5 μl Annexin V-FITC and 5 μl PI solution in each collection tube. After incubation for 15 min, cell apoptosis was analyzed using a FACS analyzer (BD, USA).

Transwell Migration Assay

The transfected 786-O cells were seeded in a medium with 10% FBS and placed in each Transwell chamber at a density of 1×10^5 cells/well. The medium containing 20% fetal bovine serum was added in the lower 24-well plate chamber. After 24 h, the bottom 786-O cells were treated with 4% polyoxymethylene for 15 min and 0.1% crystal violet for 30 min. Then, 786-O cells migrating to the lower surface of the Transwell chamber were counted using a microscope in six random fields.

Statistical Analysis

SPSS 20.0, GraphPad Prism 8.0, and R software were used for all statistical analyses. The R packages used are listed in the corresponding subheading of the *Methods* section. All statistical analyses were two-sided, and a value of $p < 0.05$ was considered statistically significant.

RESULTS

IFN-γ Response Genes Are Differentially Expressed Between RCC and Normal Kidney Tissues

To assess the characteristics of IFN-γ response genes in RCC, we compared the mRNA expression in ccRCC (n = 530), pRCC (n = 323), chRCC (n = 91), and adjacent normal kidney tissues (n = 128). The differentially expressed mRNAs are shown in a bubble chart in **Figure 1A**. The size of the circle represents statistical significance—red and blue represent significantly high or low expression in tumor tissues, respectively. Notably, most IFN-γ response genes showed markedly differential expression patterns, although some IFN-γ response genes had similar expression patterns between the three kidney cancer subtypes. For example, the expression of RBCK1 was significantly higher in RCC tumors compared with normal samples (**Figure 1B**). Significantly decreased PNP and SELP expressions in RCC samples were observed when compared with normal samples (**Figures 1C, D**).

Association Between IFN-γ Response Genes and the Clinical Features of RCC

Next, we summarized the differences in IFN-γ response mRNA signatures between different clinical stages of ccRCC, pRCC, and chRCC (**Figure 1E**). The expressions of RIPK2, RBCK1, TRAFD1, SOD2, NMI, MT2A, CD86, and CD74 were significantly increased in the advanced stages of ccRCC, and the expressions of RIPK2, RBCK1, NOD1, and CDKN1A were significantly increased in the advanced stages of pRCC. In addition, the survival analysis emphasized the prognostic significance of TRAFD1, SOD2, RIPK2, RBCK1, and MT2A as cancer-promoting factors in ccRCC and pRCC (**Figure 1F**). The survival curves of IFN-γ response signatures with significant prognostic value for ccRCC (**Supplementary Figure 1**) and pRCC patients (**Supplementary Figure 2**) are displayed. Taken together, we identified 24 IFN-γ response signatures with significantly different expressions that had strong prognostic implications among 947 RCC samples.

DNA Variations in 24 IFN-γ Response Signatures in RCC

Next, we examined DNA variation in the IFN-γ response signatures of RCC. As shown in **Figure 2A**, we investigated the profiles of SNV of the 24 IFN-γ response signatures in ccRCC (n = 370), pRCC (n = 282), and chRCC (n = 66) patients. These findings indicate a high mutation frequency of *CIITA* and *LATS2* in ccRCC; *CIITA*, *IL10RA*, and *OAS3* in pRCC; and *CSF2RB* and *CDKN1A* in chRCC. Besides, although statistical significance was not observed for gene expression or survival in the chRCC dataset, mutations in the IFN-γ response signatures predicted

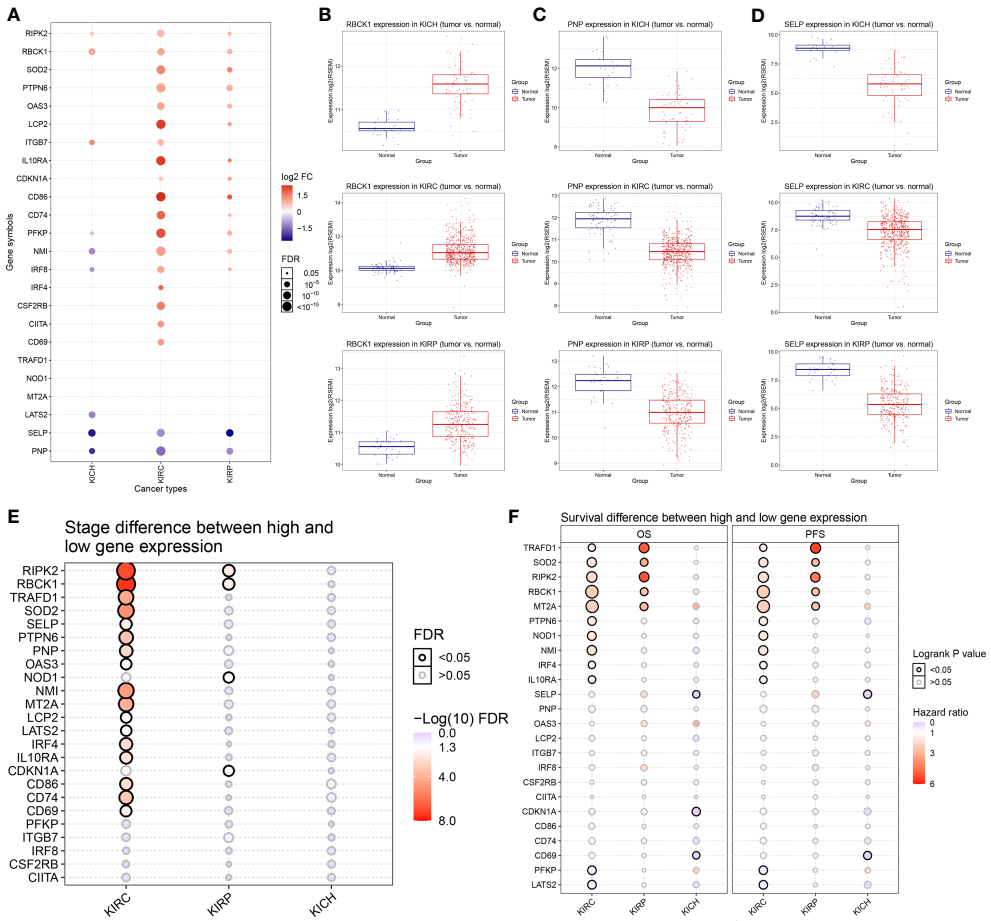

FIGURE 1 | Differentially expressed 24 IFN-γ response genes and its association with clinical features of renal cell carcinoma (RCC). **(A)** We compared the mRNA expression in clear cell RCC (ccRCC) (*n* = 530), papillary RCC (pRCC) (*n* = 323), chromophobia RCC (chRCC) (*n* = 91), and adjacent normal kidney tissues displayed using a bubble chart. The size of the circle represents statistical significance; red represents significantly high expression in tumor tissue and blue represents low. **(B–D)** Expressions of RBCK1, PNP, and SELP in RCC samples were observed in comparison with normal samples using unpaired *t*-test. **(E)** We summarized the difference of IFN-γ response signatures of mRNA expression between clinical stages in ccRCC, pRCC, and chRCC using Wilcoxon non-parametric test. **(F)** The univariate Cox survival analysis emphasized the prognostic significance of TRAFD1, SOD2, RIPK2, RBCK1, and MT2A as cancer-promoting factors of ccRCC and pRCC.

relatively poor survival for patients with chRCC (**Figure 2B**). Next, we examined the SNV of the top 10 mutated genes among IFN-γ response signatures. The most frequently mutated genes were *CIITA*, *CSF2RB*, and *OAS3* in 78 RCC samples with DNA variation (**Figure 2C**). The variant classifications, variant type, and SNV classes of IFN-γ response signatures are summarized in **Figure 2D**.

Relationship Between the CNV of the 24 IFN-γ Response Signatures and the Clinical Outcomes of RCC

After determining the DNA mutation map, we determined whether the CNV was characteristic of IFN-γ response signatures in kidney cancer. **Figure 2E** shows the CNV characteristics of IFN-γ response signatures in patients with ccRCC, pRCC, and chRCC. The CNV of SOD2, CDKN1A, and IRF4 was mainly reflected in Hete.Del, and the CNV of CD74 and LCP2RBCK1 was mainly reflected in Hete.Amp. Next, we explored the heterozygous amplification and deletion of IFN-γ response characteristics (**Figure 2F**). There was a high percentage of heterozygous CNV of IFN-γ response signatures in ccRCC, pRCC, and chRCC patients. Next, we explored the prognosis implications between CNV groups and a wild type (WT) group using the Kaplan–Meier method (**Figure 2G**). The results showed that CNV changes in many interferon-related genes showed inconsistent survival interventions for RCC patients compared with the WT group ($p < 0.05$, $\log|FC| > 1$). Next, we showed that interferon genes had a high frequency of CNV among the three kidney cancer subtypes and significantly interfered with the overall survival prognosis. For example, the CNV of IL10RA and SOD2 indicated a significantly worse overall survival (OS) for pRCC patients compared with the WT group. For chRCC patients, the CNV of CSF2RB indicated a significantly worse OS, and patients with a deletion of MT2A

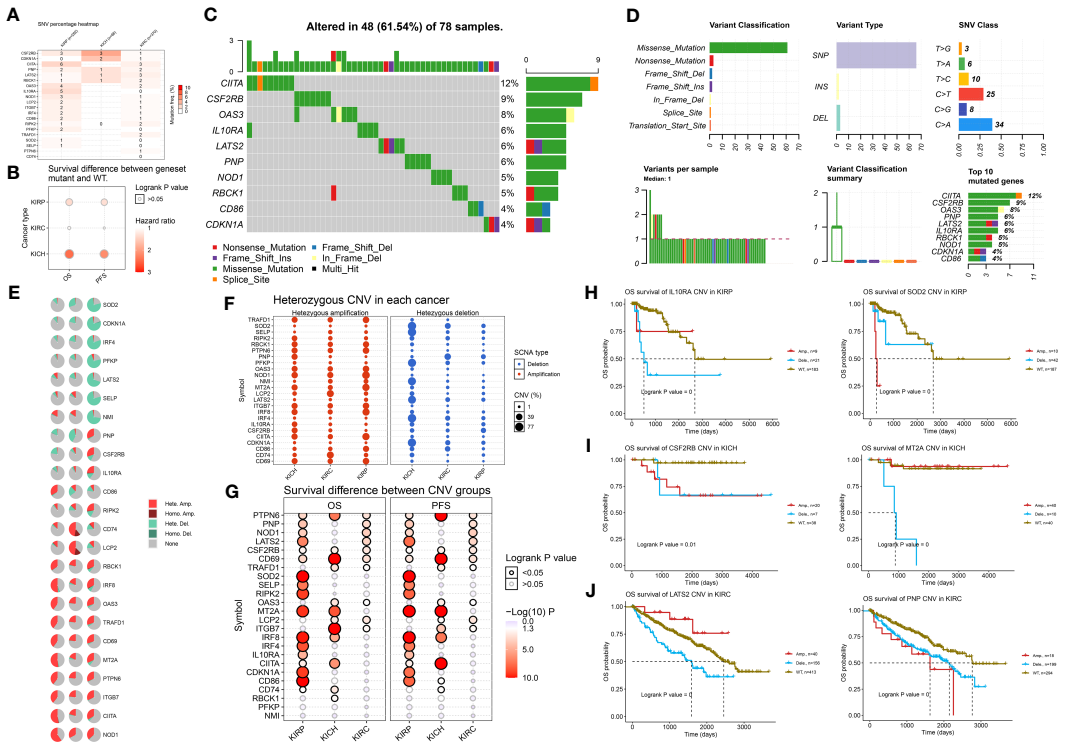

FIGURE 2 | DNA variation landscape of 24 IFN-γ response signatures of RCC. **(A)** Profiles of SNV of the 24 IFN-γ response signatures in ccRCC (n = 370), pRCC (n = 282), and chRCC (n = 66) patients were provided. **(B)** Mutation of IFN-γ response signatures was used to predict poor survival for patients with RCC. **(C)** Mutation information of IFN-γ response signatures in 78 RCC samples with DNA variation was shown in the waterfall plot, where different colors with specific annotations at the bottom meant various mutation types. **(D)** The variant classifications, variant type, and SNV classes of IFN-γ response signatures were summarized. A stacked bar plot shows the top 10 mutated genes. **(E)** Pie plot summarizes the CNV of IFN-γ response signatures in patients with ccRCC, pRCC, and chRCC. **(F)** Using bubbles to represent the percentage of heterozygous CNV, including heterozygous amplification and deletion of IFN-γ response signatures in ccRCC, pRCC, and chRCC. The bubble size is positively correlated with percentage; the bubble color blue represents deletion, and red represents amplification. **(G)** The hazard ratio and log-rank p-value through bubble color and size. The column is the gene set symbol and the row is the ccRCC, pRCC, and chRCC. The bubble color from blue to red represents the significance of log-rank p-value from low to high, and bubble size is positively correlated with the significance of log-rank p-value. **(H–J)** Kaplan–Meier curves between amplification, deletion, and wide type of the 24 IFN-γ response signatures in ccRCC, pRCC, and chRCC.

had poor outcomes compared with the WT and amplification groups. Interestingly, LATS2 had a higher CNV percentage in ccRCC SCNA deletions, whereas its amplification and deletion had significantly opposite prognostic implications compared with the WT group; the CNV of PNP indicated a significantly worse OS for ccRCC patients compared with the WT group (**Figures 2H–J**). Overall, we found a strong relationship between the CNV profiles of the 24 IFN-γ response signatures and the clinical outcomes of ccRCC, pRCC, and chRCC patients.

IPMs Significantly Predict Prognosis and Immune Cell Infiltration of ccRCC

Next, we used the LASSO regression model to derive risk characteristics of the IFN-γ response signatures for progression-free survival (PFS) and OS in ccRCC and all RCC patients (**Figures 3A, B**). Based on the median risk score, patients were divided into low- and high-risk groups. We found that the risk score increased with increased mortality events (**Figure 3C**). Next, the risk score of the 24 IPMs to predict the PFS of ccRCC patients from the TCGA was calculated (**Figure 3D**). We found that an elevated risk score of IPMs was significantly correlated with a worse prognosis for ccRCC patients (HR = 5.442, $p < 0.001$). We also conducted ROC analysis on IPMs and found AUC values with strong specificity and sensitivity (1-year = 0.737, 3-year = 0.772, 5-year = 0.813), which indicated that it is an effective and accurate marker for predicting the PFS of ccRCC patients (**Figure 3E**). In addition, we analyzed the relationship between IPMs and the amount of immune cell infiltration. The analysis demonstrated that the risk score of IPMs was significantly correlated with the upregulation of M1 macrophages and the downregulation of $CD4^+$ T cells, neutrophils, and NK cells (Spearman's correlation analysis, $p < 0.001$) (**Figure 3F**).

We also used the LASSO regression model to derive the risk characteristics of IFN-γ response genes to predict the OS of ccRCC patients (**Figures 4A, B**). Based on the median risk score of the IPMs, patients were divided into low- and high-risk groups (**Figure 4C**). **Figure 4D** shows that a higher risk score of IPMs predicted a significantly worse prognosis for ccRCC patients (HR = 3.958, $p < 0.001$). ROC analysis revealed high AUC values

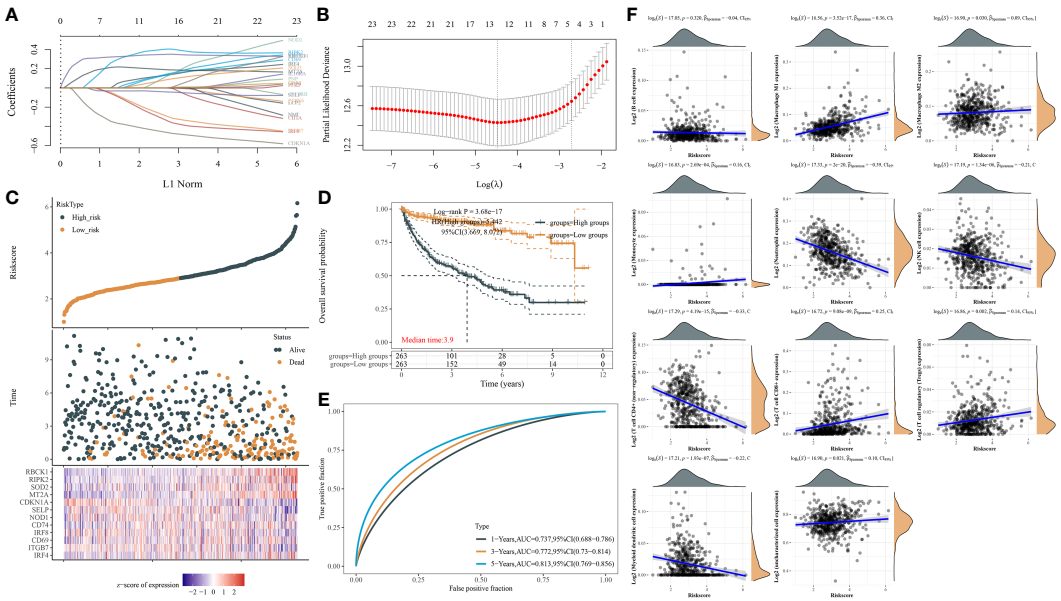

FIGURE 3 | IFN-γ response signature prediction models (IPMs) predicting progression-free survival (PFS) and immune cell infiltration of ccRCC. **(A)** Coefficients of the 24 IFN-γ response signatures are displayed by the lambda parameter. **(B)** Partial likelihood deviance *versus* log (*λ*) was drawn using LASSO Cox regression model. **(C)** The dotted line represented the median risk score and divided the patients into low-risk and high-risk groups. **(D)** Risk score of the 24 IPMs for predicting PFS of ccRCC patients from TCGA was displayed using Kaplan–Meier curves. *p*-values and hazard ratio (HR) with 95% confidence interval (CI) were generated by log-rank tests and univariate Cox proportional hazards regression. **(E)** Time-dependent ROC analysis of the IPMs was generated in predicting 1-, 3-, and 5-year progression status. **(F)** Spearman correlation analysis of IPMs and immune cell infiltration. The horizontal axis in the figure represents the expression distribution of risk score of IPMs, and the ordinate is the expression abundance of immune cell infiltration.

(1-year = 0.761, 3-year = 0.751, 5-year = 0.748) of the IPMs (**Figure 4E**). These findings indicate that IPM can be used as an independent prognostic predictor of ccRCC.

IPMs Significantly Predict the PFS and OS of All RCC Patients

In addition, we used the LASSO regression model to derive the risk characteristics of IFN-γ response signatures for PFS and OS in all RCC patients (**Supplementary Figures 3A, B**). We found that the higher the risk score, the worse the prognosis of the RCC patient (HR = 4.31, $p < 0.001$), which suggests the prognostic independence of the IPMs to predict the PFS of RCC patients (1-year AUC = 0.821, 3-year AUC = 0.757, 5-year AUC = 0.758) (**Supplementary Figures 3C–E**). We then analyzed the relationship between IPMs and immune cell infiltration of RCC and found that the risk score of IPMs had a significant positive correlation with M1 macrophages and a negative correlation with $CD4^+$ T-cell infiltration ($p < 0.001$, $|r^2| > 0.30$) (**Supplementary Figure 3F**).

Then, we investigated the prognostic effect of IPMs to predict the OS for RCC patients (**Supplementary Figure 4**). We found that the higher the risk score, the worse the prognosis of the RCC patient (HR = 5.23, $p < 0.001$) with high AUC values (1-year = 0.790, 3-year = 0.769, 5-year = 0.788), which indicated that it is an effective and accurate model to predict the prognosis of ccRCC and all RCC patients.

Identification of Differentially Expressed Genes of IPMs and Functional Annotations

We screened differentially expressed genes (DEGs) related to IPMs and performed functional annotations to identify the potential role of IPMs in ccRCC patients. First, we screened related genes according to the high- and low-risk scores of IPMs (**Figure 5A**). Then, we determined the DEGs of IPMs in ccRCC *via* hierarchical cluster analysis and analyzed their differences between tumor and normal tissues (**Figure 5B**). Finally, we conducted a selective enrichment of the Kyoto Encyclopedia of Genes and Genomes (KEGG) signaling pathway and Gene Ontology (GO) functional enrichment analysis (including biological processes, cell components, and molecular functions) of the selected DEGs of IPMs to demonstrate their main biological effects (**Figures 5C, D**). In the enrichment of GO functions, DEGs were mainly related to viral protein interactions with cytokines and cytokine receptors, type I diabetes mellitus, and viral myocarditis. In the KEGG signaling pathway, DEGs were mainly related to responses to molecules of bacterial origin, the regulation of leukocyte proliferation, and the regulation of leukocyte migration.

Construction of a Nomogram to Predict the Prognosis for ccRCC Patients

To optimize the predictive models and enhance clinical translation efficiency based on the prognostic implications of

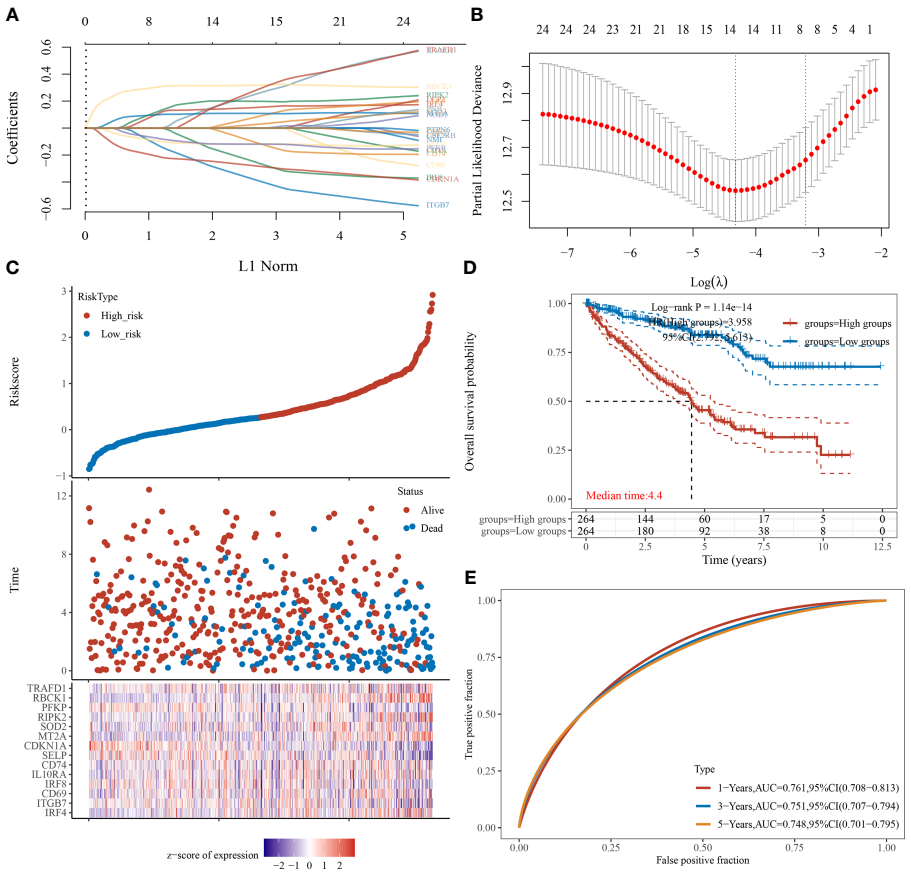

FIGURE 4 | IPMs predicting the OS of ccRCC. **(A)** Coefficients of the 24 IFN-γ response signatures are displayed by the lambda parameter. **(B)** Partial likelihood deviance *versus* log (*λ*) was drawn using LASSO Cox regression model. **(C)** The dotted line represented the median risk score and divided the patients into low-risk and high-risk groups. **(D)** Risk score of the 24 IPMs for predicting OS of ccRCC patients from TCGA was displayed using Kaplan–Meier curves. *p*-values and hazard ratio (HR) with 95% confidence interval (CI) were generated by log-rank tests and univariate Cox proportional hazards regression. **(E)** Time-dependent ROC analysis of the IPMs was generated predicting 1-, 3-, and 5-year survival status.

the 24 IFN-γ response signatures, we selected the five IFN-γ related genes (*MT2A*, *RBCK1*, *PNP*, *LATS2*, *PFKP*) with the most prognostic significance for ccRCC for use in a nomogram. Using univariate and multivariate Cox regression analyses, we found that RBCK1 was the most clinically significant factor to predict outcomes for ccRCC patients ($p < 0.01$) (**Figures 6A, B**). The constructed nomogram indicated the significant prognostic roles of RBCK1 and PFKP (C-index = 0.761) (**Figure 6C**). Then, we aimed to establish a nomogram to predict the PFS of ccRCC patients using univariate and multivariate Cox regression, and found that RBCK1 was the most clinically significant ($p = 0.027$) (**Supplementary Figures 5A, B**). The nomogram also indicated the significant prognostic role of RBCK1 (C-index = 0.761) for ccRCC patients (**Supplementary Figure 5C**).

Protein–Protein Interaction Networks and the Single-Cell Localization of RBCK1

After screening the most significant gene, *RBCK1*, we constructed a protein–protein interaction (PPI) network and performed single-cell localization analysis. We used GeneMANIA to construct a PPI network with the 24 IFN-γ response characteristics (**Figure 7A**). As shown in **Figure 7B**, RBCK1 was highly expressed in different cells in the tumor immune microenvironment (TIME), including $CD4^+$ and $CD8^+$ T cells, monocytes, macrophages, and NK cells. Using three scRNA-seq datasets, we detailed cell-type annotations at the single-cell level and focused on the tumor microenvironment of ccRCC to analyze the correlation between RBCK1 expression and immune abundance (**Figures 7C–E**). Overall, RBCK1 was widely expressed in a variety of cell types in the TIME of ccRCC and may mediate malignant clinical phenotypes by regulating the microenvironment.

Pan-Cancer Analysis of RBCK1 mRNA Differential Expression and Correlation Analysis of TIME

By single-cell analysis, we analyzed the expression of RBCK1 in pan-cancer tissues (**Figure 8A**). We analyzed the expression

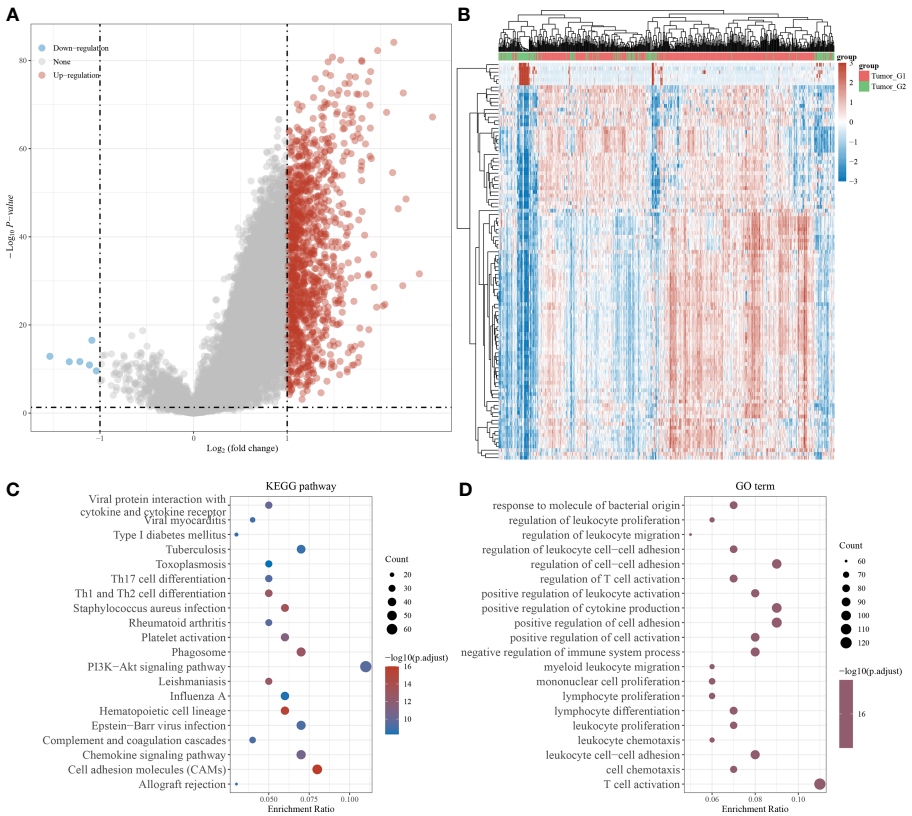

FIGURE 5 | Identification of differentially expressed genes (DEGs) of IPMs and functional annotations. **(A)** Volcano plots were constructed using fold-change values and adjusted *p* based on the high and low risk score of IPMs for predicting PFS of ccRCC patients from TCGA. The red point in the plot represents the overexpressed mRNAs and the blue point indicates the downexpressed mRNAs with statistical significance. **(B)** Hierarchical clustering analysis to identify DEGs of IPMs in ccRCC, which were differentially expressed between tumor and normal tissues. **(C, D)** The enriched KEGG signaling pathways and GO functional enrichment (including biological process, cellular component, and molecular function) analysis were selected to demonstrate the primary biological actions of major DEGs of IPMs based on ClusterProfiler package in R software.

distribution of RBCK1 in tumor and normal samples from the TCGA database and GTEx Portal and found the significantly different expression of RBCK1 in pan-cancers, such as bladder cancer, breast cancer, glioma, lung cancer, and liver cancer. Next, we analyzed the enrichment score of all TIME elements and RBCK1 in pan-cancers and found that the expression of RBCK1 was significantly correlated with increased numbers of immune cells, including B cells, Th2 cells, M1 macrophages, and the decreased numbers of $CD4^+$ T cells and Treg cells (**Figure 8B**). Moreover, we investigated the relationship between RBCK1 expression and immune checkpoint genes, including *SIGLEC15*, *IDO1*, *CD274*, *HAVCR2*, *PDCD1*, *CTLA4*, *LAG3*, and *PDCD1LG2* in pan-cancers. Interestingly, RBCK1 showed significant differential expression between cancer and normal tissues and was significantly related to tumor-infiltrating immune cells, including tumor purity and immune checkpoint molecules such as PD-L1, CTLA-4, LAG-3, and TIGIT in ccRCC (**Figure 8C**). Although RBCK1 expression was positively correlated with most cancer types, its expression had a significant negative association with immune checkpoints in thymoma samples.

Immunotherapy Efficacy, TIME Characterization, and Prognostic Implications of RBCK1 in ccRCC Patients From the FUSCC Proteomics Cohort

The TIDE algorithm was used to evaluate two different tumor immune escape mechanisms, and was used to compare $RBCK1^{high}$ and $RBCK1^{low}$ expressing groups in the ccRCC or RCC cohorts (**Figures 9A, B**). The TIDE score was significantly higher in the $RBCK1^{high}$ group compared with the $RBCK1^{low}$ group in ccRCC and RCC patients, which suggests that $RBCK1^{high}$ patients are intolerant to ICT treatment. Kruskal–Wallis analysis showed that immune checkpoints were significantly associated with the expression level of RBCK1 in ccRCC (**Figure 9B**). Besides, as shown in the revised **Supplementary Figure 6**, we enrolled a total of 136 patients with ccRCC from the RECA-EU cohort in the International Cancer Genome Consortium (ICGC) database. Consistent with TCGA database results, it suggested that TIDE score in ccRCC samples with elevated RBCK1 expression is significantly higher in samples with low RBCK1 expression (p = 2.5e-08). Immunohistochemistry staining showed significantly elevated RBCK1 expression in tumors (n = 50) compared with normal kidney samples (n = 40) from the

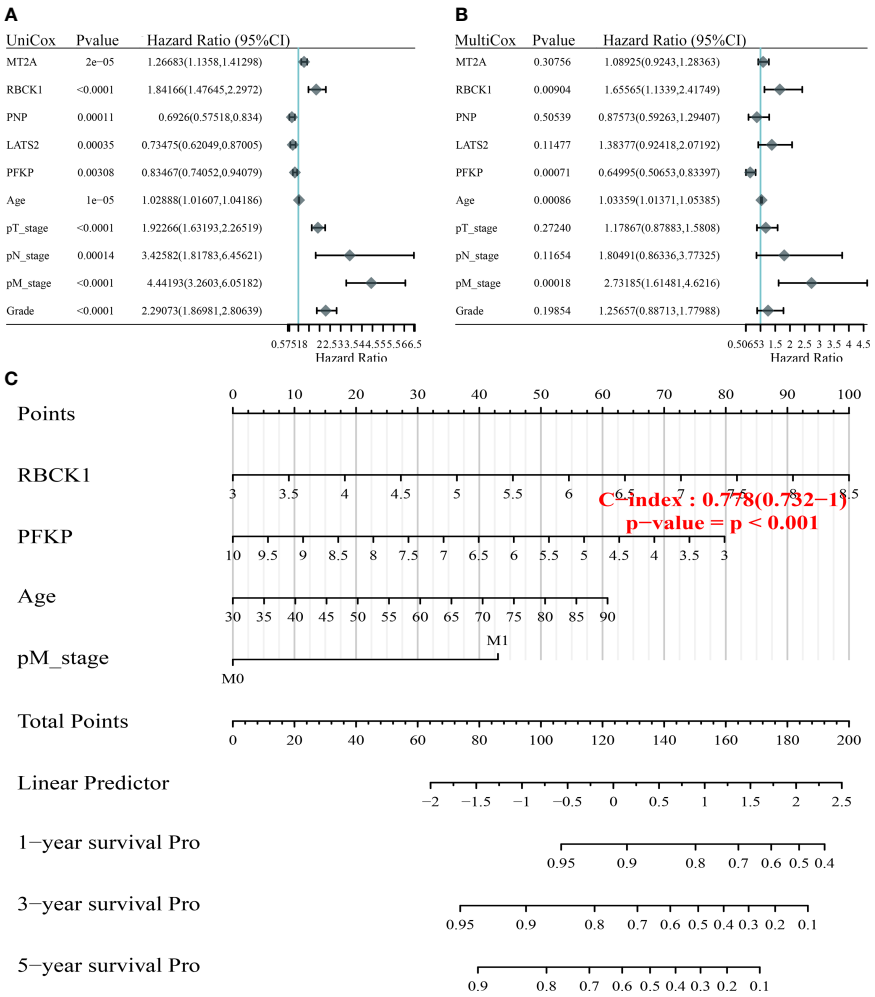

FIGURE 6 | Construction of the nomogram predicting the prognosis of ccRCC. **(A, B)** Hazard ratio and *p*-value of constituents involved in univariate and multivariate Cox regression enrolling clinicopathological features and five IFN-γ response signatures with the most prognostic significance. **(C)** The nomogram provided a graphical representation of the clinicopathological features and IFN-γ response signatures, which can be used to calculate the risk of recurrence for an individual patient by the points associated with each risk factor through the "rms" R package.

FUSCC real-world cohort ($p < 0.001$; **Figures 9C, D**). After RBCK1 expression of ccRCC was confirmed, we found a significantly decreased number of infiltrated $CD4^+$ T cells, $CD4^+FOXP3^+$ Treg cells, $CD68^+CD163^-$ M1 macrophages, and $CD56^{bight/dim}$ NK cells in the immune-cold $RBCK1^{high}$ group using opal multi-marker immunohistochemistry staining (**Figures 9E, F**). In addition to the heterogeneously distinct immune microenvironment, $RBCK1^{high}$ predicted a significantly worse prognosis than $RBCK1^{low}$ for 232 ccRCC patients in the FUSCC cohort based on proteomics sequencing data (PFS: HR = 2.541, $p < 0.001$; OS: HR = 3.296, $p < 0.001$; **Figures 9G, H**).

Inhibition of RBCK1 Attenuates Cell Proliferation and Migration and Promotes Cell Apoptosis Abilities of 786-O Cells

To further investigate the biological function of the RBCK1 in ccRCC, we used siRNA to knock down the expression of RBCK1 in the human ccRCC cell line, 786-O. The relative expression of RBCK1 was significantly inhibited in the siRNA groups compared with the negative control group ($p < 0.01$; **Figure 10A**). Furthermore, after we transfected with siRNA in human ccRCC cells, the CCK-8 and Transwell assays revealed extraordinarily markedly decreased cell proliferation and migration capacities in the siRNA groups compared with the negative control group ($p < 0.001$; **Figures 10B, C**). In addition, we assessed early and late apoptotic cell proportions using the FITC/PI kit. Cell populations with FITC−/PI−, FITC+/PI−, FITC+/PI+, and FITC−/PI+ were regarded as living, early apoptotic, late apoptotic, and necrotic cells, respectively. The results suggested significantly increased apoptotic cell percentage of the siRNA groups compared with the control group ($p < 0.001$; **Figure 10D**). Interestingly, we then analyzed the downstream signaling pathway RBCK1 was possibly involved in and found that RBCK1 inactivation significantly promotes receptor tyrosine

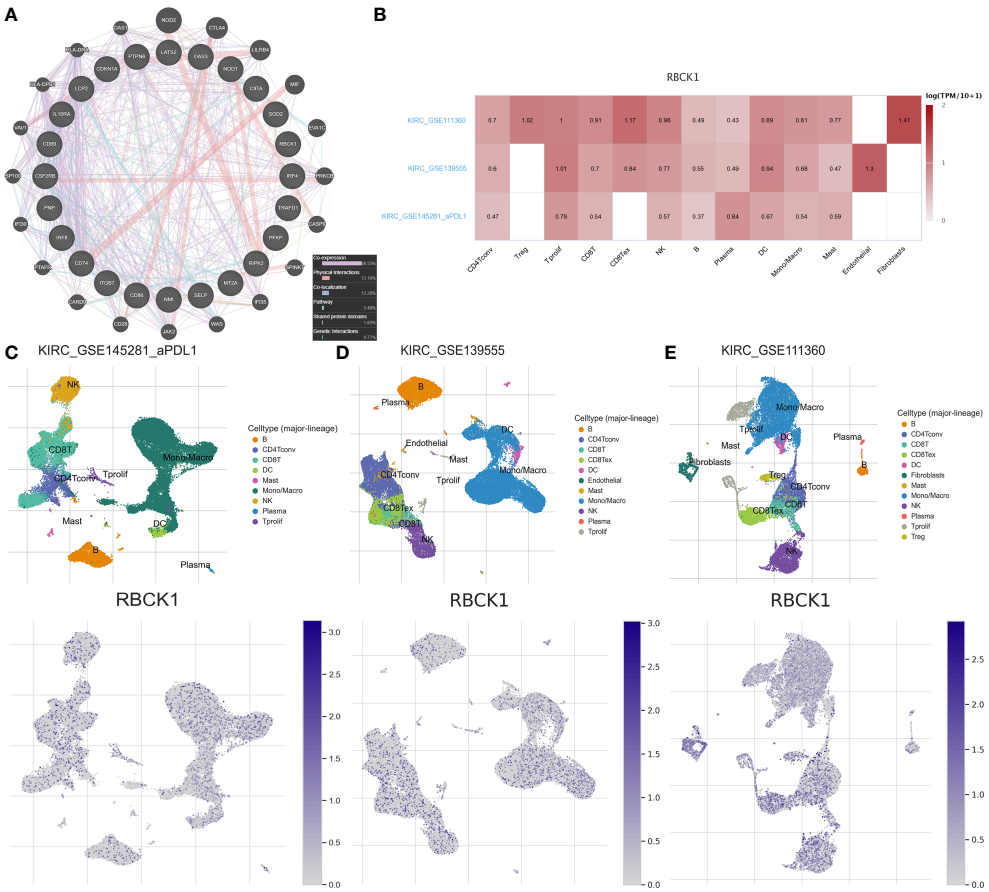

FIGURE 7 | Protein networks and single-cell localization of RBCK1. **(A)** Protein–protein interaction (PPI) network of the 24 IFN-γ response signatures was constructed using GeneMANIA. **(B)** Three scRNA-seq datasets with detailed cell-type annotation at the single-cell level focusing on the tumor microenvironment for ccRCC. GSE111360 (*n* = 2, number of cells = 23,130), GSE139555 (*n* = 3, number of cells = 49,907), and GSE145281_PDL1 (*n* = 4, number of cells = 44,220) were enrolled with correlation analyzed between *RBCK1* expression and abundance of immune cell infiltrations. The higher the expression of *RBCK1* in a single-cell subpopulation, the darker the red color is in the heatmap. **(C–E)** The heatmap showed the relatively high expression of *RBCK1* in different cell types, such as CD^{4+}, CD^{8+} T cells, monocytes, macrophages, and NK cells across the three scRNA-seq datasets.

kinases (RTK) pathway in RCC samples from TCGA ($p < 0.001$; **Figure 10E**).

DISCUSSION

The incidence of RCC is increasing and it has become the most common kidney cancer. Over the past decade, various therapeutic options have been developed including cytoreductive nephrectomy, targeted therapies, and immune checkpoint inhibitors for advanced RCC patients (18). RCC has heterogeneous genomic and clinical features, and a better understanding of the molecular biology of tumors might help in the diagnosis and choice of treatment approaches. Therefore, many biomarkers associated with treatment outcomes and disease-specific outcomes have been identified. In addition, predictive signatures have been developed based on the multi-omics analysis of renal cell carcinoma. The most well-known hallmark of RCC, especially ccRCC, is VHL inactivation (19, 20). However, VHL inactivation alone is insufficient for the induction of RCC tumorigenesis. PBRM1, BAP1, SETD2, and PTEN mutations also commonly occur in RCC (21, 22). A risk model that included PBRM1, BAP1, and TP53 mutation status was correlated with the OS and PFS of RCC patients. PBRM1 mutations occur in almost 30%–40% of ccRCC tumors (23), and patients with PBRM1 loss have a poor predicted clinical outcome (22). The recent development of ICI treatment has shifted immunotherapy into the first-line setting and the combination of target therapies and ICIs is on the horizon, and a suitable predictive signature can direct the choice of combination therapies (24). In chRCC, tumor mutation burden (TMB) is associated with tumor metastasis and tumor grade. The immune-related genes *BIRC5*, *INHBE*, and *IL20RB* were upregulated in a TMB^{high} group and were associated with a poor prognosis (25), and a combination of PD-1 and CTLA-4 blockers was suggested for the treatment of advanced renal cell carcinoma with aberrations (26).

Cancer cells are the key responders of IFN-γ in the tumor microenvironment, and IFN-γ drives immune-activated and immune-suppressive effects (27). The immune activation of

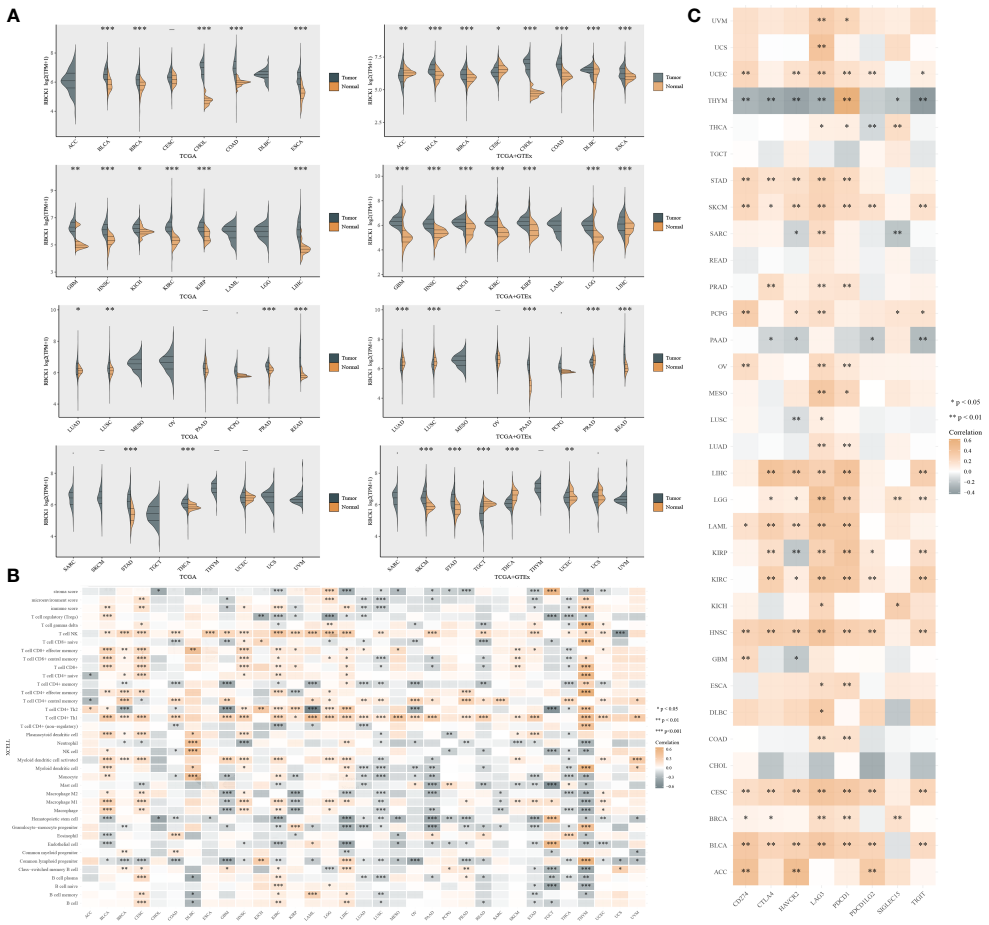

FIGURE 8 | Pan-cancer analysis of RBCK1 mRNA differential expression and correlation analysis of the tumor immune microenvironment. **(A)** The expression distribution of RBCK1 in tumor and normal samples from the TCGA database and GTEx Portal, where the horizontal axis represents different tumor tissues, and the vertical axis represents the gene expression distribution using the Wilcoxon test (*$p < 0.05$, **$p < 0.01$, ***$p < 0.001$). **(B)** Spearman correlation analysis heatmap of immune score and RBCK1 expression in over 13,000 pan-cancer tissues, where the horizontal axis represents different tumor tissues, and the vertical axis represents different immune scores. The stronger the correlation, the darker the color. **(C)** The heatmap represents the correlation between RBCK1 expression and immune checkpoints (SIGLEC15, IDO1, CD274, HAVCR2, PDCD1, CTLA4, LAG3, and PDCD1LG2) in pan-cancer tissues, where the horizontal axis represents different immune checkpoint genes, and the vertical axis represents different tumor tissues (*$p < 0.05$, **$p < 0.01$, ***$p < 0.001$).

IFN-γ on tumor cells is largely attributed to tumor cells, monocytes, endothelial cells, and fibroblasts inducing tumor cells to express MHC class I and secrete CXCL9, CXCL10, and CXCL11 to promote lymphocyte migration and inhibition of angiogenesis (28–30). Therefore, it is worth exploring which cells expressing IFN-γ in the tumor microenvironment mediate the resistance of immunotherapy and the mechanism of IFN-γ-mediated "immune-cold" tumor turning to "immune-hot," in order to design better treatment methods to balance antitumor and immune escape capacities of RCC (31, 32). In the present study, we examined the expression, prognostic implications, and copy number variation profiles of 24 IFN-γ response genes that were significantly correlated with OS and PFS for papillary, chromophobia, and clear cell RCC (n = 947). We derived a risk signature for use in a LASSO Cox regression model comprised of the IFN-γ response genes for prognosis. We found a marked upregulation of M1 macrophages and downregulation of $CD4^+$ T cells, neutrophils, and NK cells in the high-risk group, which were associated with worse OS and PFS. This suggests that the IFN-γ response gene risk signature can predict tumor-infiltrating immune cells and direct the choice of clinical immunotherapies.

RBCK1 is essential for NF-κB stimulation and mutations in RBCK1 were associated with immunodeficiency (33–35). In the present study, the prognostic nomograms were constructed to predict the OS and PFS for 530 ccRCC patients, highlighting the significant prognostic implications of RBCK1 among the 24 IFN-γ response genes. RBCK1 was co-localized with tumor-infiltrating immune cells according to the three single-cell RNA datasets. This suggested that RBCK1 expression is correlated with tumor-infiltrating immune cells. The large-scale pan-cancer analysis also showed that RBCK1 had a strong prognostic value related to the significant differential expression of mRNAs between cancer and normal tissues and

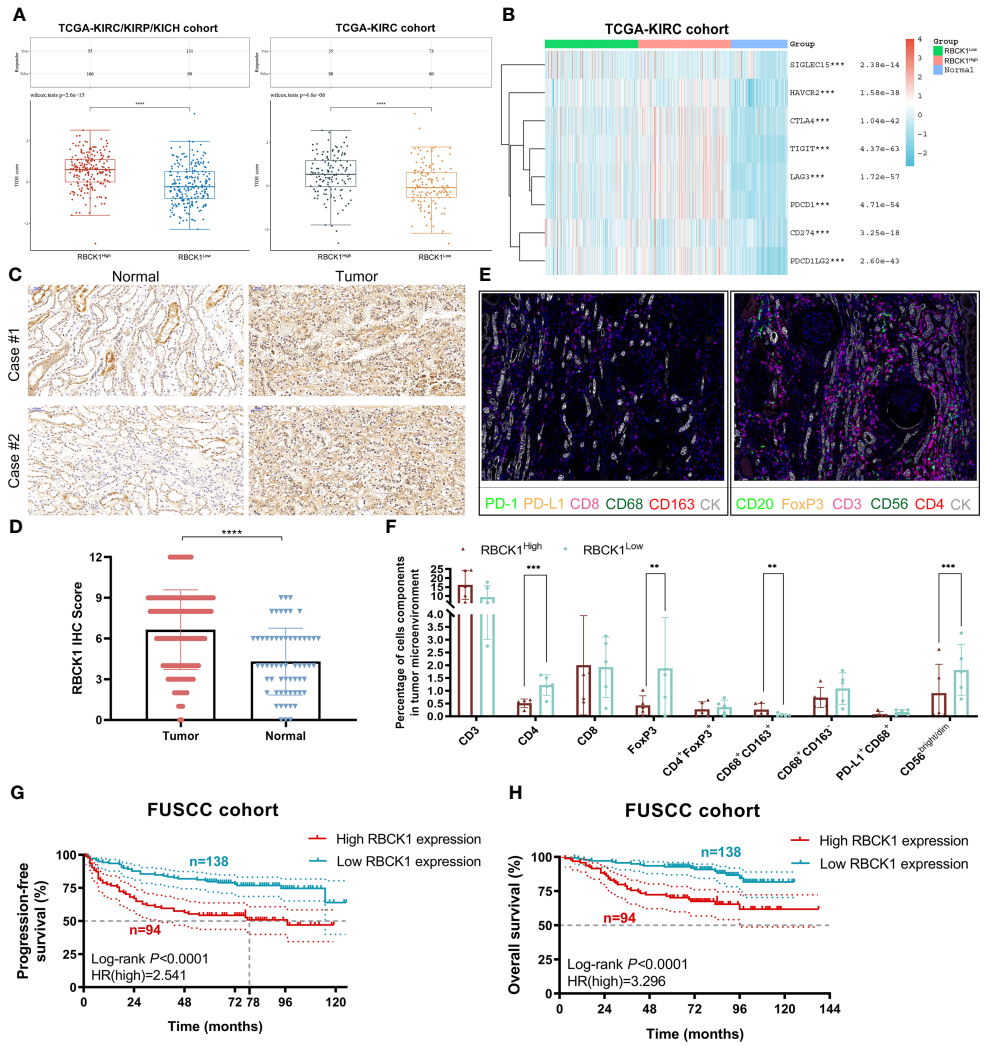

FIGURE 9 | Immunotherapy efficacy, TIME characterization, and prognostic implications of RBCK1 in ccRCC patients from the Fudan University Shanghai Cancer Center (FUSCC) proteomics cohort. **(A)** The TIDE algorithm is used to evaluate two different tumor immune escape mechanisms and was developed in RBCK1^{high} compared with low RBCK1 expression group in both ccRCC and RCC cohorts using Student's *t*-test. **(B)** The expression heatmap of immune checkpoint-related genes and RBCK1 in ccRCC and normal tissues was tested by Kruskal–Wallis, and the different colors represent the expression trend in different samples. **(C, D)** Immunohistochemistry staining showed RBCK1 expression in tumor (n = 50) and normal kidney samples (n = 40) from a real-world cohort, FUSCC, Shanghai. **(E, F)** Opal multi-marker immunohistochemistry was used on 10 ccRCC specimens to achieve six biomarker staining. The significance of the two groups of samples passed the Wilcoxon test. **(G, H)** Prognostic value of RBCK1 in predicting prognosis was assessed for 232 ccRCC patients from the FUSCC cohort based on proteomics sequencing data using the Kaplan–Meier method (**p < 0.01, ***p < 0.001, ****p < 0.0001).

was correlated with tumor-infiltrating immune cells, tumor purity, and immune microenvironment scores. The RBCK1^{high} group had a significantly higher TIDE score compared with the RBCK1^{low} group in the ccRCC or RCC cohorts, which suggests a better response to the ICTs in RCC patients with RBCK1^{high} expression. In addition, studies in a real-world cohort (232 ccRCC patients from the FUSCC cohort based on proteomics sequencing data) showed that the immune-cold RBCK1^{high} group had a worse predicted prognosis than the RBCK1^{low} group. Inhibition of RBCK1 attenuates cell proliferation and migration and promotes cell apoptotic abilities of the 786-O cell. It is a limitation of the present study that only one cell line was used. After transfected with siRNA in human ccRCC cells, extraordinarily decreased cell proliferation, migration capacities, and prominently elevated apoptosis tumor cell proportion were found in the siRNA groups compared with the negative control group. In view of the findings of this study, future research directions can focus on the problem of RBCK1-regulated tumor microenvironment disorder mediating RCC malignant biological behavior. Furthermore, regarding the observed heterogeneity between the effect estimates in the two studies (TCGA and FUSCC), it is worth noting that these are retrospective studies, and the diagnostic criteria, ascertainment, and age distribution differ between them. On the other hand, we

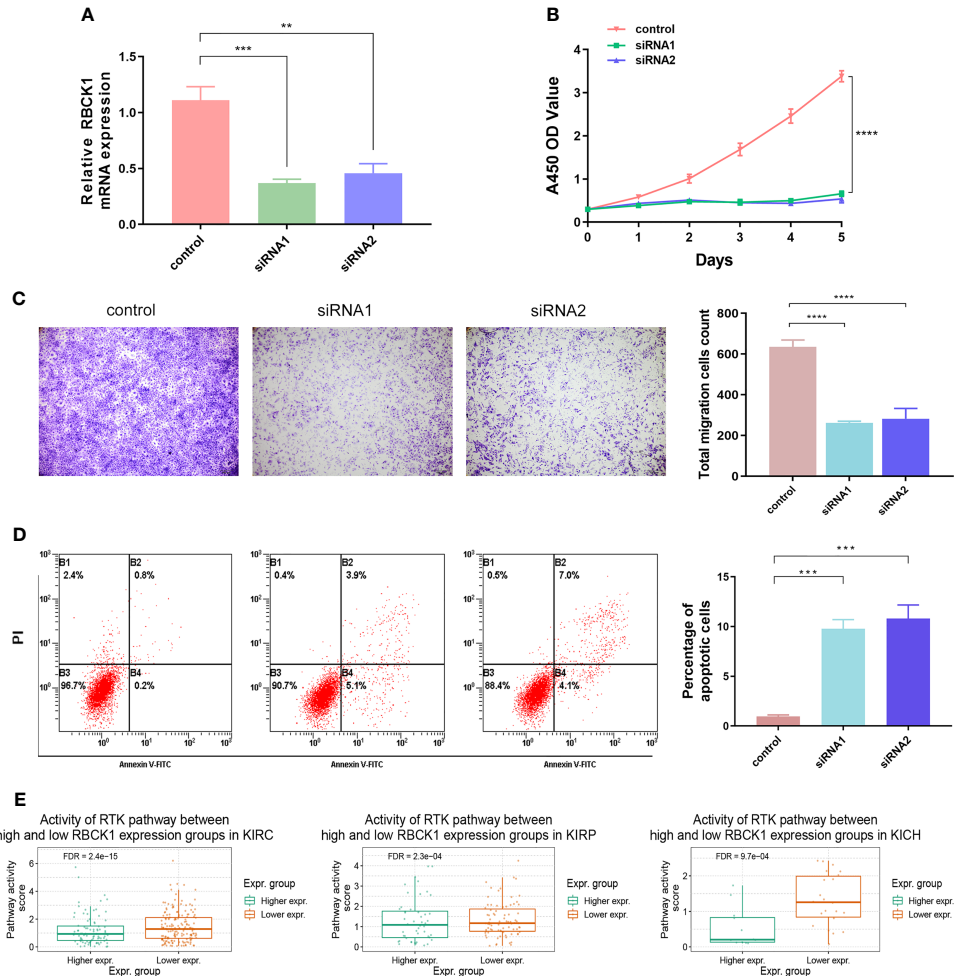

FIGURE 10 | Inhibition of RBCK1 attenuates cell proliferation and migration and promotes cell apoptosis abilities of 786-O cell. **(A)** SiRNA was used to knock down the expression of RBCK1 in the human ccRCC cell line, 786-O. **(B, C)** The CCK-8 and Transwell assays were detected after the siRNAs were transfected in human ccRCC cells. **(D)** Early and late apoptotic cell proportions using the FITC/PI kit. Cell populations with FITC−/PI−, FITC+/PI−, FITC+/PI+, and FITC−/PI+ were regarded as living, early apoptotic, late apoptotic, and necrotic cells, respectively. **(E)** Differential RBCK1 inactivation level in the score of receptor tyrosine kinase (RTK) pathway in RCC samples from TCGA (**$p < 0.01$, ***$p < 0.001$, ****$p < 0.0001$).

added the clinicopathological features of ccRCC patients and clarified that based on the retrospective study, IFN-γ response clusters and RBCK1 cannot yet be used as decision aids to spare patients from immunotherapy and/or clinical treatment management. These limitations will largely be addressed in a planned prospective multicenter research to confirm the benefits indicated from this study.

CONCLUSION

In conclusion, this study investigated IFN-γ response clusters to derive a risk signature for papillary, chromophobia, and clear cell RCC patients, which can be used for determining a clinical diagnosis. These IFN-γ response signatures improved the prognostic accuracy of immune contexture in the ccRCC microenvironment. We performed a comprehensive analysis based on multi-omics large-scale data and found that immune-cold RBCK1^{high} patients had pro-tumorigenic immune infiltration and a significantly worse outcome compared with RBCK1^{low} patients. Our discovery of these novel independent prognostic indicators in RCC highlights the relationship between tumor phenotype and immune contexture.

DATA AVAILABILITY STATEMENT

The datasets presented in this study can be found in online repositories. The names of the repository/repositories and

accession number(s) can be found below: https://www.ncbi.nlm.nih.gov/bioproject/PRJNA557348 and PRJNA557348.

ETHICS STATEMENT

The studies involving human participants were reviewed and approved by the Ethics Committee of Fudan University Shanghai Cancer Center. The patients/participants provided their written informed consent to participate in this study. Written informed consent was obtained from the individual(s) for the publication of any potentially identifiable images or data included in this article.

AUTHOR CONTRIBUTIONS

Conceptualization: WX, WZ, JT, XT, CL, WL, and JS. Formal analysis: WX, WZ, WL, GW, and XT. Funding acquisition: WX, HZ, and DY. Investigation: WX, XT, WL, JT, AA, JS, and WZ. Resources: HH, GS, GW, CL, YQ, HZ, and DY. Supervision: YQ, HH, GW, CL, HZ, and DY. Original draft: WX, WZ, WL, and JT. Review and editing: GW, CL, YQ, HZ, and DY. All authors contributed to the article and approved the submitted version.

FUNDING

This work was supported by grants from the National Key Research and Development Project (No. 2019YFC1316000); "Fuqing Scholar" Student Scientific Research Program of Shanghai Medical College, Fudan University (No. FQXZ202112B); Natural Science Foundation of China (No. 82172817); Natural Science Foundation of Shanghai (No. 20ZR1413100); and Shanghai Municipal Health Bureau (No. 2020CXJQ03).

ACKNOWLEDGMENTS

We are grateful to all patients for their dedicated participation in the current study. We thank Ms. ZOO for her work in color schemes and optimization of all the figures.

SUPPLEMENTARY MATERIAL

The Supplementary Material for this article can be found online at: https://www.frontiersin.org/articles/10.3389/fimmu.2021.734646/full#supplementary-material

REFERENCES

1. Bray F, Ferlay J, Soerjomataram I, Siegel RL, Torre LA, Jemal A. Global Cancer Statistics 2018: GLOBOCAN Estimates of Incidence and Mortality Worldwide for 36 Cancers in 185 Countries. *CA Cancer J Clin* (2018) 68 (6):394–424. doi: 10.3322/caac.21492
2. Hsieh JJ, Purdue MP, Signoretti S, Swanton C, Albiges L, Schmidinger M, et al. Renal Cell Carcinoma. *Nat Rev Dis Primers* (2017) 3:17009. doi: 10.1038/nrdp.2017.9
3. Sazuka T, Nihei N, Nakamura K, Sakamoto S, Fukasawa S, Komaru A, et al. Interferon Treatment for Japanese Patients With Favorable-Risk Metastatic Renal Cell Carcinoma in the Era of Targeted Therapy. *Korean J Urol* (2015) 56 (3):205–11. doi: 10.4111/kju.2015.56.3.205
4. Akaza H, Tsukamoto T, Onishi T, Miki T, Kinouchi T, Naito S. A Low-Dose Combination Therapy of Interleukin-2 and Interferon-Alpha Is Effective for Lung Metastasis of Renal Cell Carcinoma: A Multicenter Open Study. *Int J Clin Oncol* (2006) 11(6):434–40. doi: 10.1007/s10147-006-0596-z
5. Akaza H, Kawai K, Tsukamoto T, Fujioka T, Tomita Y, Kitamura T, et al. Successful Outcomes Using Combination Therapy of Interleukin-2 and Interferon-Alpha for Renal Cell Carcinoma Patients With Lung Metastasis. *Jpn J Clin Oncol* (2010) 40(7):684–9. doi: 10.1093/jjco/hyq027
6. Xu W, Liu WR, Xu Y, Tian X, Anwaier A, Su JQ, et al. Hexokinase 3 Dysfunction Promotes Tumorigenesis and Immune Escape by Upregulating Monocyte/Macrophage Infiltration Into the Clear Cell Renal Cell Carcinoma Microenvironment. *Int J Biol Sci* (2021) 17(9):2205–22. doi: 10.7150/ijbs.58295
7. Xu WH, Xu Y, Wang J, Wan FN, Wang HK, Cao DL, et al. Prognostic Value and Immune Infiltration of Novel Signatures in Clear Cell Renal Cell Carcinoma Microenvironment. *Aging (Albany NY)* (2019) 11(17):6999–7020. doi: 10.18632/aging.102233
8. Ngwa VM, Edwards DN, Philip M, Chen J. Microenvironmental Metabolism Regulates Antitumor Immunity. *Cancer Res* (2019) 79(16):4003–8. doi: 10.1158/0008-5472.CAN-19-0617
9. Zhang Q, Zhang L, Li L, Wang Z, Ying J, Fan Y, et al. Interferon Regulatory Factor 8 Functions as a Tumor Suppressor in Renal Cell Carcinoma and Its Promoter Methylation Is Associated With Patient Poor Prognosis. *Cancer Lett* (2014) 354(2):227–34. doi: 10.1016/j.canlet.2014.07.040
10. Yu S, Dai J, Ma M, Xu T, Kong Y, Cui C, et al. RBCK1 Promotes P53 Degradation *via* Ubiquitination in Renal Cell Carcinoma. *Cell Death Dis* (2019) 10(4):254. doi: 10.1038/s41419-019-1488-2
11. Hänze J, Wegner M, Noessner E, Hofmann R, Hegele A. Co-Regulation of Immune Checkpoint PD-L1 With Interferon-Gamma Signaling Is Associated With a Survival Benefit in Renal Cell Cancer. *Target Oncol* (2020) 15(3):377–90. doi: 10.1007/s11523-020-00728-8
12. Liu L, Zhu S. Computational Methods for Prediction of Human Protein-Phenotype Associations: A Review. *Phenomics* (2021). doi: 10.1007/s43657-021-00019-w
13. Fang Y, Shi H, Xiang T, Liu J, Liu J, Tang X, et al. Genetic Architecture of Childhood Kidney and Urological Diseases in China. *Phenomics* (2021) 1 (3):91–104. doi: 10.1007/s43657-021-00014-1
14. Wang C, Li Y, Lv J, Jin J, Hu X, et al. Recommendation for Cardiac Magnetic Resonance Imaging-Based Phenotypic Study: Imaging Part. *Phenomics* (2021). doi: 10.1007/s43657-021-00018-x
15. Xu WH, Xu Y, Tian X, Anwaier A, Liu WR, Wang J, et al. Large-Scale Transcriptome Profiles Reveal Robust 20-Signatures Metabolic Prediction Models and Novel Role of G6PC in Clear Cell Renal Cell Carcinoma. *J Cell Mol Med* (2020) 24(16):9012–27. doi: 10.1111/jcmm.15536
16. Jiang P, Gu S, Pan D, Fu J, Sahu A, Hu X, et al. Signatures of T Cell Dysfunction and Exclusion Predict Cancer Immunotherapy Response. *Nat Med* (2018) 24(10):1550–8. doi: 10.1038/s41591-018-0136-1
17. Xu W, Hu X, Anwaier A, Wang J, Liu W, Tian X, et al. Fatty Acid Synthase Correlates With Prognosis-Related Abdominal Adipose Distribution and Metabolic Disorders of Clear Cell Renal Cell Carcinoma. *Front Mol Biosci* (2020) 7:610229. doi: 10.3389/fmolb.2020.610229
18. Kotecha RR, Motzer RJ, Voss MH. Towards Individualized Therapy for Metastatic Renal Cell Carcinoma. *Nat Rev Clin Oncol* (2019) 16(10):621–33. doi: 10.1038/s41571-019-0209-1
19. Sato Y, Yoshizato T, Shiraishi Y, Maekawa S, Okuno Y, Kamura T, et al. Integrated Molecular Analysis of Clear-Cell Renal Cell Carcinoma. *Nat Genet* (2013) 45(8):860–7. doi: 10.1038/ng.2699
20. Hakimi AA, Pham CG, Hsieh JJ. A Clear Picture of Renal Cell Carcinoma. *Nat Genet* (2013) 45(8):849–50. doi: 10.1038/ng.2708
21. Voss MH, Reising A, Cheng Y, Patel P, Marker M, Kuo F, et al. Genomically Annotated Risk Model for Advanced Renal-Cell Carcinoma: A Retrospective

Cohort Study. *Lancet Oncol* (2018) 19(12):1688–98. doi: 10.1016/S1470-2045(18)30648-X
22. Hakimi AA, Chen YB, Wren J, Gonen M, Abdel-Wahab O, Heguy A, et al. Clinical and Pathologic Impact of Select Chromatin-Modulating Tumor Suppressors in Clear Cell Renal Cell Carcinoma. *Eur Urol* (2013) 63(5):848–54. doi: 10.1016/j.eururo.2012.09.005
23. Joseph RW, Kapur P, Serie DJ, Parasramka M, Ho TH, Cheville JC, et al. Clear Cell Renal Cell Carcinoma Subtypes Identified by BAP1 and PBRM1 Expression. *J Urol* (2016) 195(1):180–7. doi: 10.1016/j.juro.2015.07.113
24. Rotte A. Combination of CTLA-4 and PD-1 Blockers for Treatment of Cancer. *J Exp Clin Cancer Res* (2019) 38(1):255. doi: 10.1186/s13046-019-1259-z
25. Li L, Chen X, Hao L, Chen Q, Liu H, Zhou Q. Exploration of Immune-Related Genes in High and Low Tumor Mutation Burden Groups of Chromophobe Renal Cell Carcinoma. *Biosci Rep* (2020) 40(7):1–10. doi: 10.1042/BSR20201491
26. Wu X, Gu Z, Chen Y, Chen B, Chen W, Weng L, et al. Application of PD-1 Blockade in Cancer Immunotherapy. *Comput Struct Biotechnol J* (2019) 17:661–74. doi: 10.1016/j.csbj.2019.03.006
27. Kim EY, Ner-Gaon H, Varon J, Cullen AM, Guo J, Choi J, et al. Post-Sepsis Immunosuppression Depends on NKT Cell Regulation of mTOR/IFN-γ in NK Cells. *J Clin Invest* (2020) 130(6):3238–52. doi: 10.1172/JCI128075
28. Muntjewerff EM, Meesters LD, van den Bogaart G, Revelo NH, et al. Reverse Signaling by MHC-I Molecules in Immune and Non-Immune Cell Types. *Front Immunol* (2020) 11:605958. doi: 10.3389/fimmu.2020.605958
29. Grasso CS, Tsoi J, Onyshchenko M, Abril-Rodriguez G, Ross-Macdonald P, Wind-Rotolo M, et al. Conserved Interferon-γ Signaling Drives Clinical Response to Immune Checkpoint Blockade Therapy in Melanoma. *Cancer Cell* (2020) 38(4):500–15.e3. doi: 10.1016/j.ccell.2020.08.005
30. Kanda N, Shimizu T, Tada Y, Watanabe S. IL-18 Enhances IFN-Gamma-Induced Production of CXCL9, CXCL10, and CXCL11 in Human Keratinocytes. *Eur J Immunol* (2007) 37(2):338–50. doi: 10.1002/eji.200636420
31. Yuan Z, Yang H, Wei Y. Combined Induction With Anti-PD-1 and Anti-CTLA-4 Antibodies Provides Synergistic Antitumor Effects in DC-CIK Cells in Renal Carcinoma Cell Lines. *Int J Clin Exp Pathol* (2019) 12(1):123–32. doi: 10.32388/p5v6y2
32. Galon J, Bruni D. Approaches to Treat Immune Hot, Altered and Cold Tumours With Combination Immunotherapies. *Nat Rev Drug Discov* (2019) 18(3):197–218. doi: 10.1038/s41573-018-0007-y
33. Taminiau A, Draime A, Tys J, Lambert B, Vandeputte J, Nguyen N, et al. HOXA1 Binds RBCK1/HOIL-1 and TRAF2 and Modulates the TNF/NF-κb Pathway in a Transcription-Independent Manner. *Nucleic Acids Res* (2016) 44(15):7331–49. doi: 10.1093/nar/gkw606
34. Krenn M, Salzer E, Simonitsch-Klupp I, Rath J, Wagner M, Haack TB, et al. Mutations Outside the N-Terminal Part of RBCK1 may Cause Polyglucosan Body Myopathy With Immunological Dysfunction: Expanding the Genotype-Phenotype Spectrum. *J Neurol* (2018) 265(2):394–401. doi: 10.1007/s00415-017-8710-x
35. Liu ML, Zang F, Zhang SJ. RBCK1 Contributes to Chemoresistance and Stemness in Colorectal Cancer (CRC). *BioMed Pharmacother* (2019) 118:109250. doi: 10.1016/j.biopha.2019.109250

Conflict of Interest: The authors declare that the research was conducted in the absence of any commercial or financial relationships that could be construed as a potential conflict of interest.

The reviewer J-YZ declared a shared affiliation with several of the authors to the handling editor at the time of review. The reviewer HW declared a shared affiliation with several of the authors to the handling editor at the time of review.

Publisher's Note: All claims expressed in this article are solely those of the authors and do not necessarily represent those of their affiliated organizations, or those of the publisher, the editors and the reviewers. Any product that may be evaluated in this article, or claim that may be made by its manufacturer, is not guaranteed or endorsed by the publisher.

Citation: *Xu W, Tao J, Zhu W, Liu W, Anwaier A, Tian X, Su J, Shi G, Huang H, Wei G, Li C, Qu Y, Zhang H and Ye D (2021) Comprehensive Multi-Omics Identification of Interferon-γ Response Characteristics Reveals That RBCK1 Regulates the Immunosuppressive Microenvironment of Renal Cell Carcinoma. Front. Immunol. 12:734646. doi: 10.3389/fimmu.2021.734646*

frontiers in Immunology

ORIGINAL RESEARCH
published: 04 November 2021
doi: 10.3389/fimmu.2021.737650

Identification of Methylation Immune Subtypes and Establishment of a Prognostic Signature for Gliomas Using Immune-Related Genes

Zhengang Hu[1], Hao Zhang[1], Fan Fan[1], Zeyu Wang[1], Jiahao Xu[1], Yunying Huang[1], Ziyu Dai[1], Hui Cao[2], Xun Zhang[1], Zhixiong Liu[1,3†] and Quan Cheng[1,3,4*†]*

[1] Department of Neurosurgery, Xiangya Hospital, Central South University, Changsha, China, [2] Department of Psychiatry, The Second People's Hospital of Hunan Province, The Hospital of Hunan University of Chinese Medicine, Changsha, China, [3] National Clinical Research Center for Geriatric Disorders, Xiangya Hospital, Central South University, Changsha, China, [4] Department of Clinical Pharmacology, Xiangya Hospital, Central South University, Changsha, China

DNA methylation patterns are essential in understanding carcinogenesis. However, the relationship between DNA methylation and the immune process has not been clearly established—this study aimed at elucidating the interaction between glioma and DNA methylation, consolidating glioma classification and prognosis. A total of 2,483 immune-related genes and 24,556 corresponding immune-related methylation probes were identified. From the Cancer Genome Atlas (TCGA) glioma cohort, a total of 683 methylation samples were stratified into two different clusters using unsupervised clustering, and eight types of other cancer samples from the TCGA database were shown to exhibit excellent distributions. A total of 3,562 differentially methylated probes (DMPs) were selected and used for machine learning. A five-probe signature was established to evaluate the prognosis of glioma as well as the potential benefits of radiotherapy and Procarbazine, CCNU, Vincristine (PCV) treatment. Other prognostic clinical models, such as nomogram and decision tree, were also evaluated. Our findings confirmed the interactions between immune-related methylation patterns and glioma. This novel approach for cancer molecular characterization and prognosis should be validated in further studies.

Keywords: glioma, methylation, immune subtype, prognostic signature, pan-cancer

OPEN ACCESS

Edited by:
Qin Yan,
Yale University, United States

Reviewed by:
Suojun Zhang,
Huazhong University of Science and Technology, China
Peng Cheng,
The First Affiliated Hospital of China Medical University, China

****Correspondence:***
Quan Cheng
chengquan@csu.edu.cn
Zhixiong Liu
zhixiongliu@csu.edu.cn

†These authors have contributed equally to this work and share last authorship

Specialty section:
This article was submitted to Cancer Immunity and Immunotherapy, a section of the journal Frontiers in Immunology

Received: *07 July 2021*
Accepted: *01 October 2021*
Published: *04 November 2021*

Citation:
Hu Z, Zhang H, Fan F, Wang Z, Xu J, Huang Y, Dai Z, Cao H, Zhang X, Liu Z and Cheng Q (2021) Identification of Methylation Immune Subtypes and Establishment of a Prognostic Signature for Gliomas Using Immune-Related Genes. Front. Immunol. 12:737650. doi: 10.3389/fimmu.2021.737650

INTRODUCTION

Glioma, which develops from glial cells, is the most common type of primary central nervous system tumor (1). Therapeutic options for glioma include surgical resection, radiation, and chemotherapy. However, the overall survival (OS) time continues to be low.

Molecular markers have been shown to be efficient in predicting prognosis, including mutational status, mRNA expression, and DNA methylation. Several molecular markers

(MGMT, 1p/19q, IDH, EGFR, p53, PI3K, Rb, and RAF) have been successfully used for the classification and prediction of prognosis (2). The immune system plays a crucial role in antineoplasms (3). Apart from cancer cells, the tumor microenvironment (TME) contains various non-carcinogenic cell types, including endothelial cells, pericytes, and fibroblasts (4). Characteristically, as tumor grade increases, patients present with heightened levels of immunosuppression (5). A typical human immune response comprises humoral and cell-mediated reactions that shield the body against foreign bodies, including microscopic organisms, infections, and tumors. To prevent autoimmune responses, various immune cells such as regulatory T cells, monocytes, and neutrophils are used to suppress inflammation and maintain self-tolerance (6–8). Given that all options for managing glioma, temozolomide chemotherapy, radiotherapy, and corticosteroids, exhibit immunosuppressive effects, therapeutic options should confer less reduced side effects and clinical complications (3).

DNA methylation patterns are now perceived as heritable alterations in gene expression and are highly involved in carcinogenesis (9). A minimally invasive biopsy can improve diagnosis, treatment measures, and prediction of prognosis in cancer. Peculiar DNA methylation patterns influence critical genes of carcinogenesis and progression and inhibit some tumor suppressor genes (10). Therefore, understanding epigenetic changes can improve the characterization of malignancy patterns to predict treatment responses and prognosis (11). Even though DNA methylation patterns of specific genes have been reported, the scope of immune-related gene methylation patterns on glioma and other tumors has not been clearly established.

This study aims to classify and predict glioma outcomes by concentrating on the interaction between the immune process and methylation profile. We sought to identify immune-related probes and build an immune-related cluster using unsupervised clustering analysis. Moreover, we performed pan-cancer analysis to identify a pan-cancer immune pattern to subdivide cancer among patients. Then, we established an immune-related prognostic signature, a clinical decision tree model, and a nomogram to inform on customized therapy and prognosis.

Abbreviations: AUC, Area Under Curve; CNS, central nervous system; C-index, concordance index; CDF, cumulative distribution function; DC, dendritic cells; DCA, decision curve analysis; DEGs, differentially expressed genes; DMPs, differentially methylation probes; ebGSEA, empirical Bayes Gene Set Enrichment Analysis; GBM, glioblastoma; GEO, Gene Expression Omnibus; GO, gene ontology; GSEA, gene set enrichment analysis; IL, interleukin; LGG, lower-grade glioma; MHC, major histocompatibility complex; NFAT5, Nuclear factor of activated T cells 5; NK, natural killer; OPRK1, κ-opioid receptors 1; OS, Overall Survival; PAC, Proportion of Ambiguous Clustering; PCA, principal component analysis; PFS, Progression-Free Survival; RT/PCV, radiotherapy and Procarbazine, CCNU, Vincristine; ROC, receiver operating characteristic; TGF-β, tumor growth factor-β; TNFα, tumor necrosis factor-α; SNP, single-nucleotide polymorphism; TCGA, The Cancer Genome Atlas; TME, tumor microenvironment; TNFα, tumor necrosis factor α; ZYX, zyxin.

MATERIALS AND METHODS

Glioma Patient Data

The schematic presentation of the study is shown in **Figure 1**.

This study involved a total of 683 glioma samples from TCGA databases and were retrieved from UCSC Xena TCGA database (https://tcga.xenahubs.net). RNA-seq data of 587 glioma samples were downloaded from the TCGA database (http://cancergenome.nih.gov/). Correlative clinical traits and molecular features were also retrieved from the TCGA database. Pan-cancer data atlas were downloaded from the UCSC Xena TCGA database. The Gene Expression Omnibus (GEO) dataset (GSE48462, GSE61160, GSE36278, GSE30338, and GSE104293) was obtained from the GEO database (https://www.ncbi.nlm.nih.gov/geo/). The platform of the methylation dataset was Illumina HumanMethylation450 BeadChip (GPL13534).

Construction of Immune-Related Probes

Inclusive immune-related genes (2,483 genes) were retrieved from the ImmPort database (version: July 2020) (https://www.immport.org/shared/genelists). Corresponding probes in 450k chipset annotation file (GPL13534) were matched, after which 24,556 immune-related probes participating involved in the immune process were eventually selected.

Establishment of Immune-Related Clusters Based on Immune-Related Probes Using Consensus Clustering

We used the R package "ConsensusClusterPlus" to perform unsupervised clustering analysis (12). A total of 683 glioma samples accompanied by 24,556 immune-related probes were divided into different methylation subtypes using K-means and Euclidean distance as the baseline clustering algorithm and the similarity measure, respectively. After 1,000 iterations, the optimal k value was selected using the Proportion of Ambiguous Clustering (PAC) measure, which had the lowest PAC.

Identification of Genome-Wide Methylation Probes

R package "ChAMP" was used to preprocess and analyze the Illumina Infinium 450k DNA methylation array (13). Probes with missing values greater than 20% were deleted. Then probes were filtered by "champ.filter" to remove those with $p > 0.01$, bead count <3, noCG start, Single Nucleotide Polymorphism (SNP) (14), multihit, and those targeting the X and Y chromosomes. Other missing values were imputed by k-nearest neighbor (KNN) imputation algorithm. The normalized beta value matrix was established by "champ.norm" using the Beta MIxture Quantile dilation (BMIQ) method (15). Differential methylation probes were detected using "limma" package to calculate the p-value for differential methylation using a linear model (16). The Benjamini and Hochberg false discovery rate method was used to reduce the false positive rate (FDR) when applying multiple comparisons. Delta beta means the average discrepancy of beta value between

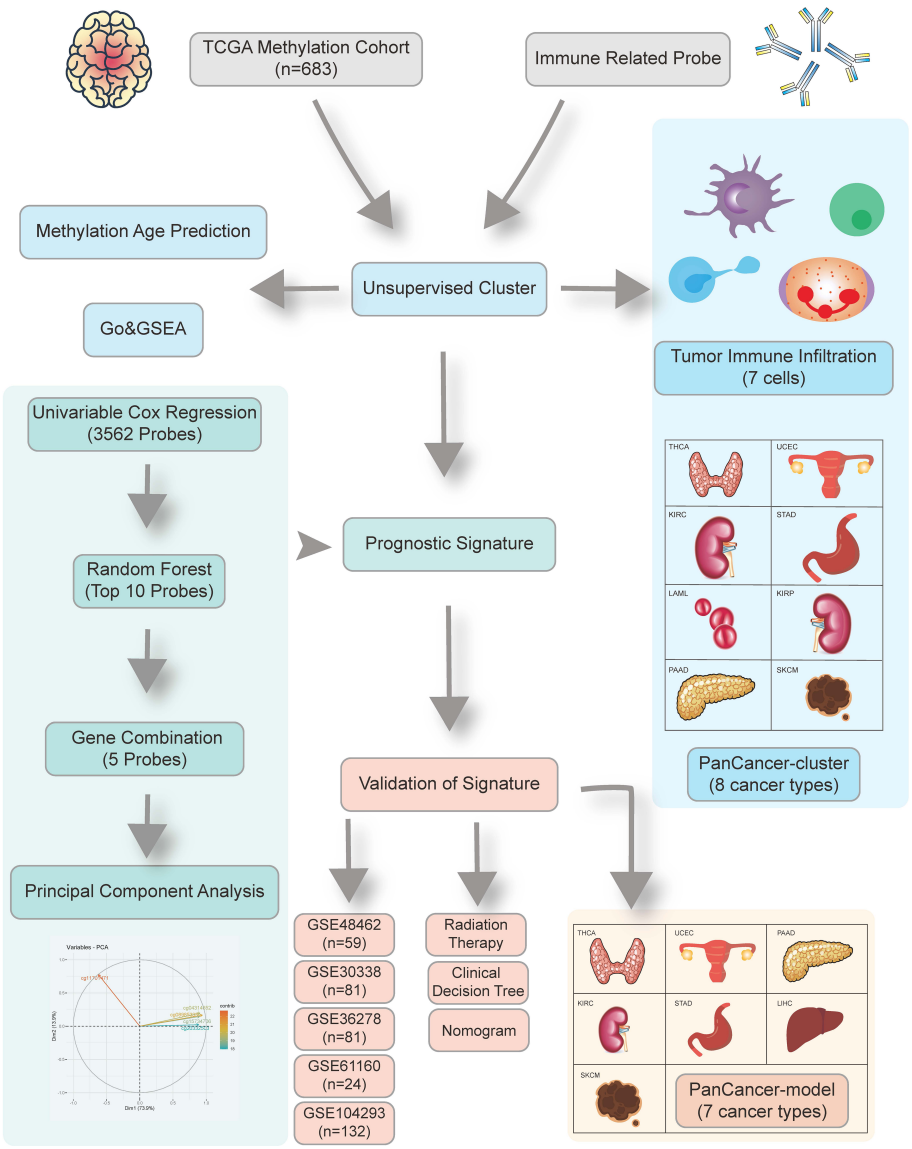

FIGURE 1 | Overview of the study design. First, we identified 24,556 candidate immune-related methylation probes. Then unsupervised cluster was used in a 683 TCGA glioma methylation cohort. A five-CpG-based prognostic signature was established and validated in five independent GEO datasets.

two different groups. Adjusted p<0.05 and delta beta>0.2 were selected as cutoff values for detecting DMPs. Simultaneously, differentially expressed genes were identified by "limma" package with 0.5 logFC cutoff and p value <0.05 (17).

Functional Annotations

Gene ontology (GO) analysis of the methylation profile was performed using "clusterProfiler" package (18). We used the Benjamini and Hochberg (BH) method to determine the adjusted p-values, and pathway in which FDR values were under 0.05 was chosen.

The Empirical Bayes Gene Set Enrichment Analysis (ebGSEA) was used to identify the exact enriched genes for specific biological terms or pathways (19). This method can be used to independently perform GSEA, regardless of DMPs or differentially methylated regions. Moreover, it can be used to identify significant genes, with the bias of inequality of CpG number corrected for each gene. GSEA of the TCGA RNA-seq cohort was estimated using the "clusterProfiler" package (18).

Profiling DNA Methylation Age and Tumor Infiltration

Based on Horvath's clock model, we used the "agep" method in the "wateRmelon" package to predict DNA methylation age from normalized methylation β values (19).

Tumor-infiltrating immune analysis of the methylation set was performed using the "EpiDish" package (20). We identified proportions of *a priori* known cell subtypes present in a sample representing a mixture of such cell types. FractionS of eight cell subtypes (B-cells, CD4+ T-cells, CD8+ T-cells, NK-cells, Monocytes, Neutrophils, Eosinophils, Neutrophils, and Eosinophils) were estimated using the Robust Partial Correlations (RPC) method and whole blood subtypes reference (21). Meanwhile, the tumor-infiltrating immune analysis of transcriptome was evaluated using the CIBERSORT algorithm (22). A total of 22 immune cells are calculated in 1,000 times permutations.

Construction and Validation of a Prognostic Model

Univariate Cox regression analyses were performed using the "survival" package with a 0.05 p-value cutoff. Then Random Forest algorithm was used to rank the top 10 methylation probes that contribute to prediction. Therefore, the "randomForestSRC" package was used, and the number of trees was 1,000. Kaplan-Meier analysis was performed to establish the best combination of the 1,023 participant model. After selecting the best combination model, exact coefficients of each probe were determined by the Principal Component Analysis (PCA) method. FactoMineR and "factoextra" package contributed to applying PCA (23). The risk score for each patient after the prognostic value of each gene signature score was obtained using the formula: risk score = SPC1i - SPC1j, where *i* represented the expression of genes with HR>1, and *j* the expression of genes with HR<1. Risk score = 10.52*cg11701471-22.14*cg04314652-21.95*cg04314652-21.34*cg20332504-24.02*cg08985333. To make the cutoff value more accurate, we employed the survival cutoff method to determine the optimal cutpoint that corresponds to the most significant relation with overall survival. The cutoff point of the high- and low-risk group in the TCGA cohort was −33.57. Receiver operating characteristic (ROC) analysis was performed using "timeROC" package (24). Clinical benefits were estimated using decision curve analysis and were established by R package "rmda" (25). Five GEO datasets (GSE48462, GSE61160, GSE36278, GSE30338, GSE104293) were chosen as validation set.

Identification of Clinical Associated Risk Model

A nomogram and corresponding calibration curve were established using the "rms" in R package. Univariate and multivariate Cox proportional hazard analyses were performed based on the risk score and clinical factors. After multivariate Cox proportional hazard analysis, factors with p<0.05 were chosen to establish the nomogram. Forest plots were constructed using the "forestplot" and "ggforest" packages. Recursive partitioning analysis was performed using the "rpart" and "rattle" packages to construct a survival-related decision tree and stratify the prognostic risk. Concordance index (C-index) and ROC analysis were used to evaluate the predictive values of survival among the different models.

Prediction of Radiotherapeutic and Chemotherapeutic Responses

The TCGA GBM cohort was used to predict patient responses to radiotherapy. The GSE48462 dataset, which was an Anaplastic Oligodendrogliomas and Oligoastrocytomas cohort treated with RT or RT/PCV, was used for the prediction of patient responses to PCV therapy (26). Samples with Illumina HumanMethylation27k BeadChip were excluded.

Statistical Analysis

Pearson correlation analyses were performed to establish correlation coefficients. The chi-square test was used to analyze count data, while the Wilcoxon rank-sum test was used to analyze continuous data. Kaplan-Meier survival analysis with log-rank test was used to assess survival differences between different groups. Data were depicted using the "ggplot2" package. The cutoff between high-risk and low-risk was determined by "surv_cutpoint" function in "survminer" package, and all the survival curves were visualized by the "survminer" package. Heatmaps are presented using the "pheatmap" package. All statistical analyses were performed by R software. p<0.05 was considered statistically significant.

RESULTS

Identification of Immune-Related Clusters

The overall design of our study is shown in **Figure 1**. We aimed at identifying immune-related clusters in the TCGA glioma cohort (n=683) by utilizing the 24,556 immune-related methylation probes using the ConsensusClusterPlus package (**Table S1**). Clinical information of the TCGA glioma cohort is shown in **Table 1**. Clustering results are presented in a cumulative distribution function (CDF) plot and a delta area plot (**Figures S1A, B**). The CDF plot and delta area plot revealed that the optimal k value for stable distribution was 2. We selected k=2 as the epitome number of clusters, and the heatmap of the consensus matrix showed satisfactory discrimination (**Figure S1C**). Kaplan-Meier survival analysis revealed that cluster2 had a more favorable prognosis (p<0.0001; **Figure 2A**). To elucidate on the immune microenvironment status between the two clusters, tumor-infiltrating immune analysis was performed in both the TCGA methylation set and the expression set (n=587). In the methylation set, we used the EpiDISH package to evaluate differences in seven immune cells, including B cells, Natural killer (NK) cells, CD4T cells, CD8T cells, monocytes, neutrophils, and eosinocytes. Levels of all the seven immune cells were significantly different (p<0.001), and cluster2 exhibited a higher enrichment score of B cells, NK cells, CD4T cells, and eosinocytes. In contrast, cluster1 exhibited a higher proportion of CD8+T cells, monocytes, and neutrophils (**Figures 2B**, **S1F**). The immune microenvironment difference in the TCGA RNA-seq cohort using the CIBERSORT algorithm (**Figures S1G**). Methylation levels between clusters 1 and 2 were significantly different (p<2.2e-16), with a higher methylation level in cluster2 (**Figure 2C**). Since the different methylation statuses may

TABLE 1 | Clinical and genetic characteristics of patients after clustering.

	GBM		LGG		TOTAL	
	Cluster1 (N=146)	Cluster2 (N=7)	Cluster1 (N=104)	Cluster2 (N=426)	Cluster1 (N=250)	Cluster2 (N=433)
Gender						
Female	60 (41%)	1 (14%)	45 (4%)	163 (38%)	105 (42%)	164 (38%)
Male	80 (55%)	5 (71%)	49 (47%)	211 (50%)	129 (52%)	216 (50%)
Missing	6 (4.1%)	1 (14.3%)	10 (9.6%)	52 (12.2%)	16 (6.4%)	53 (12.2%)
Age (years)						
<52	31 (21%)	5 (71%)	42 (40%)	292 (69%)	73 (29%)	297 (69%)
>66	48 (33%)	0 (0%)	14 (13%)	17 (4%)	62 (25%)	17 (4%)
52–66	61 (42%)	1 (14%)	38 (37%)	65 (15%)	99 (40%)	66 (15%)
Missing	6 (4.1%)	1 (14.3%)	10 (9.6%)	52 (12.2%)	16 (6.4%)	53 (12.2%)
IDH						
Mutant	2 (1%)	7 (100%)	8 (8%)	423 (99%)	10 (4%)	430 (99%)
WT	135 (92%)	0 (0%)	96 (92%)	0 (0%)	231 (92%)	0 (0%)
Missing	9 (6.2%)	0 (0%)	0 (0%)	3 (0.7%)	9 (3.6%)	3 (0.7%)
pq						
Codel	0 (0%)	0 (0%)	1 (1%)	171 (40%)	1 (0%)	171 (39%)
Non-codel	143 (98%)	7 (100%)	103 (99%)	255 (60%)	246 (98%)	262 (61%)
Missing	3 (2.1%)	0 (0%)	0 (0%)	0 (0%)	3 (1.2%)	0 (0%)
MGMT						
Methylated	56 (38%)	6 (86%)	40 (38%)	397 (93%)	96 (38%)	403 (93%)
Unmethylated	79 (54%)	0 (0%)	64 (62%)	29 (7%)	143 (57%)	29 (7%)
Missing	11 (7.5%)	1 (14.3%)	0 (0%)	0 (0%)	11 (4.4%)	1 (0.2%)
Radiation therapy						
Yes	108 (74%)	7 (100%)	70 (67%)	226 (53%)	178 (71%)	233 (54%)
No	17 (12%)	0 (0%)	21 (20%)	164 (38%)	38 (15%)	164 (38%)
Missing	21 (14.4%)	0 (0%)	13 (12.5%)	35 (8.2%)	34 (13.6%)	35 (8.1%)

contribute to biological changes, ebGSEA analysis was performed. It was found that corresponding genes of DMPs were concentrated in the cytokine-receptor pathways such as TGF–beta Receptor (TGF-β), TP53, tumor necrosis factor-alpha (TNFα), and interleukin-2 (IL-2), which implied a strong relationship between glioma tissues and inflammatory responses (**Figure 2D**). Furthermore, GO functional enrichment analysis revealed that corresponding genes of DMPs were enriched in pathways involving neutrophils, T cells, B cells, macrophages, and mast cell signaling pathways, implying that the two clusters had vital differences regarding immune status (**Figures 2E, F**).

In summary, the GO functional enrichment analysis and the association between EpiDISH and CIBERSORT results of the immune infiltrating microenvironment indicated the abnormal immune infiltrations in cluster1 might serve as prognostic indicators for strong inflammatory reactions and poor overall outcomes.

Analysis of DNA Methylation Age and Clinical and Molecular Feature

The patients in cluster1 trended to be older than cluster2 (**Figure 2G**). We identified the DNAm ages in the TCGA methylation cohort (n=683) using the "wateRmelon" package and compared them with their chronological ages. Chronological ages (Wilcoxon, p < 2.2e-16) and DNAm ages (Wilcoxon, p = 5e −06) were found to be higher in cluster1 than in cluster2. Furthermore, the correlations between chronological ages and DNAm ages were significantly high (Pearson, R=0.607), indicating that epigenetic age analysis might contribute to glioma patients' prognostic prediction (**Figure 2H**).

Moreover, we evaluated gender, histology, IDH, 1p/19q, and MGMT distributions between the two clusters. Histology, IDH, 1p/19q, and MGMT were found to be significantly distributed (Pearson's chi-squared test, p<0.001). However, no evidence was found for gender associations between the two clusters (**Figure S2A**).

We also employed the survival differences considering the types of gliomas with the cluster. In details, cluster1 enjoyed worse prognosis than cluster2 in GBM cohort (p = 0.013) and in LGG cohort (p < 2e-16). LGG cohort possessed higher survival possibilities than GBM cohort in cluster1 (p < 0.0001) and in cluster2 (p = 0.048, **Figure S2B**).

These results suggest that there is a difference in epigenetic age and clinical traits.

Differentially Methylated Probes and Differentially Expressed Genes in the Two Clusters

Then, we compared global patterns between the two clusters in the TCGA glioma methylation and expression sets. In the methylation set, package "ChAMP" was used, and 56886 DMPs were identified from Illumina Infinium 450k DNA methylation data of 683 samples according to the cutoff of Delta beta>0.2 and p value<10^-5. Compared to cluster1, 55,186 DMPs were upregulated, while 1,700 DMPs were downregulated (**Figure 3A**). At most, 5,964 DMPs were

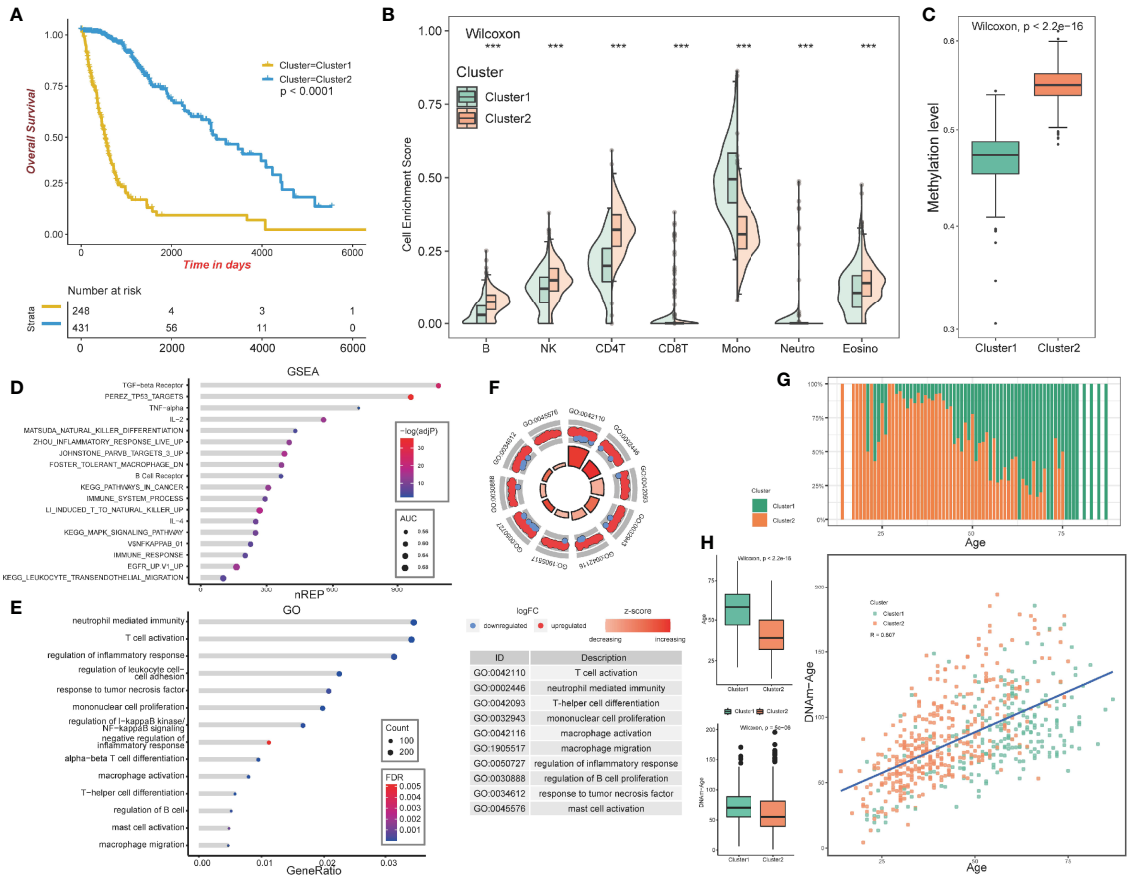

FIGURE 2 | Construction and analysis of consensus cluster. **(A)** Kaplan–Meier survival analysis of the two clusters showing clear separation. **(B)** Tumor-infiltrating immune analysis of the two clusters based on TCGA methylation set. **(C)** Methylation levels of the two clusters. **(D)** ebGSEA result of the two clusters. **(E, F)** GO functional enrichment analysis of the two clusters. **(G)** Age distribution of the two clusters. **(H)** Box plot showing the age and DNA methylation age difference between the two clusters, Scatter plot revealing correlations of the DNA methylation age-age correlation coefficients between cluster1 and cluster2. ***p <0.001.

located on chromosome 1, and at least 492 DMPs were located on chromosome 21 (**Figure 3B**). The overview of unsupervised clustering analysis of genome-wide DMPs is shown in the heatmap. Clinical and demographic features, including MGMT, IDH with codel subtype, 1p/19q, IDH, sex, age, grade, histology, and cancer type, are also shown in the heatmap (**Figure 3C**).

Differentially expressed genes (DEGs) were identified using the "limma" package in the expression section, and genes with log2FC > 0.5 and p < 0.05 were selected (**Figure 3D**). Global DEGs and clinical characteristics were visualized by heatmap (**Figure 3E**).

Pan-Cancer Analysis of Immune-Related Methylation Probes

To evaluate the methylation levels of immune-related probes in other types of TCGA cancers, we applied the unsupervised consensus clustering method to other 31 cancer types in TCGA. After selecting optimal *k*, Kaplan-Meier survival analysis was performed, with the 0.05 significant p-value cutoff. Finally, eight cancer types, including Stomach adenocarcinoma (STAD) (p=0.004), Uterine corpus endometrial carcinoma (UCEC) (p=0.011), Pancreatic adenocarcinoma (PAAD) (p=0.00018), Acute myeloid leukemia (LAML) (p=0.024), Thyroid carcinoma (THCA) (p=0.024), Kidney renal clear cell carcinoma (KIRC) (p<0.0001), Kidney renal papillary cell carcinoma (KIRP) (p<0.0001), and Skin cutaneous melanoma (SKCM), were selected (p=0.05; **Figures 4A–H**). The p-values of pairwise comparison were also identified (**Table S2**). This methylation pattern indicates that further evaluation is required.

Construction of a Prognostic DNA Methylation Signature for Glioma

To select optimal DNAm markers for glioma patients, we used 24,556 immune-related probes for differential methylation analysis of 683 TCGA tumor samples by adopting the standard of Delta beta>0.2 and p value<10^-5. A total of 3,562 probes were selected. Then univariate Cox regression analysis was

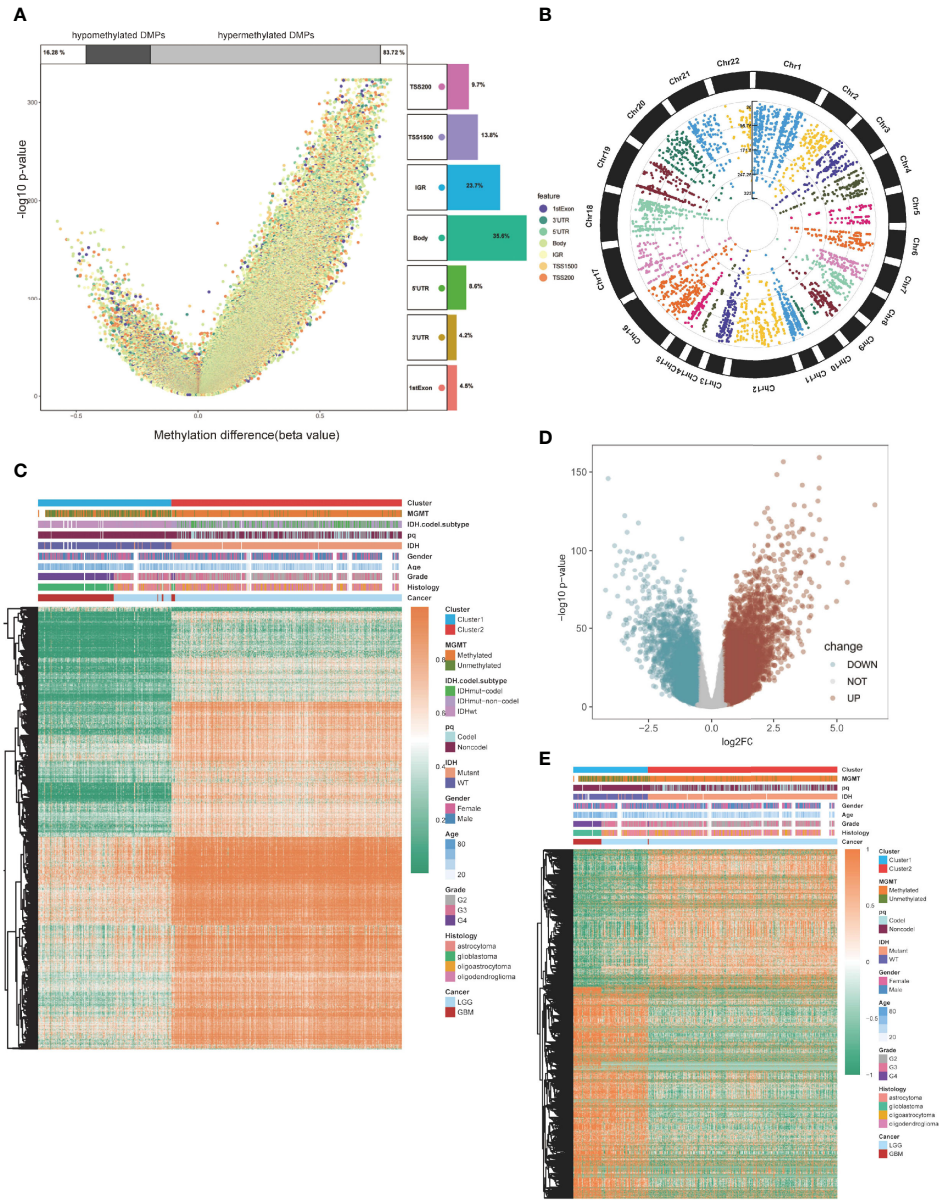

FIGURE 3 | Global DMPs and DEGs of the two clusters. **(A)** Volcano plot. Proportions of hypermethylated and hypomethylated DMPs are shown on top. The distribution of DMPs' feature is shown on the right. **(B)** The manhattan plot of the DMPs. **(C)** Heatmap of the two clusters based on the TCGA methylation set. High methylation, orange; low methylation, green. **(D)** Volcano plot of the DEGs. **(E)** Heatmap of the twp clusters based on the TCGA RNA-seq cohort. High expression, red; low expression, green.

performed with overall survival data, and all 3,562 markers were selected (**Figure 5A**; **Table S3**). After univariate Cox regression analysis, the 3,562 probes were put into machine learning algorithms, using Random Forest with overall survival profile, and 10 probes were selected (cg20332503, cg15734706, cg23505299, cg08015801, cg18443253, cg04314652, cg11701471, cg07388018, cg00732815, cg08985333) (**Figures 5B**, **S1D**). The 10 probes could form 1,023 combinations (**Table S4**), and Kaplan-Meier analysis was performed to establish the best probe combination. First, we contrasted their Log-rank p-values. However, the top 10 signature p values turned out to be close to 0 infinitely, which meant that their overall survival conditions were significantly distinct but not comparable. Therefore, we compared chi-squares (chisq) of each model and a five-probe signature (cg11701471, cg04314652, cg08985333, cg15734706, cg20332503) with the highest chi-square was selected finally (**Figure 5C**). Profile of the five methylation probes was given (**Table 2**). Then, coefficients of the signatures were determined by PCA (**Figure S1E**).

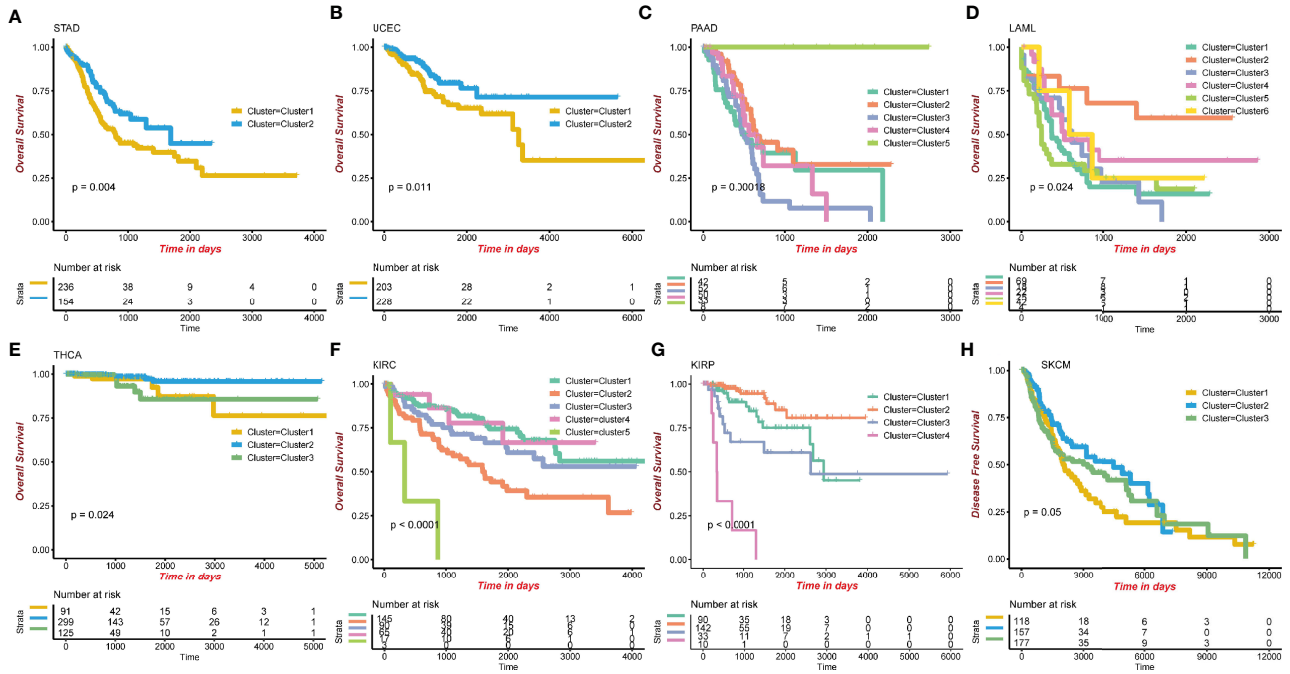

FIGURE 4 | Eight cancer types showing significant outcomes in TCGA pan-cancer survival analysis using consensus cluster. **(A)** STAD, Stomach adenocarcinoma. **(B)** UCEC, Uterine Corpus Endometrial Carcinoma. **(C)** PAAD, Pancreatic adenocarcinoma. **(D)** LAML, Acute Myeloid Leukemia. **(E)** THCA, Thyroid carcinoma. **(F)** KIRC, Kidney renal clear cell carcinoma. **(G)** KIRP, Kidney renal papillary cell carcinoma. **(H)** SKCM, Skin Cutaneous Melanoma.

Evaluation of the Signature and Pan-Cancer Analysis

By dividing the TCGA glioma cohort into high-risk groups (n=267) and low-risk groups (n=462) using the survival cutoff, high-risk patients were short-lived compared to low-risk patients (log-rank test p<0.0001) (**Figure 5D**). Beta values of the selected probes are presented in the heatmap (**Figure 5E**). We also verified the RNA-seq profiles of the five selected probes. Gene Set Enrichment Analysis (GSEA) revealed that cluster1 exhibited significant immune processes (**Figure 5F**). The RNA-seq data of the corresponding genes were also presented in the heatmap (**Figure 5G**). The impact of DNA methylation on gene expression in glioma was also evaluated. Three of five corresponding genes (cg15734706 and RARG, cg20332503 and ZYX, cg08985333 and CIITA) were considered significantly different between the high-risk group and low-risk group, and they share the same pattern that they were both hypomethylated and upregulated genes (**Figure S3A–E**). We further excavated the interaction between DNA methylation and gene expression by conducting Spearman's rank correlation analysis. It showed that cg20332503, cg15734706, and cg08985333 exhibited negative correlation, while cg20332503 ($\rho=-0.5$) and cg08985333 ($\rho=-0.6$) showed extremely high correlation (**Figure S3F–J**).

Then, we performed ROC to evaluate the predictive value of the signature, and we found that the area under curve (AUC) values of 1 to 5 years were all higher than 0.8, with the highest AUC (0.898) at 2 years (**Figure 5H**). Interestingly, there was a negative correlation between Progression-Free Survival (PFS) and risk score (Pearson, R=−0.43, p<0.00001; **Figure 5I**). The overall survival exhibited the same pattern with risk score (Pearson, R=−0.36, p<0.00001; **Figure 5J**), implying that patients with lower risk scores have better survival outcomes.

Then, we validated the performance of the signature using pan-cancer analysis. We downloaded the TCGA Illumina Infinium 450k DNA methylation pan-cancer data from UCSC Xena and calculated the risk scores. Using survival cutoff, they were distributed into high-risk groups and low-risk groups. After the Kaplan-Meier survival test, seven of 31 cancer types were selected: Skin cutaneous melanoma (SKCM) (p=0.00095), Pancreatic adenocarcinoma (PAAD) (p=0.00015), Liver hepatocellular carcinoma (LIHC) (p=0.00013), Thyroid carcinoma (THCA) (p=0.029), Kidney renal clear cell carcinoma (KIRC) (p<0.0001), Uterine corpus endometrial carcinoma (UCEC) (p=0.0071), and Stomach adenocarcinoma (STAD) (p=0.014) (**Figures S2C–I**). Pan-cancer analysis revealed a satisfactory prognostic value in glioma and the other seven cancer types.

Validation of the Signature and Its Functional Enrichment

To confirm the performance of the signature, five GEO datasets of glioma were formed as the validation groups; they were GSE48462 (n=59; p<0.0001), GSE61160 (n=24; p<0.0001), GSE36278 (n=81; p=0.006), GSE30338 (n=81; p<0.0001), and

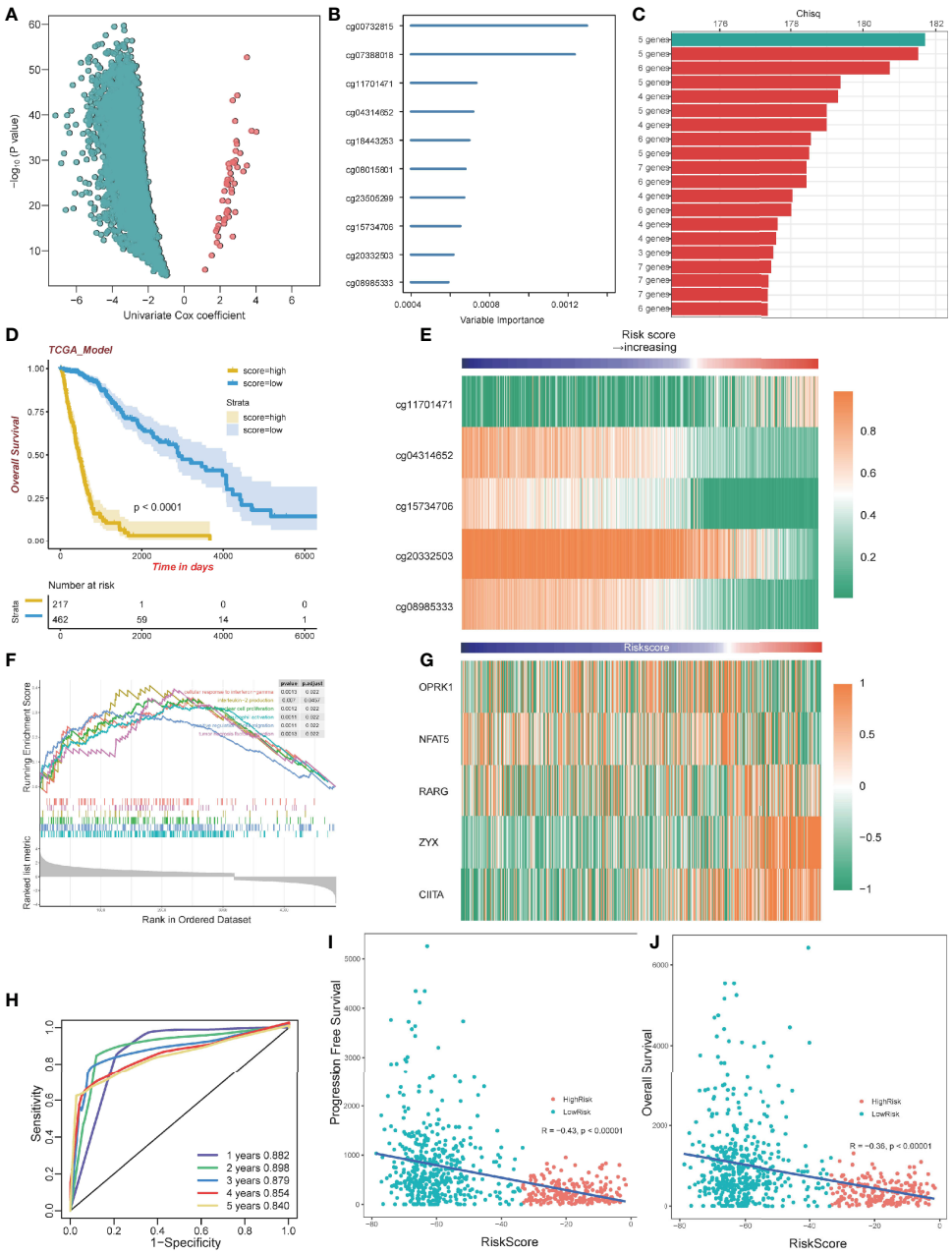

FIGURE 5 | Construction of a prognostic model. **(A)** Volcano plot showing the selected probes by univariate Cox regression analysis. The horizontal axis represents log2(HR) **(B)** Variable importance of 10 probes determined by random survival forest analysis. **(C)** Top 20 combinations of signatures were selected after Kaplan–Meier analysis according to the chi-square value. A five-probe signature with the highest chi-square was identified. All 20 signatures had a significant p-value Kaplan–Meier analysis. **(D)** Kaplan–Meier analysis of the high-risk and low-risk group. **(E)** Heatmap of the five selected methylation probes sorted by risk score. **(F)** GSEA plots for the enrichment of immunogenic and oncogenic signaling pathways from the GO. **(G)** Heatmap of gene expression corresponding to the selected five probes sorted by risk score. **(H)** ROC curve of the TCGA dataset. **(I)** The correlation between PFS time and risk score. **(J)** The correlation between OS time and risk score.

GSE104293 (n=132; p<0.0001). High-risk group patients exhibited lower survival outcomes than low-risk group patients (**Figures 6A–E**). Moreover, the ROC curve showed a competent accuracy in each validation set (**Figures 6G–J**).

Then we performed the functional enrichment analysis of the high-risk and low-risk groups. Both GO enrichment (**Figure S2J**) and ebGSEA (**Figure S2K**) pathways were related to the immune process and may participate in glioma development.

TABLE 2 | Five selected methylation probes.

	Chr	Mapinfo	Strand	Type	Gene	Feature	Cgi	UCSC_CpG_Islands_Name
cg11701471	8	54164051	R	I	***OPRK1***	5'UTR	island	chr8:54163303-54164443
cg04314652	16	69597925	F	II	***NFAT5***	TSS1500	shore	chr16:69599437-69600736
cg15734706	12	53614080	F	I	***RARG***	1stExon	island	chr12:53613716-53615103
cg20332503	7	143081287	R	II	***ZYX***	Body	shelf	chr7:143077469-143079169
cg08985333	16	10970960	F	II	***CIITA***	TSS200	shore	chr16:10972782-10973305

5'UTR, 5' untranslated region; TSS200, –200 base pairs upstream of the Transcription Start Site; TSS1500, between –200 and –1,500 base pairs upstream of the Transcription Start Site.

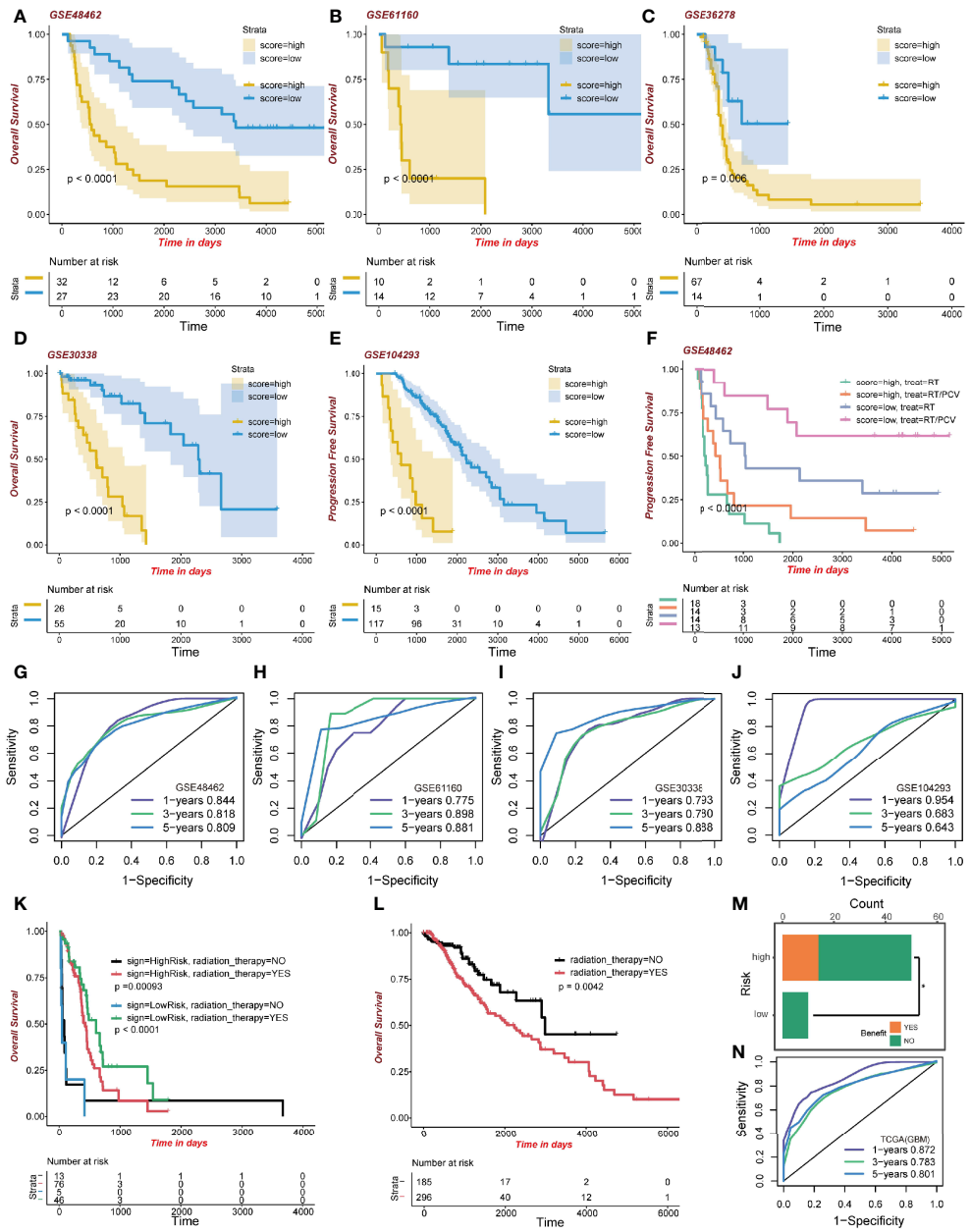

FIGURE 6 | Validation of the signature. **(A–E)** Kaplan-Meier curve of high-risk and low-risk score groups in the GEO cohort. **(F)** Kaplan-Meier survival analysis of different treatments on the GSE48462 dataset. Both high-risk and low-risk groups benefited from PCV. **(G–J)** ROC curve of the GEO dataset. **(K)** Kaplan-Meier curve of radiation therapy in the high- and low-risk GBM dataset group of TCGA. **(L)** Kaplan-Meier curve of radiation therapy in the LGG dataset group of TCGA. **(M)** Benefit from RT/PCV treatment in the GSE48462 dataset. **(N)** ROC curve of the GBM dataset group in TCGA.

GBM Patients Present Favorable Clinical Benefits to Radiotherapy

What is interesting regarding data of the training set is that GBM patients, regardless of risk scores, benefited from radiotherapy. The GBM high-risk group patients who had been administered with radiotherapy exhibited better survival outcomes (483 days median OS time) than those who did not (64 days median OS time; p=0.00093; **Figure 6K**). Moreover, the low-risk GBM group exhibited some clinical benefits from radiotherapy (579 days median OS time than 19 days median OS time, p<0.0001; **Figure 6K**). However, in the LGG group, patients receiving radiotherapy exhibited worse clinical outcomes (2,235 days median OS time than 2,988 days median OS time, p=0.0042; **Figure 6L**). We evaluated the model's predictive ability in the GBM cohort by ROC analysis (**Figure 6N**). These results revealed better radiotherapeutic outcomes.

High-Risk Group Patients Benefitted From RT/PCV Treatment

After validating the GSE48462 cohort as the glioma validation set, we evaluated the prognostic outcomes of radiotherapy and Procarbazine, CCNU, and Vincristine (RT/PCV) treatment. We found that both high-risk and low-risk group patients treated with RT/PCV had better PFS time than those treated with RT alone (p<0.0001; **Figure 6F**). Moreover, 14 (28%) high-risk patients benefited from RT/PCV treatment, 36 (72%) high-risk patients did not benefit from RT/PCV treatment, while 9 (100%) low-risk patients failed to benefit from RT/PCV treatment. There was a significant difference between the two groups (Chi-square test p<0.05), implying that the high-risk group rather than the low-risk group exhibited favorable outcomes from RT/PCV treatment (**Figure 6M**).

Construction of Clinical-Related Models to Precisely Demonstrate Risk Stratification in Glioma Patients

To validate the parameters' predictive value, we used decision curve analysis (DCA), and the risk score enjoyed the highest net benefit compared with age, gender, and grade, indicating that the risk score of models can be used as the main decision tree parameter (**Figure 7A**). Then, a total of 679 patients with detailed clinical information, including histology, grade, age, gender, status of IDH, status of pq, status of MGMT, and risk score, were selected for recursive partitioning analysis with an attempt to establish a detailed and maneuverable clinical-related model. Age and risk scores were chosen to finally establish a decision tree model. We selected two as the number of splits to prune our decision tree model since it had a relatively simple decision as well as a comparatively low standard deviation. Four risk subgroups were established based on whether the risk score was "high" or "low," together with age distribution. The low-risk group was identified when the methylation model's risk score was low regardless of age. The medium-risk group was identified when the risk score was high and the patient ages were lower than 52. Patients with high risk scores and aged between 52 and 66 years old were considered the high-risk group, while patients that were older than 66 years old were placed in the extremely high-risk group (**Figure 7B**). The four-class risk stratification suffered significantly different overall survival outcomes (p<0.0001, **Figure 7C**).

To establish an advanced prognostic evaluation model, we used univariate Cox regression analysis. Several parameters were passed through to the algorithm, and almost all variables fitted well (p<0.001) except for gender (HR=1.118, p=0.232; **Figure 7D**, **Table 3**). The multivariable Cox regression showed that grade, age, gender, IDH, and model were highly significant independent variables. In contrast, pq and MGMT did not fit well (**Figure 7E**). Therefore, we established a nomogram combined with risk scores and other significant parameters using the multivariate Cox regression (**Figure 7F**).

Calibration analysis revealed that 1-, 3-, and 5-year were significantly contiguous to the ideal 45-degree calibration line, suggesting that the nomogram had considerable high accuracy (**Figure 7G**). Then we evaluated Concordance indices (C-index) of the three models, and the nomogram had the highest goodness of fit (0.865, **Figure 7H**). Moreover, we also compared the three different models, and 1-year ROC revealed that the nomogram exhibited the most potent predictive capacity with AUC of 0.937 (**Figure 7I**).

DISCUSSION

Gliomas are among the most common types of primary tumors of the central nervous system, and aberrant DNA methylation is considered the hallmark of cancer tissues, participating in carcinogenesis, tumor immunology, and recurrence (27). Due to the contribution of the fast-growing methylation bead chip technique, it is important to obtain DNA methylation profiles.

DNA methylation in vertebrates happens at position 5′ of the cytosine ring in CpGs through a covalent obligation of methyl gathering (28, 29). The loss in DNA methylation, combing the silenced tumor suppressor genes, is considered a dangerous hallmark and poor prognosis in most cancer types (30–33). Our findings are in tandem with those of previous studies. After clustering, the average methylation level of cluster1 was significantly lower than that of cluster2, indicating that cluster1 exhibited a poor prognosis. Kaplan-Meier survival analysis confirmed this idea because the overall survival outcomes of cluster1 were impressively lower than cluster2.

Another important finding was the methylation scope of immune infiltration. We postulated that cluster2 exhibited immunity and living conditions. All seven immune cells showed a significant difference, and cluster2 exhibited a higher enrichment score of B cells, NK cells, CD4T cells, and eosinocytes. In contrast, cluster1 exhibited a higher proportion of CD8+T cells, monocytes, and neutrophils. This finding is in tandem with those of the work of other studies. For example, a higher proportion of B cells is associated with increased immunity, thereby enhancing the antitumor effect leading to better prognostic outcomes (34). NK cells are the prototype innate lymphoid cells that fight against microbial contamination and tumors (35). CD4+T cells can secrete IFN-γ, IL-2, and TNFα cytokines to interfere with tumor development. Cluster2 was found to have a higher immune score and an ideal OS time, which validated the previous findings. Meanwhile, functional annotations also

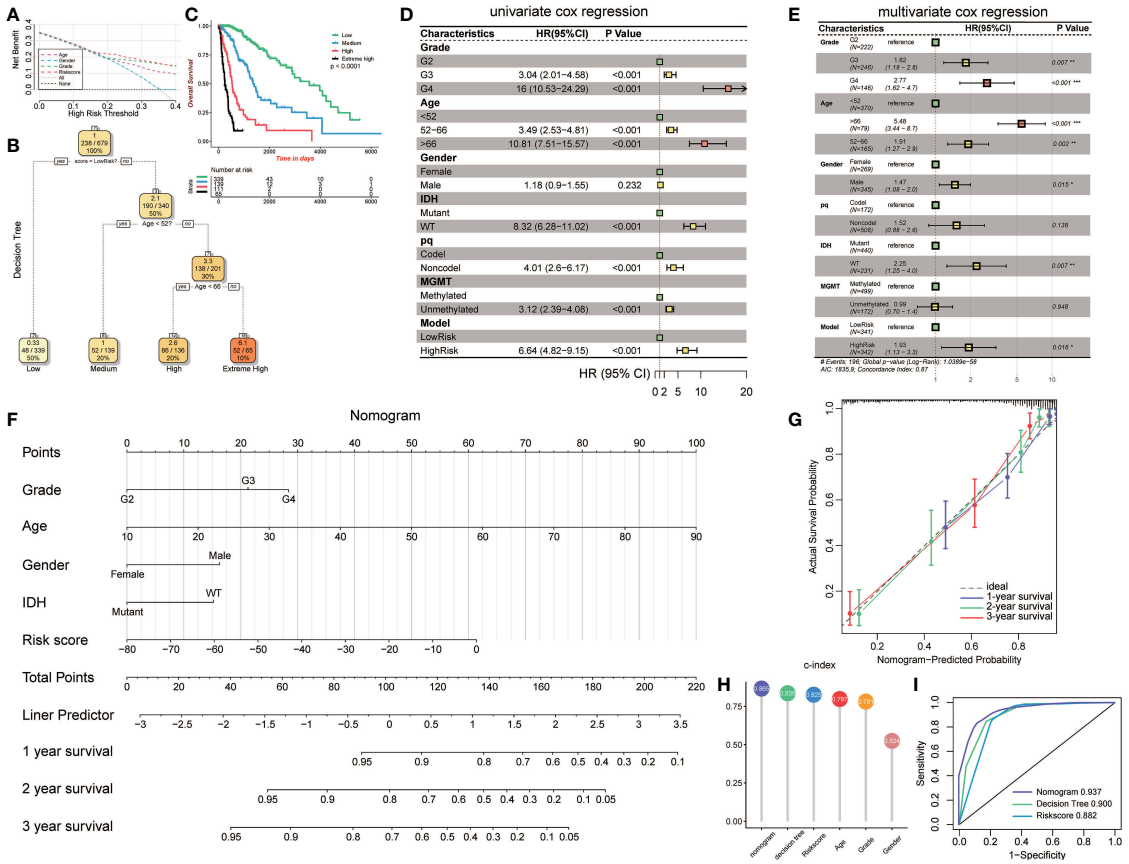

FIGURE 7 | Construction and validation of the clinic-associated model. **(A)** Decision curve analysis (DCA) for age, gender, grade, and risk score, revealing the risk score revealed better survival outcomes than the other variables. **(B)** Patients with risk score and age were used to set up a detailed glioma risk stratification. **(C)** Kaplan-Meier survival analysis of the four precise risk subtypes in the TCGA dataset. **(D)** Forest plot of the univariate Cox proportional-hazards model survival analysis of various parameters. **(E)** Forest plot of multivariate Cox proportional-hazards model survival analysis of various parameters. **(F)** Details of the nomogram. **(G)** Calibration curve showing a high accuracy of the nomogram. **(H)** Comparison of the predictive power of multiple models. **(I)** ROC curve of the nomogram, decision tree, and risk score model in 1 year. HR, hazard ratio; CI, confidence interval. *p<0.05; **p<0.01; ***p <0.001.

TABLE 3 | Univariate Cox regression of clinical features.

Variable	Coef	HR	z	P	CI (lower)	CI (upper)
Histology	−0.27172	0.76207	−4.90692	9.25E-07	0.683692	0.849434
Grade	1.453439	4.277799	13.59881	4.07E-42	3.469318	5.274686
Age	0.068908	1.071338	12.81726	1.31E-37	1.060108	1.082686
Gender	0.165048	1.17945	1.19585	0.231755	0.899909	1.545825
IDH	2.11895	8.322394	14.78035	1.96E-49	6.283733	11.02247
pq	1.388133	4.007361	6.305825	2.87E-10	2.60303	6.169326
MGMT	1.139027	3.123729	8.330238	8.07E-17	2.389379	4.083773
Risk	−1.89371	0.150512	−11.5915	4.55E-31	0.109272	0.207316
Risk score	0.051468	1.052815	16.8548	9.67E-64	1.046533	1.059135

supported our idea since DMPs were enriched in TGF-β, IL-2, TNF-α, NK cells, and B cell receptors.

Epigenetic age acceleration is a new marker for cancer prognosis. We calculated the epigenetic age of each patient. Although the average DNAm age of cluster2 was still lower than that of cluster1, more patients in cluster1 had lower DNAm age than their chronological age. This finding is in concordance with that from earlier studies that decelerated DNAm age may result in poorer prognosis (36, 37). The strong correlation between methylation age and veritable age reveals the stability of the prediction.

We performed an integrative analysis of the TCGA Pan-cancer tumors based on other 31 cancer types. Eventually, eight

cancer types were selected. Clustering based on immune-related methylation probes revealed an important common role of the immune markers, and the exact immune pattern and pathways need further evaluation. Moreover, we tested the signature on other cancers, and the seven cancer types showed affable results. One unanticipated finding was that LIHC was not concluded in clustering, but was well-distributed when tested using the signature. In the meantime, LAML and KIRP were excluded when tested using the signature. We hypothesized that there is a general DNA methylation pattern among these cancers. Thus, more studies are recommended to test this hypothesis.

Univariate Cox regression, Random Forest, and PCA were performed to construct the best prognostic signatures. To elucidate on the five probes' biological roles, we performed GO and GSEA analysis, and the results were highly associated with immune system processes. In detail, four negative coefficient probes (gene) were cg04314652 (NFAT5), cg15734706 (RARG), cg20332503 (ZYX), and cg08985333 (CIITA). We revealed the impact of DNA methylation on gene expression in glioma, and three genes exhibited hypomethylation-upregulated DNA methylation patterns. Immunological processes of the five genes were identified to establish the signature mechanism. Nuclear factor of activated T cell 5 (NFAT5) is involved in neuroinflammation (38), and NFAT5 levels correspond to glioma pathological grade (39). Retinoic acid receptor γ (RARG) belongs to the nuclear receptor superfamily (40), and elevated RARG levels may contribute to an unfavorable outcome in LAML (41). Zyxin (ZYX) has been shown to enhance the invasion of hepatocellular carcinoma (42) and oral squamous cell carcinoma cells (43). Overexpression of ZYX is also involved in invasion and unfavorable prognosis of GBM (44). CIITA, a key regulator of the controlling major histocompatibility complex (MHCII) gene, is regulated by NFAT5 (45). The only positive coefficient probe was cg11701471 (OPRK1). In previous studies, κ-opioid receptors 1 (OPRK1) were shown to suppress lung cancer growth, suggesting a tumor-suppressive gene (46, 47). In summary, all the negative coefficient probes are tumor-genesis, and the positive one is tumor-suppressive. Since a higher risk score indicates poor prognosis, it can be hypothesized that DNA methylation silences its corresponding gene expression by hypermethylating CpG islands, shore, and shelf in the promoter regions or gene body. Previous studies of CIITA and NFAT5 strengthen the reliability of the signature.

We validated the prognostic signature using five GEO databases and the TCGA cohort itself. The risk score was associated with overall OS and PFS time. Moreover, low-risk GBM patients were more sensitive to radiation therapy. A possible explanation might be that radiation therapy activates more antitumor immune cells in higher immune cohorts, such as regulating dendritic cells (DC). Regulated DC recognizes and phagocytoses tumor cells and induces the release of inflammatory factors such as IFN-γ, IL-2, and TNFα from immune cells. Another interesting finding was that LGG patients enjoyed even worse overall survival time after radiotherapy. The benefit of radiotherapy in patients with LGG has long been controversial, and the EORTC 22845 randomized trial showed that median overall survival was similar between the radiotherapy and control groups (48). Combined with our findings, high-dose radiotherapy may lead to contrary effects such as neurotoxicity during the management of LGG patients. In the GSE48462 dataset, we found that in this LGG cohort, 14 (28%) high-risk patients benefited from RT/PCV, while no low-risk patients benefited from RT/PCV, suggesting further studies are needed to evaluate the value of PCV treatment in LGG.

Prediction of prognosis based on epigenetic change is not comprehensive. First, we confirmed that the risk score was a reliable predictor of survival through DCA. We further constructed a decision tree model to improve the risk stratification accuracy. Several factors were put into the machine learning algorithm, and the risk score was selected as a major factor, while age was selected as the secondary factor. The maneuverable decision tree helps clinicians to conveniently evaluate the patient risks. Moreover, we developed a complex nomogram model for a more accurate risk and survival outcome assessment. The nomogram model exhibited the highest concordance index when compared to other models and factors. It also exhibited the highest accuracy when compared to the decision tree and risk score model.

One limitation of our study is that bioinformatic methods were used for all analyses. Given the complicated DNA methylation pattern and intricate immune process, more experiments are needed and there exists abundant room for further progress in determining the pan-cancer immune pattern.

DATA AVAILABILITY STATEMENT

The datasets presented in this study can be found in online repositories. The names of the repository/repositories and accession number(s) can be found in the article/**Supplementary Material**.

AUTHOR CONTRIBUTIONS

ZH, HZ, FF, QC, ZW, YH, ZL, and XZ designed and drafted the manuscript. ZH, HZ, QC, ZD, HC, FF, JX, and ZL wrote figure legends and revised the manuscript. ZH, HZ, JX, and XZ conducted data analysis. All authors contributed to the article and approved the submitted version.

FUNDING

This work was supported by the National Natural Science Foundation of China (Nos. 82073893, 81703622, 81472693, and 81873635), China Postdoctoral Science Foundation (No. 2018M633002), Hunan Provincial Natural Science Foundation of China (No. 2018JJ3838, 2018SK2101), and the Hunan Provincial Health and Health Committee Foundation of China (C2019186).

SUPPLEMENTARY MATERIAL

The Supplementary Material for this article can be found online at: https://www.frontiersin.org/articles/10.3389/fimmu.2021.737650/full#supplementary-material

REFERENCES

1. Ostrom QT, Patil N, Cioffi G, Waite K, Kruchko C, Barnholtz-Sloan JS. CBTRUS Statistical Report: Primary Brain and Other Central Nervous System Tumors Diagnosed in the United States in 2013-2017. *Neuro Oncol* (2020) 22 (12 Suppl 2):iv1–iv96. doi: 10.1093/neuonc/noaa200
2. Ludwig K, Kornblum HI. Molecular Markers in Glioma. *J Neurooncol* (2017) 134(3):505–12. doi: 10.1007/s11060-017-2379-y
3. Lim M, Xia Y, Bettegowda C, Weller M. Current State of Immunotherapy for Glioblastoma. *Nat Rev Clin Oncol* (2018) 15(7):422–42. doi: 10.1038/s41571-018-0003-5
4. Quail DF, Joyce JA. Microenvironmental Regulation of Tumor Progression and Metastasis. *Nat Med* (2013) 19(11):1423–37. doi: 10.1038/nm.3394
5. El Andaloussi A, Lesniak MS. CD4+ CD25+ FoxP3+ T-Cell Infiltration and Heme Oxygenase-1 Expression Correlate With Tumor Grade in Human Gliomas. *J Neurooncol* (2007) 83(2):145–52. doi: 10.1007/s11060-006-9314-y
6. Ooi YC, Tran P, Ung N, Thill K, Trang A, Fong BM, et al. The Role of Regulatory T-Cells in Glioma Immunology. *Clin Neurol Neurosurg* (2014) 119:125–32. doi: 10.1016/j.clineuro.2013.12.004
7. Quail DF, Joyce JA. The Microenvironmental Landscape of Brain Tumors. *Cancer Cell* (2017) 31(3):326–41. doi: 10.1016/j.ccell.2017.02.009
8. Locarno CV, Simonelli M, Carenza C, Capucetti A, Stanzani E, Lorenzi E, et al. Role of Myeloid Cells in the Immunosuppressive Microenvironment in Gliomas. *Immunobiology* (2020) 225(1):151853. doi: 10.1016/j.imbio.2019.10.002
9. Hao X, Luo H, Krawczyk M, Wei W, Wang W, Wang J, et al. DNA Methylation Markers for Diagnosis and Prognosis of Common Cancers. *Proc Natl Acad Sci USA* (2017) 114(28):7414–9. doi: 10.1073/pnas.1703577114
10. Ceccarelli M, Barthel FP, Malta TM, Sabedot TS, Salama SR, Murray BA, et al. Molecular Profiling Reveals Biologically Discrete Subsets and Pathways of Progression in Diffuse Glioma. *Cell* (2016) 164(3):550–63. doi: 10.1016/j.cell.2015.12.028
11. Han L, Yuan Y, Zheng S, Yang Y, Li J, Edgerton ME, et al. The Pan-Cancer Analysis of Pseudogene Expression Reveals Biologically and Clinically Relevant Tumour Subtypes. *Nat Commun* (2014) 5:3963. doi: 10.1038/ncomms4963
12. Wilkerson MD, Hayes DN. ConsensusClusterPlus: A Class Discovery Tool With Confidence Assessments and Item Tracking. *Bioinformatics* (2010) 26 (12):1572–3. doi: 10.1093/bioinformatics/btq170
13. Morris TJ, Butcher LM, Feber A, Teschendorff AE, Chakravarthy AR, Wojdacz TK, et al. ChAMP: 450k Chip Analysis Methylation Pipeline. *Bioinformatics* (2014) 30(3):428–30. doi: 10.1093/bioinformatics/btt684
14. Zhou W, Laird PW, Shen H. Comprehensive Characterization, Annotation and Innovative Use of Infinium DNA Methylation BeadChip Probes. *Nucleic Acids Res* (2017) 45(4):e22. doi: 10.1093/nar/gkw967
15. Teschendorff AE, Marabita F, Lechner M, Bartlett T, Tegner J, Gomez-Cabrero D, et al. A Beta-Mixture Quantile Normalization Method for Correcting Probe Design Bias in Illumina Infinium 450 K DNA Methylation Data. *Bioinformatics* (2013) 29(2):189–96. doi: 10.1093/bioinformatics/bts680
16. Smyth GK. Linear Models and Empirical Bayes Methods for Assessing Differential Expression in Microarray Experiments. *Stat Appl Genet Mol Biol* (2004) 3:Article3. doi: 10.2202/1544-6115.1027
17. Ritchie ME, Phipson B, Wu D, Hu Y, Law CW, Shi W, et al. Limma Powers Differential Expression Analyses for RNA-Sequencing and Microarray Studies. *Nucleic Acids Res* (2015) 43(7):e47. doi: 10.1093/nar/gkv007
18. Yu G, Wang LG, Han Y, He QY. Clusterprofiler: An R Package for Comparing Biological Themes Among Gene Clusters. *Omics* (2012) 16(5):284–7. doi: 10.1089/omi.2011.0118
19. Dong D, Tian Y, Zheng SC, Teschendorff AE. ebGSEA: An Improved Gene Set Enrichment Analysis Method for Epigenome-Wide-Association Studies. *Bioinformatics* (2019) 35(18):3514–6. doi: 10.1093/bioinformatics/btz073
20. Zheng SC, Breeze CE, Beck S, Teschendorff AE. Identification of Differentially Methylated Cell Types in Epigenome-Wide Association Studies. *Nat Methods* (2018) 15(12):1059–66. doi: 10.1038/s41592-018-0213-x
21. Teschendorff AE, Breeze CE, Zheng SC, Beck S. A Comparison of Reference-Based Algorithms for Correcting Cell-Type Heterogeneity in Epigenome-Wide Association Studies. *BMC Bioinf* (2017) 18(1):105. doi: 10.1186/s12859-017-1511-5
22. Newman AM, Liu CL, Green MR, Gentles AJ, Feng W, Xu Y, et al. Robust Enumeration of Cell Subsets From Tissue Expression Profiles. *Nat Methods* (2015) 12(5):453–7. doi: 10.1038/nmeth.3337
23. Lê S, Josse J, Husson F. FactoMineR: An R Package for Multivariate Analysis. *J Stat Software* (2008) 25:1–18. doi: 10.18637/jss.v025.i01
24. Blanche P, Dartigues JF, Jacqmin-Gadda H. Estimating and Comparing Time-Dependent Areas Under Receiver Operating Characteristic Curves for Censored Event Times With Competing Risks. *Stat Med* (2013) 32 (30):5381–97. doi: 10.1002/sim.5958
25. Vickers AJ, Cronin AM, Elkin EB, Gonen M. Extensions to Decision Curve Analysis, a Novel Method for Evaluating Diagnostic Tests, Prediction Models and Molecular Markers. *BMC Med Inf Decis Making* (2008) 8:53. doi: 10.1186/1472-6947-8-53
26. van den Bent MJ, Erdem-Eraslan L, Idbaih A, de Rooi J, Eilers PH, Spliet WG, et al. MGMT-STP27 Methylation Status as Predictive Marker for Response to PCV in Anaplastic Oligodendrogliomas and Oligoastrocytomas. A Report From EORTC Study 26951. *Clin Cancer Res* (2013) 19(19):5513–22. doi: 10.1158/1078-0432.Ccr-13-1157
27. Witt H, Gramatzki D, Hentschel B, Pajtler KW, Felsberg J, Schackert G, et al. DNA Methylation-Based Classification of Ependymomas in Adulthood: Implications for Diagnosis and Treatment. *Neuro Oncol* (2018) 20 (12):1616–24. doi: 10.1093/neuonc/noy118
28. Arber W, Linn S. DNA Modification and Restriction. *Annu Rev Biochem* (1969) 38:467–500. doi: 10.1146/annurev.bi.38.070169.002343
29. Yarus M. Recognition of Nucleotide Sequences. *Annu Rev Biochem* (1969) 38:841–80. doi: 10.1146/annurev.bi.38.070169.004205
30. Feinberg AP, Tycko B. The History of Cancer Epigenetics. *Nat Rev Cancer* (2004) 4(2):143–53. doi: 10.1038/nrc1279
31. Herman JG, Baylin SB. Gene Silencing in Cancer in Association With Promoter Hypermethylation. *N Engl J Med* (2003) 349(21):2042–54. doi: 10.1056/NEJMra023075
32. Egger G, Liang G, Aparicio A, Jones PA. Epigenetics in Human Disease and Prospects for Epigenetic Therapy. *Nature* (2004) 429(6990):457–63. doi: 10.1038/nature02625
33. Klutstein M, Nejman D, Greenfield R, Cedar H. DNA Methylation in Cancer and Aging. *Cancer Res* (2016) 76(12):3446–50. doi: 10.1158/0008-5472.Can-15-3278
34. Yuen GJ, Demissie E, Pillai S. B Lymphocytes and Cancer: A Love-Hate Relationship. *Trends Cancer* (2016) 2(12):747–57. doi: 10.1016/j.trecan.2016.10.010
35. Morvan MG, Lanier LL. NK Cells and Cancer: You can Teach Innate Cells New Tricks. *Nat Rev Cancer* (2016) 16(1):7–19. doi: 10.1038/nrc.2015.5
36. Perna L, Zhang Y, Mons U, Holleczek B, Saum KU, Brenner H. Epigenetic Age Acceleration Predicts Cancer, Cardiovascular, and All-Cause Mortality in a German Case Cohort. *Clin Epigenet* (2016) 8:64. doi: 10.1186/s13148-016-0228-z
37. Yang Z, Wong A, Kuh D, Paul DS, Rakyan VK, Leslie RD, et al. Correlation of an Epigenetic Mitotic Clock With Cancer Risk. *Genome Biol* (2016) 17(1):205. doi: 10.1186/s13059-016-1064-3
38. Jeong GR, Im SK, Bae YH, Park ES, Jin BK, Kwon HM, et al. Inflammatory Signals Induce the Expression of Tonicity-Responsive Enhancer Binding Protein (TonEBP) in Microglia. *J Neuroimmunol* (2016), 295:21-9. doi: 10.1016/j.jneuroim.2016.04.009
39. Yu H, Zheng J, Liu X, Xue Y, Shen S, Zhao L, et al. Transcription Factor NFAT5 Promotes Glioblastoma Cell-Driven Angiogenesis *via* SBF2-AS1/miR-338-3p-Mediated EGFL7 Expression Change. *Front Mol Neurosci* (2017) 10:301. doi: 10.3389/fnmol.2017.00301
40. Chambon P. A Decade of Molecular Biology of Retinoic Acid Receptors. *FASEB J* (1996) 10(9):940–54. doi: 10.1096/fasebj.10.9.8801176
41. Qin YZ, Huang XJ, Zhu HH. Identification of a Novel CPSF6-RARG Fusion Transcript in Acute Myeloid Leukemia Resembling Acute Promyelocytic Leukemia. *Leukemia* (2018) 32(10):2285–7. doi: 10.1038/s41375-018-0095-z
42. Sy SM, Lai PB, Pang E, Wong NL, To KF, Johnson PJ, et al. Novel Identification of Zyxin Upregulations in the Motile Phenotype of Hepatocellular Carcinoma. *Mod Pathol* (2006) 19(8):1108–16. doi: 10.1038/modpathol.3800626
43. Yamamura M, Noguchi K, Nakano Y, Segawa E, Zushi Y, Takaoka K, et al. Functional Analysis of Zyxin in Cell Migration and Invasive Potential of Oral Squamous Cell Carcinoma Cells. *Int J Oncol* (2013) 42(3):873–80. doi: 10.3892/ijo.2013.1761

44. Wen XM, Luo T, Jiang Y, Wang LH, Luo Y, Chen Q, et al. Zyxin (ZYX) Promotes Invasion and Acts as a Biomarker for Aggressive Phenotypes of Human Glioblastoma Multiforme. *Lab Invest* (2020) 100(6):812–23. doi: 10.1038/s41374-019-0368-9
45. Buxadé M, Huerga Encabo H, Riera-Borrull M, Quintana-Gallardo L, López-Cotarelo P, Tellechea M, et al. Macrophage-Specific MHCII Expression is Regulated by a Remote Ciita Enhancer Controlled by NFAT5. *J Exp Med* (2018) 215(11):2901–18. doi: 10.1084/jem.20180314
46. Yamamizu K, Furuta S, Hamada Y, Yamashita A, Kuzumaki N, Narita M, et al. K Opioids Inhibit Tumor Angiogenesis by Suppressing VEGF Signaling. *Sci Rep* (2013) 3:3213. doi: 10.1038/srep03213
47. Yamamizu K, Hamada Y, Narita M. κ Opioid Receptor Ligands Regulate Angiogenesis in Development and in Tumours. *Br J Pharmacol* (2015) 172 (2):268–76. doi: 10.1111/bph.12573
48. van den Bent MJ, Afra D, de Witte O, Ben Hassel M, Schraub S, Hoang-Xuan K, et al. Long-Term Efficacy of Early Versus Delayed Radiotherapy for Low-Grade Astrocytoma and Oligodendroglioma in Adults: The EORTC 22845 Randomised Trial. *Lancet* (2005) 366(9490):985–90. doi: 10.1016/s0140-6736(05)67070-5

Conflict of Interest: The authors declare that the research was conducted in the absence of any commercial or financial relationships that could be construed as a potential conflict of interest.

Publisher's Note: All claims expressed in this article are solely those of the authors and do not necessarily represent those of their affiliated organizations, or those of the publisher, the editors and the reviewers. Any product that may be evaluated in this article, or claim that may be made by its manufacturer, is not guaranteed or endorsed by the publisher.

frontiers in Oncology

ORIGINAL RESEARCH
published: 10 November 2021
doi: 10.3389/fonc.2021.734853

Disulfiram Improves the Anti-PD-1 Therapy Efficacy by Regulating PD-L1 Expression *via* Epigenetically Reactivation of IRF7 in Triple Negative Breast Cancer

Xin Zheng, Zijian Liu, Mi Mi, Qiuyue Wen, Gang Wu and Liling Zhang *

Cancer Center, Union Hospital, Tongji Medical College, Huazhong University of Science and Technology, Wuhan, China

OPEN ACCESS

Edited by:
Mingzhu Yin,
Central South University, China

Reviewed by:
Mien-Chie Hung,
China Medical University, Taiwan
Steven F. Gameiro,
McMaster University, Canada

***Correspondence:**
Liling Zhang
lily-1228@hotmail.com

Specialty section:
This article was submitted to Cancer Immunity and Immunotherapy, a section of the journal Frontiers in Oncology

Received: *01 July 2021*
Accepted: *20 October 2021*
Published: *10 November 2021*

Citation:
Zheng X, Liu Z, Mi M, Wen Q, Wu G and Zhang L (2021) Disulfiram Improves the Anti-PD-1 Therapy Efficacy by Regulating PD-L1 Expression via Epigenetically Reactivation of IRF7 in Triple Negative Breast Cancer. Front. Oncol. 11:734853. doi: 10.3389/fonc.2021.734853

Immune checkpoint blockade (ICB), particularly programmed death 1 (PD-1) and its ligand (PD-L1), has shown considerable clinical benefits in patients with various cancers. Many studies show that PD-L1 expression may be biomarkers to help select responders for anti-PD-1 treatment. Therefore, it is necessary to elucidate the molecular mechanisms that control PD-L1 expression. As a potential chemosensitizer and anticancer drug, disulfiram (DSF) kills tumor cells *via* regulating multiple signaling pathways and transcription factors. However, its effect on tumor immune microenvironment (TIME) remains unclear. Here, we showed that DSF increased PD-L1 expression in triple negative breast cancer (TNBC) cells. Through bioinformatics analysis, we found that DNMT1 was highly expressed in TNBC tissue and PD-L1 was negatively correlated with IRF7 expression. DSF reduced DNMT1 expression and activity, and hypomethylated IRF7 promoter region resulting in upregulation of IRF7. Furthermore, we found DSF enhanced PD-L1 expression *via* DNMT1-mediated IRF7 hypomethylation. In *in vivo* experiments, DSF significantly improved the response to anti-PD-1 antibody (Ab) in 4T1 breast cancer mouse model. Immunohistochemistry staining showed that granzyme B+ and CD8+ T cells in the tumor tissues were significantly increased in the combination group. By analyzing the results of the tumor tissue RNA sequencing, four immune-associated pathways were significantly enriched in the DSF joint anti-PD-1 Ab group. In conclusion, we found that DSF could upregulate PD-L1 in TNBC cells and elucidated its mechanism. Our findings revealed that the combination of DSF and anti-PD-1 Ab could activate TIME to show much better antitumor efficacy than monotherapy.

Keywords: disulfiram, triple negative breast cancer, immune checkpoint blockade, PD-L1, DNMT1, IRF7

INTRODUCTION

Breast cancer (BC) is one of the most frequent diseases and the leading cause of cancer death among females (1). Although molecular targeted therapy such as trastuzumab, pertuzumab, lapatinib has achieved good curative effects on human epidermal growth factor receptor-2 (HER-2)-positive BC, there is limited efficacious treatment options for triple negative BC (TNBC) (2). TNBC (progesterone receptor, estrogen receptor, and HER-2 negative BC) is an aggressive subtype of BC that accounts for 15–20% of BC patients, with very poor prognosis (3). There is an urgent need to explore novel therapeutic strategies to improve the clinical outcomes of TNBC patients.

Over the last decades, immunotherapy, especially immune checkpoint inhibitors, has shown considerable clinical benefits in patients with various cancers (4–6). T cell surface expressing PD-1 plays a vital role in negatively regulating the functions of antitumor T cell effector upon interacting with its PD-L1 expressed on tumor cell surface. In the tumor microenvironment (TME), inducing PD-L1 expression can lead to PD-1-mediated T cell exhaustion, thus suppressing the antitumor cytotoxic T cell response (7). Such negative interaction can be inhibited by anti-PD-1/anti-PD-L1 antibodies (Abs). PD-1/PD-L1 checkpoint blockades have been approved by the FDA in various cancers, including lung cancer, Hodgkin lymphoma, and BC (8–10). Although pembrolizumab has been approved in TNBC, the overall response rate was only 18.5%, reported in KEYNOTE-012 trial (11). Therefore, improving the therapeutic effect of anti-PD-1 antibody (Ab) in TNBC patients is urgent and valuable.

Numerous studies have identified biomarkers predicting response of anti-PD-1 therapy, and found that tumor mutational load, dense CD8+ T-cell infiltrates, and PD-L1 expression may be biomarkers to help select responders to anti-PD-1 Ab (12–15). In the TME, PD-L1 expression is regulated at epigenetic, transcriptional, and post-transcriptional levels. At epigenetic level, inhibiting DNA methylation upregulates the expression of PD-L1. Several studies reported that DNA methyltransferase (DNMT) inhibitors decitabine and azacytidine could increase PD-L1 expression level and enhance anti-PD-1 Ab therapeutic efficacy in tumor cells (16–18). At transcriptional level, several transcriptional factors, such as NF-κB, STAT3, and interferon regulatory factor 7 (IRF7), are involved in PD-L1 expression (19, 20). IRF7, a master regulator of type I interferon response, can upregulate PD-L1 expression through PD-L1 promoter binding. Recent study reported that hypomethylating IRF7 by decitabine resulted in elevated levels both IRF7 and PD-L1 (21). Restoration of IRF7 can also affect the activation of immune cells, leading to a remodeling of TME (21–23). As such, we may infer that regulation of DNMT1/IRF7/PD-L1 could sensitize TNBC cells through inducing PD-L1 by DNMT1 inhibitors.

Besides decitabine and azacytidine are DNMT inhibitors, which have won FDA approval for treating myelodysplastic syndromes, disulfiram (DSF) also acts as a DNMT inhibitor. DSF has been employed to treat alcohol use disorders for over sixty years. Increasing evidences indicate that DSF can be repurposed as a novel anti-cancer drug by regulating tumor cell growth, angiogenesis, apoptosis, epithelial-to-mesenchymal transition (EMT) and stemness (24–26). Lin and colleagues reported that DSF monotherapy inhibited DNMT1 catalytical activity and resulted in inhibition of prostate cancer growth (27). However, Dastjerdi and colleagues failed to confirm the DNA demethylation effect of DSF in pancreatic cancer cell line (28). The discrepancy of DSF on DNMT activity perhaps is due to different cancer types or others. Whether DSF has potent DNA demethylation function in TNBC needs to be further explored. Furthermore, Zhou et al. reported that DSF combined with copper upregulated PD-L1 expression by inhibiting PARP1 activity in hepatocellular carcinoma (11). Moreover, a recent study demonstrated that DSF combined with an anti-PD-1 Ab synergistically suppressed tumor growth by targeting FROUNT (also known as NUP85) function and elevated the number of CD8+ T cells in the tumors (29). Accordingly, DSF could enhance the responsiveness to immune checkpoint blockade (ICB) therapy; however, the underlying mechanism remains unclear (30).

DNMT1 plays an essential role in tumorigenesis of TNBC involving suppression of estrogen receptor expression, promotion of epithelial-to-mesenchymal transition (EMT), and induction of stemness in TNBC (31). Although targeting DNMT1 in TNBC by azacytidine did not show sufficient efficacy (32, 33), combination of decitabine and anti-PD-1 Ab may sensitize TNBC patients for anti-PD-1 therapy by inducing the expression of PD-L1, and the regimen is currently investigated in the neoadjuvant setting (NCT02957968). In this study, we explored whether epigenetic regulation associated with DNA methylation could underlie increasing PD-L1 expression by DSF. We found that DSF inhibited DNMT1 activity, thus leading to IRF7 hypomethylation and PD-L1 upregulation in TNBC cell lines. We further observed that co-treatment of DSF and anti-PD-1 Ab increased CD8+ tumor infiltrating lymphocytes (TIL) and enhanced the therapeutic effects of ICB *in vivo*.

RESULTS

DSF Inhibits DNMT1 Expression and Activity in TNBC Cells

The mRNA expression of DNMT1 was remarkably higher in TNBC/basal-like subtype (BLS; n=135) than in normal breast tissue (NBT; n=112; p=3.00×10−36) based on Gene Expression Profiling Interactive Analysis 2 (GEPIA2) in **Figure 1A**. To investigate the DNA demethylation effect of DSF in TNBC cell lines, we tested the protein levels of DNMT1 in human BT-549 and MDA-MB-231 cell lines exposed to DSF at different does for 48 h by western blot. As shown in **Figures 1B, C**, the DNMT1 expression was significantly reduced by DSF. At transcription level, a consistent phenomenon was observed in human MDA-MB-231 cells and BT-549 cells exposed to the indicated concentrations of DSF for 48 h in **Figure 1D**. Further experiments showed that the activity of DNMT was also

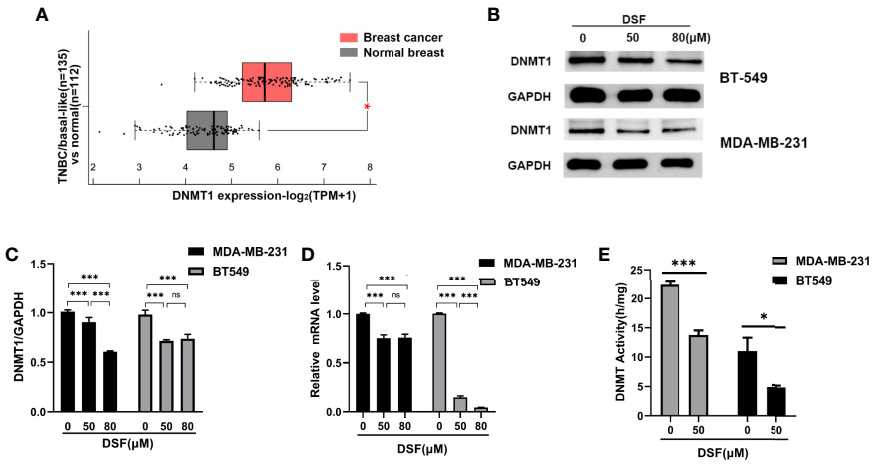

FIGURE 1 | DSF inhibits DNMT1 expression and activity *in vitro*. **(A)** Gene expression analysis of DNMT1 using GEPIA2 database based on the TCGA database. Box plots represent the gene expression level in terms of log2 (TPM+1) in the tumor (TNBC/basal-like subtype, red, n=135) and normal breast tissue (gray, n=112) samples, respectively. **(B)** DNMT1 expression in human BT-549 and MDA-MB-231 cells by Western blotting after treatment with different doses of DSF for 48 h. **(C)** Quantitative analysis of DNMT1 expression after different doses of DSF for 48 h through ImageJ intensity measurements. **(D)** The relative mRNA expression levels of DNMT1 in human MDA-MB-231 cells and BT-549 cells treated with indicated concentration of DSF for 48 h. **(E)** DNMT1 enzyme activity assays in human MDA-MB-231 and BT-549 cells treated with indicated concentration of DSF for 48 h. *p < 0.05, ***p < 0.001. ns, no statistic significance.

inhibited by DSF in BT-549 and MDA-MB-231 cells exposed to DSF for 48 h (**Figure 1E**).

DSF Upregulates IRF7 by Hypomethylating IRF7 in TNBC Cells

We explored whether DSF can affect the methylation level of IRF7 by affecting DNMT1, thereby regulating its expression. First, we analyzed the hypomethylation status of IRF7 promoter regions assessed by bisulfite sequencing analysis in the human MDA-MB-231 cells and BT-549 cells exposed to DSF (**Figure 2A**). To unravel the underlying relationship between the expression and the DNA methylation level of IRF7 in BC, we analyzed data from 1,217 patients in TCGA. The tumor samples are divided into high methylation groups (n=24) and low methylation groups (n= 206). In **Figure 2B**, the violin-box plot revealed that IRF7 mRNA expression was negatively correlated with its DNA methylation level. Gene expression analysis of IRF7 using GEPIA2 database based on the TCGA and GTEx database. Box plots represent the gene expression level in terms of log2 (TPM+1) in the tumor (TNBC/basal-like subtype, red, n=135) and normal breast tissue (gray, n=291) samples, respectively (**Figure 2C**). As presented in **Figure 2D**, the results showed that there was a negative correlation between IRF7 mRNA expression and DNA-methylated CpG islands in the gene body region, especially the promoter region. The immunoblot results revealed that the protein levels of IRF7 were upregulated in human BT549 cells and MDA-MB-231 cells exposed to DSF at different doses for 48 h (**Figures 2E, F**). Next, real-time PCR (RT-PCR) was conducted to determine the mRNA expression of IRF7. Notably, the expression level of IRF7 was remarkably upregulated in human MDA-MB-231 cells and BT-549 cells exposed to the indicated concentration of DSF for 48 h (**Figure 2G**).

DSF Increases PD-L1 Expression in TNBC Cell Lines

Type I interferon regulated by IRFs can induce PD-L1 expression (34). We observed that the mRNA expression of PD-L1 was positively associated with IRF7 in BC patients from TCGA database (R=0.21, p<0.001) in **Figure 3A**. Human BT-549 and MDA -MB-231 cells were exposed to DSF for 48 h at doses 50 and 80 μM. DSF treatments significantly increased surface PD-L1 level and induced a twofold increase in PD-L1 levels. Flow cytometry and immunoblotting showed that PD-L1 protein expression was upregulated in the human MDA-MB-231 and BT549 cells after DSF treatment in **Figures 3B–E**. In human BT-549 cells, RT-PCR analysis further indicated that DSF treatment upregulated the mRNA expression of PD-L1 (**Figure 3F**), suggesting that DSF controls PD-L1 expression at the transcriptional levels. Upregulation of PD-L1 surface expression was found in human BT-549 cell line treated with DSF. Collectively, these findings show that DSF can upregulate the transcription and surface expression of PD-L1 in TNBC cell lines.

DSF Regulates PD-L1 Expression Through IRF7

To investigate if DSF regulated PD-L1 through IRF7 in TNBC cell lines, we then detected whether the human BT-549 and MDA-MB-231 cells transfected with siRNA-IRF7 can significantly attenuate the upregulation of PD-L1 caused by DSF treatment in membrane protein level (**Figure 4A**). Next, the mRNA expression of PD-L1 was quantified by RT-PCR after DSF/si-RNA-IRF7 treatment. The results showed that when combined with si-RNA-IRF7, the upregulating effects of DSF on PD-L1 were significantly reduced. The level of PD-L1

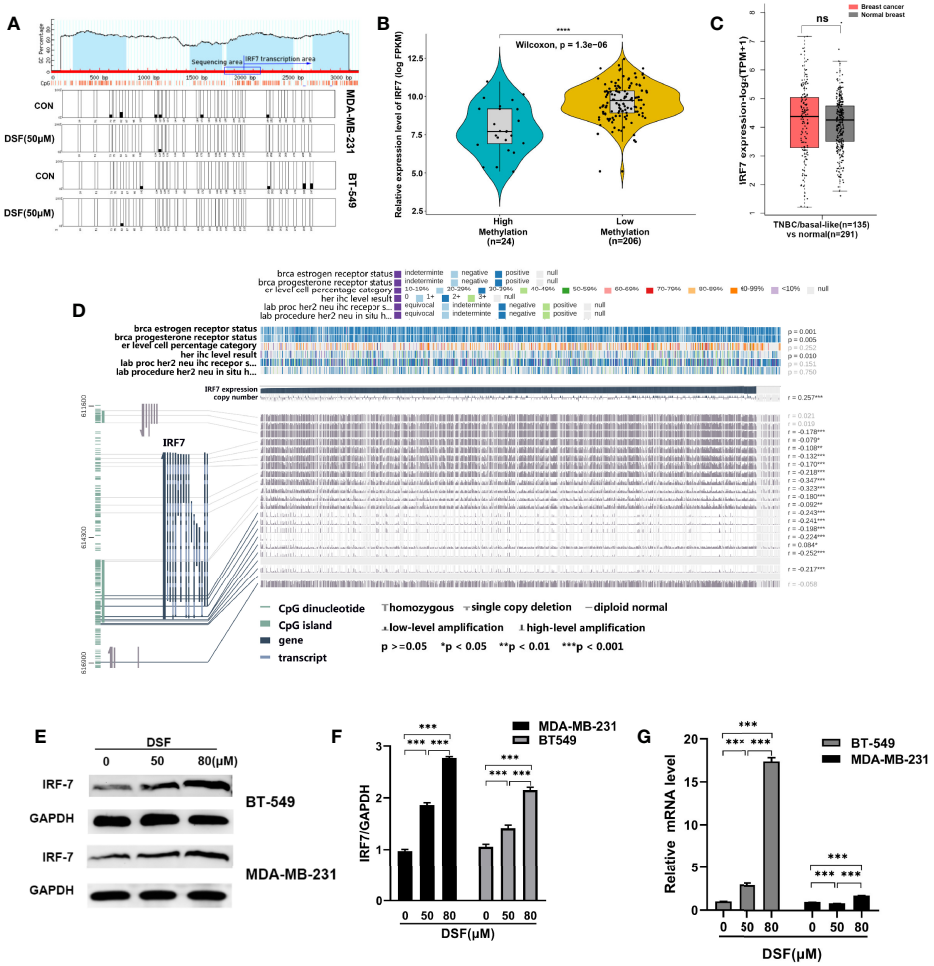

FIGURE 2 | DSF upregulates IRF7 by hypomethylating IRF7. **(A)**The hypomethylation status of IRF7 promoter regions assessed by bisulfite sequencing analysis in the human MDA-MB-231 cells and BT-549 cells treated with DSF (50 μM) for 48 h. **(B)** The negative relationship between the mRNA expression of IRF7 and the methylation level of IRF7. The samples in TCGA are divided into high methylation groups (green, n=24) and low methylation groups (yellow, n= 206). **(C)** Gene expression analysis of IRF7 using GEPIA2 database based on the TCGA and GTEx database. Box plots represent the gene expression level in terms of log2 (TPM+1) in the tumor (TNBC/basal-like subtype, red, n=135) and normal breast tissue (gray, n=291) samples, respectively. **(D)** Visualization of TCGA data for IRF7 expression in 1,217 patients using MEXPRESS. The samples are ordered by their expression value. This view shows the relationship between IRF7 expression and methylation around CpG island and promoter region, clinical features, as well as CNVs. Statistical significance was indicated in the right side. **(E)** IRF7 expression in human BT-549 and MDA-MB-231 cells by Western blotting after treatment with different doses of DSF for 48 h. **(F)** Quantitative analysis of IRF7 expression after different doses of DSF for 48 h through ImageJ intensity measurements. **(G)** The relative mRNA expression levels of IRF7 in human MDA-MB-231 cells and BT-549 cells treated with indicated concentration of DSF for 48 h. ***p < 0.001, ****p < 0.0001. ns, no statistic significance.

transcription was significantly inhibited after knocking down IRF7 (**Figure 4B**). Western blot was applied to verify that si-RNA-IRF7 can cancel PD-L1 upregulation by DSF at the total protein level (**Figure 4C**). These results implicated that the regulation effects of DSF on PD-L1 was mediated by IRF7.

Combination of Anti-PD-1 Therapy With DSF Improved Antitumor Activity

Increasing PD-L1 expression could improve the response to PD-1 blockade therapy. Thus, we explored combined efficiency of anti-PD-1 Ab and DSF *in vivo*. The schedule of animal experiments was shown in a flowchart (**Figure 5A**). The results showed that DSF reduced the tumor burden moderately, anti-PD-1 Ab inhibited tumor growth slightly, and the co-treatment strategy exhibited higher antitumor efficacy than each treatment alone (**Figures 5B, C**). In addition, mice can tolerate this combination treatment well. Immunohistochemistry (IHC) analysis demonstrated that both PD-L1 expression was upregulated in the DSF group as well as the DSF and anti-PD-1 Ab co-treatment group, while the population of tumor-infiltrating CD8+ T cells was downregulated in the tumor tissues of mice treated with DSF alone. Furthermore, the population of granzyme B+, CD8+ in the tumor tissue was significantly increased in the combination group, suggesting

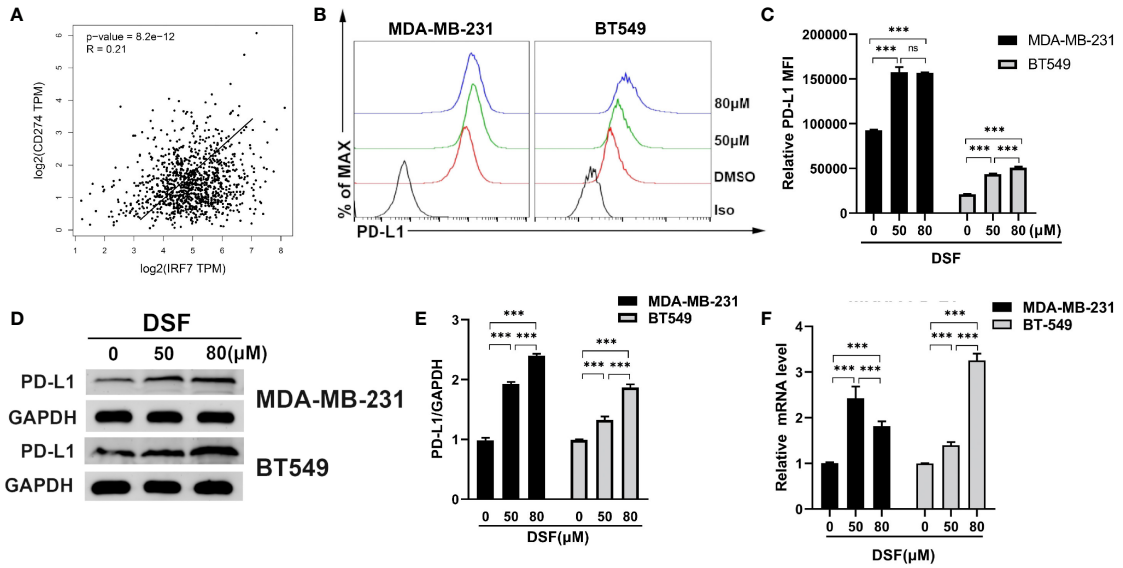

FIGURE 3 | DSF increases PD-L1 expression *in vitro*. **(A)** The positive relationship between the mRNA expression of PD-L1 and IRF-7 in breast cancer. **(B)** Flow cytometry result of surface level of PD-L1 on MDA-MB-231 cell and BT-549 cell treated with different doses of DSF for 48 h. **(C)** The quantification of relative mean fluorescence intensity (MFI) of PD-L1 on MDA-MB-231 cell and BT-549 cell treated with different doses of DSF for 48 h. **(D)** PD-L1 protein expression after DSF treatment. MDA-MB-231 and BT-549 cells were treated with different doses of DSF for 48 h, and PD-L1 protein levels were analyzed by Western blotting. **(E)** Quantitative analysis of PD-L1 expression after different doses of DSF for 48 h through ImageJ intensity measurements. **(F)** The relative mRNA expression levels of PD-L1 in human MDA-MB-231 cells and BT-549 cells treated with indicated concentration of DSF for 48 h. ***p < 0.001. ns, no statistic significance.

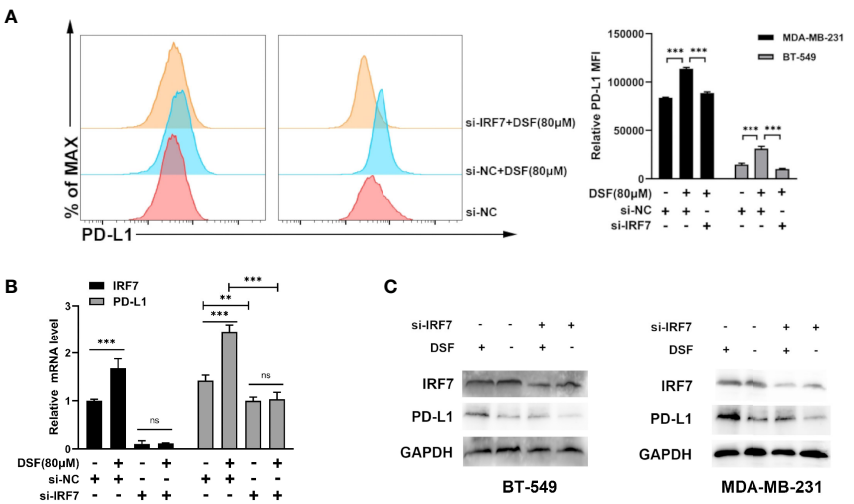

FIGURE 4 | DSF regulates PD-L1 expression through IRF7. **(A)** The MDA-MB-231 cell and BT-549 cell transfected with siRNA-IRF7 were treated with DSF for 48 h, and PD-L1 expression was measured by flow cytometry analysis. Right panel, quantification of relative MFI. **(B)** The mRNA expression level of IRF7 and PD-L1 in the MDA-MB-231 cell transfected with siRNA-IRF7 or siRNA-NC after the treatment of indicated concentration of DSF for 48 h. **(C)** The protein level of IRF7 and PD-L1 in MDA-MB-231 cell and BT-549 cell treated with siRNA-IRF7 or treated with siRNA-IRF7 or siRNA-NC were measured by western blotting after treatment with indicated doses of DSF for 48 h. **p < 0.01, ***p < 0.001. ns, no statistic significance.

that the combined treatment could improve T cell activities in mice. Taken together, these findings illustrated that DSF combined with anti-PD-1 Ab had potential therapeutic benefits (**Figures 5D, F**). Finally, we detected the expression of DNMT1 and IRF7 in mice tissues. DNMT1 was downregulated and IRF7 upregulated in the DSF group and the DSF and anti-PD-1 Ab co-treatment group, which was consistent with the results *in vitro* (**Figures 5E, F**).

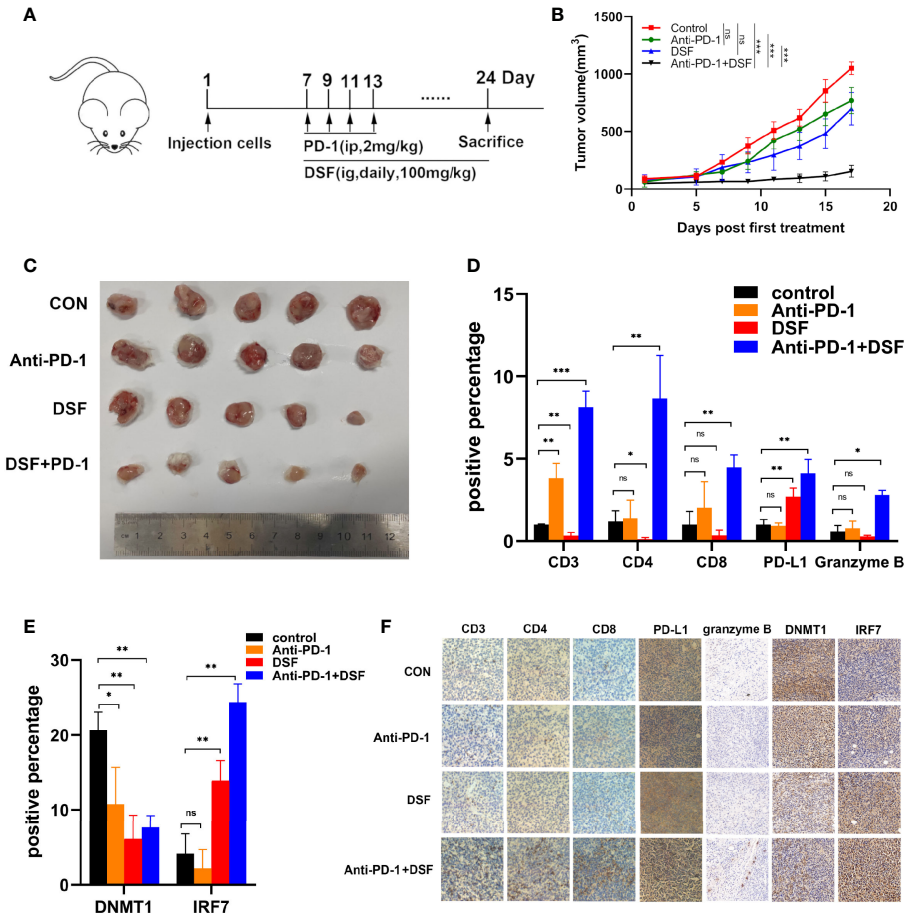

FIGURE 5 | The combination of anti-PD-1 therapy with DSF improves antitumor activity. **(A)** BALB/c mice were inoculated s.c. with 4T1 cells. Seven days after inoculation, mice began to receive DSF (i.g., daily, 100 mg/kg), anti-PD-1 blocking antibodies (i.p., four times, 2 mg/kg), a combination of reagents or solvent control as indicated. **(B)** Representative photographs of 4T1 tumor of the mice after treatment with DSF and/or anti-PD-1 blocking antibody. **(C)** 4T1 implanted tumor-bearing mice were randomly enrolled in different treatment groups as indicated. For each treatment group, tumor volumes were measured every 3 days and plotted individually. **(D)** The positive percentage of CD3, CD4, CD8, PD-L1, and granzyme B in 4T1 tumors. **(E)** The positive percentage of DNMT1 and IRF7 in 4T1 tumors. **(F)** Immunohistochemical staining for CD3, CD4, CD8, PD-L1, granzyme B, DNMT1, and IRF7 in 4T1 tumors. *p < 0.05, **p < 0.01, ***p < 0.001. ns, no statistic significance.

The Modulation of TIME in the Co-Combination of DSF and the Anti-PD-1 Ab

To further explore the effects of DSF and anti-PD-1 blocking Ab co-treatment on the immune microenvironment in 4T1 mouse xenograft tumor model, the expression profiles of immune microenvironment-related genes in the four groups were analyzed by RNA-seq. Notably, the gene expression profile of DSF and anti-PD-1 Ab co-treatment group was significantly different from other three groups (**Figure 6A**). For further validation of DSF and anti-PD-1 blocking Ab co-treatment as a potential immune regulator, we measured the tendency of residential immune cells in different treatment groups by calculating the degree of immune infiltration through MCP counter in R. We found the tumors in DSF group were in a low immune activation state (**Figure 6B**). This might be due to the upregulated expression of PD-L1 by DSF in tumor cells resulted in an impaired T cell function. To further explore the potential molecular mechanism of DSF regulating tumor immune function, the GO and KEGG pathway enrichment analysis was done to reveal the inactive state of immune-associated pathways (**Figure 6C**), such as Th1 and Th2 cell differentiation (Q<0.01), as well as antigen processing and presentation (Q<0.01). We speculated that the co-treatment of DSF and anti-PD-1 Ab can overcome the immunological side effects caused by DSF. To reveal the differences in biological function between the anti-PD-1 Ab group and the DSF and anti-PD-1 Ab co-treatment group, gene set enrichment analysis (GSEA) was performed (**Figure 6D**). The results indicated that four pathways (i.e., Th1 and Th2 cell differentiation, antigen processing and presentation, natural killer cell-mediated cytotoxicity, and T cell receptor signal transduction) were significantly enriched in the combination groups, whereas no pathway was markedly enriched in anti-PD-1 blocking Ab groups (P<0.05).

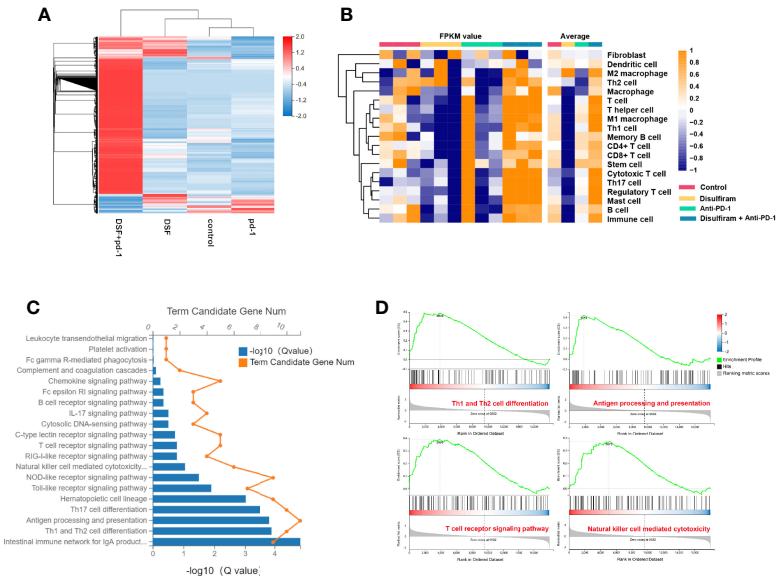

FIGURE 6 | The modulation of tumor immune microenvironment in the combination of DSF and anti-PD-1 therapy. **(A)** Heat map shows gene expression profiles of a selected list of the immune microenvironment showing fold changes in the groups of control, DSF, anti-PD-1 antibody, combination. **(B)** The MCP counter algorithm was utilized to analyze the degree of infiltration of immune cells with mRNA expression in the groups of control, DSF, pd-1, combination. **(C)** The Gene ontology (GO) and Kyoto Encyclopedia of Genes and Genomes (KEGG) functional enrichment analyses of mRNAs in the groups of control *vs* DSF. **(D)** KEGG functional enrichment analysis of the anti-PD-1 blocking antibody groups and the combination of DSF and the anti-PD-1 blocking antibody groups based on GSEA.

MATERIALS AND METHODS

Cell Culture

Human BC cell lines BT-549, MDA-MB-231 and mouse BC cell line 4T1 were supplied by ATCC. BT549 was cultured in RPMI 1640 (Thermo Scientific HyClone, USA), while MDA-MB-231 and 4T1 were cultured in DMEM (Thermo Scientific HyClone) containing 1% penicillin-streptomycin and 10% fetal bovine serum (FBS), followed by incubation in an atmosphere of 5% CO2 at 37°C.

Reagents and Abs

DSF was obtained from Sigma (USA) and then dissolved in DMSO. siRNA of IRF7 (5′-TCGAGTGCTTCCTTATGGA- 3′) (RiboBio, Guangzhou, China). Anti-DNMT1, IRF7, PD-L1, granzyme B, CD3, CD4, CD8, and GAPDH Abs were obtains from ABclonal (Wuhan, China). PE-conjugated PD-L1 Ab were obtained from BioLegend (San Diego, CA, USA). The DNMT Activity/Inhibition Assay Ultra Kit (Colorimetric) was purchased from EpiGentek (USA). The anti-PD-1 blocking Ab were obtained from Innovent Biologics (China).

Immunoblotting

The cells were rinsed twice with pre-cold PBS and lysed in RIPA Buffer for 15 min, followed by centrifugation (15,000 rpm, 15 min, 4°C). Total protein content was measured using the BCA kit (Beyotime). After separation on 10% SDSPAGE, the samples were transferred onto a PVDF membrane. Subsequently, the membrane was inhibited with 5% skimmed milk in 0.1% TBST for 1 h, and then exposed to primary Abs at 4°C. On the next day, the membranes were rinsed thrice with TBST for 15 min and exposed to the corresponding secondary Ab (1:4,000 dilution, Servicebio, Wuhan, China) for 1 h. After washing, the protein blots were detected using a SuperSignal West Pico Chemiluminescent Substrate (Pierce, USA). GAPDH was employed as an internal control for normalization.

RT-PCR

Total RNA was extracted with Total RNA Kit I (Omega, USA). cDNA synthesis was conducted with SYBR® Premix Ex TaqTM II (Takara Bio, Japan) by following the manufacturer's protocols. RT-PCR was performed on a Step One Plus RT-PCR system (Applied Biosystems) using SYBR Green Mastermix (Takara Bio). The sequences of the primers used are as follows: DNMT1 F: 5′5-CGGCAGACCATCAGGCATTCTAC-3′ and R: 5′-CACACC TCACAGACGCCACATC-3′; IRF7 F: 5′-CTCCTTGGAG AGATCAGCAG-3′, and R: 5′-CAGCGG-AAGTTGGTTTTCC-3′; PD-L1 F: 5′-GCTGCACTAATTGTCTATTG-GG-3′ and R: 5′-CACAGTAATTCGCTTGTAGTCG-3′; GAPDH F: 5′-ACCA CAGTCCATGCCATCAC-3′ and R: 5′-TCCACCACCCT GTTGCTGTA-3′.

Flow Cytometric Analysis

The harvested cells were incubated with PE-conjugated PD-L1 Ab (BioLegend) for 30 min at 4°C, rinsed twice with 4°C PBS, evaluated with flow cytometry, and analyzed by FACSDiva Software (BD Bioscience, NJ, USA).

Bisulfite Sequencing PCR

MDA-MB-231 and BT-549 cells (1×10^5/wells) were grown on 6 cm dishes for 24 h, and then exposed to vehicle or the corresponding drugs for 48 h. Then, genomic DNA was extracted, followed by bisulfite treatment using the Qiagen EpiTect kit. PCR cycle (98°C for 30 s; followed by 35 cycles of 98°C for 10 s, 60°C for 30 s, and 72°C for 10 s; 72°C for 2 min; 4°C hold) was conducted with Q5 Hot Start High-Fidelity Master Mix (NEB). Methyl Primer Express™ v1.0 (ThermoFisher) was used to design primer sequences for IRF7 promoter region (F: 5′-TTGGGTTGTAGTGGAGTGGTTTTATT-3′; R: 5′-CATCTCTCAAACTCCCCCAACTCTT-3′). The PCR products were detected through electrophoresis and purified by Gel and PCR Clean-up System (Promega). After purification, Zero Blunt™ TOPO™ PCR Cloning Kit (Invitrogen) was used to insert the products into pCR™4Blunt-TOPO® Vector. Lastly, Sanger sequencing (Sangon) was carried out.

Data Collection and Methylation and Copy Number Variation Analysis

The gene expression RNAseq data (1,104 tumor tissues and 113 normal tissues) of the cohort: Genomic Data Commons Cancer Genome Atlas-Breast Cancer (GDC TCGA-BRCA) were obtained from the https://xenabrowser.net/datapages/. Total BC specimens were ordered according to methylation score levels. The beta-value cutoff ranges for hypermethylation and hypomethylation were 0.7–0.5 and 0.3–0.25, respectively (35, 36). R 3.6.0 was used to analyze the relationship between the level of IRF7 methylation and transcription. MEXPRESS is an easy-to-use tool for visualizing gene expression, DNA methylation, clinical TCGA data, and the relationship among them (37). Given the important effects of methylation and CNVs on gene expression, MEXPRESS was used to explore the association between IRF7 expression and methylation/CNVs.

Gene Correlation and Gene Expression Analysis

GEPIA database (http://gepia.cancer-pku.cn/index.html) was employed to verify the significant relation between IRF7 and PD-L1, and the Pearson correlation was used to analyze the correlation between the two genes. The gene transcript expression in TNBC/basal-like compared with normal breast cases in TCGA and GTEx data cohorts by GEPIA2 (http://gepia2.cancer-pku.cn/). The p-value were set as 0.01.

siRNA Transfection

siRNA targeting IRF7 was supplied by RiboBio (China). After transfection with siRNA (50 nM), the cells were analyzed by GenMute transfection reagent (SL100568; SignaGen Laboratories, China) as per the manufacturer's protocol.

Animal Experiments

BALB/c mice (4–6 weeks old, female) were procured from Beijing HFK Bioscience (China) and maintained under SPF conditions in accordance with the animal care guidelines of Huazhong University of Science and Technology (HUST). The experimental protocol was approved by the Ethical Committee of HUST. 4T1 cells (1×10^6) were subcutaneously transplanted into the right flank of mice. The tumor-bearing mice were randomly categorized into four groups (n = 5/group): control; anti-PD-1 blocking Ab i.p.; DSF p.o; anti-PD-1 blocking Ab + DSF. Tumor dimension was assessed by vernier caliper, and tumor volume was calculated as follows: $0.5\times width^2\times length$. After 28 days, the mice were sacrificed, and the subcutaneous tumors was isolated, recorded, and subsequently analyzed. DSF (100 mg/kg) was administered daily *via* the p.o. route starting from day 7 after tumor implantation and continuously for 3 weeks. Anti-PD-1 blocking Ab (200 μg; BE101, BioXCell) was administered i.p. every other day for four times starting from day 7 after tumor implantation. The mice in control group were treated with solvent (5% Tween 80, 30% PEG300, and 2% DMSO). Tumor size was recorded using a digital caliper every 3 days and calculated as follows: $0.5\times width^2\times length$.

Staining of Tumor Tissue Sample

4T1 xenografted tumors in BALB/c mice were formalin-fixed and embedded in paraffin. Briefly, after deparaffinization, rehydration, and antigen retrieval, tissue sections were exposed to primary antibody (DNMT1, IRF7, PD-L1, granzyme B, CD3, CD4, or CD8). Then, the sections were exposed to biotinylated goat-anti-mouse IgG secondary antibody and streptavidin-conjugated HRP, and finally developed with 3,3′-diaminobenzidine (DAB). Images were collected using a high-resolution slide scanning system (3DHISTECH Ltd, Pannoramic MIDI). Image-pro Plus 6.0 software (Media Cybernetics, Inc., Rockville, MD, USA) was used to select the same brown color as the unified standard for judging the positivity of all photos, and the positive area of each photo was obtained by analyzing each photo.

RNA Deep Sequencing

Total RNA was isolated from the 4T1 xenografted tumors tissue sample using TRIzol Reagent (Invitrogen, USA), and then subjected to RNA deep sequencing with MGISEQ2000 platform at Beijing Genomics Institute (BGI, China). The obtained sequencing reads were expressed as the FPKM (fragments per kilobase of exon per million reads) for each transcript. KEGG and single sample GSEA (ssGSEA) analyses were described in the previous study (38). The R-3.4.3 software tools were used to perform bioinformatics analysis and generate figures.

Statistical Analysis

The data were shown as mean ± S.E. Statistical tests were performed by GraphPad Prism v8.0 and R language v3.4.3. Unpaired Student's t-test ($n<30$) and Wilcoxon test ($n>30$) were used to compare the difference between two groups. Level of significance was set as $p<0.05$. The Pearson correlation was used to analyze the correlation between the two genes.

DISCUSSION

Despite anti-PD-1 therapy has shown promising clinical benefits in patients with TNBC, a significant fraction of patients remains

unresponsive to this therapy. The key to improve the anti-PD-1 therapy is the formation of combination therapies (39). Accumulating evidences have indicated that altered PD-L1 expression by small molecules can modify the efficacy of anti-PD-1 therapy in preclinical phase (40–42). In this work, as **Figure 7** shows, we found that DSF could upregulate PD-L1 expression through hypomethylating IRF7 *via* inhibition of DNMT1 activity and expression, and improve the anti-PD-1 therapy by modulating TIME. Although increased PD-L1 expression represents an immunosuppression status, DSF combined with anti-PD-1 Ab could overcome it.

IRF7 is an important regulator of type I IFN responses, and its transactivation can amplify the generation of type I IFNs *via* a positive feedback loop (43). IRF7 was found by Bidwell et al. to be overexpressed in NBT and primary BC tissue, while much lower expressed in bone metastasis (23). Restoration of IRF7 inhibited bone metastasis of BC cells by inducing the production of type I IFNs, and caused an increasing of CD8+ T cells in the blood samples of 4T1 tumor-bearing mice. Lan et al. reported that the upregulated expression of IRF7 in doxorubicin- and methotrexate-treated tumor cells could induce a switching from the myeloid-derived suppressor cell-mediated immune responses to the CD4+/CD8+ T cell-dependent anticancer responses through constitutive activation of type I IFN pathway (22). However, IRF7 is also reported to enhance constitutive PD-L1 expression, independent of IFN induce, resulting in decreasing CD8+ TIL expansion (21). IRF7 has the potential to exert multifaced effects on regulating TME (44). The expression of IRF7 can be epigenetically regulated by DNA methylation (45). DNMT inhibitors, decitabine and azacytidine, can induce the DNA hypomethylation of IRF promoter leading to transcriptional activation of IRF7 (46). In our study, DSF acted as a DNMT1 inhibitor and upregulated IRF7 expression by DNA hypomethylation, whose effect is similar to other DNMT inhibitors.

PD-L1 expression is one of the biomarkers to help select patients for anti-PD-1 therapy. Increasing evidence has shown that abnormal PD-L1 expression can affect the efficacy of anti-PD-1 therapy (42, 47). PD-L1 expression can be regulated by transcriptional control. Transcriptional factors, such as MYC, BRD4 and IRF1, participate in the activation of PD-L1 by binding to its promoter. IRF7 could also directly bind to PD-L1 promoter and enhance its transcriptional expression (9). Our study, like many other literatures, showed a positive correlation between PD-L1 and IRF7 at both transcriptional and protein levels in TNBC (48, 49). However, Chang and colleagues showed that PD-L1 protein level is negatively correlated with IRF7 in lung squamous cell cancer tissues, which may result from the effect of PD-1/PD-L1 reverse signaling on eIF2α/ATF4 activation with subsequent downregulation of IRF7 expression (50). DSF-induced PD-L1 expression was abolished by IRF7 knockdown in our study, suggesting that DSF upregulated PD-L1 expression *via* IRF7 restoration. Additionally, although DSF epigenetically restoration of IRF7, immunological suppressive TME was observed in tumors treated by DSF (**Figure 6**). We speculate the reason might be constitutively expression of PD-L1, which was mediated by IRF7 directly promoting transcription of PD-L1, leading to abrogating CD8+ TIL expansion (21).

DSF, an old anti-alcohol drug, has been shown to possess anticancer effects on various malignancies for many years. However, recent study reported that DSF combined with copper (DSF/Cu2+) could inhibit tumor proliferation in immunodeficient mice but failed in immunocompetent mice (45). Zhou and colleagues further found DSF combined with copper (DSF/Cu2+) was reported to upregulate PD-L1 expression by suppressing PARP1/GSK3β in hepatocellular carcinoma cells and ultimately prevented CD8+ TIL infiltration (51). However, co-treatment of DSF/Cu2+ and anti-PD-1 Ab improved antitumor immunity in mice and showed better antitumor activity than the monotherapy. Terashima et al. demonstrated that DSF inhibited FROUNT and suppressed macrophage deposition and its tumor-promoting potential (29). In our study, co-treatment of DSF and anti-PD-1 Ab noticeably elevated the population of granzyme B-positive CD8+ TIL and synergistically inhibited tumor growth compared to monotherapy. In contrast, anti-PD-1 Ab alone showed no growth inhibitory effect on 4T1 tumors with low CD8+ TIL, which is concordant with other studies (52).

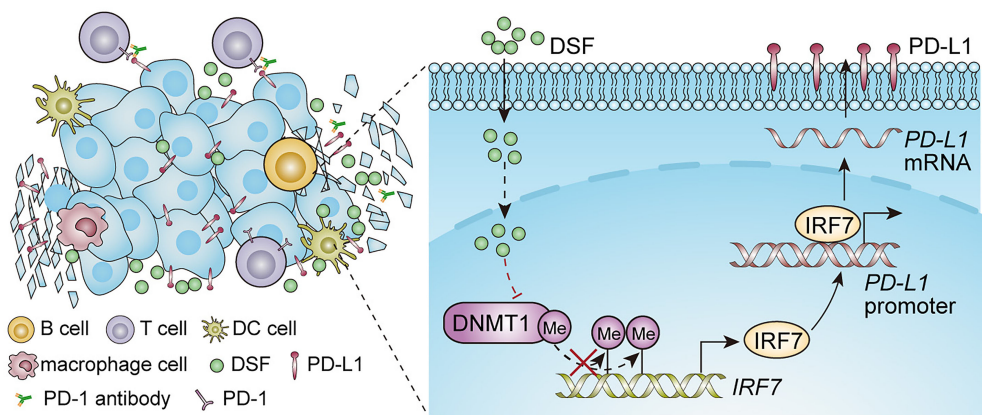

FIGURE 7 | An illustration of the proposed working model. Synergistic effect of DSF and PD-1 blocking antibody in the treatment of triple negative breast cancer.

Concordant with other studies, we found DSF treatment alone did not exert antitumor effects along with upregulated PD-L1 expression as well as a decreased immune cell infiltration in immunocompetent mice model, and we also observed that co-treatment of DSF and anti-PD-1 Ab improved the efficiency of anticancer with increased CD8+ TIL and activated antitumor immune pathway (29, 51). Furthermore, our RNA-seq results indicated that the combination of DSF and anti-PD-1 Ab reversed the immunological suppressive effects caused by DSF, and four pathways (i.e., Th1 and Th2 cell differentiation, antigen processing and presentation, natural killer cell-mediated cytotoxicity, and T cell receptor signal transduction) were significantly enriched in the combination groups, whereas no pathway was markedly enriched in anti-PD-1 blocking Ab groups.

A large number of studies have proved that DSF has superior anti-BC effects *in vitro* and *in vivo*, providing a new potential direction for TNBC treatment (53–55). A phase II trial of copper and DSF against metastatic BC (NCT03323346) was carried out to provide clinical evidence for introducing this novel combination therapy to metastatic BC patients who had failed conventional systemic or locoregional therapy. Our results indicated that the supplement of DSF to the anti-PD-1 therapy could improve the therapeutic efficacy than the monotherapy.

In conclusion, our findings demonstrate that DSF upregulates PD-L1 expression *via* DNMT1-mediated IRF7 hypomethylation and restoration in TNBC, and enhances the antitumor potential of anti-PD-1 Ab by modulating TME in **Figure 7**. DSF combined with anti-PD-1 Ab could serve as a novel option for relapse or metastatic TNBC.

DATA AVAILABILITY STATEMENT

The datasets presented in this study can be found in online repositories. The names of the repository/repositories and accession number(s) can be found below: (https://www.ncbi.nlm.nih.gov/gds/), GSE186885.

ETHICS STATEMENT

The animal study was reviewed and approved by Ethical Committee of Huazhong University of Science and Technology.

AUTHOR CONTRIBUTIONS

LZ and GW designed the experiments. XZ, ZL, MM, and QW performed experiments, data collection, and analysis. XZ and LZ analyzed data and drafted the manuscript. All authors contributed to the article and approved the submitted version.

FUNDING

This work was supported by grant from the National Natural Science Foundation of China (no. 81672940) and the Clinical Research Physician Program of Tongji Medical College, Huazhong University of Science and Technology (no. 5001530053).

REFERENCES

1. Siegel RL, Miller KD, Fuchs HE, Jemal A. Cancer Statistics, 2021. *CA Cancer J Clin* (2021) 71:7–33. doi: 10.3322/caac.21654
2. Perou CM, Sorlie T, Eisen MB, van de Rijn M, Jeffrey SS, Rees CA, et al. Molecular Portraits of Human Breast Tumours. *Nature* (2000) 406:747–52. doi: 10.1038/35021093
3. Foulkes WD, Smith IE, Reis-Filho JS. Triple-Negative Breast Cancer. *N Engl J Med* (2010) 363:1938–48. doi: 10.1056/NEJMra1001389
4. Reck M, Rodriguez-Abreu D, Robinson AG, Hui R, Csoszi T, Fulop A, et al. Pembrolizumab Versus Chemotherapy for PD-L1-Positive Non-Small-Cell Lung Cancer. *N Engl J Med* (2016) 375:1823–33. doi: 10.1056/NEJMoa1606774
5. Voorwerk L, Slagter M, Horlings HM, Sikorska K, van de Vijver KK, de Maaker M, et al. Immune Induction Strategies in Metastatic Triple-Negative Breast Cancer to Enhance the Sensitivity to PD-1 Blockade: The TONIC Trial. *Nat Med* (2019) 25:920–8. doi: 10.1038/s41591-019-0432-4
6. Larkin J, Chiarion-Sileni V, Gonzalez R, Grob JJ, Cowey CL, Lao CD, et al. Combined Nivolumab and Ipilimumab or Monotherapy in Untreated Melanoma. *N Engl J Med* (2015) 373:23–34. doi: 10.1056/NEJMoa1504030
7. Ribas A, Wolchok JD. Cancer Immunotherapy Using Checkpoint Blockade. *Science* (2018) 359:1350–5. doi: 10.1126/science.aar4060
8. Mavratzas A, Seitz J, Smetanay K, Schneeweiss A, Jager D, Fremd C. Atezolizumab for Use in PD-L1-Positive Unresectable, Locally Advanced or Metastatic Triple-Negative Breast Cancer. *Future Oncol* (2020) 16:4439–53. doi: 10.2217/fon-2019-0468
9. Goodman A, Patel SP, Kurzrock R. PD-1-PD-L1 Immune-Checkpoint Blockade in B-Cell Lymphomas. *Nat Rev Clin Oncol* (2017) 14:203–20. doi: 10.1038/nrclinonc.2016.168
10. Gong J, Chehrazi-Raffle A, Reddi S, Salgia R. Development of PD-1 and PD-L1 Inhibitors as a Form of Cancer Immunotherapy: A Comprehensive Review of Registration Trials and Future Considerations. *J Immunother Cancer* (2018) 6:8. doi: 10.1186/s40425-018-0316-z
11. Nanda R, Chow LQ, Dees EC, Berger R, Gupta S, Geva R, et al. Pembrolizumab in Patients With Advanced Triple-Negative Breast Cancer: Phase Ib KEYNOTE-012 Study. *J Clin Oncol* (2016) 34:2460–7. doi: 10.1200/JCO.2015.64.8931
12. Gibney GT, Weiner LM, Atkins MB. Predictive Biomarkers for Checkpoint Inhibitor-Based Immunotherapy. *Lancet Oncol* (2016) 17:e542–51. doi: 10.1016/S1470-2045(16)30406-5
13. Yi M, Jiao D, Xu H, Liu Q, Zhao W, Han X, et al. Biomarkers for Predicting Efficacy of PD-1/PD-L1 Inhibitors. *Mol Cancer* (2018) 17:129. doi: 10.1186/s12943-018-0864-3
14. Cristescu R, Mogg R, Ayers M, Albright A, Murphy E, Yearley J, et al. Pan-Tumor Genomic Biomarkers for PD-1 Checkpoint Blockade-Based Immunotherapy. *Science* (2018) 362:3593. doi: 10.1126/science.aar3593
15. Lu S, Stein JE, Rimm DL, Wang DW, Bell JM, Johnson DB, et al. Comparison of Biomarker Modalities for Predicting Response to PD-1/PD-L1 Checkpoint Blockade: A Systematic Review and Meta-Analysis. *JAMA Oncol* (2019) 5:1195–204. doi: 10.1001/jamaoncol.2019.1549
16. Li H, Chiappinelli KB, Guzzetta AA, Easwaran H, Yen RW, Vatapalli R, et al. Immune Regulation by Low Doses of the DNA Methyltransferase Inhibitor 5-Azacitidine in Common Human Epithelial Cancers. *Oncotarget* (2014) 5:587–98. doi: 10.18632/oncotarget.1782
17. Chatterjee A, Rodger EJ, Ahn A, Stockwell PA, Parry M, Motwani J, et al. Marked Global DNA Hypomethylation Is Associated With Constitutive PD-L1 Expression in Melanoma. *iScience* (2018) 4:312–25. doi: 10.1016/j.isci.2018.05.021

18. Huang KC, Chiang SF, Chen WT, Chen TW, Hu CH, Yang PC, et al. Decitabine Augments Chemotherapy-Induced PD-L1 Upregulation for PD-L1 Blockade in Colorectal Cancer. *Cancers (Basel)* (2020) 12:462. doi: 10.3390/cancers12020462
19. Jin X, Ding D, Yan Y, Li H, Wang B, Ma L, et al. Phosphorylated RB Promotes Cancer Immunity by Inhibiting NF-kappaB Activation and PD-L1 Expression. *Mol Cell* (2019) 73:22–35 e6. doi: 10.1016/j.molcel.2018.10.034
20. Chen S, Crabill GA, Pritchard TS, McMiller TL, Wei P, Pardoll DM, et al. Mechanisms Regulating PD-L1 Expression on Tumor and Immune Cells. *J Immunother Cancer* (2019) 7:305. doi: 10.1186/s40425-019-0770-2
21. Lai Q, Wang H, Li A, Xu Y, Tang L, Chen Q, et al. Decitibine Improve the Efficiency of Anti-PD-1 Therapy *via* Activating the Response to IFN/PD-L1 Signal of Lung Cancer Cells. *Oncogene* (2018) 37:2302–12. doi: 10.1038/s41388-018-0125-3
22. Lan Q, Peyvandi S, Duffey N, Huang YT, Barras D, Held W, et al. Type I Interferon/IRF7 Axis Instigates Chemotherapy-Induced Immunological Dormancy in Breast Cancer. *Oncogene* (2019) 38:2814–29. doi: 10.1038/s41388-018-0624-2
23. Bidwell BN, Slaney CY, Withana NP, Forster S, Cao Y, Loi S, et al. Silencing of Irf7 Pathways in Breast Cancer Cells Promotes Bone Metastasis Through Immune Escape. *Nat Med* (2012) 18:1224–31. doi: 10.1038/nm.2830
24. Skrott Z, Mistrik M, Andersen KK, Friis S, Majera D, Gursky J, et al. Alcohol-Abuse Drug Disulfiram Targets Cancer *via* P97 Segregase Adaptor NPL4. *Nature* (2017) 552:194–9. doi: 10.1038/nature25016
25. Han D, Wu G, Chang C, Zhu F, Xiao Y, Li Q, et al. Disulfiram Inhibits TGF-Beta-Induced Epithelial-Mesenchymal Transition and Stem-Like Features in Breast Cancer *via* ERK/NF-Kappab/Snail Pathway. *Oncotarget* (2015) 6:40907–19. doi: 10.18632/oncotarget.5723
26. Choi SA, Choi JW, Wang KC, Phi JH, Lee JY, Park KD, et al. Disulfiram Modulates Stemness and Metabolism of Brain Tumor Initiating Cells in Atypical Teratoid/Rhabdoid Tumors. *Neuro Oncol* (2015) 17:810–21. doi: 10.1093/neuonc/nou305
27. Lin J, Haffner MC, Zhang Y, Lee BH, Brennen WN, Britton J, et al. Disulfiram is a DNA Demethylating Agent and Inhibits Prostate Cancer Cell Growth. *Prostate* (2011) 71:333–43. doi: 10.1002/pros.21247
28. Dastjerdi MN, Babazadeh Z, Salehi M, Hashemibeni B, Kazemi M. Comparison of the Anti-Cancer Effect of Disulfiram and 5-Aza-CdR on Pancreatic Cancer Cell Line PANC-1. *Adv BioMed Res* (2014) 3:156. doi: 10.4103/2277-9175.137866
29. Terashima Y, Toda E, Itakura M, Otsuji M, Yoshinaga S, Okumura K, et al. Targeting FROUNT With Disulfiram Suppresses Macrophage Accumulation and its Tumor-Promoting Properties. *Nat Commun* (2020) 11:609. doi: 10.1038/s41467-020-14338-5
30. Deng S, Hu Q, Zhang H, Yang F, Peng C, Huang C. HDAC3 Inhibition Upregulates PD-L1 Expression in B-Cell Lymphomas and Augments the Efficacy of Anti-PD-L1 Therapy. *Mol Cancer Ther* (2019) 18:900–8. doi: 10.1158/1535-7163.MCT-18-1068
31. Wong KK. DNMT1: A Key Drug Target in Triple-Negative Breast Cancer. *Semin Cancer Biol* (2021) 72:198–213. doi: 10.1016/j.semcancer.2020.05.010
32. Braiteh F, Soriano AO, Garcia-Manero G, Hong D, Johnson MM, Silva Lde P, et al. Phase I Study of Epigenetic Modulation With 5-Azacytidine and Valproic Acid in Patients With Advanced Cancers. *Clin Cancer Res* (2008) 14:6296–301. doi: 10.1158/1078-0432.CCR-08-1247
33. Connolly RM, Li H, Jankowitz RC, Zhang Z, Rudek MA, Jeter SC, et al. Combination Epigenetic Therapy in Advanced Breast Cancer With 5-Azacitidine and Entinostat: A Phase II National Cancer Institute/Stand Up to Cancer Study. *Clin Cancer Res* (2017) 23:2691–701. doi: 10.1158/1078-0432.CCR-16-1729
34. Xiao W, Klement JD, Lu C, Ibrahim ML, Liu K. IFNAR1 Controls Autocrine Type I IFN Regulation of PD-L1 Expression in Myeloid-Derived Suppressor Cells. *J Immunol* (2018) 201:264–77. doi: 10.4049/jimmunol.1800129
35. Men C, Chai H, Song X, Li Y, Du H, Ren Q. Identification of DNA Methylation Associated Gene Signatures in Endometrial Cancer *via* Integrated Analysis of DNA Methylation and Gene Expression Systematically. *J Gynecol Oncol* (2017) 28:e83. doi: 10.3802/jgo.2017.28.e83
36. Shinawi T, Hill VK, Krex D, Schackert G, Gentle D, Morris MR, et al. DNA Methylation Profiles of Long- and Short-Term Glioblastoma Survivors. *Epigenetics* (2013) 8:149–56. doi: 10.4161/epi.23398
37. Koch A, De Meyer T, Jeschke J, Van Criekinge W. MEXPRESS: Visualizing Expression, DNA Methylation and Clinical TCGA Data. *BMC Genomics* (2015) 16:636. doi: 10.1186/s12864-015-1847-z
38. Liu Z, Mi M, Li X, Zheng X, Wu G, Zhang L. lncRNA OSTN-AS1 May Represent a Novel Immune-Related Prognostic Marker for Triple-Negative Breast Cancer Based on Integrated Analysis of a ceRNA Network. *Front Genet* (2019) 10:850. doi: 10.3389/fgene.2019.00850
39. Chowdhury PS, Chamoto K, Honjo T. Combination Therapy Strategies for Improving PD-1 Blockade Efficacy: A New Era in Cancer Immunotherapy. *J Intern Med* (2018) 283:110–20. doi: 10.1111/joim.12708
40. Ahmad G, Mackenzie GG, Egan J, Amiji MM. DHA-SBT-1214 Taxoid Nanoemulsion and Anti-PD-L1 Antibody Combination Therapy Enhances Antitumor Efficacy in a Syngeneic Pancreatic Adenocarcinoma Model. *Mol Cancer Ther* (2019) 18:1961–72. doi: 10.1158/1535-7163.MCT-18-1046
41. Cai S, Chen Z, Wang Y, Wang M, Wu J, Tong Y, et al. Reducing PD-L1 Expression With a Self-Assembled Nanodrug: An Alternative to PD-L1 Antibody for Enhanced Chemo-Immunotherapy. *Theranostics* (2021) 11:1970–81. doi: 10.7150/thno.45777
42. Hogg SJ, Vervoort SJ, Deswal S, Ott CJ, Li J, Cluse LA, et al. BET-Bromodomain Inhibitors Engage the Host Immune System and Regulate Expression of the Immune Checkpoint Ligand PD-L1. *Cell Rep* (2017) 18:2162–74. doi: 10.1016/j.celrep.2017.02.011
43. Zitvogel L, Galluzzi L, Kepp O, Smyth MJ, Kroemer G. Type I Interferons in Anticancer Immunity. *Nat Rev Immunol* (2015) 15:405–14. doi: 10.1038/nri3845
44. Musella M, Manic G, De Maria R, Vitale I, Sistigu A. Type-I-Interferons in Infection and Cancer: Unanticipated Dynamics With Therapeutic Implications. *Oncoimmunology* (2017) 6:e1314424. doi: 10.1080/2162402X.2017.1314424
45. Lu R, Au WC, Yeow WS, Hageman N, Pitha PM. Regulation of the Promoter Activity of Interferon Regulatory Factor-7 Gene. *Activation Interferon Silencing Hypermethylation J Biol Chem* (2000) 275:31805–12. doi: 10.1074/jbc.M005288200
46. Chiappinelli KB, Strissel PL, Desrichard A, Li H, Henke C, Akman B, et al. Inhibiting DNA Methylation Causes an Interferon Response in Cancer *via* dsRNA Including Endogenous Retroviruses. *Cell* (2015) 162:974–86. doi: 10.1016/j.cell.2015.07.011
47. Sen T, Rodriguez BL, Chen L, Corte CMD, Morikawa N, Fujimoto J, et al. Targeting DNA Damage Response Promotes Antitumor Immunity Through STING-Mediated T-Cell Activation in Small Cell Lung Cancer. *Cancer Discovery* (2019) 9:646–61. doi: 10.1158/2159-8290.CD-18-1020
48. Lu C, Redd PS, Lee JR, Savage N, Liu K. The Expression Profiles and Regulation of PD-L1 in Tumor-Induced Myeloid-Derived Suppressor Cells. *Oncoimmunology* (2016) 5:e1247135. doi: 10.1080/2162402X.2016.1247135
49. Wrangle J, Wang W, Koch A, Easwaran H, Mohammad HP, Vendetti F, et al. Alterations of Immune Response of Non-Small Cell Lung Cancer With Azacytidine. *Oncotarget* (2013) 4:2067–79. doi: 10.18632/oncotarget.1542
50. Chang LC, Chen TP, Kuo WK, Hua CC. The Protein Expression of PDL1 Is Highly Correlated With Those of Eif2alpha and ATF4 in Lung Cancer. *Dis Markers* (2018) 2018:5068701. doi: 10.1155/2018/5068701
51. Zhou B, Guo L, Zhang B, Liu S, Zhang K, Yan J, et al. Disulfiram Combined With Copper Induces Immunosuppression *via* PD-L1 Stabilization in Hepatocellular Carcinoma. *Am J Cancer Res* (2019) 9:2442–55.
52. Draganov D, Han Z, Rana A, Bennett N, Irvine DJ, Lee PP. Ivermectin Converts Cold Tumors Hot and Synergizes With Immune Checkpoint Blockade for Treatment of Breast Cancer. *NPJ Breast Cancer* (2021) 7:22. doi: 10.1038/s41523-021-00229-5
53. Kim JY, Lee N, Kim YJ, Cho Y, An H, Oh E, et al. Disulfiram Induces Anoikis and Suppresses Lung Colonization in Triple-Negative Breast Cancer *via* Calpain Activation. *Cancer Lett* (2017) 386:151–60. doi: 10.1016/j.canlet.2016.11.022
54. Chen D, Cui QC, Yang H, Dou QP. Disulfiram, a Clinically Used Anti-Alcoholism Drug and Copper-Binding Agent, Induces Apoptotic Cell Death in Breast Cancer Cultures and Xenografts *via* Inhibition of the Proteasome Activity. *Cancer Res* (2006) 66:10425–33. doi: 10.1158/0008-5472.CAN-06-2126
55. Kim YJ, Kim JY, Lee N, Oh E, Sung D, Cho TM, et al. Disulfiram Suppresses Cancer Stem-Like Properties and STAT3 Signaling in Triple-Negative Breast

Cancer Cells. *Biochem Biophys Res Commun* (2017) 486:1069–76. doi: 10.1016/j.bbrc.2017.03.164

Conflict of Interest: The authors declare that the research was conducted in the absence of any commercial or financial relationships that could be construed as a potential conflict of interest.

Publisher's Note: All claims expressed in this article are solely those of the authors and do not necessarily represent those of their affiliated organizations, or those of the publisher, the editors and the reviewers. Any product that may be evaluated in this article, or claim that may be made by its manufacturer, is not guaranteed or endorsed by the publisher.

frontiers in Immunology

ORIGINAL RESEARCH
published: 25 November 2021
doi: 10.3389/fimmu.2021.706936

Identification of Immune-Related lncRNA Prognostic Signature and Molecular Subtypes for Glioblastoma

Wanli Yu[1,2†], Yanan Ma[3†], Wenbin Hou[4†], Fang Wang[5], Wan Cheng[6], Feng Qiu[7], Pengfei Wu[8,9,10,11*] and Guohua Zhang[12*]*

[1] Department of Neurosurgery, Gaoxin Hospital of The First Affiliated Hospital of Nanchang University, Nanchang, China, [2] Department of Neurosurgery, The First Affiliated Hospital of Nanchang University, Nanchang, China, [3] Laboratory of Medical Genetics, Harbin Medical University, Harbin, China, [4] Department of Urology, The Second Affiliated Hospital of Harbin Medical University, Harbin, China, [5] Department of Neurosurgery, The Second Affiliated Hospital of Harbin Medical University, Harbin, China, [6] The Laboratory of Artificial Intelligence and Bigdata in Ophthalmology, The Affiliated Eye Hospital of Nanjing Medical University, Nanjing, China, [7] Oncology Department, Gaoxin Hospital of The First Affiliated Hospital of Nanchang University, Nanchang, China, [8] Department of Neurosurgery, The First Affiliated Hospital of USTC, Division of Life Sciences and Medicine, University of Science and Technology of China, Hefei, China, [9] Anhui Provincial Stereotactic Neurosurgical Institute, Hefei, China, [10] Anhui Province Key Laboratory of Brain Function and Brain Disease, Hefei, China, [11] Anhui Provincial Clinical Research Center for Neurosurgical Disease, Hefei, China, [12] Central Laboratory, Gaoxin Hospital of The First Affiliated Hospital of Nanchang University, Nanchang, China

OPEN ACCESS

Edited by:
Mingzhu Yin,
Central South University, China

Reviewed by:
Zongqiang Huang,
First Affiliated Hospital of Zhengzhou University, China
Hongzhe Guo,
Harbin Institute of Technology, China
Tao Zhennan,
Nanjing Drum Tower Hospital, China

***Correspondence:**
Guohua Zhang
zhgh71@163.com
Pengfei Wu
wupengfei1992@126.com
Feng Qiu
lukeqiubmu@163.com

†These authors have contributed equally to this work

Specialty section:
This article was submitted to Cancer Immunity and Immunotherapy, a section of the journal Frontiers in Immunology

Received: *08 May 2021*
Accepted: *25 October 2021*
Published: *25 November 2021*

Citation:
Yu W, Ma Y, Hou W, Wang F, Cheng W, Qiu F, Wu P and Zhang G (2021) Identification of Immune-Related lncRNA Prognostic Signature and Molecular Subtypes for Glioblastoma. Front. Immunol. 12:706936. doi: 10.3389/fimmu.2021.706936

Background: Glioblastoma multiforme (GBM) is extensively genetically and transcriptionally heterogeneous, which poses challenges for classification and management. Long noncoding RNAs (lncRNAs) play a critical role in the development and progression of GBM, especially in tumor-associated immune processes. Therefore, it is necessary to develop an immune-related lncRNAs (irlncRNAs) signature.

Methods: Univariate and multivariate Cox regression analyses were utilized to construct a prognostic model. GBM-specific CeRNA and PPI network was constructed to predict lncRNAs targets and evaluate the interactions of immune mRNAs translated proteins. GO and KEGG pathway analyses were used to show the biological functions and pathways of CeRNA network-related immunity genes. Consensus Cluster Plus analysis was used for GBM gene clustering. Then, we evaluated GBM subtype-specific prognostic values, clinical characteristics, genes and pathways, immune infiltration access single cell RNA-seq data, and chemotherapeutics efficacy. The hub genes were finally validated.

Results: A total of 17 prognostically related irlncRNAs were screened to build a prognostic model signature based on six key irlncRNAs. Based on GBM-specific CeRNAs and enrichment analysis, *PLAU* was predicted as a target of lncRNA-H19 and mainly enriched in the malignant related pathways. GBM subtype-A displayed the most favorable prognosis, high proportion of genes (*IDH1*, *ATRX*, and *EGFR*) mutation, chemoradiotherapy, and low risk and was characterized by low expression of four high-risk lncRNAs (*H19*, *HOTAIRM1*, *AGAP2-AS1*, and *AC002456.1*) and one mRNA *KRT8*. GSs with poor survival were mainly infiltrated by mesenchymal stem cells (MSCs) and astrocyte, and were more sensitive to gefitinib and roscovitine. Among GSs, three hub genes KRT8, NGFR, and TCEA3, were screened and validated to potentially play feasible oncogenic roles in GBM.

Conclusion: Construction of lncRNAs risk model and identification of GBM subtypes based on 17 irlncRNAs, which suggesting that irlncRNAs had the promising potential for clinical immunotherapy of GBM.

Keywords: glioblastoma, immune-related lncRNAs, biomarker, prognostic signature, immune infiltration

INTRODUCTION

Glioblastoma multiforme (GBM) is the most frequent intracranial primary malignancy in adults. Despite standard treatment, the median survival of GBM patients is less than 14 months (1). In the latest glioma classification, molecular features are considered as classifiers in conjunction with histopathological appearance (2). Emerging biosomics studies have improved the diagnosis and treatment strategies for GBM to some extent but have not yet achieved satisfactory results due to the complex pathogenesis and molecular heterogeneity of GBM. Therefore, more studies are urgently needed to explore the mechanisms involved and to identify novel biomarkers to predict the prognosis and therapeutic effects of GBM.

Long noncoding RNA (lncRNA) is a noncoding RNA with a length of more than 200 nucleotides (3). The discovery of lncRNAs has uncovered new horizons in the pathological processes of multiple diseases, including cancer initiation and progression (4). Recent studies have shown that lncRNAs can influence the tumor immune microenvironment (TIM) by regulating inflammation and participating in immune gene expression (5, 6). For example, lncRNA nuclear-enriched abundant transcript 1 (*NEAT1*) affects cytokine response and induces IGs expression through the regulation of interleukin (IL)-8 transcription (7). LncRNA-*Cox2* participates in inflammatory gene expression in macrophages *via* regulating chromatin complex remodeling (8). Zhao et al. showed that the lncRNA *SNHG14/miR-5590-3p/ZEB1* positive feedback loop can regulate the PD-1/PD-L1 checkpoint to promote diffuse large B cell lymphoma progression and immune evasion (9). Increasing studies reporting on the mechanism of irlncRNAs in multiple cancers (10), the ambiguous relationship between lncRNAs, and the tumor immune microenvironment have been gradually unveiled. However, the relationship between lncRNAs and tumor immune microenvironment is rarely studied in GBM. Therefore, identification of the irlncRNAs signature may provide a new insight for predicting prognosis and individualized treatment of GBM.

In this study, we identified six key irlncRNA signatures (*H19*, *ST3GAL6-AS1*, *AL162231.2*, *SOX21-AS1*, *AC006213.5*, and *AC002456.1*), which concluded that the risk model indeed had a good predictive outcome. GBM-specific CeRNAs were constructed to predict irlncRNAs targets. GO and KEGG pathway enrichment analysis was used to explore target functions. The PPI network was performed to identify the interactions of proteins translated from mRNAs in the CeRNA network. Furthermore, GS-A showed better prognosis among the identified four GSs (A-D). GSs-specific prognostic value, clinical characteristics, genes and pathways, immune infiltration, and chemotherapeutic drug sensitivity were evaluated. Three hub genes, KRT8, NGFR, and TCEA3, were screened and validated among GSs. These results suggested that the irlncRNAs had the promising potential for clinical immunotherapy of GBM.

Abbreviations: GBM, glioblastoma multiforme; lncRNAs, long noncoding RNAs; irlncRNAs, immune-related lncRNAs; GSs, GBM subtypes; PRirlncRNAs, prognostically related irlncRNAs; GTEx, genotype-tissue expression; TCGA, The Cancer Genome Atlas; CGGA, Chinese Glioma Genome Atlas; GEO, Gene Expression Omnibus; OS, overall survival; IGs, immunity genes; NEAT1, nuclear-enriched abundant transcript 1; TIM, tumor immune microenvironment; DE, differentially expressed; IG, immune genes; PPI, protein–protein interaction; GO, Gene Ontology; KEGG, Kyoto Encyclopedia of Genes and Genomes; GSEA, Gene Set Enrichment Analysis; ROC, receiver operating characteristic; TMA, temozolomide; FC, fold change; CDF, cumulative distribution function; CM, consensus matrix; BP, biological processes; MF, molecular function; CC, cellular component; IDH, isocitrate dehydrogenase; MGMT, O6-methylguanine DNA methyltransferase; EGFR, epidermal growth factor receptor; HOTAIRM1, HOXA transcript antisense RNA myeloid-specific 1; AGAP2-AS1, AGAP2 antisense RNA 1; KRT8, keratin 8; NGFR, nerve-growth-factor receptor; TCEA3, transcription elongation factor A3; PTTG1, pituitary tumor transforming gene 1.

MATERIALS AND METHODS

Acquisition and Processing of GBM Expression and Clinicopathological Data

RNA-seq transcriptome data of healthy samples were obtained from the GTEx database (11) (http://commonfund.nih.gov/GTEx/). The RNA-seq transcriptome data and clinicopathological data of the GBM samples were downloaded from the TCGA database (http://cancergenome.nih.gov/). Samples and patients with incomplete clinical information were excluded, and conformers are shown in **Table S1**. Two available matrices were merged, normalized with the *limma* package of R software, and obtained the differentially expressed (DE) genes. The input file is FPKM, and the output file is log $^{(x + 1)}$. The scRNA-seq data of human GBM samples, accession number GSE168004, were obtained from the Gene Expression Omnibus (GEO, http://www.ncbi.nlm.nih.gov/geo/) database. The cutoff criteria were set as $|$ log2 fold change (FC) $|$ > 0.5 and $p < 0.05$.

Identification of Immune-Related lncRNAs (irlncRNAs)

The immune genes (IGs) list was downloaded from the IMMPORT shared database (12) (https://www.immport.org/) and the Molecular Signatures Database v 7.0 (http://www.gsea-msigdb.org/gsea/index.jsp/). The correlation between genes was calculated to obtain irlncRNAs. Correlation coefficient >0.4 and p<0.001 were used as the threshold.

Establishment of the Immune-Related Risk Prognostic Model

Univariate and multivariate Cox regression analyses were performed to identify significant lncRNAs for construction of the prognostic signature. A risk score was calculated based on each patient's lncRNAs expression level by the following formula: *Risk score* $(RS) = \Sigma_{i=1}^{N} \quad Expi * \beta i$ (N is the number of relative lncRNAs, Expi represents the expression value of each lncRNA, and βi is the regression coefficient of the multivariate Cox analysis for the target lncRNA). By setting the median value of the risk score as the cutoff value in the training set and the whole set, GBM patients were divided into high- and low-risk groups. Related files for constructing the immune-related risk prognostic model are displayed in **Table S2**.

Evaluation and Validation of a Risk Prognostic Model

The predictive ability of the prognostic model was evaluated by a series of analyses: Kaplan-Meier survival analysis, time-dependent ROC curve analyses, univariate Cox regression analysis, and multivariate Cox regression analysis for comparison of the survival between the high- and low-risk groups in the training, testing, and whole cohorts using the R packages *survival* and *survivalROC*. In addition, the signature derived from this study was compared with these three other signature ROC curves (13–15). We analyzed the ROC curve differences between prognostic models and clinicopathological features.

Construction of a CeRNA Network and a Protein–Protein Interaction (PPI) Network

The miRcode database (16) was performed to match differentially expressed and prognostically related irlncRNAs and miRNAs. Three databases, miRTarBase (17), miRDB (18), and TargetScan (19), were used to predict miRNA target genes. The interactions between miRNAs and lncRNAs or mRNAs were integrated to construct a CeRNA regulatory network. The mRNAs were enrolled in a PPI network through the STRING database (https://string-db.org/) with a confidence score > 0.7. Cytoscape (version 3.8.1) was used to visualize the CeRNA and PPI networks.

Functional and Pathway Enrichment Analyses

We used the "clusterProfiler" package to perform Gene Ontology (GO) and Kyoto Encyclopedia of Genes and Genomes (KEGG) enrichment analysis of CeRNA network-related IGs to explore potential biological functions and pathways. The cutoff criterion was set at $p < 0.05$. Additionally, KEGG pathway analysis of KRT8 was performed using the Gene Set Enrichment Analysis (GSEA) software (www.gsea-msigdb.org). The cutoff criterion was set at $p < 0.05$.

Identification of GBM Subtypes in Risk Prognostic Model

Unsupervised consensus clustering was conducted to identify a novel immune classification of GBM based on the prognostic irlncRNAs using the *ConsensusClusterPlus* package (50 iterations, resample rate of 80%). The consensus cumulative distribution function (CDF), consensus matrix (CM), and consensus heatmap were performed to determine the optimal number of clusters.

Analysis of Clinical Characters and Molecular Differences in GBM Subtypes

Survival analysis and valuable clinical information (**Table S3**) were compared between the different subtypes. The Wilcoxon rank test was used to identify differentially expressed molecules among subtypes. The cutoff criteria were set as $|\log2FC| > 0.3$ and $p < 0.05$.

Immune Microenvironment Exploration for GBM Subtypes Access scRNA-seq Data

The Seurat package was performed for quality control, statistical analysis, and exploration of the scRNA-seq data. The quality control standards were genes detected in >3 cells; cells with >50 total detected genes and cells with ≤5% of mitochondria-expressed genes were included. PCA was used to discriminate available dimensions with a p value < 0.05. Then, dimensionality reduction and cluster classification analysis were performed using a t-distributed stochastic neighbor embedding (tSNE) algorithm. The limma package was applied for differential expression analysis to identify the marker genes of each cluster with p value < 0.05 and $|\log2[\text{fold change (FC)}]| > 0.5$. Based on marker gene populations, different cell clusters were annotated by the singleR package and then manually validated and corrected with the CellMarker database. The corresponding cell surface marker genes for the annotation of cell clusters are listed in **Table S4**.

Exploration of Candidate Small Molecule Agents

To evaluate the significance of this prognostic model in clinical treatment, the IC_{50} of common administrating chemotherapeutic agents in the GBM dataset TCGA project was calculated. The IC_{50} difference analysis was performed between the high-risk and low-risk groups using the Wilcoxon signed-rank test. Box plots were obtained using *pRRophetic* and *ggplot2* to show the results.

Preparation for Human GBM Samples

GBM tissues and normal brain tissues were obtained from patients treated at First Affiliated Hospital of Nanchang University who provided informed consent. The study was approved by the hospital's institutional ethics committee. GBM tissue was collected and immediately stored in an environment at −80°C.

Quantitative Real-Time RT-PCR (qRT-PCR) Analysis

Total RNA extracted from transfected cells was reverse-transcribed with RT reagent Kit gDNA Eraser (TaKaRa) and detected by SYBR-Green (TaKaRa). The PCR primers are listed in **Table S5**.

Western Blot Assays

Western blot (WB) assays were performed as described previously (20). The antibodies used are listed in **Table S6**.

Statistical Analysis

All analysis was carried out by R version 3.6.1 and corresponding packages. Kruskal–Wallis test was used to compare the divergence between multiple groups. Chi-square test or Fisher exact test was used for statistics on clinical information. A Bonferroni test was used to correct the p-value. Kaplan–Meier curves analysis was used to assess survival differences of the subtype. The correlation was determined by Pearson correlation analysis. $p < 0.05$ was regarded as statistically significant.

RESULTS

Selection of DElncRNAs, DEimmune genes (DEIGs), and irlncRNAs in GBM

A filtering flow chart for the study is shown in **Figure 1**. The 1,520 DElncRNAs with 396 upregulated and 1,124 downregulated were identified between normal and GBM tissues. Analogously, we also identified 358 upregulated and 196 downregulated IGs. The corresponding heatmaps are displayed in **Figure S2**. Based on 396 upregulated lncRNAs and 554 DEIGs, 224 irlncRNAs were obtained by correlation analysis (**Tables S7**–**S9**).

Construction of irlncRNAs Model in GBM

The data of GBM patients were allocated randomly to the training and validation cohort. The 224 irlncRNAs were subjected to univariate Cox regression analysis (**Table S10**) followed by Lasso regression (**Table S11** and **Figures 2A–D**) in the training set to obtain 17 PRirlncRNAs ($p < 0.05$; **Table S12** and **Figure 2E**) and a risk score prognostic model constituted based on 6 key irlncRNAs. The risk score for each sample was calculated based on the expression levels of these six lncRNAs (**Figure 2F**). The coefficient of each gene was calculated by multivariate Cox regression analysis (**Table 1**).

$$\begin{aligned}\text{Risk score} = {} & (0.14{*}H19) + (-0.51{*}ST3GAL6-AS1) + \\ & (-0.32{*}AL162231.2) + (-1.09{*}SOX21-AS1) + \\ & (-0.39{*}AC006213.5) + (0.50{*}AC002456.1).\end{aligned}$$

Evaluation and Validation of irlncRNAs Signature in GBM

The irlncRNAs signature is a robust prognostic tool for GBM. Risk curves and scatter plots showed the risk score and survival status of each GBM patient in the training (**Figure 2G**), testing (**Figure S3A**), and total sets (**Figure S1A**). The low-risk group had a lower risk coefficient and mortality than the high-risk group. The heatmap of the irlncRNAs signature in the training (**Figure 2H**; **Table S13**), testing (**Figure S3B**; **Table S14**), and total sets (**Figure S1B**) revealed that GBM with high prognostic scores expressed high-risk irlncRNAs (*H19*, *AL162231.2*, *AC002456.1*), whereas GBM with low prognostic scores expressed protective irlncRNAs (*ST3GAL6-AS1*, *SOX21-AS1*, *AC006213.5*). Based on the median risk score in the training set, GBM patients were divided into high- and low-risk cohorts. Survival curves indicated that patients in the low-risk group had a longer median OS compared with the high-risk group (**Figure 2I**); further examinations were performed in the test (**Figure S3C**) and whole sets (**Figure S1C**) by the same algorithmic cutoff in order to evaluate the accuracy of the prognostic signature. Both groups yielded similar results, suggesting that the prognostic signature was effective. In addition, the promising predictive value for the GBM special model in the training set was demonstrated by ROC curve analysis (**Figure 2J** 1-year AUC = 0.792, 2-year AUC = 0.922, 3-year AUC = 0.981), which validated the results of the model in the testing set (**Figure S3D**; 1-year AUC = 0.703, 2-year AUC = 0.657, 3-year AUC = 0.669) and the whole set (**Figure S1D**; 1-year AUC = 0.744, 2-year AUC = 0.756, 3-year AUC = 0.838). The multi-index ROC analysis revealed that the AUC of the prognostic model was significantly better than those of other clinicopathological indicators (**Figure 2K**) (such as age, gender, therapy, molecular typing, etc.). Compared with three existing lncRNA-related signatures (13–15) (**Figure 2L**), the excellent predictive viability of our model is further demonstrated. Together, these data illustrate the excellent identification of high-risk patients using our model.

IrlncRNAs Prognostic Model Is an Independent Prognostic Factor for GBM

Univariate and multivariate Cox regression analyses were performed to verify that the irlncRNAs model was an independent prognostic factor for GBM in the training set. The univariate Cox analysis revealed that gender, radiotherapy, MGMT status, and risk score were dramatically associated with the OS (**Figure S4A**), while the multivariate analysis revealed that gender, MGMT status, and risk score were identified as independent prognostic factors (**Figure S4B**).

Construction of the CeRNA and PPI Network and Functional Enrichment Analysis in GBM

Of the 224 irlncRNAs, 17 lncRNAs were associated with prognosis. Based on matching analysis of 17 PRirlncRNAs and 554 DEIGs, a total of 5 irlncRNAs and 16 miRNAs paired into 31 irlncRNAs–miRNA interactions, while 16 miRNAs and 27 DEIGs matched to form 35 miRNA–DEIGs interactions. Finally, 5 irlncRNAs, 16 miRNAs, and 27 DEIGs were used to construct lncRNA–miRNA–mRNA regulatory networks (**Table S15** and **Figure 3A**).

Furthermore, the PPI network was constructed to identify the interactions of proteins translated from mRNAs in the CeRNA network (**Figure 3B**). We found that some genes with high combined score including *TGFBR1-TGFBR2*, *JAG2-NOTCH2*, *ETS1-SP1*, *NRAS-PDGFRA*, and *BDNF-TRAF6* were mainly enriched in the "Human T-cell leukemia virus 1 infection," "IL-17 signaling pathway," "TGF-beta signaling pathway," and "PD-L1 expression and PD-1 checkpoint pathway in cancer pathway."

GO (**Table S16**) and KEGG (**Table S17**) pathway enrichment analyses demonstrated that the GBM-specific CeRNA network

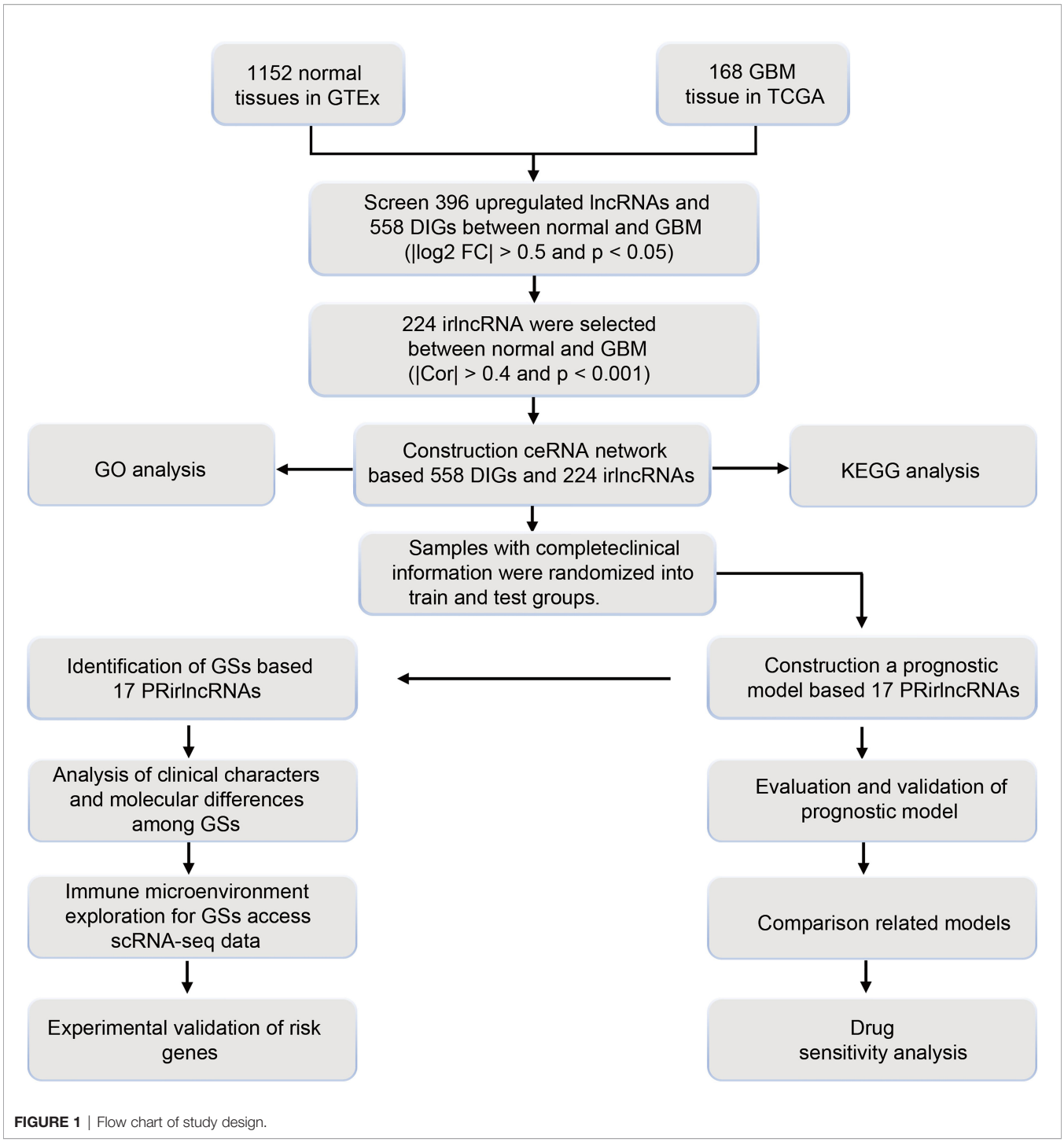

FIGURE 1 | Flow chart of study design.

might be involved in the neoplastic process by regulating these biological functions and pathways. GO functional analysis showed that DEIGs involved in the CeRNA network were enriched in BPs, including regulation of vasculature development, response to oxidative stress, and positive regulation of epithelial cell proliferation. The enrichment of MF is mainly related to the membrane signal, and CC is protein binding (**Figures 3C, D**). CeRNA network-related IGs were significantly enriched in KEGG pathways, namely, MAPK signaling pathway, cytokine–cytokine receptor interaction, PI3K-Akt signaling pathway, and multiple cancers (**Figures 3E–F**).

Four Subtypes of GBM Were Identified and Correlated With Prognosis

Based on 17 PRirlncRNAs, Consensus Cluster Plus was utilized to identify the different subtypes (K = 2-9) among the risk model.

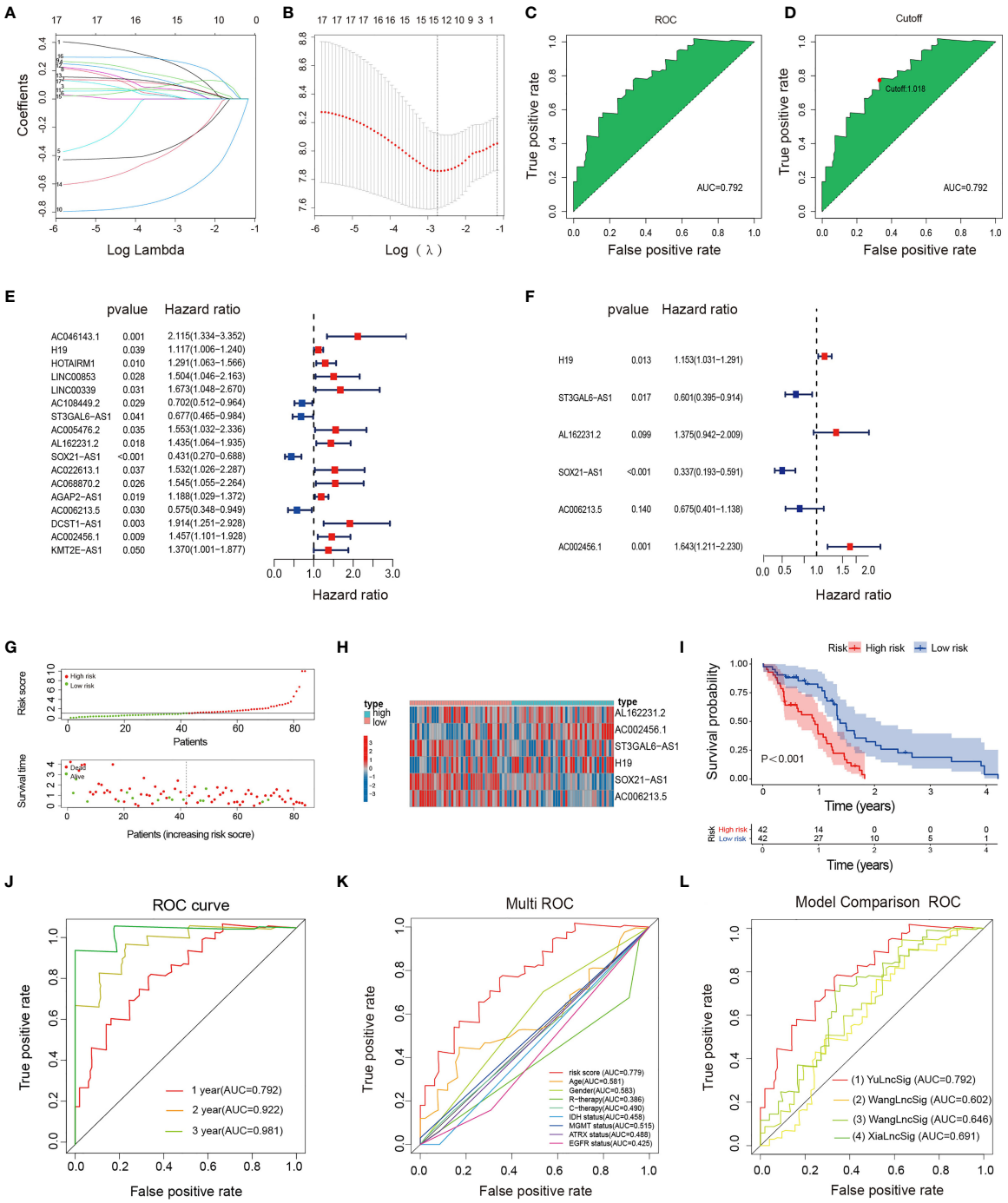

FIGURE 2 | Construction, evaluation, and comparison of a risk signature. **(A)** LASSO coefficient profiles of the 17 irlncRNAs in the training set. **(B)** A coefficient profile plot was generated against the log (lambda) sequence. Selection of the optimal parameter (lambda) in the LASSO model. **(C, D)** The AUC value and cutoff point obtained in the training set. **(E)** Forest plot of 17 irlncRNAs selected by univariate Cox regression analysis associated with GBM survival in the training set. **(F)** Forest plot of six irlncRNAs selected by multivariate Cox regression analysis associated with GBM survival and construction risk model. **(G)** Risk score and survival status analysis of irlncRNAs prognostic signature. **(H)** The expression pattern of irlncRNAs prognostic signature in the low- and high-risk groups. **(I)** Survival analysis of irlncRNAs prognostic signature. **(J)** ROC curve analysis within 1, 2, and 3 years. **(K)** Multivariate ROC curve analysis showing that the superior prognostic performance of the irlncRNAs prognostic model compared to other clinical indicators. **(L)** AUCs of the ROCs for our and the three other gene signatures.

TABLE 1 | Coefficients based on a multivariate Cox regression analysis of the selected lncRNAs.

Gene	Coef	HR	HR.95L	HR.95H	p-value
H19	0.143	1.153	1.031	1.291	0.013
ST3GAL6-AS1	-0.509	0.600	0.395	0.914	0.017
AL162231.2	0.319	1.375	0.942	2.009	0.099
SOX21-AS1	-1.087	0.337	0.193	0.591	0.000
AC006213.5	-0.392	0.675	0.401	1.138	0.140
AC002456.1	0.497	1.643	1.211	2.230	0.001

HR, hazard ratio.

According to the cumulative distribution function (CDF) curves, tracking pot, Delta area pot, and CM heatmap (**Figures 4A–D**), when k=4, the sample cluster was stable and robust. As a result, patients could be classified into four GSs (**Table S18**): A (n = 23, 27.4%), B (n = 24, 28.6%), C (n = 28, 33.3%), and D (n = 9, 10.7%). Kaplan-Meier survival analysis indicated that patients with GS-A showed the best OS compared to patients with cluster B, C, or D (p=0.007; **Figure 4E**).

Revelation of Clinical Characters, Molecular Differences, and Pathway Analysis for GBM Subtypes

Clinicopathological variables and molecular differences were compared among the four subtypes. Heatmap of 17 irlncRNAs illustrated the clinical features and molecular differences among the four subtypes (**Figures 5A**). The results revealed that GS-A patients are characterized by a high mutation rate of genes including *IDH1*, *ATRX*, and *EGFR*, a high rate of chemoradiotherapy, and a high rate of the low-risk group (**Figures 5B–G**).

Subsequently, difference analysis identified 10 lncRNAs (**Table S19**) and 14 mRNAs (**Table S20**) among the four subtypes (**Figures 6A, B**). The results revealed that 6 of the 14 mRNAs were risk genes, and 4 (KRT8, NGFR, TCEA3, and PTTG1) of the risk genes were highly expressed in GBM compared with normal tissues. Thus, these four risk factors, as hub genes, may play an important role in the malignant behavior of GBM.

In addition, patients with GS-A patients are characterized by low expression of four high-risk lncRNA (*H19*, *HOTAIRM1*, *AGAP2-AS1*, *AC002456.1*) and one high-risk gene *KRT8*. GSEA showed that functional pathways involved in RTK8 were mainly immune cell and tumor-related signaling pathways, such as the T cell receptor, apoptosis, or JAK/STATA signaling pathway (**Figures 6C–E**).

GSVA enrichment analysis showed the activation states of biological pathways including the regulation of autophagy, the apoptosis, the Wnt signaling pathway, the NOTCH signaling pathway, the ERBB signaling pathway, the RIG like receptor signaling pathway, and the NOD-like receptor signaling pathway in GS-A (**Figures 6F–H**).

Exploration of Immune Microenvironment for GBM Subtypes Access scRNA-seq Data

Eight cell clusters with different annotations were identified by scRNA-seq data, revealing cellular heterogeneity in GBM tumors. A total of 4,210 cluster markers were identified from all 8 clusters by differential analysis (**Table S21**). Clusters 0 and 4, containing 398 cells, were annotated as GBM MSCs; clusters 1, 2, 3, 5, 6, and 7, containing 792 cells, were annotated as the astrocytes (**Figures 7A–F** and **Table S22**).

Among the six risk genes of GBM subtypes, two genes, OLFM1 and TENM2, with low expression in GBM were excluded. Searching of the remaining four hub genes (GS-A: KRT8; GS-B: NGFR; GB-C: TCEA3; GB-D: PTTG1) in different GSs with clustering markers revealed that GBM may infiltrate immune cells. KRT8, belonging to Cluster 0, was annotated as GBM MSCs; NGFR, belonging to Clusters 0 and 4, was annotated as GBM MSCs; TCEA3, belonging to Clusters 0, 1, 2, 3, 4, and 5, was annotated as GBM MSCs and astrocyte; PTTG1, belonging to Clusters 2, 3, 4, 5, 6, and 7, was annotated as GBM MSCs and astrocyte (**Figures 7G–J**).

Screening of the Related Small Candidate Drugs With irlncRNAs Signature

An attempt was made to screen out chemotherapeutic agents that are sensitive to the high-risk group in the TCGA project of the GBM dataset. We found that the high-risk score correlated with a lower half inhibitory concentration (IC_{50}) of chemotherapeutic drugs such as Gefitinib (p= 0.015) and Roscovitine (p= 0.035), whereas it correlated with the higher IC_{50} of axitinib (p=0.039) and thapsigargin (p=0.0041) (**Figures S4A–D**).

Validation of the Hub Genes in Clinical Tissues

The K-M survival curve from the TCGA database was performed to explore the potential role of the individual hub gene in OS. Three of the four hub genes showed significant predictions of poor OS ($P < 0.05$, **Figures 8A–C**). To further verify the expression level of hub genes in GBM samples, we generated RT-qPCR to calculate the mRNA levels of the three hub genes. As illustrated in **Figures 8D–F**, the expressions of KRT8, NGFR, and TCEA3 were significantly upregulated in GBM tissues compared with normal tissues. Subsequently, WB was used to evaluate the expression level of three proteins. As shown in **Figures 8G–I**, the expression levels of three proteins in GBM tissues were higher than those in normal brain tissues.

DISCUSSION

GBM cells form a complex tumor microenvironment that supports malignant tumor progression and immune escape (21).

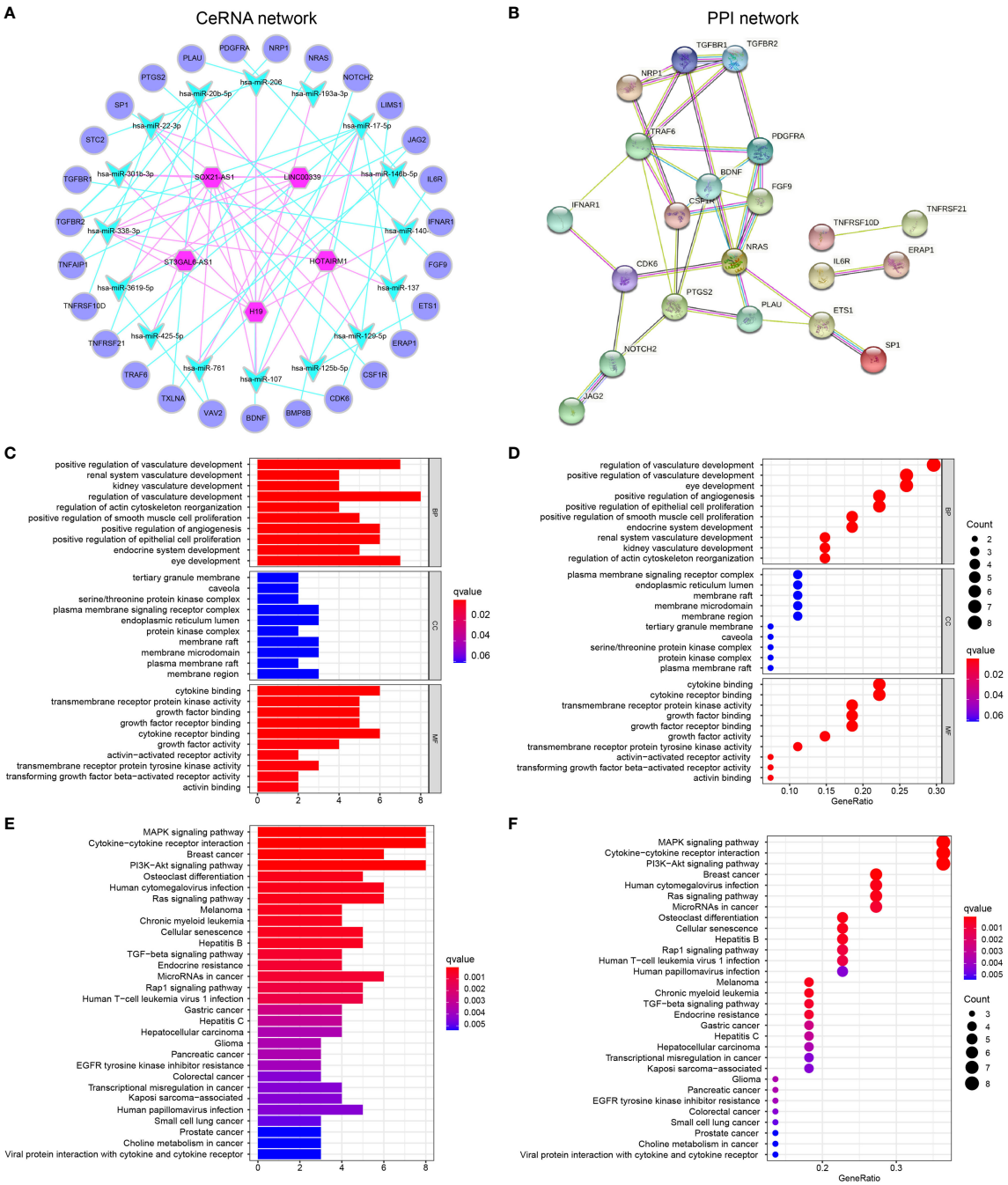

FIGURE 3 | GBM-specific CeRNA network, PPI network, and functional enrichment analysis **(A)** A total of 31 irlncRNAs–miRNA interactions and 35 miRNA–DEIGs interactions construct the lncRNA–miRNA–mRNA regulatory networks. **(B)** PPI network displayed the interactions of proteins translated from IGs in the CeRNA network. **(C, D)** GO enrichment analysis **(E, F)** KEGG pathway enrichment analysis.

Novel immunotherapy within the tumor microenvironment has been uncovered that exerts antitumor immune response *via* targeting immunoregulatory cells or immunosuppressive factors (22). Accumulating evidence suggests that abnormal lncRNAs servers as new markers contribute to antitumor immunoreactivity (23, 24). It is of great significance to understand the tumor immune microenvironment driven by lncRNAs, to construct a clinical prognosis model, and to screen new markers for providing risk stratification and targets for immunotherapy.

In this study, 224 irlncRNAs were analyzed between tumor and normal tissues, 17 PRirlncRNAs were obtained by using the univariate Cox regression analysis, LASSO regression analysis

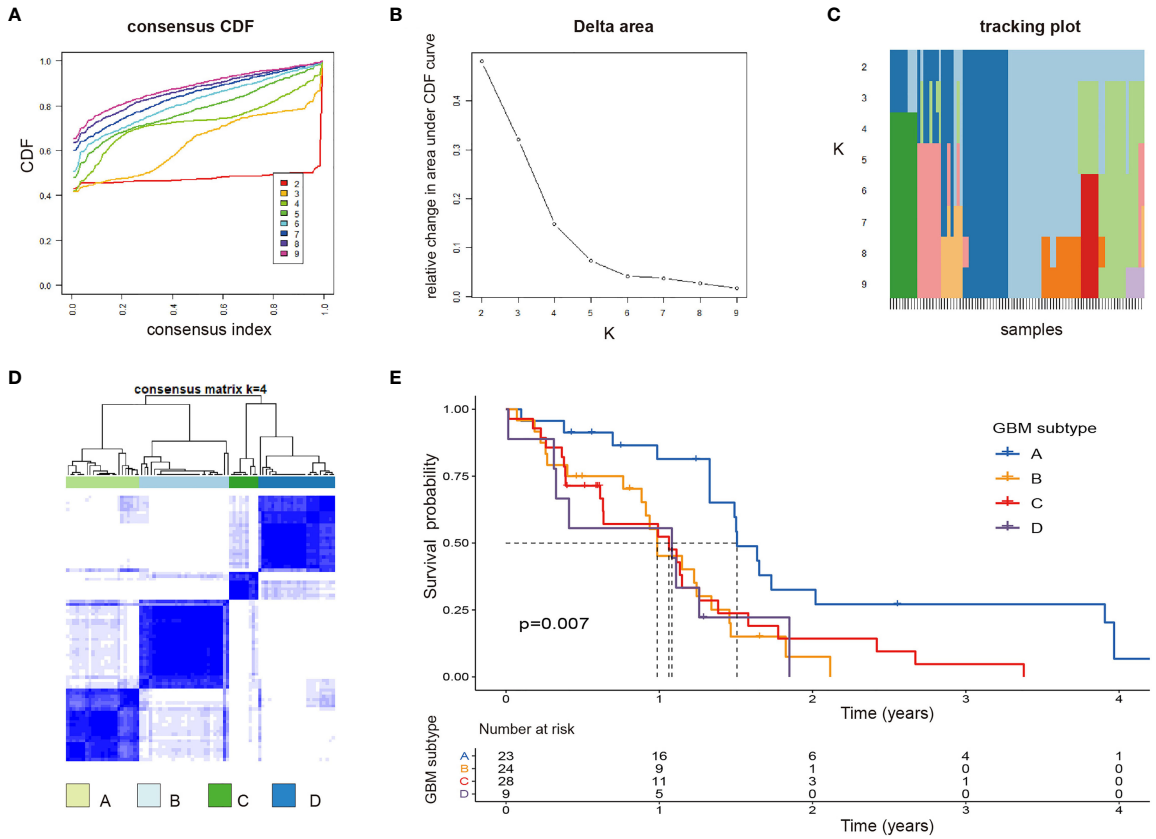

FIGURE 4 | Identification of potential GBM subtypes **(A–C)** Cumulative distribution function curve, delta area, and tracking plot of immune-related lncRNA in GBM. **(D)** Consensus clustering matrix for k = 4, which was the optimal cluster number in the TCGA training cohort. **(E)** Patients in the GBM subtype-A experienced a longer survival time.

was used to identify 6 key lncRNAs, and multivariate Cox regression analysis was applied to calculate coefficients and construct the risk model. We found that patients in the low-risk group had longer survival than those in the high-risk group. Subsequently, we established forest plots and ROC plots including age, sex, radiotherapy, chemotherapy, gene (*IDH*, *MGMT*, *ATRX*, and *EGFR*) mutation status, and risk scores. By plotting risk heatmap, risk curve, ROC curve, and survival curve, it was concluded that the risk model indeed had a good predictive effect. Meanwhile, we obtained similar results in the validation set.

The immune alterations driven by lncRNAs in GBM have also been preliminarily investigated (20, 25). Among the six key lncRNAs, *H19*, *AL162231.2*, and *AC002456.1* were risk factors for the prognosis of GBM, while *ST3GAL6-AS1*, *SOX21-AS1*, and *AC006213.5* were protective factors. LncRNA *H19* as the first discovered classical regulator lncRNA is involved in the regulation of multiple cancers, including GBM (26, 27). *H19* is overexpressed in glioma tissues, negatively correlates with patient survival, and promotes tumor growth by silencing relevant microRNAs (27, 28). *H19* has a potential reference value for glioma remission and immunotherapy. *ST3GAL6-AS1* and *SOX21-AS1* as protective factors have been reported in cancers, lncRNA *ST3GAL6-AS1* overexpression significantly reduces colorectal cancer cell tumorigenesis and metastasis (29), and lncRNA *SOX21-AS1* significantly suppresses tumorigenesis in cervical cancer (30), oral cancer (31), and GBM (32). Relevant literature reports for *AL162231.2*, *AC002456.1*, and *AC006213.5* are sparse.

Identifying the targets of lncRNAs is a key step in exploring their functions. An immune-related CeRNA network was constructed to predict lncRNAs targets, and a PPI network was used to evaluate the interactions of translated proteins from mRNAs in the CeRNA network. The CeRNA network enabled not only a deeper understanding of the communication between RNAs and a more comprehensive analysis of the complex gene interactions underlying carcinogenesis but also the identification of novel biomarkers. Among the prognostic biomarkers involved in the GBM-specific CeRNA and PPI network, the most significant difference gene was *PLAU* (encoding urokinase-type plasminogen activator; uPA), which was overexpressed, was the target of lncRNA *H19*, and was enriched in the KEGG pathway, namely, MicroRNAs in cancer, NF-kappa B signaling pathway, transcriptional misregulation in cancer, and proteoglycans in

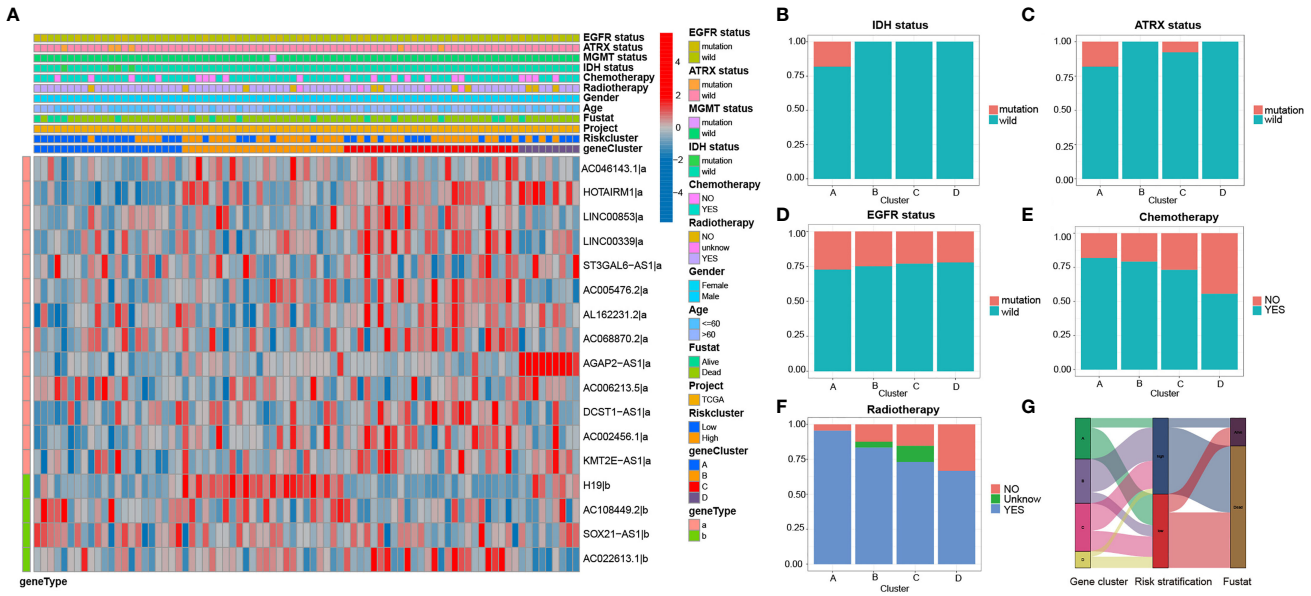

FIGURE 5 | Heatmap and clinicopathological features of four GBM subtypes **(A)** The heatmap and clinicopathological features of the 4 clusters based on the expression patterns of the 17 irlncRNAs in the training set. **(B–F)** Distribution ratio of IDH/ATRX/EGFR status and chemotherapy and radiotherapy in GBM subtypes. **(G)** Sankey diagram showing the prognosis of four GBM subtypes.

cancer pathways. Moreover, the protein pair with the highest combined score was *TGFBR1–TGFBR2*. *PLAU* is frequently upregulated in GBM (33, 34) and promotes cell invasion by *PLAUR* (*PLAU* receptor) binding and activation of extracellular proteases (35). *TGFBR1* and *TGFBR2* have been identified in GBM as a *TGF-β* signaling upstream receptor (36), which has been well known to be a key regulator of migration phenotype in GBM cells (37). In our analysis, lncRNA *H19* may exert biological activity by targeting miR-193a-3p to regulate gene *PLAU* expression. Therefore, it is meaningful to construct immune-related CeRNA and PPI networks in GBM to mine novel biomarkers, predict prognosis, and guide therapy.

In addition to identifying candidate biomarkers in GBM, GSs are also the key to improve personalized treatment (38). Based on 17 PRirlncRNAs, we can classify GBM patients into 4 GSs (A-D). Then, we assessed subtype-specific prognostic values, clinical characteristics, genes and pathways, immune infiltration, and chemotherapeutic drug sensitivity. Our results revealed that GS-A patients displayed the most favorable prognosis, which were characterized by a high mutation rate of genes including *IDH1*, *ATRX* and *EGFR*. Previously published reports indicated that *IDH*, *ATRX* and *EGFR* mutation status significantly influenced the prognosis of glioma patients (39). Such as, *IDH* mutations are frequent in infiltrating astrocytomas (grades II and III) and secondary *GBMs* (1). Primary GBMs typically lack *IDH* mutations and demonstrate *EGFR*, *PDGFRA*, *TP53*, *PTEN*, *NF1*, and *TERT* promoter mutations (40). These classical biomarkers have been integrated into multiple classification schemes and applied to an accurate clinical decision-making process. We observed that GBM with GS-A were characterized by four high-risk lncRNAs (*H19*, *HOTAIRM1*, *AGAP2-AS1*, and *AC002456.1*) and one high-risk mRNA *KRT8* with a low expression level. Among these lncRNAs and mRNAs, lncRNA *HOXA* transcript antisense RNA myeloid-specific 1 (*HOTAIRM1*) participates in the reprogramming of chromatin organization and proliferation and metastasis of cancer (32), which has been found to be highly expressed in a variety of tumors including GBM (41). LncRNA *AGAP2* antisense RNA 1 (*AGAP2-AS1*), transcribed from a gene located at 12q14.1, a novel cancer-related lncRNA, was dysregulated in cancers (42). In GBM, lncRNA *HOTAIRM1* (43, 44) and *AGAP2-AS1* (45, 46), as oncogenic factors, promoted tumorigenesis, predicted a poor clinical outcome, and were potential biomarkers and therapeutic targets. Keratin 8 (KRT8), a major component of the intermediate filament cytoskeleton, promotes tumor progression and metastasis of various cancers (47–49). In our analysis, GS-A was positively correlated with autophagy, the apoptosis, the Wnt signaling pathway, the NOTCH signaling pathway, the ERBB signaling pathway, the RIG like receptor signaling pathway, and the NOD-like receptor signaling pathway. KRT8 may exert its biological activity through regulating the T cell receptor, apoptosis, or the JAK/STATA signaling pathway.

The efficacy of immunotherapy strongly depends on intertumoral tumor-infiltrating immune cells (50). Combining the risk gene of GSs and scRNA-seq data reveals poor prognosis GBM tumor-infiltrating immunoreactive cells. Park et al. demonstrated that high expression on macrophage signatures of GBM patients predicted suboptimal survival (51), which was consistent with our analysis. We observed that the major tumor-

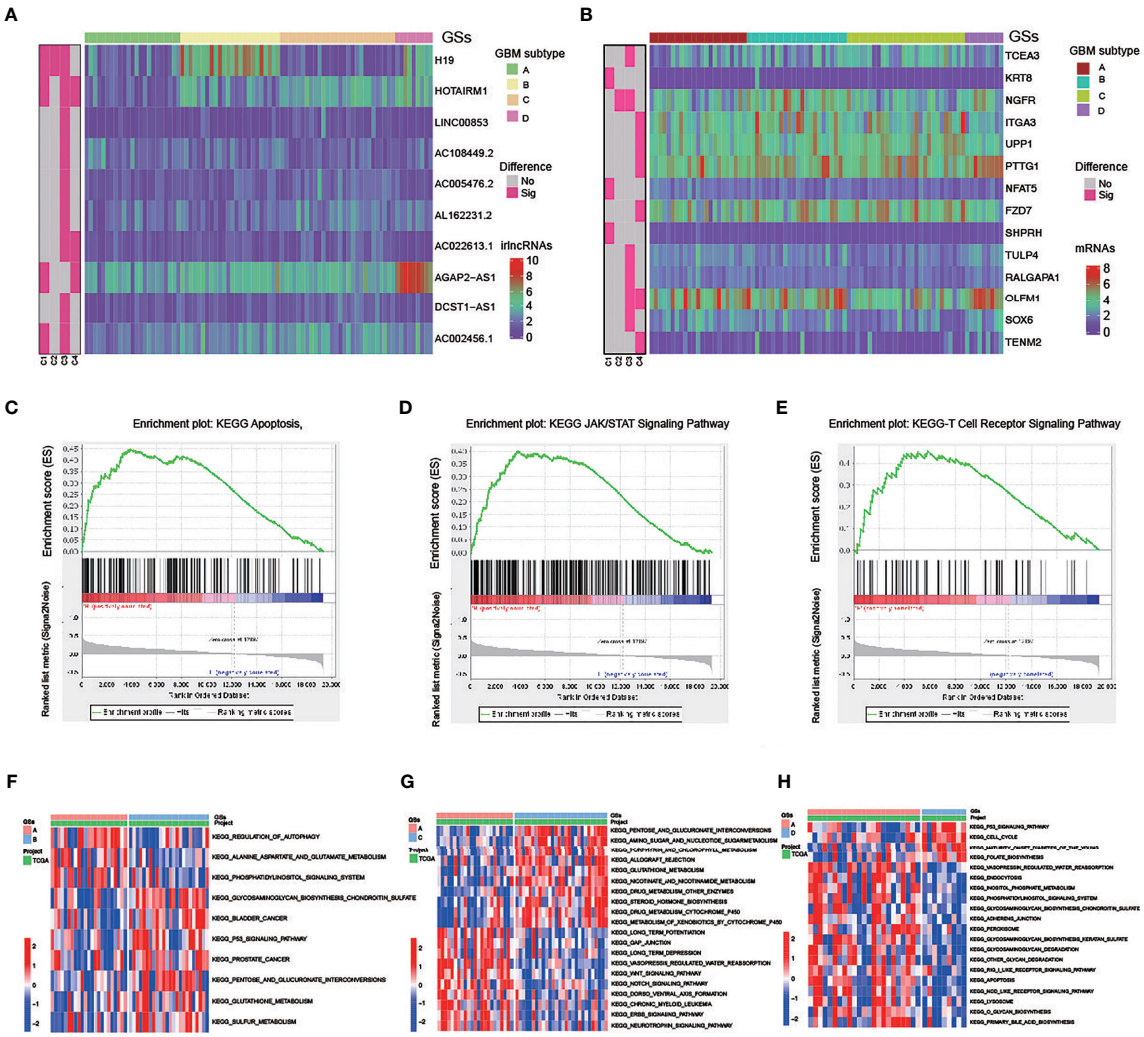

FIGURE 6 | Molecular difference analysis of four GBM subtypes **(A, B)** Heatmaps of 10 differentially expressed irlncRNAs **(A)** and 14 mRNAs **(B)** between the 4 GBM subtypes. **(C–E)** GSEA showing that the functional pathways involved in RKT8 were mainly immune cell- and tumor-related signaling pathways. **(F–H)** GSVA enrichment analysis showing the activation states of biological pathways in GSs.

infiltrating immune cells in GBM with poor prognosis were MSCs and astrocyte. Radfar et al. demonstrated that nonspecific activation of $CD4^+$ T cells dramatically enhanced the cytotoxicity of four chemotherapeutic agents including TMZ, paclitaxel (Pax), Carbo, and 5-FU in cancers (52). Patients with more infiltrated $CD8^+$ T cells had a better response to pembrolizumab treatment than those with less infiltrated cells (53). Our model suggested that high risk was associated with sensitivity to chemotherapeutics such as gefitinib and roscovitine, and GS-A patients in low risk were more sensitive to axitinib and thapsigargin.

Our survival analysis and *in vitro* study showed that three of the four hub genes showed significant predictions of poor OS, and the mRNA and protein levels of KRT8, NGFR, and TCEA3 were significantly upregulated in GBM tissues compared with normal tissues. The above results indicated that these proteins encoded by the hub genes may play a feasible oncogenic role in GBM.

CONCLUSION

In this study, based on 17 PRirlncRNAs, we not only constructed a six-key irlncRNAs prognostic signature but also identified four subtypes of GBM, which had a potential prognostic value. In GBM, lncRNA *H19* may exert biological activity by targeting miR-193a-3p to regulate gene *PLAU* expression; KRT8, NGFR, and TCEA3 may stimulate novel strategies for immunotherapy of GBM patients. Interestingly, KRT8 may exert its biological activity through regulating the T cell receptor, apoptosis, or the JAK/STATA signaling pathway.

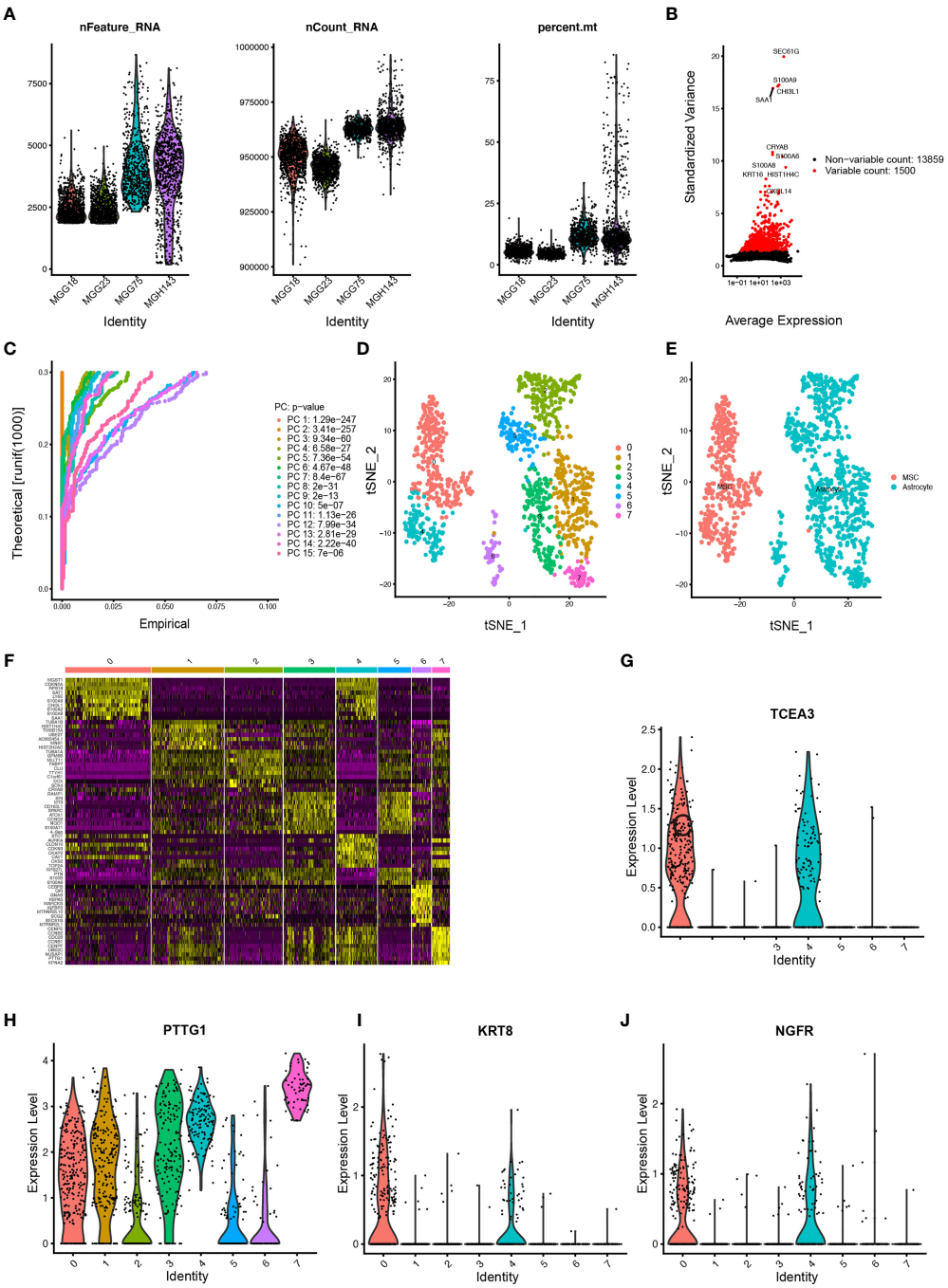

FIGURE 7 | Estimation of tumor-infiltrating cells for GBM subtypes based on scRNA-seq data **(A)** After quality control of the 3,483 cells from the tumor cores of 4 human GBM samples, 1,190 cells were included in the analysis. **(B)** The variance diagram shows 13,859 corresponding genes throughout all cells from GBMs. The red dots represent highly variable genes, and the black dots represent nonvariable genes. The top 10 most variable genes are marked in the plot. **(C)** PCA identified the 15 PCs with an estimated p value < 0.05. **(D)** All eight clusters of cells in GBMs were annotated by singleR and CellMarker according to the composition of the marker genes. **(E)** The tSNE algorithm was applied for dimensionality reduction with the 20 PCs, and 8 cell clusters were successfully classified. **(F)** The differential analysis identified 4,210 marker genes. The top 20 marker genes of each cell cluster are displayed in the heatmap. A total of 68 genes are listed beside of the heatmap after omitting the same top marker genes among clusters. The colors from purple to yellow indicate the gene expression levels from low to high. **(G–J)** Expression profiles of the four risk genes in eight cell clusters.

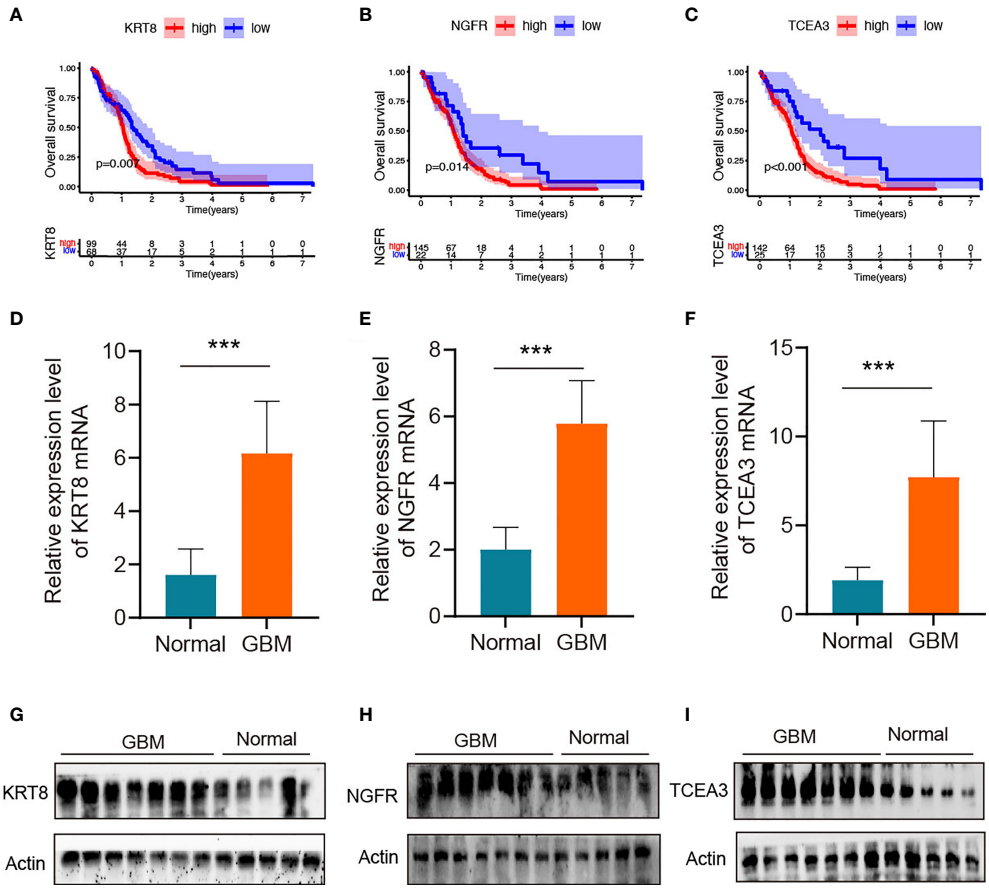

FIGURE 8 | Validation of the hub genes in clinical tissues **(A–C)** Kaplan–Meier survival curves for patients of GBM with high and low gene expression in the TCGA dataset. **(D–F)** qRT-PCR of KRT8, NGFR, and TCEA3 in clinical human GBM samples and normal brain tissues. The expression levels were normalized to β-actin. ***P < 0.001. **(G–I)** The protein expression of KRT8, NGFR, and TCEA3 in clinical human GBM tissues and normal tissues was detected by WB.

Highlights

1. Transcriptome and clinical information from 168 GBM samples was employed to screen 17 immune related lncRNAs (irlncRNAs) associated with prognosis.
2. 17 PRirlncRNAs were screen to construct a signature of 6 key irlncRNAs, which showing a good predictive effect, and similar results in the validation set.
3. GBM-specific immune CeRNA and PPI networks were constructed to predict lncRNAs targets and evaluate the interactions and functions of immune mRNAs translated proteins based on 17 PRirlncRNAs.
4. Four GBM subtypes (A–D) were identified based on 17 PRirlncRNAs, and we evaluated subtype-specific prognostic values, clinical characteristics, genes and pathways, immune infiltration, and chemotherapeutics efficacy.
5. Construction of the lncRNAs risk model and identification of GBM subtypes under immune environment, suggesting that KRT8, NGFR, TCEA3, and irlncRNAs had promising potential for clinical immunotherapy of GBM.

DATA AVAILABILITY STATEMENT

The datasets presented in this study can be found in online repositories. The names of the repository/repositories and accession number(s) can be found in the article/**Supplementary Material**.

ETHICS STATEMENT

Consent for participation for all patients was obtained through The Genotype-Tissue Expression (GTEx) Project, The Cancer Genome Atlas (TCGA) Project, and the Gene Expression Omnibus (GEO) database. Paraffin-embedded GBM tissues and normal brain tissues were obtained from patients who provided informed consent under an Institutional Ethics Committee-approved study from the First Affiliated Hospital of Nanchang University.

AUTHOR CONTRIBUTIONS

All authors contributed to the analysis of data in this study. Conception and design: GZ, FQ and PW. Acquisition, analysis and interpretation of data: WY, WH and FW; Writing, review, and/or revision of the manuscript: WY; Administrative,

technical, or material support: YM and PW. Study supervision: YM and WC. All authors contributed to the article and approved the submitted version.

FUNDING

This work was supported by the Project of Nanchang Science and Technology Support Plan of Jiangxi Province, China (HONGKO Zi [2021] 129) and the National Institute of Health Grant (5R01AR067319-04. 09/2015-07/2020).

ACKNOWLEDGMENTS

The reviewers are grateful for their helpful comments on this article.

SUPPLEMENTARY MATERIAL

The Supplementary Material for this article can be found online at: https://www.frontiersin.org/articles/10.3389/fimmu.2021.706936/full#supplementary-material

REFERENCES

1. Aldape K, Zadeh G, Mansouri S, Reifenberger G, von Deimling A. Glioblastoma: Pathology, Molecular Mechanisms and Markers. *Acta Neuropathol* (2015) 129:829–48. doi: 10.1007/s00401-015-1432-1
2. Louis DN, Perry A, Reifenberger G, von Deimling A, Figarella-Branger D, Cavenee WK, et al. The 2016 World Health Organization Classification of Tumors of the Central Nervous System: A Summary. *Acta Neuropathol* (2016) 131:803–20. doi: 10.1007/s00401-016-1545-1
3. Bhan A, Soleimani M, Mandal SS. Long Noncoding RNA and Cancer: A New Paradigm. *Cancer Res* (2017) 77:3965–81. doi: 10.1158/0008-5472.CAN-16-2634
4. Martens-Uzunova ES, Bottcher R, Croce CM, Jenster G, Visakorpi T, Calin GA. Long Noncoding RNA in Prostate, Bladder, and Kidney Cancer. *Eur Urol* (2014) 65:1140–51. doi: 10.1016/j.eururo.2013.12.003
5. Statello L, Guo CJ, Chen LL, Huarte M. Gene Regulation by Long non-Coding RNAs and its Biological Functions. *Nat Rev Mol Cell Biol* (2021) 22:96–118. doi: 10.1038/s41580-020-00315-9
6. Mathy NW, Chen XM. Long non-Coding RNAs (lncRNAs) and Their Transcriptional Control of Inflammatory Responses. *J Biol Chem* (2017) 292:12375–82. doi: 10.1074/jbc.R116.760884
7. Hirose T, Virnicchi G, Tanigawa A, Naganuma T, Li R, Kimura H, et al. NEAT1 Long Noncoding RNA Regulates Transcription via Protein Sequestration Within Subnuclear Bodies. *Mol Biol Cell* (2014) 25:169–83. doi: 10.1091/mbc.e13-09-0558
8. Hu G, Gong AY, Wang Y, Ma S, Chen X, Chen J, et al. LincRNA-Cox2 Promotes Late Inflammatory Gene Transcription in Macrophages Through Modulating SWI/SNF-Mediated Chromatin Remodeling. *J Immunol* (2016) 196:2799–808. doi: 10.4049/jimmunol.1502146
9. Zhao L, Liu Y, Zhang J, Liu Y, Qi Q. LncRNA SNHG14/miR-5590-3p/ZEB1 Positive Feedback Loop Promoted Diffuse Large B Cell Lymphoma Progression and Immune Evasion Through Regulating PD-1/PD-L1 Checkpoint. *Cell Death Dis* (2019) 10:731. doi: 10.1038/s41419-019-1886-5
10. Hu Q, Ye Y, Chan LC, Li Y, Liang K, Lin A, et al. Oncogenic lncRNA Downregulates Cancer Cell Antigen Presentation and Intrinsic Tumor Suppression. *Nat Immunol* (2019) 20:835–51. doi: 10.1038/s41590-019-0400-7
11. Tang Z, Li C, Kang B, Gao G, Li C, Zhang Z. GEPIA: A Web Server for Cancer and Normal Gene Expression Profiling and Interactive Analyses. *Nucleic Acids Res* (2017) 45:W98–W102. doi: 10.1093/nar/gkx247
12. Shen S, Wang G, Zhang R, Zhao Y, Yu H, Wei Y, et al. Development and Validation of an Immune Gene-Set Based Prognostic Signature in Ovarian Cancer. *EBioMedicine* (2019) 40:318–26. doi: 10.1016/j.ebiom.2018.12.054
13. Wang W, Zhao Z, Yang F, Wang H, Wu F, Liang T, et al. An Immune-Related lncRNA Signature for Patients With Anaplastic Gliomas. *J Neurooncol* (2018) 136:263–71. doi: 10.1007/s11060-017-2667-6
14. Wang X, Gao M, Ye J, Jiang Q, Yang Q, Zhang C, et al. An Immune Gene-Related Five-lncRNA Signature for to Predict Glioma Prognosis. *Front Genet* (2020) 11:612037. doi: 10.3389/fgene.2020.612037
15. Xia P, Li Q, Wu G, Huang Y. An Immune-Related lncRNA Signature to Predict Survival In Glioma Patients. *Cell Mol Neurobiol* (2021) 41:365–75. doi: 10.1007/s10571-020-00857-8
16. Herbst RS, Heymach JV, Lippman SM. Lung Cancer. *N Engl J Med* (2008) 359:1367–80. doi: 10.1056/NEJMra0802714
17. Siegel RL, Miller KD, Jemal A. Cancer Statistics, 2019. *CA Cancer J Clin* (2019) 69:7–34. doi: 10.3322/caac.21551
18. Lin JJ, Cardarella S, Lydon CA, Dahlberg SE, Jackman DM, Janne PA, et al. Five-Year Survival in EGFR-Mutant Metastatic Lung Adenocarcinoma Treated With EGFR-TKIs. *J Thorac Oncol* (2016) 11:556–65. doi: 10.1016/j.jtho.2015.12.103
19. Slack FJ, Chinnaiyan AM. The Role of Non-Coding RNAs in Oncology. *Cell* (2019) 179:1033–55. doi: 10.1016/j.cell.2019.10.017
20. Wu P, Cai J, Chen Q, Han B, Meng X, Li Y, et al. Lnc-TALC Promotes O(6)-Methylguanine-DNA Methyltransferase Expression via Regulating the C-Met Pathway by Competitively Binding With miR-20b-3p. *Nat Commun* (2019) 10:2045. doi: 10.1038/s41467-019-10025-2
21. Hanahan D, Coussens LM. Accessories to the Crime: Functions of Cells Recruited to the Tumor Microenvironment. *Cancer Cell* (2012) 21:309–22. doi: 10.1016/j.ccr.2012.02.022
22. Pitt JM, Marabelle A, Eggermont A, Soria JC, Kroemer G, Zitvogel L. Targeting the Tumor Microenvironment: Removing Obstruction to Anticancer Immune Responses and Immunotherapy. *Ann Oncol* (2016) 27:1482–92. doi: 10.1093/annonc/mdw168
23. Li Y, Jiang T, Zhou W, Li J, Li X, Wang Q, et al. Pan-Cancer Characterization of Immune-Related lncRNAs Identifies Potential Oncogenic Biomarkers. *Nat Commun* (2020) 11:1000. doi: 10.1038/s41467-020-14802-2
24. Atianand MK, Caffrey DR, Fitzgerald KA. Immunobiology of Long Noncoding RNAs. *Annu Rev Immunol* (2017) 35:177–98. doi: 10.1146/annurev-immunol-041015-055459
25. Peng Z, Liu C, Wu M. New Insights Into Long Noncoding RNAs and Their Roles in Glioma. *Mol Cancer* (2018) 17:61. doi: 10.1186/s12943-018-0812-2
26. Brannan CI, Dees EC, Ingram RS, Tilghman SM. The Product of the H19 Gene may Function as an RNA. *Mol Cell Biol* (1990) 10:28–36. doi: 10.1128/MCB.10.1.28
27. Jia P, Cai H, Liu X, Chen J, Ma J, Wang P, et al. Long non-Coding RNA H19 Regulates Glioma Angiogenesis and the Biological Behavior of Glioma-Associated Endothelial Cells by Inhibiting microRNA-29a. *Cancer Lett* (2016) 381:359–69. doi: 10.1016/j.canlet.2016.08.009
28. Deng Y, Zhou L, Yao J, Liu Y, Zheng Y, Yang S, et al. Associations of lncRNA H19 Polymorphisms at MicroRNA Binding Sites With Glioma Susceptibility and Prognosis. *Mol Ther Nucleic Acids* (2020) 20:86–96. doi: 10.1016/j.omtn.2020.02.003
29. Hu J, Shan Y, Ma J, Pan Y, Zhou H, Jiang L, et al. LncRNA ST3Gal6-AS1/ST3Gal6 Axis Mediates Colorectal Cancer Progression by Regulating Alpha-2,3 Sialylation *via* PI3K/Akt Signaling. *Int J Cancer* (2019) 145:450–60. doi: 10.1002/ijc.32103
30. Wang R, Li Y, Du P, Zhang X, Li X, Cheng G. Hypomethylation of the lncRNA SOX21-AS1 has Clinical Prognostic Value in Cervical Cancer. *Life Sci* (2019) 233:116708. doi: 10.1016/j.lfs.2019.116708
31. Yang CM, Wang TH, Chen HC, Li SC, Lee MC, Liou HH, et al. Aberrant DNA Hypermethylation-Silenced SOX21-AS1 Gene Expression and its Clinical Importance in Oral Cancer. *Clin Epigenet* (2016) 8:129. doi: 10.1186/s13148-016-0291-5
32. Wang Z, Ji X, Gao L, Guo X, Lian W, Deng K, et al. Comprehensive In Silico Analysis of a Novel Serum Exosome-Derived Competitive Endogenous RNA Network for Constructing a Prognostic Model for Glioblastoma. *Front Oncol* (2021) 11:553594. doi: 10.3389/fonc.2021.553594

33. Bernhart E, Damm S, Wintersperger A, DeVaney T, Zimmer A, Raynham T, et al. Protein Kinase D2 Regulates Migration and Invasion of U87MG Glioblastoma Cells *In Vitro*. *Exp Cell Res* (2013) 319:2037–48. doi: 10.1016/j.yexcr.2013.03.029
34. Dikshit B, Irshad K, Madan E, Aggarwal N, Sarkar C, Chandra PS, et al. FAT1 Acts as an Upstream Regulator of Oncogenic and Inflammatory Pathways, *via* PDCD4, in Glioma Cells. *Oncogene* (2013) 32:3798–808. doi: 10.1038/onc.2012.393
35. Blasi F, Carmeliet P. uPAR: A Versatile Signalling Orchestrator. *Nat Rev Mol Cell Biol* (2002) 3:932–43. doi: 10.1038/nrm977
36. Vinchure OS, Sharma V, Tabasum S, Ghosh S, Singh RP, Sarkar C, et al. Polycomb Complex Mediated Epigenetic Reprogramming Alters TGF-Beta Signaling via a Novel EZH2/miR-490/TGIF2 Axis Thereby Inducing Migration and EMT Potential in Glioblastomas. *Int J Cancer* (2019) 145:1254–69. doi: 10.1002/ijc.32360
37. Paw I, Carpenter RC, Watabe K, Debinski W, Lo HW. Mechanisms Regulating Glioma Invasion. *Cancer Lett* (2015) 362:1–7. doi: 10.1016/j.canlet.2015.03.015
38. Berger AC, Korkut A, Kanchi RS, Hegde AM, Lenoir W, Liu W, et al. A Comprehensive Pan-Cancer Molecular Study of Gynecologic and Breast Cancers. *Cancer Cell* (2018) 33:690–705 e699. doi: 10.1016/j.ccell.2018.03.014
39. van Tellingen O, Yetkin-Arik B, de Gooijer MC, Wesseling P, Wurdinger T, de Vries HE. Overcoming the Blood-Brain Tumor Barrier for Effective Glioblastoma Treatment. *Drug Resist Update* (2015) 19:1–12. doi: 10.1016/j.drup.2015.02.002
40. Appin CL, Brat DJ. Biomarker-Driven Diagnosis of Diffuse Gliomas. *Mol Aspects Med* (2015) 45:87–96. doi: 10.1016/j.mam.2015.05.002
41. Pastori C, Kapranov P, Penas C, Peschansky V, Volmar CH, Sarkaria JN, et al. The Bromodomain Protein BRD4 Controls HOTAIR, a Long Noncoding RNA Essential for Glioblastoma Proliferation. *Proc Natl Acad Sci USA* (2015) 112:8326–31. doi: 10.1073/pnas.1424220112
42. Hellner KA. [Night Blindness and Retinopathy in Systemic Diseases]. *Verh Dtsch Ges Inn Med* (1976) 82 Pt 1:580–3.
43. Li Q, Dong C, Cui J, Hong X. Over-Expressed lncRNA HOTAIRM1 Promotes Tumor Growth and Invasion Through Up-Regulating HOXA1 and Sequestering G9a/EZH2/Dnmts Away From the HOXA1 Gene in Glioblastoma Multiforme. *J Exp Clin Cancer Res* (2018) 37:265. doi: 10.1186/s13046-018-0941-x
44. Xie P, Li X, Chen R, Chen Y, Liu D, Liu W, et al. Upregulation of HOTAIRM1 Increases Migration and Invasion by Glioblastoma Cells. *Aging (Albany NY)* (2020) 13:2348–64. doi: 10.18632/aging.202263
45. Luo W, Li X, Song Z, Zhu X, Zhao S. Long non-Coding RNA AGAP2-AS1 Exerts Oncogenic Properties in Glioblastoma by Epigenetically Silencing TFPI2 Through EZH2 and LSD1. *Aging (Albany NY)* (2019) 11:3811–23. doi: 10.18632/aging.102018
46. Luo X, Tu T, Zhong Y, Xu S, Chen X, Chen L, et al. AGAP2-AS1 May Promote the Occurrence and Development of Glioblastoma by Sponging miR-9-5p: Evidence From a ceRNA Network. *Front Oncol* (2021) 11:607989. doi: 10.3389/fonc.2021.607989
47. Ramanand SG, Chen Y, Yuan J, Daescu K, Lambros MB, Houlahan KE. The Landscape of RNA Polymerase II-Associated Chromatin Interactions in Prostate Cancer. *J Clin Invest* (2020) 130:3987–4005. doi: 10.1172/JCI134260
48. Fang J, Wang H, Liu Y, Ding F, Ni Y, Shao S, et al. High KRT8 Expression Promotes Tumor Progression and Metastasis of Gastric Cancer. *Cancer Sci* (2017) 108:178–86. doi: 10.1111/cas.13120
49. Xie L, Dang Y, Guo J, Sun X, Xie T, Zhang L, et al. High KRT8 Expression Independently Predicts Poor Prognosis for Lung Adenocarcinoma Patients. *Genes (Basel)* (2019) 10. doi: 10.3390/genes10010036
50. McGranahan N, Furness AJ, Rosenthal R, Ramskov S, Lyngaa R, Saini SK, et al. Clonal Neoantigens Elicit T Cell Immunoreactivity and Sensitivity to Immune Checkpoint Blockade. *Science* (2016) 351:1463–9. doi: 10.1126/science.aaf1490
51. Iglesia MD, Parker JS, Hoadley KA, Serody JS, Perou CM, Vincent BG. Genomic Analysis of Immune Cell Infiltrates Across 11 Tumor Types. *J Natl Cancer Inst* (2016) 108. doi: 10.1093/jnci/djw144
52. Radfar S, Wang Y, Khong HT. Activated CD4+ T Cells Dramatically Enhance Chemotherapeutic Tumor Responses *In Vitro* and *In Vivo*. *J Immunol* (2009) 183:6800–7. doi: 10.4049/jimmunol.0901747
53. Garon EB, Hellmann MD, Rizvi NA, Carcereny E, Leighl NB, Ahn MJ, et al. Five-Year Overall Survival for Patients With Advanced NonSmall-Cell Lung Cancer Treated With Pembrolizumab: Results From the Phase I KEYNOTE-001 Study. *J Clin Oncol* (2019) 37:2518–27. doi: 10.1200/JCO.19.00934

Conflict of Interest: The authors declare that the research was conducted in the absence of any commercial or financial relationships that could be construed as a potential conflict of interest.

Publisher's Note: All claims expressed in this article are solely those of the authors and do not necessarily represent those of their affiliated organizations, or those of the publisher, the editors and the reviewers. Any product that may be evaluated in this article, or claim that may be made by its manufacturer, is not guaranteed or endorsed by the publisher.

frontiers in Immunology

MINI REVIEW
published: 30 November 2021
doi: 10.3389/fimmu.2021.724200

SNAIL1: Linking Tumor Metastasis to Immune Evasion

Xiaolong Tang[1], *Xue Sui*[1], *Liang Weng*[2,3,4,5,6,7*] *and Yongshuo Liu*[8,9*]

[1] Department of Laboratory Medicine, Binzhou Medical University, Binzhou, China, [2] Department of Oncology, Xiangya Cancer Center, Xiangya Hospital, Central South University, Changsha, China, [3] Key Laboratory of Molecular Radiation Oncology Hunan Province, Xiangya Hospital, Central South University, Changsha, China, [4] Hunan International Science and Technology Collaboration Base of Precision Medicine for Cancer, Xiangya Hospital, Central South University, Changsha, China, [5] Hunan Provincial Clinical Research Center for Respiratory Diseases, Xiangya Hospital, Central South University, Changsha, China, [6] Institute of Gerontological Cancer Research, National Clinical Research Center for Gerontology, Changsha, China, [7] Center for Molecular Imaging of Central South University, Xiangya Hospital, Changsha, China, [8] Department of Clinical Laboratory, Binzhou Medical University Hospital, Binzhou, China, [9] Biomedical Pioneering Innovation Center (BIOPIC), Beijing Advanced Innovation Center for Genomics, Peking-Tsinghua Center for Life Sciences, Peking University Genome Editing Research Center, State Key Laboratory of Protein and Plant Gene Research, School of Life Sciences, Peking University, Beijing, China

The transcription factor Snail1, a key inducer of epithelial-mesenchymal transition (EMT), plays a critical role in tumor metastasis. Its stability is strictly controlled by multiple intracellular signal transduction pathways and the ubiquitin-proteasome system (UPS). Increasing evidence indicates that methylation and acetylation of Snail1 also affects tumor metastasis. More importantly, Snail1 is involved in tumor immunosuppression by inducing chemokines and immunosuppressive cells into the tumor microenvironment (TME). In addition, some immune checkpoints potentiate Snail1 expression, such as programmed death ligand 1 (PD-L1) and T cell immunoglobulin 3 (TIM-3). This mini review highlights the pathways and molecules involved in maintenance of Snail1 level and the significance of Snail1 in tumor immune evasion. Due to the crucial role of EMT in tumor metastasis and tumor immunosuppression, comprehensive understanding of Snail1 function may contribute to the development of novel therapeutics for cancer.

Keywords: Snail1, EMT, signaling pathway, ubiquitination, methylation, acetylation, tumor immunity

OPEN ACCESS

Edited by:
Qin Yan,
Yale University, United States

Reviewed by:
Khaled Murshed,
Hamad Medical Corporation, Qatar
Dongdong Zhang,
Institute of Biophysics (CAS), China

***Correspondence:**
Liang Weng
wengliang@csu.edu.cn
Yongshuo Liu
liuyongshuo@pku.edu.cn

Specialty section:
This article was submitted to Cancer Immunity and Immunotherapy, a section of the journal Frontiers in Immunology

Received: *12 June 2021*
Accepted: *15 November 2021*
Published: *30 November 2021*

Citation:
Tang X, Sui X, Weng L and Liu Y (2021) SNAIL1: Linking Tumor Metastasis to Immune Evasion. Front. Immunol. 12:724200. doi: 10.3389/fimmu.2021.724200

INTRODUCTION

Metastasis is one of the most prominent features of malignant tumors and is the leading cause of death in tumor patients (1). Tumor metastasis is a multi-step process in which EMT has a crucial regulatory role. During the process of EMT, epithelial cells lose their cell polarity and cell–cell adhesion, and transit to quasi-mesenchymal cell states, thus increasing their migration and invasion properties (2). Recent studies indicated that tumor progression and metastasis are closely related to epigenetic modifications and the immune system. It was reported that immune checkpoint molecules such as PD-L1 are involved in EMT regulation, while EMT can also induce immunosuppression and immune evasion in tumors (3).

The Snail family of zinc finger transcription factors comprises three members in vertebrates, Snail1 (Snail), Snail2 (Slug), Snail3 (Smuc) (4, 5). Snail1 and Snail2 down-regulate the expression of many target proteins associated with EMT. Among them, the most significant one is E-cadherin (6).

Due to the critical role of Snail1 in EMT, this mini review focuses on how appropriate Snail1 levels are maintained in cells, with emphasis on the role of epigenetic and UPS in the regulation of Snail1. Furthermore, we also discuss the involvement of Snail1 in tumor immune evasion, a role which has made it a promising therapeutics target in tumor treatment.

STRUCTURAL AND FUNCTIONAL CHARACTERISTICS OF SNAIL1

In all Snail family members, the amino terminal end contains a highly conserved SNAG domain, which functions as a transcriptional repressor domain (7). The fingers correspond to the C2H2 type and bind to the upstream regulatory region of target genes for gene specific transcriptional inhibition (8). The central region of Snail2 includes the Slug domain, while Snail1 has two defined functional domains in this region: a regulatory domain containing an Xpo1/CRM1 mediated nuclear export signal (NES) (9) and a serine-rich domain involved in the regulation of its stability (10) **(Figure 1A)**.

Snail1, as a transcriptional repressor, is implicated in the regulation of other tumor metastasis suppressors, such as the epithelial marker E-cadherin (11). Previous studies reported that SNAG domain of Snail1 couples on the *CDH1* (which encodes E-cadherin) promoter (12), and recruits histone deacetylase (HDAC). Subsequently, Snail1, HDAC1, HDAC2 and mSin3A conjointly form a multi-molecular complex that further inhibits the expression of E-cadherin (13). Furthermore, Snail1 interacts with the H3K9 methyltransferase G9A or SUV39H1 and recruits it to the *CDH1* promoter for transcriptional inhibition in breast cancer (14, 15), collectively resulting in the occurrence of EMT.

THE SIGNALING PATHWAYS INVOLVED IN SNAIL1 EXPRESSION

The expression of Snail1 is regulated by many signaling pathways both at the transcriptional and protein level (16, 17) **(Figure 1B)**. Physiologically, these signaling pathways control normal cell morphology, proliferation, differentiation, and apoptosis. However, abnormal activation of these signaling pathways contribute to the initiation and progression of tumors activated (18, 19).

TGF-β Pathway

The transforming growth factor-β (TGF-β) was described as an inducer of EMT during the development of tumor (20). Mechanistically, TGF-β binds to its receptor TβRII and TβRI, which subsequently phosphorylates its downstream targets, including members of the SMAD family of signal transducers, SMAD2 and SMAD3 (21), forming a heterooligomeric complex

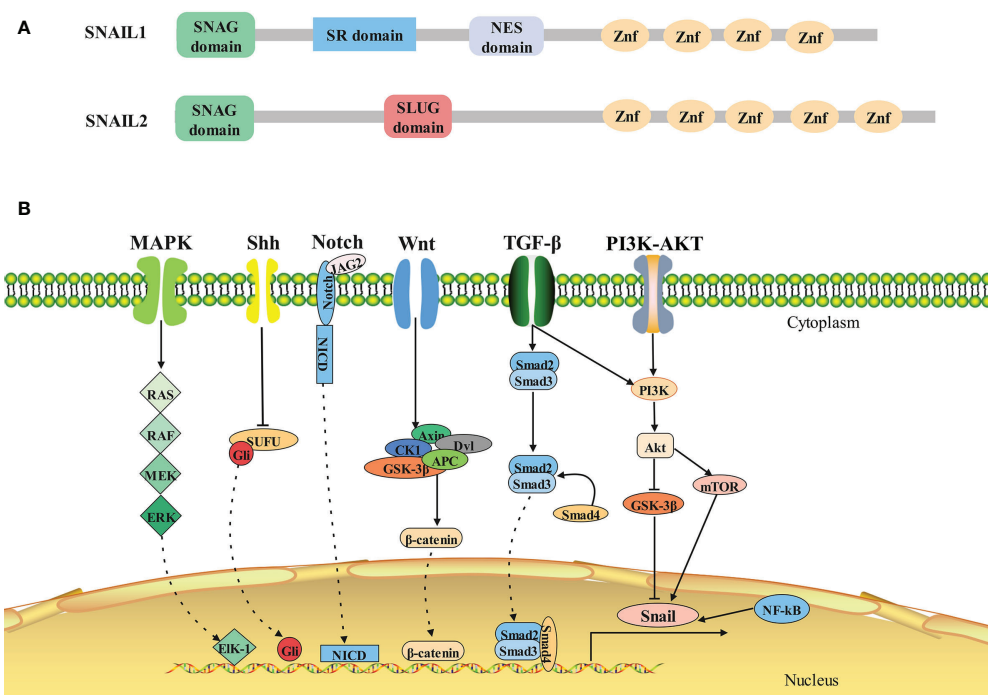

FIGURE 1 | Structure and signaling pathways of SNAIL1. **(A)**Architecture of SNAIL1 in human. Composite of the overall structure of Snail1 and Snail2, which shows the relative positions of the SNAG domain, the zinc fingers (I–V), and the Slug-specific boxes, NES domain and serine-rich domain. **(B)**The molecular signaling pathways of SNAIL1. Snail1 is regulated by several signaling pathways that promote its expression. From left to right: MAPK, Shh, Notch, Wnt, TGF-β, PI3K-AKT, and NF-κB signaling pathway.

with SMAD4 (22). Then this SMAD complex translocates to the nucleus and functions as a transcription factor to regulate the transcription of target genes such as Snail1 in human tumors (16, 21, 23–25).

PI3K-Akt Pathway

The phosphatidylinositol 3-kinase (PI3K)-Akt signaling pathway is hyperactivated or altered in many cancer types (26–28) and regulates a broad range of cellular processes (29, 30). It is well known that Akt can phosphorylate and inhibit GSK-3β activity, subsequently suppressing the GSK-3β-mediated phosphorylation of Snail1 and facilitating its stabilization and nuclear localization, which ultimately promotes EMT widely presenting in a variety of tumors (31–36). In addition to GSK-3β, PI3K-Akt also activates mTOR, thereby potentiating Snail1 expression in gastric, breast, pancreatic and ovarian cancer (37–40). Furthermore, some studies also indicate TGF-β regulates Snail1 expression *via* the Akt/GSK-3β signaling pathway in osteosarcoma and ovarian clear cell carcinoma (41, 42).

Wnt Pathway

In the presence of Wnt signaling, the destruction complex (APC, Dvl, Axin, GSK-3β, CK1) reduces the phosphorylation and ubiquitination of β-catenin (43).Thus, levels of cytoplasmic β-catenin rise, which translocates to the nucleus and induces transcription of pro-invasive factors (44–46). Moreover, β-catenin/T-cell factor (TCF) transcriptional complex regulates Snail1 *via* Axin2-mediated nuclear export of GSK-3β in breast cancer (47).

Notch Pathway

Notch signaling is generated through the interaction between Notch receptors and ligands such as Jagged-2 (JAG2) (48). Notch is released into the cytoplasm by intracellular segment (NICD) after being sheared three times (49), and then enters the nucleus to bind to the Snail1 promoter, directly stimulating transcription (50).

Shh Pathway

Sonic Hedgehog (Shh) is a lipid-modified secreted protein that couples to Patched receptor (51). In the presence of Hedgehog signaling, Smoothened is relieved from Patched-mediated suppression due to the Hedgehog-dependent internalization of Patched, which leads to inactivation of SUFU for the stabilization and nuclear accumulation of Gli family members (51, 52). So far, Shh-mediated Gli1 activation was reported to induce the expression of Snail1 in a variety of cancers, such as breast, skin, ovarian, pancreatic, neuroendocrine cancer and basal cell carcinoma (45, 53–57).

MAPK Pathway

The Ras/Raf/MEK/ERK pathway is the most important signaling cascade among all MAPK signal (58). Once activated, ERK translocates to the nucleus, binds to and regulates the activity of the transcription factor Elk-1 through phosphorylation (58). Of note, activation of Elk1 facilitates recruitment of phosphorylated mitogen and stress activated protein kinase 1 (MSK1), which in turn enhances histone H3 acetylation and phosphorylation (serine 10) of Snail1 promoter, ultimately promoting the transcription of Snail1 (59). Furthermore hepatocyte growth factor (HGF) could induce transcription of Snail1 by activating MAPK signaling pathway in liver cancer (60).

NF-κB Pathway

The over-activation of nuclear factor-κB (NF-κB) with a role in the inflammatory response, immune response and cell apoptosis, is associated with multifarious tumors (61). Previous studies have demonstrated that the activation of the NF-κB pathway blocked the degradation and promoted the transcription of Snail1 (62), subsequently facilitating the migration and invasion in breast, colorectal, gastric cancers, cholangiocarcinoma and malignant human keratinocyte (63–66).

REGULATION OF SNAIL1 EXPRESSION BY UBIQUITIN-PROTEASOME STSTEM

Ubiquitin mediates protein degradation *via* binding to lysine residues of the substrate proteins (67). It is highly conserved in eukaryotic cells and can also function as a signaling molecule to modulate protein function (68). Its eight residues including M1, K6, K11, K27, K29, K33, K48, and K63 are used as attachment sites to form polyubiquitin chains (69). The most abundant chain types are K48, which are usually degraded by the 26S proteasome (68).

Degradation of SNAIL1 by UPS

Snail1 is an extremely unstable protein, β-TrCP1 was first reported to be involved in Snail1 ubiquitination *via* GSK-3β mediated phosphorylation of S96 and S100 residues on Snail1 (10). In contrast, Snail1 is ubiquitinated independently of GSK-3β phosphorylation by FBXL14 through K98, 137, and 146 residues (70). Interestingly, miR-27a can directly down-regulate the expression of FBXO45, resulting in reduced Snail1 degradation (71). In breast cancer, the S11 residue of Snail1 is phosphorylated by PKD1, which promotes the ubiquitination and degradation of Snail1 by FBXO11 (72, 73), while FBXO22 depends on GSK-3β (74). In addition, it has been reported that PPIL2, SPSB3 and TRIM21 are involved in ubiquitination and degradation of Snail1 (75–77). In gastric cancer, phosphorylation of Snail1 is required for the F-box domain of FBXO31 to function (78), FBXW7 inhibits metastasis in part by binding to Snail1 (79) and FBXL5 promotes poly-ubiquitination of Snail1 at K85, K146 and K234 residues (80, 81). In Non-small cell lung cancer, both β-TrCP2 and FBXW7 are absolutely implicated in ubiquitination and degradation of Snail1 (82, 83). In cervical cancer, HECTD1-mediated degradation of Snail1 occurs in the cytoplasm rather than in the nucleus (84). Finally, other E3 ligases such as TRIM50 and CHIP, are also involved in regulation of Snail1 in hepatocarcinoma and ovarian cancer, respectively (85, 86).

So far, some molecular targets have been found based on the above E3 ligases, which are potential therapeutic targets.

LINC00511 and EBV-miR-Bart10-3p both inhibit β-TrCP1 and prevent Snail1 degradation in triple negative breast cancer and nasopharyngeal carcinoma, respectively (87, 88). In non-small cell lung cancer, the expression of the β-TrCP2 is inhibited by miR-106b-25 (83), while FBXW7 agonist (Oridonin) contributes to the degradation of Snail1 (89). In hepatocellular carcinoma, miR-1306-3p directly targets FBXL5 to suppress Snail1 degradation (90). Likewise, miR-27a immediately down-regulate the expression of FBXO45 (91). Particularly, BRD4 identifies acetylated K146 and K187 on Snail1 in an acetylation-dependent manner to prevent its degradation by FBXL14 and β-TrCP1 in gastric cancer (92). Inversely, Metformin is beneficial to the expression of LKB1, thereby strengthening the capacity of FBXL14 in pancreatic cancer (93) **(Figure 2A)**.

Stabilizing the Expression of SNAIL1 by DUBs

Ubiquitination is a reversible process and ubiquitin moieties are removed from polypeptides by deubiquitinases (DUBs) (94). Currently, plentiful DUBs are involved in the occurrence, progression, and drug resistance of cancer (95–97). In esophageal squamous cell carcinoma, OTUB1 inhibits the ubiquitination and degradation of SMAD2/3, leading to strengthen TGF-β signaling and stabilization of Snail1 expression (98, 99). Interestingly, USP26 is a specific deubiquitinase of Snail1 and significantly increases its stability by combining with the zinc finger domain at the Snail1, an essential region for its stability and nuclear localization (100, 101). In addition, EIF3H and PSMD14 have also been found to be involved in Snail1 deubiquitination (102, 103). In breast cancer, DUB3 couples on SNAG domain of Snail1 and inhibits ubiquitination of Snail1 mediated by FBXL14 and β-TrCP1 (104). Analogously, CSN2 removes the ubiquitination of Snail1 *via* disrupting its binding to GSK-3β and β-TrCP (62). In lung cancer, CSN5 and USP37 significantly stabilize the expression of Snail1. More importantly, USP37 is closely associated with increased mortality and metastasis rates (105, 106). In glioblastoma, USP3 also hydrolyzes FBXO11 or FBXW1-induced polyubiquitination chain on Snail1, resulting in increased aggressiveness and tumorigenicity (107). Similarly, high expression of OTUB1 in gliomas is associated with poor prognosis (108). In colorectal cancer, up-regulation of USP47 is mediated by SOX9, leading to an increase in Snail1 deubiquitination under hypoxia condition (109). In gastric cancer, USP29 enhanced the interaction between Snail1 and SCP1, causing both dephosphorylation and deubiquitination of Snail1 (110).

EPIGENETIC MODIFICATION IN SNAIL1 REGULATION

Epigenetic abnormalities have been linked to many human diseases, including cancer (111, 112). Particularly, methylation and acetylation are involved in Snail1-mediated tumor metastasis **(Figure 2A)**.

Methylation of SNAIL1

DNA methylation is an important mechanism of epigenetic gene regulation, which primarily occurs at CpG dinucleotide within gene promoters by a covalent modification of cytosine residues *via* DNA methyltransferase (DNMT) enzymes (113). It was previously reported that DNA methylation in the first intron region of Snail1 was negatively correlated with its transcription level, but its expression was increased when treated with DNMT inhibitor 5-Aza-2 '-deoxycytidine in trophoblast cells (114). Uniformly, the chromatin remodeling factor ARID2 represses EMT of hepatocellular carcinoma by recruiting DNMT1 to Snail1 promoter, which increases promoter methylation and inhibits its transcription (115). Recently, m6A RNA methylation is an emerging epigenetic modification, which has been associated with the progression of several cancers (116, 117). Interestingly, m6A is methylated by Methyltransferase-like 3 (METTL3) to accelerate Snail1 expression in HeLa cells (118), which is equivalent to indirect regulation of Snail1 by methylation.

Acetylation of SNAIL1

Protein acetylation was originally discovered on histones in the nucleus and involved in gene transcription (119). Subsequently, non-histone proteins were increasingly found to also undergo acetylation (120). In nasopharyngeal carcinoma, the glucose metabolizing enzyme PDHE1α facilitates H3K9 acetylation on the Snail1 promoter to enhance cell motility and thereby drive cancer metastasis (121). Inversely, HOPX mediates epigenetic silencing of Snail1 transcription through the enhancement of histone H3K9 deacetylation in the Snail1 promoter (122). In lung cancer cells, p300 acetylates Snail1 at K187 (123), and CREB-binding protein (CBP) interacts with and acetylates Snail1 at K146 and K187, which prevents formation of the repressor complex (124). As mentioned above, BRD4 recognizes acetylated K146 and K187 on Snail1 to prevent it from being degraded by E3 ligases in gastric cancer (92).

At present, histone deacetylase inhibitors (HDACIs) are now emerging as a new class of anticancer agents (125, 126). However, HDACIs stabilize surprisingly Snail1 expression through several mechanisms in hepatocellular carcinoma: HDACIs up-regulate Snail1 at the transcriptional level by promoting SMAD2/3 phosphorylation and nuclear translocation (127). Posteriorly, HDACIs regulate the stabilization of Snail1 *via* up-regulating the expression of CSN2, which interacts with Snail1 to expose its acetylation site, leading to inhibit degradation of Snail1 *via* preventing its phosphorylation and ubiquitination (127). Coincidentally, this phenomenon was also observed in CNE2 cells (128). Accordingly, more cautions should be exercised in the usage of medicines such as HDACIs, as they may increase the risk of tumor metastasis.

BIDIRECTIONAL REGULATION OF SNAIL1 AND TUMOR IMMUNE ENVIRONMENT IN TUMOR PROGRESSION

Tumorigenesis and progression are influenced by tumor microenvironment and controlled by the host immune system

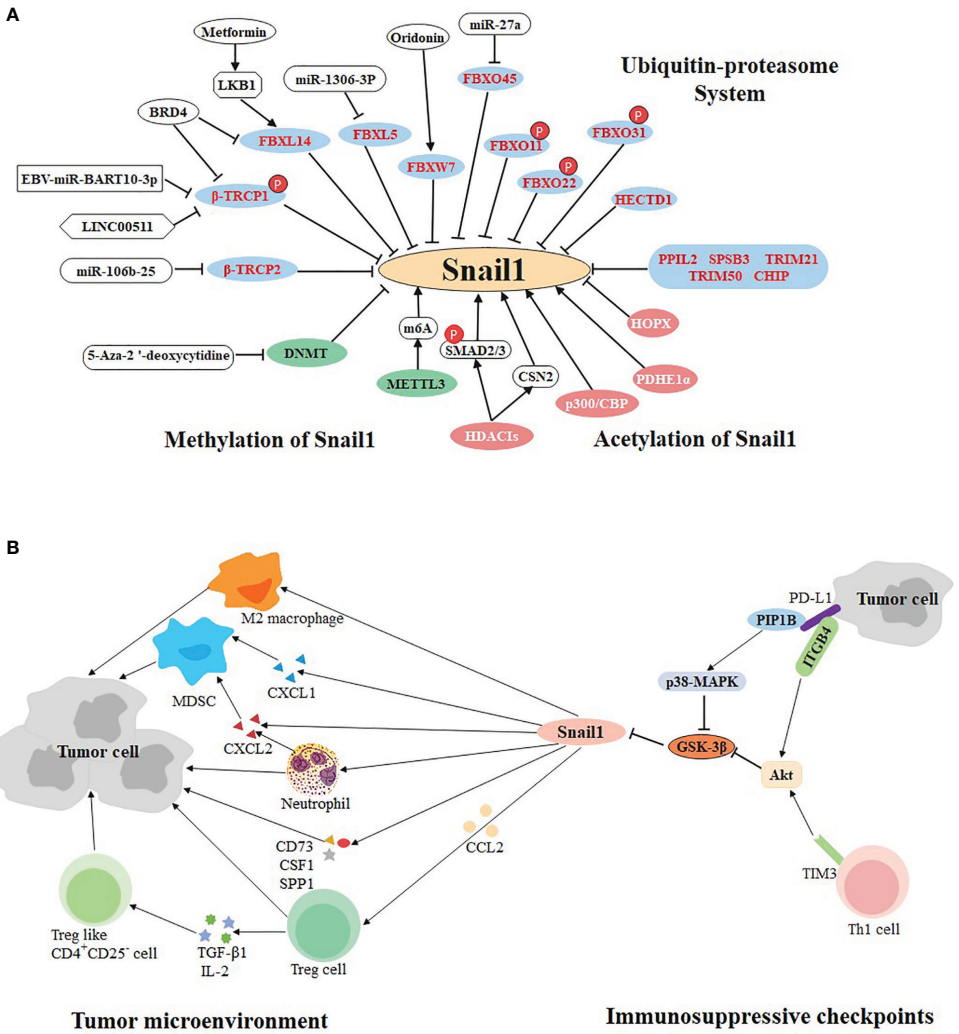

FIGURE 2 | Multifaceted regulation of SNAIL1. **(A)** Ubiquitination, methylation, and acetylation regulate the expression of SNAIL1. The ubiquitin E3 ligases in the blue circle negatively regulate the expression of Snail1. Small molecule compounds or drugs directly or indirectly act on E3 ligase to promote or inhibit the expression of Snail1. Molecules in the green and pink circles participate in methylation and acetylation of Snail1, respectively. **(B)** Bidirectional regulation of SNAIL1 and tumor immune environment. Snail1 recruits immunosuppressive cells (including Treg, MDSCs, M2 macrophages, neutrophils, and Treg-like CD4+CD25- cells) to participate in the formation of tumor microenvironment via cytokines, chemokines and their receptors. In addition, immunosuppressive checkpoints PD-L1 and TIM-3 can regulate the expression of Snail1 through different molecular pathways.

(129). In addition to malignant cells, adipocytes, fibroblasts, tumor vasculature, lymphocytes, dendritic cells, and cancer-associated fibroblasts are present in the tumor microenvironment (130). The last decade has witnessed dramatic advances in cancer treatment through immunotherapy such as immune checkpoints inhibitors, which are the most popular and promising treatment at present (131). Recently, the bidirectional regulation of immune checkpoints and EMT was uncovered *via* Snail1 (**Figure 2B**).

Immunosuppressive Checkpoints Regulate SNAIL1 Expression

So far, two immune checkpoint proteins PD-L1 and TIM-3 have been found to regulate Snail1 expression. PD-L1, which accumulates to high level on the surface of some tumor cells, can bind to PD-1 and induce T cells exhaustion, thereby mediating tumor immune escape and potentiating tumor progression (132, 133). Histochemical staining of 477 lung adenocarcinoma specimens showed a positive correlation between the expression of PD-L1 and Snail1 (134). Two studies showed that PD-L1 can inhibit GSK3β activity *via* binding to tyrosine phosphatase PTP1B or integrin β4 to activate p38-MAPK or Akt activity, respectively. Through this mechanism, PD-L1 can inhibit GSK3β-mediated phosphorylation, ubiquitination, and degradation of Snail1, thereby promoting EMT and the metastatic potential of breast cancer and cervical cancer (135, 136).

TIM-3 contains an immunoglobulin and a mucin-like domain and was originally identified as a receptor expressed on Th1 cells (137). The silencing of TIM-3 was accompanied by a

decrease in Snail1 expression, indicating that TIM-3 may be involved in metastasis of osteosarcoma and hepatocellular carcinoma (138–140). Due to the lack of research in this aspect, it is only known that TIM-3 induces EMT to stimulate the metastasis of esophageal squamous cell carcinoma at least partly through the Akt/GSK-3β/Snail1 signaling pathway (141).

The role of SNAIL1 in Tumor Immune Evasion

Increasing evidence suggests that Snail1 is also involved in immune escape from tumors, which can accelerate cancer metastasis. Previous research has reported the quantity of tumor-specific infiltrating lymphocytes and the systemic immune response increased *via* silencing Snail1 in melanoma (142), suggesting that Snail1 is visibly involved in tumor immunity. Firstly, Snail1 recruits CD4+FOXP3+Treg cells into the tumor microenvironment through C-C motif chemokine ligand 2 (CCL2) (143). In a mouse model of lung cancer, Snail1 was also found to increase intratumoral C-X-C chemokine ligand 2 (CXCL2) secretion and neutrophil infiltration (144). In ovarian cancer, Snail1 accelerates cancer progression *via* up-regulation of CXCL1 and CXCL2 as well as recruitment of myeloid-derived suppressor cells (MDSCs) (145), which plays a vital role in cancer immunosuppression, tumor angiogenesis, drug resistance and promotion of tumor metastasis (146, 147). In cholangiocarcinoma, Snail1 appears to produce immunosuppressive natural T-regulatory like CD4+CD25- cells, in part by mediating the T regulatory-inducible cytokines such as TGF-β1 and IL-2 (148). In addition, Snail1 induces M2 polarization of tumor-associated macrophages and facilitates tumor growth in head and neck cancer (149). A recent study showed that the high expression of Snail1 in mesenchymal tumor cell induces the expression of several cytokines (CD73, CSF1, SPP1), which collectively expedites the assembly of tumor immunosuppressive microenvironments (2). All these lines of evidence strongly confirm that Snail1 effectively promotes tumor cells to secrete chemokines or cytokines, which recruits various immunosuppressive cells to the tumor microenvironment and provides an appropriate environment for tumor metastasis.

SUMMARY AND FUTURE PERSPECTIVES

Physiologically, Snail1 participates in embryo implantation and initiation, wound healing, and cell survival (8, 150, 151). In addition, as we discussed above, Snail1 is a crucial target involved in tumor metastasis and immune escape, and can endow tumor cells with the characteristics of stem cells (5). What's more, Snail1 overexpression was found to be a potential risk factor of neoplasm recurrence in various cancers, such as cutaneous squamous cell carcinoma, clear cell renal cell carcinoma, ameloblastic carcinoma, non-muscle-invasive bladder, colon and non-small-cell lung cancer (152–157). Consistent with tumor relapse, Snail1 overexpression also indicates poor prognosis in several types of cancers (158–161). Taken together, Snail1 can function as a biomarker to predict tumor relapse and patient prognosis.

Snail1 also hold critical role in cancer treatment, increasing evidence suggested that Snail1 is implicated in chemotherapy and radiotherapy resistance. For instance, silencing Snail1 was found to be beneficial in enhancing the sensitivity of gemcitabine therapy in pancreatic ductal carcinoma (162, 163) and increasing radiosensitivity in hypopharyngeal carcinoma (164). Furthermore, Snail1 contributes to the resistance of glioblastoma cells to temozolomide *via* the IL-6-STAT3-Snail1 pathway (165) and colorectal cancer cells to 5-fluorouracil by facilitating the expression of the ABCB1 resistance gene (166). In addition, Snail1 overexpression could induce tumor stem cell-like phenotype and generate chemotherapy resistance to oxaliplatin in colorectal cancer (167). Collectively, chemotherapy or radiotherapy combined with Snail1 inhibitors such as CYD19 (168), GN-25 (169) and Co (III)-Ebox (170) may be a promising therapeutic approach to combat tumors. At present, it has not yet been reported whether Snail1 is involved in immune checkpoint blockade. Due to knockdown of Snail1 decreases the infiltration of immunosuppressive cells in the tumor microenvironment, it is possible targeting Snail1 could enhance the anti-tumor effect. Accordingly, further development of novel Snail1 inhibitors and investigation of the safety of these compounds is urgently need for conquering cancer in future.

AUTHOR CONTRIBUTIONS

XT and XS were responsible for the primary review of literature, consolidation of information, and writing. LW and YL guided and supervised this study. All authors contributed to the article and approved the submitted version.

FUNDING

This work was supported by National Natural Science Foundations of China (81802400 to YL, 81900199 and 81974465 to LW), China Postdoctoral Science Foundation (2020M670053 to YL), Hunan province natural science funds for Excellent Young Scholars (2019JJ30043 to LW) and the recruitment program for Huxiang talents (2019RS1009 to LW).

REFERENCES

1. Lin Y, Xu J, Lan H. Tumor-Associated Macrophages in Tumor Metastasis: Biological Roles and Clinical Therapeutic Applications. *J Hematol Oncol* (2019) 12:76. doi: 10.1186/s13045-019-0760-3
2. Dongre A, Rashidian M, Eaton EN, Reinhardt F, Thiru P, Zagorulya M, et al. Direct and Indirect Regulators of Epithelial-Mesenchymal Transition-Mediated Immunosuppression in Breast Carcinomas. *Cancer Discov* (2021) 11:1286–305. doi: 10.1158/2159-8290.CD-20-0603
3. Messeha SS, Zarmouh NO, Soliman K. Polyphenols Modulating Effects of PD-L1/PD-1 Checkpoint and EMT-Mediated PD-L1 Overexpression in Breast Cancer. *Nutrients* (2021) 13:1718–9. doi: 10.3390/nu13051718
4. Hemavathy K, Ashraf SI, Ip YT. Snail/slug Family of Repressors: Slowly Going Into the Fast Lane of Development and Cancer. *Gene* (2000) 257:1–12. doi: 10.1016/s0378-1119(00)00371-1

5. Wang Y, Shi J, Chai K, Ying X, Zhou BP. The Role of Snail in EMT and Tumorigenesis. *Curr Cancer Drug Targets* (2013) 13:963–72. doi: 10.2174/15680096113136660102
6. Whiteman EL, Liu CJ, Fearon ER, Margolis B. The Transcription Factor Snail Represses Crumbs3 Expression and Disrupts Apico-Basal Polarity Complexes. *Oncogene* (2008) 27:3875–9. doi: 10.1038/onc.2008.9
7. Chiang C, Ayyanathan K. Snail/Gfi-1 (SNAG) Family Zinc Finger Proteins in Transcription Regulation, Chromatin Dynamics, Cell Signaling, Development, and Disease. *Cytokine Growth Factor Rev* (2013) 24:123–31. doi: 10.1016/j.cytogfr.2012.09.002
8. Nieto MA. The Snail Superfamily of Zinc-Finger Transcription Factors. *Nat Rev Mol Cell Biol* (2002) 3:155–66. doi: 10.1038/nrm757
9. Dominguez D, Montserrat-Sentis B, Virgos-Soler A, Guaita S, Grueso J, Porta M, et al. Phosphorylation Regulates the Subcellular Location and Activity of the Snail Transcriptional Repressor. *Mol Cell Biol* (2003) 23:5078–89. doi: 10.1128/MCB.23.14.5078-5089.2003
10. Zhou BP, Deng J, Xia W, Xu J, Li YM, Gunduz M, et al. Dual Regulation of Snail by GSK-3beta-Mediated Phosphorylation in Control of Epithelial-Mesenchymal Transition. *Nat Cell Biol* (2004) 6:931–40. doi: 10.1038/ncb1173
11. Hanahan D, Weinberg RA. Hallmarks of Cancer: The Next Generation. *Cell* (2011) 144:646–74. doi: 10.1016/j.cell.2011.02.013
12. Gall TM, Frampton AE. Gene of the Month: E-Cadherin (CDH1). *J Clin Pathol* (2013) 66:928–32. doi: 10.1136/jclinpath-2013-201768
13. Peinado H, Ballestar E, Esteller M, Cano A. Snail Mediates E-Cadherin Repression by the Recruitment of the Sin3A/histone Deacetylase 1 (HDAC1)/HDAC2 Complex. *Mol Cell Biol* (2004) 24:306–19. doi: 10.1128/MCB.24.1.306-319.2004
14. Dong C, Wu Y, Yao J, Wang Y, Yu Y, Rychahou PG, et al. G9a Interacts With Snail and is Critical for Snail-Mediated E-Cadherin Repression in Human Breast Cancer. *J Clin Invest* (2012) 122:1469–86. doi: 10.1172/JCI57349
15. Dong C, Wu Y, Wang Y, Wang C, Kang T, Rychahou PG, et al. Interaction With Suv39H1 is Critical for Snail-Mediated E-Cadherin Repression in Breast Cancer. *Oncogene* (2013) 32:1351–62. doi: 10.1038/onc.2012.169
16. Odero-Marah V, Hawsawi O, Henderson V, Sweeney J. Epithelial-Mesenchymal Transition (EMT) and Prostate Cancer. *Adv Exp Med Biol* (2018) 1095:101–10. doi: 10.1007/978-3-319-95693-0_6
17. Vu T, Datta PK. Regulation of EMT in Colorectal Cancer: A Culprit in Metastasis. *Cancers (Basel)* (2017) 9:171. doi: 10.3390/cancers9120171
18. Nieszporek A, Skrzypek K, Adamek G, Majka M. Molecular Mechanisms of Epithelial to Mesenchymal Transition in Tumor Metastasis. *Acta Biochim Pol* (2019) 66:509–20. doi: 10.18388/abp.2019_2899
19. Liu X, Yun F, Shi L, Li ZH, Luo NR, Jia YF. Roles of Signaling Pathways in the Epithelial-Mesenchymal Transition in Cancer. *Asian Pac J Cancer Prev* (2015) 16:6201–6. doi: 10.7314/apjcp.2015.16.15.6201
20. Xu J, Lamouille S, Derynck R. TGF-Beta-Induced Epithelial to Mesenchymal Transition. *Cell Res* (2009) 19:156–72. doi: 10.1038/cr.2009.5
21. Miyazono K. Transforming Growth Factor-Beta Signaling in Epithelial-Mesenchymal Transition and Progression of Cancer. *Proc Jpn Acad Ser B Phys Biol Sci* (2009) 85:314–23. doi: 10.2183/pjab.85.314
22. Vincent T, Neve EP, Johnson JR, Kukalev A, Rojo F, Albanell J, et al. A SNAIL1-SMAD3/4 Transcriptional Repressor Complex Promotes TGF-Beta Mediated Epithelial-Mesenchymal Transition. *Nat Cell Biol* (2009) 11:943–50. doi: 10.1038/ncb1905
23. Jiang X, Zhang Z, Song C, Deng H, Yang R, Zhou L, et al. Glaucocalyxin A Reverses EMT and TGF-Beta1-Induced EMT by Inhibiting TGF-Beta1/Smad2/3 Signaling Pathway in Osteosarcoma. *Chem Biol Interact* (2019) 307:158–66. doi: 10.1016/j.cbi.2019.05.005
24. Tong X, Wang S, Lei Z, Li C, Zhang C, Su Z, et al. MYOCD and SMAD3/SMAD4 Form a Positive Feedback Loop and Drive TGF-Beta-Induced Epithelial-Mesenchymal Transition in Non-Small Cell Lung Cancer. *Oncogene* (2020) 39:2890–904. doi: 10.1038/s41388-020-1189-4
25. Li C, Ao H, Chen G, Wang F, Li F. The Interaction of CDH20 With Beta-Catenin Inhibits Cervical Cancer Cell Migration and Invasion *via* TGF-Beta/Smad/SNAIL Mediated EMT. *Front Oncol* (2019) 9:1481. doi: 10.3389/fonc.2019.01481
26. Costa R, Han HS, Gradishar WJ. Targeting the PI3K/AKT/mTOR Pathway in Triple-Negative Breast Cancer: A Review. *Breast Cancer Res Treat* (2018) 169:397–406. doi: 10.1007/s10549-018-4697-y
27. Chen H, Zhou L, Wu X, Li R, Wen J, Sha J, et al. The PI3K/AKT Pathway in the Pathogenesis of Prostate Cancer. *Front Biosci (Landmark Ed)* (2016) 21:1084–91. doi: 10.2741/4443
28. Marquard FE, Jucker M. PI3K/AKT/mTOR Signaling as a Molecular Target in Head and Neck Cancer. *Biochem Pharmacol* (2020) 172:113729. doi: 10.1016/j.bcp.2019.113729
29. Ersahin T, Tuncbag N, Cetin-Atalay R. The PI3K/AKT/mTOR Interactive Pathway. *Mol Biosyst* (2015) 11:1946–54. doi: 10.1039/c5mb00101c
30. Porta C, Paglino C, Mosca A. Targeting PI3K/Akt/mTOR Signaling in Cancer. *Front Oncol* (2014) 4:64. doi: 10.3389/fonc.2014.00064
31. Zhao GX, Xu YY, Weng SQ, Zhang S, Chen Y, Shen XZ, et al. CAPS1 Promotes Colorectal Cancer Metastasis *via* Snail Mediated Epithelial Mesenchymal Transformation. *Oncogene* (2019) 38:4574–89. doi: 10.1038/s41388-019-0740-7
32. Liu JJ, Li LZ, Xu P. Upregulation of TRPM8 can Promote the Colon Cancer Liver Metastasis Through Mediating Akt/GSK-3 Signal Pathway. *Biotechnol Appl Biochem* (2021) 0:1–10. doi: 10.1002/bab.2102
33. Lan Y, Han J, Wang Y, Wang J, Yang G, Li K, et al. STK17B Promotes Carcinogenesis and Metastasis *via* AKT/GSK-3beta/Snail Signaling in Hepatocellular Carcinoma. *Cell Death Dis* (2018) 9:236. doi: 10.1038/s41419-018-0262-1
34. Liu H, Xu L, He H, Zhu Y, Liu J, Wang S, et al. Hepatitis B Virus X Protein Promotes Hepatoma Cell Invasion and Metastasis by Stabilizing Snail Protein. *Cancer Sci* (2012) 103:2072–81. doi: 10.1111/cas.12017
35. Gao Y, Zheng H, Li L, Zhou C, Chen X, Zhou X, et al. KIF3C Promotes Proliferation, Migration, and Invasion of Glioma Cells by Activating the PI3K/AKT Pathway and Inducing EMT. *BioMed Res Int* (2020) 2020:6349312. doi: 10.1155/2020/6349312
36. Chen L, Wu Q, Xu X, Yang C, You J, Chen F, et al. Cancer/testis Antigen LDHC Promotes Proliferation and Metastasis by Activating the PI3K/Akt/GSK-3beta-Signaling Pathway and the in Lung Adenocarcinoma. *Exp Cell Res* (2021) 398:112414. doi: 10.1016/j.yexcr.2020.112414
37. Wu YJ, Lin SH, Din ZH, Su JH, Liu CI. Sinulariolide Inhibits Gastric Cancer Cell Migration and Invasion Through Downregulation of the EMT Process and Suppression of FAK/PI3K/AKT/mTOR and MAPKs Signaling Pathways. *Mar Drugs* (2019) 17:668. doi: 10.3390/md17120668
38. Cheng Y, Pan Y, Pan Y, Wang O. MNX1-AS1 is a Functional Oncogene That Induces EMT and Activates the AKT/mTOR Pathway and MNX1 in Breast Cancer. *Cancer Manag Res* (2019) 11:803–12. doi: 10.2147/CMAR.S188007
39. Sharma N, Nanta R, Sharma J, Gunewardena S, Singh KP, Shankar S, et al. PI3K/AKT/mTOR and Sonic Hedgehog Pathways Cooperate Together to Inhibit Human Pancreatic Cancer Stem Cell Characteristics and Tumor Growth. *Oncotarget* (2015) 6:32039–60. doi: 10.18632/oncotarget.5055
40. Lau MT, Leung PC. The PI3K/Akt/mTOR Signaling Pathway Mediates Insulin-Like Growth Factor 1-Induced E-Cadherin Down-Regulation and Cell Proliferation in Ovarian Cancer Cells. *Cancer Lett* (2012) 326:191–8. doi: 10.1016/j.canlet.2012.08.016
41. Yu B, Jiang K, Zhang J. MicroRNA-124 Suppresses Growth and Aggressiveness of Osteosarcoma and Inhibits TGF-Beta-Mediated AKT/GSK-3beta/SNAIL-1 Signaling. *Mol Med Rep* (2018) 17:6736–44. doi: 10.3892/mmr.2018.8637
42. Matsumoto T, Yokoi A, Hashimura M, Oguri Y, Akiya M, Saegusa M. TGF-Beta-Mediated LEFTY/Akt/GSK-3beta/Snail Axis Modulates Epithelial-Mesenchymal Transition and Cancer Stem Cell Properties in Ovarian Clear Cell Carcinomas. *Mol Carcinog* (2018) 57:957–67. doi: 10.1002/mc.22816
43. Schaefer KN, Peifer M. Wnt/Beta-Catenin Signaling Regulation and a Role for Biomolecular Condensates. *Dev Cell* (2019) 48:429–44. doi: 10.1016/j.devcel.2019.01.025
44. Clevers H, Nusse R. Wnt/beta-Catenin Signaling and Disease. *Cell* (2012) 149:1192–205. doi: 10.1016/j.cell.2012.05.012
45. Li X, Deng W, Lobo-Ruppert SM, Ruppert JM. Gli1 Acts Through Snail and E-Cadherin to Promote Nuclear Signaling by Beta-Catenin. *Oncogene* (2007) 26:4489–98. doi: 10.1038/sj.onc.1210241

46. Schmalhofer O, Brabletz S. Brabletz T. E-Cadherin, Beta-Catenin, and ZEB1 in Malignant Progression of Cancer. *Cancer Metastasis Rev* (2009) 28:151–66. doi: 10.1007/s10555-008-9179-y
47. Yook JI, Li XY, Ota I, Hu C, Kim HS, Kim NH, et al. Weiss SJ. A Wnt-Axin2-GSK3beta Cascade Regulates Snail1 Activity in Breast Cancer Cells. *Nat Cell Biol* (2006) 8:1398–406. doi: 10.1038/ncb1508
48. Houde C, Li Y, Song L, Barton K, Zhang Q, Godwin J, et al. Overexpression of the NOTCH Ligand JAG2 in Malignant Plasma Cells From Multiple Myeloma Patients and Cell Lines. *Blood* (2004) 104:3697–704. doi: 10.1182/blood-2003-12-4114
49. Kopan R, Ilagan MX. The Canonical Notch Signaling Pathway: Unfolding the Activation Mechanism. *Cell* (2009) 137:216–33. doi: 10.1016/j.cell.2009.03.045
50. Wang Z, Li Y, Kong D, Sarkar FH. The Role of Notch Signaling Pathway in Epithelial-Mesenchymal Transition (EMT) During Development and Tumor Aggressiveness. *Curr Drug Targets* (2010) 11:745–51. doi: 10.2174/138945010791170860
51. Carballo GB, Honorato JR, de Lopes G, Spohr T. A Highlight on Sonic Hedgehog Pathway. *Cell Commun Signal* (2018) 16:11. doi: 10.1186/s12964-018-0220-7
52. Katoh Y, Katoh M. Hedgehog Signaling, Epithelial-to-Mesenchymal Transition and miRNA (Review). *Int J Mol Med* (2008) 22:271–5. doi: 10.3892/ijmm_00000019
53. Riaz SK, Ke Y, Wang F, Kayani MA, Malik M. Influence of SHH/GLI1 Axis on EMT Mediated Migration and Invasion of Breast Cancer Cells. *Sci Rep* (2019) 9:6620. doi: 10.1038/s41598-019-43093-x
54. Ke Z, Caiping S, Qing Z, Xiaojing W. Sonic Hedgehog-Gli1 Signals Promote Epithelial-Mesenchymal Transition in Ovarian Cancer by Mediating PI3K/AKT Pathway. *Med Oncol* (2015) 32:368. doi: 10.1007/s12032-014-0368-y
55. Feldmann G, Dhara S, Fendrich V, Bedja D, Beaty R, Mullendore M, et al. Blockade of Hedgehog Signaling Inhibits Pancreatic Cancer Invasion and Metastases: A New Paradigm for Combination Therapy in Solid Cancers. *Cancer Res* (2007) 67:2187–96. doi: 10.1158/0008-5472.CAN-06-3281
56. Fendrich V, Waldmann J, Esni F, Ramaswamy A, Mullendore M, Buchholz M, et al. Snail and Sonic Hedgehog Activation in Neuroendocrine Tumors of the Ileum. *Endocr Relat Cancer* (2007) 14:865–74. doi: 10.1677/ERC-07-0108
57. Li X, Deng W, Nail CD, Bailey SK, Kraus MH, Ruppert JM, et al. Snail Induction is an Early Response to Gli1 That Determines the Efficiency of Epithelial Transformation. *Oncogene* (2006) 25:609–21. doi: 10.1038/sj.onc.1209077
58. Guo YJ, Pan WW, Liu SB, Shen ZF, Xu Y, Hu LL. ERK/MAPK Signalling Pathway and Tumorigenesis. *Exp Ther Med* (2020) 19:1997–2007. doi: 10.3892/etm.2020.8454
59. Hsu YL, Hou MF, Kuo PL, Huang YF, Tsai EM. Breast Tumor-Associated Osteoblast-Derived CXCL5 Increases Cancer Progression by ERK/MSK1/Elk-1/Snail Signaling Pathway. *Oncogene* (2013) 32:4436–47. doi: 10.1038/onc.2012.444
60. Grotegut S, von Schweinitz D, Christofori G, Lehembre F. Hepatocyte Growth Factor Induces Cell Scattering Through MAPK/Egr-1-Mediated Upregulation of Snail. *EMBO J* (2006) 25:3534–45. doi: 10.1038/sj.emboj.7601213
61. Dolcet X, Llobet D, Pallares J, Matias-Guiu X. NF-kB in Development and Progression of Human Cancer. *Virchows Arch* (2005) 446:475–82. doi: 10.1007/s00428-005-1264-9
62. Wu Y, Deng J, Rychahou PG, Qiu S, Evers BM, Zhou BP. Stabilization of Snail by NF-kappaB is Required for Inflammation-Induced Cell Migration and Invasion. *Cancer Cell* (2009) 15:416–28. doi: 10.1016/j.ccr.2009.03.016
63. Yang Y, Li Y, Wang K, Wang Y, Yin W, Li L. P38/NF-Kappab/Snail Pathway is Involved in Caffeic Acid-Induced Inhibition of Cancer Stem Cells-Like Properties and Migratory Capacity in Malignant Human Keratinocyte. *PloS One* (2013) 8:e58915. doi: 10.1371/journal.pone.0058915
64. Zhang K, Zhaos J, Liu X, Yan B, Chen D, Gao Y, et al. Activation of NF-B Upregulates Snail and Consequent Repression of E-Cadherin in Cholangiocarcinoma Cell Invasion. *Hepatogastroenterology* (2011) 58:1–7. doi: 10.1186/1746-160X-7-15
65. Zhu QC, Gao RY, Wu W, Qin HL. Epithelial-Mesenchymal Transition and Its Role in the Pathogenesis of Colorectal Cancer. *Asian Pac J Cancer Prev* (2013) 14:2689–98. doi: 10.7314/apjcp.2013.14.5.2689
66. Li J, Deng Z, Wang Z, Wang D, Zhang L, Su Q, et al. Zipper-Interacting Protein Kinase Promotes Epithelial-Mesenchymal Transition, Invasion and Metastasis Through AKT and NF-kB Signaling and Is Associated With Metastasis and Poor Prognosis in Gastric Cancer Patients. *Oncotarget* (2015) 6:8323–38. doi: 10.18632/oncotarget.3200
67. Swatek KN, Komander D. Ubiquitin Modifications. *Cell Res* (2016) 26:399–422. doi: 10.1038/cr.2016.39
68. Nandi D, Tahiliani P, Kumar A, Chandu D. The Ubiquitin-Proteasome System. *J Biosci* (2006) 31:137–55. doi: 10.1007/BF02705243
69. Wu X, Luo Q, Liu Z. Ubiquitination and Deubiquitination of MCL1 in Cancer: Deciphering Chemoresistance Mechanisms and Providing Potential Therapeutic Options. *Cell Death Dis* (2020) 11:556. doi: 10.1038/s41419-020-02760-y
70. Vinas-Castells R, Beltran M, Valls G, Gomez I, Garcia JM, Montserrat-Sentis B, et al. The Hypoxia-Controlled FBXL14 Ubiquitin Ligase Targets SNAIL1 for Proteasome Degradation. *J Biol Chem* (2010) 285:3794–805. doi: 10.1074/jbc.M109.065995
71. Xu M, Zhu C, Zhao X, Chen C, Zhang H, Yuan H, et al. Atypical Ubiquitin E3 Ligase Complex Skp1-Pam-Fbxo45 Controls the Core Epithelial-to-Mesenchymal Transition-Inducing Transcription Factors. *Oncotarget* (2015) 6:979–94. doi: 10.18632/oncotarget.2825
72. Jin Y, Shenoy AK, Doernberg S, Chen H, Luo H, Shen H, et al. FBXO11 Promotes Ubiquitination of the Snail Family of Transcription Factors in Cancer Progression and Epidermal Development. *Cancer Lett* (2015) 362:70–82. doi: 10.1016/j.canlet.2015.03.037
73. Zheng H, Shen M, Zha YL, Li W, Wei Y, Blanco MA, et al. PKD1 Phosphorylation-Dependent Degradation of SNAIL by SCF-FBXO11 Regulates Epithelial-Mesenchymal Transition and Metastasis. *Cancer Cell* (2014) 26:358–73. doi: 10.1016/j.ccr.2014.07.022
74. Sun R, Xie HY, Qian JX, Huang YN, Yang F, Zhang FL, et al. FBXO22 Possesses Both Protumorigenic and Antimetastatic Roles in Breast Cancer Progression. *Cancer Res* (2018) 78:5274–86. doi: 10.1158/0008-5472.CAN-17-3647
75. Jia Z, Wang M, Li S, Li X, Bai XY, Xu Z, et al. Wu H. U-Box Ubiquitin Ligase PPIL2 Suppresses Breast Cancer Invasion and Metastasis by Altering Cell Morphology and Promoting SNAI1 Ubiquitination and Degradation. *Cell Death Dis* (2018) 9:63. doi: 10.1038/s41419-017-0094-4
76. Liu Y, Zhou H, Zhu R, Ding F, Li Y, Cao X, et al. SPSB3 Targets SNAIL for Degradation in GSK-3beta Phosphorylation-Dependent Manner and Regulates Metastasis. *Oncogene* (2018) 37:768–76. doi: 10.1038/onc.2017.370
77. Jin Y, Zhang Y, Li B, Zhang J, Dong Z, Hu X, et al. TRIM21 Mediates Ubiquitination of Snail and Modulates Epithelial to Mesenchymal Transition in Breast Cancer Cells. *Int J Biol Macromol* (2019) 124:846–53. doi: 10.1016/j.ijbiomac.2018.11.269
78. Zou S, Ma C, Yang F, Xu X, Jia J, Liu Z. FBXO31 Suppresses Gastric Cancer EMT by Targeting Snail1 for Proteasomal Degradation. *Mol Cancer Res* (2018) 16:286–95. doi: 10.1158/1541-7786.MCR-17-0432
79. Li H, Wang Z, Zhang W, Qian K, Xu W, Zhang S. Fbxw7 Regulates Tumor Apoptosis, Growth Arrest and the Epithelial-to-Mesenchymal Transition in Part Through the RhoA Signaling Pathway in Gastric Cancer. *Cancer Lett* (2016) 370:39–55. doi: 10.1016/j.canlet.2015.10.006
80. Wu W, Ding H, Cao J, Zhang W. FBXL5 Inhibits Metastasis of Gastric Cancer Through Suppressing Snail1. *Cell Physiol Biochem* (2015) 35:1764–72. doi: 10.1159/000373988
81. Vinas-Castells R, Frias A, Robles-Lanuza E, Zhang K, Longmore GD, Garcia DHA, et al. Nuclear Ubiquitination by FBXL5 Modulates Snail1 DNA Binding and Stability. *Nucleic Acids Res* (2014) 42:1079–94. doi: 10.1093/nar/gkt935
82. Xiao G, Li Y, Wang M, Li X, Qin S, Sun X, et al. FBXW7 Suppresses Epithelial-Mesenchymal Transition and Chemo-Resistance of Non-Small-Cell Lung Cancer Cells by Targeting Snai1 for Ubiquitin-Dependent Degradation. *Cell Prolif* (2018) 51:e12473. doi: 10.1111/cpr.12473
83. Savita U, Karunagaran D. MicroRNA-106b-25 Cluster Targets Beta-TRCP2, Increases the Expression of Snail and Enhances Cell Migration and Invasion in H1299 (Non Small Cell Lung Cancer) Cells. *Biochem Biophys Res Commun* (2013) 434:841–7. doi: 10.1016/j.bbrc.2013.04.025
84. Wang X, De Geyter C, Jia Z, Peng Y, Zhang H. HECTD1 Regulates the Expression of SNAIL: Implications for Epithelialmesenchymal Transition. *Int J Oncol* (2020) 56:1186–98. doi: 10.3892/ijo.2020.5002

85. Ma X, Ma X, Qiu Y, Zhu L, Lin Y, You Y, et al. TRIM50 Suppressed Hepatocarcinoma Progression Through Directly Targeting SNAIL for Ubiquitous Degradation. *Cell Death Dis* (2018) 9:608. doi: 10.1038/s41419-018-0644-4
86. Park SM, Park SH, Ryu KJ, Kim IK, Han H, Kim HJ, et al. Downregulation of CHIP Promotes Ovarian Cancer Metastasis by Inducing Snail-Mediated Epithelial-Mesenchymal Transition. *Mol Oncol* (2019) 13:1280–95. doi: 10.1002/1878-0261.12485
87. Liu R, Wang L, Gan T, Pan T, Huang J, Bai M. Long Noncoding RNA LINC00511 Promotes Cell Growth and Invasion in Triple-Negative Breast Cancer by Interacting With Snail. *Cancer Manag Res* (2019) 11:5691–9. doi: 10.2147/CMAR.S203455
88. Yan Q, Zeng Z, Gong Z, Zhang W, Li X, He B, et al. EBV-miR-BART10-3p Facilitates Epithelial-Mesenchymal Transition and Promotes Metastasis of Nasopharyngeal Carcinoma by Targeting BTRC. *Oncotarget* (2015) 6:41766–82. doi: 10.18632/oncotarget.6155
89. Zhang Y, Zhang X, Ye M, Jing P, Xiong J, Han Z, et al. FBW7 Loss Promotes Epithelial-to-Mesenchymal Transition in Non-Small Cell Lung Cancer Through the Stabilization of Snail Protein. *Cancer Lett* (2018) 419:75–83. doi: 10.1016/j.canlet.2018.01.047
90. He ZJ, Li W, Chen H, Wen J, Gao YF, Liu YJ. miR-1306-3p Targets FBXL5 to Promote Metastasis of Hepatocellular Carcinoma Through Suppressing Snail Degradation. *Biochem Biophys Res Commun* (2018) 504:820–6. doi: 10.1016/j.bbrc.2018.09.059
91. Lin M, Wang ZW, Zhu X. FBXO45 is a Potential Therapeutic Target for Cancer Therapy. *Cell Death Discovery* (2020) 6:55. doi: 10.1038/s41420-020-0291-2
92. Qin ZY, Wang T, Su S, Shen LT, Zhu GX, Liu Q, et al. BRD4 Promotes Gastric Cancer Progression and Metastasis Through Acetylation-Dependent Stabilization of Snail. *Cancer Res* (2019) 79:4869–81. doi: 10.1158/0008-5472.CAN-19-0442
93. Song L, Guo J, Chang R, Peng X, Li J, Xu X, et al. LKB1 Obliterates Snail Stability and Inhibits Pancreatic Cancer Metastasis in Response to Metformin Treatment. *Cancer Sci* (2018) 109:1382–92. doi: 10.1111/cas.13591
94. Komander D, Clague MJ, Urbe S. Breaking the Chains: Structure and Function of the Deubiquitinases. *Nat Rev Mol Cell Biol* (2009) 10:550–63. doi: 10.1038/nrm2731
95. Cheng J, Guo J, North BJ, Wang B, Cui CP, Li H, et al. Functional Analysis of Deubiquitylating Enzymes in Tumorigenesis and Development. *Biochim Biophys Acta Rev Cancer* (2019) 1872:188312. doi: 10.1016/j.bbcan.2019.188312
96. Wei R, Liu X, Yu W, Yang T, Cai W, Liu J, et al. Deubiquitinases in Cancer. *Oncotarget* (2015) 6:12872–89. doi: 10.18632/oncotarget.3671
97. Tanguturi P, Kim KS, Ramakrishna S. The Role of Deubiquitinating Enzymes in Cancer Drug Resistance. *Cancer Chemother Pharmacol* (2020) 85:627–39. doi: 10.1007/s00280-020-04046-8
98. Herhaus L, Al-Salihi M, Macartney T, Weidlich S, Sapkota GP. OTUB1 Enhances TGFbeta Signalling by Inhibiting the Ubiquitylation and Degradation of Active SMAD2/3. *Nat Commun* (2013) 4:2519. doi: 10.1038/ncomms3519
99. Zhou H, Liu Y, Zhu R, Ding F, Cao X, Lin D, et al. OTUB1 Promotes Esophageal Squamous Cell Carcinoma Metastasis Through Modulating Snail Stability. *ONCOGENE* (2018) 37:3356–68. doi: 10.1038/s41388-018-0224-1
100. Li L, Zhou H, Zhu R, Liu Z. USP26 Promotes Esophageal Squamous Cell Carcinoma Metastasis Through Stabilizing Snail. *Cancer Lett* (2019) 448:52–60. doi: 10.1016/j.canlet.2019.02.007
101. Ning B, Zhao W, Qian C, Liu P, Li Q, Li W, et al. USP26 Functions as a Negative Regulator of Cellular Reprogramming by Stabilising PRC1 Complex Components. *Nat Commun* (2017) 8:349. doi: 10.1038/s41467-017-00301-4
102. Guo X, Zhu R, Luo A, Zhou H, Ding F, Yang H, et al. EIF3H Promotes Aggressiveness of Esophageal Squamous Cell Carcinoma by Modulating Snail Stability. *J Exp Clin Cancer Res* (2020) 39:175. doi: 10.1186/s13046-020-01678-9
103. Zhu R, Liu Y, Zhou H, Li L, Li Y, Ding F, et al. Deubiquitinating Enzyme PSMD14 Promotes Tumor Metastasis Through Stabilizing SNAIL in Human Esophageal Squamous Cell Carcinoma. *Cancer Lett* (2018) 418:125–34. doi: 10.1016/j.canlet.2018.01.025
104. Wu Y, Wang Y, Lin Y, Liu Y, Wang Y, Jia J, et al. Dub3 Inhibition Suppresses Breast Cancer Invasion and Metastasis by Promoting Snail1 Degradation. *Nat Commun* (2017) 8:14228. doi: 10.1038/ncomms14228
105. Watanabe K, Yokoyama S, Kaneto N, Hori T, Iwakami Y, Kato S, et al. COP9 Signalosome Subunit 5 Regulates Cancer Metastasis by Deubiquitinating SNAIL. *Oncotarget* (2018) 9:20670–80. doi: 10.18632/oncotarget.25060
106. Cai J, Li M, Wang X, Li L, Li Q, Hou Z, et al. USP37 Promotes Lung Cancer Cell Migration by Stabilizing Snail Protein *via* Deubiquitination. *Front Genet* (2019) 10:1324. doi: 10.3389/fgene.2019.01324
107. Fan L, Chen Z, Wu X, Cai X, Feng S, Lu J, et al. Ubiquitin-Specific Protease 3 Promotes Glioblastoma Cell Invasion and Epithelial-Mesenchymal Transition *via* Stabilizing Snail. *Mol Cancer Res* (2019) 17:1975–84. doi: 10.1158/1541-7786.MCR-19-0197
108. Xu L, Li J, Bao Z, Xu P, Chang H, Wu J, et al. Silencing of OTUB1 Inhibits Migration of Human Glioma Cells *In Vitro*. *Neuropathology* (2017) 37:217–26. doi: 10.1111/neup.12366
109. Choi BJ, Park SA, Lee SY, Cha YN, Surh YJ. Hypoxia Induces Epithelial-Mesenchymal Transition in Colorectal Cancer Cells Through Ubiquitin-Specific Protease 47-Mediated Stabilization of Snail: A Potential Role of Sox9. *Sci Rep* (2017) 7:15918. doi: 10.1038/s41598-017-15139-5
110. Qian W, Li Q, Wu X, Li W, Li Q, Zhang J, et al. Deubiquitinase USP29 Promotes Gastric Cancer Cell Migration by Cooperating With Phosphatase SCP1 to Stabilize Snail Protein. *Oncogene* (2020) 39:6802–15. doi: 10.1038/s41388-020-01471-0
111. Hogg SJ, Beavis PA, Dawson MA, Johnstone RW. Targeting the Epigenetic Regulation of Antitumour Immunity. *Nat Rev Drug Discovery* (2020) 19:776–800. doi: 10.1038/s41573-020-0077-5
112. Dawson MA, Kouzarides T. Cancer Epigenetics: From Mechanism to Therapy. *Cell* (2012) 150:12–27. doi: 10.1016/j.cell.2012.06.013
113. Baylin SB, Herman JG. DNA Hypermethylation in Tumorigenesis: Epigenetics Joins Genetics. *Trends Genet* (2000) 16:168–74. doi: 10.1016/s0168-9525(99)01971-x
114. Chen Y, Wang K, Qian CN, Leach R. DNA Methylation Is Associated With Transcription of Snail and Slug Genes. *Biochem Biophys Res Commun* (2013) 430:1083–90. doi: 10.1016/j.bbrc.2012.12.034
115. Jiang H, Cao HJ, Ma N, Bao WD, Wang JJ, Chen TW, et al. Chromatin Remodeling Factor ARID2 Suppresses Hepatocellular Carcinoma Metastasis *via* DNMT1-Snail Axis. *Proc Natl Acad Sci U S A* (2020) 117:4770–80. doi: 10.1073/pnas.1914937117
116. Liu ZX, Li LM, Sun HL, Liu SM. Link Between M6a Modification and Cancers. *Front Bioeng Biotechnol* (2018) 6:89. doi: 10.3389/fbioe.2018.00089
117. Sun T, Wu R, Ming L. The Role of M6a RNA Methylation in Cancer. *BioMed Pharmacother* (2019) 112:108613. doi: 10.1016/j.biopha.2019.108613
118. Li J, Chen F, Peng Y, Lv Z, Lin X, Chen Z, et al. N6-Methyladenosine Regulates the Expression and Secretion of TGFbeta1 to Affect the Epithelial-Mesenchymal Transition of Cancer Cells. *CELLS-BASEL* (2020) 9:296. doi: 10.3390/cells9020296
119. Guo P, Chen W, Li H, Li M, Li L. The Histone Acetylation Modifications of Breast Cancer and Their Therapeutic Implications. *Pathol Oncol Res* (2018) 24:807–13. doi: 10.1007/s12253-018-0433-5
120. Narita T, Weinert BT, Choudhary C. Functions and Mechanisms of Non-Histone Protein Acetylation. *Nat Rev Mol Cell Biol* (2019) 20:156–74. doi: 10.1038/s41580-018-0081-3
121. Zhang J, Jia L, Liu T, Yip YL, Tang WC, Lin W, et al. Mtorc2-Mediated PDHE1alpha Nuclear Translocation Links EBV-LMP1 Reprogrammed Glucose Metabolism to Cancer Metastasis in Nasopharyngeal Carcinoma. *Oncogene* (2019) 38:4669–84. doi: 10.1038/s41388-019-0749-y
122. Ren X, Yang X, Cheng B, Chen X, Zhang T, He Q, et al. HOPX Hypermethylation Promotes Metastasis *via* Activating SNAIL Transcription in Nasopharyngeal Carcinoma. *Nat Commun* (2017) 8:14053. doi: 10.1038/ncomms14053
123. Chang R, Zhang Y, Zhang P, Zhou Q. Snail Acetylation by Histone Acetyltransferase P300 in Lung Cancer. *Thorac Cancer* (2017) 8:131–7. doi: 10.1111/1759-7714.12408
124. Hsu DS, Wang HJ, Tai SK, Chou CH, Hsieh CH, Chiu PH, et al. Acetylation of Snail Modulates the Cytokinome of Cancer Cells to Enhance the

Recruitment of Macrophages. *Cancer Cell* (2014) 26:534–48. doi: 10.1016/j.ccell.2014.09.002
125. West AC, Johnstone RW. New and Emerging HDAC Inhibitors for Cancer Treatment. *J Clin Invest* (2014) 124:30–9. doi: 10.1172/JCI69738
126. Lakshmaiah KC, Jacob LA, Aparna S, Lokanatha D, Saldanha SC. Epigenetic Therapy of Cancer With Histone Deacetylase Inhibitors. *J Cancer Res Ther* (2014) 10:469–78. doi: 10.4103/0973-1482.137937
127. Xu W, Liu H, Liu ZG, Wang HS, Zhang F, Wang H, et al. Histone Deacetylase Inhibitors Upregulate Snail *via* Smad2/3 Phosphorylation and Stabilization of Snail to Promote Metastasis of Hepatoma Cells. *Cancer Lett* (2018) 420:1–13. doi: 10.1016/j.canlet.2018.01.068
128. Jiang GM, Wang HS, Zhang F, Zhang KS, Liu ZC, Fang R, et al. Histone Deacetylase Inhibitor Induction of Epithelial-Mesenchymal Transitions *via* Up-Regulation of Snail Facilitates Cancer Progression. *Biochim Biophys Acta* (2013) 1833:663–71. doi: 10.1016/j.bbamcr.2012.12.002
129. Lei X, Lei Y, Li JK, Du WX, Li RG, Yang J, et al. Immune Cells Within the Tumor Microenvironment: Biological Functions and Roles in Cancer Immunotherapy. *Cancer Lett* (2020) 470:126–33. doi: 10.1016/j.canlet.2019.11.009
130. Arneth B. Tumor Microenvironment. *Med (Kaunas)* (2019) 56:15. doi: 10.3390/medicina56010015
131. Li B, Chan HL, Chen P. Immune Checkpoint Inhibitors: Basics and Challenges. *Curr Med Chem* (2019) 26:3009–25. doi: 10.2174/0929867324666170804143706
132. Han Y, Liu D, Li L. PD-1/PD-L1 Pathway: Current Researches in Cancer. *Am J Cancer Res* (2020) 10:727–42.
133. Yi M, Jiao D, Xu H, Liu Q, Zhao W, Han X, et al. Biomarkers for Predicting Efficacy of PD-1/PD-L1 Inhibitors. *Mol Cancer* (2018) 17:129. doi: 10.1186/s12943-018-0864-3
134. Kim S, Koh J, Kim MY, Kwon D, Go H, Kim YA, et al. PD-L1 Expression is Associated With Epithelial-to-Mesenchymal Transition in Adenocarcinoma of the Lung. *Hum Pathol* (2016) 58:7–14. doi: 10.1016/j.humpath.2016.07.007
135. Chen C, Li S, Xue J, Qi M, Liu X, Huang Y, et al. PD-L1 Tumor-Intrinsic Signaling and Its Therapeutic Implication in Triple-Negative Breast Cancer. *JCI Insight* (2021) 6:e131458. doi: 10.1172/jci.insight.131458
136. Wang S, Li J, Xie J, Liu F, Duan Y, Wu Y, et al. Programmed Death Ligand 1 Promotes Lymph Node Metastasis and Glucose Metabolism in Cervical Cancer by Activating Integrin Beta4/SNAI1/SIRT3 Signaling Pathway. *Oncogene* (2018) 37:4164–80. doi: 10.1038/s41388-018-0252-x
137. Monney L, Sabatos CA, Gaglia JL, Ryu A, Waldner H, Chernova T, et al. Th1-Specific Cell Surface Protein Tim-3 Regulates Macrophage Activation and Severity of an Autoimmune Disease. *Nature* (2002) 415:536–41. doi: 10.1038/415536a
138. Shang Y, Li Z, Li H, Xia H, Lin Z. TIM-3 Expression in Human Osteosarcoma: Correlation With the Expression of Epithelial-Mesenchymal Transition-Specific Biomarkers. *Oncol Lett* (2013) 6:490–4. doi: 10.3892/ol.2013.1410
139. Lin H, Yang B. Teng M. T-Cell Immunoglobulin Mucin-3 as a Potential Inducer of the Epithelial-Mesenchymal Transition in Hepatocellular Carcinoma. *Oncol Lett* (2017) 14:5899–905. doi: 10.3892/ol.2017.6961
140. Feng ZM, Guo SM. Tim-3 Facilitates Osteosarcoma Proliferation and Metastasis Through the NF-kappaB Pathway and Epithelial-Mesenchymal Transition. *Genet Mol Res* (2016) 15:10.4238/gmr.15037844. doi: 10.4238/gmr.15037844
141. Shan B, Man H, Liu J, Wang L, Zhu T, Ma M, et al. TIM-3 Promotes the Metastasis of Esophageal Squamous Cell Carcinoma by Targeting Epithelial-Mesenchymal Transition *via* the Akt/GSK-3beta/Snail Signaling Pathway. *Oncol Rep* (2016) 36:1551–61. doi: 10.3892/or.2016.4938
142. Kudo-Saito C, Shirako H, Takeuchi T, Kawakami Y. Cancer Metastasis is Accelerated Through Immunosuppression During Snail-Induced EMT of Cancer Cells. *Cancer Cell* (2009) 15:195–206. doi: 10.1016/j.ccr.2009.01.023
143. Kudo-Saito C, Shirako H, Ohike M, Tsukamoto N, Kawakami Y. CCL2 is Critical for Immunosuppression to Promote Cancer Metastasis. *Clin Exp Metastasis* (2013) 30:393–405. doi: 10.1007/s10585-012-9545-6
144. Faget J, Groeneveld S, Boivin G, Sankar M, Zangger N, Garcia M, et al. Neutrophils and Snail Orchestrate the Establishment of a Pro-Tumor Microenvironment in Lung Cancer. *Cell Rep* (2017) 21:3190–204. doi: 10.1016/j.celrep.2017.11.052
145. Taki M, Abiko K, Baba T, Hamanishi J, Yamaguchi K, Murakami R, et al. Snail Promotes Ovarian Cancer Progression by Recruiting Myeloid-Derived Suppressor Cells *via* CXCR2 Ligand Upregulation. *Nat Commun* (2018) 9:1685. doi: 10.1038/s41467-018-03966-7
146. Gabrilovich DI. Myeloid-Derived Suppressor Cells. *Cancer Immunol Res* (2017) 5:3–8. doi: 10.1158/2326-6066.CIR-16-0297
147. Kumar V, Patel S, Tcyganov E, Gabrilovich DI. The Nature of Myeloid-Derived Suppressor Cells in the Tumor Microenvironment. *Trends Immunol* (2016) 37:208–20. doi: 10.1016/j.it.2016.01.004
148. Qian Y, Yao W, Yang T, Yang Y, Liu Y, Shen Q, et al. aPKC-Iota/P-Sp1/Snail Signaling Induces Epithelial-Mesenchymal Transition and Immunosuppression in Cholangiocarcinoma. *Hepatology* (2017) 66:1165–82. doi: 10.1002/hep.29296
149. Hsieh CH, Tai SK, Yang MH. Snail-Overexpressing Cancer Cells Promote M2-Like Polarization of Tumor-Associated Macrophages by Delivering MiR-21-Abundant Exosomes. *Neoplasia* (2018) 20:775–88. doi: 10.1016/j.neo.2018.06.004
150. Du F, Yang R, Ma HL, Wang QY, Wei SL. Expression of Transcriptional Repressor Slug Gene in Mouse Endometrium and Its Effect During Embryo Implantation. *Appl Biochem Biotechnol* (2009) 157:346–55. doi: 10.1007/s12010-008-8521-8
151. Swain SD, Grifka-Walk HN, Gripentrog J, Lehmann M, Deuling B, Jenkins B, et al. Slug and Snail Have Differential Effects in Directing Colonic Epithelial Wound Healing and Partially Mediate the Restitutive Effects of Butyrate. *Am J Physiol Gastrointest Liver Physiol* (2019) 317:G531–44. doi: 10.1152/ajpgi.00071.2019
152. Liu W, Liu Y, Liu H, Zhang W, An H, Xu J. Snail Predicts Recurrence and Survival of Patients With Localized Clear Cell Renal Cell Carcinoma After Surgical Resection. *Urol Oncol* (2015) 33:69.e1–10. doi: 10.1016/j.urolonc.2014.08.003
153. Gou Y, Ding W, Xu K, Wang H, Chen Z, Tan J, et al. Snail is an Independent Prognostic Indicator for Predicting Recurrence and Progression in Non-Muscle-Invasive Bladder Cancer. *Int Urol Nephrol* (2015) 47:289–93. doi: 10.1007/s11255-014-0874-z
154. Oh KY, Yoon HJ, Lee JI, Ahn SH, Hong SD. Twist and Snail Expression in Tumor and Stromal Cells of Epithelial Odontogenic Tumors. *J Oral Pathol Med* (2017) 46:127–33. doi: 10.1111/jop.12479
155. Wang G, Ma W, Li Y, Jiang Y, Ma G, Zhang X, et al. Prognostic Value of Twist, Snail and E-Cadherin Expression in Pathological N0 Non-Small-Cell Lung Cancer: A Retrospective Cohort Study. *Eur J Cardiothorac Surg* (2018) 54:237–45. doi: 10.1093/ejcts/ezy022
156. Rashed HE, Hussein S, Mosaad H, Abdelwahab MM, Abdelhamid MI, Mohamed SY, et al. Prognostic Significance of the Genetic and the Immunohistochemical Expression of Epithelial-Mesenchymal-Related Markers in Colon Cancer. *Cancer Biomark* (2017) 20:107–22. doi: 10.3233/CBM-170034
157. Zhao G, Kim KY, Zheng Z, Oh Y, Yoo DS, Lee ME, et al. AXIN2 and SNAIL Expression Predict the Risk of Recurrence in Cutaneous Squamous Cell Carcinoma After Mohs Micrographic Surgery. *Oncol Lett* (2020) 19:2133–40. doi: 10.3892/ol.2020.11324
158. Kwon CH, Park HJ, Choi JH, Lee JR, Kim HK, Jo HJ, et al. Snail and Serpina1 Promote Tumor Progression and Predict Prognosis in Colorectal Cancer. *Oncotarget* (2015) 6:20312–26. doi: 10.18632/oncotarget.3964
159. van Nes JG, de Kruijf EM, Putter H, Faratian D, Munro A, Campbell F, et al. Co-Expression of SNAIL and TWIST Determines Prognosis in Estrogen Receptor-Positive Early Breast Cancer Patients. *Breast Cancer Res Treat* (2012) 133:49–59. doi: 10.1007/s10549-011-1684-y
160. Mikami S, Katsube K, Oya M, Ishida M, Kosaka T, Mizuno R, et al. Expression of Snail and Slug in Renal Cell Carcinoma: E-Cadherin Repressor Snail is Associated With Cancer Invasion and Prognosis. *Lab Invest* (2011) 91:1443–58. doi: 10.1038/labinvest.2011.111
161. Shin NR, Jeong EH, Choi CI, Moon HJ, Kwon CH, Chu IS, et al. Overexpression of Snail is Associated With Lymph Node Metastasis and Poor Prognosis in Patients With Gastric Cancer. *BMC Cancer* (2012) 12:521. doi: 10.1186/1471-2407-12-521
162. Zheng X, Carstens JL, Kim J, Scheible M, Kaye J, Sugimoto H, et al. Epithelial-To-Mesenchymal Transition is Dispensable for Metastasis But Induces Chemoresistance in Pancreatic Cancer. *Nature* (2015) 527:525–30. doi: 10.1038/nature16064

163. Richards KE, Zeleniak AE, Fishel ML, Wu J, Littlepage LE, Hill R. Cancer-Associated Fibroblast Exosomes Regulate Survival and Proliferation of Pancreatic Cancer Cells. *Oncogene* (2017) 36:1770–8. doi: 10.1038/onc.2016.353
164. Wang H, Wang Z, Li Y, Lu T, Hu G. Silencing Snail Reverses Epithelial-Mesenchymal Transition and Increases Radiosensitivity in Hypopharyngeal Carcinoma. *Onco Targets Ther* (2020) 13:497–511. doi: 10.2147/OTT.S237410
165. Liang H, Chen G, Li J, Yang F. Snail Expression Contributes to Temozolomide Resistance in Glioblastoma. *Am J Transl Res* (2019) 11:4277–89.
166. Wang H, Li JM, Wei W, Yang R, Chen D, Ma XD, et al. Regulation of ATP-Binding Cassette Subfamily B Member 1 by Snail Contributes to Chemoresistance in Colorectal Cancer. *Cancer Sci* (2020) 111:84–97. doi: 10.1111/cas.14253
167. Fan F, Samuel S, Evans KW, Lu J, Xia L, Zhou Y, et al. Overexpression of Snail Induces Epithelial-Mesenchymal Transition and a Cancer Stem Cell-Like Phenotype in Human Colorectal Cancer Cells. *Cancer Med* (2012) 1:5–16. doi: 10.1002/cam4.4
168. Li HM, Bi YR, Li Y, Fu R, Lv WC, Jiang N, et al. A Potent CBP/p300-Snail Interaction Inhibitor Suppresses Tumor Growth and Metastasis in Wild-Type P53-Expressing Cancer. *Sci Adv* (2020) 6:eaaw8500. doi: 10.1126/sciadv.aaw8500
169. Azmi AS, Bollig-Fischer A, Bao B, Park BJ, Lee SH, Yong-Song G, et al. Systems Analysis Reveals a Transcriptional Reversal of the Mesenchymal Phenotype Induced by SNAIL-Inhibitor GN-25. *BMC Syst Biol* (2013) 7:85. doi: 10.1186/1752-0509-7-85
170. Harney AS, Meade TJ, LaBonne C. Targeted Inactivation of Snail Family EMT Regulatory Factors by a Co(III)-Ebox Conjugate. *PloS One* (2012) 7: e32318. doi: 10.1371/journal.pone.0032318

Conflict of Interest: The authors declare that the research was conducted in the absence of any commercial or financial relationships that could be construed as a potential conflict of interest.

Publisher's Note: All claims expressed in this article are solely those of the authors and do not necessarily represent those of their affiliated organizations, or those of the publisher, the editors and the reviewers. Any product that may be evaluated in this article, or claim that may be made by its manufacturer, is not guaranteed or endorsed by the publisher.

frontiers in Immunology

ORIGINAL RESEARCH
published: 08 March 2022
doi: 10.3389/fimmu.2022.740960

Cross-Talk Between m^{6}A- and m^{5}C-Related lncRNAs to Construct a Novel Signature and Predict the Immune Landscape of Colorectal Cancer Patients

Wei Song, Jun Ren, Rensheng Xiang, Wenzheng Yuan and Tao Fu *

Department of Gastrointestinal Surgery II, Renmin Hospital of Wuhan University, Wuhan, China

Background: N6-methyladenosine (m^{6}A) and 5-methylcytosine (m^{5}C) can modify long non-coding RNAs (lncRNAs), thereby affecting tumorigenesis and tumor progression. However, there is a lack of knowledge regarding the potential roles and cross-talk of m^{6}A- and m^{5}C-related lncRNAs in the tumor microenvironment (TME) and their effect on prognosis.

Methods: We systematically evaluated the expression patterns of m^{6}A- and m^{5}C-related lncRNAs in 1358 colorectal cancer (CRC) samples from four datasets. Consensus clustering was conducted to identify molecular subtypes of CRC, and the clinical significance, TME, tumor-infiltrating immune cells (TIICs), and immune checkpoints in the different molecular subtypes were analyzed. Finally, we established a m^{6}A- and m^{5}C-related lncRNA signature and a prognostic nomogram.

Results: We identified 141 m^{6}A- and m^{5}C-related lncRNAs by co-expression analysis, among which 23 lncRNAs were significantly associated with the overall survival (OS) of CRC patients. Two distinct molecular subtypes (cluster A and cluster B) were identified, and these two distinct molecular subtypes could predict clinicopathological features, prognosis, TME stromal activity, TIICs, immune checkpoints. Next, a m^{6}A- and m^{5}C-related lncRNA signature for predicting OS was constructed, and its predictive capability in CRC patients was validated. We then constructed a highly accurate nomogram for improving the clinical applicability of the signature. Analyses of clinicopathological features, prognosis, TIICs, cancer stem cell (CSC), and drug response revealed significant differences between two risk groups. In addition, we found that patients with a low-risk score exhibited enhanced response to anti-PD-1/L1 immunotherapy. Functional enrichment analysis showed that these lncRNAs related to the high-risk group were involved in the development and progression of CRC.

Conclusions: We conducted a comprehensive analysis of m^{6}A- and m^{5}C-related lncRNAs in CRC and revealed their potential functions in predicting tumor-immune-stromal microenvironment, clinicopathological features, and prognosis, and determined

OPEN ACCESS

Edited by:
Mingzhu Yin,
Central South University, China

Reviewed by:
Jinhui Liu,
Nanjing Medical University, China
Lianze Chen,
China Medical University, China

****Correspondence:***
Tao Fu
tfu001@whu.edu.cn

Specialty section:
This article was submitted to Cancer Immunity and Immunotherapy, a section of the journal Frontiers in Immunology

Received: *14 July 2021*
Accepted: *09 February 2022*
Published: *08 March 2022*

Citation:
Song W, Ren J, Xiang R, Yuan W and Fu T (2022) Cross-Talk Between m^{6}A- and m^{5}C-Related lncRNAs to Construct a Novel Signature and Predict the Immune Landscape of Colorectal Cancer Patients. Front. Immunol. 13:740960. doi: 10.3389/fimmu.2022.740960

their role in immunotherapy. These findings may improve our understanding of the cross-talk between m^{6}A- and m^{5}C-related lncRNAs in CRC and pave a new road for prognosis assessment and more effective immunotherapy strategies.

Keywords: colorectal cancer, long non-coding RNA, m^{6}A regulators, m^{5}C regulators, tumor microenvironment, immunotherapy

INTRODUCTION

Colorectal cancer (CRC) is one of the most common and lethal cancers of the digestive system, and it remains a challenging issue globally (1). Colonoscopy is available currently, and such early screening methods can effectively prevent the occurrence of CRC, but its hidden onset, long evolution time, and high malignancy grade have frequently led to poor prognosis (2, 3). CRC is characterized by inherent biological invasiveness as well as specific radiological and chemical resistance that result in high recurrence rates and progression in patients. Although different treatments, such as surgery, chemotherapy, radiotherapy, and some new immunotherapies, are currently applied, their clinical benefits remain unsatisfactory (4). Therefore, efficient prognostic biomarkers and functional signatures may be beneficial to realize individualized survival predictions and provide patients with an optimal therapeutic approach.

Long non-coding RNAs (lncRNAs), a sequence made up of more than 200 bp but lacking protein encoding capability, are transcribed by RNA polymerase II; they play a crucial regulatory role at the transcriptional, post-transcriptional, and epigenetic levels, and are involved in multiple aspects of gene regulation and numerous biological processes (5). Accumulating evidence has shown that lncRNAs can directly combine with DNA, RNA, or proteins to regulate gene expression in the form of RNA at various levels, thus resulting in the alteration of multiple physiological and pathological processes, including cell proliferation, migration, metabolism, and immunity (6, 7). Many researchers have explored the lncRNA expression profile of CRC and found that lncRNAs can serve as biomarkers of CRC prognosis and diagnosis (8, 9). Of note, lncRNA modification can change transcript stability and gene expression, causing regulatory abnormalities, which in turn influence tumorigenesis and cancer progression (10).

To date, more than 170 post-transcriptional modifications in RNA have been discovered, most of which are distributed in highly abundant non-coding RNAs (ncRNAs), such as transfer RNA (tRNA) and ribosomal RNA (rRNA), and small nuclear RNA (snRNA), and are involved in ncRNA biogenesis, metabolism, and other biological functions (11, 12). Among these modifications, the most frequent are N6-methyladenosine (m^{6}A), 5-methylcytosine (m^{5}C), N1-methyladenosine (m^{1}A), adenosine to inosine transition (A-to-I), and pseudouridine (Ψ). To date, several chemically modified lncRNAs have been identified in cancers (12), and there may be some competitive compensation interactions between these modifications.

m^{6}A modification, the most common post-transcriptional modification of mRNAs and ncRNAs, plays a vital role in RNA maturation, export, stability, translation, export, and decay (13, 14). To date, m^{6}A modifications have been identified in more than 7,600 genes and 300 non-coding RNAs in mammals (10). As an invertible and dynamic RNA epigenetic process, the molecular components of m^{6}A include intracellular methyltransferases ("writers"), demethylases ("erasers"), and signal transducers ("readers"), which regulate gene expression and are associated with various biological functions, such as RNA splicing, export, stability, translation, and ncRNA biogenesis (15, 16). Accumulating evidence has shown that changes in m^{6}A modification patterns are related to the tumorigenesis and progression of various types of cancer (17–19). Abnormal m^{6}A methylation levels can affect the self-renewal of cancer stem cells, tumor immune response, microRNA (miRNA) editing, promotion of cancer cell proliferation, and resistance to radiotherapy or chemotherapy (20–23). For example, mediated by m^{6}A modification, CBX8 interacts with KMT2b and Pol II to promote LGR5 expression, which contributes to increasing cancer stemness and decreasing chemosensitivity in colon cancer (22). METTL3-mediated m^{6}A modification was found to promote the proliferation of bladder cancer by promoting pri-miR221 and pri-miR222 maturation (23). YTHDF3 recognizes and binds to m^{6}A-modified lncRNA GAS5, promoting its degradation, which elevates YAP expression and exacerbates CRC (24).

m^{5}C is another abundant RNA modification in humans (25). It occurs when the fifth carbon of RNA cytosine is modified by methylation (26). This modification was first reported in rRNA, and later reported in other RNAs, such as mRNAs and ncRNAs (rRNAs, tRNAs, lncRNAs, and eRNAs) (27). The distribution of m^{5}C methylation modification varies greatly in different kinds of RNAs and species. Like other type of RNA methylation, m^{5}C methylation modification is a reversible process regulated by methylases and demethylases, and can only be biologically activated by methylation binding proteins (26). Just like m^{6}A, m^{5}C plays critical roles in RNA stability, translation, and nuclear transport (25, 28). Aberrant expression of m^{5}C has been found to play carcinogenic roles in several cancers, including gastric cancer (29), bladder cancer (28), and pancreatic cancer (30).

The tumor microenvironment (TME) has been recognized as an important component of malignant tumor tissues and plays various roles in tumorigenesis, tumor progression, metastasis, treatment resistance, and disease recurrence (31). The complex interaction between tumor cells and the TME plays an essential role in tumor development. Tumors can affect their microenvironment, promoting tumor angiogenesis and inducing immune tolerance by releasing cell signaling molecules. The TME can regulate cancer progression, and

tumor-infiltrating immune cells (TIICs) within this environment are reported to be of great value in predicting cancer prognosis (32).

To fully elucidate how the regulatory network of m^{6}A- and m^{5}C-related lncRNAs affects the TME, there is an urgent need for understanding the crosstalk between these different patterns of changes in lncRNAs. The two RNA modifications in lncRNAs may form an important and complex cellular regulatory network in CRC. The understanding of this network may provide important insights into the underlying mechanism of CRC tumorigenesis and may open up new therapeutic possibilities for CRC. In the present study, we explored genomic alterations in 1358 CRC samples from The Cancer Genome Atlas (TCGA) and Gene Expression Omnibus (GEO) datasets to comprehensively evaluate the roles of m^{6}A- and m^{5}C-related lncRNAs. We revealed two distinct molecular subtypes that can be used to predict clinicopathological features, prognosis, TME stromal activity, TIICs, and immune checkpoints. We further established a set of scoring system to predict OS for CRC patients. The current investigation will contribute to great progresses on the exploration of prognostic m^{6}A- and m^{5}C-related lncRNAs and shed new light on the possible mechanisms of CRC development.

MATERIALS AND METHODS

Data Sources

A map illustrating the process of this study is shown in **Figure 1**. Gene expression (fragments per kilobase million, FPKM) and the relevant the corresponding prognostic and clinicopathological data of CRC were downloaded from The Cancer Genome Atlas (TCGA) database (https://portal.gdc.cancer.gov/) and the gene expression omnibus (GEO) database (https://www.ncbi.nlm.nih.gov/geo/). GTF files were downloaded from Ensembl (http://asia.ensembl.org/index.html) for accurate distinguishing of mRNAs and lncRNAs. Three GEO CRC cohorts (GSE39582, GSE17536, GSE38832) and TCGA cohort were obtained for subsequent analysis (**Table S1**). We downloaded the raw "CELL" files and performed background adjustment and quantile normalization. The FPKM values of TCGA-COAD/READ were transformed into Transcripts Per kilobase Million (TPM) as previously described. Three GEO datasets were combined, and the "Combat" algorithm was used to eliminate the batch effect. We excluded data from patients who had no survival information. Detailed information on CRC patients is shown in **Table S1**. Clinical variables involved age, sex, tumor location, TNM stage, KRAS mutation, BRAF mutation, follow-up time, and survival status.

Identification of m^{6}A- and m^{5}C-Related lncRNAs

Based on published data, 23 recognized m^{6}A and 15 m^{5}C regulators were obtained, including writers, erasers, and readers. The list of m^{6}A and 15 m^{5}C regulators is provided in **Table S2**. The correlation between lncRNAs and the expression of m^{6}A- and m^{5}C-related genes was analyzed using the Pearson correlation test. LncRNAs with |correlation coefficients| > 0.4 and P < 0.001 were identified as m^{6}A- and m^{5}C-related lncRNAs, respectively. Next, the intersection between the m^{6}A- and m^{5}C-related lncRNAs was considered as a candidate lncRNA. To screen for m^{6}A- and m^{5}C-related lncRNAs that were highly correlated with OS, univariate Cox regression analysis was performed (P < 0.05) based on lncRNAs from three GEO datasets.

Consensus Clustering Analysis of m^{6}A- and m^{5}C-Related lncRNAs

The "ConsensusClusterPlus" package in R was used for consensus unsupervised clustering analysis to classify patients into distinct molecular subtypes according to the expression of m^{6}A- and m^{5}C-related lncRNAs obtained from univariate Cox

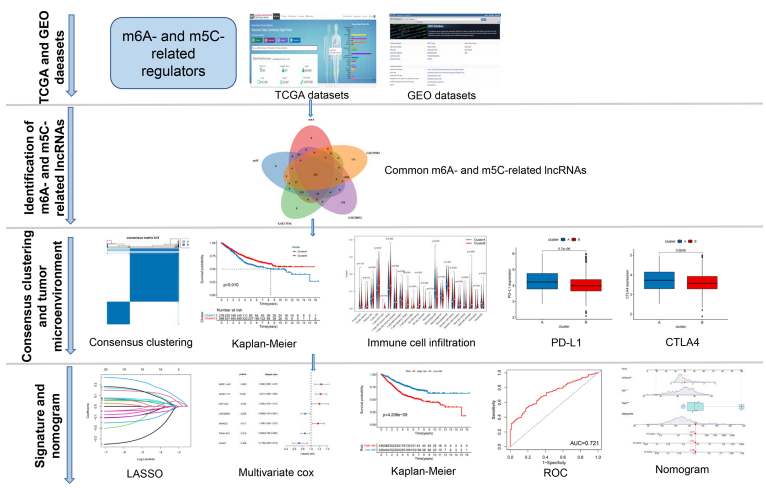

FIGURE 1 | The entire analytical process of the study.

regression analysis. Clustering was conducted based on the following criteria. Firstly, the cumulative distribution function curve increased gradually and smoothly. Secondly, there was no group with a small sample size. Lastly, after clustering, the intra-group correlation increased, whereas the inter-group correlation decreased. To investigate the differences in biological processes between m^{6}A- and m^{5}C-related lncRNAs, we conducted Gene Set Variation Analysis (GSVA) enrichment analysis using the "GSVA" R package. The gene set "c2.cp.kegg.v7.2" and "clusterProfiler" R package was used to perform functional annotation for m^{6}A- and m^{5}C-related lncRNAs, with the cutoff value of adjusted p-value < 0.05.

Clinical Significance of the Molecular Subtypes

To explore the clinical significance of the molecular subtypes in CRC, we investigated the relationship between the molecular subtypes, clinical characteristics, and prognosis. The patient characteristics included age, sex, tumor location, TNM stage, KRAS mutation, and BRAF mutation. Subsequently, the differences in OS between different clusters were calculated using the Kaplan-Meier method and visualized by using the "survival" and "survminer" modules in the R software.

Evaluation of TME and TIICs

We employed the Estimation of Stromal and Immune cells in Malignant Tumors using Expression algorithm (ESTIMATE) to evaluate the immune score and stroma score of each CRC sample (33). In addition, the CIBERSORT (https://cibersort.stanford.edu/) algorithm was utilized to precisely measure the fractions of 22 human immune cell subsets in CRC samples (34).

Establishment and Evaluation of the m^{6}A- and m^{5}C-Related lncRNA Signature

A total of 878 CRC patients from the three GEO datasets were used to construct a m^{6}A- and m^{5}C-related prognostic signature. Briefly, based on m^{6}A- and m^{5}C-related prognostic lncRNAs identified by univariate Cox regression analysis, the Lasso Cox regression algorithm was used to minimize the risk of over-fitting and remove highly related genes using the "glmnet" R package. A 10-fold cross validation was conducted to identify the optimal lambda value. Next, the screened lncRNAs were subjected to multivariate Cox proportional hazard regression analysis to obtain the optimal lncRNAs and establish a prognostic signature using the training set.

The following formula was used:

$$Risk\ \ Score = \Sigma(Expi * Coefi)$$

Expi is the expression level of the lncRNA, and *Coefi* is the estimated regression coefficient of the lncRNA. The median value of the risk score was used as the cutoff for the risk score, and the patients were assigned to a high- (risk score > median value) or low-risk group (risk score > median value). We performed survival analysis between the two risk groups to detect whether the difference in OS was subsistent. A receiver operating characteristic (ROC) curve was also generated for further assessment of the predictive ability of the signature. Moreover, the accuracy of the model was validated using the TCGA cohort by the same method. To investigate whether the signature can predict patient response to immune checkpoint blockade therapy, the IMvigor210 cohort was downloaded from the website http://research-pub.gene.com/IMvigor210CoreBiologies/, which is a study cohort of atezolizumab in patients with locally advanced or metastatic urothelial carcinoma (35).

Tissue Samples

A total of six pairs of colorectal tissue samples and paired adjacent normal colorectal tissues derived from surgically resected specimens were stored at −70°C until expression analysis. Tissues were attained during surgery prior to receiving chemo/radiotherapy. The study was approved by the ethical committee of the Renmin Hospital of University of Wuhan University. All subjects gave written informed consent in accordance with the Declaration of Helsinki.

RNA Isolation and Quantitative Real Time-PCR (RT-qPCR)

Total RNA from tissues of CRC patients was extracted using the TRIzol reagent (Invitrogen, Carlsbad, CA, USA) according to the manufacturer's instructions. We synthesized cDNA from RNA using the PrimeScript RT reagent kit (Takara, Japan). qPCR analysis was conducted with SYBR Green Premix Ex Taq (TaKaRa, Japan) and according to the standard program on CFX-96 (Bio-Rad Laboratories, Inc., USA). Gene expression levels were normalized to GAPDH levels, and the relative expression level was calculated using the $2^{-\Delta\Delta Cq}$ method.

Clinical Correlation and Stratification Analyses of the Prognostic Signature

To explore the association of the signature with the clinicopathological features (age, sex, tumor location, TNM stage, KRAS mutation, and BRAF mutation) of CRC, the correlation between the signature and clinicopathological variables of CRC was assessed using the Chi-square test and visualized using the "pheatmap" package and "ggpubr" in the R software. To assess whether risk scores and clinicopathological characteristics can be used as independent prognostic factors, we subjected the training and testing sets to univariate and multivariate cox regression analyses. Moreover, stratified analysis was carried out to confirm whether the signature retains its predictive ability in various subgroups. These variables include age (< 60 and > 60 years), gender (female and male), tumor stage (I-II and III-IV), T stage (T1-2 and T3-4), N stage (N0 and N1-3), M stage (M0 and M1), tumor location (left-side and right-side), KRAS mutation (yes and no), and BRAF mutation (yes and no). To quantitatively evaluate CRC prognosis in clinical practice, a nomogram was generated by the "rms" package based on the outcome of the independent prognosis analysis. In the nomogram scoring system, each variable was matched with a score, and the total score was obtained by adding the scores across all variables of each sample. Time-dependent ROC curves for 3, 5, and 10 years

were used to evaluate the nomogram. Calibration curves were drawn to depict the predictive value between the predicted 3-, 5-, and 10-year survival events and the virtual observed outcomes.

Drug Sensitivity and Cancer Stem Cell (CSC) Analyses

To explore differences in therapeutic effects of chemotherapeutic drugs in patients across the high- and low-risk groups, R package "pRRophetic" was used to predict the half-maximal inhibitory concentration (IC50), which could construct a ridge regression signature based on TCGA gene expression profiles and Genomics of Drug Sensitivity in Cancer cell line expression spectrum (36). In addition, we also analyzed the relationship between the risk score and cancer stem cell (CSC).

Functional Enrichment Analysis

To explore the differences in biological process between the different risk groups, we performed GO and KEGG pathway analysis using the "clusterProfiler" R package. Samples with p-value < 0.05 were considered significantly enriched.

Statistical Analyses

All statistical analyses were implemented using R version 4.1.0. Statistical significance was set at p-value < 0.05. The Kruskal-Wallis test was used to analyze differences between three or more groups. The results of immune infiltration assay were analyzed using the 'gsva' package in R. The Kaplan-Meier plot was used to generate survival curves, and Log-rank test was performed to evaluate significant differences. Univariate and multivariate Cox proportional hazard regression analyses were utilized to determine whether the m^{6}A- and m^{5}C-related lncRNA signature can be an independent prognostic factor. For visual risk prediction, the nomogram was created by the "Survival" and "RMS" packages of R.

RESULTS

Identification of m^{6}A- and m^{5}C-Related lncRNAs in CRC

The entire analytical process used in this research is displayed in **Figure 1**. The gene expression and corresponding clinicopathological data were downloaded from the TCGA and GEO databases. To gain a comprehensive understanding of the expression patterns of the m^{6}A- and m^{5}C-related lncRNAs involved in tumorigenesis, 1364 CRC samples from four eligible CRC cohorts, namely TCGA-COAD/READ (n = 486), GSE39582 (n = 579), GSE17536 (n = 177), and GSE38832 (n = 122), were integrated in our study for further analysis. Detailed information on 1364 CRC patients is shown in **Table S1**. We extracted 14087 lncRNAs from the TCGA database in total, and 23 were recognized as m^{6}A and 15 as m^{5}C regulators from previous publications, respectively. Through co-expression analysis, we identified 1524 m^{6}A- and 1581 m^{5}C-related lncRNAs (|correlation coefficient| > 0.4, p-value < 0.001), respectively (**Table S3**). Consequently, a total of 1401 common lncRNAs were selected from the intersection of 1524 m^{6}A- and 1581 m^{5}C-related lncRNAs (**Figure S1A**). After intersecting lncRNAs obtained from three other GEO datasets, a total of 141 common lncRNAs of m^{6}A- and m^{5}C-related lncRNAs were identified and used for subsequent analysis (**Figure S1B**; **Table S4**). To confirm whether the 141 lncRNAs were correlated with the OS of CRC patients, we performed univariate Cox regression analysis based on the patients from three GEO datasets to identify the prognostic value of the m^{6}A- and m^{5}C-related lncRNAs. Twenty-one lncRNAs related to OS time (p-value < 0.05) were screened out and applied in the following analysis (**Figure 2A**).

Consensus Clustering Analysis for m^{6}A- and m^{5}C-Related lncRNAs

To understand the effect of m^{6}A- and m^{5}C-related lncRNAs on CRC development, consensus unsupervised clustering analysis was conducted on the expression level of 21 m^{6}A- and 15 m^{5}C-related lncRNAs obtained from univariate Cox regression analysis. The optimal number of clusters was determined according to the cumulative distribution function and clinical significance. We choose the value of k = 2 as the appropriate number of clusters for further analysis. Finally, two subtypes were determined and dubbed cluster A (n = 279) and cluster B (n = 599) (**Figure 2B**).

Correlation of Molecular Subtypes to Characteristics and Survival

To further examine the clinicopathological characteristics of the two subtypes identified by consensus clustering, the clinicopathological features of different subtypes of CRC patients were compared. Significant differences in the expression of m^{6}A- and m^{5}C-related lncRNAs and clinicopathological characteristics between the two subtypes were observed (**Figure 2C**). As shown in **Figure 2C**, Cluster B was preferentially related to younger age (p-value < 0.05) and lower TNM stage (p-value < 0.05), compared to cluster A. In addition, prognostic analysis of the two subtypes showed that patients with subtype B had longer OS than their counterparts with subtype A (**Figure 2D**). Taken together, clustering subtypes are significantly correlated with the heterogeneity of CRC.

Characteristics of TME and TIICs in Distinct Subtypes

To identify the biological significance of the two distinct subtypes, we conducted GSVA enrichment analysis. Cluster A was significantly enriched in stromal and oncogenic activation pathways, such as the ECM receptor interaction, colorectal cancer, TGF-β signaling pathway, cell adhesion, and other cancer-related pathways (**Figure 3A**). Cluster B was enriched in pathways related to metabolism, including glyoxylate and dicarboxylate metabolism, pyruvate metabolism, and Drug metabolism-other enzymes (**Figure 3A**).

To investigate the role of m^{6}A- and m^{5}C-related lncRNAs in the TME of CRC, we analyzed the relationship between the two subtypes and 22 human immune cell subsets of every CRC

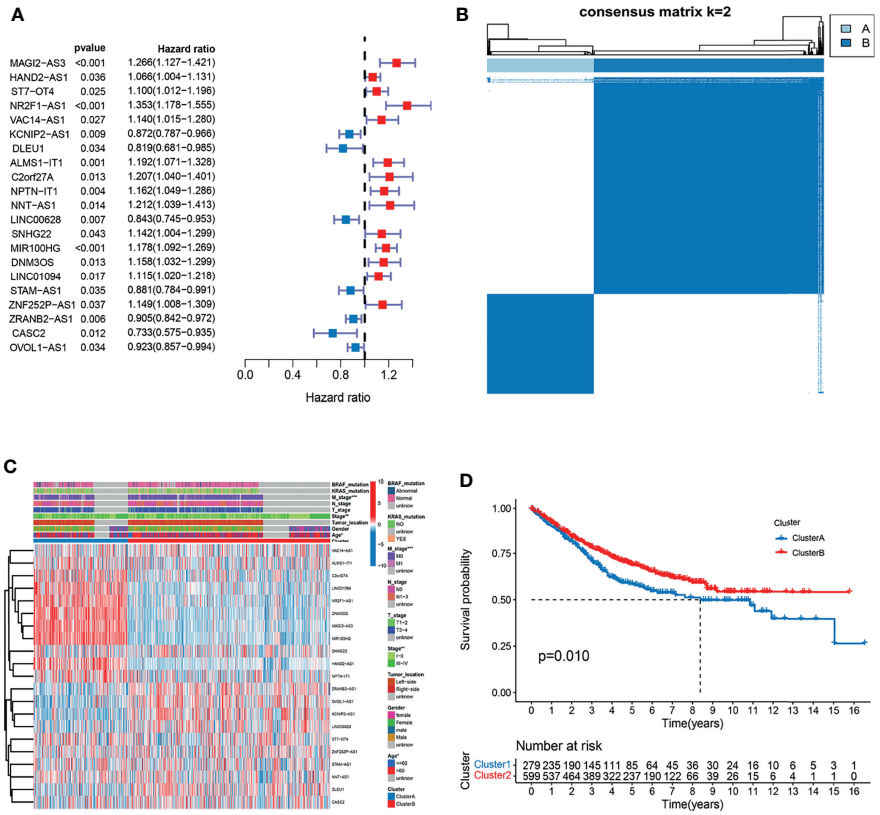

FIGURE 2 | Analysis of the clinical characteristics, outcome, and expression level of m^{6}A- and m^{5}C-related lncRNAs between two distinct subtypes of samples divided by consistent clustering. **(A)** Univariate analysis revealed 21 lncRNAs related to overall survival (OS) time. **(B)** Consensus clustering analysis and the correlation area of the clusters when k = 2. **(C)** Differences in clinicopathologic features and the expression level of m^{6}A- and m^{5}C-related lncRNAs between the two distinct subtypes. **(D)** Kaplan-Meier curves of OS for patients with the two colorectal cancer (CRC) subtypes.

sample by the CIBERSORT algorithm (**Table S5**). The results revealed the differences in the infiltration level of most immune cells between the two subtypes (**Figure 3B**). Violin plots showed that follicular helper T cells, M0, M1, and M2 macrophages, resting mast cells, eosinophils, and neutrophils exhibited significantly higher infiltration rates in the subtype A group than in the subtype B group, whereas memory B cells, plasma cells, CD8+ T cells, resting memory CD4+ T cells, regulatory T cells, gamma delta T cells, resting NK cells, monocytes, resting dendritic cells, and activated mast cells had significantly lower infiltration rates in the subtype A group than in the subtype B group (**Figure 3B**). Similarly, the expression levels of PD-L1, CTAL-4, and HAVCR2 in cluster A were higher, and the expression levels of PD1 were lower (**Figures 3C–F**). In addition, we evaluated the TME score (stromal score, immune score, and estimate score) of the two subtypes by the ESTIMATE package. Higher stromal scores or immune scores represented higher relative content of stromal cells or immunocytes in the TME, and estimate scores indicated the aggregation of stromal scores or immune scores in the TME. The results showed that cluster A was significantly correlated to stromal score, immune score, and estimate score (**Figures 3G–I**).

Construction of m^{6}A- and m^{5}C-Related lncRNA Prognostic Signature

To further explore the prognostic value of m^{6}A- and m^{5}C-related lncRNAs in CRC, LASSO Cox regression and multivariate Cox proportional hazard regression analyses for those 21 m^{6}A- and m^{5}C-related lncRNAs were conducted to further select a robust and effective risk model for prognosis prediction. A total of 16 prognosis-associated lncRNAs were screened by LASSO regression analysis (**Figure 4A**) and partial likelihood deviance (**Figure 4B**). Subsequently, we performed multivariate Cox regression analysis on the 16 prognosis-associated lncRNAs based on the AIC value, and finally obtained 7 lncRNAs, namely NR2F1-AS1, ALMS1-IT1, NNT-AS1, LINC00628, SNHG22, STAM-AS1, and CASC2, including 4 high-risk lncRNAs (NR2F1-AS1, ALMS1-IT1, NNT-AS1, and SNHG22) and 3 low-risk lncRNAs (LINC00628, STAM-AS1, and CASC2) (**Figure 4C**). The risk score of each patient in the training set was calculated based on the regression coefficient and expression level of m^{6}A- and m^{5}C-related prognostic lncRNAs. The expression levels of the eight genes used to construct the risk score in the high and low risk groups are shown in **Figure S2**. Patients with a score lower than the median risk score were categorized into the low-risk group (n = 436),

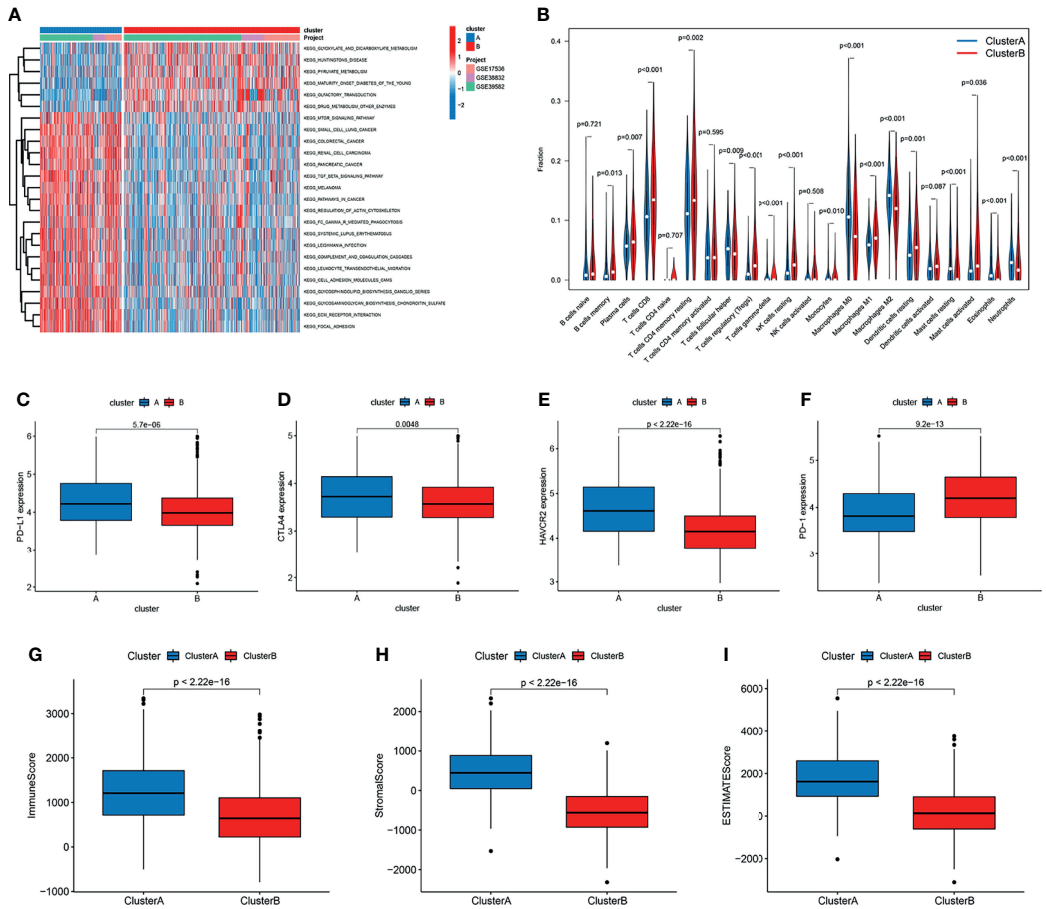

FIGURE 3 | Correlation of tumor immune cell microenvironment to two colorectal cancer (CRC) subtypes. **(A)** GSVA enrichment analysis showing the activation states of biological pathways in the two distinct subtypes. The activated pathways are marked with red color, and the inhibited pathways are marked with blue color. **(B)** The infiltration levels of 22 immune cell types in the two subtypes. **(C–F)** The expression of tumor immune checkpoints (PD-L1, CTAL-4, HAVCR2, and PD-1), in the two subtypes. **(G–I)** TME score (stromal score, immune score, and estimate score) in the two subtypes.

whereas those with a score greater than median risk score were allocated to the high-risk group (n = 436). Compared with subtype B, subtype A showed significantly increased risk score. The distribution of patients in the two subtypes and two risk subgroups is shown in **Figures 4D, E**. The risk distribution plot based on the signature revealed that survival times decreased, whereas mortality rates increased with increasing risk scores (**Figures 4F, G**). Survival analysis revealed that the prognosis of patients in the low-risk score group was better than that in the high-risk score group (log-rank test, p-value < 0.001; **Figure 4H**). In addition, the time-dependent ROC curves showed that the AUC in the training set was 0.721 (**Figure 4I**).

To validate the prognostic performance of the signature, we calculated risk scores across the TCGA set (**Figure 5A**). Patients were also stratified into high- or low-risk groups based on the same formula as that for the training set. The risk scores and survival status of patients of the low- and high-risk groups are shown in **Figures 5A, B**. Survival analysis revealed a significantly better prognosis in the low-risk group, compared to the high-risk group (log-rank; p-value < 0.05; **Figure 5C**), with the AUC of the ROC greater than 0.7 (**Figure 5D**), indicating that the signature had excellent ability to predict the survival of CRC patients.

Validation of the Expression Levels of Eight lncRNAs of Prognostic Signature

To further verify the accuracy of the m^{6}A- and m^{5}C-related lncRNA signature, the expression levels of seven prognostic lncRNAs were measured in six CRC tissues and adjacent normal tissues using RT-qPCR. As shown in **Figure S3**, the expression levels of ALMS1-IT1, NNT-AS1, SNHG22, and STAM-AS1 were significantly upregulated in CRC tissues, whereas NR2F1-AS1, LINC00628, and CASC2 expression was downregulated in CRC tissues compared with that in the corresponding normal tissues.

Clinical Correlation Analysis and Stratification Analysis of the Prognostic Signature

To examine the association of the signature with the clinicopathological characteristics of CRC, we determined the

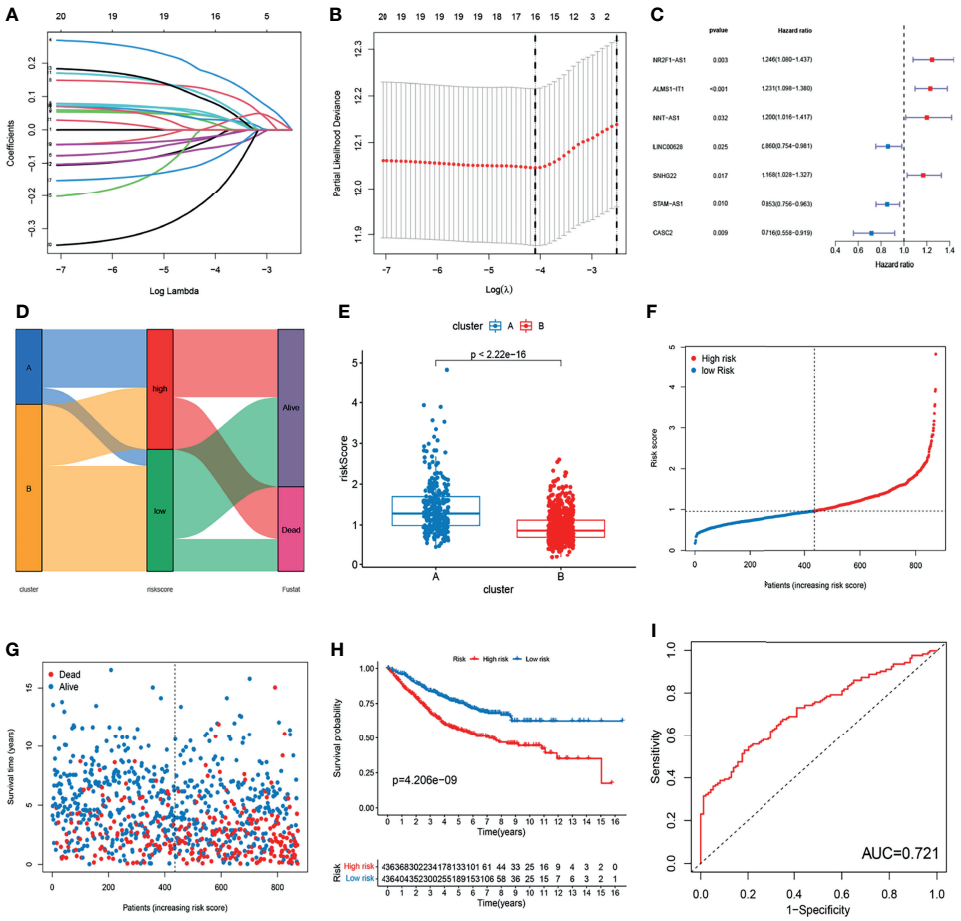

FIGURE 4 | Construction of m^{6}A- and m^{5}C-related lncRNA signature using the training set. **(A, B)** LASSO regression analysis and partial likelihood deviance of prognostic lncRNAs. **(C)** Forest plot of multivariate cox regression analysis of prognostic lncRNAs. **(D)** Alluvial diagram of subtypes distribution in groups with different risk score and survival outcomes. **(E)** Correlation between the two subtypes and the different risk scores of the signature. **(F, G)** The ranked dot plot indicates the risk score distribution and scatter plot presenting patient survival status. **(H)** KM analysis of overall survival (OS) between the two groups. **(I)** Receiver operating characteristic (ROC) curve of the m^{6}A- and m^{5}C-related lncRNA signature.

correlation between the signature and different clinical characteristics of CRC (age, sex, tumor location, TNM stage, KRAS mutation, and BRAF mutation). The risk scores in the T3-4, N1-3, M1, and stage III-IV, subgroups were significantly higher than those in the stage T0-2, N0, M0, and stage I-II subgroups (p-value < 0.05; **Figures 6A–D**). To determine whether this prognostic signature might independently predict the prognosis for CRC patients, we combined the clinical features (age, gender, tumor location, TNM stage, and KRAS mutation) with the risk scores of the prognostic signature in univariate and multivariate Cox regression analyses. As shown in **Figures 6E. F**, the age, TNM stage, and risk score in the GEO group showed significant differences, and the results were consistent with those in the TCGA group (**Figures 6G, H**). Moreover, to assess whether the signature retains its predictive ability in various subgroups, we stratified subgroups by age (age ≤ 60 and age > 60), gender (female and male), tumor location (left-side and right side), TNM stage (stage I-II and stage III-IV), and KRAS mutation (yes and no). As shown in **Figure S4**, the OS of low-risk patients based on age (p-value < 0.001), gender (p-value = 0.003 in male), tumor location (p-value = 0.008 in left-side and p-value = 0.040 in right side), TNM stage (p-value = 0.045 in stage I-II and p-value < 0.001 in stage III-IV), and KRAS mutation (p-value = 0.022 in yes and p-value = 0.028 in no) was significantly higher than that of high-risk patients.

m^{6}A- and m^{5}C-Related lncRNA Signature in Anti-PD-1/L1 Immunotherapy

To investigate whether the signature can predict patient response to immune checkpoint blockade therapy, we calculated the risk score in an anti-PD-L1 cohort (IMvigor210). Patients with a low-risk score exhibited significantly clinical benefits and significantly favorable OS (**Figure S5A**). Furthermore, patients in the CR/PR group had a lower risk score, suggesting that patients in the low risk-score group a significant therapeutic advantages and clinical response to anti-PD-1/L1 immunotherapy compared to those in the high risk-score group (**Figure S5B**).

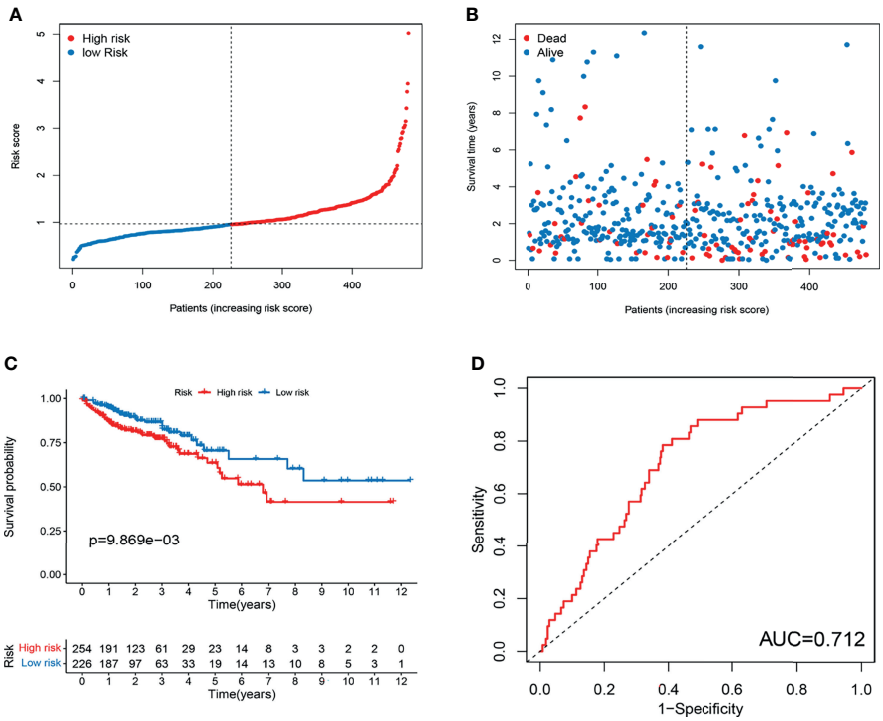

FIGURE 5 | Evaluation of m^{6}A- and m^{5}C-related lncRNA signature in TCGA set. **(A)** The ranked dot plot indicates the risk score distribution. **(B)** Scatter plot presenting the patient survival status. **(C)** KM analysis of overall survival (OS) between the two groups. **(D)** Receiver operating characteristic (ROC) curve of the m^{6}A- and m^{5}C-related lncRNA signature.

Relationship Between the Signature and the CSC Index and Sensitivity to Chemotherapeutic Agents

We analyzed the correlation between the two subtypes and the CSC index. As shown in **Figures 7A, B**, there was a significant difference in CSC indexes between high-risk and low-risk groups. Distinct CRC subgroups in the signature should guide clinical treatment. Thus, we compared the sensitivity of high-risk and low-risk groups to common anticancer drugs to identify potential CRC treatment modalities. Patients in the high-risk group may be sensitive to Cisplatin, Gemcitabine, lapatinib, Nilotinib, and Pazopanib, while those in the low-risk group was more sensitive to Paclitaxel (**Figures 7C–H**). Under these circumstances, it is possible that these drugs could be employed for the treatment of CRC with a high risk in the future.

Development of a Nomogram for Predicting Survival

To establish a quantitative method to predict the prognosis of CRC patients, we built a nomogram to predict the 3-, 5-, and 10-year OS of CRC patients. All variables that were significant (age, stage, and risk score) in the multivariate analysis were enumerated in the nomogram according to the algorithm. The nomogram displays an example of a patient to predict survival probability. The variable scores were summed to obtain the total points, and the total point line is shown at the bottom of the nomogram, which can predict the probability of OS at 3-, 5-, and 10 years (**Figure 8A**). We performed AUC experiments on the nomogram model and found that it had a higher accuracy in predicting OS at 3-, 5-, and 10-years in the GEO and TCGA sets (**Figures 8B, C**). Calibration curves were drawn to depict the predictive value between the predicted 3-, 5-, and 10-year survival events and the virtual observed outcomes in the GEO and TCGA sets (**Figures 8D, E**), which showed that the nomogram model was highly accurate, affirming its practicability in predicting patient prognosis.

GO and KEGG Analysis

To determine the potential biological processes and signaling pathways related to the signature, we performed GO terms and KEGG pathway analysis of the low- and high-risk groups. The "limma" R package was used to identify the differentially expressed genes (DEGs) between the high- and low-risk groups with the criteria of $|\log FC| > 1$ and adjusted p-value < 0.05. The results of GO functional annotation analysis of the DEGs showed that the most significantly enriched biological processes included extracellular matrix organization, extracellular structure organization, and external encapsulating structure organization. The most significantly enriched cellular components included collagen-containing extracellular matrix, endoplasmic reticulum lumen, and apical part of cell. The most significantly enriched molecular functions included extracellular matrix structural constituent, glycosaminoglycan binding, and

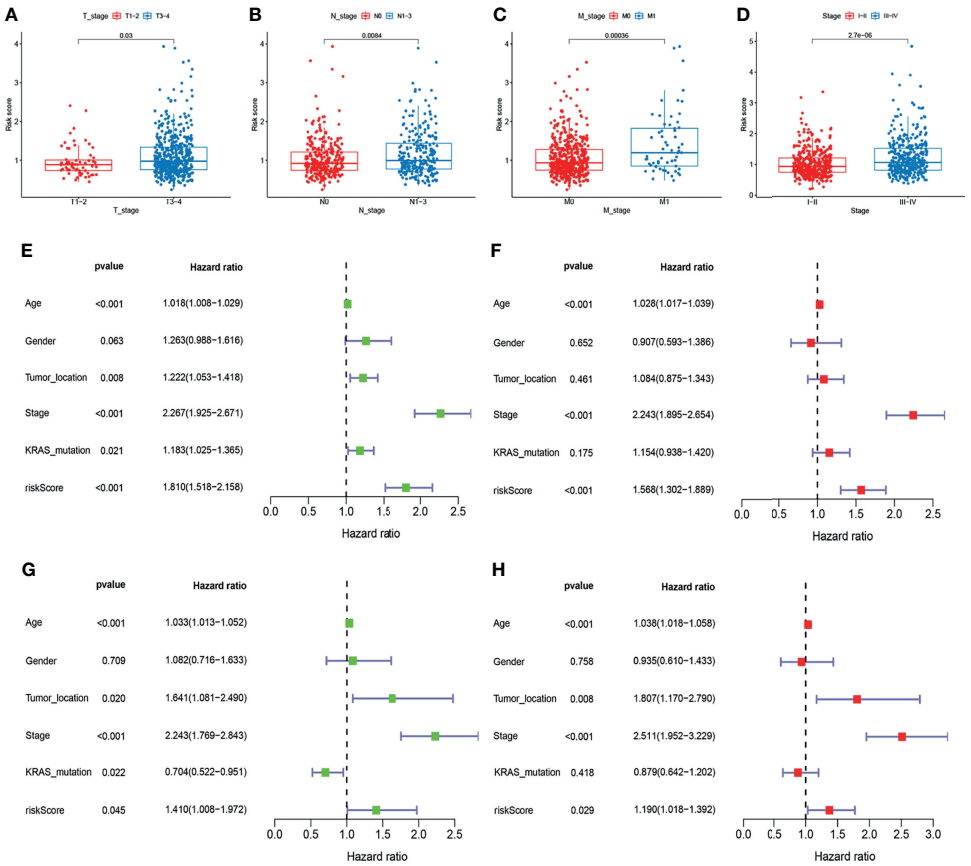

FIGURE 6 | Correlation and independent prognosis analysis of risk score and clinicopathological variables in colorectal cancer (CRC). **(A–D)** Correlation between the risk score and T, N, and M stage, and TNM stage. **(E, F)** Univariate and multivariate analyses showed the prognostic value of the lncRNA signature in the GEO set. **(G, H)** Univariate and multivariate analyses showed the prognostic value of the lncRNA signature in the TCGA set.

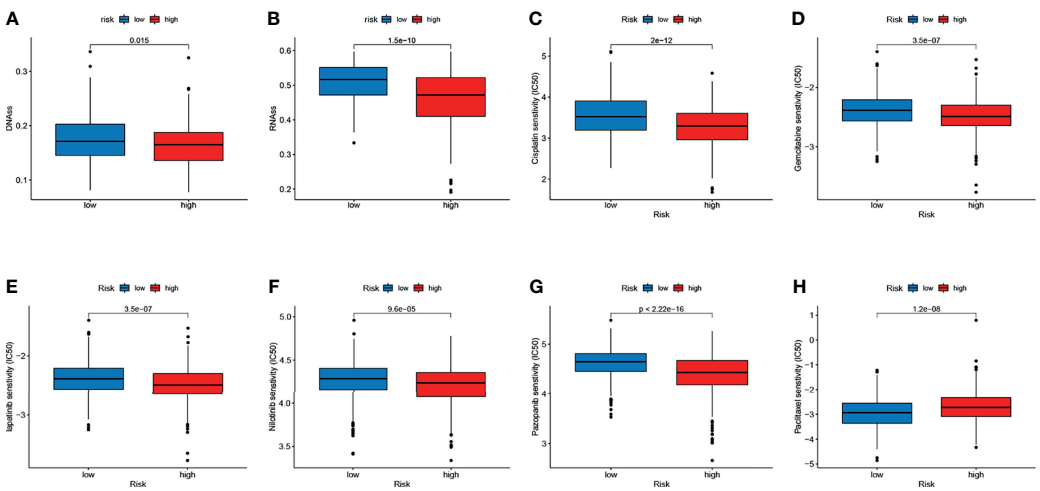

FIGURE 7 | Relationship between the signature and the CSC index and sensitivity to chemotherapeutic agents. **(A, B)** Correlation between the risk score and CSC index. **(C–H)** The IC50 values of six chemotherapeutic drugs in the high- and low-risk groups.

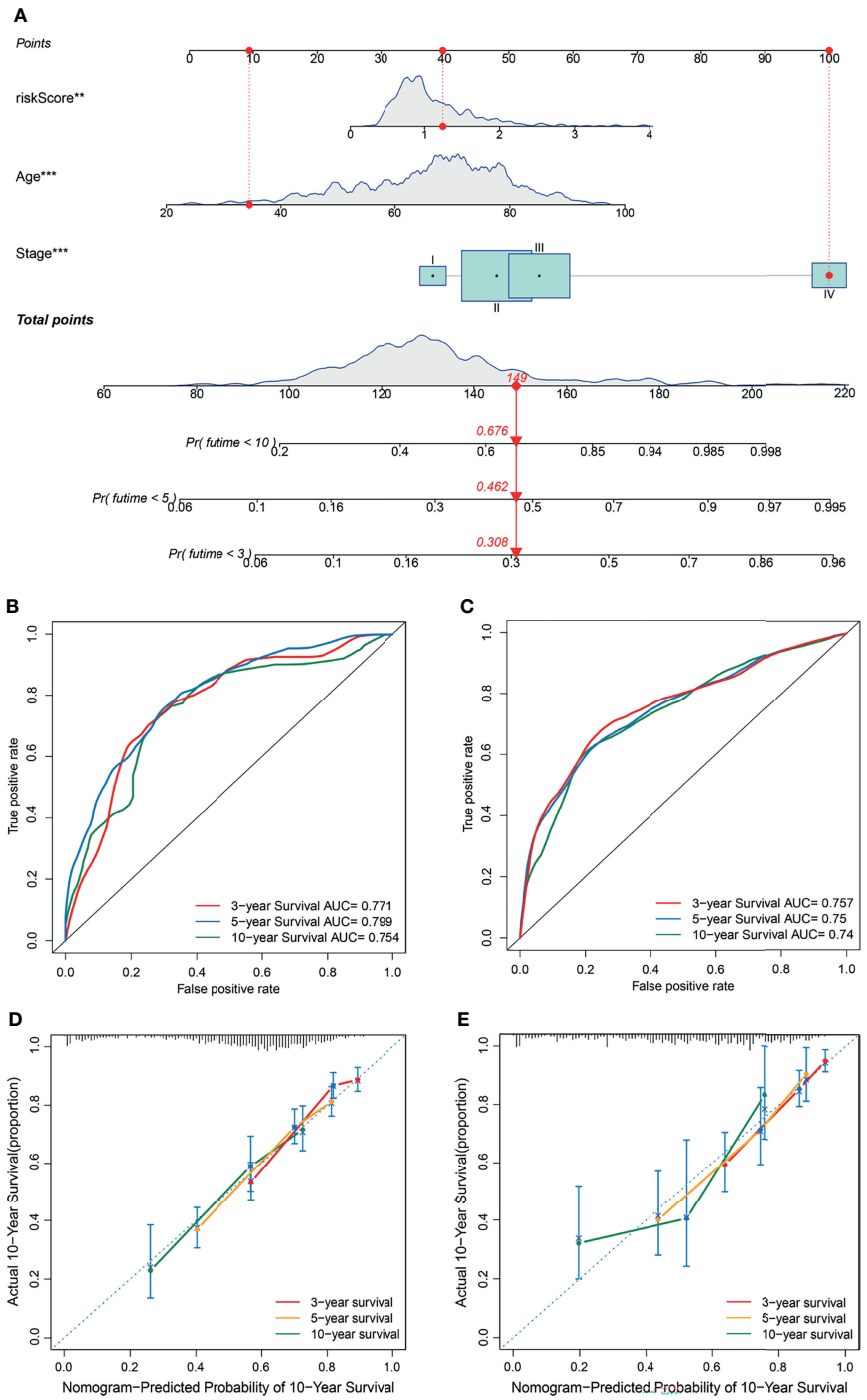

FIGURE 8 | Construction and validation of a nomogram. **(A)** A nomogram for predicting the overall survival (OS) of colorectal cancer (CRC) patients at 3-, 5-, and 10-years in the GEO set. **(B, C)** Receiver operating characteristic (ROC) curves for predicting the 3-, 5-, and 10-year ROC curves in the GEO cohort **(B)** and TCGA set **(C)**. **(D, E)** Calibration curves of the nomogram for predicting 3- and 5-year OS in the GEO cohort **(D)** and TCGA set **(E)**.

sulfur compound binding (**Figure S6A**). KEGG pathway enrichment analysis for the DEGs showed that the significantly enriched pathways included PI3K-Akt signaling pathway, the ECM-receptor interaction, focal adhesion, proteoglycans in cancer, and Transcriptional misregulation in cancer (**Figure S6B**; **Table S6**). Notably, most of these functions were significantly correlated with the occurrence and development of tumors.

DISCUSSION

CRC is a heterogeneous and highly malignant tumor with high morbidity and mortality (37). Owing to the phenotype and genetic heterogeneity of CRC, the accuracy of conventional methods using clinical features in predicting individual outcome and survival is still limited. Accurate prognostic prediction and individualized clinical treatment strategy are the basis of precision medicine (38). Most of the established clinical markers for treatment response and prognosis of CRC are based on clinical features, and their accuracy and specificity are limited. Traditional AJCC TNM staging is mainly based on anatomical information and cannot adequately assess the prognosis of CRC patients. Therefore, exploring the molecular mechanisms and screening reliable CRC-specific genomic signatures are urgently needed to improve prognosis assessment and individualized treatment.

Following in-depth studies of post-transcriptional modifications, researchers gradually realized the importance of epitranscriptomics in CRC. Increasing studies have confirmed and highlighted the potential effects of several common modifications in lncRNAs (m^{6}A and m^{5}C) on cancer development and progression. As the most abundant post-transcriptional modification in eukaryotic ncRNAs, m^{6}A has a huge effect on their maturation, export, stability, translation, export, and decay (13, 14). Previous studies have shown that m^{6}A "writers" and "erasers" could adjust the levels of m^{6}A modification in lncRNAs to regulate binding sites to m^{6}A "reader" proteins. Different m^{6}A "reader" proteins recognize and bind to methylated lncRNAs to exert different functions. Liu et al. (39) revealed that the specific m^{6}A readers YTHDF1 and YTHDF2 can read m^{6}A motifs and regulate the stability (and decay) of the lncRNA THOR, thereby regulating the proliferation, migration, and invasion of cancer cells. The m^{6}A regulators reportedly act as a lncRNA structural switch, participate in the lncRNA-mediated competing endogenous RNA model, and enhance the stability of lncRNA to serve its functions, thereby influencing tumor initiation and progression. For example, m^{6}A-induced LNCAROD can promote the development of head and neck squamous cell cancer by forming a ternary complex with YBX1 and HSPA1A (40). The m^{6}A mark increased the stability of lncRNA FAM225A, which promotes nasopharyngeal carcinoma progression by acting as ceRNA to sponge miR-590-3p/miR-1275 (41).

m^{5}C is distributed widely in lncRNAs and involved in various biological processes related to the occurrence and progression of tumors. In a previous study, quantitative mapping of m^{5}C sites in *Arabidopsis thaliana* on a transcriptome range revealed more than 1000 m^{5}C sites in mRNA, lncRNAs, and other non-coding RNAs (42). He et al. (43) found that m^{5}C methylation in lncRNAs occurred more frequently in hepatocellular carcinoma than in the adjacent non-tumor tissues, and a higher number of methylated genes were upregulated. Sun et al. (44) revealed that H19 lncRNA modified by the m5A "writer" NSUN2 promoted the occurrence and development of hepatocellular carcinoma by recruiting the G3BP1 oncoprotein. These lncRNAs can be upregulated or downregulated to promote cancer cell proliferation and migration. Although significant progress has been made in the field of epitranscriptomics and lncRNA research, little is known about the functional role of lncRNAs in cancers or their complete mechanism of action. To advance individualized therapies based on lncRNAs, it is important to clarify the interactions between the chemical modifications that occur in lncRNAs. Moreover, it is necessary to further study m^{6}A- and m^{5}C-related lncRNAs to clarify their potential regulatory mechanism in the TME.

In the present study, we identified 1401 m^{6}A- and m^{5}C-related lncRNAs by Pearson's correlation analysis between 23 m^{6}A regulators, 15 m^{5}C regulators, and lncRNAs, and we screened out 21 prognostic lncRNAs. We detected two distinct molecular subtypes based on the 21 prognostic lncRNAs, and determined that cluster A was significantly associated with advanced clinicopathological features and worse survival outcomes. The TME characteristics and the proportions of 22 TIICs were significantly different between the two subtypes. This CRC subtype was also characterized by a significant stroma activation status, including the EMT and TGF-β signaling pathways. These findings suggested that m^{6}A- and m^{5}C-related lncRNAs might serve as a valid prognostic biomarker and predictor for evaluating the clinical outcome and immunotherapy response of CRC patients. Therefore, we conducted LASSO Cox regression and multivariate Cox proportional hazard regression analyses to construct a robust and effective prognostic signature. Patients in the high- and low-risk groups divided by risk scores exhibited significantly different clinicopathological characteristics and survival outcomes. In addition, there was a significant difference in CSC indexes between high-risk and low-risk groups. We also found that patients in the high-risk group may be sensitive to Cisplatin, Gemcitabine, lapatinib, Nilotinib, and Pazopanib. Under these circumstances, it is possible that these drugs could be employed for the treatment of CRC with a high risk in the future. Functional enrichment analysis showed that these lncRNAs related to the high-risk group were involved in the development and progression of CRC. Last, a nomogram was constructed based on age, tumor stage, and risk score to further improve the performance and facilitate the use of the m^{6}A- and m^{5}C-related lncRNA signature. The m^{6}A- and m^{5}C-related lncRNA signature can be used for prognosis stratification of CRC patients, and will assist with understanding the molecular mechanism of CRC and provide new ideas for targeting therapies.

The immune system plays a complex role in cancer development and substantially affects CRC progression. The prognosis of CRC after conventional chemotherapy is poor, with high levels of tumor neoantigens, tumor infiltrating lymphocytes, and checkpoints. There is growing evidence that the TME, in which immune cells and molecules are important components, plays a crucial role in tumor development, and that the degree of immune cell infiltration is highly correlated with patient prognosis (45). The TME that surrounds tumor cells is composed of TIICs, mesenchymal cells, endothelial cells, inflammatory mediators, and ECM molecules (46). Evidence has shown that the TME has significant effects on tumor growth and development, therapeutic resistance, and clinical outcome (47). In this study, we discovered that the TME characteristics and proportions of 22 TIICs were significantly different between

the two molecular subtypes. This suggests the critical role of m^{6}A- and m^{5}C-related lncRNAs in CRC progression. A previous study showed that high density of plasma cells can predict a relatively auspicious signal for the prognosis of CRC patients (48), which is consistent with our finding that plasma cells were more clustered in subtype B than in subtype A. Previous studies revealed that tumor-infiltrating B cells were associated with favorable outcomes in CRC (48, 49). Patients with metastatic CRC who exhibit high infiltration of B cells have significantly lower risk for disease recurrence and prolonged OS (49). In our study, there was no significant difference in the degree of naive B cell infiltration between the two subtypes, but the infiltration level of memory B cells in subtype A, which had worse OS, was significantly lower than that in subtype B. This indicates that B cell infiltration inhibits tumor invasion and metastasis in CRC, consistent with previous studies (48, 49).

Increasing evidence shows that memory T cells, effector T cells, and T cell differentiation play an important role in the immune defense of CRC (50). T cells can be classified into CD4+ and CD8+ T cells, and the former can further differentiate into regulatory T cells (Tregs) and follicular helper T cells. Tregs are responsible for maintaining the balance of immune responses and preventing excessive immune responses, and they are thought to be involved in the escape of cancer from the host immune system [51]. Gamma delta T cells can effectively recognize and kill CRC cells, thereby suppressing tumor progression via multiple mechanisms (51). The densities of tumor-infiltrating T cells in CRC tissues were higher than that in the normal tissues, and higher densities indicated a good prognosis (51–53). In this study, subtype B, which had a better prognosis, exhibited higher immune infiltration of CD4+ and CD8+ T cells, suggesting that they play a positive role during CRC development. Tumor-associated macrophages are divided into two main phenotypes: M1 macrophages (which inhibit cancer progression) and M2 macrophages (which promote cancer progression). M1 macrophages participate in a positive immune response and exert the function of immune surveillance by secreting proinflammatory cytokines and chemokines as well as presenting antigens. M2 macrophages have weak antigen-presenting ability and participate in immune regulation by secreting inhibitory cytokines to downregulate the immune response (54). CRC has a high level of MMP-9, which can degrade collagen in the type IV basement membrane, thereby promoting metastasis (55). In this study, we found that infiltration of M1 macrophages was higher in subtype B with a better prognosis, whereas the level of M2 macrophage infiltration was higher in subtype A with a poorer prognosis, consistent with known findings.

In recent years, with in-depth research on tumor immunology and molecular biology, immunotherapy has provided a new direction for tumor treatment. Tumor immunotherapy aims to activate the human immune system, kill tumor cells and tissues through autoimmune function, and restore the normal antitumor immune response of the body by restarting and maintaining the tumor-immune cycle to control and eliminate tumors (56, 57). This therapy includes monoclonal antibody immune checkpoint inhibitors, therapeutic antibodies, cancer vaccines, cell therapy, and small-molecule inhibitors. Recently, immune checkpoint therapies targeting PD-1 (PDCD1), PD-L1, CTLA-4, and HAVCR2 have gained attention, and clinical studies have shown that they are reliable in terms of safety and efficacy (58, 59). Mismatch repair-defective CRC account for 14% of all CRCs (60). Patients with microsatellite instability have a higher response to PD-1 treatment. In this study, we found that the proportion of microsatellite instability was higher in subtype B with a poor prognosis. Immune checkpoint inhibitors have recently been used to treat CRC (61). In this study, we also conducted correlational analysis for the two subtypes and the expression of tumor immune checkpoint genes (PD-1, PD-L1, CTLA-4, and HAVCR2), and our results revealed that subtype A was positively associated with the expression of PD-L1, HAVCR2, and CTLA-4. PD-1 is an inhibitory receptor expressed on the surface of activated T cells with two ligands, PD-L1 and PD-L2. PD-1 acts as a "brake" in tumor immunity and inflammation reactions. PD-L1 is generally widely expressed on the surface of epithelial cells, endothelial cells, and tumor cells. In this study, we found that patients with low risk scores exhibited significant therapeutic advantages and clinical response to anti-PD-1/L1 immunotherapy compared to those with high-risk scores, suggesting that the established signature will contribute to predicting patient responses to anti-PD-1/L1 immunotherapy. CTLA-4 exists on the surface of T cells and can prevent B7 from binding to the CD28 receptor on T cells, thereby inhibiting immune stimulation (62). PD-1, PD-L1, and CTLA-4 inhibitors have been widely applied for different types of solid tumors (63–65). Tremelimumab is an anti-CTLA-4 monoclonal human antibody that is well-tolerated by CRC patients who have poor response to other immunotherapies (66). HAVCR2, namely, TIM-3, which inhibits tumor immunity with depletion of T cells, is a negative regulator of immune check points. The immune checkpoint blockade for HAVCR2 has achieved encouraging efficacy in the medical treatment of advanced non-small cell lung cancer (67) and hepatocellular carcinoma (68). Thus, we can conclude that the high-risk CRC patients with higher expression of PD-L1, CTLA-4, and HAVCR2 may respond to immune checkpoint blockade.

The proposed signature contained eight m^{6}A- and m^{5}C-related lncRNAs. Among the seven lncRNAs, four have been shown to be involved in the development and progression of in CRC and other kinds of malignancies, namely NNT-AS1, CASC2, ALMS1-IT1, SNHG22, LINC00628, and NR2F1-AS1. NNT-AS1 is an oncogene associated with worse OS in CRC. Wang et al. (69) revealed that NNT-AS1 was significantly upregulated in CRC tissues and was clearly linked to clinical stage, lymph node metastasis, vessel invasion, and worse OS and progression-free survival. Silencing of NNT-AS1 suppressed cell proliferation, migration, and invasion by activating the MAPK/Erk and EMT signaling pathways. Moreover, a high NNT-AS1 expression level was also observed in the serum and exosomes of CRC patients, and was associated with an advanced tumor stage. Knockdown of NNT-AS1 impaired the proliferation, migration, and invasion of CRC cells *via* regulation of the miRNA-496/Ras-related protein Rap-2c axis

(70). In this study, NNT-AS1 was found to be a risk factor, which is inconsistent with the findings of previous studies. LncRNA CASC2 has been reported to be a tumor suppressor in CRC, and its low expression was significantly more frequent in the advanced TNM stage. Its overexpression suppressed proliferation of CRC cell and tumor growth *via* the miR-18a/STAT3 axis (71). CASC2 was also found to enhance berberine-induced cytotoxicity in CRC cells by silencing BCL2 (72). Luan and colleagues recently reported that ALMS1-IT1 promoted the malignant progression of lung adenocarcinoma through AVL9-mediated activation of the cyclin-dependent kinase pathway (73). SNHG22 has been detected to be overexpressed and to act as an oncogene in multiple cancers, including CRC (74, 75). Yao et al. (75) revealed that SNHG22 promoted CRC cell growth, migration, and invasion through SNHG22/miR-128-3p/E2F3 axis. LINC00628 has been reported to inhibit the malignant progression of cancer through different mechanisms, such as binding to EZH2 to regulate the p57 or H3K27me3 level (76, 77), and interacting with the promoter of LAMA3 or VEGFA (78, 79). In present study, we also found that LINC00628 was CRC suppressor, which is inconsistent with the findings of previous studies.

CONCLUSIONS

Our comprehensive analysis of two types of RNA modifications revealed their potential functions in the tumor-immune-stromal microenvironment, cancer clinicopathological features, and cancer prognosis, and we determined their therapeutic liability in targeted therapy and immunotherapy. These findings highlight the crucial clinical implications of the cross-talk of m^{6}A- and m^{5}C-related lncRNAs and provide new ideas for guiding personalized immune immunotherapy strategies for CRC patients.

DATA AVAILABILITY STATEMENT

The datasets analyzed for this study can be found in the TCGA-COAD/READ project (http://www.cancer.gov/tcga) and GEO (https://www.ncbi.nlm.nih.gov/geo/query/acc.cgi?acc=GSE39582/GSE17536/GSE38832).

AUTHOR CONTRIBUTIONS

WS, JR, RSX, and TF made substantial contributions to the conception, design, interpretation, and preparation of the final manuscript. WS, JR, RSX, and TF participated in the coordination of data acquisition and data analysis, and reviewed the manuscript.

FUNDING

This work was supported by the Talent Introduction Fund of Wuhan University Renmin Hospital (grant number NA to TF).

ACKNOWLEDGMENTS

We thank the reviewers for their constructive comments.

SUPPLEMENTARY MATERIAL

The Supplementary Material for this article can be found online at: https://www.frontiersin.org/articles/10.3389/fimmu.2022.740960/full#supplementary-material

REFERENCES

1. Arnold M, Sierra MS, Laversanne M, Soerjomataram I, Jemal A, Bray F. Global Patterns and Trends in Colorectal Cancer Incidence and Mortality. *Gut* (2017) 66:683–91. doi: 10.1136/gutjnl-2015-310912
2. Pinsky PF, Schoen RE. Contribution of Surveillance Colonoscopy to Colorectal Cancer Prevention. *Clin Gastroenterol Hepatol* (2020) 18:2937–2944.e2931. doi: 10.1016/j.cgh.2020.01.037
3. Yachida S, Mizutani S, Shiroma H, Shiba S, Nakajima T, Sakamoto T, et al. Metagenomic and Metabolomic Analyses Reveal Distinct Stage-Specific Phenotypes of the Gut Microbiota in Colorectal Cancer. *Nat Med* (2019) 25:968–76. doi: 10.1038/s41591-019-0458-7
4. Dekker E, Tanis PJ, Vleugels JLA, Kasi PM, Wallace MB. Colorectal Cancer. *Lancet (Lond Engl)* (2019) 394:1467–80. doi: 10.1016/S0140-6736(19)32319-0
5. Kopp F, Mendell JT. Functional Classification and Experimental Dissection of Long Noncoding RNAs. *Cell* (2018) 172:393–407. doi: 10.1016/j.cell.2018.01.011
6. Huarte M. The Emerging Role of lncRNAs in Cancer. *Nat Med* (2015) 21:1253–61. doi: 10.1038/nm.3981
7. Sanchez Calle A, Kawamura Y, Yamamoto Y, Takeshita F, Ochiya T. Emerging Roles of Long Non-Coding RNA in Cancer. *Cancer Sci* (2018) 109:2093–100. doi: 10.1111/cas.13642
8. Bian Z, Zhang J, Li M, Feng Y, Wang X, Zhang J, et al. LncRNA-FEZF1-AS1 Promotes Tumor Proliferation and Metastasis in Colorectal Cancer by Regulating PKM2 Signaling. *Clin Cancer Res: An Off J Am Assoc Cancer Res* (2018) 24:4808–19. doi: 10.1158/1078-0432.Ccr-17-2967
9. Xu M, Xu X, Pan B, Chen X, Lin K, Zeng K, et al. LncRNA SATB2-AS1 Inhibits Tumor Metastasis and Affects the Tumor Immune Cell Microenvironment in Colorectal Cancer by Regulating SATB2. *Mol Cancer* (2019) 18:135. doi: 10.1186/s12943-019-1063-6
10. Meyer KD, Saletore Y, Zumbo P, Elemento O, Mason CE, Jaffrey SR, et al. Comprehensive Analysis of mRNA Methylation Reveals Enrichment in 3' UTRs and Near Stop Codons. *Cell* (2012) 149:1635–46. doi: 10.1016/j.cell.2012.05.003
11. Wiener D, Schwartz S. The Epitranscriptome Beyond m^{6}A. *Nat Rev Genet* (2021) 22:119–31. doi: 10.1038/s41576-020-00295-8
12. Han X, Wang M, Zhao YL, Yang Y, Yang YG. RNA Methylations in Human Cancers. *Semin Cancer Biol* (2020) 75:97–115. doi: 10.1016/j.semcancer.2020.11.007
13. Du K, Zhang L, Lee T, Sun T. m^{6}A RNA Methylation Controls Neural Development and Is Involved in Human Diseases. *Mol Neurobiol* (2019) 56:1596–606. doi: 10.1007/s12035-018-1138-1
14. Wang S, Sun C, Li J, Zhang E, Ma Z, Xu W, et al. Roles of RNA Methylation by Means of N(6)-Methyladenosine (m^{6}A) in Human Cancers. *Cancer Lett* (2017) 408:112–20. doi: 10.1016/j.canlet.2017.08.030
15. Chen XY, Zhang J, Zhu JS. The Role of m^{6}A RNA Methylation in Human Cancer. *Mol Cancer* (2019) 18:103. doi: 10.1186/s12943-019-1033-z
16. Ma S, Chen C, Ji X, Liu J, Zhou Q, Wang G, et al. The Interplay Between m^{6}A RNA Methylation and Noncoding RNA in Cancer. *J Hematol Oncol* (2019) 12:121. doi: 10.1186/s13045-019-0805-7

17. Liu T, Wei Q, Jin J, Luo Q, Liu Y, Yang Y, et al. The m^{6}A Reader YTHDF1 Promotes Ovarian Cancer Progression *via* Augmenting EIF3C Translation. *Nucleic Acids Res* (2020) 48:3816–31. doi: 10.1093/nar/gkaa048
18. Zhang B, Wu Q, Li B, Wang D, Wang L, Zhou Y L. m^{6}A Regulator-Mediated Methylation Modification Patterns and Tumor Microenvironment Infiltration Characterization in Gastric Cancer. *Mol Cancer* (2020) 19:53. doi: 10.1186/s12943-020-01170-0
19. Liu J, Eckert MA, Harada BT, Liu SM, Lu Z, Yu K, et al. m^{6}A mRNA Methylation Regulates AKT Activity to Promote the Proliferation and Tumorigenicity of Endometrial Cancer. *Nat Cell Biol* (2018) 20:1074–83. doi: 10.1038/s41556-018-0174-4
20. He X, Tan L, Ni J, Shen G. Expression Pattern of m^{6}A Regulators Is Significantly Correlated With Malignancy and Antitumor Immune Response of Breast Cancer. *Cancer Gene Ther* (2021) 28:188–96. doi: 10.1038/s41417-020-00208-1
21. Du J, Ji H, Ma S, Jin J, Mi S, Hou K, et al. m^{6}A Regulator-Mediated Methylation Modification Patterns and Characteristics of Immunity and Stemness in Low-Grade Glioma. *Brief Bioinform* (2021). doi: 10.1093/bib/bbab013
22. Zhang Y, Kang M, Zhang B, Meng F, Song J, Kaneko H, et al. m^{6}A Modification-Mediated CBX8 Induction Regulates Stemness and Chemosensitivity of Colon Cancer *via* Upregulation of LGR5. *Mol Cancer* (2019) 18:185. doi: 10.1186/s12943-019-1116-x
23. Han J, Wang JZ, Yang X, Yu H, Zhou R, Lu HC, et al. METTL3 Promote Tumor Proliferation of Bladder Cancer by Accelerating Pri-Mir221/222 Maturation in m^{6}A-Dependent Manner. *Mol Cancer* (2019) 18:110. doi: 10.1186/s12943-019-1036-9
24. Ni W, Yao S, Zhou Y, Liu Y, Huang P, Zhou A, et al. Long Noncoding RNA GAS5 Inhibits Progression of Colorectal Cancer by Interacting With and Triggering YAP Phosphorylation and Degradation and Is Negatively Regulated by the m^{6}A Reader YTHDF3. *Mol Cancer* (2019) 18:143. doi: 10.1186/s12943-019-1079-y
25. Yang X, Yang Y, Sun BF, Chen YS, Xu JW, Lai WY, et al. 5-Methylcytosine Promotes mRNA Export - NSUN2 as the Methyltransferase and ALYREF as an M(5)C Reader. *Cell Res* (2017) 27:606–25. doi: 10.1038/cr.2017.55
26. Trixl L, Lusser A. The Dynamic RNA Modification 5-Methylcytosine and Its Emerging Role as an Epitranscriptomic Mark. *Wiley Interdiscip Rev RNA* (2019) 10:e1510. doi: 10.1002/wrna.1510
27. Schaefer M. RNA 5-Methylcytosine Analysis by Bisulfite Sequencing. *Methods Enzymology* (2015) 560:297–329. doi: 10.1016/bs.mie.2015.03.007
28. Chen X, Li A, Sun BF, Yang Y, Han YN, Yuan X, et al. 5-Methylcytosine Promotes Pathogenesis of Bladder Cancer Through Stabilizing mRNAs. *Nat Cell Biol* (2019) 21:978–90. doi: 10.1038/s41556-019-0361-y
29. Mei L, Shen C, Miao R, Wang JZ, Cao MD, Zhang YS, et al. RNA Methyltransferase NSUN2 Promotes Gastric Cancer Cell Proliferation by Repressing P57(Kip2) by an M(5)C-Dependent Manner. *Cell Death Dis* (2020) 11:270. doi: 10.1038/s41419-020-2487-z
30. Yang R, Liang X, Wang H, Guo M, Shen H, Shi Y, et al. The RNA Methyltransferase NSUN6 Suppresses Pancreatic Cancer Development by Regulating Cell Proliferation. *EBioMedicine* (2021) 63:103195. doi: 10.1016/j.ebiom.2020.103195
31. Runa F, Hamalian S, Meade K, Shisgal P, Gray PC, Kelber JA. Tumor Microenvironment Heterogeneity: Challenges and Opportunities. *Curr Mol Biol Rep* (2017) 3:218–29. doi: 10.1007/s40610-017-0073-7
32. Lee SS, Cheah YK. The Interplay Between MicroRNAs and Cellular Components of Tumour Microenvironment (TME) on Non-Small-Cell Lung Cancer (NSCLC) Progression. *J Immunol Res* (2019) 2019:3046379. doi: 10.1155/2019/3046379
33. Yoshihara K, Shahmoradgoli M, Martínez E, Vegesna R, Kim H, Torres-Garcia W, et al. Inferring Tumour Purity and Stromal and Immune Cell Admixture From Expression Data. *Nat Commun* (2013) 4:2612. doi: 10.1038/ncomms3612
34. Newman AM, Liu CL, Green MR, Gentles AJ, Feng W, Xu Y, et al. Robust Enumeration of Cell Subsets From Tissue Expression Profiles. *Nat Methods* (2015) 12:453–7. doi: 10.1038/nmeth.3337
35. Mariathasan S, Turley SJ, Nickles D, Castiglioni A, Yuen K, Wang Y, et al. Tgfβ Attenuates Tumour Response to PD-L1 Blockade by Contributing to Exclusion of T Cells. *Nature* (2018) 554:544–8. doi: 10.1038/nature25501
36. Geeleher P, Cox NJ, Huang RS. Clinical Drug Response can be Predicted Using Baseline Gene Expression Levels and *In Vitro* Drug Sensitivity in Cell Lines. *Genome Biol* (2014) 15:R47. doi: 10.1186/gb-2014-15-3-r47
37. Bray F, Ferlay J, Soerjomataram I, Siegel RL, Torre LA, Jemal A. Global Cancer Statistics 2018: GLOBOCAN Estimates of Incidence and Mortality Worldwide for 36 Cancers in 185 Countries. *CA Cancer J Clin* (2018) 68:394–424. doi: 10.3322/caac.21492
38. Arnedos M, Soria JC, Andre F, Tursz T. Personalized Treatments of Cancer Patients: A Reality in Daily Practice, a Costly Dream or a Shared Vision of the Future From the Oncology Community? *Cancer Treat Rev* (2014) 40:1192–8. doi: 10.1016/j.ctrv.2014.07.002
39. Liu H, Xu Y, Yao B, Sui T, Lai L, Li Z. A Novel N6-Methyladenosine (m^{6}A)-Dependent Fate Decision for the lncRNA THOR. *Cell Death Dis* (2020) 11:613. doi: 10.1038/s41419-020-02833-y
40. Ban Y, Tan P, Cai J, Li J, Hu M, Zhou Y, et al. LNCAROD Is Stabilized by m^{6}A Methylation and Promotes Cancer Progression *via* Forming a Ternary Complex With HSPA1A and YBX1 in Head and Neck Squamous Cell Carcinoma. *Mol Oncol* (2020) 14:1282–96. doi: 10.1002/1878-0261.12676
41. Zheng ZQ, Li ZX, Zhou GQ, Lin L, Zhang LL, Lv JW, et al. Long Noncoding RNA FAM225A Promotes Nasopharyngeal Carcinoma Tumorigenesis and Metastasis by Acting as ceRNA to Sponge miR-590-3p/miR-1275 and Upregulate Itgb3. *Cancer Res* (2019) 79:4612–26. doi: 10.1158/0008-5472.Can-19-0799
42. David R, Burgess A, Parker B, Li J, Pulsford K, Sibbritt T, et al. Transcriptome-Wide Mapping of RNA 5-Methylcytosine in Arabidopsis mRNAs and Noncoding RNAs. *Plant Cell* (2017) 29:445–60. doi: 10.1105/tpc.16.00751
43. He Y, Shi Q, Zhang Y, Yuan X, Yu Z. Transcriptome-Wide 5-Methylcytosine Functional Profiling of Long Non-Coding RNA in Hepatocellular Carcinoma. *Cancer Manage Res* (2020) 12:6877–85. doi: 10.2147/cmar.S262450
44. Sun Z, Xue S, Zhang M, Xu H, Hu X, Chen S, et al. Aberrant NSUN2-Mediated M(5)C Modification of H19 lncRNA is Associated With Poor Differentiation of Hepatocellular Carcinoma. *Oncogene* (2020) 39:6906–19. doi: 10.1038/s41388-020-01475-w
45. Seager RJ, Hajal C, Spill F, Kamm RD, Zaman MH. Dynamic Interplay Between Tumour, Stroma and Immune System can Drive or Prevent Tumour Progression. *Convergent Sci Phys Oncol* (2017) 3:34002. doi: 10.1088/2057-1739/aa7e86
46. Turley SJ, Cremasco V, Astarita JL. Immunological Hallmarks of Stromal Cells in the Tumour Microenvironment. *Nat Rev Immunol* (2015) 15:669–82. doi: 10.1038/nri3902
47. Hinshaw DC, Shevde LA. The Tumor Microenvironment Innately Modulates Cancer Progression. *Cancer Res* (2019) 79:4557–66. doi: 10.1158/0008-5472.Can-18-3962
48. Berntsson J, Nodin B, Eberhard J, Micke P, Jirström K. Prognostic Impact of Tumour-Infiltrating B Cells and Plasma Cells in Colorectal Cancer. *Int J Cancer* (2016) 139:1129–39. doi: 10.1002/ijc.30138
49. Meshcheryakova A, Tamandl D, Bajna E, Stift J, Mittlboeck M, Svoboda M, et al. B Cells and Ectopic Follicular Structures: Novel Players in Anti-Tumor Programming With Prognostic Power for Patients With Metastatic Colorectal Cancer. *PloS One* (2014) 9:e99008. doi: 10.1371/journal.pone.0099008
50. Zhang L, Yu X, Zheng L, Zhang Y, Li Y, Fang Q, et al. Lineage Tracking Reveals Dynamic Relationships of T Cells in Colorectal Cancer. *Nature* (2018) 564:268–72. doi: 10.1038/s41586-018-0694-x
51. Ma R, Yuan D, Guo Y, Yan R, Li K. Immune Effects of γδ T Cells in Colorectal Cancer: A Review. *Front Immunol* (2020) 11:1600. doi: 10.3389/fimmu.2020.01600
52. Kuwahara T, Hazama S, Suzuki N, Yoshida S, Tomochika S, Nakagami Y, et al. Intratumoural-Infiltrating CD4 + and Foxp3 + T Cells as Strong Positive Predictive Markers for the Prognosis of Resectable Colorectal Cancer. *Br J Cancer* (2019) 121:659–65. doi: 10.1038/s41416-019-0559-6
53. Governa V, Trella E, Mele V, Tornillo L, Amicarella F, Cremonesi E, et al. The Interplay Between Neutrophils and CD8(+) T Cells Improves Survival in Human Colorectal Cancer. *Clin Cancer Res: an Off J Am Assoc Cancer Res* (2017) 23:3847–58. doi: 10.1158/1078-0432.Ccr-16-2047
54. Pan Y, Yu Y, Wang X, Zhang T. Tumor-Associated Macrophages in Tumor Immunity. *Front Immunol* (2020) 11:583084. doi: 10.3389/fimmu.2020.583084
55. Zeng ZS, Huang Y, Cohen AM, Guillem JG. Prediction of Colorectal Cancer Relapse and Survival *via* Tissue RNA Levels of Matrix Metalloproteinase-9.

J Clin Oncol: Off J Am Soc Clin Oncol (1996) 14:3133–40. doi: 10.1200/jco.1996.14.12.3133
56. Riley RS, June CH, Langer R, Mitchell MJ. Delivery Technologies for Cancer Immunotherapy. *Nat Rev Drug Discovery* (2019) 18:175–96. doi: 10.1038/s41573-018-0006-z
57. Kennedy LB, Salama AKS. A Review of Cancer Immunotherapy Toxicity. *CA Cancer J Clin* (2020) 70:86–104. doi: 10.3322/caac.21596
58. Yaghoubi N, Soltani A, Ghazvini K, Hassanian SM, Hashemy SI. PD-1/PD-L1 Blockade as a Novel Treatment for Colorectal Cancer. *Biomed Pharmacother* (2019) 110:312–8. doi: 10.1016/j.biopha.2018.11.105
59. Rotte A. Combination of CTLA-4 and PD-1 Blockers for Treatment of Cancer. *J Exp Clin Cancer Res* (2019) 38:255. doi: 10.1186/s13046-019-1259-z
60. Ward R, Meagher A, Tomlinson I, O'Connor T, Norrie M, Wu R, et al. Microsatellite Instability and the Clinicopathological Features of Sporadic Colorectal Cancer. *Gut* (2001) 48:821–9. doi: 10.1136/gut.48.6.821
61. Marin-Acevedo JA, Dholaria B, Soyano AE, Knutson KL, Chumsri S, Lou Y. Next Generation of Immune Checkpoint Therapy in Cancer: New Developments and Challenges. *J Hematol Oncol* (2018) 11:39. doi: 10.1186/s13045-018-0582-8
62. Feng M, Zhao Z, Yang M, Ji J, Zhu D. T-Cell-Based Immunotherapy in Colorectal Cancer. *Cancer Lett* (2021) 498:201–9. doi: 10.1016/j.canlet.2020.10.040
63. Franklin C, Livingstone E, Roesch A, Schilling B, Schadendorf D. Immunotherapy in Melanoma: Recent Advances and Future Directions. *Eur J Surg Oncol: J Eur Soc Surg Oncol Br Assoc Surg Oncol* (2017) 43:604–11. doi: 10.1016/j.ejso.2016.07.145
64. Specenier P. Ipilimumab in Melanoma. *Expert Rev Anticancer Ther* (2016) 16:811–26. doi: 10.1080/14737140.2016.1211936
65. Kooshkaki O, Derakhshani A, Safarpour H, Najafi S, Vahedi P, Brunetti O, et al. The Latest Findings of PD-1/PD-L1 Inhibitor Application in Gynecologic Cancers. *Int J Mol Sci* (2020) 21:5034. doi: 10.3390/ijms21145034
66. Chung KY, Gore I, Fong L, Venook A, Beck SB, Dorazio P, et al. Phase II Study of the Anti-Cytotoxic T-Lymphocyte-Associated Antigen 4 Monoclonal Antibody, Tremelimumab, in Patients With Refractory Metastatic Colorectal Cancer. *J Clin Oncol: Off J Am Soc Clin Oncol* (2010) 28:3485–90. doi: 10.1200/jco.2010.28.3994
67. Rocco D, Gregorc V, Della Gravara L, Lazzari C, Palazzolo G, Gridelli C. New Immunotherapeutic Drugs in Advanced Non-Small Cell Lung Cancer (NSCLC): From Preclinical to Phase I Clinical Trials. *Expert Opin Investig Drugs* (2020) 29:1005–23. doi: 10.1080/13543784.2020.1793956
68. Tan S, Xu Y, Wang Z, Wang T, Du X, Song X, et al. Tim-3 Hampers Tumor Surveillance of Liver-Resident and Conventional NK Cells by Disrupting PI3K Signaling. *Cancer Res* (2020) 80:1130–42. doi: 10.1158/0008-5472.Can-19-2332
69. Wang Q, Yang L, Hu X, Jiang Y, Hu Y, Liu Z, et al. Upregulated NNT-AS1, a Long Noncoding RNA, Contributes to Proliferation and Migration of Colorectal Cancer Cells *In Vitro* and *In Vivo*. *Oncotarget* (2017) 8:3441–53. doi: 10.18632/oncotarget.13840
70. Yin H, Hu J, Ye Z, Chen S, Chen Y. Serum Long Non−Coding RNA NNT −AS1 Protected by Exosome Is a Potential Biomarker and Functions as an Oncogene via the Mir−496/RAP2C Axis in Colorectal Cancer. *Mol Med Rep* (2021) 24:585. doi: 10.3892/mmr.2021.12224
71. Huang G, Wu X, Li S, Xu X, Zhu H, Chen X. The Long Noncoding RNA CASC2 Functions as a Competing Endogenous RNA by Sponging miR-18a in Colorectal Cancer. *Sci Rep* (2016) 6:26524. doi: 10.1038/srep26524
72. Dai W, Mu L, Cui Y, Li Y, Chen P, Xie H, et al. Long Non−Coding RNA CASC2 Enhances Berberine−Induced Cytotoxicity in Colorectal Cancer Cells by Silencing BCL2. *Mol Med Rep* (2019) 20:995–1006. doi: 10.3892/mmr.2019.10326
73. Luan T, Zhang TY, Lv ZH, Guan BX, Xu JY, Li J, et al. The lncRNA ALMS1-IT1 may Promote Malignant Progression of Lung Adenocarcinoma *via* AVL9-Mediated Activation of the Cyclin-Dependent Kinase Pathway. *FEBS Open Bio* (2021) 11:1504–15. doi: 10.1002/2211-5463.13140
74. Mao X, Ji T, Liu A, Weng Y. ELK4-Mediated lncRNA SNHG22 Promotes Gastric Cancer Progression Through Interacting With EZH2 and Regulating miR-200c-3p/Notch1 Axis. *Cell Death Dis* (2021) 12:957. doi: 10.1038/s41419-021-04228-z
75. Yao J, Wang C, Dong X, Zhang Y, Li Y, Zhou H, et al. lncRNA SNHG22 Sponges Mir−128−3p to Promote the Progression of Colorectal Cancer by Upregulating E2F3. *Int J Oncol* (2021) 59:71. doi: 10.3892/ijo.2021.5251
76. Zhang MC, Zhang L, Zhang MQ, Yang GX, Wang FZ, Ding P, et al. Downregulated LINC00628 Aggravates the Progression of Colorectal Cancer *via* Inhibiting P57 Level. *Eur Rev Med Pharmacol Sci* (2020) 24:1763–70. doi: 10.26355/eurrev_202002_20353
77. Zhang ZZ, Zhao G, Zhuang C, Shen YY, Zhao WY, Xu J, et al. Long Non-Coding RNA LINC00628 Functions as a Gastric Cancer Suppressor *via* Long-Range Modulating the Expression of Cell Cycle Related Genes. *Sci Rep* (2016) 6:27435. doi: 10.1038/srep27435
78. Chen Q, Wang D, Li Y, Yan S, Dang H, Yue H, et al. LINC00628 Suppresses Migration and Invasion of Hepatocellular Carcinoma by Its Conserved Region Interacting With the Promoter of VEGFA. *J Cell Physiol* (2019) 234:15751–62. doi: 10.1002/jcp.28233
79. Xu SF, Zheng Y, Zhang L, Wang P, Niu CM, Wu T, et al. Long Non-Coding RNA LINC00628 Interacts Epigenetically With the LAMA3 Promoter and Contributes to Lung Adenocarcinoma. *Mol Ther Nucleic Acids* (2019) 18:166–82. doi: 10.1016/j.omtn.2019.08.005

Conflict of Interest: The authors declare that the research was conducted in the absence of any commercial or financial relationships that could be construed as a potential conflict of interest.

Advantages of publishing in Frontiers

OPEN ACCESS
Articles are free to read for greatest visibility and readership

FAST PUBLICATION
Around 90 days from submission to decision

HIGH QUALITY PEER-REVIEW
Rigorous, collaborative, and constructive peer-review

TRANSPARENT PEER-REVIEW
Editors and reviewers acknowledged by name on published articles

Frontiers
Avenue du Tribunal-Fédéral 34
1005 Lausanne | Switzerland

Visit us: www.frontiersin.org
Contact us: frontiersin.org/about/contact

REPRODUCIBILITY OF RESEARCH
Support open data and methods to enhance research reproducibility

DIGITAL PUBLISHING
Articles designed for optimal readership across devices

FOLLOW US
@frontiersin

IMPACT METRICS
Advanced article metrics track visibility across digital media

EXTENSIVE PROMOTION
Marketing and promotion of impactful research

LOOP RESEARCH NETWORK
Our network increases your article's readership